

NATIONAL AERONAUTICS AND SPACE ADMINISTRATION

Space Programs Summary 37-45, Vol. IV
Supporting Research and Advanced Development

For the Period April 1 to May 31, 1967

FACILITY FORM 802

N67-34761
(ACCESSION NUMBER)

363
(PAGES)

CR-89450
(NASA CR OR TMX OR AD NUMBER)

N67-34781
(THRU)

~~1~~ 30
(CODE)

~~1~~ 30
(CATEGORY)

JET PROPULSION LABORATORY
CALIFORNIA INSTITUTE OF TECHNOLOGY
PASADENA, CALIFORNIA

June 30, 1967

NATIONAL AERONAUTICS AND SPACE ADMINISTRATION

Space Programs Summary 37-45, Vol. IV

Supporting Research and Advanced Development

For the Period April 1 to May 31, 1967

JET PROPULSION LABORATORY
CALIFORNIA INSTITUTE OF TECHNOLOGY
PASADENA, CALIFORNIA

June 30, 1967

PRECEDING PAGE BLANK NOT FILMED.

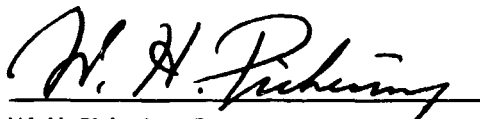
Preface

The Space Programs Summary is a six-volume bimonthly publication designed to report on JPL space exploration programs and related supporting research and advanced development projects. The titles of all volumes of the Space Programs Summary are:

- Vol. I. *The Lunar Program* (Confidential)
- Vol. II. *The Planetary-Interplanetary Program* (Confidential)
- Vol. III. *The Deep Space Network* (Unclassified)
- Vol. IV. *Supporting Research and Advanced Development* (Unclassified)
- Vol. V. *Supporting Research and Advanced Development* (Confidential)
- Vol. VI. *Space Exploration Programs and Space Sciences* (Unclassified)

The Space Programs Summary, Vol. VI, consists of: an unclassified digest of appropriate material from Vols. I, II, and III; an original presentation of the JPL quality assurance and reliability efforts, and the environmental- and dynamic-testing facility-development activities; and a reprint of the space science instrumentation studies of Vols. I and II.

Approved by:



W. H. Pickering, Director

Jet Propulsion Laboratory

PRECEDING PAGE BLANK NOT FILMED.

PRECEDING PAGE BLANK NOT FILMED.

Contents

SYSTEMS DIVISION

I. Systems Analysis	1	✓
A. Optimum Strategies for Selecting Midcourse Correction Aiming Points NASA Code 125-17-05-02, T. H. Thornton, Jr.	1	
B. Analysis of a Low-Thrust Solar-Electric Jupiter Flyby Mission NASA Code 684-30-01-10, C. G. Sauer	3	
C. A Note on Diverse Methods for Obtaining the Mean, Variance, and Higher Moments in Discrete Probability Theory NASA Code 129-04-01-01, H. Lass and C. B. Solloway	6	
D. A New Approach to the Calculus of Brownian Motion NASA Code 129-04-01-01, S. R. McReynolds	9	
E. The Implementation of a Method of Optimal Data Compression by Using Polynomials NASA Code 129-04-01-01, W. Kizner	12	
F. Magnitude of Second-Degree Harmonics in Lunar Gravity Field NASA Code 814-12-02-01, J. Lorell	13	
References	15	
II. Computation and Analysis	17	✓
A. Planetary Masses for Ephemeris Development NASA Code 129-04-04-02, J. D. Mulholland	17	
B. Studies in Orbit Correction Theory NASA Code 129-04-04-02, J. D. Mulholland	19	
References	21	

GUIDANCE AND CONTROL DIVISION

III. Spacecraft Power	22	✓
A. Photovoltaic Supporting Development NASA Code 120-33-01-06, J. D. Sandstrom and E. Castle	22	
B. 20-W/lb Technology Development Program NASA Code 120-33-01-02, D. W. Ritchie	28	
C. Thermionic Development NASA Code 120-33-02-01 and 120-27-06-07, P. Rouklove	31	
References	41	
IV. Guidance and Control Research	42	✓
A. Reduction of Plasma Maintenance Voltage With Magnetic Field NASA Code 129-02-01-07, K. Shimada	42	
B. Noise of Unipolar Space-Charge-Limited Current in Solids NASA Code 129-02-05-09, M-A. Nicolet	45	

PRECEDING PAGE BLANK NOT FILMED.

Contents (contd)

C. Solid-State Triode: Gate Electrode Fabrication <i>NASA Code 129-02-05-09, A. Shumka</i>	46
D. Response Times and Sterilizability of Evaporated Thin Film CdS Photodetectors <i>NASA Code 129-02-05-01, R. J. Stirn</i>	48
References	56

ENGINEERING MECHANICS DIVISION

V. Applied Mechanics	57 ✓
A. ELAS Computer Program for Equilibrium Analysis of Linear Structures <i>NASA Codes 124-08-06-03 and 128-32-05-04, S. Utku and F. Akyuz</i>	57

ENVIRONMENTAL SIMULATION DIVISION

VI. Aerodynamics Facilities	61 ✓
A. Biplanar Optical System for Nonplanar Free-Flight Testing <i>NASA Code 124-07-04-01, H. P. Holway</i>	61
B. Hypersonic Boom Study <i>NASA Code 124-07-04-02, R. Kerr</i>	66
C. Air Radiation Measurements <i>NASA Code 124-07-04-02, G. M. Thomas and W. A. Monard</i>	67
D. X-15 Research Vehicle <i>NASA Code 124-07-04-01, D. Kurtz</i>	68
E. Wedge Wake Studies <i>NASA Code 124-07-04-01, R. Kerr</i>	69
Reference	70

PROPULSION DIVISION

VII. Solid Propellant Engineering	71 ✓
A. Applications Technology Satellite Motor Development <i>NASA Code 630-01-00-55, R. G. Anderson and R. A. Grippi</i>	71
B. Potential Binder Curing Reactions <i>NASA Code 128-32-05-10-55, J. Hutchison and H. Marsh, Jr.</i>	77
C. Pintle Nozzle Thrust Vector Control <i>NASA Code 128-32-06-01, L. Strand</i>	83
D. Low-Pressure Combustion Studies <i>NASA Code 128-32-06-01, L. Strand</i>	85
References	90

Contents (contd)

VIII. Polymer Research	92 ✓
A. Characterization Studies on Polyurethane Elastomers <i>NASA Code 128-32-05-02, R. F. Fedors and R. F. Landel</i>	92
B. Structure—Property Relationships for Polymers. Part I: Influence of the Chemical Nature of an Elastomer on Stress—Strain Response <i>NASA Code 128-32-05-02, R. F. Fedors and R. F. Landel</i>	99
C. The Suitability of Thermoplastic Rubbers as Binders for Composite Solid Propellants, Interim Report II <i>NASA Code 128-32-05-02, B. G. Moser and R. F. Landel</i>	105
D. The Relationship Between Stress and Strain in Multiaxial Deformations of Elastomers <i>NASA Code 128-32-05-02, W. D. Hutchinson</i>	109
E. Poly(isobutylene) Prepolymers <i>NASA Code 128-32-05-03, J. D. Ingham</i>	113
F. Method for Measuring the Internal Gas Pressure of Rigid Closed-Cell Foam <i>NASA Code 186-68-13-03, E. F. Cuddihy and J. Moacanin</i>	115
G. Dielectric Strength of Rigid Urethane Foam <i>NASA Code 186-68-13-03, J. Moacanin, J. Farrar, and I. N. Einhorn</i>	118
References	126
IX. Propulsion Research and Advanced Concepts	129 ✓
A. Liquid MHD Power Conversion <i>NASA Code 120-27-06-03, D. G. Elliott, D. J. Cerini, and L. G. Hays</i>	129
B. Reactivity Effects From Fuel Displacement in a Small Thermionic Reactor <i>NASA Code 120-27-06-02, H. Gronroos and J. P. Davis</i>	136
C. Comparison of Enthalpy Measurements Obtained in an Internal High-Temperature Flow of Argon as Determined by Conservation of Energy, a Calorimetric Probe, a Flowmeter, and Spectroscopy <i>NASA Code 129-01-09-04, P. F. Massier, L. H. Back, and E. J. Roschke</i>	141
D. Analog Studies of Thermionic Reactor Dynamics <i>NASA Code 120-27-06-02, H. Gronroos</i>	151
E. Flow Visualization Studies Demonstrating the Effects of a Transverse Gas Velocity on a Glow Discharge <i>NASA Code 128-31-06-06, J. A. Gardner</i>	162
F. Influence of Swirl on the Velocity Distribution in a Constant-Diameter Duct When the Swirling Flow Is Injected Perpendicular to the Axis of the Duct <i>NASA Code 128-31-06-08, P. F. Massier and E. J. Roschke</i>	167
References	176

Contents (contd)

X.	Liquid Propulsion	179 ✓
	A. Advanced Liquid Propulsion Systems <i>NASA Codes 721-12-03-01 and 731-12-03-03, L. R. Toth, H. B. Stanford, and W. F. MacGlashan</i>	179
	B. Resonant Combustion <i>NASA Code 128-31-06-01, R. M. Clayton</i>	184
	C. Injector Development: Stream Separation Experiments <i>NASA Code 731-12-03-02, R. W. Riebling</i>	192
	References	196

SPACE SCIENCES DIVISION

XI.	Lunar and Planetary Instruments	197 ✓
	A. Development of Wet Chemical Process Control Circuitry <i>NASA Code 189-55-02-04, J. R. Clark</i>	197
XII.	Space Instruments	203 ✓
	A. Surface Temperature of Mars <i>NASA Code 185-47-26-01, J. H. Shaw and P. W. Schaper</i>	203
	B. Complete Error Analysis of Relative and Absolute Orientation in Extraterrestrial Mapping Techniques <i>NASA Code 125-24-01-09, M. Benes</i>	209
	References	221
XIII.	Science Data Systems	222 ✓
	A. Video Film Converter <i>NASA Code 125-23-02-01, R. D. Brandt</i>	222
	B. Cycle Length Versus Initial State for Linear Feedback Shift Registers <i>NASA Code 186-68-03-03, M. Perlman</i>	225
	C. Spacecraft Woven Plated Wire Memory <i>NASA Code 186-68-03-04, W. J. Rousey</i>	228
	Reference	234
XIV.	Lunar and Planetary Sciences	235 ✓
	A. Spectral Reflectance of Silicate Rock Powders <i>NASA Code 185-41-08-01, J. B. Adams and A. L. Filice</i>	235
	B. Cloud-Top Pressure and Abundance of Hydrogen in the Atmosphere of Venus <i>NASA Code 185-37-26-16, J. E. Beckman</i>	236
	C. Use of the Visible and Near-IR Spectrum in Analysis of the Lunar Surface <i>NASA Code 185-42-20-01, A. L. Filice</i>	236

Contents (contd)

D. Linear Martian Features on <i>Mariner IV</i> Frames 3 and 11	
NASA Code 185-37-20-12, J. Negus deWys	240
References	242
XV. Fluid Physics	244 ✓
A. The Density Disturbance Ahead of a Sphere in Rarefied Supersonic Flow	
NASA Code 129-01-10-01, D. A. Russell	244
B. The Stability of Viscous Three-Dimensional Disturbances in the Laminar Compressible Boundary Layer: Part I	
NASA Code 129-01-09-01, L. M. Mack	247
References	250
XVI. Physics	251 ✓
A. The Polar Substorm—Flow of Magnetic Flux Tubes and Auroral Effects	
NASA Code 129-02-07-02, G. Atkinson	251
B. The Dynamitron Accelerator as a Source of Thermal Neutrons	
NASA Code 129-02-03-08, R. H. Parker, E. L. Haines, A. B. Whitehead, and W. F. Wegst	255
C. The Algebra of Fermi-Dirac Operators and Its Application to the Many-Body Problem	
NASA Code 129-02-07-02, M. M. Saffren	256
References	257

TELECOMMUNICATIONS DIVISION

XVII. Communications Systems Research	259 ✓
A. Block Coding and Synchronization Study	
NASA Code 125-21-02-03, J. Stiffler and A. Balakrishnan	259
B. Combinatorial Communication	
NASA Code 125-21-01-01, H. Rumsey, Jr., and L. Baumert	267
C. Propagation Studies	
NASA Code 125-21-02-04, P. Reichley	270
D. Communications Systems Development	
NASA Code 150-22-11-08, W. C. Lindsey and A. J. Viterbi	276
E. Information Processing	
NASA Code 150-22-11-09, S. Zohar	297
F. Data Compression Techniques	
NASA Code 150-22-17-08, I. Eisenberger	303
References	309

Contents (contd)

TELECOMMUNICATIONS DIVISION

XVIII. Communications Elements Research	313	✓
A. RF Techniques: 90-GHz mm Wave Work <i>NASA Code 125-21-04, W. V. T. Rusch, S. D. Slobin, and C. T. Stelzried</i>	313	
B. Quantum Electronics: Optical Communications Components <i>NASA Code 125-22-02-01, M. S. Schumate and J. C. Siddoway</i>	316	
C. Propagation Studies: Planetary Entry Blackout <i>NASA Code 150-22-11-11, G. S. Levy</i>	318	
D. Low Noise Transponder Preamplifier Research <i>NASA Code 150-22-17-01, W. H. Higa</i>	321	
E. Thermally Isolated Transmission Lines <i>NASA Code 150-22-11-07, C. T. Stelzried, T. Y. Otschi, and D. L. Mullen</i>	322	
F. RF Breakdown Studies <i>NASA Codes 125-22-01-02 and 125-22-02-01, R. Woo and H. Erpenbach</i>	323	
G. Spacecraft Antenna Studies <i>NASA Codes 186-68-04-06, 186-68-04-02, and 125-21-02-02, K. Woo and R. M. Dickinson</i>	331	
References	336	
XIX. Spacecraft Radio	338	✓
A. Spacecraft Guidance Radar Beam Configuration Performance II <i>NASA Code 186-68-02-14, R. L. Harttor</i>	338	
B. Performance Margin and Cost Tradeoff for Spacecraft Telecommunication System Design <i>NASA Code 186-68-04-11, M. K. Tam</i>	343	

ADVANCED STUDIES

XX. Future Projects	353	✓
A. Mission to a Comet: Constraints and Background Information <i>NASA Code 684-30-01-10, R. G. Brereton and R. L. Newburn</i>	353	
References	361	

1.3 Systems Analysis
SYSTEMS DIVISION

A. Optimum Strategies for Selecting Midcourse Correction Aiming Points, T. H. Thornton, Jr.

This summary describes two strategies for selecting interplanetary midcourse correction aiming points when such aiming points are restricted by a planetary quarantine constraint.

With reference to Fig. 1, we define the following quantities: let R_c be the capture radius of the target; x_1 and x_2 be coordinates aligned with the minor and major axes, respectively, of the midcourse correction dispersion ellipse; α_1 and α_2 be the center of the final success zone; R_s be the final success zone radius; and μ_1 and μ_2 be the first midcourse correction aiming point. The vectors R and T are shown to illustrate the B-plane.

It will be assumed that the size of the midcourse correction dispersion ellipse is not a function of μ_1 and μ_2 . This assumes large B-plane errors prior to the midcourse correction.

It should be noted that the orientation of the midcourse error ellipse is fixed and does not change with

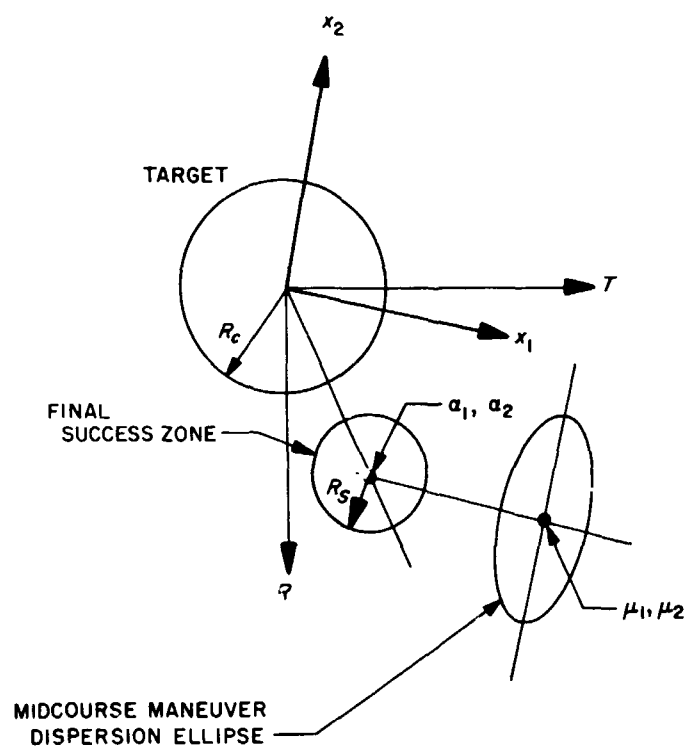


Fig. 1. Coordinate definition

BLANK PAGE

μ_1 or μ_2 , and that some orientations, and hence some trajectories, are more favorable than others.

The first aiming point strategy that we will consider is that which maximizes the probability of being within the final success zone after the first midcourse correction, subject to a planetary quarantine constraint P_1 . This strategy also minimizes the probability of needing additional interplanetary corrections.

Let $p(x_1, x_2, \sigma_1, \sigma_2, \mu_1, \mu_2)$ be the B-space error density function after the correction. We wish to obtain the maximum:

$$\max_{\mu_1, \mu_2} \iint_{R_c} p \, dx_1 \, dx_2 \quad (1)$$

subject to

$$\iint_{R_c} p \, dx_1 \, dx_2 = P_1 \quad (2)$$

The equality is used in Eq. (2), and we shall modify the final answer to account for the desired inequality. Now, unless the problem is trivial, R_c will be small compared to σ_1 and σ_2 , and P_1 will be small compared to unity; thus Eqs. (1) and (2) can be written as

$$\left. \begin{aligned} \max_{\mu_1, \mu_2} p(\alpha_1, \alpha_2, \sigma_1, \sigma_2, \mu_1, \mu_2) \\ p(0, 0, \sigma_1, \sigma_2, \mu_1, \mu_2) = \frac{P_1}{\pi R_c^2} \end{aligned} \right\} \quad (3)$$

Since p is of the form

$$p = \frac{1}{2\pi\sigma_1\sigma_2} \exp - \frac{1}{2} \left[\frac{(x_1 - \mu_1)^2}{\sigma_1^2} + \frac{(x_2 - \mu_2)^2}{\sigma_2^2} \right] \quad (4)$$

Eq. (3) can be written as

$$\left. \begin{aligned} \min_{\mu_1, \mu_2} \left[\frac{(\alpha_1 - \mu_1)^2}{\sigma_1^2} + \frac{(\alpha_2 - \mu_2)^2}{\sigma_2^2} \right] \\ \frac{\mu_1^2}{\sigma_1^2} + \frac{\mu_2^2}{\sigma_2^2} = \text{constant} \end{aligned} \right\} \quad (5)$$

Forming

$$\frac{(\alpha_1 - \mu_1)^2}{\sigma_1^2} + \frac{(\alpha_2 - \mu_2)^2}{\sigma_2^2} + \lambda \left[\frac{\mu_1^2}{\sigma_1^2} + \frac{\mu_2^2}{\sigma_2^2} \right] \quad (6)$$

it follows that

$$\frac{\alpha_1 - \mu_1}{\mu_1} = \frac{\alpha_2 - \mu_2}{\mu_2} = \lambda \quad (7)$$

or

$$\frac{\mu_1}{\mu_2} = \frac{\alpha_1}{\alpha_2} \quad (8)$$

This states that the first midcourse aiming point μ_1, μ_2 should be along the line joining the center of the target planet and α_1, α_2 . It is obvious that we have a maximum to Eq. (1) when μ_1, μ_2 is on the same side of the planet as α_1, α_2 and a minimum to Eq. (1) when μ_1, μ_2 is on the opposite side of the planet. The actual values of μ_1 and μ_2 are selected to satisfy Eq. (1).

In conclusion

$$\left. \begin{aligned} \max_{\mu_1, \mu_2} \iint_{R_c} p \, dx_1 \, dx_2 \\ \iint_{R_c} p \, dx_1 \, dx_2 \leq P_1 \end{aligned} \right\} \quad (9)$$

so that

$$\left. \begin{aligned} \text{yields} \\ \frac{\mu_1}{\mu_2} = \frac{\alpha_1}{\alpha_2} \\ \text{with } \mu_1 \text{ and } \mu_2 \text{ being determined from} \\ \iint_{R_c} p \, dx_1 \, dx_2 = P_1 \end{aligned} \right\} \quad (10)$$

noting that $\mu_1^2 + \mu_2^2$ must be greater than $\alpha_1^2 + \alpha_2^2$.

If the probability of being in the final success zone after the first midcourse correction is small, one may wish to choose the first midcourse correction aiming point to minimize the expected square of the miss rather than to maximize the immediate probability of success. This will, in some cases, decrease the chances of a third interplanetary correction while increasing the chances of the second interplanetary correction. We shall consider this as a possible second strategy.

Let m_1, m_2 be sample miss coordinates in the x_1, x_2 system after the first midcourse correction. We wish to

$$\min_{\mu_1, \mu_2} E[(m_1 - \alpha_1)^2 + (m_2 - \alpha_2)^2] \quad (11)$$

so that

$$\iint p dx_1 dx_2 = P_1 \quad (12)$$

Now

$$E[(m_1 - \alpha_1)^2] = \sigma_1^2 + (\mu_1 - \alpha_1)^2 \quad (13)$$

Using Eq. (13) and the assumptions of the constraint Eq. (5), we write Eqs. (11) and (12) as

$$\left. \begin{aligned} \min_{\mu_1, \mu_2} [(\mu_1 - \alpha_1)^2 + (\mu_2 - \alpha_2)^2] \\ \frac{\mu_1^2}{\sigma_1^2} + \frac{\mu_2^2}{\sigma_2^2} = \text{constant} \end{aligned} \right\} \quad (14)$$

It follows that

$$\alpha_2 \mu_1 + \left(\frac{\sigma_1^2}{\sigma_2^2} - 1 \right) \mu_1 \mu_2 - \left(\frac{\sigma_1^2}{\sigma_2^2} \alpha_1 \right) \mu_2 = 0 \quad (15)$$

It is noted that if $\sigma_1 = \sigma_2$, Eq. (15) becomes Eq. (8), and the two strategies are equal. Also as σ_1 becomes large compared to σ_2 , μ_1 approaches α_1 ; that is, the point α_1, α_2 will be along the minor axis of the dispersion ellipse.

B. Analysis of a Low-Thrust Solar-Electric Jupiter Flyby Mission, C. G. Sauer

The following presents some preliminary results of a trajectory analysis of a low-thrust solar-electric flyby mission to Jupiter. In order to accurately evaluate the potential capability of a low-thrust solar-electric propulsion vehicle for a specific mission, it is first necessary to conduct a comprehensive analysis covering a relatively large range of flight time and departure dates. In this preliminary analysis it is also desirable to place as few restrictions as possible on the vehicle, specifying only those parameters which characterize the particular vehicle or propulsion system being investigated. The particular parameters being fixed for this investigation include the launch vehicle characteristics, the low-thrust

powerplant specific mass, and the propulsion system efficiency function.

The specific launch vehicle being considered is the *Atlas SLV3C/Centaur* whose performance is described in Ref. 1. This launch vehicle has approximately a 1200-kg payload capability at parabolic escape speed.

There are a number of vehicle or flight parameters which are free and capable of being optimized. These include, in addition to the flight path, the departure energy, the powerplant mass of the low-thrust vehicle and the exhaust velocity or specific impulse of the propulsion system. A conservative value of 30 kg/kW for the powerplant specific mass was used in this analysis. Any decrease in this value would, of course, result in a direct increase in useful payload.

The optimization of the powerplant mass and exhaust velocity is accomplished using the methods described in Ref. 2 so as to result in maximum gross payload into an inpowered trajectory past Jupiter.

A range of departure dates of about 450 days was covered to include a full synodic period of the earth and Jupiter, the earliest departure date corresponding to April 28, 1975. A range of flight times of 600 to 1000 days was included to provide a reasonably comprehensive coverage. Because the inclination of the Jovian orbit to the ecliptic plane is only 1.3 deg, and because the arrival planet was close to a node during the arrival times investigated, it was possible to perform the analysis using a two-dimensional model with a consequent saving in computing time. A program which numerically integrated the two-body equations of motion and Euler-Lagrange equations and solves the two-point boundary value problem is used for the analysis (Ref. 3).

1. Optimization of the Departure Energy

Since the low-thrust vehicle is a rather low performance vehicle, optimization of the launch vehicle and low-thrust vehicle results in hyperbolic or near-hyperbolic escape from the earth using the high-thrust launch vehicle. The methods described in SPS 37-36, Vol. IV, pp. 14-19, were used in computing the effects of the departure planet on the two-body optimization formulation described in Ref. 3. The effects of the departure planet in the analysis was included by incorporating an "asymptotic velocity bias" at the start of the trajectory which was a function of the departure energy, the gravitational attraction of the planet, and the initial thrust acceleration of the low-thrust

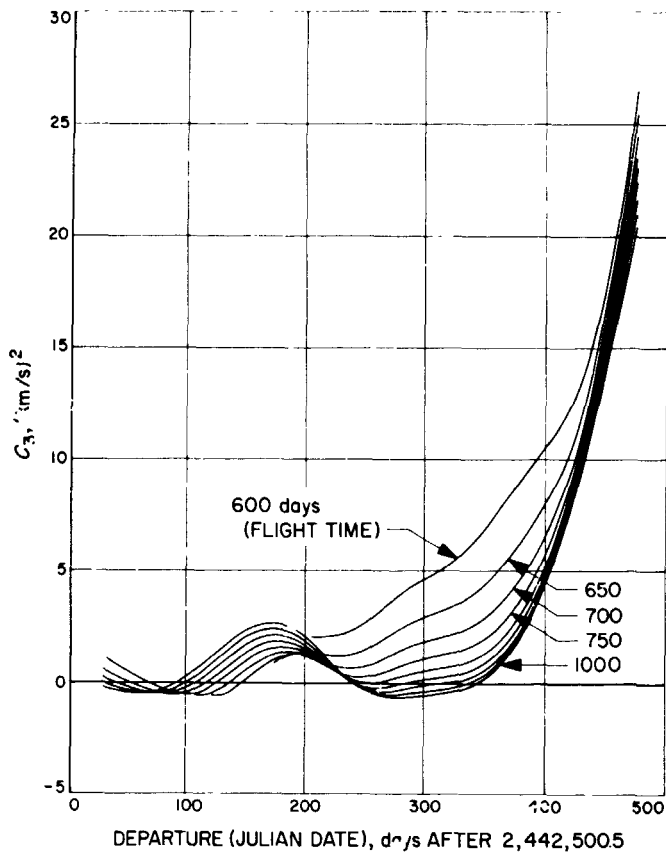


Fig. 2. Jupiter flyby optimum C: departure date, 1975

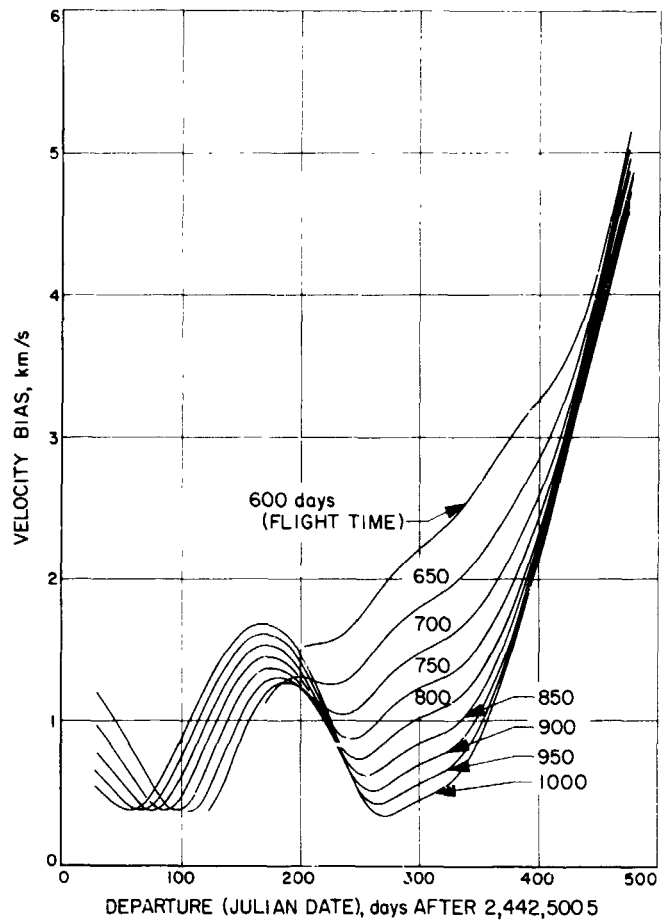


Fig. 3. Velocity bias versus departure date

vehicle. The direction of this velocity was also optimized. The results of the optimization of the departure energy is shown in Fig. 2. In this figure, C_3 is twice the specific energy at departure. Figure 3 presents the corresponding magnitude of the asymptotic velocity bias applied at the start of the trajectory. Note that although slightly negative values of departure energy are realized, nevertheless, the resulting velocity bias is never less than around 300 m/s.

2. Vehicle Masses

The initial mass of the low-thrust vehicle is solely a function of the magnitude of the departure energy and is shown in Fig. 4. Note that the earliest launch dates correspond to transfer angles of more than one revolution and hence may be designated as indirect transfer trajectories, the vehicle coming significantly inside the orbit of the earth. The latest launch dates correspond to a more direct transfer with much shorter transfer angles, these trajectories when optimized requiring, in general, high values of departure energy.

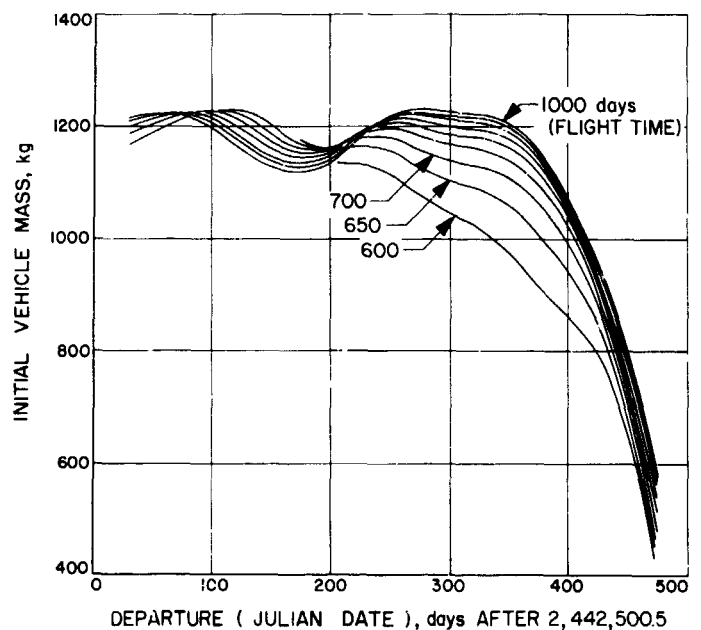


Fig. 4. Initial vehicle mass versus departure date

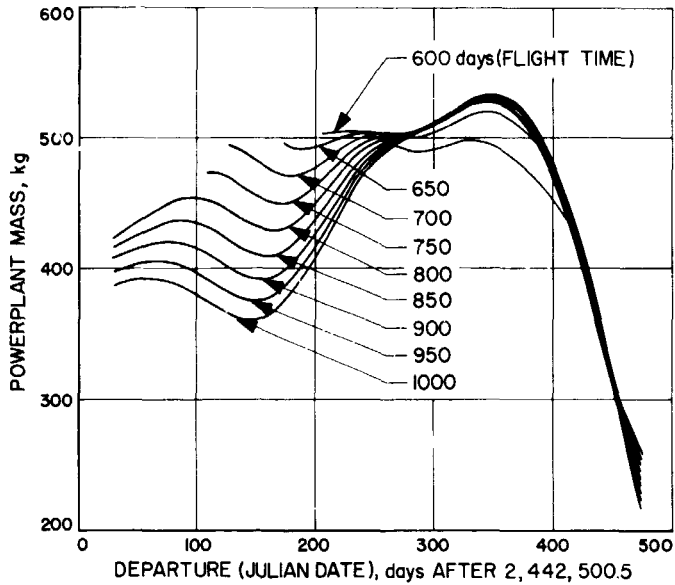


Fig. 5. Powerplant mass versus departure date

Figure 5 presents the optimized powerplant mass. The corresponding output electrical power to the propulsion system may be found by dividing the powerplant mass by the powerplant specific mass of 30 kg/kW.

Figure 6 gives the gross payload capability of this vehicle. Note that a larger payload is possible on any particular departure date by increasing the flight time.

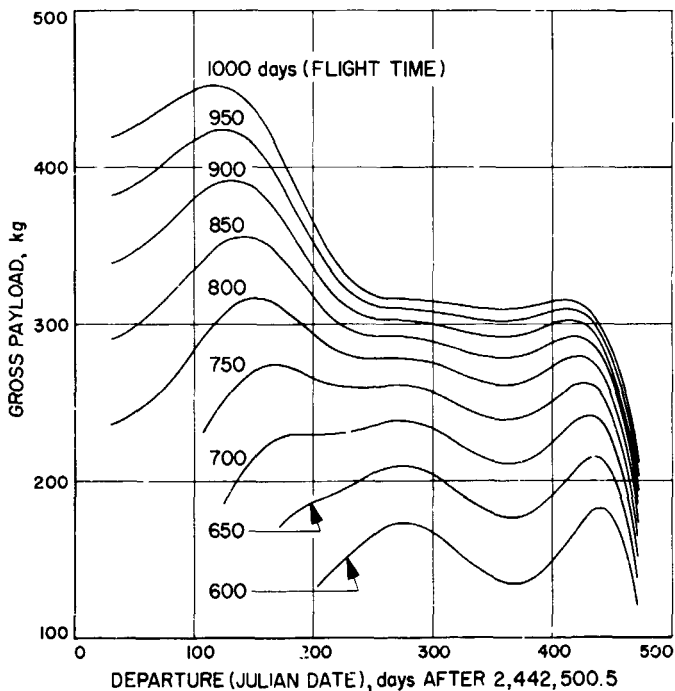


Fig. 6. Gross payload versus departure date

The maxima occurring for the early launch dates correspond to the indirect transfers mentioned previously. The maxima occurring late in the launch period correspond to direct transfer trajectories.

3. Exhaust Velocity

The optimized values of exhaust velocity are shown in Fig. 7. Note that the longer flight times require higher values of exhaust velocity.

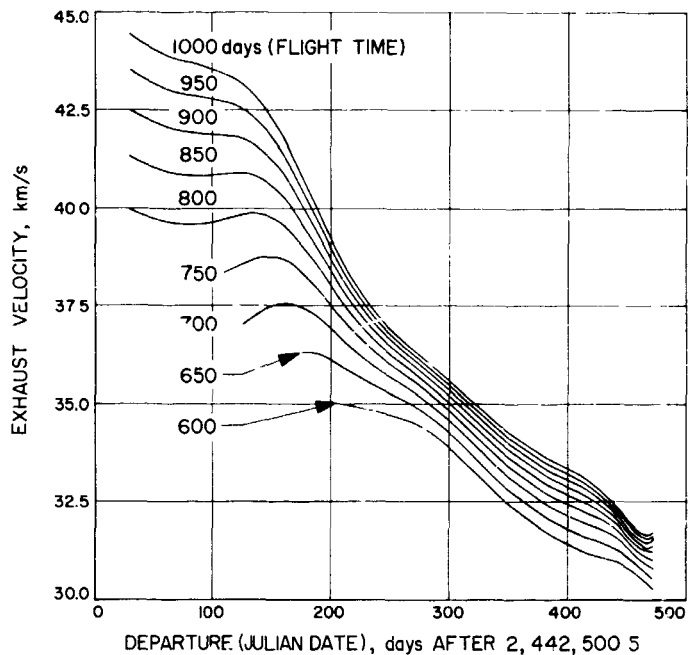


Fig. 7. Optimum exhaust velocity versus departure date

The form of the efficiency function for the particular propulsion system being considered is given in Appendix A of Ref. 4, for a mercury bombardment engine under development by the Hughes Aircraft Company. This efficiency function η is closely approximated by the following analytic form given in Ref. 2,

$$\eta = \frac{0.79c^2}{c^2 + (22.45)^2} \quad (1)$$

where c is the effective exhaust velocity of the propulsion system.

The last three figures present several trajectory-related parameters which are of interest. Figure 8 presents the hyperbolic approach velocity at Jupiter for the trajectories being considered. The indirect transfer trajectories

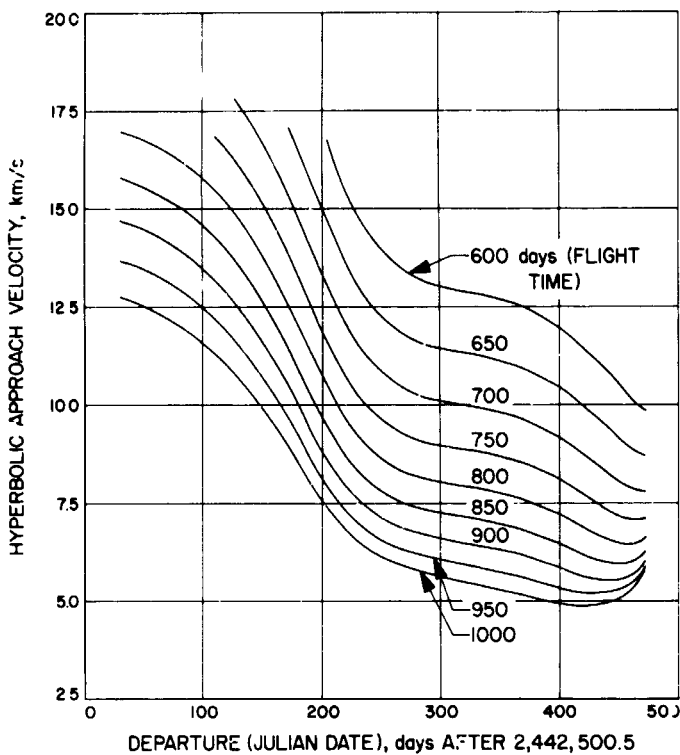


Fig. 8. Hyperbolic approach velocity versus departure date

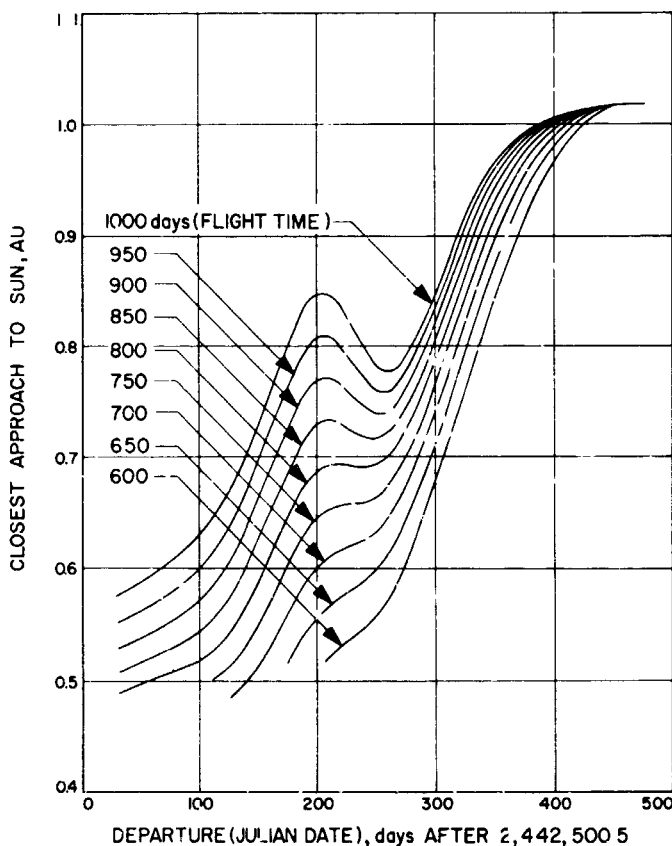


Fig. 9. Closest approach to sun versus departure date

result in generally high values of approach hyperbolic velocity.

Figure 9 shows the minimum distance of closest approach of the vehicle to the sun. The indirect transfer trajectories require very close approaches to the sun of 0.5 to 0.6 AU, these close approaches possibly severely compromising the design of the vehicle.

The resulting total propulsion time required by the low-thrust propulsion system is shown in Fig. 10. Note that the indirect transfer trajectories require longer operating times and a corresponding decrease in reliability of the thrusters.

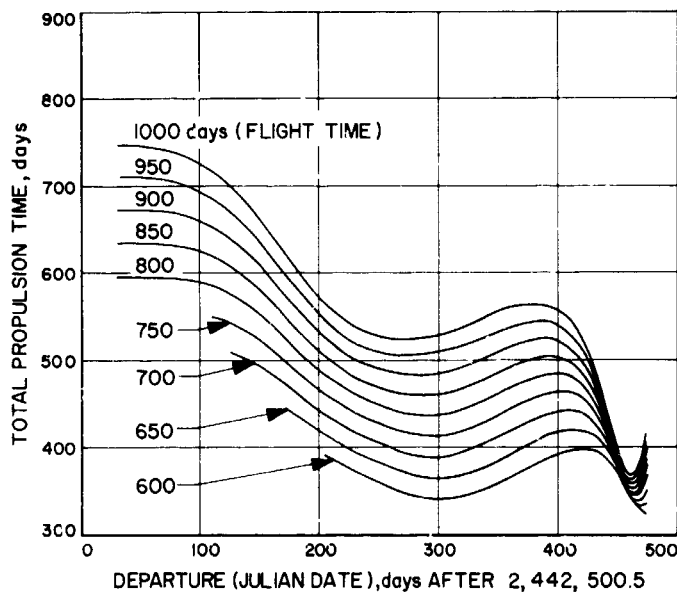


Fig. 10. Total propulsion time versus departure date

C. A Note on Diverse Methods for Obtaining the Mean, Variance, and Higher Moments in Discrete Probability Theory

H. Lass and C. B. Solloway

In discrete probability theory there are various methods available to obtain the moments of the distribution. Generating functions are applicable when the frequency function has an explicit form or can be expressed by means of a difference equation. Occasionally one can set up directly the difference equation for the mean, as in the case of the gambler ruin problem to be discussed. However, to our knowledge, this method has not been exploited for a calculation of the variance. The method for calculating the variance will depend on the known fact that the second moment about a point is simply the variance plus the square of the distance from the mean to the point in

question, often called the translation theorem. We will now exhibit this method by means of various examples.

1. Example 1

Let us consider the standard problem involving independent Bernoulli trials. Let p be the probability of success and let $q = 1 - p$ be the probability of a failure for a single trial. For n trials we wish to determine the mean and variance for the random variable describing the number of successes. Since

$$p_k = \binom{n}{k} p^k q^{n-k}, k = 0, 1, 2, \dots, n,$$

represents the probability of obtaining exactly k successes in n trials, the moment generating function becomes

$$M(\theta) = \sum_{k=0}^n p_k e^{k\theta} = (pe^\theta + q)^n,$$

from which one quickly deduces that $\mu = M'(0) = np$, $\mu_2 = M''(\theta=0) = npq + n^2p^2$, and $\sigma^2 = \mu_2 - \mu^2 = npq$.

An alternative approach is to let

$$\xi = x_1 + x_2 + \dots + x_n \quad (1)$$

with $x_i = 1$ for a success and $x_i = 0$ for a failure on the i th trial, $i = 1, 2, \dots, n$. Thus ξ is a random variable representing the number of successes in n trials. It is simple to deduce that $E(x_i) = p$, $V(x_i) = pq$. Thus $\mu = E(\xi) = np$ and $\sigma^2 = V(\xi) = npq$.

Let us now obtain these results by means of difference equations. If μ_n is the mean number of successes in n trials, then $\mu_n = \mu_{n-1} + p$, since μ_{n-1} is the mean number of successes on the first $(n-1)$ trials, μ_{n-1} , with the addition of one more success which can be obtained with probability p on the last trial. From $\mu_0 = 0$ it follows that $\mu_n = np$.

Now let σ_n^2 be the variance for n trials. With probability p a success will occur on the first trial, so that the mean number of successes will be $1 + (n-1)p$, since $(n-1)$ trials remain. The distance of this point to $\mu_n = np$ is $|1 - p| = q$. With probability q , a failure occurs on the first trial and the mean number of successes is $(n-1)p$

whose distance from μ_n is p . From the translation theorem it follows that

$$\begin{aligned} \sigma_n^2 &= p[\sigma_{n-1}^2 + q^2] + q[\sigma_{n-1}^2 + p^2] \\ &= \sigma_{n-1}^2 + pq \end{aligned} \quad (2)$$

so that $\sigma_n^2 = npq$, since $\sigma_0^2 = 0$.

2. Example 2

We consider that one-dimensional random walk problem with p the probability of taking a unit step to the right and $q = 1 - p$ the probability of taking a unit step to the left. Starting at the origin we wish to determine the mean distance and variance from the origin after n independent moves.

If μ_n is the mean distance from the origin after n moves, it follows that

$$\begin{aligned} \mu_n &= p[1 + \mu_{n-1}] + q[-1 + \mu_{n-1}] \\ &= \mu_{n-1} + p - q \end{aligned} \quad (3)$$

so that $\mu_n = n(p - q)$, since $\mu_0 = 0$.

Now with probability p , the first move is to the right ($x = 1$) and the mean distance from the origin after $(n-1)$ subsequent moves is $1 + (n-1)(p - q)$, whose distance from $\mu_n = n(p - q)$ is $(1 - p + q) = 2q$. A similar argument if the first move is to $x = -1$ yields a distance of $2p$, and the translation theorem gives

$$\begin{aligned} \sigma_n^2 &= p(\sigma_{n-1}^2 + 4q^2) + q(\sigma_{n-1}^2 + 4p^2) \\ &= \sigma_{n-1}^2 + 4pq \end{aligned} \quad (4)$$

yielding $\sigma_n^2 = 4pqn$.

These results can be obtained easily by considering $\xi = x_1 + x_2 + \dots + x_n$, with $x_i = 1, -1$ with probabilities p and q , respectively. Thus $E(x_i) = p - q$, $V(x_i) = 4pq$ yield the results above.

3. Example 3

Let μ be the mean number of trials until two consecutive successes occur for the case of Bernoulli trials (see Example 1). Now one can be successful by obtaining successes on the first two trials, or by failing on the first trial and subsequently obtaining two consecutive successes, or by obtaining a success on the first trial, a failure

on the second trial, and subsequently obtaining two consecutive successes. Thus

$$\mu = 2p^2 + q(1 + \mu) + pq(2 + \mu) \quad (5)$$

which yields $\mu = (p + 1)/p^2$.

From the translation theorem it follows that

$$\sigma^2 = p^2 \left(2 - \frac{p+1}{p^2} \right)^2 + q(\sigma^2 + 1) + pq(\sigma^2 + 2) \quad (6)$$

which yields $\sigma^2 = (1 + 2p - 2p^2 - p^3)/p^4$.

By letting p_k represent the probability that two consecutive successes occur for the first time on the k th trial, one can deduce that $p_k = qp_{k-1} + pqp_{k-2}$, $k \geq 3$, with $p_1 = 0$, $p_2 = p^2$. From

$$\mu = \sum_2^{\infty} kp_k = \sum_3^{\infty} kp_k + 2p^2$$

one can obtain the above results for μ . Similarly one can obtain σ^2 of Eq. (6).

Another method for obtaining μ is to note if v_n is the probability that two consecutive successes occur on the n th trial, but not necessarily for the first time, then $\lim_{n \rightarrow \infty} v_n = p^2q + p^4q + \dots = p^2/(1 + p)$, and from a known result that $\mu = \lim_{n \rightarrow \infty} 1/v_n$ we obtain $\mu = (1 + p)/p^2$.

4. Example 4

For Bernoulli trials let μ_k be the mean number of trials until the k th success occurs. Then $\mu_k = p(1 + \mu_{k-1}) + q(1 + \mu_k)$, so that $\mu_k = \mu_{k-1} + 1/p$, and $\mu_k = k/p$.

To obtain the variance, we note that if a success occurs on the first trial, the mean number of trials to obtain k successes is $(1 + (k-1)/p)$ whose distance from $\mu_k = k/p$ is q/p ; if a failure occurs, the mean number of trials will be $1 + k/p$, whose distance from μ_k is unity. From the translation theorem it follows that

$$\sigma_k^2 = p \left(\sigma_{k-1}^2 + \frac{q^2}{p^2} \right) + q(\sigma_{k-1}^2 + 1) \quad (7)$$

which yields $\sigma_k^2 = (q/p^2)k$.

5. Example 5: The Gambler Ruin Problem

Consider a fair game in which A and B exchange one unit per game. If A starts with a units and B starts with b units, we wish to determine the mean number of games played until either A or B is ruined. This problem is solved in probability texts by letting μ_n be the mean number of games played until A or B is ruined if A has n units. Then, $\mu_n = \frac{1}{2}(\mu_{n+1} + 1) + \frac{1}{2}(\mu_{n-1} + 1)$, with $\mu_0 = 0$, $\mu_{a+b} = 0$. The solution is $\mu_n = (a + b)n - n^2$, so that $\mu = \mu_a = ab$, a startling result.

We obtain now the variance by means of the translation theorem. Let σ_n^2 be the variance for the number of games to be played until A or B is ruined if A has n units. With probability $p = \frac{1}{2}$, A will gain one unit after the first game, so that the mean number of games that would be played is $1 + (a + b)(n + 1) - (n + 1)^2$, whose distance from $\mu_n = (a + b)n - n^2$ is $|a + b - 2n|$, with a similar result if A loses the first game.

Thus

$$\sigma_n^2 = \frac{1}{2} [\sigma_{n+1}^2 + (a + b - 2n)^2] + \frac{1}{2} [\sigma_{n-1}^2 + (a + b - 2n)^2] \quad (8)$$

with $\sigma_0^2 = \sigma_{a+b}^2 = 0$. The solution of Eq. (8) is

$$\sigma^2 = \sigma_a^2 = \frac{ab}{3}(a^2 + b^2 - 2) \quad (9)$$

6. Example 6

For n Bernoulli trials let E be the event that a success is followed by a failure. We wish to determine the mean and variance for the event E . Thus

$$\mu_n = \mu_{n-1} + pq \quad (10)$$

since p is the fraction of sample sequences which end with a success on the $(n-1)$ th trial, and q is the probability that a failure occurs on the last trial yielding one further E . Hence $\mu_n = (n-1)pq$.

Now let z represent the number of times the event E occurs in n trials, x the number of times E occurs in $(n-1)$ trials, and let $y = 1$ if E occurs on the last trial, otherwise $y = 0$. Thus $z = x + y$, and $E(z^2) = E(x^2) + E(y^2) + 2E(xy)$, so that

$$\mu_n^{(2)} = \mu_{n-1}^{(2)} + pq + 2pq\mu_{n-2} \quad (11)$$

with $\mu_n^{(2)}$ the second moment for the event E . The solution of Eq. (11) yields

$$\left. \begin{aligned} \mu_n^{(2)} &= pq + (pq - 6p^2q^2)(n - 2) \\ &\quad + p^2q^2(n - 2)(n + 3) \\ \sigma_n^2 &= \mu_n^{(2)} - (\mu_n)^2 = pq[(5pq - 1) + (1 - 3pq)n] \end{aligned} \right\} (12)$$

7. Example 7

For n Bernoulli trials let us consider the mean number of runs. For example, the sequence 00 1 000 11 0, has five runs. If μ_n is the mean number of runs, then $\mu_n = \mu_{n-1} + 2pq$, since an additional run is obtained on the last trial if a *zero* follows a *one* (failure follows a success) or a *one* follows a *zero*, with probability $2pq$. Hence $\mu_n = 1 + 2pq(n - 1)$.

A simple technique for obtaining μ_n is the following: Let x_1, x_2, \dots, x_n denote a sequence of *zeros* and *ones*. Consider

$$z = 1 + f(x_1, x_2) + f(x_2, x_3) + \dots + f(x_{n-1}, x_n) \quad (13)$$

with $f(x_i, x_{i+1}) = 1$ if $x_i \neq x_{i+1}$, and $f(x_i, x_{i+1}) = 0$ if $x_i = x_{i+1}$. Thus z represents the number of runs for any given sequence. Since $E[f(x_i, x_{i+1})] = 2pq$, we obtain $\mu_n = E(z) = 1 + 2pq(n - 1)$. By considering $E(z^2)$ one can obtain the variance σ_n^2 .

In conclusion, higher moments can be obtained by means of translation theorems. Thus

$$\begin{aligned} E[(z - z_0)^3] &= E\{[(z - \mu) + (\mu - z_0)]^3\} \\ &= E[(z - \mu)^3] + 3(\mu - z_0)E[(z - \mu)^2] \\ &\quad + (\mu - z_0)^3 \end{aligned} \quad (14)$$

can be used to obtain third moments about the mean.

For n Bernoulli trials we obtain from Eq. (14),

$$\begin{aligned} \tau_n &= q[\tau_{n-1} - 3p(n - 1)pq - p^3] \\ &\quad + p[\tau_{n-1} + 3q(n - 1)pq + q^3] \\ &= \tau_{n-1} + pq(q - p) \end{aligned} \quad (15)$$

which yields $\tau_n = npq(q - p)$, the third moment.

D. A New Approach to the Calculus of Brownian Motion, S. R. McReynolds

1. Introduction

Stochastic calculus is the mathematics of continuous stochastic processes. The stochastic process concerned here is Brownian motion. The fundamental problem in stochastic calculus is to furnish a mathematical model for such processes and to provide the tools which enable one to solve physical problems.

The common working model for most stochastic processes is the stochastic differential equation. For Brownian motion it [Langevin's Equation] has the form

$$\dot{x} = f(x, t) + \sigma(x, t)w(t) \quad (1)$$

where $x(t)$ is the Brownian motion process, and $w(t)$ is referred to as "white noise," which is not a well-defined process from either a mathematical or physical standpoint. Equation (1) must be interpreted by means of the integral equation

$$x(T) = x(0) + \int_0^T f(x, t) dt + \int_0^T \sigma(x, t) dz(t) \quad (2)$$

Here $z(t) = \int_0^t w(t) dt$ is a well-defined Markov process (a Wiener process) with the conditional transition density function

$$P(z(t_1) | z(t_0)) = \frac{1}{[2\pi |t_1 - t_0|]^{1/2}} \exp\left[-\frac{[x(t_1) - x(t_0)]^2}{2 |t_1 - t_0|}\right] \quad (3)$$

Sample functions of the Wiener process are continuous and well-defined.

The difficulty in interpreting Eq. (2) arises in connection with the second integral

$$I = \int_0^T \sigma(x(t), t) dt \quad (4)$$

The problem is due to the fact that sample functions $z(t)$ are not of bounded variation. Hence the above integral cannot be defined in the normal Riemann-Lebesgue sense. Thus in order to give Eq. (4) a precise mathematical meaning, another approach to the subject of calculus is required. This other approach is provided by stochastic calculus.

The first rigorous treatment of stochastic integrals was provided by Norbert Wiener (Ref. 5), who treated the class of integrals of the form

$$W = \int_0^T L(t) dz(t)$$

If the σ appearing in Eqs. (3) and (4) does not depend upon $x(t)$, then the Wiener integral is applicable.

The first attempt to rigorously define the more general class of integrals was provided by Ito (Ref. 6). Later his work was extended to a more general class of processes by Doob (Ref. 7). At the heart of Ito's calculus is the definition stochastic integrals of the form

$$J = \int_0^T L(z(t), t) dz(t) \quad (6)$$

where $z(t)$ is the fundamental Wiener process. [This integral is slightly different from the one in Eq. (4) but in defining Eq. (6) the meaning of Eq. (4) emerges.]

Recently, alternate definitions of the integral appearing in Eq. (6) have been provided by Stratonovich (Ref. 8) and Gray and Caughey (Ref. 9). These last two definitions which are equivalent, generally yield a different value than obtained from Ito's definition. In general, one can show that there are an infinite numbers of ways of defining the integral appearing in Eq. (6). To see this, let α be a real number on the closed interval $[0, 1]$, then define

$$J(\alpha) = \lim_{\delta \rightarrow 0} \sum_{i=0}^{n-1} L((1-\alpha)z(t_i) + \alpha z(t_{i+1}), t_i) [z(t_{i+1}) - z(t_i)]$$

$\delta = \max_{0 \leq i < n} |t_{i+1} - t_i|$ is the mesh of a partition $0 = t_0 < t_1 < \dots < t_n = T$ of the closed interval $[0, T]$. $J(0)$ coincides in the Ito integral, and $J(1/2)$ yields Stratonovich's and Gray and Caughey's value of the integral. To see that $J(\alpha_1) \neq J(\alpha_2)$ generally holds if $\alpha_1 \neq \alpha_2$, consider the difference $J(\alpha_2) - J(\alpha_1)$. Expanding each term about the previous mesh point, one obtains

$$J(\alpha_2) - J(\alpha_1) = \sum_{i=0}^{n-1} (\alpha_2 - \alpha_1) L_z(z(t_i), t_i) [z(t_{i+1}) - z(t_i)]^2 + \sum_{i=0}^{n-1} O[z(t_{i+1}) - z(t_i)]$$

Employing arguments similar to Stratonovich's (Ref. 8), one can show that as $\delta \rightarrow 0$ the above becomes

$$J(\alpha_2) - J(\alpha_1) = (\alpha_2 - \alpha_1) \int_0^T L_z(z(t), t) dt$$

Thus unless $L_z = 0$, $J(\alpha_1)$ and $J(\alpha_2)$ generally differ. This result demonstrates that stochastic calculus is fundamentally different than ordinary calculus.

From the preceding observation it appears that an infinite number of stochastic calculi are possible. This is disturbing from a mathematical standpoint and hence one may wonder perhaps if one of the many possible calculi represents a true extension of ordinary calculus. In this paper we wish to provide an answer to this conjecture. We assert that the stochastic calculus defined by Gray and Caughey (Ref. 9) and Stratonovich (Ref. 8) is the true extension of ordinary calculus. Our argument for this conclusion in this paper will be based upon philosophical and esthetic arguments rather than practical arguments employed by Stratonovich (Ref. 8), Gray and Caughey (Ref. 9), and McReynolds (Ref. 10).¹ In the process of providing these arguments, we shall give an original development of stochastic calculus.

2. The Main Arguments

In the introduction it was seen that there are many ways to define a stochastic integral if the criteria of existence and uniqueness were the only ones used. However, there are other criteria which are applied to mathematical constructions. One such criterion applied to boundary value problems and functionals is that of continuity. The origin of this criterion stems from the philosophical view, formulated by Poincaré, that the main role of mathematics is to deal with physical problems. The notion of continuity was initially formulated by Hadamard (Ref. 11) in his doctrine that mathematics should be concerned with "well-set" problems. A well-set problem is one whose solution depends continuously on the input. Hadamard's doctrine is a natural consequence of Poincaré's, because nature primarily consists of well-set (i.e., stable) processes.

Another criterion that may be applied to mathematical constructs is that of simplicity. The criterion forces us to accept simple extensions of previous definitions if they exist. Often a simple extension of a definition is provided by the notion of continuity. In order to satisfy

¹The practical argument is that their calculus is easier to use, because many of the techniques used in ordinary calculus may be applied.

the criterion of simplicity such an extension must be employed if possible.

As we shall see, an application of these two criteria, which are closely related, will provide a unique definition of the stochastic integral in Eq. (6).

3. The Fundamental Definition of Stochastic Integral

In this section the notion of continuity shall be employed to provide a fundamental definition of stochastic integrals. To obtain the proper generalization of the Riemann-Stieltjes integral let us apply the technique of imbedding continuity described in the previous section.

Definition

Let $x^n(t)$ be a sequence of continuous piecewise differentiable functions that converge pointwise to the Brownian motion function $x(t)$. Then define

$$I = \int_0^T L(x(t), t) dx(t)$$

by

$$I = \lim_{n \rightarrow \infty} \int_0^T L(x^n(t), t) dx^n(t) \quad (7)$$

Before the above definition can be accepted, it is necessary to show that it results in a unique definition of the integral for a sufficiently wide class of $L(x, t)$. One class of functions is given as follows:

Theorem

Let $L(x)$ be a function for which there exists a differential function $F(x)$ such that $(\partial F(x))/\partial x = L(x)$, then

$$F(x(T)) - F(x(0)) = \int_0^T L(x(t)) dx(t) \quad (8)$$

with probability 1.

Proof

If $x^n(t)$ is continuous and piecewise differentiable, then the fundamental law of calculus implies

$$F(x^n(T)) - F(x^n(0)) = \int_0^T L(x^n(t)) dx^n(t) \quad (9)$$

Hence if $x^n(t) \rightarrow x(t)$ pointwise as $n \rightarrow \infty$, taking the limits of both sides of Eq. (9) yields Eq. (8).

An example of these integrals is given by

$$I_0 = \int_0^T x dx$$

Doob (Ref. 7, p. 443) showed that the Ito value of integral $I_0 = J(0)$ is given by

$$I_0 = \frac{1}{2} [x^2(T) - x^2(0)] - \frac{1}{2} T$$

Our value for the integral is given by

$$I_0 = \frac{1}{2} [x^2(T) - x^2(0)]$$

The fundamental definition given above satisfies the metamathematical criteria of simplicity and continuity. It also is justified from pure physical arguments. The physical argument, presented elegantly by Gray and Caughey (Ref. 9), is based upon the observation that the physical process $x(t)$ is really of bounded variation, and hence the physical quantity that corresponds to the stochastic integral can be defined by means of the Riemann integral.

Since the Ito integral does not approximate the physical (Riemann) integral, Gray and Caughey (Ref. 9) differentiate between physical Brownian motion and mathematical Brownian motion. However, we accept the philosophical tenet that it is the role of mathematics to formulate physical problems; then the Ito definition of the stochastic integral must be abandoned and the new definition must be accepted.

4. The Fundamental Approximation Formula

Next the fundamental approximation formula is established for stochastic integrals and differential equations. This approximation formula for stochastic integrals, which is equivalent to the ones obtained by Stratonovich and Gray and Caughey, is

$$I \cong \sum_{i=0}^{n-1} L(x(t_i), t_i) [x(t_{i+1}) - x(t_i)] + \frac{1}{2} L_x(x(t_i), t_i) [x(t_{i+1}) - x(t_i)]^2 \quad (10)$$

The above approximation formula is arrived at by the following consideration (suggested by Frost in Ref. 12). Suppose that L is continuous. Then

$$L(x(t), t) = L(x(t_i), t) + L_x(x(s), t) [x(t) - x(t_i)]$$

where $t_i \leq s(t) \leq t$. Integrating the above expression with respect to dx over the interval $[t_i, t_{i+1}]$ yields

$$\int_{t_i}^{t_{i+1}} L(x(t), t) dx(t) = \int_{t_i}^{t_{i+1}} [L(x(t_i), t) + L_x(x(s(t)), t) [x(t) - x(t_i)]] dx(t)$$

Now if $L(x(t_i), t)$ and $L(x(s(t)), t)$ are approximated by $L(x(t_i), t_i)$ and $L(x(t_i), t_i)$ in the above expression, which seems reasonable if L and L_x are continuous, then

$$\int_{t_i}^{t_{i+1}} L(x(t), t) dx(t) \cong L(x(t_i), t_i) [x(t_{i+1}) - x(t_i)] + \frac{1}{2} L_x(x(t_i), t_i) [x(t_{i+1}) - x(t_i)]^2$$

Summing the above expressions obtained for each time interval $[t_i, t_{i+1}]$ $i = 0, \dots, n-1$, yields the formula in Eq. (10). It can be shown that, with some assumptions on L , the approximation formula converges to the actual value of the integral in the mean squared sense as the mesh shrinks to zero. The proof is omitted here.

Applying the above approximating formula to the integral Eq. (2) results in the following approximating formula for stochastic differential equations.

$$x(t_{i+1}) = x(t_i) + (t_{i+1} - t_i) t(x(t_i), t_i) + \sigma(x(t_i), t_i) [z(t_{i+1}) - z(t_i)] + \frac{1}{2} \frac{\partial \sigma}{\partial x} (x(t_i), t_i) \times \sigma(x(t_i), t_i) [z(t_{i+1}) - z(t_i)]^2 \quad (11)$$

The last term on the right-hand side of the above expression is omitted from Ito's approximation. This expression has been derived by Wong and Zakai (Ref. 13).

5. Properties of the New Stochastic Calculus

As noted in Refs. 8, 9, and 10 the new stochastic calculus shares many of the properties found in ordinary calculus. Standard techniques, such as change of variables, integration by parts, etc., hold for the new calculus but do not hold for Ito's calculus. From the approach suggested in this paper, it is evident why the new calculus does have

the same properties as the classical calculus. For example, let us consider the integration by parts formula

$$\int_0^T f(x(t), t) dg(x(t), t) = f(x(t), t) g(x(t), t) \Big|_{t=0}^{t=T} - \int_0^T g(x(t), t) df(x(t), t) \quad (12)$$

We shall assume that f and g are differentiable. Now if $x^n(t)$ is a differentiable approximation to $x(t)$, ordinary calculus implies

$$\int_0^T f(x^n(t), t) dg(x^n(t), t) = f(x^n(t), t) g(x^n(t), t) \Big|_{t=0}^{t=T} - \int_0^T g(x^n(t), t) df(x^n(t), t)$$

The limit of the above equation as $n \rightarrow \infty$, yields Eq. (12). Similarly, other rules found in ordinary calculus can be shown to hold for stochastic calculus.

6. Conclusion

In this article there is presented a logical and simple way to extend the definition of the Riemann-Lebesgue integral to include stochastic integrals. The philosophical tradition behind modern mathematics suggests that this new calculus replace the currently popular Ito calculus. An important property of this new calculus is that all the conventional rules found in ordinary calculus may be applied.

E. The Implementation of a Method of Optimal Data Compression by Using Polynomials, W. Kizner

In SPS 37-43, Vol. IV, pp. 1-7 the author discusses the use of polynomials in the enhancement of data and as a means of data compression. A theorem is proved which shows that if $f(x)$ is analytic on the interval $[-1, 1]$ then the coefficients of the Chebyshev series expansion of $f(x)$, a_n , satisfy

$$\overline{\lim} (|a_n|)^{1/n} = \frac{1}{R} \quad (1)$$

and R is the parameter of the ellipse E_R , with foci at ± 1 , within which $f(x)$ is analytic. If R is known, then there exist bounds for $|a_n|$ of the form

$$|a_n| \leq K p^n \quad n = 0, 1, 2, \dots \quad (2)$$

where $p = (1/R) + \epsilon$, for any $\epsilon > 0$, and K a constant. It can be shown that corresponding to a given ϵ there exists a smallest constant K for which Eq. (2) holds. A bound for $|a_n|$, such as given by Eq. (2), is then used to enhance the data by putting in an *a priori* value of zero for $|a_n|$ and a corresponding variance $(Kp^n)^2$. Thus the series need never be truncated (at least not for mathematical reasons).

Suppose now that R is not known but we are given a finite number of $|a_n|$, $n = 0, 1, 2, \dots, m$, and we wish to estimate K and p in Eq. (2) in order to improve the estimate. Obviously from a strict mathematical point of view it is impossible to obtain the bound Eq. (2) no matter how large m is, but in practice there is usually a simple pattern for the size of the coefficients.

From Eqs. (1) and (2) it follows that there will be infinite number of $|a_n|$ for which

$$K \left(\frac{1}{R} - \epsilon \right)^n \leq |a_n| \leq K \left(\frac{1}{R} + \epsilon \right)^n \quad (3)$$

Thus one method of estimating $1/R$ and K is to show that many points of $|a_n|$ cluster about an experimentally determined curve $\bar{K} \bar{p}^n$, and that there exists no such curve for a larger value of \bar{p} .

The method we are using to find \bar{K} and \bar{p} is to take the logarithm of $|a_n|$ for $n = 0, 1, 2, \dots, m$ for a range of n in which $|a_n|$ can be accurately determined, and to fit this finite set of values with a line using the l_1 norm,² or minimizing the sum of the absolute values of the deviations from the line. This norm is the least sensitive to large residuals, which we must expect. After a first approximation is obtained, the $|a_n|$ which lie significantly below the line is dropped. This method should work well if enough terms are used and the singularities in the complex plane are used and the singularities in the complex plane are of the types discussed by Elliott (Ref. 14), such as poles, where the behavior for large n of $|a_n|$ is fairly closely approximated by an expression such as $\bar{K} \bar{p}^n$ multiplied by a rapidly oscillating function whose amplitude is unity.

F. Magnitude of Second-Degree Harmonics in Lunar Gravity Field, J. Lorell

1. Introduction

In conjunction with the selenodesy experiment (SPS 37-43, Vol. IV, pp. 22-31) which is using the *Lunar*

²Fitting of l_1 was programmed by Dr. R. J. Hanson of JPL.

Orbiter tracking data to determine the moon's gravity field, it is important to obtain independent non-orbiter estimates of the gravity field coefficients where possible. Earth-based measurements of various types can yield such information. Thus, studies of the lunar librations have yielded, according to Jeffreys (Ref. 15), the values (assuming a uniform density moon).

$$L' = \frac{3}{2}(C-A)/Ma^2 = (377 \pm 2) \times 10^{-6}$$

$$K' = \frac{3}{2}(B-A)/Ma^2 = (126 \pm 2) \times 10^{-6}$$

in which A, B, C are the three moments of inertia about the principal axes, M is the mass of the moon, and a its mean equatorial radius. These values may be converted to values of the harmonic coefficients C_{20} and C_{22} :

$$C_{20} = \frac{2}{3} \left(L' - \frac{1}{2} K' \right) = (-209.3 \pm 2.0) \times 10^{-6}$$

$$C_{22} = \frac{1}{6} K' = (21.0 \pm 0.4) \times 10^{-6}$$

The uncertainties indicated here reflect the estimated accuracy of the measurements based on the assumed model. However, unaccounted for biases and/or model errors could increase these uncertainties appreciably.

The remaining second-degree harmonics C_{21} , S_{21} , and S_{22} must be zero, since the reference coordinate system coincides with the principal axes.

In the usual treatment of lunar librations it is assumed that except for small perturbations, the moon rotates uniformly about its polar axis within a period of one month. The polar axis is inclined to the ecliptic at an angle of about $1^\circ 32' 39''$. Deviations from this motion are referred to as the physical librations of the moon, and these never exceed about $2'$.

Implicit in the librations theory is the assumption that the principal axes of inertia of the moon are appropriately oriented. In particular, the polar axis is that of largest moment of inertia C , and the smallest moment of inertia A is the one about the axis through the moon's zero meridian, i.e., the meridian with mean position on the earth-moon line. Plummer (Ref. 16) shows that for dynamic stability it is necessary that $C > B > A$.

If, however, due to effects unaccounted for in the theory the principal axes fail to coincide with the coordinate axes as assumed, the harmonics C_{21} , S_{21} , and S_{22} would no longer be zero; their actual size would be a function of the magnitude of the angles between the two sets of axes. The harmonics C_{20} and C_{22} would be affected also.

Derivation of appropriate formulas follow.

2. Relations Between the Second-Degree Gravity Harmonics and the Directions of the Principal Axes

It can be shown that (Ref. 17):

$$Ma^2 C_{20} = \int \rho(z^2 - \frac{1}{2}x^2 - \frac{1}{2}y^2) d\tau = -C + \frac{1}{2}A + \frac{1}{2}B$$

$$Ma^2 C_{22} = \int \rho(\frac{1}{4}x^2 - \frac{1}{4}y^2) d\tau = \frac{1}{4}(B-A)$$

$$Ma^2 C_{21} = \int \rho zx d\tau = I_{zx}$$

$$Ma^2 S_{21} = \int \rho yz d\tau = I_{yz}$$

$$Ma^2 S_{22} = \frac{1}{2} \int \rho xy d\tau = \frac{1}{2} I_{xy}$$

in which ρ is the density and the integration is taken over the moon's volume.

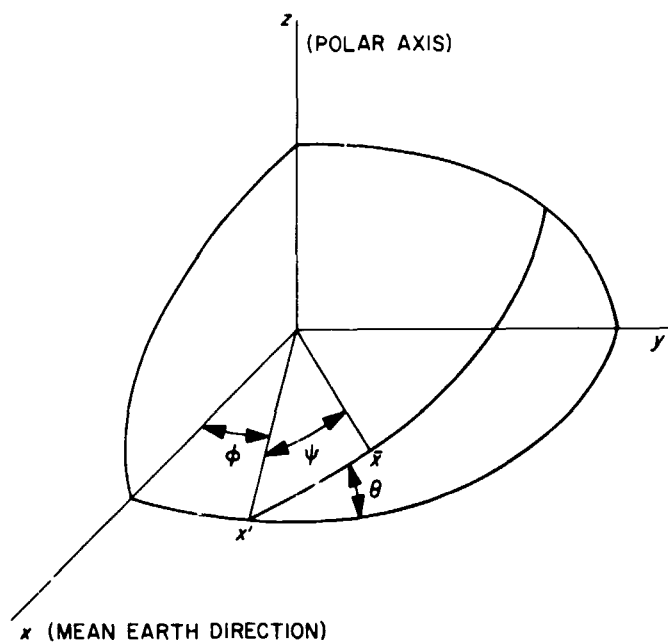


Fig. 11. Angles between principal axes and coordinate axes

Assume that the Euler angles ϕ , θ , and ψ (Fig. 11) between the coordinate axes and the principal axes are small, i.e.,

$$\phi \ll 1, \quad \theta \ll 1, \quad \psi \ll 1$$

Then, the transformation to principal axes is given by (Ref. 18):

$$\begin{pmatrix} x \\ y \\ z \end{pmatrix} = \begin{pmatrix} 1 - \frac{1}{2}\phi^2 - \frac{1}{2}\psi^2 - \phi\psi & \phi + \psi & \psi\theta \\ -\phi - \psi & 1 - \frac{1}{2}\theta^2 - \frac{1}{2}\phi^2 - \frac{1}{2}\psi^2 - \psi\phi & \theta \\ \theta\phi & -\theta & 1 - \frac{1}{2}\theta^2 \end{pmatrix} \begin{pmatrix} \bar{x} \\ \bar{y} \\ \bar{z} \end{pmatrix}$$

in which the principal axis coordinates are \bar{x} , \bar{y} , \bar{z} . Terms through second order in the small angles have been retained.

Substituting in the expressions for the harmonics yields finally

$$C_{20} - \bar{C}_{20} = \frac{3}{2}\theta^2 (C_{20} - 2C_{22})$$

$$C_{22} - \bar{C}_{22} = -\theta^2 C_{20} - (2\phi^2 + 2\psi^2 + 4\phi\psi) C_{22}$$

$$C_{21} = \theta(\psi C_{20} + 4\phi C_{22})$$

$$S_{21} = \theta C_{20}$$

$$S_{22} = -2(\phi + \psi) C_{22}$$

in which the barred coefficients are referred to the principal axes.

3. Numerical Values

It is seen from the formulas of Sect. 2 that the change in C_{20} and C_{22} due to a small rotation of the principal axes is of second order in the angles. For rotations of less than a degree, for example, each angle would be less than 0.02 rad and (using Jeffreys' values for C_{20} , C_{22} given above):

$$\frac{\Delta C_{20}}{C_{20}} \sim 6 \times 10^{-4}$$

$$\frac{\Delta C_{22}}{C_{22}} \sim 6 \times 10^{-3}$$

Furthermore, \bar{C}_{20} is larger (in absolute magnitude) than C_{20} , since both quantities are negative.

Of the remaining second-degree harmonics, C_{21} is of second order in the angles, and S_{21} and S_{22} are of first order. Their magnitude for the rotation through 1 deg assumed above are:

$$C_{21} \sim 0.11 \times 10^{-6}$$

$$S_{21} \sim 4 \times 10^{-6}$$

$$S_{22} \sim 1.6 \times 10^{-6}$$

On the other hand, it is difficult to reconcile the observations of the lunar librations with values of the Euler angles as large as 1 deg. For example, Jeffreys' analysis yields an uncertainty in the inclination of the lunar equator of at most 30", and this should be a bound on θ . Thus,

$$\theta < 0.00015$$

whence both C_{21} and S_{21} become negligibly small with respect to their effect on a lunar orbiter. However, S_{22} which does not contain the factor θ could possibly be significant if the principal axis in the earth direction were appreciably off the x -axis.

4. Conclusions

It has been shown that the effects of small malorientations of the moon's principal axes are reflected in the second-degree gravity harmonics. Using what appear to be the best non-orbiter estimate of the moon's principal axes directions and moments of inertia, the results indicate that C_{21} and S_{21} are negligibly small.

References

1. *Launch Vehicle Estimating Factors for Generating OSSA Prospectus 1967*, National Aeronautics and Space Administration, Washington, D.C., November 1966.
2. Melbourne, W. G., and Sauer, C. G., "Payload Optimization for Power-Limited Vehicles," *Progress in Astronautics and Aeronautics Vol. 9. Electric Propulsion Development*, pp. 617-645, Academic Press, New York, N.Y., 1963.
3. Melbourne, W. G., and Sauer, C. G., "Optimum Thrust Programs for Power-Limited Propulsion Systems," *Astronaut. Acta*, Vol. VIII, Fasc. 4, 1962.
4. Table A-1, Solar-Powered Electric Propulsion Summary Report, Hughes Aircraft Company, Report SD-60374R, December 1966.
5. Wiener, N., "Generalized Harmonic Analysis," *Acta Math.*, Vol. 55, pp. 117-258, 1930.
6. Ito, K., "Stochastic Integral," *Proc. Imp. Acad. Tokyo*, Vol. 20, pp. 519-524, 1944.
7. Doob, J. L., *Stochastic Processes*, John Wiley & Sons, New York, N.Y., 1953.

References (con'd)

8. Stratonovich, R. L., "A New Representation for Stochastic Integrals and Equations," *J. SIAM Control*, Vol. 4, No. 2, 1966.
9. Gray, A. H., and Caughey, T. K., "A Controversy in Problems Involving Random Parametric Excitation," *J. of Math and Physics*, Vol. 44, pp. 288-296, Sept. 1965.
10. McReynolds, S. R., "A New Approach to Stochastic Calculus," delivered at the Seminar on Guidance Theory and Trajectory Analysis, NASA-ERC, Cambridge, Mass., June 1, 1967.
11. Hadamard, J., *Lectures on Cauchy's Problem in Linear Partial Differential Equations*, Yale University Press, New Haven, Conn., 1923.
12. Frost, P. A., "A New Form of Representation of Stochastic Integrals and Equations by R. L. Stratonovich," TR 7050-d, Systems Theory Laboratory, Stanford Electronics Laboratory, Stanford University, Stanford, Calif., Aug. 1966.
13. Wong, E., and Zakai, M., "On the Relation Between Ordinary and Stochastic Differential Equations," *Int. J. Eng. Sci.*, Vol. 3, pp. 213-229, 1965.
14. Elliott, E., "The Evaluation and Determination of the Coefficients in the Chebyshev Series Expansion of a Function," *Mathematics of Computation*, Vol. 18, No. 86, p. 274, 1964.
15. Jeffreys, H., "On the Figure of the Moon," *Monthly Notices of the Royal Astronomical Society*, Vol. 122, pp. 421-432, 1961.
16. Plummer, H. C., *An Introductory Treatise on Dynamical Astronomy*, Chap. XXIII, Cambridge University Press, New York, N.Y., 1918.
17. Clemence, G. M., and Brouwer, D., *Celestial Mechanics*, Chap. III, Academic Press, New York, N.Y., 1961.
18. Goldstein, H., *Classical Mechanics*, Sec. 4-4, Addison-Wesley Publishing Company, Inc. Reading, Mass., 1959.

N67-34763

II. Computation and Analysis

SYSTEMS DIVISION

A. Planetary Masses for Ephemeris Development,

J. D. Mulholland

Unlike the ephemerides used in the more traditional areas of astronomical research, ephemerides for space vehicle trajectory computations should conform as closely as practicable to the most accurate model of the solar system available. Complete conformity is not possible, for a variety of reasons; the principal barrier is the time and expense required to compute a new ephemeris. It is necessary to weigh the desire for the "best" ephemeris in terms of the real benefit to be attained by the recomputation. Improvements will always be possible, but they need not be executed unless the attendant decreases of uncertainties in the coordinates are significant.

The versions of the JPL ephemeris tape system currently in use are based on solar system models that are far from adequate. In fact, it is hardly proper to dignify the underlying structures with the designation "model," because of their lack of internal consistency (SPS 37-29, Vol. IV, pp. 61-65). The ephemeris improvement effort has recently entered a new phase, intended to render the ephemeris more consistent as well as more accurate. This effort is characterized by two new features: (1) simultaneous numerical integration of the equations of motion of all of

the major planets, and (2) differential correction of these integrations to fit observational data, both optical and radar. The ephemerides which arise from this effort will thus be freed from the mutual inconsistencies between the various planetary theories. It will be possible, also, to introduce improved astronomical constants without necessarily undermining the bases of the computation. It is imperative that this work begin with the most reliable estimates available for the planetary masses. In this article, we propose a set of mass values that we believe best satisfies this condition at the present time. For purposes of comparison, Table 1 lists the masses used in JPL development ephemeris 3 (Ref. 1).

Table 1. Mass values from Reference 1

Planet	Inverse mass
Mercury	6 000 000
Venus	408 000
Earth-moon	329 390
Mars	3 093 500
Jupiter	1 047.355
Saturn	3 501.6
Uranus	22 869
Neptune	19 314
Pluto	360 000

BLANK PAGE

The work by Clemence (Ref. 2) supplies the model for constructing the present system of masses. It is a definitive discussion of the state of knowledge of the masses to 1964. Since that time, however, several new determinations have been made and some old ones have been discredited. In that which follows, we have combined the still-valid data of Ref. 2 with the newer determinations. The resulting system represents weighted means of all data cited, the weights being assigned as inversely proportional to the squares of the formal errors cited. Table 2 lists the mass determinations that were used in constructing the recommended masses.

No discussion is necessary for those entries in Table 2 which have been adopted from Ref. 2, as they are fully treated therein. Some comment, however, needs to be made about the additions to and omissions from that collection:

Mercury: Rabe's mass determination based on the orbit of Eros has been recently invalidated by Rabe and Francis.¹ Eros' orbit is apparently incapable of yielding reliable masses for any planet other than earth.

Venus: Rabe's mass is omitted for the reason cited above. Anderson's (Ref. 3) value is a refinement of that of Anderson, Null, and Thornton cited in Ref. 2. The value of Ash, et al. (Ref. 4), is based on differential corrections to the planetary ephemerides, based on Washington transit circle observations (1950-65) and radar bounce observations (1959-66) taken at Lincoln Laboratory, Arecibo, and Crimea.

Earth-moon: The value attributed to Rabe and Francis results from a rediscussion of Rabe's earlier work on the orbit of Eros, thus supplanting Rabe's value from Ref. 2. The comments on Ash's mass of Venus apply here also. The value attributed to Sjogren, et al. (Ref. 5), represents a weighted mean of the separate values obtained from tracking the *Ranger VI-IX* vehicles. The remarkable consistency of the recent determinations has prompted me to discard the older determinations entirely. The effect of including them would not have been significant.

Mars: As with Mercury and Venus, Rabe's value is discarded. The comments on Ash's mass of Venus apply here also. Null's (Ref. 6) determination results from a definitive discussion of the *Mariner IV* flight path.

Jupiter: The mass of this planet is currently the subject of an intensive, broad-based attack by traditional cy-

¹M. P. Francis, private communication.

Table 2. Independent mass determinations

Mercury			
1.	5 970 000	± 455 000	Duncombe, 1958
2.	5 980 000	170 000	Makover and Boklan, 1961
3.	6 021 000	53 000	Ash, Shapiro, and Smith ⁽⁴⁾ , 1967
Venus			
1.	409 300	± 1 400	Clemence, 1943
2.	404 700	800	Jones, 1926
3.	408 945	300	Duncombe, 1963
4.	408 505	6	Anderson ⁽³⁾ , 1967
5.	408 250	120	Ash, Shapiro, and Smith ⁽⁴⁾ , 1967
Earth-moon			
1.	328 906	± 6	Radar, 1961-63
2.	328 900	60	Ash, Shapiro, and Smith ⁽⁴⁾ , 1967
3.	328 899	15	Rabe and Francis, 1966
4.	328 900	1	Sjogren, et al. ⁽⁵⁾ , 1966
Mars			
1.	3 088 000	± 5 000	van den Bosch, 1927
2.	3 111 000	9 000	Ash, Shapiro, and Smith ⁽⁴⁾ , 1967
3.	3 098 600	600	Null, Gordon, and Tito ⁽⁶⁾ , 1967
Jupiter			
1.	1 047.39	± 0.03	Clemence, 1961
2.	1 047.40	0.03	de Sitter, 1915
3.	1 047.4	0.4	Kulikov, 1950
4.	1 047.558	0.40	Samter, 1910
5.	1 047.57	0.06	Osten, 1928
6.	1 047.387	0.008	O'Handley, 1967
Saturn			
1.	3 496	± 3	van den Bosch, 1927
2.	3 494.8	1.3	Jeffreys, 1954
3.	3 499.7	0.4	Clemence, 1960
Uranus			
1.	22 934	± 6	Harris, 1950
2.	22 239	89	Hill, 1898
3.	22 530	50	van den Bosch, 1927
Neptune			
1.	19 094	± 22	Gaillot, 1910
2.	18 889	62	van Biesbroeck, 1957
Pluto			
1.	400 000	± 40 000	Brouwer, 1955

Note: Superscript numerals are bibliographic reference numbers. All data not so designated are from Ref. 2 or private communication.

cal procedures. The value attributed to O'Handley² arises from the first to be completed of a related series of investigations. It is based on a discussion (to be published in the *Astronomical Papers of the American Ephemeris*) of the observations of minor planet Cybele.

No discussion is necessary for Saturn, Uranus, Neptune, or Pluto.

²D. O'Handley, private communication.

Table 3. Recommended values of planetary masses

Mercury	6 017 000	±	50 000
Venus	408 504	±	6
Earth-moon	328 900	±	1
Mars	3 098 500	±	600
Jupiter	1 047.3908	±	0.0074
Saturn	3 499.2	±	0.4
Uranus	22 930	±	6
Neptune	19 071	±	21
Pluto	400 000	±	40 000

1. Recommended Planetary Masses

Table 3 presents the weighted mean values of the data in Table 2. These may be regarded as the most reliable system of masses available at the instant of this writing. I have recommended that they be adopted for the current phase of ephemeris development. I also propose that they be recommended, on the same grounds, to other agencies and organizations concerned with spacecraft trajectories.

One may note in passing that the spacecraft tracking data are so overwhelmingly powerful that the masses given in Table 3 for those planets which have been the object of spacecraft missions are essentially the values derived from those missions.

2. Lunar Mass

Numerical integration of the lunar motion is not being contemplated for the near future. We shall continue to use the present combination (Ref. 7) of evaluation of a revised Brown Lunar Theory adjusted to reflect improved values of certain constants. The present version of the lunar ephemeris is constructed with a value of the earth-moon mass ratio

$$\mu^{-1} = 81.30$$

but is recommended for the use with $\mu^{-1} = 81.302$, with a properly determined scaling factor. We do not propose to change this at the present time, but for the sake of completeness Table 4 is included. The weighted mean shown represents the best available estimate at this time, but it

Table 4. Earth-moon mass ratio

81.3030 ± 0.0050	Ash, Shapiro, and Smith ⁽⁴⁾ , 1967
81.3001 ± 0.0013	Anderson ⁽⁵⁾ , 1967
81.3020 ± 0.0017	Sjogren, et al. ⁽⁶⁾ , 1966
81.3011 ± 0.0049	Sjogren, et al. ⁽⁶⁾ , 1966
81.3015 ± 0.0016	Null, Gordon, and Tito ⁽⁹⁾ , 1967
Weighted mean = 81.3011 ± 0.0008	

Note: Superscript numerals are reference numbers.

is not recommended for use until the present approach to the lunar ephemeris is abandoned.

The two values cited for Sjogren, et al., correspond to the values from *Rangers VI-IX* and *Ranger III*, respectively.

B. Studies in Orbit Correction Theory, J. D. Mulholland

In many problems, it is still either useful or necessary to consider geometrically simple approximations to the motion of a celestial object. In these cases, orbit improvement consists of differentially correcting some appropriate set of geometric elements of this "mean orbit," a process that is often taken for granted as a routine task, reduced to "turning the crank." While this is often a valid judgement, it is not necessarily so. This article is a progress report on an investigation intended to clarify some of the questions associated with the construction of the equations of condition in such problems and to quantify the results where possible.

The first phase of this work (Ref. 8), a study of differential correction formulae in a Hansen-type satellite theory, is reported elsewhere and will not be discussed here.

The current phase is concerned with the practical effects of misinterpretation of the usual formulation of the differential correction relations in rectangular coordinates (Ref. 9) for a Keplerian reference orbit used as a nominal in the computation of special perturbations. The basic relation for a differential correction is

$$\delta \mathbf{r} = \left[\frac{\partial \mathbf{r}}{\partial \eta_i} \right] \{ \delta \eta_i \} \quad (1)$$

where \mathbf{r} is the position vector and η_i represents the six Keplerian elements or their equivalents. Some or all of the partial derivatives are usually stated in the form

$$\frac{\partial \mathbf{r}}{\partial \eta_j} = \phi(\eta_i, \mathbf{r}, \dot{\mathbf{r}}) \quad (2)$$

For example, the derivative with respect to the mean anomaly at the epoch M_0 is

$$\frac{\partial \mathbf{r}}{\partial M_0} = \frac{\dot{\mathbf{r}}}{n} \quad (3)$$

where n is the Keplerian mean motion.

In the application hypothesized above, the relations (2) are frequently evaluated incorrectly. Numerical tests now under way indicate that the penalties can be quite severe. The trouble arises in the following way: The derivative expressions are intended for the correction of a Keplerian approximation to the real trajectory. Properly speaking, they should be evaluated using only the data for the nominal (Keplerian) orbit. On the other hand, the numerical integration yields the coordinates and velocities in the *perturbed* orbit. One may reason that these values of r and \dot{r} may be used in the relations (2) with perfect safety, thus avoiding what may seem to be the redundant computation of position and velocity in the nominal orbit.

A systematic test of the validity of such an approach, using actual perturbed orbits, would involve a rather large expenditure of computer time. It is possible, however, to construct an analog to the real problem which requires no numerical integration of perturbed orbits. In a Hansen-type theory, one relates the osculating radial distance r to the nominal radial distance ρ by the relation

$$r = (1 + v) \rho, \quad -v_1 \leq v \leq +v_1 \quad (4)$$

where v is a perturbation quantity bounded by the extreme values $\pm v_1$. Now, the osculating radial distance r in true Keplerian motion may be written as

$$r = (1 + v) a, \quad -e \leq v \leq +e \quad (5)$$

where a is the semimajor axis and e the eccentricity of the ellipse. The formal similarity of Eqs. (4) and (5) is quite obvious. One may contend that the departures from nominal motion caused by in-plane perturbations of size v are comparable to the departures of circular motion from elliptic motion with eccentricity e .

If we adopt an elliptic nominal orbit and regard the associated circular orbit as providing the "perturbed" position and velocity, then the situation that we wish to study is equivalent to that of correcting the elliptic nominal using the circular r and \dot{r} in conjunction with the elliptic elements. For purposes of comparison, we have chosen to perform tests on the effects of computing the equations of condition in three ways:

- Case 1: Elliptic elements, elliptic state vector
- Case 2: Elliptic elements, circular state vector
- Case 3: Circular elements, circular state vector

Case 3 corresponds to correcting a nominal orbit using osculating data only.

Only preliminary results have been obtained from the study at this time, but they are both unambiguous and significant. The ratio σ/σ_0 of rms residual after differential correction to that before the correction seems to be the one most significant measure of the effectiveness of the process, and this quantity is plotted in Fig. 1 as a function of the maximum "perturbation" e . Several noteworthy features may be seen in this plot:

- (1) For each case, the variation is nearly linear with e .
- (2) There is little difference between Case 2 and Case 3, with each having slopes near unity.
- (3) Case 1 is more effective than Cases 2 or 3 by an order of magnitude.

The near-linearity is not expected to extend to extremely high values of e .

The data of Fig. 1 are based on one case only and the slopes of the curves may not be universally valid. Nonetheless, the curves show relationships *with one another* that probably are general. Further studies are under way which will determine these questions.

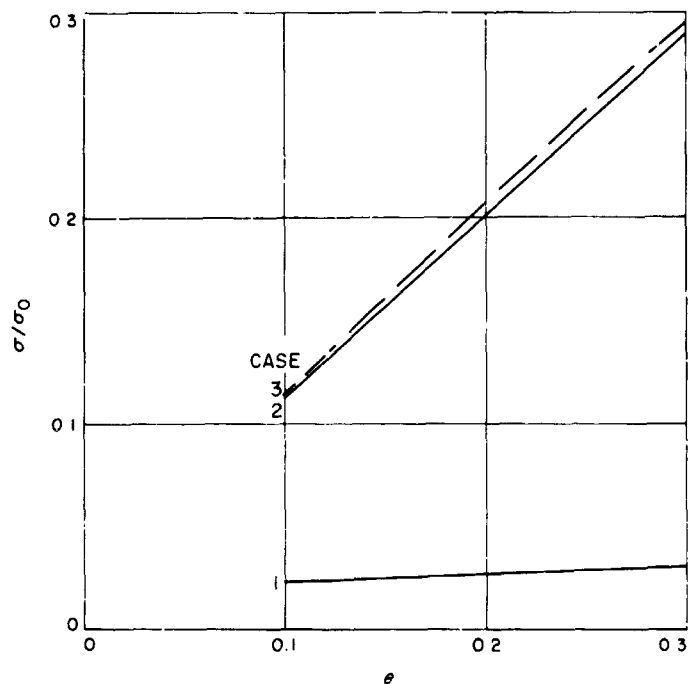


Fig. 1. Effectiveness of differential correction procedures

References

1. Peabody, P. R., Scott, J. F., and Orozco, E. G., "JPL Ephemeris Tapes E9510, E9511, and E9512," Technical Memorandum 33-167, Jet Propulsion Laboratory, Pasadena, California, March 2, 1964.
2. Clemence, G. M., "Masses of the Principal Planets," *Trans. Intern. Astron. Union*, Vol. 12B, pp. 60C-614, Academic Press, 1966.
3. Anderson, J. D., "Determination of the Masses of the Moon and Venus and the Astronomical Unit from Radio Tracking Data of the *Mariner II* Spacecraft," Technical Report 32-816, Jet Propulsion Laboratory, Pasadena, California, in press.
4. Ash, M. E., Shapiro, I. I., and Smith, W. B., "Astronomical Constants and Planetary Ephemerides Deduced From Radar and Optical Observations," *Astron. J.*, Vol. 22, pp. 338-350, 1967.
5. Sjogren, W. L., Trask, D. W., Vegos, C. J., and Wollenhaupt, W. R., "Physical Constants as Determined From Radio Tracking of the Ranger Lunar Probes," Technical Report 32-1057, Jet Propulsion Laboratory, Pasadena, California, December 30, 1966.
6. Null, G., Gordon, H. J., and Tito, D. A., "*Mariner IV* Flight Path and Its Determination from Tracking Data," Technical Report 32-1108, Jet Propulsion Laboratory, Pasadena, California, in press.
7. Mulholland, J. D. and Block, N., "JPL Lunar Ephemeris Number 4," Technical Memorandum 33-346, Jet Propulsion Laboratory, Pasadena, California, April 15, 1967.
8. Mulholland, J. D., "Differential Correction of Non-Keplerian Reference Orbits," *Astron. J.*, Vol. 72, August 1967, in press.
9. Brouwer, D., and Clemence, G. M., *Methods of Celestial Mechanics*, pp. 235-247. Academic Press, New York, 1961.

N67-34764

III. Spacecraft Power

GUIDANCE AND CONTROL DIVISION

A. Photovoltaic Supporting Development,

J. D. Sandstrom and E. Castle

The function of the photovoltaic laboratory at JPL is to aid the solar panel engineer in solar panel design by supplying him with solar cell performance characteristics that are obtained empirically under known and controlled environments. This is accomplished by performing tests on individual cells or matrices of cells (submodules) under test conditions that simulate the actual temperatures, solar intensities, and space environment to which the panel will be exposed. Experience over the past years has shown this technique to be a valid method for predicting the performance of a solar panel within heliocentric distances equivalent to Mars-Venus missions. Also, the goal of JPL's photovoltaic laboratory is to aid in the design of solar panels for future deep space missions to regions not presently explored.

To enable the Laboratory to meet its immediate and long term objectives, several photovoltaic evaluation systems are currently in operation to measure the electrical characteristics of the various solar cells in use today.

At present, the "workhorse" light source used to illuminate test specimens has been tungsten at a color temperature of 2800°K. The tungsten light test facility is shown in Fig. 1. Though the spectral characteristics of tungsten are different from space sunlight, industry generally employs this source because of stability, ease of operation, and low cost. Solar cells, however, are spectrally selective; in order to properly use the tungsten source, quite extensive calibration of the cell and tungsten relative to sunlight is required. In many cases involving solar cell development, a source of solar simulation is employed. Presented in Fig. 2 is a small simulator used in the JPL photovoltaic laboratory specifically for evaluation of individual silicon solar cells at intensity levels of one solar constant or less. The simulator is the OCLI Model 31. This device allows reproduction of the solar spectrum in the region of response of silicon solar cells through the mixing of two light sources, xenon and tungsten.

A third and the most flexible light source in use in the laboratory is a Spectrolab X25L solar simulator. This simulator utilizes a 19-lens lenticular system that filters a

BLANK PAGE

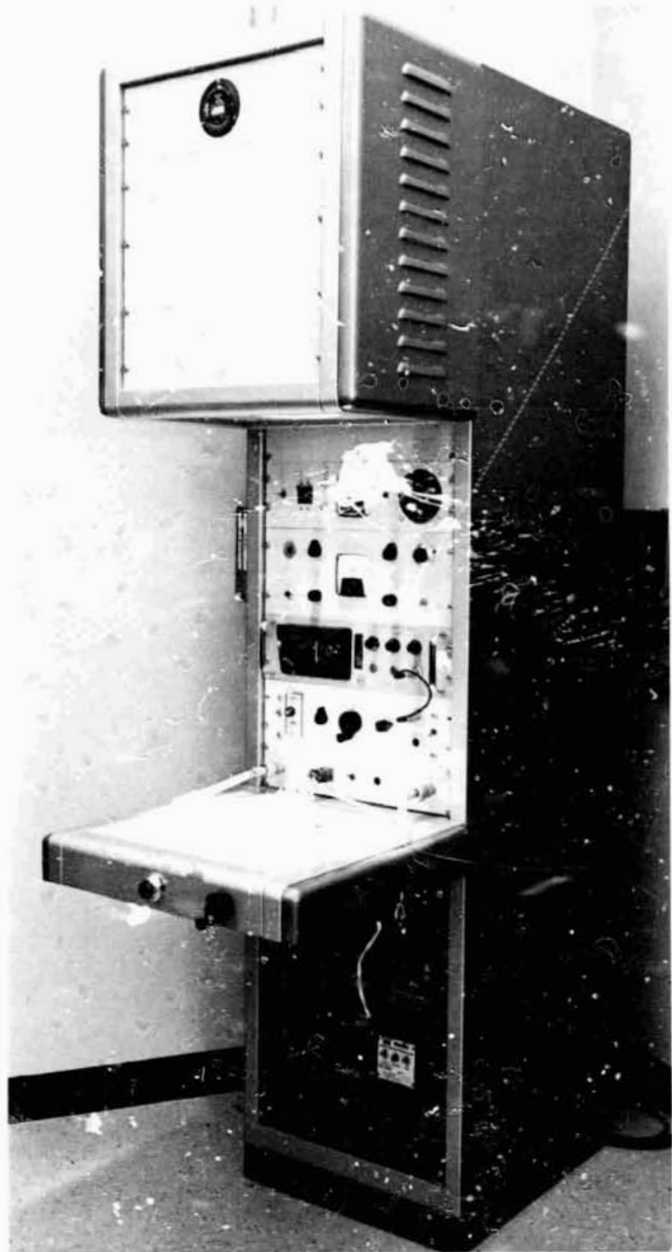


Fig. 1. Tungsten tower

2.5-kW xenon source such that the resultant spectral distribution is essentially that of sunlight. The source has been calibrated using various solar cells that JPL has flown during the past 6 yr in conjunction with the solar cell standardization program. The cells used in this program fit into several categories: those that were unfiltered, those filtered with a $0.41\mu\text{m}$ cutoff interference filter, those with bandpass filters (approximately $0.1\mu\text{m}$ transmission), and those that were filtered to pass energy in the infrared or ultraviolet portions of the spectrum. The measured output (short circuit current) of these cells in the X25L



Fig. 2. OCLI solar simulator



Fig. 3. Thermal-vacuum test facility

illumination, standardized with a balloon-calibrated solar cell, shows 2% agreement with their air mass zero output.

In order to perform temperature-intensity parametric studies on solar cells, a thermal-vacuum test facility has

been developed (Fig. 3). The system is illustrated diagrammatically in Fig. 4. The thermal-vacuum test facility allows the study of solar cell behavior over an extremely wide range of temperatures and solar flux levels. Fig. 5 shows a typical test fixture mounted in the vacuum chamber. This particular test specimen consists of 2×2 -cm,

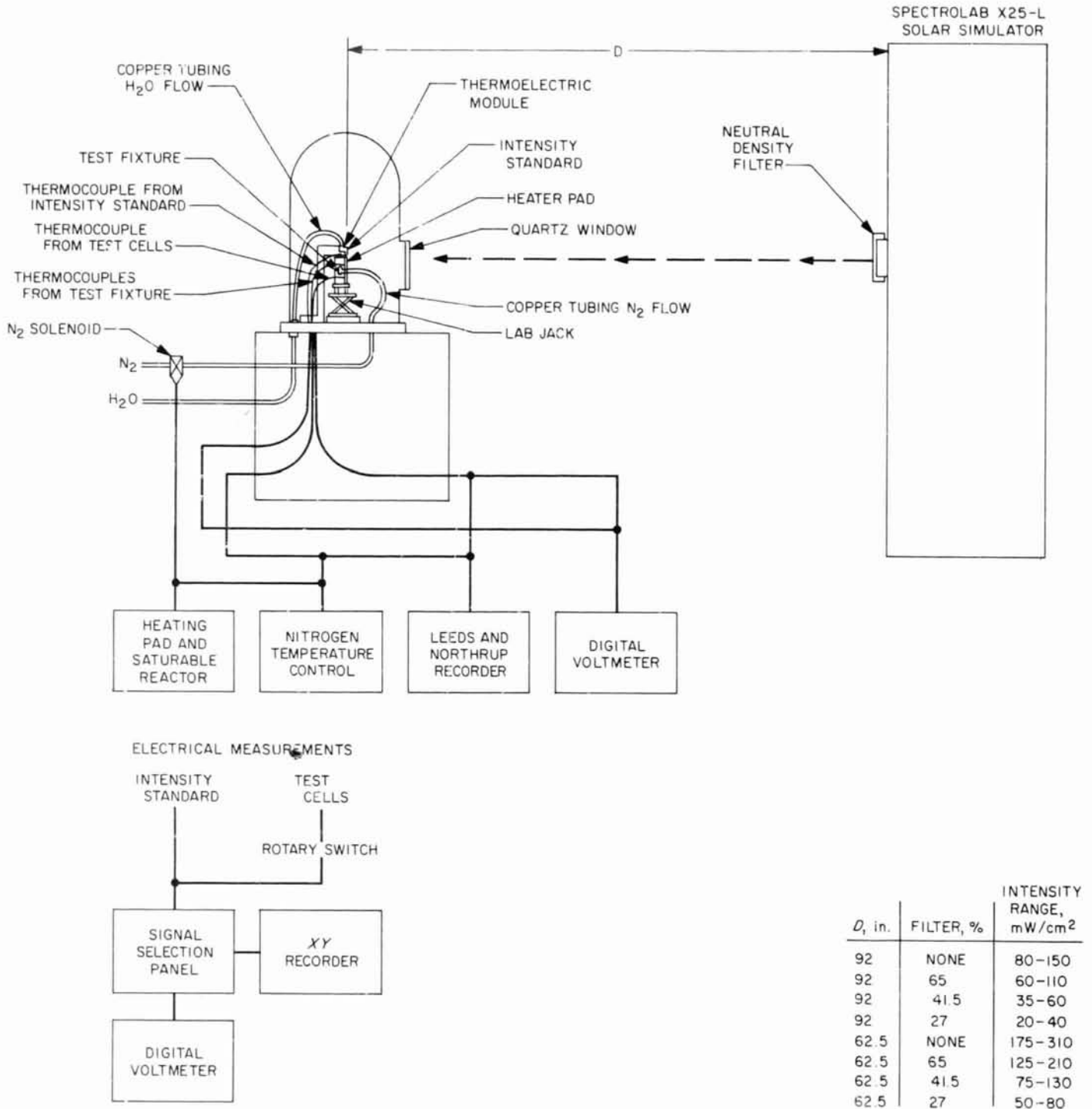


Fig. 4. Thermal-vacuum test facility diagram

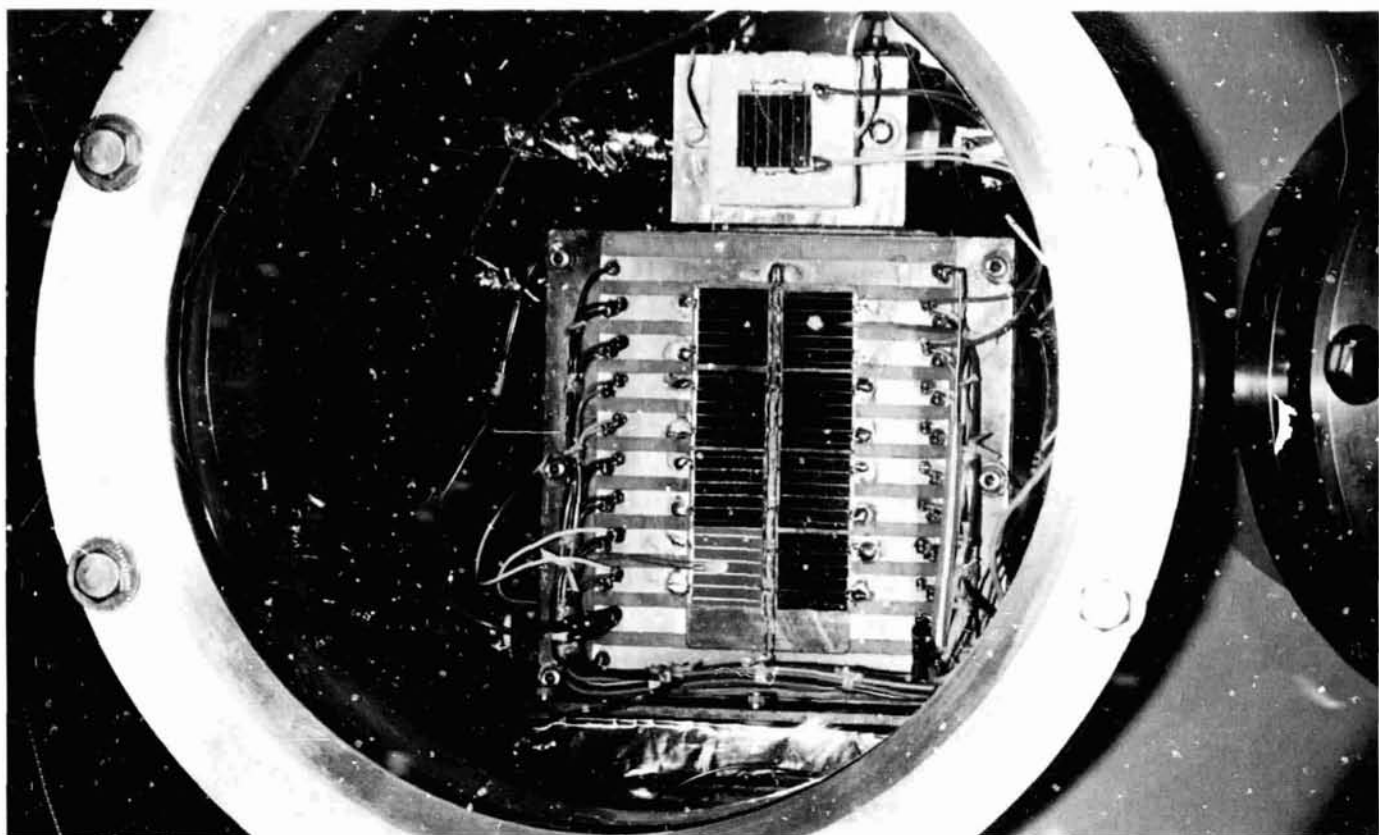


Fig. 5. Specimen test fixture

8-mil N-P silicon solar cells. The cell at the top of the picture is the intensity reference cell, which is thermally and electrically isolated from the primary test fixture. Thus, the intensity standard can be maintained at a constant temperature independently of the test specimens. The curves presented in Fig. 6 represent the average current-voltage ($I-V$) characteristic obtained from the 8-mil cells shown being tested in Fig. 5. The data indicate the relative outputs of these cells at nominal temperatures and at solar flux levels expected to be encountered by a solar panel at various planet heliocentric distances.

To facilitate meeting the objectives of testing solar cells in a thermal-vacuum environment, a special system designed for testing solar cell assemblies in a simulated space environment has been developed. The test facility consists of a space simulator specifically designed for testing sample sections of an array. This chamber is used in conjunction with a solar simulator, as shown in Fig. 7. The system is shown diagrammatically in Fig. 8 and consists of a 3×1.5 -ft cylindrical vacuum chamber incorporating a highly absorbent, liquid nitrogen cooled shroud. Test

assemblies mounted at the rear of the chamber and illuminated with simulated sunlight through a 7-in. diameter quartz window can be evaluated relative to their static and dynamic thermal conditions in space. Thus the thermal equilibrium vacuum chamber will allow tests to be performed on individual cells, submodules, and submodule assemblies under simulated space conditions that are anticipated for a particular application or mission.

The test programs that are being conducted at present, or that will be implemented in the next few months, include the evaluation of the characteristics of currently available silicon solar cells, such as single-crystal P on N or N on P and ion-implanted cells, polycrystalline (dendritic) cells, and thin film cadmium sulfide (CdS) cells. This will be done experimentally by means of the solar simulator and thermal-vacuum system, and theoretically by means of an appropriate computer program. Fig. 9 is the schedule of events through the end of CY 1967. The data obtained from these investigations will be used to determine the design changes necessary to optimize solar cells and, ultimately, composite solar panels for use under various environmental conditions.

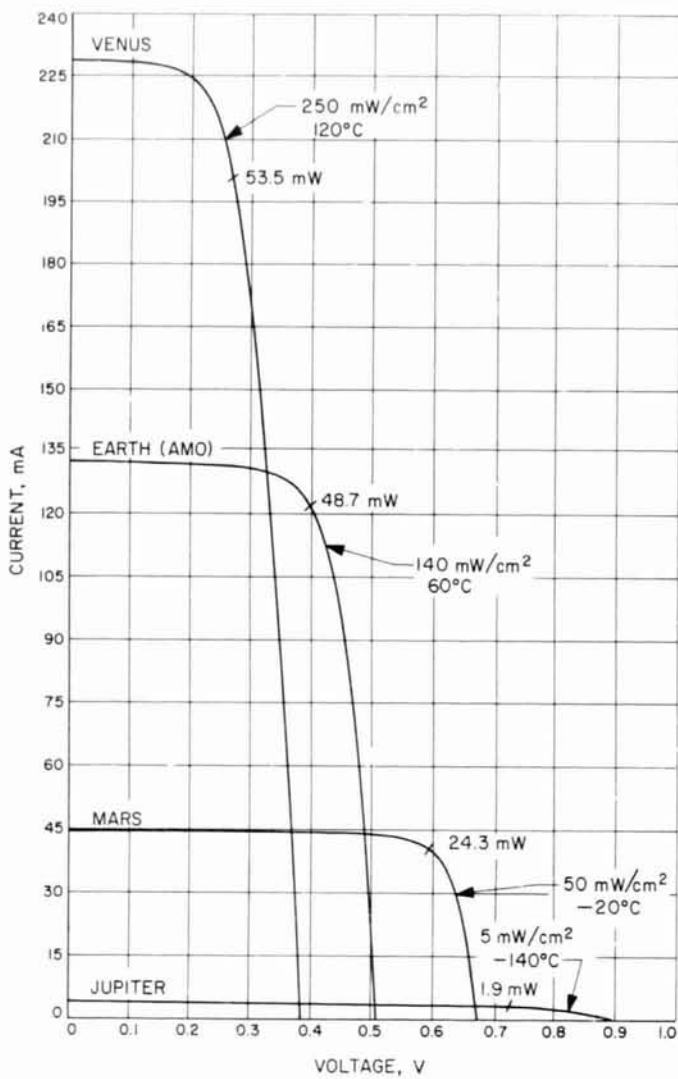


Fig. 6. Current-voltage characteristic of 0.008-in. N-P solar cell at planet heliocentric encounter distances

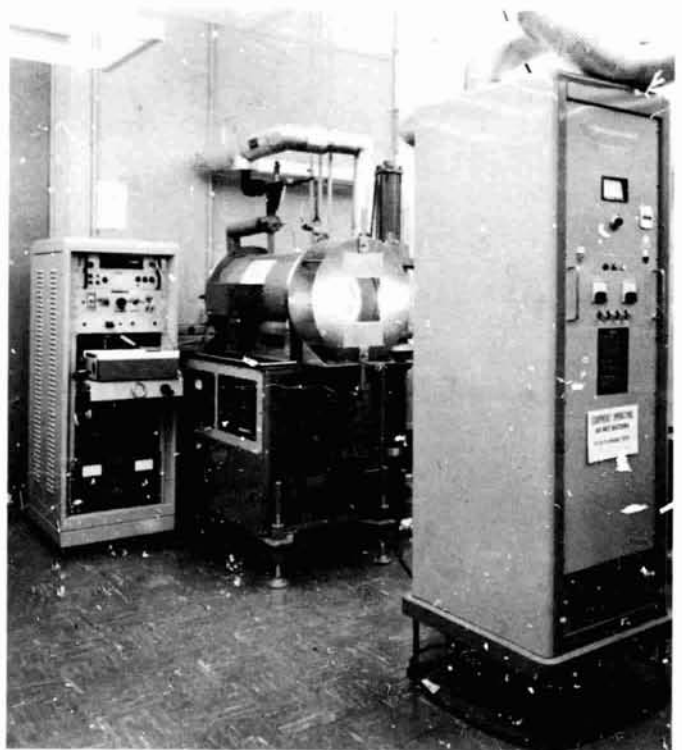


Fig. 7. Thermal equilibrium test facility

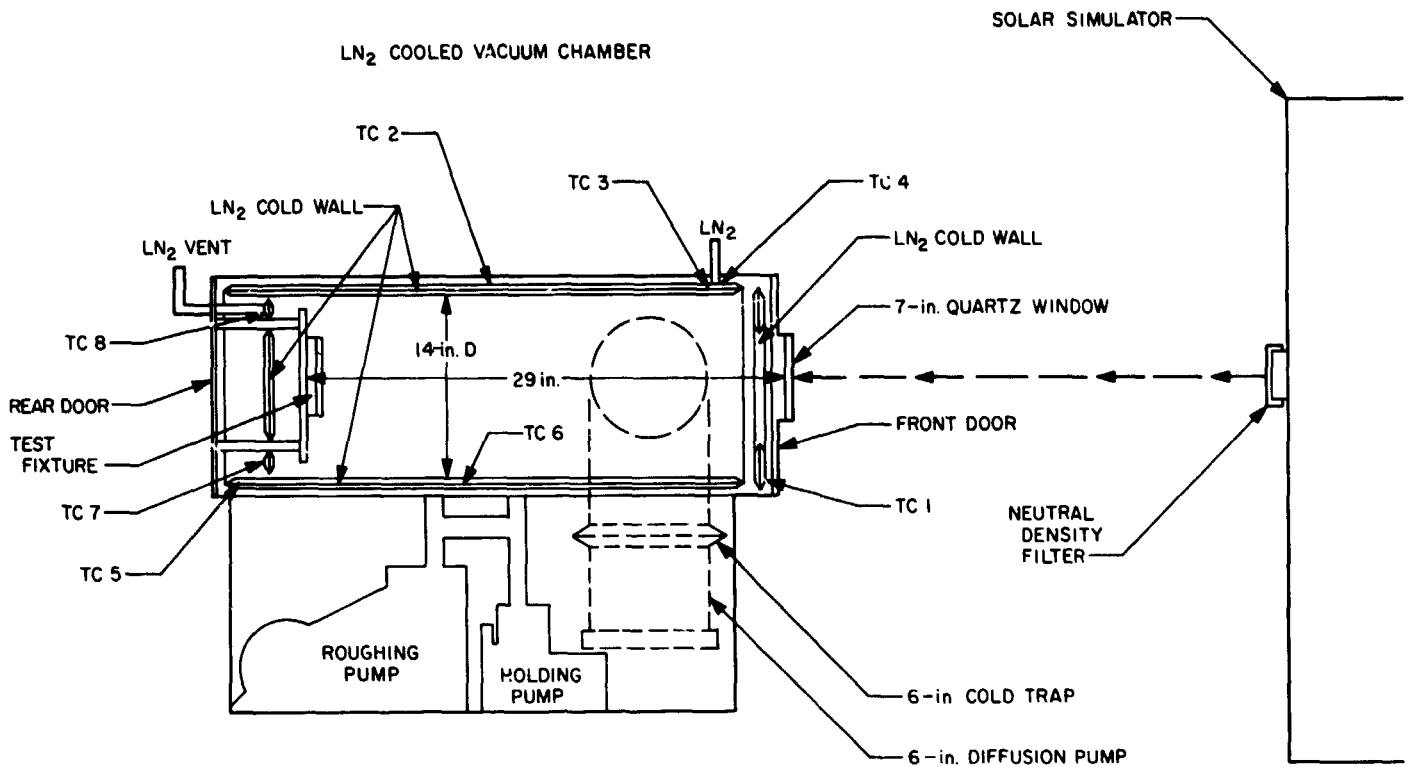


Fig. 8. Diagram of thermal equilibrium test facility

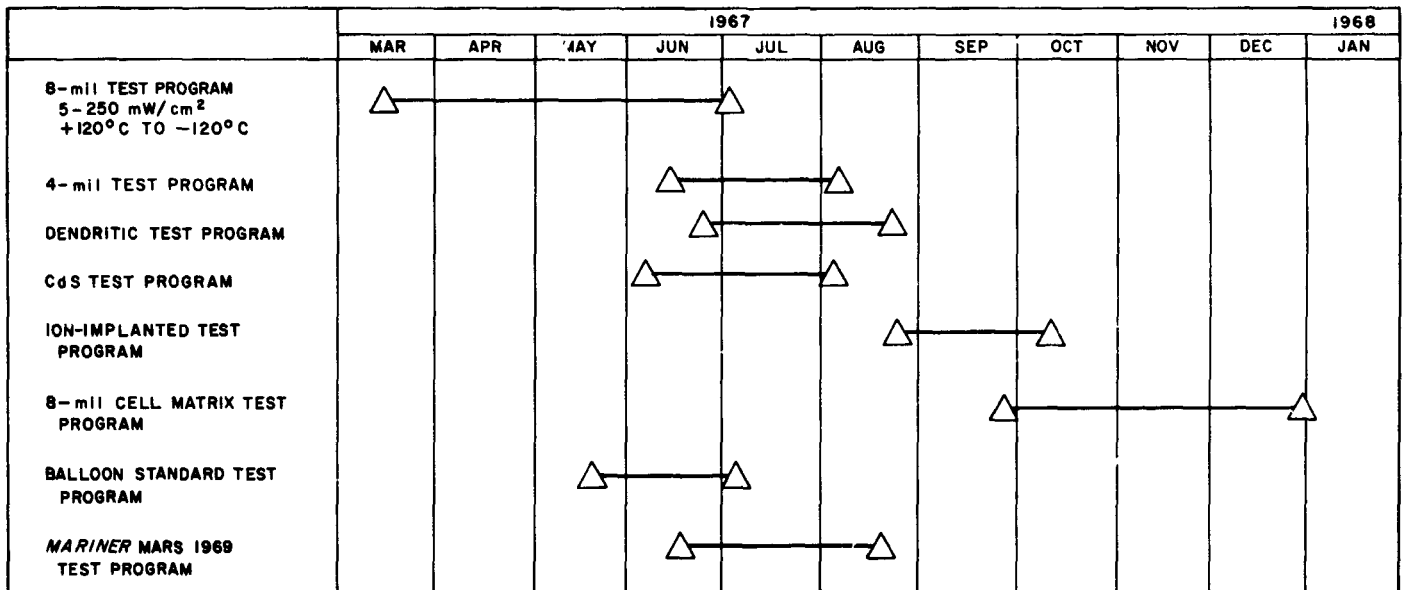


Fig. 9. Photovoltaic supporting development solar cell electrical test program

B. 20-W/lb Technology Development Program,
D. W. Ritchie

1. Introduction

The purpose of this program is to develop the necessary technology to achieve a power density of 20 W/lb for a folding, modular solar array having a deployed area of 1,250 ft². It is anticipated that by CY 1969 the technology to fabricate and assemble 20 W/lb arrays of up to 50 kW will be achieved. The present program is planned as a three-phase effort (Fig. 10).

The Phase I effort will include a thorough detailed evaluation of the earlier preliminary design, culminating in a detailed design, subject to JPL review. Experimental verification of the design data, assumptions, and criteria used in the detail design will be undertaken. Materials, components, and processes will be investigated for compatibility with the solar panel assembly design, the space environment, and suitability for the intended use. Experimental fabrication of beryllium spars and intercostals will be undertaken, and these structures will be tested to obtain

verification of the assumed damping, resonant frequency, and bending modes. Experimental fabrication will identify tooling requirements and fabrication processes to be used in Phases II and III. Sample panels will be fabricated to evaluate methods of mounting 8-mil solar cells and 3-mil coverglass on fiberglass substrates. These sample panels will be subjected to electrical and environmental testing to provide design data and confidence in the semi-rigid panel concept.

The sample panel sizes will be determined to provide data as to the effect of sinusoidal vibration, complex Gaussian noise excitation, and acoustic excitation on the semirigid concept. Data will be obtained for thermal cycling, thermal shock, and extreme temperatures. The completion of the Phase I effort will culminate in a detailed solar array design with ground support equipment (GSE) design requirements established, and experimental test verification of sample assemblies and materials.

The Phase II and III efforts, grossly defined, will include experimental fabrication of limited subpanel structures

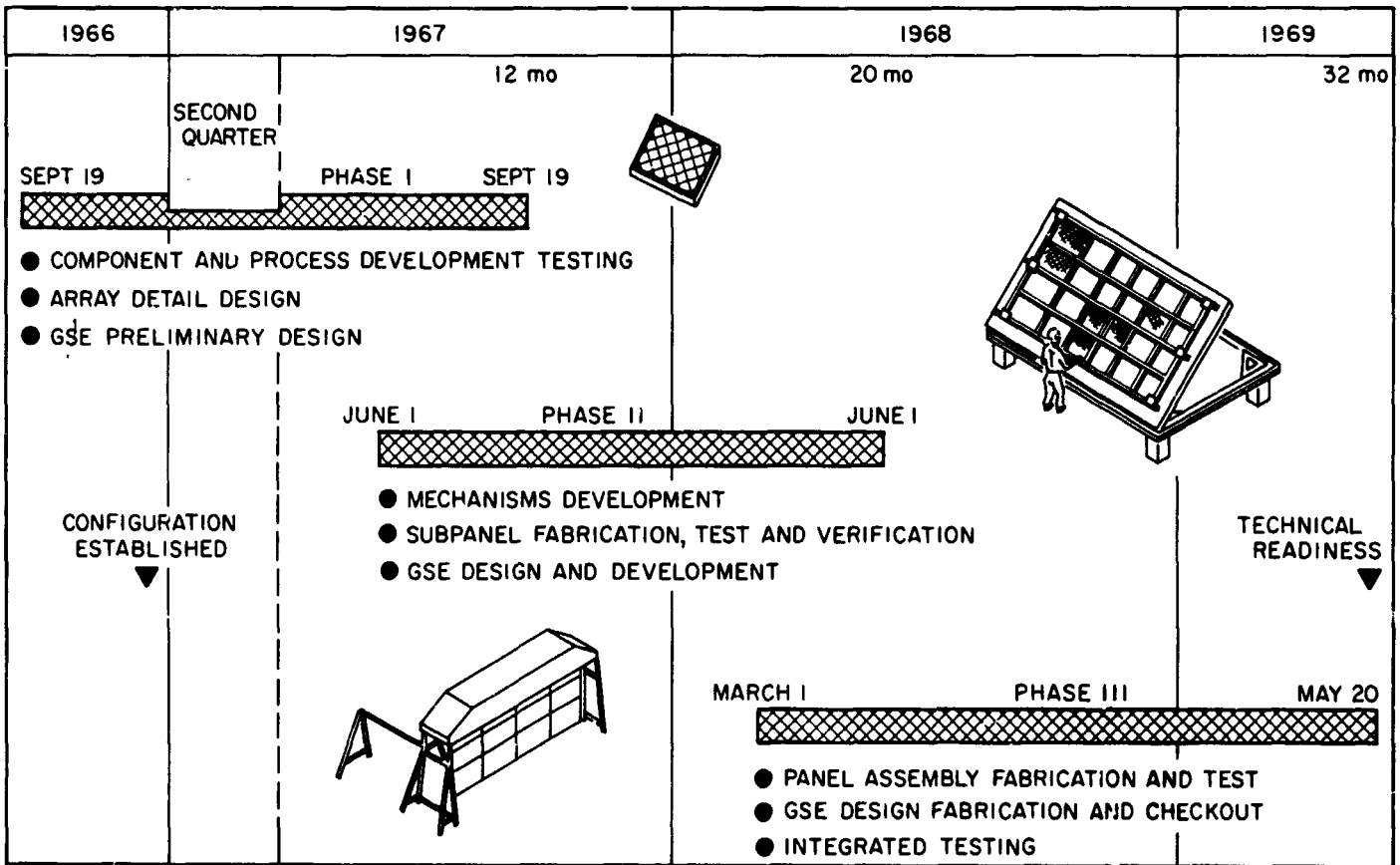


Fig. 10. Large area solar array program phasing

with partial coverage of active solar cells. Deployment dynamics will be investigated for verification of deployment method and support of the simulated zero-g deployment system. Full-size subpanels will be subjected to electrical and environmental tests to establish confidence in the design produced in the Phase I effort.

Manufacture and test of a full size (1250 ft²) solar panel assembly consisting of 13 subpanels will be undertaken. The test will include environmental testing in the launch configuration, and a series of tests simulating zero-g deployment.

2. Program Status

JPL Contract 951653, for Phase I, was initiated with the Boeing Company in September 1966. Presently the program is in the eighth month of activities. The basic folding

modular solar array concept of this program is shown in Fig. 11. The Phase I contracted effort consists of six separate tasks:

Task 1. An analysis and evaluation of the solar array baseline design configuration established in an earlier feasibility study.

Task 2. Development of over-all program plans.

Task 3. Test program to provide design data and establish material limitations.

Task 4. Detail design of the solar panel assembly.

Task 5. Preliminary design of ground support equipment.

Task 6. Documentation and reporting.

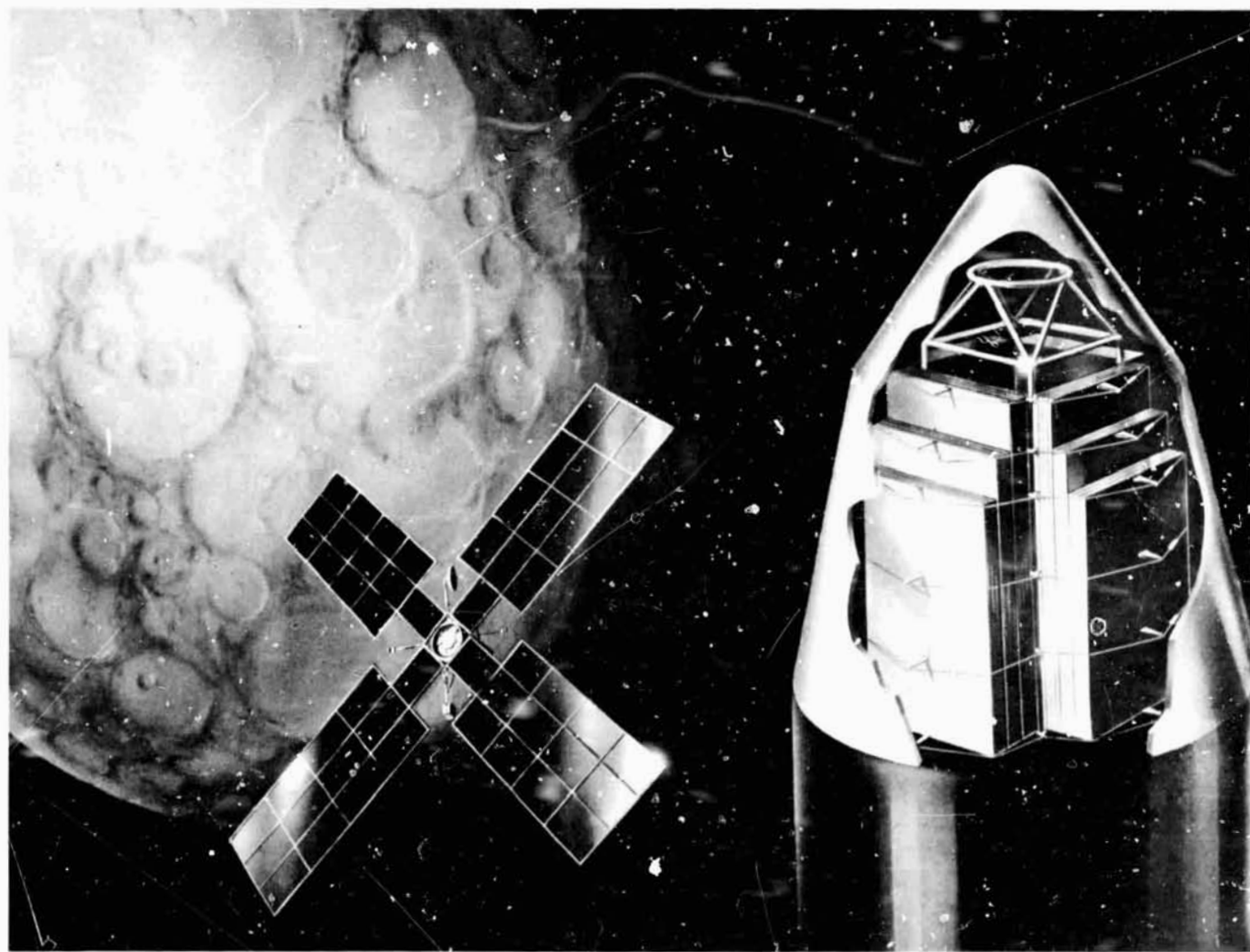


Fig. 11. Folding array concept

Tasks 3, 4, and 5 are the major design and development efforts necessary to meet the Phase I program objectives. Shown in Fig. 12 is a block diagram reflecting the design approach and the relationship among these three tasks. The detail design of the solar panel assembly is 45% complete and is being supported heavily by structures analyses and results of the task 3 test program. The task 3 test support program is to provide design limitations on materials and a limited amount of design, manufacturing, and test verification. The task 3 program is broken down into structures (SCS), electrical (SCE), and solar assembly tests (SCC). The major portion of task 3 is devoted to the SCS test program, which includes evaluation of manufacturing development techniques and materials. The SCS test includes testing on materials and structural components and also, the fabrication of a 16-ft² test panel. Presently in the SCS test series, tests have been completed on the following for establishing or verifying design limitations:

SCS 1 • Tensile strength and modulus of elasticity of fiberglass tape at temperatures between -320°F and 167°F.

SCS 3 • Tensile properties of beryllium as a function of temperature (-200, 70, and 300°F).

SCS 4 • Compressive characteristics of beryllium sheet material at +70 and 300°F.

SCS 5 • Plane strain toughness properties of beryllium sheets by inducing controlled flaws.

SCS 6 • Shear strength of adhesive bond joints assembled from beryllium to beryllium, beryllium to titanium, and beryllium to fiberglass as a function of temperature.

SCS 7 • Beryllium-forming temperatures for acceptable 90-deg bends at 3T, 4T, 5T, and 6T bend radii of wrought material.

The SCS series of tests completed to date indicates that original design assumptions on materials can be met and that in some areas close manufacturing control is needed. One main problem area exists in the forming of beryllium channels. Some of these problems are flaw determination, etching material control, and matching techniques. Beryllium channel beams up to 30 in. long have been completed with limited success.

The SCC solar cell tests are nearly completed and have investigated the manufacturability of 8-mil, solderless solar cells into matrices. During this series of tests, manufacturing techniques were developed for pulse soldering interconnection, filtering bond line thickness control assembly, and determination of assembly degradation of the electrical characteristics of these cells (Fig. 13). At present, it appears that cells can be assembled onto the webbed substrate with adhesive thickness control and electrical degradation maintained at less than 5%.

After completing 8 mo of design and development on the 20 W/lb solar array technology development effort,

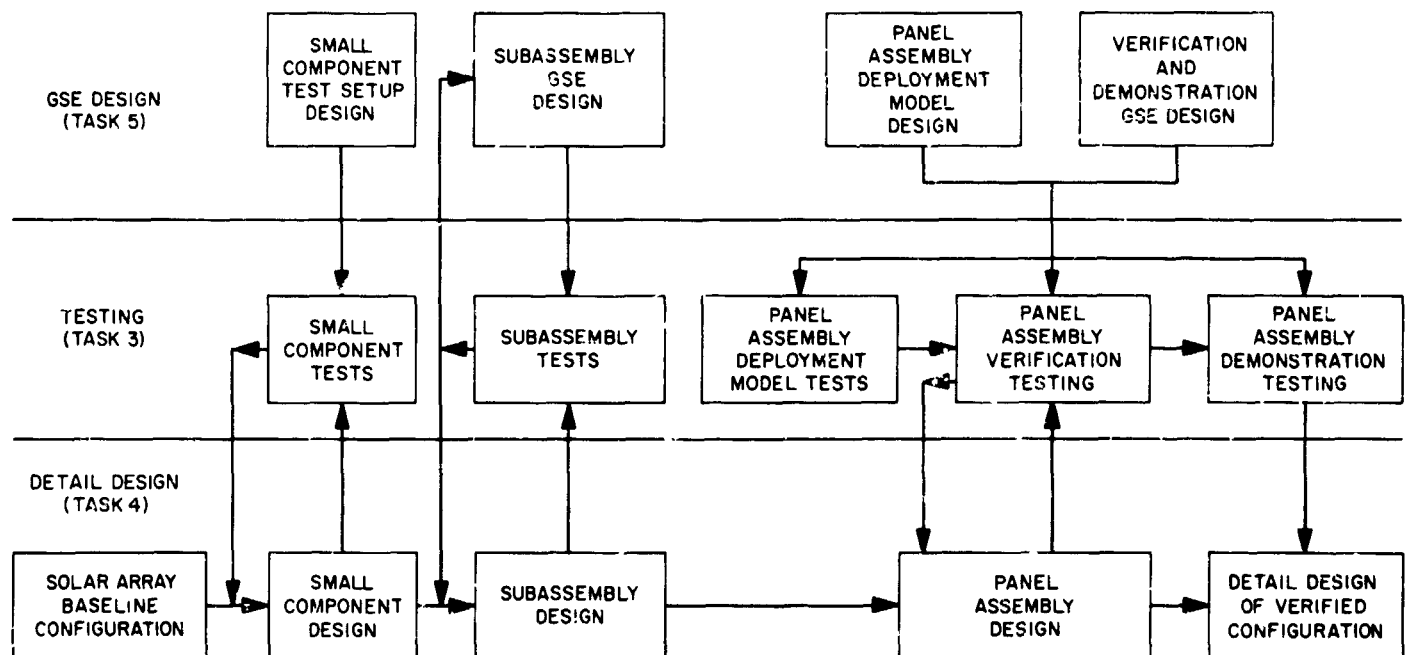


Fig. 12. Design approach

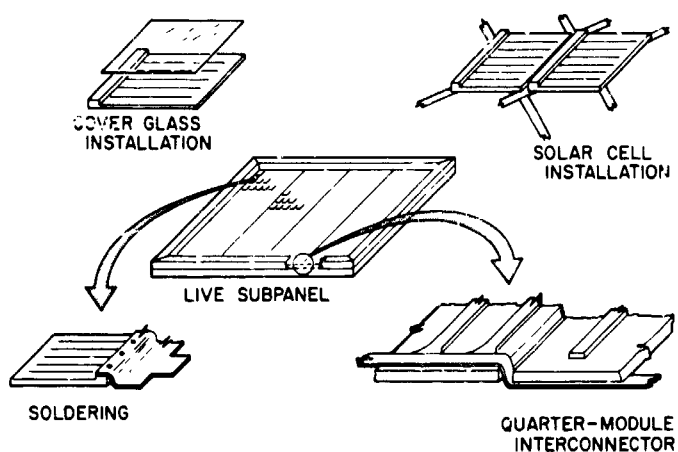


Fig. 13. Electrical power component tests

no insurmountable problems have been uncovered. Some of the major milestones of the Phase I contract are to be encountered in the third and fourth quarter of this effort. These include the successful manufacturing and assembly of the 16-ft² sample panel, the completion of its testing, and the forming, assembly, and testing of a 13-ft long beryllium spar.

C. Thermionic Development, P. Rouklove

The development of thermionic energy conversion systems is continuing at JPL, with emphasis on converter and generator development. Efforts have also been applied in the field of thermal energy distribution. The "heat pipe," a relatively new and novel device, appears very promising, and its application and utilization are being actively pursued by JPL.

1. Converter Test:

Several converters of the advanced technology were tested at JPL. The designs of similar converters were discussed in SPS 37-31, Vol. 4, pp. 58-59 and Fig. 14. In the present iteration of the original design, several modifications were included. The emitter is now formed by a rhenium polycrystalline slab, replacing the original tantalum-rhenium sandwich construction. In the sandwich construction, deficiencies were observed as the result of the diffusion of the tantalum into the rhenium (SPS 37-39, Vol. IV, pp. 66-67). As result of the change and because of difficulties of maintaining the proper bonding of rhenium to tantalum in the high temperature region, the thin, reentrant, emitter supporting sleeve was also made out of rhenium. It was welded to the niobium part of the metal-to-ceramic structure near the seal, in a region where the temperature was lower ($\approx 700^{\circ}\text{C}$). The complete

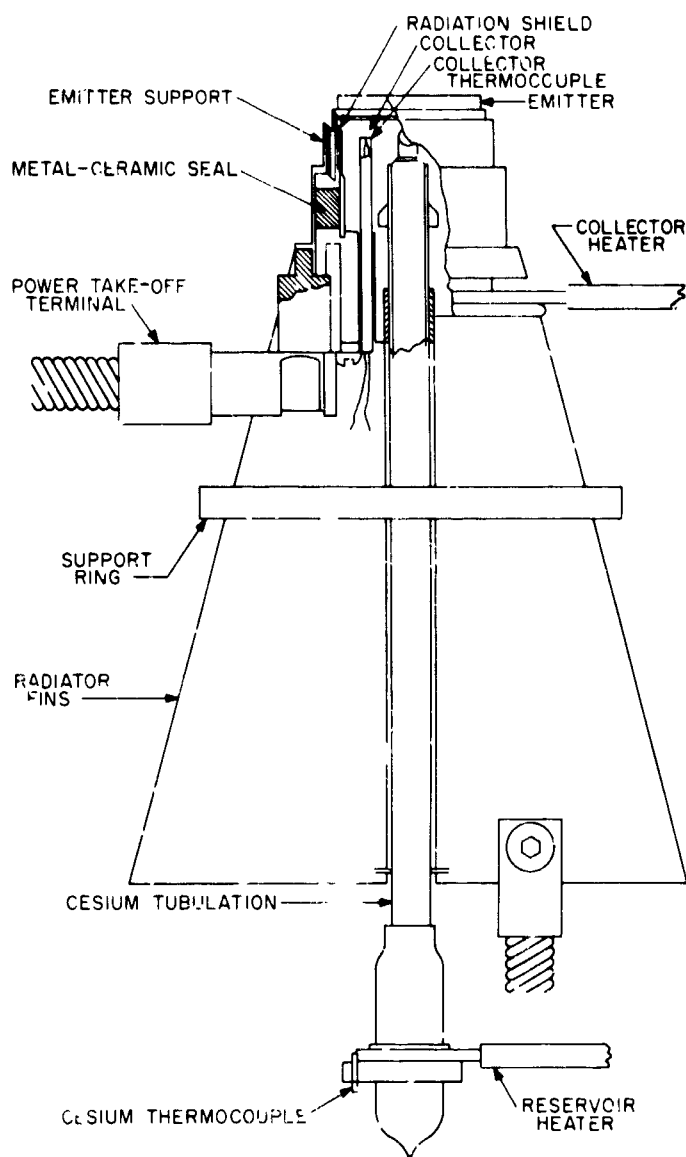


Fig. 14. Series 9 thermionic converter

assembly, prior to its incorporation into a converter, was thermal-cycled and found to be leak-tight. In all the converters tested the collector was molybdenum, with different surface finishes. The test results of two such converters built by Thermo Electron Engineering Co., Waltham, Mass. (TEECO) are reported.

a. Converter T-204. The results of the parametric tests of converter T-204 are graphically presented in Fig. 15 for four values of emitter temperature, and are summarized in Table 1 for two values of voltage output. As in all converters of this design, the thermocouple registering the collector temperature was embedded in the collector body with its sensing head 0.080 in. from the collector surface.

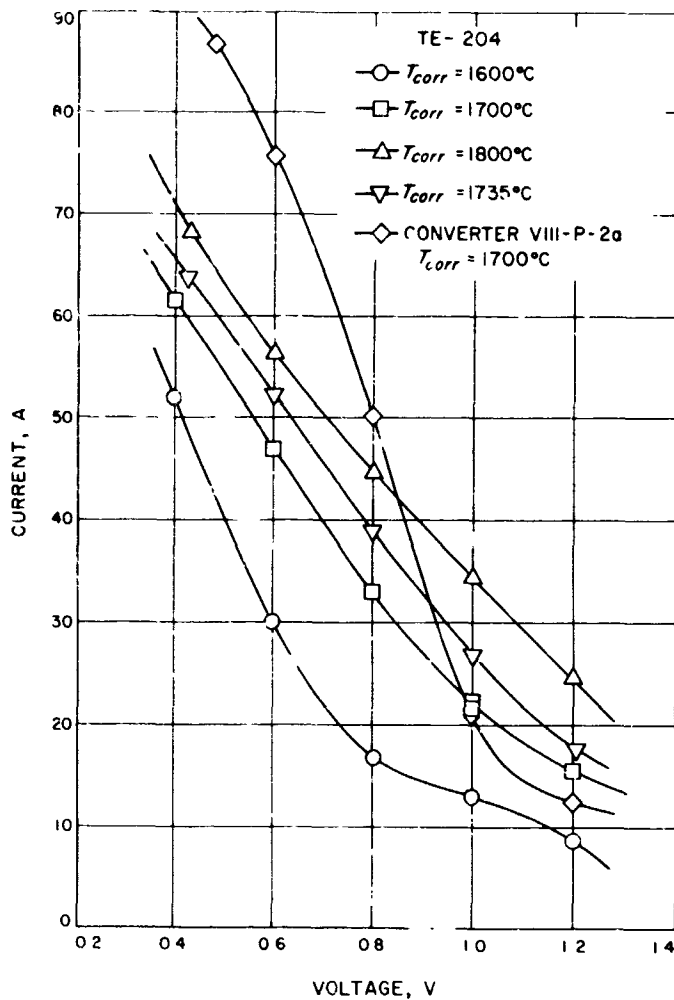


Fig. 15. TE-204 I-V characteristics

Included in Fig. 15 are results of the parametric tests of converter VIII-P 2, another prototype converter built in 1964 with 2.0 cm² of collector area, as compared with the 2.5 cm² collector area of converter T-204. It appears

that no major improvements in converter performances were achieved in converter T-204. The power density for T-204 at 1800°C emitter temperature was 12.6 W/cm² as compared to 28.5 W/cm² demonstrated in the older prototype.

Measurements were made of the collector and emitter work functions, assuming an emitter surface area of 2.75 and 2.55 cm² for the collector. The emitter work function was observed at three ratios of emitter-to-reservoir temperature (T_e/T_{cs}): 3.38, 5.57, and 3.76 resulting in calculated work functions (Φ_e) of 2.83, 3.08, and 3.27 eV, respectively. The apparent collector work function was observed at collector-to-reservoir temperature ratios (T_c/T_{cs}) of 1.51, 1.43, and 1.44, yielding collector work functions (Φ_c) of 1.55, 1.57, and 1.58 eV, respectively.

Attempts made to measure the interelectrode spacing by the cesium conduction method at first produced meaningless values because of imperfections in the measurement techniques. These were improved (SPS 37-43, Vol. IV, pp. 108-112), resulting in an average value of the interelectrode spacing of 1.6 mil as compared to a value of 1.8 mil spacing calculated by the manufacturer. During the measurement, difficulties were observed in optimizing the converter performance in the high emitter temperature range. This difficulty was traced to deficiencies in the heating and radiating properties of the cesium reservoir, which were corrected in converter T-204 by applying a high-emissivity coating on the cesium reservoir, and were eliminated in the next prototype converter (T-205).

b. Converter T-205. Converter T-205 was also built by GECo with an all-rhenium emitter and emitter support structure. The collector was molybdenum, but in converter T-205 the collector face was machine-polished, as

Table 1. Converter performance

Parameters	Converter T-204 (2.5 cm ²)						Converter VIII-17 (2 cm ²)					
	1576	1576	1705	1706	1765	1768	1558	1553	1647	1647	1740	1743
T emitter, °C (observed)	1576	1576	1705	1706	1765	1768	1558	1553	1647	1647	1740	1743
T collector, °C (measured)	609	681	784	860	831	903	477	594	613	700	628	715
V output, V	0.8	0.6	0.8	0.6	0.5	0.6	0.8	0.6	0.8	0.6	0.8	0.6
I output, A	17.0	30.2	29.0	52.4	44.6	56.3	11.4	34.1	34	54	53.4	72.2
V open circuit, V	1.2	1.2	1.5	1.5	1.7	1.7	2.25	2.0	2.1	1.85	1.84	1.78
W output, W	13.6	18.2	31.2	31.4	35.7	33.8	—	—	29.8	32.4	42.7	43.3
W input, W	222	258	351	392.5	398	434	170	240	291	350	383	470
Efficiency, %	6.12	7.02	8	8	8.97	7.79	5.6	9.5	9.4	9.3	11.2	9.2
Cs reservoir input power, W	5.6	3.96	0	0	0	0	2.32	1.35	1.39	0.88	1.29	0.84
Cs reservoir, °C	294	309	327	342	339	351	294	307	313	317	350	354
Radiator, °C	466	500	542	570	564	587	407	492	504	554	576	599
Vacuum, torr 10 ⁻⁷	7	9	4	4	5	5	4	4	3	3	2.8	2.8
Pyrometer correction, °C	23	23	32	32	35	35	47	47	55	55	60	60

opposed to the electro-etching used in converter T-204. The emitter in both cases was electro-etched and thermally stabilized. During the fabrication of converter T-205 the converter twice developed leaks which were repaired, the converter being re-outgassed and re-cesiated.

The results of the parametric measurements performed on converter T-205 can be observed in Fig. 16 and are summarized, again for two values of voltage output, in Table 2.

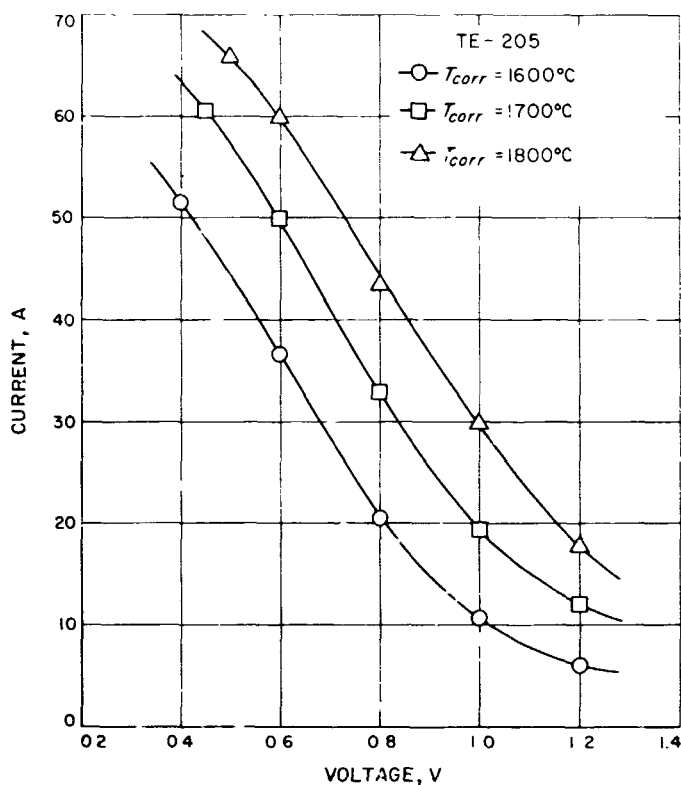


Fig. 16. TE-205 converter characteristics

The measurements of the emitter and collector work functions were performed assuming again a surface of 2.75 cm² for the emitter and 2.5 cm² in case of the collector. The emitter work function measurements were performed at T_e/T_{cs} ratios of 3.96, 4.17, 3.76, and 3.54, yielding respective values of emitter work function of 3.22, 3.49, 3.00, and 2.87 eV. In the case of the collector work function, the ratios of T_c/T_{cs} were 1.70, 1.60, 1.53, and 1.45 and resulted in values of the apparent collector work function of 1.30, 1.35, 1.41, and 1.49 eV. The emitter work function values agree with those observed in converter T-204 and other converters with rhenium emitters. The collector work function, however, was lower in case of converter T-205 than that observed in converter T-204 (1.58 eV in T-204 versus 1.49 eV in the case of T-205). This difference was attributed to a possible contamination of the collector surface by adsorbed gases, as result of the double re-cesiation operation. Such contamination could have a marked influence on the converter's performance (SPS 37-29, Vol. IV, pp. 20-25).

The measurement of the interelectrode spacing by the cesium conduction technique yielded a value of 3.0 mils by "curve fitting" and 2 to 2.5 mils by direct measurements. The value assumed by the manufacturer was 4.0 mils.

During the measurements, consistent discrepancies were observed between the test data supplied by the manufacturer and the data observed at JPL (Fig. 17). These discrepancies may be attributed to differences in the emitter surface temperatures as the result of differences in the pyrometer corrections and also to differences in the shapes of the electron bombardment filaments. These differences could have induced errors in the observed emitter temperature and the thermal flux distribution

Table 2. Converter performance

Parameters	T-205 (2.5 cm ²)						VIII-P-2 (2 cm ²)					
	1585	1583	1660	1659	1760	1758	1575	1575	1676	1675	1775	1775
T emitter, °C (observed)	1585	1583	1660	1659	1760	1758	1575	1575	1676	1675	1775	1775
T collector, °C (measured)	675	749	767	849	864	951	405	447	608	724	719	789
V output, V	0.8	0.6	0.8	0.6	0.8	0.6	0.8	0.6	0.8	0.6	0.8	0.6
I output, A	22.6	375	33	50	43.5	60	11.4	19.4	50.3	76	68.1	88.0
V open circuit, V	1.55	1.6	1.6	16.5	1.7	1.75	2.2	2.25	2.2	1.8	1.96	1.8
W output, W	18.08	22.5	26.4	30.0	34.8	36.0	9.12	11.64	40.65	47.6	54.5	53
W input, W	245.1	286.0	314	361.4	402	456	208	226	385	464	525	558
Efficiency, %	7.37	7.86	8.4	8.3	8.66	7.9	4.38	7.26	10.56	9.83	10.4	9.48
Cesium reservoir input, W	5.12	4.95	7.6	8.4	9.45	9.45	2.56	1.87	0.75	—	—	—
T cesium reservoir, °C	289	297	331	350	362	369	296	298	330	353	352	363
T radiator, °C	480	512	524	554	564	589	327	342	450	501	500	529
Vacuum, torr 10 ⁻¹	2	3	2	3	3	4	20	20	20	20	20	20
Pyrometer corrections, °C	37	37	41	41	44	44	25	25	25	25	25	25

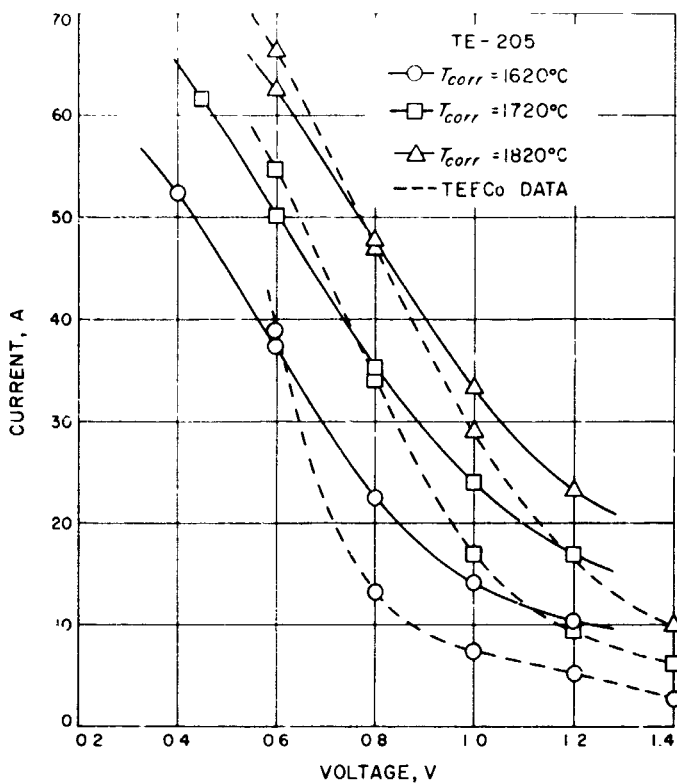


Fig. 7. Measurement comparison

along the emitter of between 11 and 15°C, as can be observed by comparing the curves in Figs. 16 and 17. In all cases it was noted that the collector surface temperature was too high for an optimum output. The low performance observed in this converter could be attributed at least partially to these excessive collector temperatures, which are the result of excessive collector barrel length and a deficiency in the radiator area and radiative coating emissivity.

c. Converter VIII-R-2. The converter VIII-R-2 is similar in construction to other converters of the series VIII (SPS 37-31, Vol. IV, pp. 53-58 and Fig. 18), except that the emitter was built of a single rhenium slab 120 mils thick, and the emitter supporting sleeve was also made out of thin rhenium tubing. Such construction was first tested under the thermal energy storage (TES) program (SPS 37-36, Vol. IV, p. 46) and was found to be successful.

Converter VIII-R-2 was built by TEECo as part of an evaluation program in which four identical converters were to be supplied. Two of the converters were to contain "cesium only"; the two others were to be built with cesium and additives. The converters supplied were to be evaluated at JPL for performance and life time. Difficulties were encountered during the program in: procurement of leak-tight thin-wall rhenium tubing; the

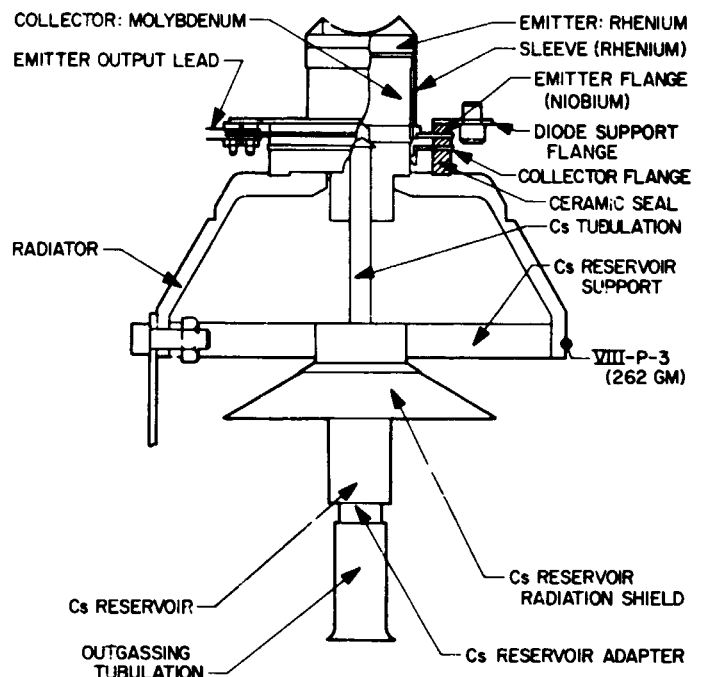


Fig. 18. Series VIII converter

evaluation of the thermal conductivity of bulk rhenium material (Refs. 1 and 2); and the selection of appropriate additive. The latter problem, in which cesium fluoride, selected as a first approach, will be replaced by oxygen, is still under investigation.

The results of the parametric tests of converter VIII-R-2 are presented in Fig. 19 for three values of emitter temperature and are compared with typical values observed in other converters of the series VIII. The differences in performance could not be satisfactorily explained. They may be the result of a larger-than-anticipated thermal drop through the rhenium emitter slug, resulting in a cooler-than-calculated emitter surface temperature.

The emitter and collector work-function measurements yielded an average value for the emitter work function of 3.41 eV and a value of 1.69 eV for the collector work function. The interelectrode spacing, computed by a curve-fitting method from the cesium conduction data, was estimated to be 2.5 mils.

u. Converter VIII-S-14 tests in a simulated generator environment. During the tests of the thermionic generator JG-3 (SPS 37-40, Vol. IV, p. 9) it was observed that for similar emitter hohlraum temperatures, the behavior of the converters was different when tested individually, than when mounted in a generator block. It was hypothesized that the differences in heat rejection from the

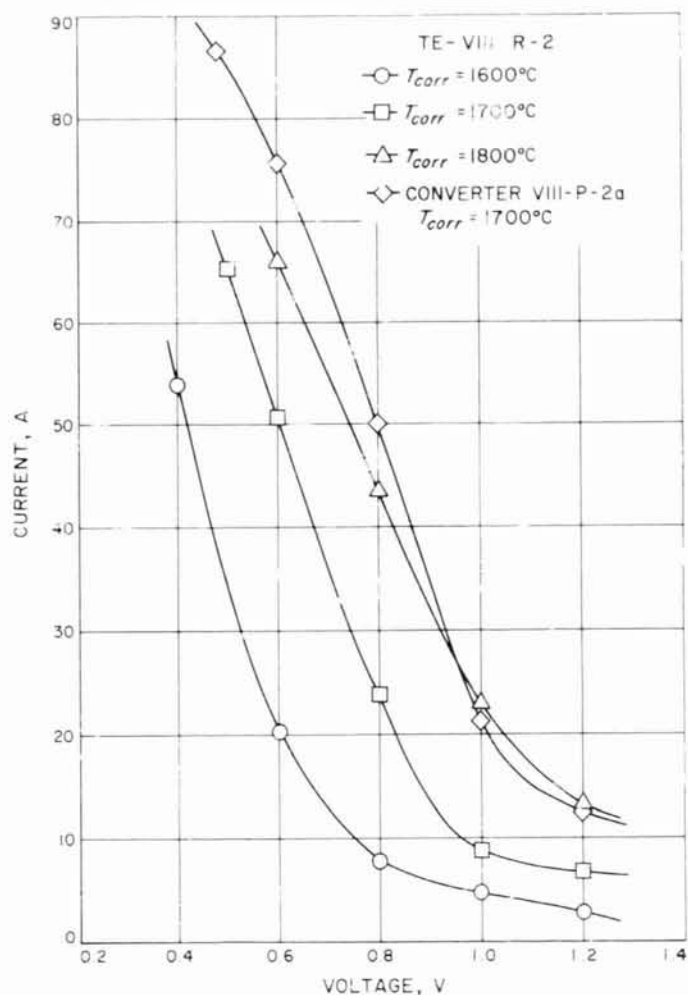


Fig. 19. VIII-R-2 converter characteristics

emitter sleeve changed its thermal expansion, thus increasing the interelectrode spacing in the converters. Experiments were performed to simulate the generator conditions by surrounding the converter with a heavy molybdenum block (Fig. 20). The performance of the converter in all cases indicated a sharp decrease when compared with the data observed for the same converter without the molybdenum block. The comparative data is presented in Fig. 21. This decrease in performance was attributed to an increase in the interelectrode spacing as the result of the larger expansion of the thin emitter sleeve.

Calculations of thermal expansion with and without the moly block¹ were performed for a low current, high voltage (1.2 V) output to minimize the thermal effects of I²R heating. The assumed heat distribution along the emitter sleeve for an observed emitter temperature of 1700°C is

¹S. S. Laebbers, private communication.

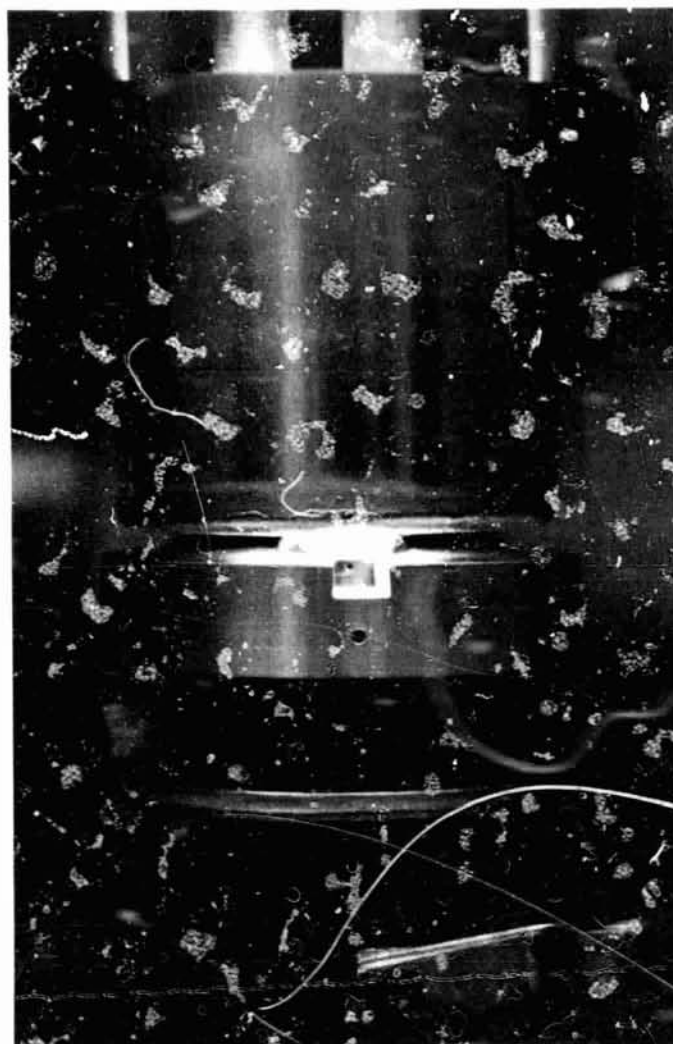


Fig. 20. Converter in-block simulation

Table 3. Differential expansion measurement conditions

Measurement performed at low current, high voltage (1.2 V) for minimum I ² R heating, emitter temperature 1700°C (corrected)		
Parameters	Without block	With block
Temperature collector ₁ , °C	514	568
Temperature collector ₂ , °C	475	531
Temperature seal, °C	561	612

Note: See Fig. 23 for collector thermocouple locations.

presented in Fig. 22. The thermal conditions as observed in support of these calculations are presented in Table 3 and the significant dimensions are indicated in Fig. 23. The calculations for the expansion of the emitter sleeve, collector and seal, with and without the moly block, performed using the dimensions presented in Fig. 23 and the

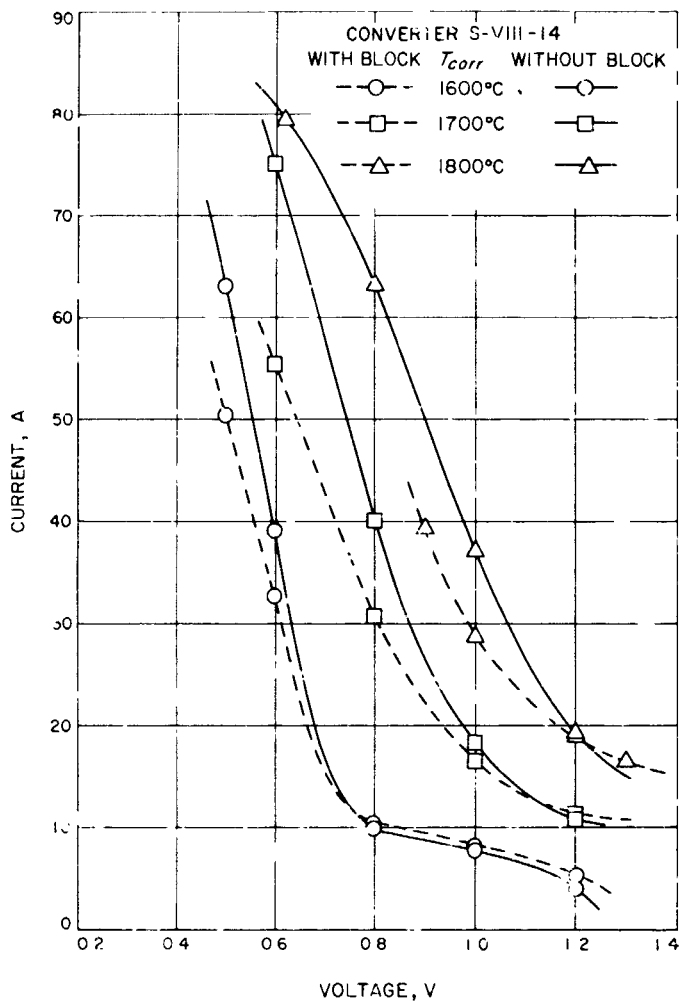


Fig. 21. Converter performance comparison

Table 4. Interelectrode spacing, differential expansions^a

Parameters	Without moly block, mil	With moly block, mil
Sleeve	+ 2.75	+ 5.12
Collector	-1.56	-1.72
Seal	+0.54	+0.62
Total	1.73	4.02

^aAssuming thermal distribution, as per Fig. 22
 $\alpha_{TA} = 6.5 \times 10^{-6}/^{\circ}\text{C}$
 $\alpha_{Mo} = 5.4 \times 10^{-6}/^{\circ}\text{C}$
 $\alpha_{Nb} = 8.1 \times 10^{-6}/^{\circ}\text{C}$

assumed thermal distribution, are presented in Table 4. The differential expansion appears to increase the interelectrode spacing by 2.3 mils when the converter was tested with the molybdenum block. This expansion appears to be too large, a 1 to 1.5-mil expansion being a more likely figure, but the calculations and the test results confirm that a significant increase in interelectrode spacing

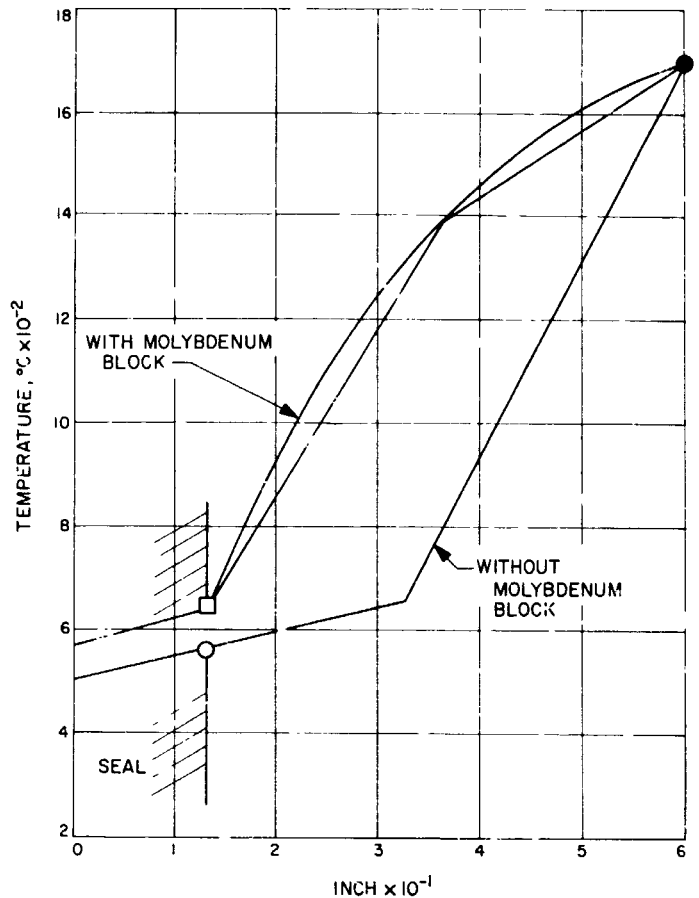


Fig. 22. Temperature profiles

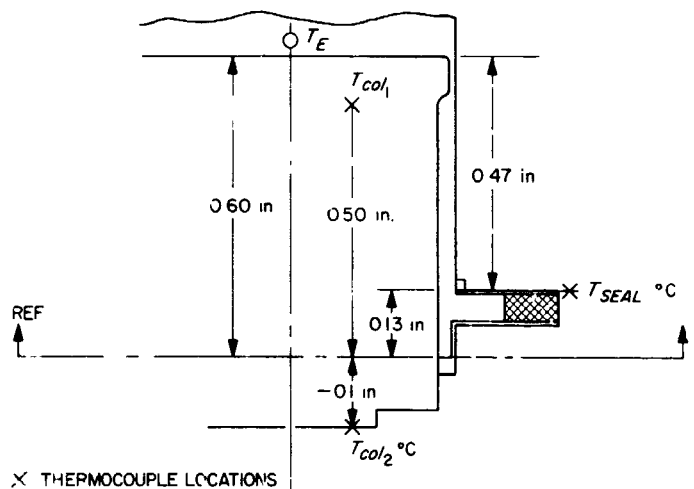


Fig. 23. Constructional dimensions

ing occurs when the converters operate in an enclosed condition such as presented by a generator block. The changes in the values of the voltage-current characteristics, observed by inserting the converters into the generator, correspond to those observed during the tests

performed with and without the molybdenum block, using converter VIII-S-14. This again supports the assumption that the increase in interelectrode spacing was responsible for the difference in converter behavior observed during the generator tests.

2. Heat Pipe

The transmission and distribution of the heat generated from a thermal source, such as the concentrated solar energy flux absorbed by the walls of a cavity, or the heat resulting from the decay of radioisotopes, can present significant engineering problems. Experimental data obtained during solar tests of thermionic generators indicated that the solar heat concentrated in the focal spot of a parabolic mirror could not be distributed evenly along a long cavity by multiple reflection without a very large thermal loss penalty. This fact restricts the size and geometry of solar thermionic generators. The heat produced by the decay of many isotopes has too low a thermal flux density to be directly used in thermionic energy conversion. The large volume of some isotope materials required can create difficulties in extracting the heat from the isotope mass because of the generally low thermal conductance of the fuel form. This low thermal conductance could result in a large thermal drop between the center and the outer surface of the isotope mass, creating excessive temperatures in the region of the centerline.

The addition of metallic doping to the fuel form could increase its thermal conductance, but will further decrease its thermal density, resulting in an increase of the required fuel inventory. Other problems such as attachment of a heavy fuel-capsule mass to the emitter slab, the effect of this mass during inflight shock and vibration, and the possibility of secondary radiations from the inclusions in the fuel, also create additional difficulties.

The use of relatively heavy metal radiator fins for heat rejection is limited by the heat conduction in the metal, the heat rejection capability of the fin surface, the dimensional and weight constraints imposed by the view angle factors, and the generator geometry and location on the spacecraft.

The high thermal conductance device (Ref. 3) commonly known as a "heat pipe" appears as a solution to the many problems involving the transfer and distribution of heat.

a. Heat pipe considerations. In its simplest form, the heat pipe consists of a hollow evacuated container of cylindrical, rectangular, or other geometry, the inner

walls of which are lined with a continuous capillary structure (Fig. 24). This capillary is saturated by a wetting liquid. The shape of the capillary (mesh, grooves, corrugation, or combination of the same) has some influence on the heat transfer, and the choice of the fluid used is limited by its wettability of the wick, compatibility with the heat pipe materials and by the operating temperature of the heat pipe. The heat supplied at the heat input end of the container converts the liquid into vapor, an action which absorbs large quantities of thermal energy (heat of vaporization). The vapor is transported along the hollow center of the container to the thermal output end of the pipe where it condenses to liquid, thus releasing the heat of vaporization. The liquid saturates the wick and travels by capillary action to the evaporation section at a rate determined by its physical properties, and the constructional characteristics of the capillary system. The heat pipe is thus a double-phase system with a continuous recirculation of the boiling and condensing fluid between a heat source and a heat sink. The liquid flow rate

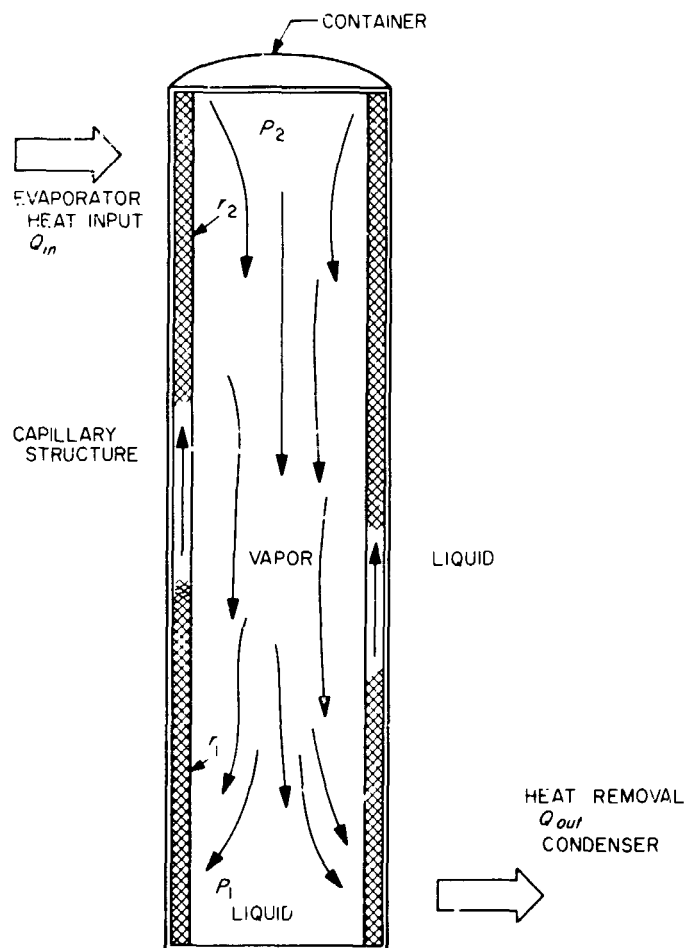


Fig. 24. Heat pipe schematic

required to successfully transfer large amounts of heat is relatively small. A flow rate of 2.7 cm³/s of lithium is capable of operating a heat pipe with a heat transfer of 2 thermal kW at 1300°C, while a mass flow rate of 1.5 g/s is sufficient to transfer 3.5 thermal kW at 2000°C in a tungsten-silver heat pipe.

The maximum heat transfer capability of a heat pipe, when operating free of external forces is:

$$Q = K \left[\frac{L y^2 \rho_v \rho_L}{b \eta l} \right]^{1/3}$$

where

Q = heat transfer, cal/s

L = heat of vaporization, cal/g

y = surface tension, dyn/cm

ρ_v = density of vapor, g/cm³

ρ_L = density of liquid, g/cm³

η = liquid viscosity, P

b = capillary constant ($\cong 16$ for groove, $\cong 20$ for wire mesh)

K = geometrical constant (function of the pipe geometry), cm^{5/3}

l = length of pipe, cm

Table 5. Properties of heat pipe fluids

Fluids	Melting point, °C	Boiling point, °C	Density, g/cm ³ at melting point	Latent heat vaporization, cal/g	Surface tension dyn/cm at melting point
Water	0	100	1.0	538	75
Indium	156	2087	7.0	468	630
Cesium	29	705	1.8	146	55
Potassium	64	760	0.82	496	100
Sodium	98	883	0.93	1005	190
Lead	327	1737	10.5	205	450
Lithium	179	1317	0.51	4680	398
Silver	960	2212	9.3	446	930

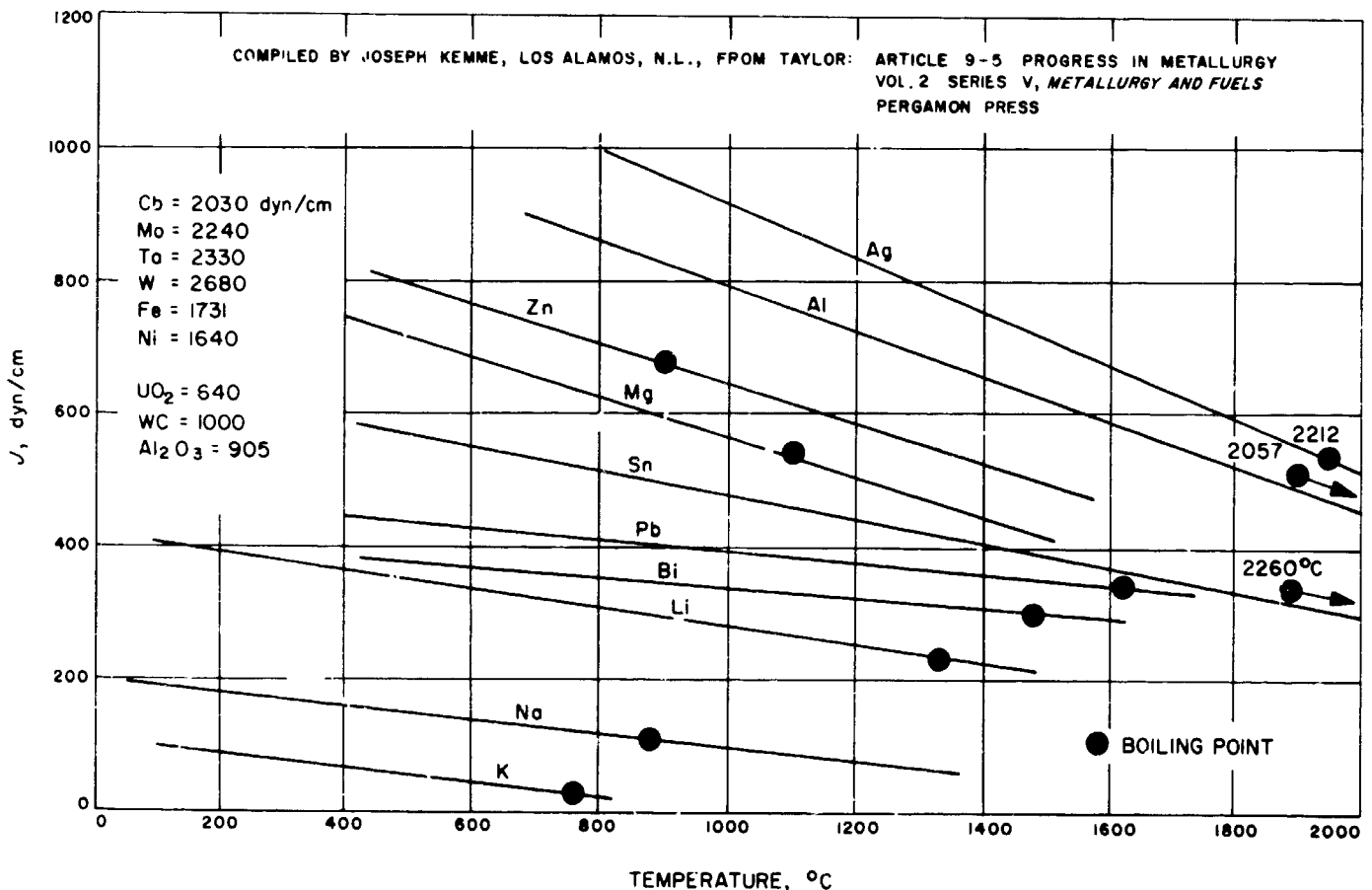


Fig. 25. Surface tension of metals

The maximum heat-carrying capacity of a heat pipe is roughly proportional to the square of the pipe diameter, inversely proportional to the length, and is also dependent upon the fluid viscosity, number and shape of the capillaries, etc.

A theoretical analysis (Ref. 4) performed to compare a tantalum solid rod with a tungsten-silver heat pipe of same cross section indicated that the heat transfer for the heat pipe was 10,000 times larger than for the rod. It was calculated that the heat pipe can transfer 520 times more heat per unit weight than any solid rod of the same cross section.

The outstanding characteristics of several materials considered as fluids for the heat pipe are presented in Fig. 25 and Table 5. The total thermal power transfer capability versus the operating temperatures, calculated for a unit heat pipe (1-in. diameter, 1-ft length) with a woven mesh is presented in Fig. 26. The effect of the optimization of the wick dimensions for maximum heat transfer is illustrated for sodium in Fig. 27. The limiting factors determining the range of operation of a heat pipe are the vapor pressure of the working fluid at operating temperatures, the compatibility of the fluid with the wick and container materials, the strength of the container material at the operating temperatures, and the phenomenon of nucleated wick boiling. The vapor pressures, at different temperatures, of several materials considered as possible working fluids for the heat pipe are presented in Fig. 28. In general, the selection of the fluid is performed based on an operating vapor pressure of 1 to 2 atm.

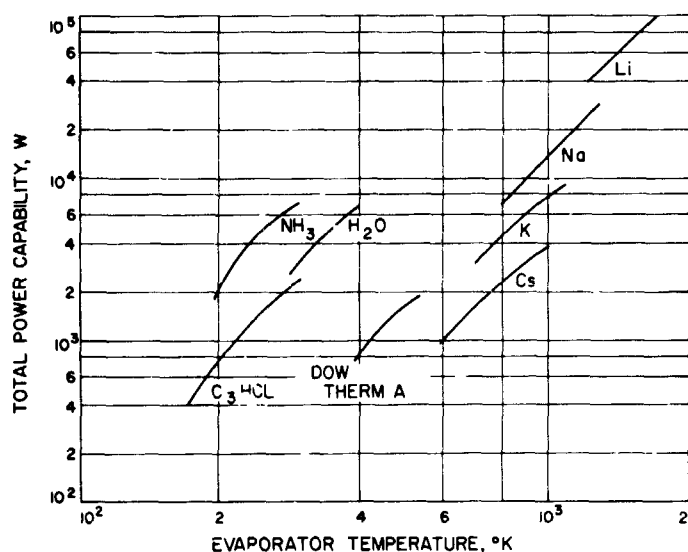


Fig. 26. Heat-carrying capacity of unit heat pipe

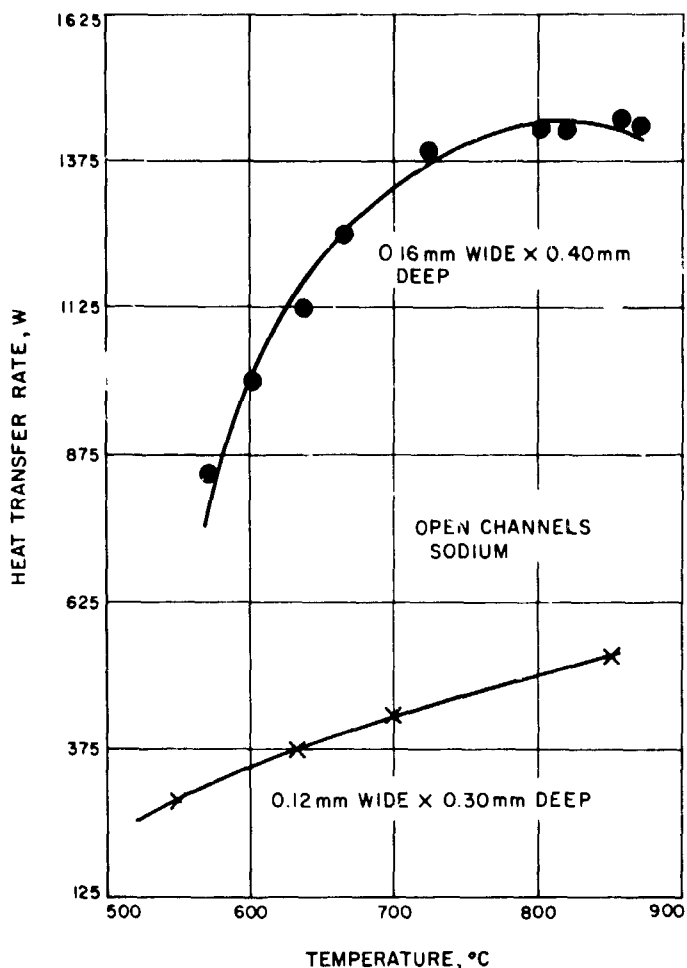


Fig. 27. Wick optimization

The heat pipe has several characteristics which help to make its application attractive:

- (1) It is practically isothermic axially or radially.
- (2) It is an extremely efficient heat transfer device.
- (3) It can operate as a thermal flux transformer.
- (4) It allows the separation of the thermal source from the point of utilization.
- (5) It can have a temperature-flattening effect.

Two parallel applications of the heat pipe are being pursued by JPL. Under contract with Radio Corporation of America (RCA), Lancaster, Pa., an effort is being pursued to integrate the heat pipe with thermionic converters. The heat pipe is used as a means of supplying heat to the emitters of the thermionic energy converters. The goal of the effort is the integration of the thermionic energy conversion with an isotopic thermal source. The second effort,

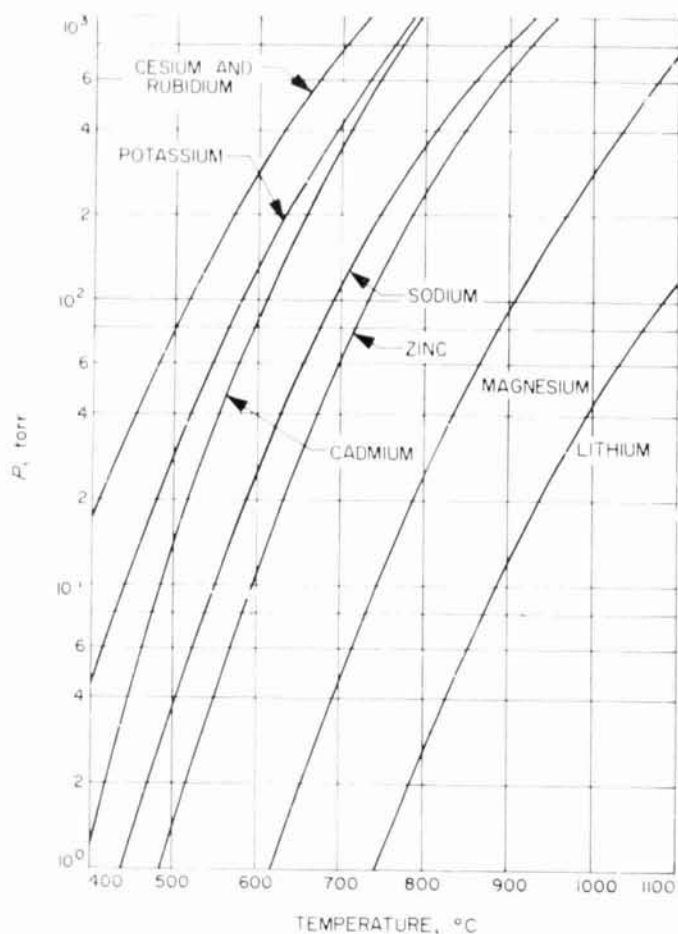


Fig. 28. Vapor pressures

being pursued at TEECo, covers the use of the heat pipe as a means for heat rejection from the collector of the thermionic converter, to replace the conventional radiator.

Under the RCA effort several outstanding achievements have been made. A heat pipe operating in the temperature range between 1500 and 1600°C has successfully achieved 8700 h of continuous operation, transmitting 5 kWt with a ΔT (between ends of the heat pipe) of less than 7°C (Fig. 29). Another heat pipe 32 in. long transmitted a maximum heat flux of 18.5 kWt with a ΔT of 10°C at 1500°C. Experiments in thermal density concentration demonstrate the possibility of concentration ratios of 10 to 1 (21 thermal W/cm² input-210 thermal W/cm² output) at 1500°C and 4.5 kWt.

An experimental heat pipe has been built and successfully operated to demonstrate not only the possibility of axial heat transfer but also the radial. This double-wall heat pipe shows valuable design approaches to solve the problems of increasing the surface utilization.

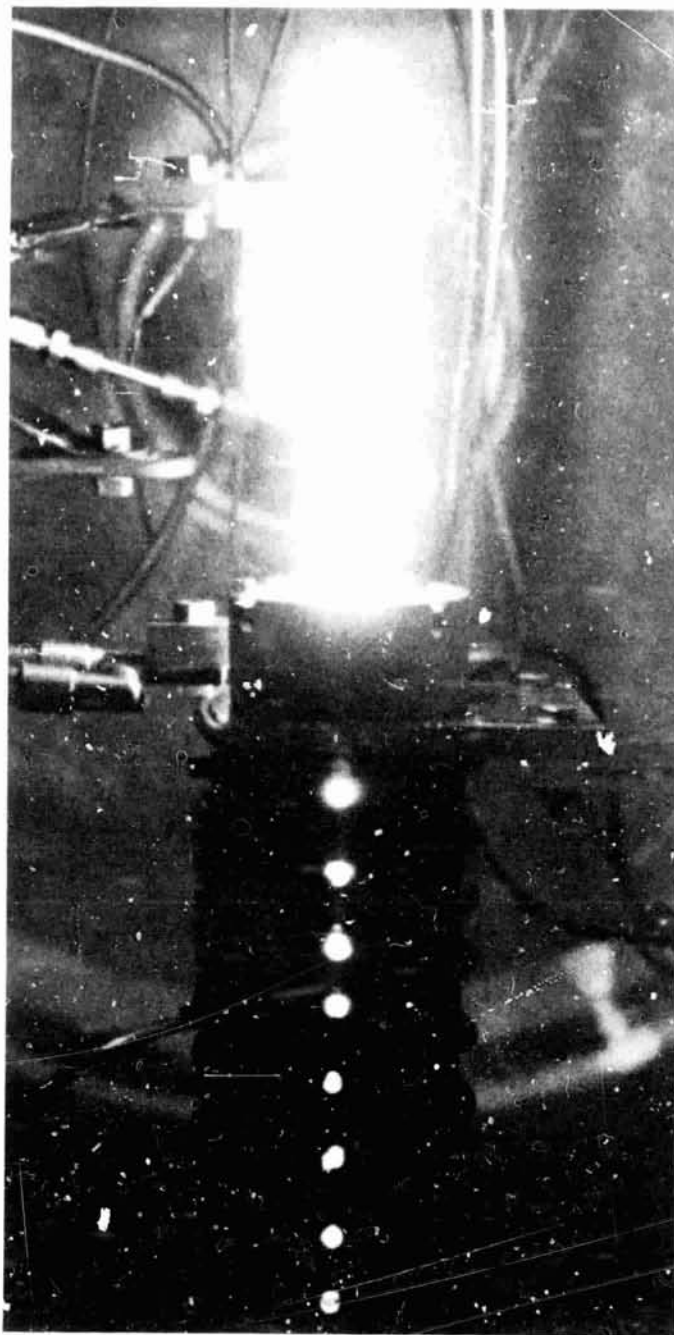


Fig. 29. Heat pipe in operation

The heat pipe and a thermionic converter have been successfully integrated. Using electrical resistance heating, the system demonstrated an efficiency of 13.4%, the emitter of the converter operating at 1490°C. The output of the converter was 250 A at 0.665 V. This effort is now being continued with emphasis on the improvement in the wick structure to demonstrate a minimum heat transfer capacity of 20,000 thermal W and the successful integration and operation of two thermionic converters for

1000 h of continuous operation. The minimum output of the system was fixed at 225 electrical W.

The effort at TEECo has as a goal the incorporation of the heat pipe concept to transfer heat between the collector face and a radiator of a thermionic converter. The thermionic structure of the series IX converters was retained, and a suitable heat pipe structure was added to the collector. The walls of the heat pipe were designed to act as the radiator. The concept is shown in Fig. 30. The fluid selected for the heat pipe operation is sodium with niobium being used as the container. Calculations performed on the thermal/electrical energy balance in the converter indicated a requirement of heat rejection of 150 W.

Considering a radiator emittance of 3.92 W/cm^2 the radiator area should be approximately 37.5 cm^2 , and with a total emissivity of 0.85, should operate at 951°K . The calculated heat pipe dimensions are:

Vapor conduit length, 9.75 cm (3.85 in.)

Vapor conduit cross section, 1.60 cm^2

Capillary mesh wire diameter, 0.0025 cm

Fluid flow (sodium), $3.75 \times 10^{-3} \text{ g/s}$

The minimum permissible number of capillaries was calculated to be 800 for a pressure drop of $1.03 \times 10^4 \text{ dyn/cm}^2$. Two wraps of 400 mesh size capillary were selected. The total weight of the converter was calculated to be 70.7 g, resulting in a minimum specific weight of 4 lb/kW.

Experiments performed on such a structure outlined areas of trouble, specifically, the weld between the fluid

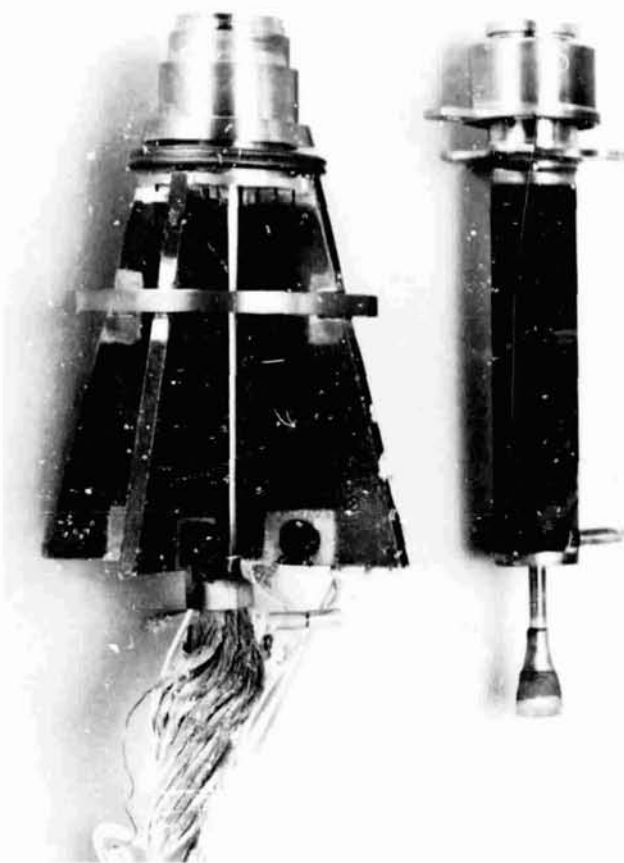


Fig. 30. TEECo converter-heat pipe

filling pipe and the heat pipe. Also, a severe reaction was observed when the high-emissivity coating (chromium oxide) embrittled the niobium heat pipe after a bake-out at 1400°C .

References

1. Kitrilakis, S., et al., JPL Contract 950671, Task IV, "Final Report," Vol. 1, pp. III 43-52. Jet Propulsion Laboratory, Pasadena, California.
2. June, C. K., and Hoch, M., "Thermal Conductivity of TA, W, Rh, TA-10% W at Temperature Range $1500-2800^\circ\text{C}$." University of Cincinnati, Ohio.
3. Grover, G. M., et al., "Structure of Very High Thermal Conductance," *J. Appl. Phys.*, p. 1990, 1964; Cotter, T. P., "Theory of Heat Pipes," LA-3247. Los Alamos Scientific Laboratory, New Mexico, March 26, 1965.
4. Deverall, J. E., and Kemme, J. E., "High Thermal Conductance Devices Using the Boiling of Lithium or Silver," LA-3211. Los Alamos Scientific Laboratory, New Mexico, October 1964.

N67-34765

IV. Guidance and Control Research

GUIDANCE AND CONTROL DIVISION

A. Reduction of Plasma Maintenance Voltage With Magnetic Field, K. Shimada

1. Introduction

Thermionic energy converters are considered as potential energy-conversion devices having a medium power capability. They already have shown substantial progress in their power output (18 W/cm^2), efficiency (14%), and in prolonged operation (10,000 h/diode). However, further improvement in the output voltage is highly desirable for the device to become operational since the over-all efficiency of the energy-conversion system, which includes power conditioners and the interconnecting bus-bars between thermionic energy converters, becomes higher as the output voltage of the converters becomes larger.

One approach in increasing the output voltage is to choose or to prepare the electrode surfaces so that a desired contact potential can be maintained at reduced cesium pressures. This approach would result indirectly in the reduction of electron scattering by electron-neutral

collisions (transport losses). Another approach is to reduce collisional losses, inelastic as well as elastic ones, by reducing cesium pressures. In the latter approach, the electron space charge must be neutralized by ions which are generated without expending those electrons which are to reach the collector for the production of electrical power output. In order to achieve such a mode of operation, the surface ionization must be copious and/or the interelectrode gap must be extremely small. Use of an auxiliary discharge was examined by various investigators with limited success.

In contrast to the aforementioned methods, we have chosen a method of producing ions in the interelectrode space using principles similar to those which govern the Penning-type discharge. We have designed an experimental cesium diode which has electron-emitting side walls in addition to the planar part of the emitter. A magnetic field is applied externally with its direction normal to the surface of the planar part of the emitter. Consequently, only those electrons emitted from the side wall are subjected to the Lorentz force created by the transverse magnetic field. These electrons move in

BLANK PAGE

circular paths as they traverse from emitter to collector under the influence of the external magnetic field. Since they are accelerated through the emitter sheath as they enter the interelectrode space, and since they traverse a distance substantially longer than the electron mean-free-path, which by choosing the cesium pressure can be made approximately equal to the gap between the planar parts of the electrodes, these electrons can make ionizing collisions with cesium atoms in the interelectrode space.

Preliminary measurements of the plasma maintenance voltage of our experimental cesium diode indicate that a reduction of this voltage from 1.75 to 1.35 V can be achieved with the application of an external magnetic field of the order of 100 G.

2. Experiments

A specially designed thermionic cesium diode was fabricated at Thermo Electron Engineering Co., Waltham, Mass. This diode has tantalum electrodes; the emitter has electron-emitting side walls in addition to the planar emitter area which is parallel to the planar collector face. The interelectrode distance is 0.028 in. between two planar surfaces of electrodes; the height of the emitter side wall is also 0.028 in. In other words, the emitter forms a shallow cup which is loosely fitted with the collector at its opening, as shown in Fig. 1. The diode is placed in a vacuum bell jar which is pumped down to the 5×10^{-8} -torr range with a 400-l/s vac-ion pump. The emitter of the experimental diode is heated by a Pierce-type electron gun (SPS 37-41, Vol. IV, pp. 46-48) which is physically separated from the diode by a distance of approximately 5 in. This method of heating is selected in order to make accurate determination of the emitter heating power; the direct radiation heating by the gun filament, which contributes to the emitter heating in ordinary methods, is eliminated in our method since the gun filament is far removed from the emitter surface. Also, a solenoid installed in the extra space

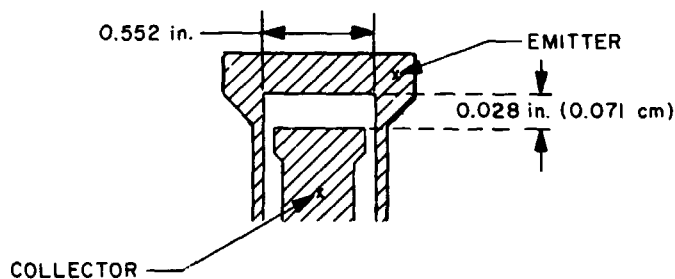


Fig. 1. Emitter-collector structure

between the gun and the emitter provides the external magnetic field in the emitter region of the experimental cesium diode. The solenoid is water-cooled and can provide a dc magnetic field having an intensity up to 400 G at its center, where the emitter of the test diode is located. Emitter temperatures are measured at a black-body hole (depth-to-diameter ratio = 8) by a calibrated Mikro-Werk Optical pyrometer. Temperatures of the cesium reservoir (T_{cs}) and the collector radiator (T_c) are measured by uninterrupted chromel-alumel thermocouples. Cesium reservoir temperatures are maintained within $\pm 0.5^\circ\text{C}$ during measurements which require constant T_{cs} .

The volt-ampere characteristics were examined for a range of cesium temperatures between 130 and 200°C , and for a range of emitter temperatures between 900 and 1700°C . It was quickly found that the external magnetic field had an appreciable effect only for cesium temperatures between 130 and 150°C . In fact, such temperatures

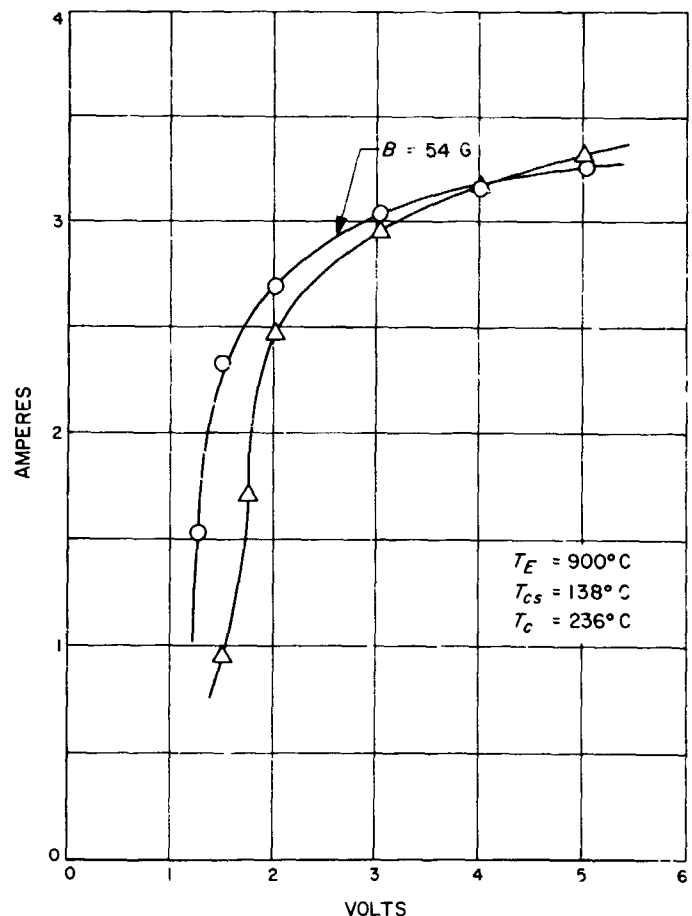


Fig. 2. Volt-ampere curves: $T_E = 900^\circ\text{C}$,
 $T_{CS} = 138^\circ\text{C}$, $T_C = 236^\circ\text{C}$

fall in a range where the electron-neutral mean-free-path is comparable with the interelectrode spacing of 0.028 in. (0.071 cm). Optimum emitter temperatures which yield significant current through the diode are then determined to be approximately 1000°C.

The diode is operated in the plasma mode (SPS 37-44, Vol. IV, pp. 59-63) where a positive voltage as large as 5 V is applied to the collector, with respect to the emitter of the diode.

The volt-ampere characteristics are obtained point-by-point after thermal equilibrium is reached at each data point. Heat-balance data are also obtained at corresponding points of the volt-ampere characteristics. Results obtained by the heat-balance experiments were reported in SPS 37-44, Vol. IV, pp. 59-63.

Typical volt-ampere curves are shown in Figs. 2, 3, and 4. Also shown in the figures are the volt-ampere

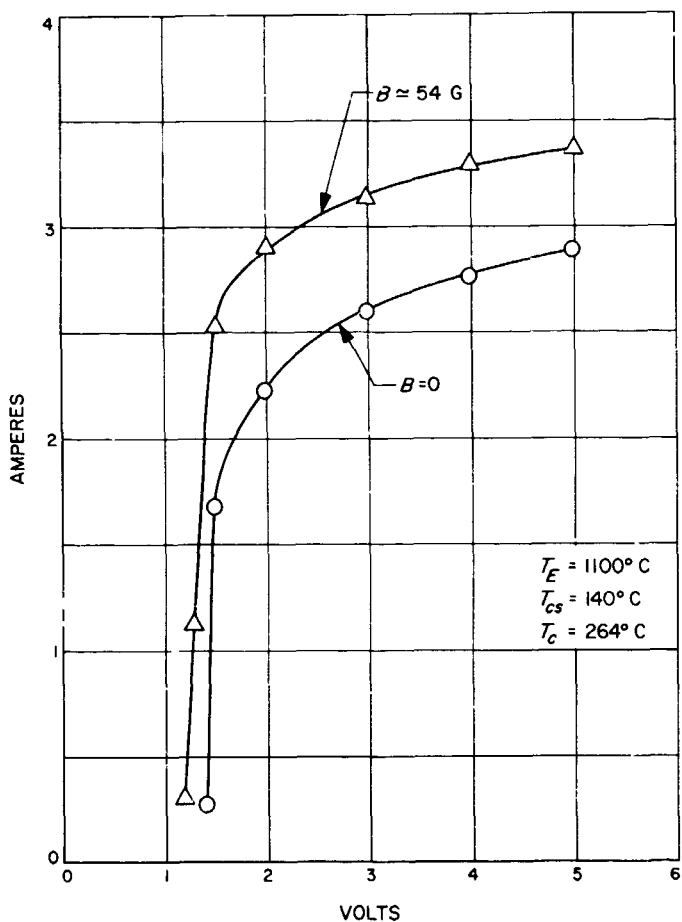


Fig. 3. Volt-ampere curves: $T_E = 1100^\circ\text{C}$, $T_{CS} = 140^\circ\text{C}$, $T_C = 264^\circ\text{C}$

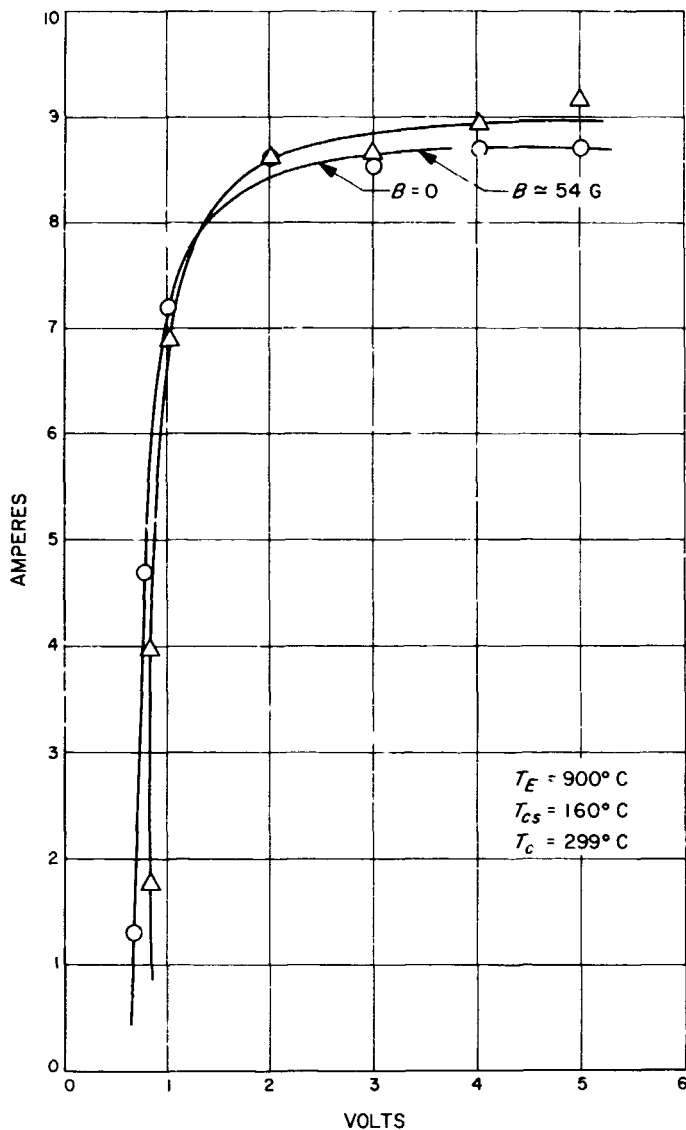


Fig. 4. Volt-ampere curves: $T_E = 900^\circ\text{C}$, $T_{CS} = 160^\circ\text{C}$, $T_C = 299^\circ\text{C}$

characteristics obtained after an external magnetic field is applied.

3. Discussion

An ion current as large as 30% of the total current flows through the diode when it is operated in the plasma mode. The magnitude of the ion current is considerably larger than that which is found in conventional thermionic energy converters operating in an ignited mode. The emitter work function of the experimental diode is approximately 2 V, which is 0.5 V lower than the value expected from the Warner-Rasor theory of cesiated surfaces. Further study of such behavior in the plasma mode is now in progress.

The effects of an applied magnetic field are noticeable only when $T_{cs} \approx 130^\circ\text{C}$, at which the electron-neutral mean-free-path is approximately 0.2 cm; the interelectrode gap is approximately one-third of the mean-free-path at this temperature. At a current of 2 A (0.75 A/cm²), the voltage drop across the diode is 1.75 V when the diode is not immersed in a magnetic field, whereas it is 1.35 V when the magnetic field of 54 G is applied. An increase of the saturation current is also noticed at an emitter temperature of 1100°C and a cesium temperature of 140°C. The amount of this increase is approximately 30%, nearly double that which is expected from the additional emission from the side wall of the emitter. This will be investigated further with an experimental diode having different side-wall areas.

In conclusion, the external magnetic field exhibits positive results in reducing the voltage drop in the plasma only when the cesium pressure is such that the electron-neutral mean-free-path is comparable to the interelectrode gap. Heat-balance experiments are expected to provide further insight into the process of ion formation in a diode which is operating in a mode similar to Penning's discharge.

B. Noise of Unipolar Space-Charge-Limited Current in Solids, M-A. Nicolet¹

1. Introduction

It has been stated in the literature that unipolar space-charge-limited current (sclc) should exhibit reduced shot noise (Ref. 1). The prediction is based on the analogy which exists between sclc in a solid and in vacuum, where shot noise is known to be reduced by a space-charge suppression factor $F < 1$. An analysis has recently been published which attempts to establish the fact more rigorously (Ref. 2). Experimental verifications are still awaited. This article points out that there is at least one *limiting* case of operation of sclc in a solid in which shot noise may be suppressed little, if at all, and for which no analogous situation exists in vacuum.

Sclc in its pure form, free of any trapping, has been observed mainly in germanium and silicon (Refs. 3, 4). In both cases, it was found that, in general, the free charge carriers are not in thermal equilibrium with the lattice. Rather, it is more proper to assume that the charge car-

riers are tepid or hot, in which case the value v of the drift velocity depends upon the strength E of the electric field as $v \approx E^{1/n}$, with $n = 2$ for tepid and $n = \infty$ for hot-charge carriers. In this latter alternative, the charge carriers move at a constant "saturation velocity" v_s , independent of the field strength. Hot-charge carriers are observed regularly in the upper voltage and current range of sclc in Ge and Si. The V-I characteristic in this range of operation can be interpreted satisfactorily by assuming that: (1) the charge carriers move at constant saturation velocity v_s throughout the base width of the diode, and (2) diffusion and initial velocities of emission are negligible (SPS 37-37, Vol. IV, pp. 64-68).

2. Noise

The shot noise predicted under these conditions must be uncorrelated, because the model allows neither for a virtual emitter nor for an influence on the charge motion by Coulomb interaction. A power spectrum for the shot noise can then be obtained by finding the differential current pulse $i(t)$ due to the transit across the base of an individual charge moving at constant speed v_s . The Fourier transform $F(\omega)$ of this current pulse and its average rate of occurrence I/q determine the power spectrum $W(\omega)$ according to

$$W(\omega) = 2(I/q)|F(\omega)|^2 \quad (1)$$

where I is the dc current flowing through the device, provided that the charge carriers are emitted into the base in a truly random sequence (Ref. 5). Rewriting $F(\omega)$ by setting $F(\omega) = qN(\omega)$, one obtains

$$W(\omega) = 2qI|N(\omega)|^2 \quad (2)$$

Figs. 5 and 6 show the result of such an analysis for the five distinct cases of planar ($k \rightarrow 1$), cylindrical and spherical geometries ($k \geq 1$ each). Details on the calculations of $i(t)$ are given elsewhere (Ref. 6). The transform $F(\omega)$ can be obtained analytically only in the planar case. Numerical integrations have been used for all other results.

3. Discussion

The validity of this approach may be questioned on two grounds. The justification of the model is based on experimental V-I characteristics. These measurements may be relatively insensitive to the details of the charge and field distribution in the vicinity of the emitter, while shot noise suppression may be critically sensitive to these details.

¹At the California Institute of Technology, performing work supported by JPL.

The assumptions of constant drift velocity and negligible diffusion are certainly poorest at precisely this location, so that noise suppression may actually persist even if the $V-I$ characteristic indicates velocity saturation. An answer to this objection could be furnished either by analyzing more sophisticated models or by experimental investigations.

Another flaw resides in the use of the current pulse $i(t)$. While in vacuum diodes such a pulse could actually be measured and is the consequence of the transit of an electron through the cathode-anode spacing, the meaning of $i(t)$ in the solid-state analogue is merely that of an average. The scattering of charge carriers in their path from emitter to collector by the lattice will introduce a fine structure on $i(t)$, the detail of which depends on the microscopic behavior of the charge carrier. Information of this type can be obtained only by abandoning the phenomenological description in terms of a mobility or drift velocity and replacing it by a complete microscopic picture of the dynamics and statistics of this motion. If m is the average number of scattering events during the transit time T_0 of a charge from emitter to collector, one would expect that for frequencies beyond m/T_0 the model based on $i(t)$ breaks down completely. It is difficult to make a more accurate statement without additional analysis.

The saturation velocities of electrons and holes in Ge and Si lie between 6 and 11×10^6 cm/s in the range of 77°K to room temperature. For a typical base width of

10 μ , this places the transit time in the neighborhood of 1 and 2×10^{-12} s, corresponding to submillimeter wavelengths at the point $\omega T_0 = 1$ in Figs. 5 and 6. Experimental techniques in that frequency range are difficult. There is little prospect for experimental data to shed light on this question in the immediate future. Experiments on the noise of unipolar sclc are thus most attractive in connection with the presence and/or absence of shot noise suppression at moderate and low frequencies, and as a function of the dc operating point. Practical limitations, such as power dissipation and long-term stability of the device, noise figure of the amplifier, its bandwidth and the possibility of $1/f$ noise may make such measurements rather difficult, though.

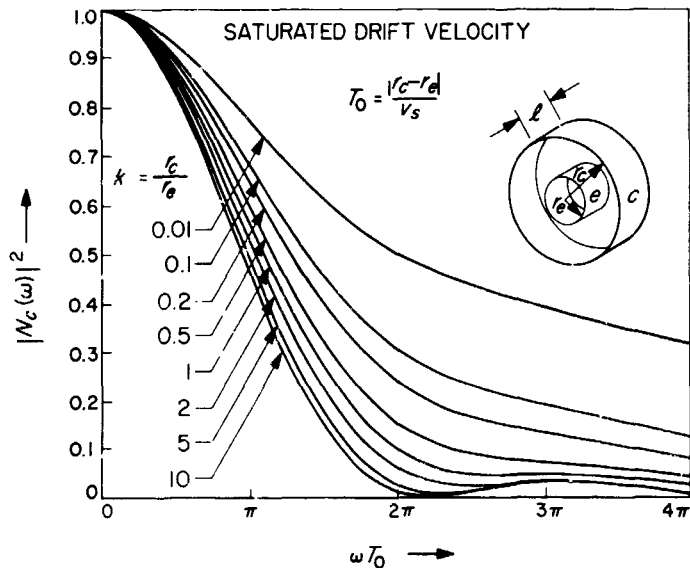


Fig. 5. Power spectrum of shot noise for unipolar sclc in a cylindrical device

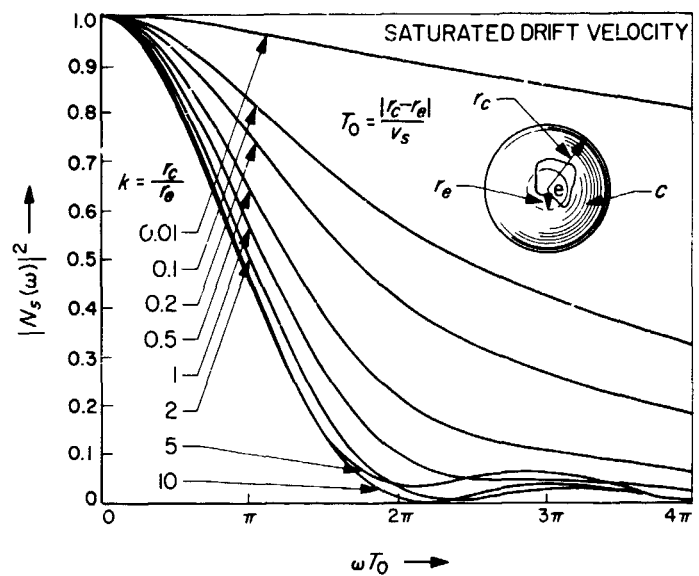


Fig. 6. Power spectrum of shot noise for unipolar sclc in a spherical device

C. Solid-State Triode: Gate Electrode Fabrication, A. Shumka

1. Introduction

Control and modulation of space-charge-limited current (sclc) in solids are essential if a solid-state triode is to be realized. Previous work has established the existence of sclc electron and hole currents in n^+pn^+ and p^+vp^+ germanium solid-state diodes respectively (SPS 37-39, Vol. IV, pp. 44-50 and Ref. 7). We will describe an approach for achieving control and modulation of these currents.

The solid-state triode offers several attractive features as a useful device: (1) it would have a good frequency

response because the charge transport is by drift; (2) it would be relatively insensitive to temperature changes because of the weak dependence of mobility on temperature; (3) it would be a majority carrier device and should have a low susceptibility to radiation damage; (4) it would be a low-noise device due to noise suppression by the space charge; and (5) it would have a high input impedance.

2. Model

The crucial part of a solid-state triode is the gate electrode by which control and modulation of sclc can be achieved. A gate electrode that would satisfy these requirements is shown in Fig. 7. It consists of a set of

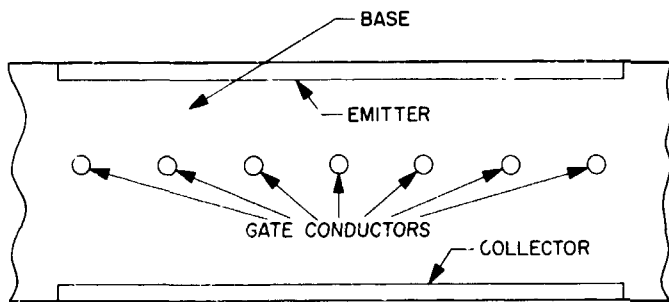


Fig. 7. Cross section of an ideal solid-state triode

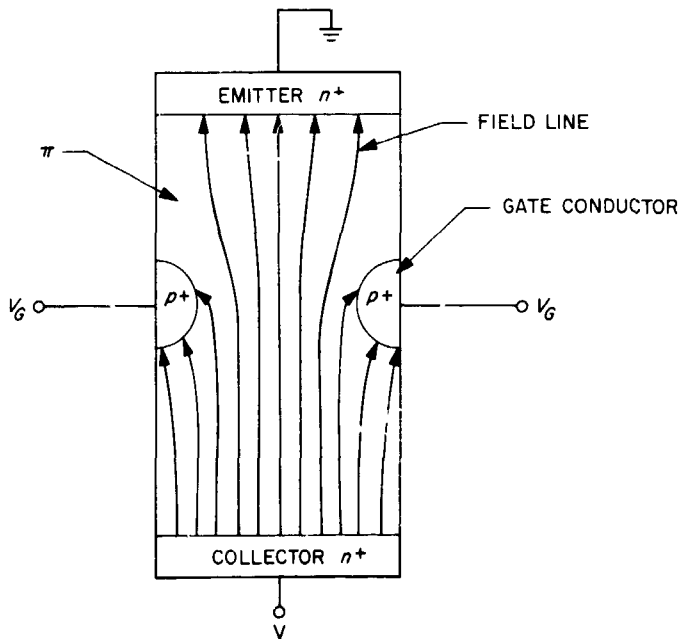


Fig. 8. Electric field line distribution in a solid-state triode for $V_g \leq 0$ V

closely spaced parallel conductors (p -type) embedded in the base of an $n^+ \pi n^+$ solid-state diode. Operation of the solid-state triode can best be understood from Fig. 8, in which a segment of a solid-state triode is shown. In Fig. 8, field lines emanating from the collector terminate on the emitter and on the gate. This is not a concise representation of the actual situation because some of these field lines will terminate on the injected charge carriers and on the fixed impurity ions present in the base. However, this distribution is used in order to obtain a simple qualitative picture of the solid-state triode.

The emitter current (electron current) is directly related to the number of field lines terminating on the emitter. This number can be modulated by varying the gate voltage. That is, if the voltage between the collector and the gate is increased while that between the emitter and collector is kept constant, fewer field lines will terminate on the emitter. The amount by which the emitter current changes for a given change of the gate voltage will depend largely on the position of the gate electrode with respect to the emitter, and also upon the separation distance between the gate conductors. The gate is neither a source nor a sink for the injected carriers but is capacitively coupled with the emitter. It is through this coupling that modulation takes place. An analogous structure in which n^+ -type conductors are embedded in the base of a $p^+ \pi p^+$ solid-state diode can also be used for scl hole-current control.

3. Experiment

There are several problems involved in the fabrication of a solid-state triode with the structure shown in Fig. 7. First, the gate conductors are buried in the base. Second, these conductors must be uniformly spaced and accurately positioned. Finally, the inserted gate conductors should not introduce any contaminants into the base. The difficulty of embedding the gate conductors can be bypassed provided that equally spaced channels (grooves) are cut in the solid-state diodes, as shown in Fig. 9. Alloyed into these channels are the gate conductors. These channels should not appreciably deteriorate the performance because those portions of the emitter and base that are normally shielded from the collector by the gate electrode are removed. The channels will provide a means of uniformly spacing and of accurately positioning the gate conductors. Furthermore, the alloying of these gate conductors can be accomplished without introducing any contaminants into the base.

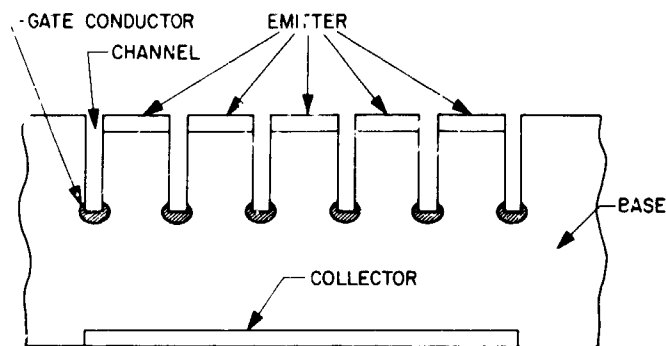


Fig. 9. A proposed solid-state triode with gate conductors alloyed into the channels

The simplest and most basic structure for a solid-state triode is one which contains only two gate conductors. For example, the solid-state triode shown in Fig. 9 can be considered to contain five of these structures in parallel. Consequently, all that is required is to investigate the feasibility of fabricating this structure.

A wire saw was used to cut two parallel and closely spaced channels in an $n^+ \pi n^+$ germanium solid-state diode. The cutting operation was as follows. A nichrome wire (5-mil diameter) was pulled across the surface of a germanium wafer onto which an abrasive slurry (0- to 3- μ grinding compound) was continuously fed. Wire speed and slurry consistency were such as to cut a groove 2.5 mils deep in approximately 15 min. A micro-positioner accurately positioned the wafer with respect to the wire. The depth of the cut was periodically monitored with a calibrated microscope.

A sketch of the first fabricated solid-state triode is shown in Figs. 10 (a) and (b). The channels were 10 mils wide and 2.5 mils deep, and the mesa was 4 mils wide. Three grooves were cut by the wire saw to obtain a channel 10 mils wide. The gate conductors less than 2 mils wide were alloyed into the mesa wall. Channels were cut in more than 20 samples to determine the accuracy of the wire-saw technique. Results indicate that the tolerances are ± 0.1 mils for the mesa width and ± 0.2 mils for the channel depth.

There are several limitations to the wire-saw technique. First, the mesa walls are curved because of the wire geometry. Second, it is difficult to monitor accurately the channel depth, as is evident from the ± 0.2 -mil tolerance given to this dimension. A new sabre saw is presently being designed which would circumvent these limitations. Essentially, it is a reciprocating blade saw

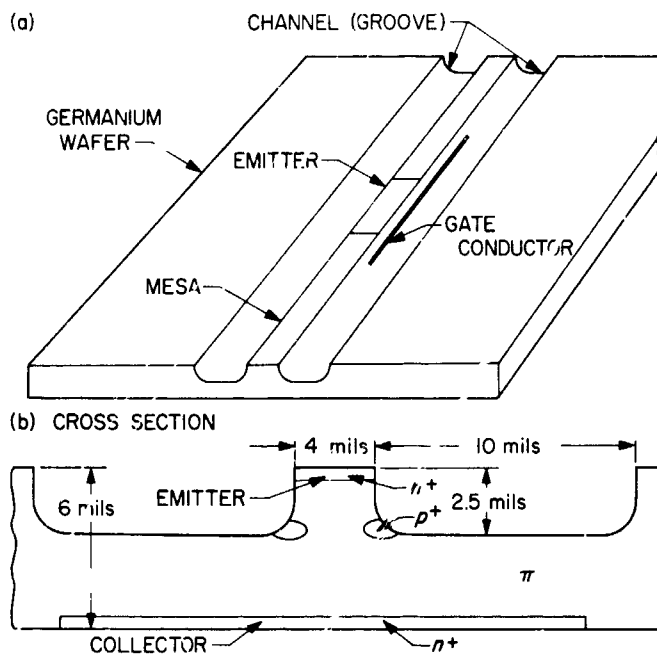


Fig. 10. Fabricated solid-state triode

which is accurately machined. A blade of rectangular cross section will be used in order to form rectangular channels. This setup will also permit the use of a very sensitive dial gauge to accurately monitor the channel depth. By ganging several saws it may be feasible to cut all of the channels in one operation.

The present investigations clearly show that it is feasible to accurately cut channels into which gate conductors can be alloyed. Preliminary electrical measurements on the first fabricated solid-state triodes indicate that the sclc can be controlled and modulated. The electrical results and a description of the alloying process will be given in a future SPS.

D. Response Times and Sterilizability of Evaporated Thin Film CdS Photodetectors.

R. J. Stirn

1. Introduction

In SPS 37-41, Vol. IV, pp. 41-46, some major features of recrystallized evaporated thin films of photoconducting cadmium sulfide (CdS) were presented. These films were first developed by Prof. K. W. Böer at the University of Delaware (Ref. 8). Compared to the sintered CdS photodetectors presently being used on spacecraft (Ref. 9), these recrystallized films have significantly improved electrical properties.

In the following article, we shall compare representative samples of the two types of photocells. In particular, the decay and rise times for signal light intensities of 0.05 and 0.5 ft-cd and bias light intensities of 0, 0.05, and 0.5 ft-cd are presented. The response of the cells to light with the above intensities, and chopped at a rate of 10 and 50 Hz, is also shown. Lastly, the effect of heat sterilizing the samples at 135°C for various lengths of time is given.

2. Experimental Detail

Samples of the recrystallized CdS films were supplied by the Allen-Bradley Company. Their sample (ST-11) reported on here was treated to maximize the response times at very low light intensities (SPS 37-41, Vol. IV, p. 44). Its resistance is quite high—100 MΩ at 2 ft-cd; however, optimized electrode patterns and doping can bring this value down by a factor of 20 or more.²

One of the Clairex photocells reported on here is from the series CL 705. Cells from this series are used presently as sun and planet sensors on *Mariner*-class spacecraft, for example.

Also included for comparison is a new type Clairex photocell (CL 705 HL). This cell, still of the sintered CdS variety, has a speed of response that has been greatly improved over those of the CL 705 series.

The samples were biased with 4.5 V for all measurements. Photocurrents were measured with a Keithley picoammeter (Model 416) in the range from 10^{-9} to 10^{-5} A. Currents larger than 10^{-5} A were measured with a standard Weston milliammeter (Model 931).

Changes in the photocurrent in response to pulsed illumination were monitored on an oscilloscope connected across a resistor in series with the photocell. The value of the resistor was chosen to be much less than the cell resistance at all light intensities. This is required so that the measured response times are those of the photoconducting cell only.

The sources of both signal and bias illuminations were GE 1630 lamps operated at the rated voltage of 6.5 V and current of 2.75 A. The color temperature was estimated to be about 2600°K under these conditions. Distances from sample to light source were set to yield a maximum intensity of approximately 10 ft-cd. Lower light intensities were obtained with neutral density filters in

various combinations. Filters with densities greater than 1.5 (about 3% transmission) were avoided as spectrophotometer readings indicated that they were not truly neutral. The light intensities were calibrated with a Spectra Pritchard photometer. Chopped light was obtained with a variable-speed motor and a mechanical shutter designed to give a 50% duty cycle, i.e., equal times under light and dark conditions. Quantitative values for the response times were measured by using a Nikon F camera body as a "single shot" shutter. The flash synchronization on the camera provided a useful trigger for the oscilloscope, as light intensities were too low to use a standard silicon photodiode for this purpose. The finite speed of the Nikon shutter limited measurements to response times greater than 500 μs.

3. Experimental Results

a. Photoresponse. The peak response of relatively pure photoconducting CdS occurs near a wavelength of 5200 Å because of its band gap of 2.4 eV. The Allen-Bradley sample ST-11, which is recrystallized using Cu as a catalyst (SPS 37-41, Vol. IV, pp. 41-46), shows a peak response at 6000 Å. This is similar to that found for Cu-doped single crystals of CdS (Ref. 10). The peak response of the Clairex photocells reported on here is approximately 5500 Å.

The response of the three cells at room temperature as a function of light intensity is shown in Fig. 11 for a

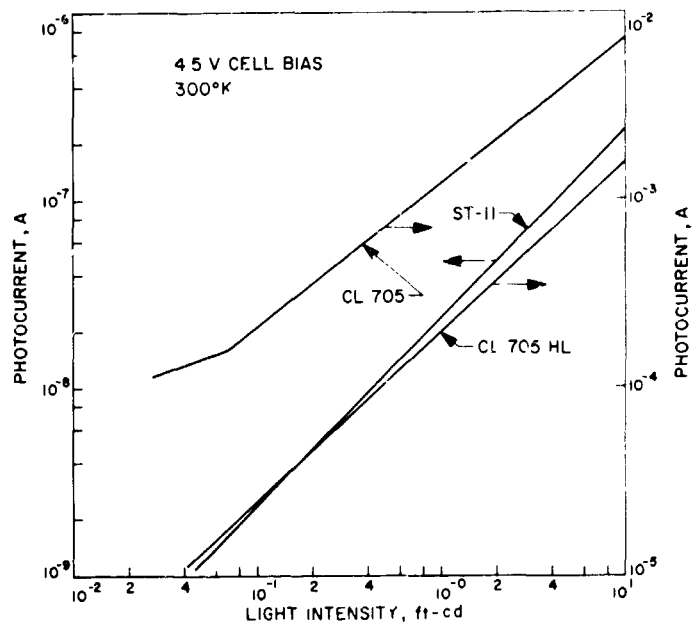


Fig. 11. Photocurrent vs light intensity

²J. W. Feitknecht, private communication, 1967.

range of intensities from 0.02 to 10 ft-cd. For this range of intensities, the Allen-Bradley sample is linear, while the Clairex samples show a sublinear behavior. A model for the sublinear response has been proposed by Rose (Ref. 11). Its main feature is an exponential distribution of electron-trapping states.

Because of the cell geometries, the Clairex cells are lower in resistance by factors of 10^4 and 10^5 . However, the light-to-dark ratios, i.e., the sensitivities, are about the same for all three samples.

The type of data shown in Fig. 11 and a photocell's dark resistance are very sensitive indicators of the effect of higher temperatures. The effects of sterilizing at 135°C will be discussed in another section.

b. Response times (without bias illumination). The rise and decay times of the three types of photocells were measured for two low-level light intensities, 0.5 and 0.05 ft-cd. These intensities correspond roughly to those that a planet detector would "see" when pointed at Mars about 24 h before encounter, with and without optics, respectively.

Figs. 12 and 13 are reproductions of the Polaroid prints taken of the oscilloscope tracings. Differences in the response times between the three samples are immediately apparent. The Clairex cell CL 705 in particular is much the slowest in response.

The rise and decay times of a photoconductor are not the same in general, though both are governed by the presence of electron traps. When the number of traps is large compared to the number of free carriers, the decay time is related to the thermal emptying of these traps and hence to the trap activation energy. However, upon an increase in light intensity, any increase in the number of free carriers in the conduction band must necessarily be accompanied by the same increase in the number of trapped carriers. Thus the rise time is more directly related to the ratio of the number of trapping states to the number of free carriers, and not to the trap activation energy.

Numerical values of the response times are given in Table 1. These values were obtained by defining the rise time as the time required for the photocurrent to rise or decay to a value of $1/e$ or 37% of the final steady-state value.

Table 1. CdS photodetector response times, ms

Signal	0.05 ft-cd				0.5 ft-cd			
	Zero		0.5 ft-cd		Zero		0.5 ft-cd	
	Rise	Decay	Rise	Decay	Rise	Decay	Rise	Decay
ST-11	95	5	1	1	12	1	<0.5	<0.5
CL 705	720	100	28	24	180	25	38	16
CL 705 HL	120	65	4	3	44	12	3	3
CL 705 HL after 16 h of 135°C heating	200	25			40	4	2	2
CL 705 HL after 32 h of 135°C heating	280	300			50	50	20	26
ST-11 after 104 h of 135°C heating	95	5			12	1	<0.5	<0.5

c. Response times (with bias illumination). When an additional amount of light is used as a bias, the number of free carriers is increased relative to the number of trapping states. This in turn shortens the response times and tends to equalize the rise and decay times. This is because the relative influence of the electron traps is reduced and the response times are then related more to the free carrier lifetime. The latter depends on the recombination cross sections and is independent of the light intensity.

Figs. 14 and 15 show the effect of a bias illumination of 0.5 ft-cd on two of the samples. The extracted response times are given in Table 1. It is seen that a small amount of bias light, which is readily obtained from electroluminescent panels, for example, dramatically improves the response times.

d. Response to chopped light. Since photodetectors are often used in a bridge configuration whose output is fed into a servo loop, the response of the three samples to periodically chopped light was observed. Representative results are shown in Figs. 16 and 17.

Fig. 16 compares the three samples exposed to light of 0.5 ft-cd intensity chopped at a rate of 10 Hz. There was no bias illumination. The faster response time of sample ST-11 is immediately apparent.

Fig. 17 gives the same comparison for light of 0.5 ft-cd intensity chopped at a rate of 50 Hz. A constant bias illumination of 0.5 ft-cd was employed in this example.

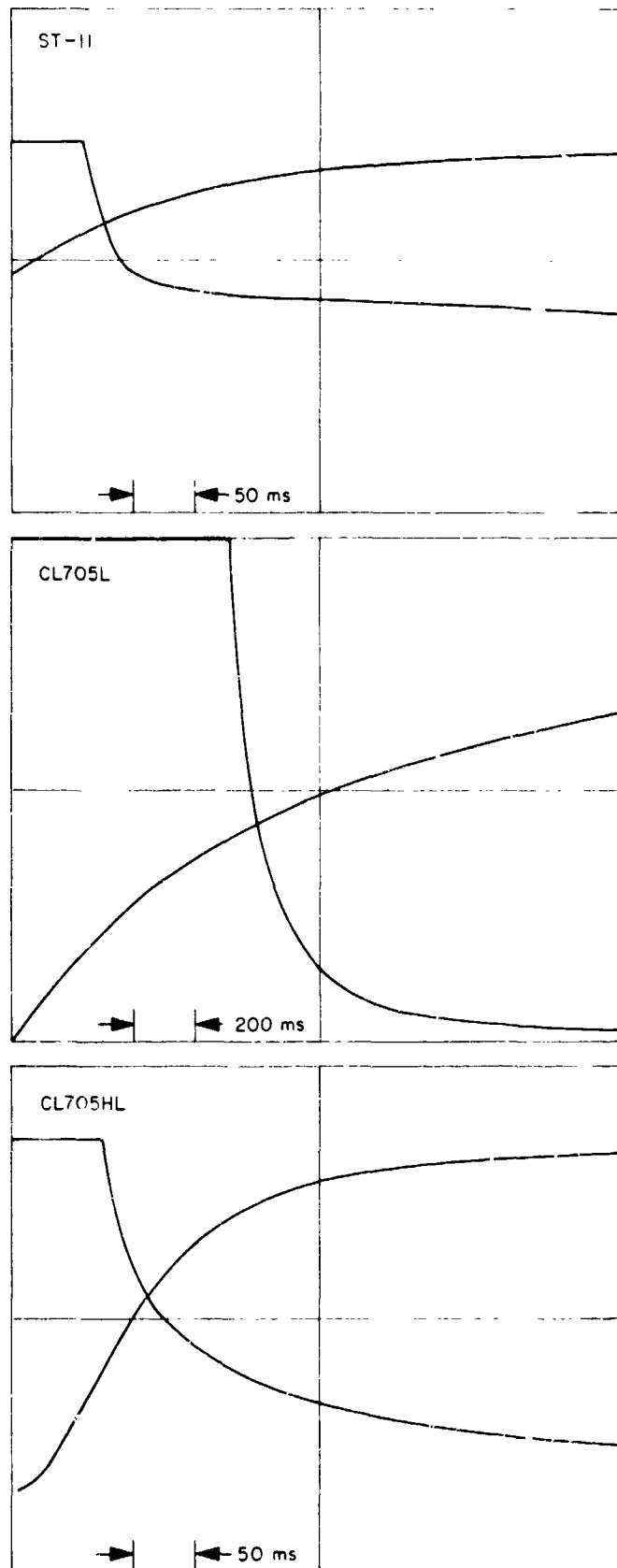


Fig. 12. Photocurrent rise and decay for 0.05 ft-cd signal and zero bias illumination

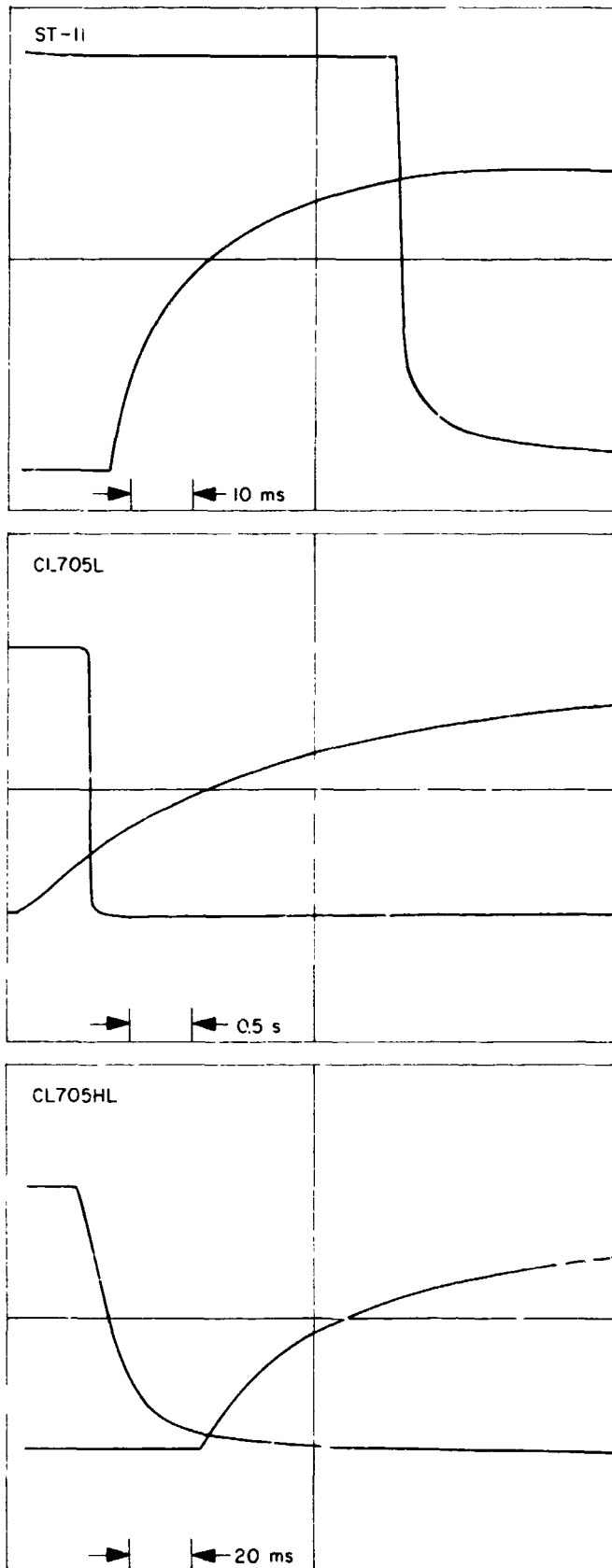


Fig. 13. Photocurrent rise and decay for 0.5 ft-cd signal and zero bias illumination

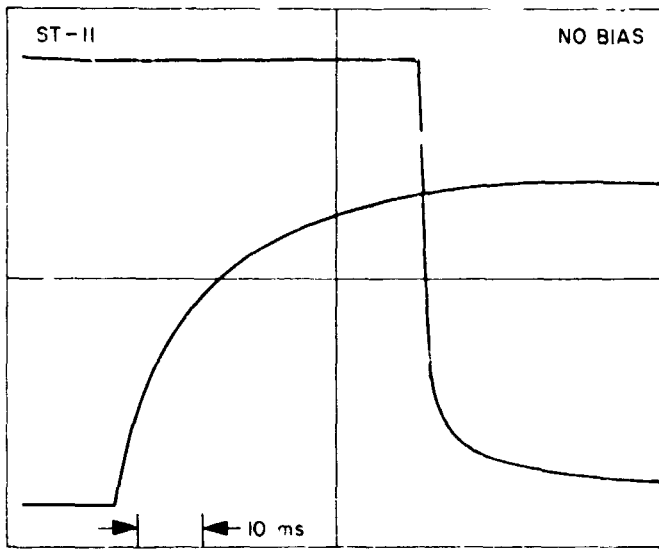


Fig. 14. Effect of 0.5 ft-cd bias illumination for ST-11 with signal intensity of 0.5 ft-cd

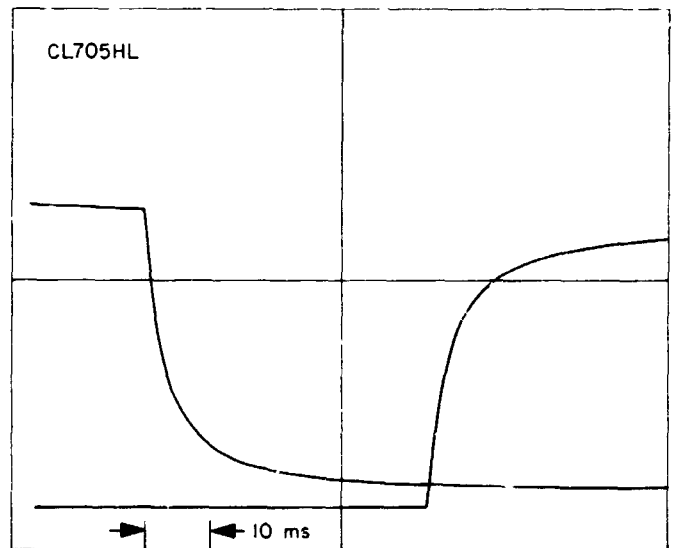
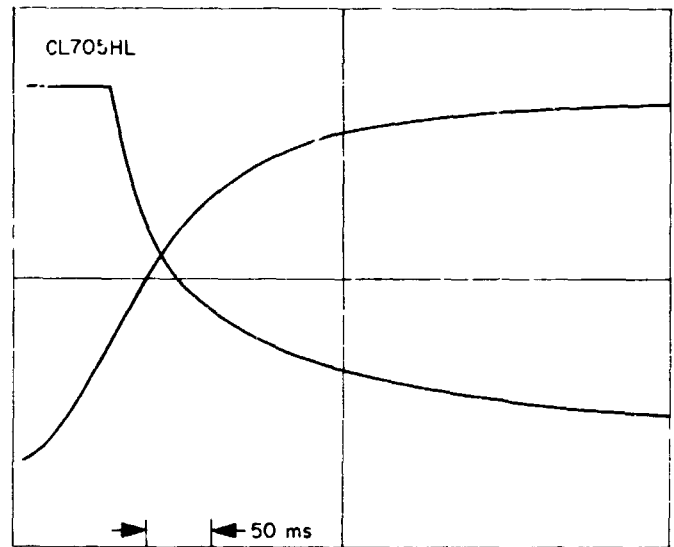


Fig. 15. Effect of 0.5 ft-cd bias illumination for CL 705 HL with signal intensity of 0.05 ft-cd

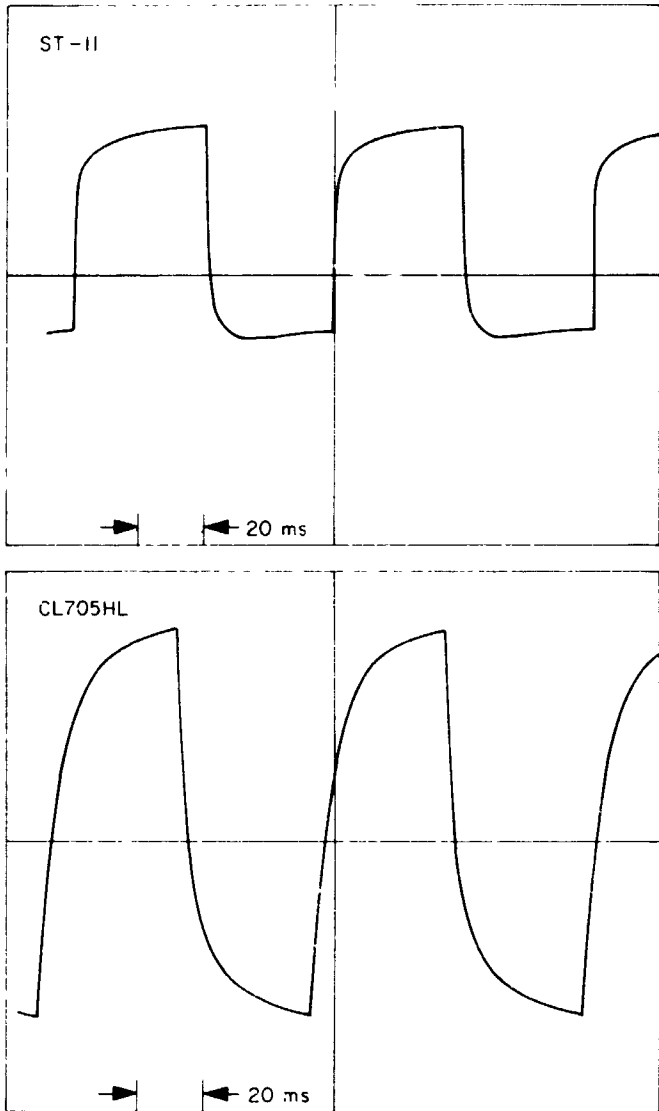


Fig. 16. Response to 0.5 ft-cd signal chopped at 10 Hz with zero bias illumination

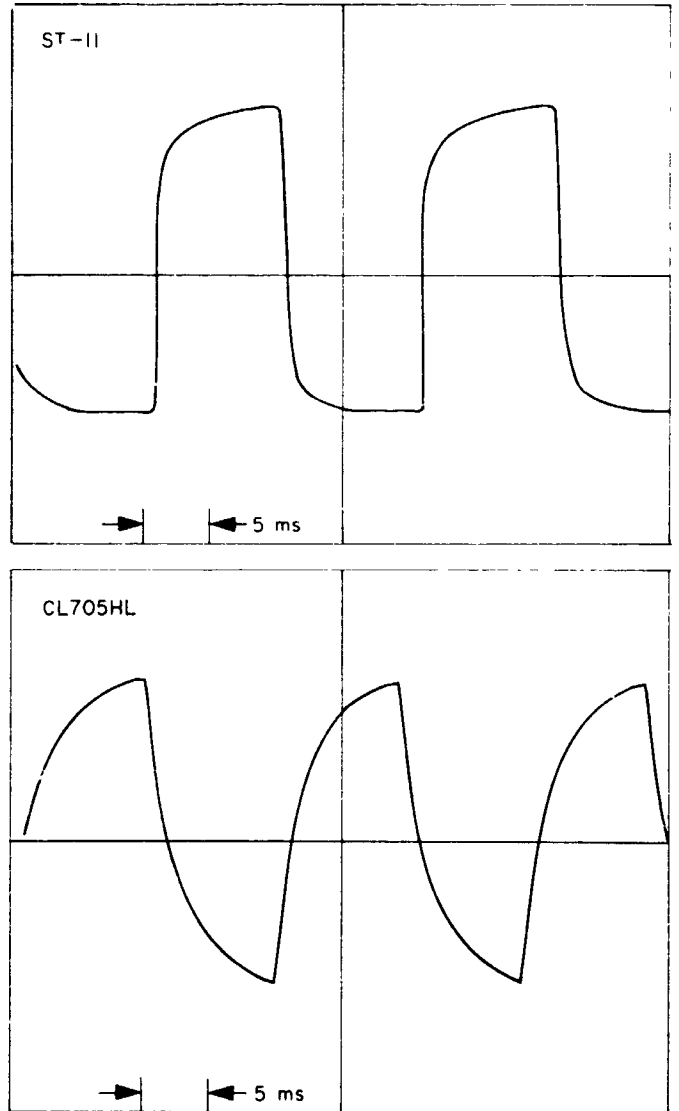


Fig. 17. Response to 0.5 ft-cd signal chopped at 50 Hz with 0.5 ft-cd bias illumination

e. Effect of sterilization. Besides having longer response times, commercial CdS photodetectors invariably fail when exposed to sterilization temperatures for the required length of time. Because of their sintered formation, these cells have many grain boundaries and defects which, in conjunction with dopants and impurities, form associated defects. The latter easily disassociate upon heating, perhaps forming new defects which remain after cooling. The photoconductivity and electrical conductivity are very sensitive to the type and number of such associated defects. Recrystallized layers of CdS have far fewer intrinsic defects and hence are less susceptible to these changes. In addition, a new method for forming ohmic contacts was developed by Hall and Böer (Ref. 12 and SPS 37-41, Vol. IV). Such contacts, which remain unchanged up to temperatures of 200 to 300°C are used on sample ST-11.

Fig. 18 shows the results of heating ST-11 to 135°C in 8-h cycles. The solid line is the response curve before this test. It is seen that the linear behavior (slope equals one) was preserved throughout the test and that the resistance did not change by more than a factor of two. Moreover, the sample had previously been exposed to 72 h of 135°C heating before delivery to JPL. Thus, the final run, indicated by the squares, is actually the conclusion of a total heating of 104 h. Subsequent response time measurements like those in subsections *b* and *c* showed no changes, as noted in the final entry in Table 1.

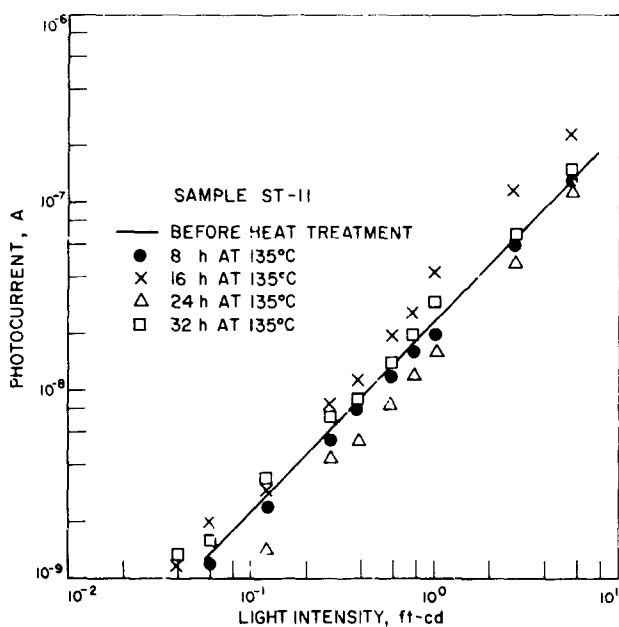


Fig. 18. Effect of sterilizing temperatures on ST-11

The photoresponse curve for CL 705 HL (Fig. 19) showed no effect upon 8 h of heating, but this sample *increased* in resistance after 16 h. Additional heating *lowered* the resistance and began to decrease the photo-sensitivity rapidly. After a total of 32 h of heating, the sample was highly conducting and showed almost no response to light. The small response remaining did have a measurable time constant, however. The values for some representative light intensities are given in Table 1. The response times have changed, but not so drastically as the sensitivity. Another sample, not discussed here, failed completely after approximately 32 h of heating.

4. Conclusions

The results of the previous sections show that the recrystallized layers of CdS are far superior to the sintered layers with respect to response times at low light levels and the ability to survive heat sterilization. However, there are additional important characteristics that remain to be investigated. Mainly these involve relative stability with time and temperature when a pair of photocells is placed in a bridge circuit.

For example, a matched pair of photocells must show a small relative drift ($\pm 5\%$) with respect to each other in their resistivity versus light-intensity characteristics: (1) for moderate temperature changes of -5 to 40°C (both cells at the same temperature), (2) for changes caused by sterilization, and (3) for long-term changes over 1 yr.

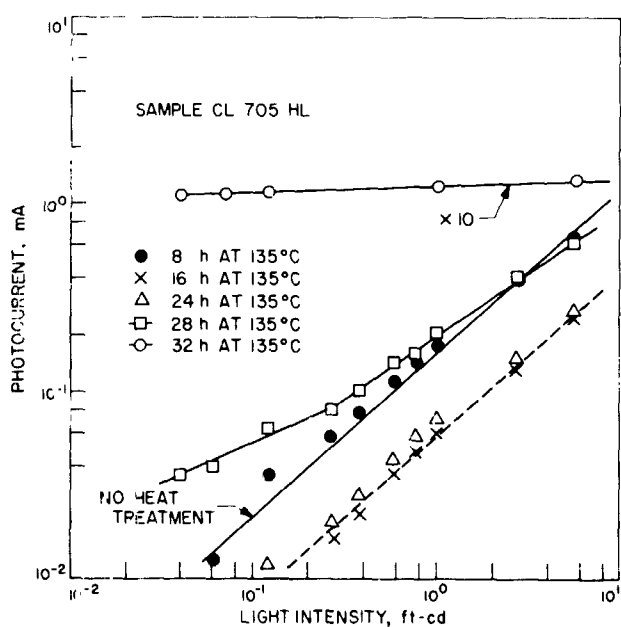


Fig. 19. Effect of sterilizing temperatures on CL 705 HL

It will also be necessary for both of the matched cells to have a temperature coefficient of resistance of approximately 1% /°C in the temperature range of -5 to 40°C.

Optimization of such characteristics will modify the sensitivity and perhaps the response times. Measurements of all these parameters will have to be made when a larger supply of the recrystallized photocells becomes available.

References

1. Webb, P. W., and Wright, G. T., "The Dielectric Triode: a Low-Noise Solid-State Amplifier," *J. Brit. IRE*, Vol. 23, pp. 111-112, 1962.
2. van der Ziel, A., "Low Frequency Noise Suppression in Space Charge Limited Solid-State Diodes," *Solid-State Electronics*, Vol. 9, pp. 123-127, 1966.
3. Shumka, A., and Nicolet, M-A., "Space-Charge-Limited Current in Germanium." Proceedings of the 7th International Conference on the Physics of Semiconductors, p. 621, Dunod, Paris, 1964.
4. Denda, S., and Nicolet, M-A., "Pure Space-Charge-Limited Electron Current in Silicon," *J. Appl. Phys.*, Vol. 37, 1966.
5. van der Ziel, A., *Noise*, p. 321. Prentice-Hall, New York, 1954.
6. Rodriguez, V., and Nicolet, M-A., "Differential Impulse Response of Unipolar Space-Charge-Limited Current," *J. Appl. Math. Phys.*, Vol. 18, pp. 280-289, 1967.
7. Shumka, A., "Space-Charge-Limited Current in Germanium," Division of Engineering and Applied Science Report. California Institute of Technology, Pasadena, California, May 1964.
8. Böer, K. W., Esbitt, A. S., and Kaufman, W. M., *J. Appl. Phys.*, Vol. 37, p. 2664, 1966.
9. *Photoconductor Cells*, Clairex Corporation, 8 West 30th Street, New York, 1966.
10. Bube, R. H., *Photoconductivity of Solids*, p. 168. John Wiley & Sons, Inc., New York, 1960.
11. Rose, A., *Concepts in Photoconductivity and Allied Problems*, p. 38. Interscience Publishers, New York, 1963.
12. Hall, R. B., and Böer, K. W., *J. Appl. Phys.* Vol. 37, p. 4739, 1966.

V. Applied Mechanics

ENGINEERING MECHANICS DIVISION

A. ELAS Computer Program for Equilibrium

Analysis of Linear Structures,¹ S. Utku and F. Akyuz

1. Introduction

The finite element method, being a special Ritz procedure, constitutes one of the most versatile and general tools for the numerical analysis of structures, especially those having complex geometry, general material properties, and complex boundary conditions. Parallel to its development, various computer programs based on various philosophies of composition have been prepared by many authors. Yet none of these programs seem to be able to reflect the complete spectrum of capabilities offered by the analytical studies prepared in this area. The most important barriers encountered in preparing a program to match the available analytical capabilities are the computing time, the storage capacity of the computer, and the round-off errors, since the amount of data and the computations are excessively large. These factors are not completely independent of each other, i.e., the computer time increases drastically by increasing the storage capacity of the computer with the use

of out-of-core devices. The use of double precision arithmetic to decrease the effect of round-off errors decreases the storage capacity. Although a given equilibrium problem can be solved with the help of some of the existing programs by spending a rather long computer time, these programs are impractical for the repeated solution of a given problem, as in the case of nonlinear analysis, convergence studies, parametric study of the structures, etc.

A computer program which will be the first step toward the nonlinear analysis of the structures must be as efficient as possible in the sense of using minimum core memory space, shortening the computation time, and reducing round-off errors. This concept leads to the following direct conclusions concerning the philosophy of composition for such a program:

- (1) Avoid out-of-core operations by eliminating, as much as possible, the features which are not of direct concern to the problem that is being solved.
- (2) At the earliest stage of computations, eliminate all the data and information which are not needed later, and the corresponding operations, and minimize sorting and matrix operations.

¹This program, developed in the Structures and Dynamics Research Group of the Applied Mechanics Section, is partially supported by the Propellant Stress Analysis Program.

BLANK PAGE

The application of these concepts, with additional versatile capabilities for the solution of the large class of linear equilibrium problems arising in practice, has been incorporated into a program called ELAS.

2. Description of ELAS and Its Capabilities

ELAS is written in FORTRAN II, rather than in FORTRAN IV language, in order to save some of the core storage which is being used for the standard input/output package. The displacement method of analysis, starting from an extremum formulation, has been chosen for solution of the problems. In this method the coefficient matrix of the equations, in general, is band-limited. Only the coefficients within the band which are being used are stored; therefore, considerable amounts of storage location are saved, and the computation time and the round-off errors are minimized.

Some of the special features of ELAS are:

- (1) The types of structural problems which can be handled are: analysis of trusses and frames, stretching and bending of plates and shells, two- and three-dimensional elastic solids, axisymmetrical shells and solids. These structures may be of any geometry. There is no limitation as to the force and displacement boundary conditions.
- (2) The dynamic memory allocation allows the use of adequate amount of storage for different types of problems. This feature also gives the user access to larger core memory capacity after only minor changes in the program.
- (3) The bandwidth of the stiffness matrix depends on the composition of the structure, but also it is related to the nodal point labeling. Favorable labeling of a given structure is time consuming and a difficult task for the user in most cases. Internal relabeling which minimizes the bandwidth is possible with ELAS; therefore, the reduction of necessary storage is automated as a possible option.
- (4) The boundary conditions and any *a priori* known relation between displacement unknowns may be imposed at the time of the assembly of the coefficient matrix and the load vector. This eliminates, in many cases, the use of considerable portions of the memory, which will be otherwise occupied by the coefficients of the equations to be eliminated later. The displacement boundary conditions which can be imposed are zero displacement, a known

displacement, and general linear dependence between displacement components. Discrete and/or continuous force boundary conditions and body forces may be automatically accounted for.

- (5) For structure of two- or three-dimensional continua the stresses are computed at the nodal points by using the best fit strain tensor in this region. Therefore, the stresses computed at the nodal points are better approximations than those obtained by most other methods.
- (6) The structural material can be isotropic, orthotropic, or generally anisotropic, homogeneous or nonhomogeneous. The effect of temperature changes for all types of structures; the effect of temperature gradients for frames, plates, and shells can be computed. The body forces due to an arbitrary constant acceleration field can be considered.
- (7) The coordinates, the boundary conditions, and element mesh topology data can be automatically generated for a given class of problems by supplying the necessary corresponding subroutines. The program can be used for specific purposes, such as to relabel any structure for bandwidth minimization up to 540 nodes, or to solve only for displacement unknowns. The equilibrium check is possible and the complete set of forces at the nodal points can be computed.
- (8) The capacity depends on the type and the number of types of elements which are being used on the bandwidth and on the number of unsuppressed degrees of freedom. For an average type of problem, 500-700 unknowns can be handled by the IBM 7094, 32K computer. These figures correspond approximately to trusses with 200 nodes, three-dimensional frames with 100 nodes, plane elasticity problems with 350 nodes, and three-dimensional elasticity problems with 200 nodes. In a given problem, 99 different types of material, temperature, thickness, etc., may be used. Successive sets of data corresponding to different problems can be loaded in a single run, without any restriction on their number.

3. Conclusion

For the problems which have been solved so far by ELAS on the IBM 7094, Model I computer, the computer time did not exceed 3 min. This figure is the actual order of magnitude of time spent for the largest problems which can be handled by this program. It is of

an order of magnitude less than the time required to solve the same problems with most of the programs in this area.

The development of a program for nonlinear, step-by-step analysis can follow the philosophy of ELAS with a few specific changes and additional routines.

As it is indicated by the title of this article, ELAS is only for the equilibrium problems of structures. The eigenvalue problems and the propagation problems, e.g., natural vibrations and forced response, are not included. However, for these problems the discretization and the overall stiffness matrix generation operations can be performed by ELAS.

Vi. Aerodynamics Facilities

ENVIRONMENTAL SIMULATION DIVISION

A. Biplanar Optical System for Nonplanar Free-Flight Testing, H. P. Holway

The concept of splitting the schlieren light path to permit viewing from two angles and recording the resultant images on a single frame of a high-speed 35mm movie camera was tested and first reported in SPS 37-37, Vol. IV, pp. 100-101. Improvements were made, tested, and again reported in SPS 37-38, Vol. IV, pp. 65-71. As a result of these two tests a set of precision mirrors were manufactured and Test 20-645 was conducted to evaluate these as well as the new Photo-sonics 35mm full-frame camera. Figure 1 shows the new mirrors in their positions relative to the tunnel viewing windows, and Fig. 2 is a schematic of the biplanar optics inserted into the standard schlieren optics of the wind tunnel.

The camera used for this test is shown in Fig. 3. It is capable of frame rates from 500 to 2500 frames/s and the strobe light source is synchronized with the camera prism by means of a reluctance pickup. The timing of the flash with the prism is very critical, and considerable effort was applied in this area since the first film showed that a portion of the image was cut off. A method of checking the mirror adjustments which eliminates the time-consuming and expensive film processing is being devised.

A recent change in the launch-gun location caused severe shocks from the centerbody to impinge on the models at $M = 4.0$ during this test. This was corrected by changing the Mach number to 3.0 and reducing the dynamic pressure to 50 cm Hg. At these conditions the test proceeded to completion. Ten flights were made, using 10-deg half-angle cones, launch angles of 20 and 30 deg, and axial rotation rates of 1000 to 3000 rev/min.

While operating, timing, and alignment problems plagued the early part of the test, the resulting films with the new mirrors show a definite improvement in quality. To compare the results with a previous biplanar test, Fig. 4 shows a single frame from each mirror system. The quality obtained with the new mirrors is an obvious improvement and, with care, a second iteration of the aligning procedure should eliminate the minor problems in the images.

The biplanar optical system for observing nonplanar free-flight models is but one part of the overall technique. A second-generation launch gun, now being manufactured, will project the models into the center of the viewing rhombus and increase the maximum launch velocities from 90 to 150 ft/s. The entire system is expected to be operational by the fall of 1967 in preparation for a scheduled nonplanar test.

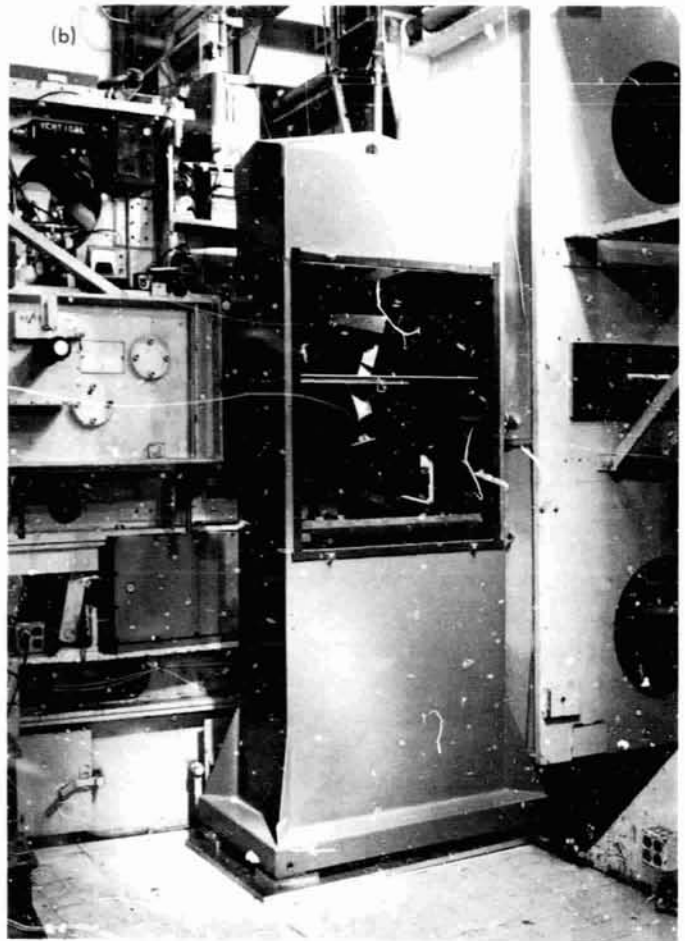
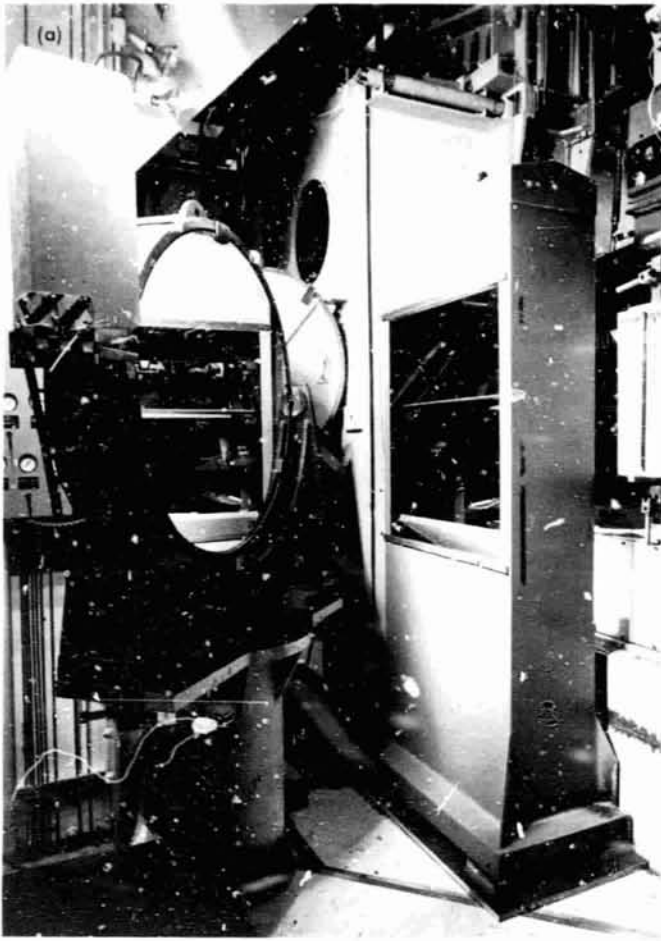


Fig. 1. Biplanar mirror assembly in position: (a) north side, (b) south side

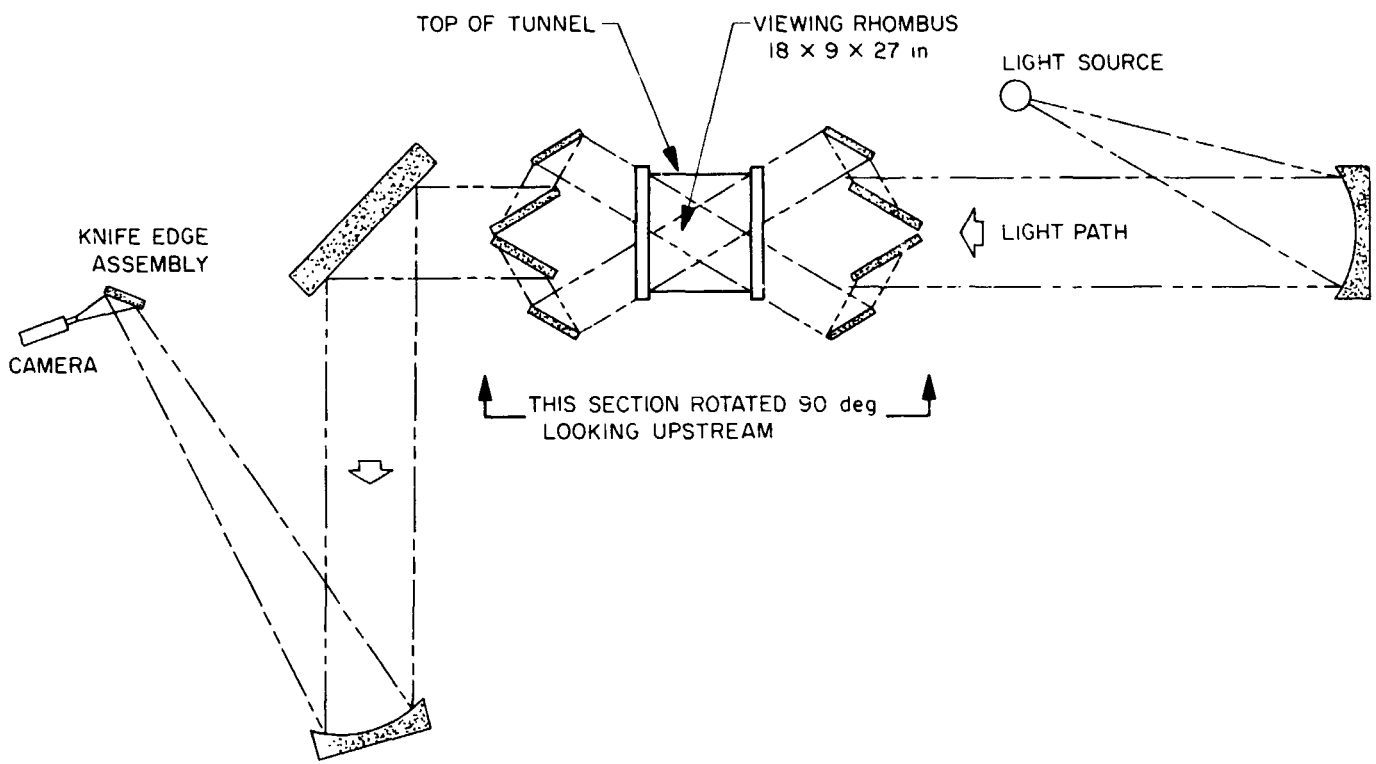


Fig. 2. Nonplanar free-flight schlieren system

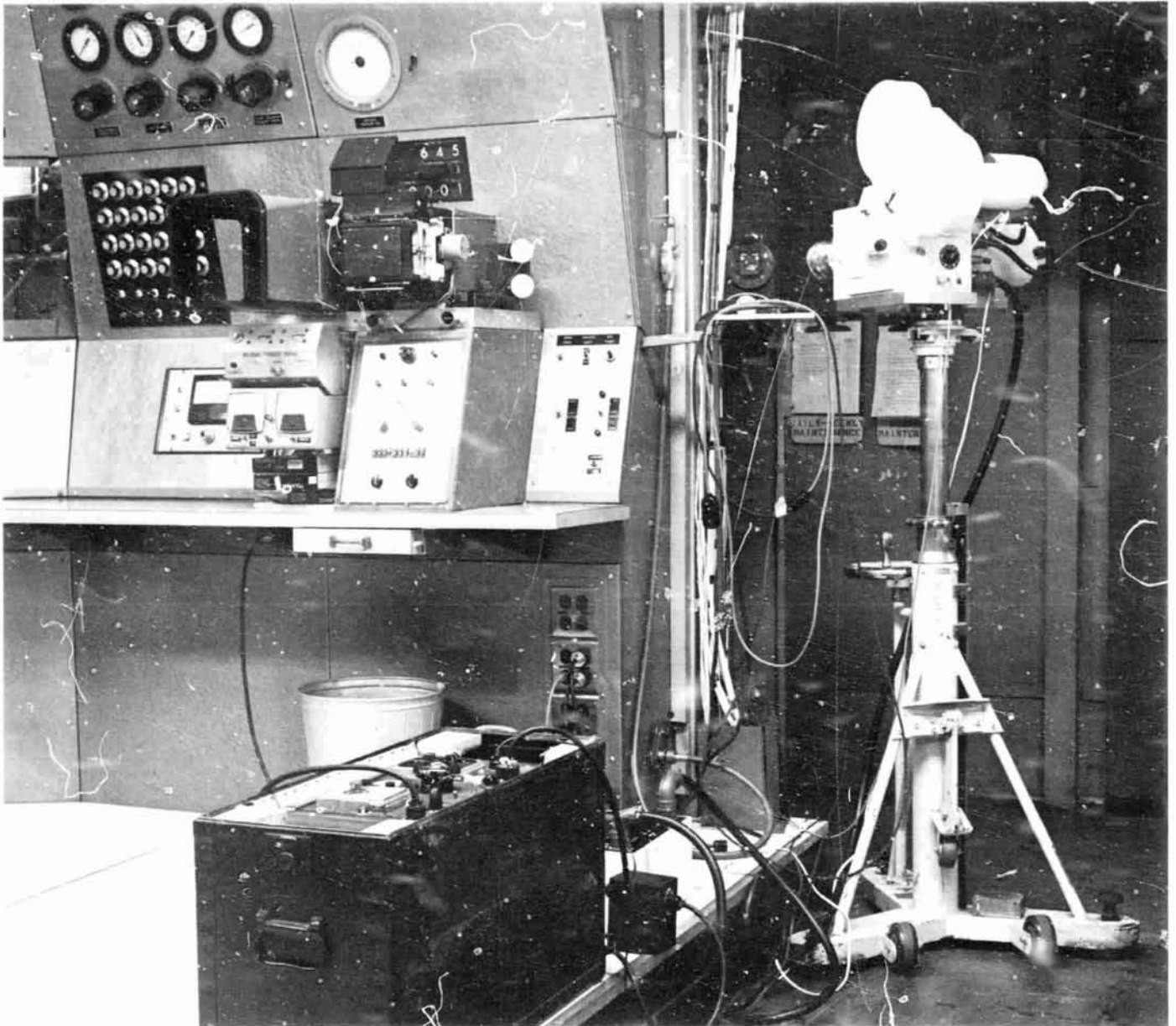


Fig. 3. Photosonics full-frame 35mm camera and controls

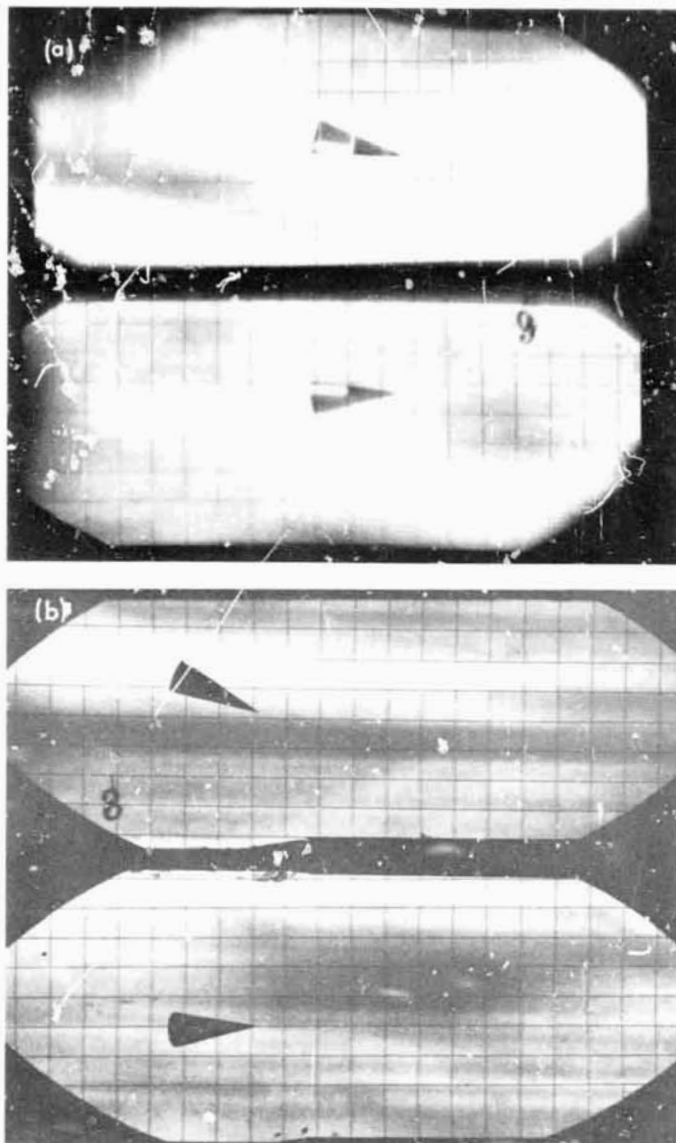


Fig. 4. Test film: (a) steady-state light source (prototype mirrors), (b) strobe light source (precision mirrors)

B. Hypersonic Boom Study, R. Kerr

Wind Tunnel Test 21-199 was conducted in order to measure the pressure signatures from hypersonic aircraft at a distance of one model length directly below the model, and to record the normal and moment forces acting on the aircraft. This test was performed in cooperation with NASA Ames Research Center (ARC), Moffett Field, California.

Five models were tested: a cone-cylinder, three hypersonic aircraft, and the X-15. These models are shown in Fig. 5. Each model was sting-mounted in the wind tunnel on ARC's $\frac{1}{4}$ -in. two-component strain gage balance, with the nose of the model located approximately 35 in. upstream from the centerline of the viewing window. The model and its sting were mounted on a vertical strut through the cooling-shield inlet located in the ceiling, and a static pressure probe was mounted to a separate

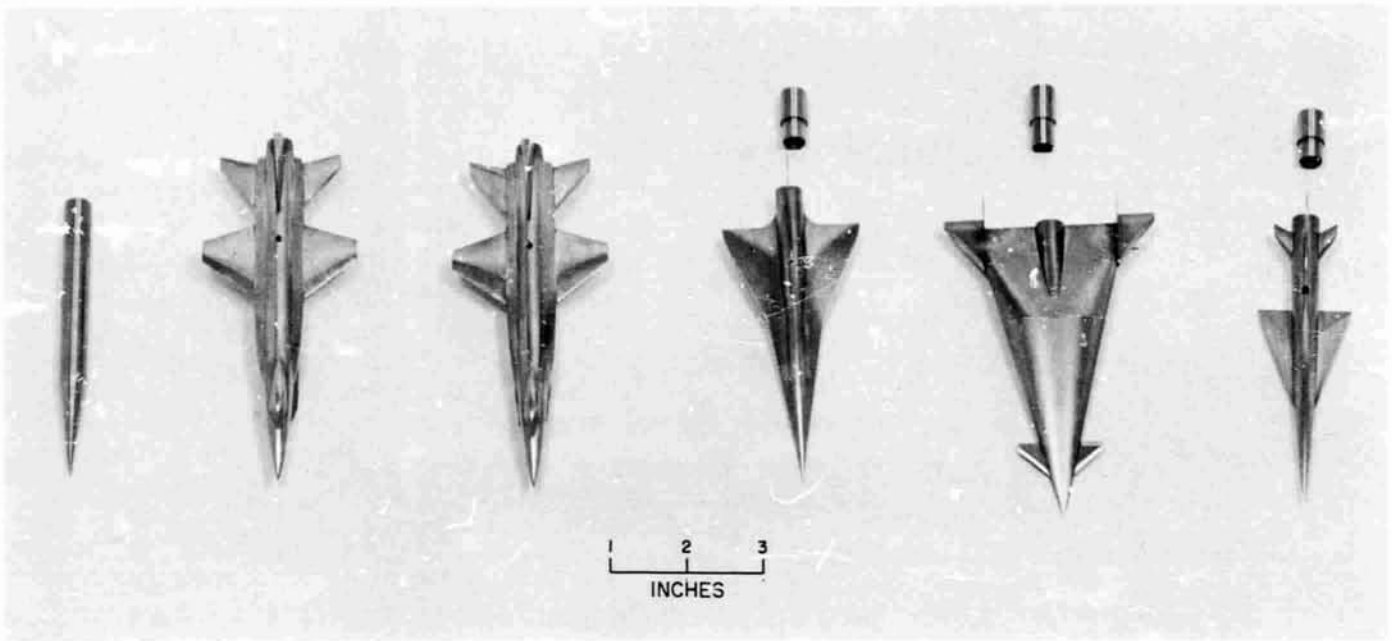


Fig. 5. Wind-tunnel test models

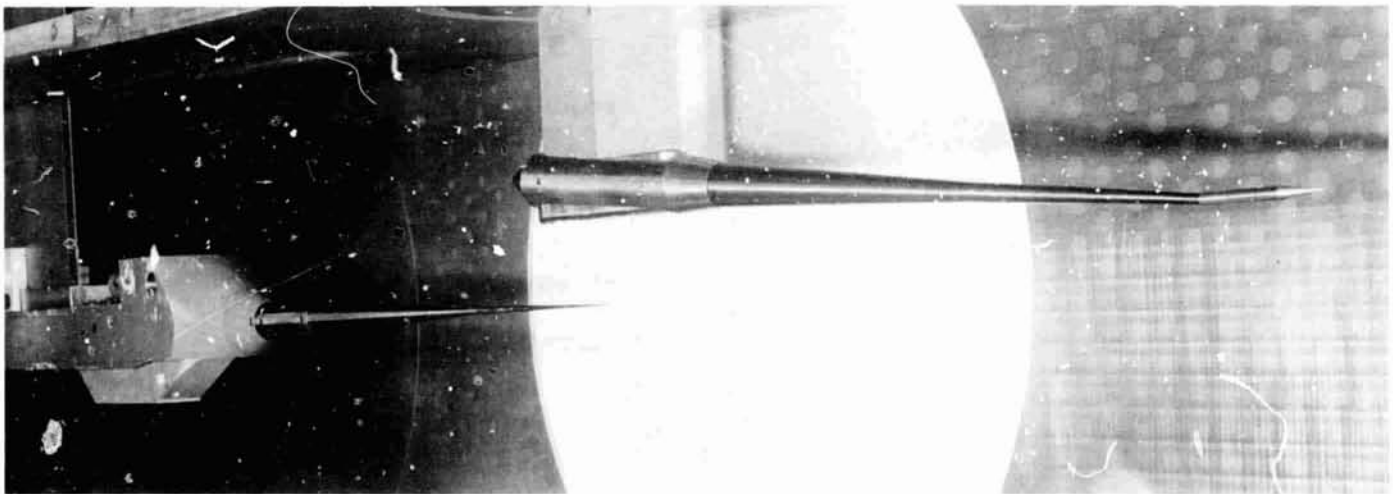


Fig. 6. Model installation set-up

traversing rig which could move in both the horizontal and vertical directions. This installation set-up is shown in Fig. 6, with the cone-cylinder model installed on the balance at zero angle-of-attack.

The aerodynamic parameters were Mach numbers M of 4.0 and 5.5, with a range in Reynolds number $(Re)/in.$ of 0.122×10^6 to 0.185×10^6 . The test variables included an angle-of-attack α of 0, 3, and 5 deg for each of the models, and a range in the horizontal position of the static-pressure probe sufficient to record all of the shocks and expansions created from the model. This static pressure from the probe was fed into a differential transducer, with a static-pressure port on the tunnel sidewall feeding into the other side of the transducer. In this manner, the overpressure through the shock waves, Δp , was measured directly.

A pressure signature is illustrated for the X-15 and the delta-body in Figs. 7 and 8, respectively, with the over-

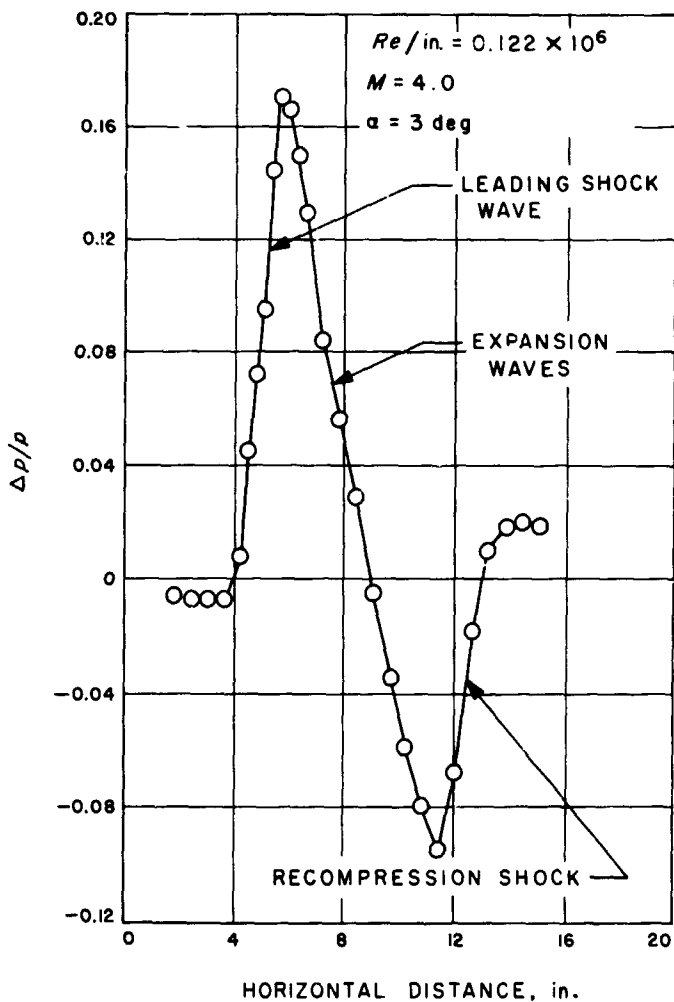


Fig. 7. X-15 pressure signature

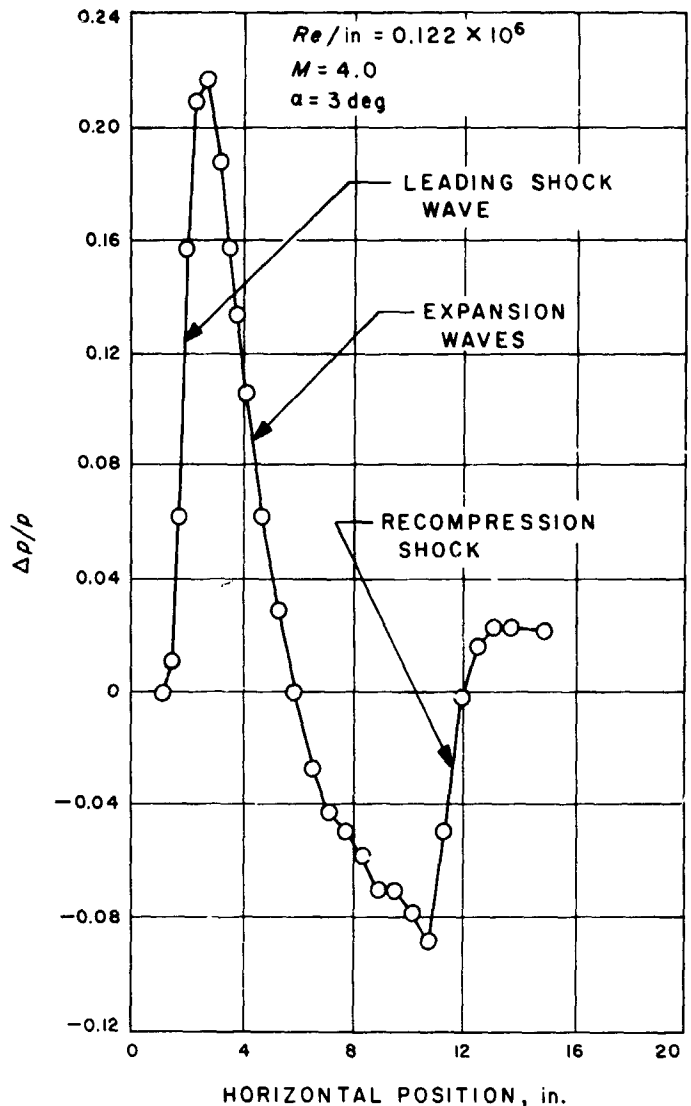


Fig. 8. Delta-body pressure signature

pressure being ratioed to the tunnel free-stream static pressure. It can be seen from schlieren photographs of previous investigations that a model's nose and wing shocks blend together at a distance of one model length away, for high supersonic Mach numbers. This explains why there is generally only one shock in the pressure signatures before the recompression shock.

C. Air Radiation Measurements, G. M. Thomas and W. A. Menard

The important sources of radiation from high-temperature equilibrium air have been studied both experimentally and analytically (Ref. 1). Measurements were made of the equilibrium radiation behind the bow shock at the nose of a model located along the axis of

an electric arc-driven shock tube over the temperature range from 9000 to 15,000°K. Spectral measurements were made over the 0.3- to 1.1- μ spectral region while total radiation measurements covered the 0.3- to 2.7- μ region. Calculations were made of the continua of singly ionized N and O atoms employing non-hydrogenic cross sections for low, principal quantum-number levels. The measured spectrum exceeded the positive ion continuum by a large factor at 10,000°K and this discrepancy was attributed to the existence of a negative nitrogen ion continua. Cross sections for the negative continua were

deduced from the data. Bound-bound transitions were also considered in the analysis and are shown to be an important radiation source. The major conclusion was that the dominant sources of radiation in this experiment were the N⁻ continua and atomic line radiation.

D. X-15 Research Vehicle, D. Kurtz

Wind Tunnel Tests 21-201 and 20-643 were recently performed on NASA's extended performance version of the X-15. The research vehicle will be used as a flying test bed for a small ramjet mounted on the lower vertical stabilizer, or ventral (Fig. 9).

The purpose of the force tests was to supply the X-15 ground simulator with sufficient stability and control data to familiarize pilots with the flight characteristics and related aerodynamic effects of the ramjet encountered in flight.

The investigation was performed at Mach numbers M of 1.47, 3.01, and 6.57 and Reynolds numbers Re of 0.26×10^6 , 0.36×10^6 , and 0.23×10^6 , respectively.

A six-component internal strain-gage balance was used to readout all force data. Schlieren photos were taken to observe and study shock impingement on the ramjet inlet (Fig. 10) and the consequent disturbance to the operational effectiveness. Preliminary evaluation indicates this to be a possible problem area.

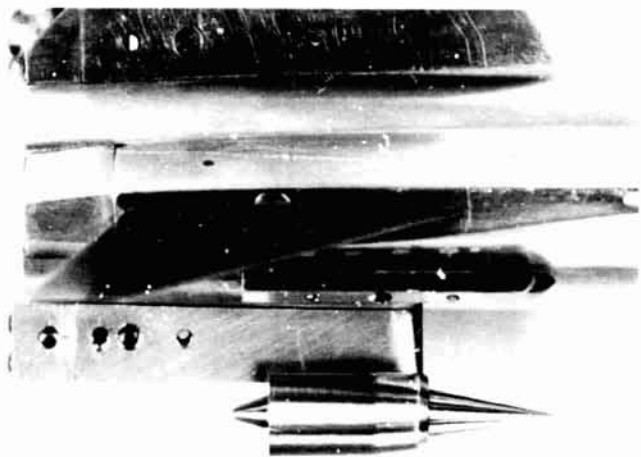


Fig. 9. Extended performance X-15 with ramjet mounted on lower ventral

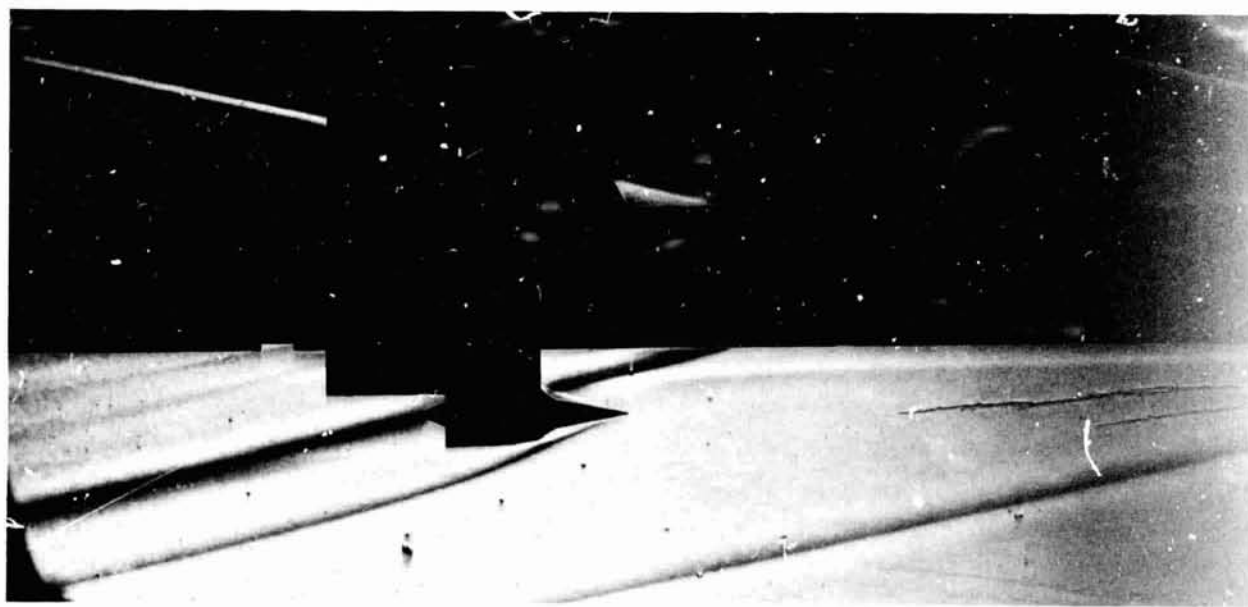


Fig. 10. X-15 with ramjet $M = 6.57$, $Re = 0.23 \times 10^6$

E. Wedge Wake Studies, R. Kerr

Wind Tunnel Test 20-644 was conducted in order to make detailed flow measurements in the near wake of a slender two-dimensional wedge with injection of gaseous nitrogen or helium from the base. This test was performed in cooperation with Thompson Ramo Woolridge Systems of Redondo Beach, California. The test was conducted in the 20-in. supersonic wind tunnel at a Mach number of 4.0 and a Reynolds number/in. of 0.304×10^6 .

The model, shown in Figs. 11 and 12, was a 6-deg half-angle wedge with a porous base 1 in. high through

which a gas could be injected into the flow. A "saw-tooth" trip was used on the leading edges to trip the model boundary layers and thus insure fully turbulent flow at the high Reynolds number. The model also had internal cooling passages through which liquid nitrogen could be circulated. This allows testing to be done in either an adiabatic- or cold-wall condition, although all runs for this test were at the adiabatic-wall condition. The wedge spanned the width of the tunnel and was mounted to the tunnel sidewalls at zero angle-of-attack

Pitot surveys, hot-wire anemometer surveys, and centerline static pressure measurements were made in the

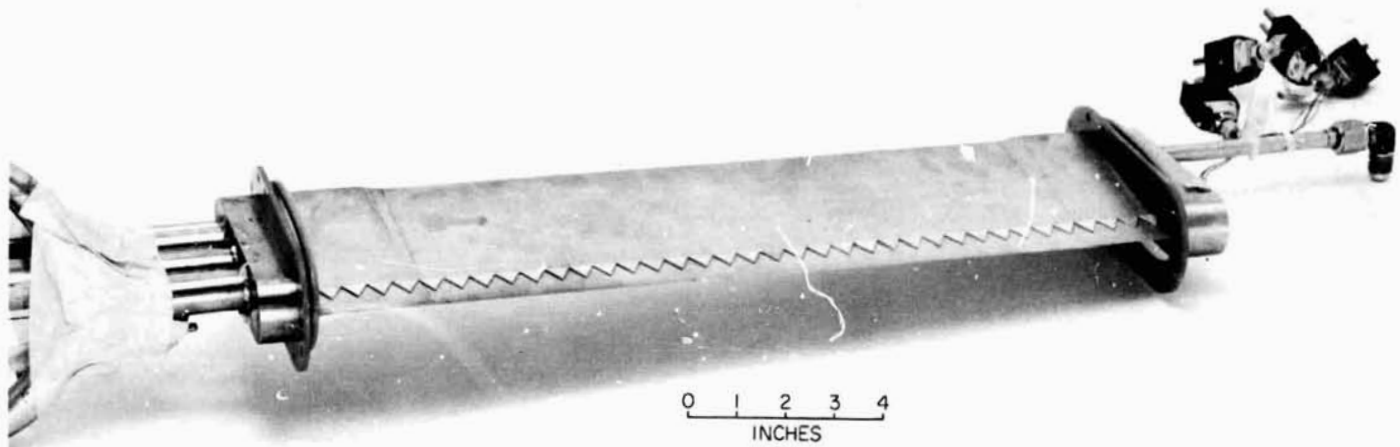


Fig. 11. Leading edge of model showing the boundary-layer trips

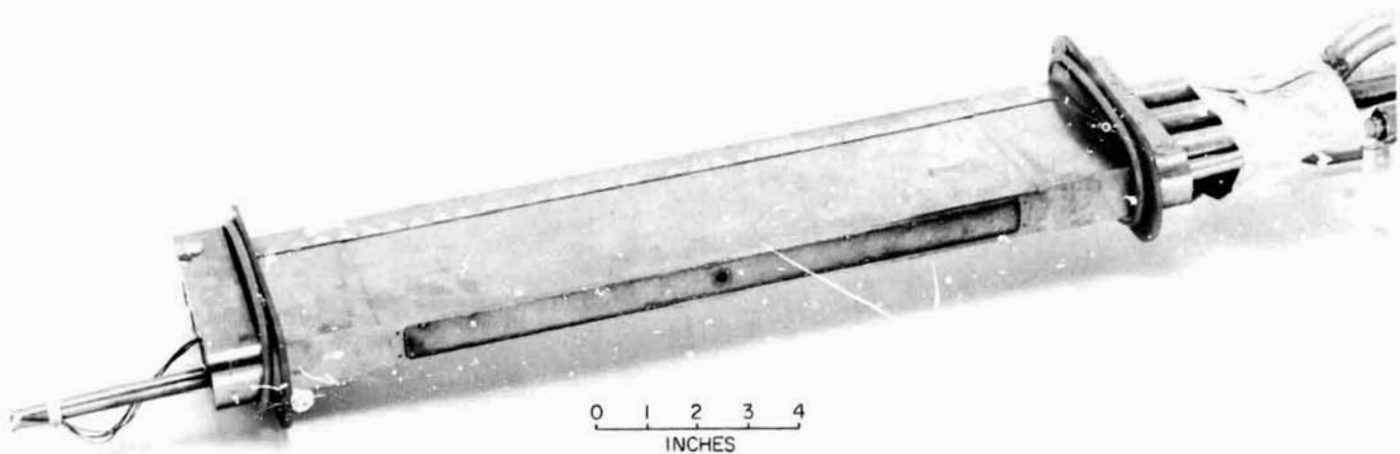


Fig. 12. Rear of model showing the porous base and base pressure port

wake by mounting the probes on a traversing rig which could move in the horizontal and vertical directions. In addition to these wake measurements, model surface pressures and temperatures were recorded. All of these measurements were made for a total of 7 different injection rates for both the gaseous nitrogen and helium. The nitrogen and helium were used because their transport properties are quite distinct from each other, and the effect of this variation was compared for identical injection rates and tunnel conditions.

One of the most troublesome regions for theoretical analysis of the flow field about a body having a blunt base is the reverse flow region in the near wake which dominates the initial conditions for the calculation of the

wake development. For this reason, the model was designed to allow for aft-facing pressure probes to be installed in the base pressure port. Various lengths of both pitot and static probes were used here to determine the centerline Mach number of the reverse flow, thus helping to define the location of the rear stagnation point in addition to measuring the magnitude of the velocities in this region.

The data show that small rates of injection of gaseous nitrogen or helium from the base of the model can cause significant changes in the wake structure. These changes consist of an unusually uniform pressure distribution along the wake axis and a tendency of the wake neck to "open up," causing the wake shock to be shifted outward from the wake axis and become greatly weakened.

Reference

1. Thomas, G. M., and Menard, W. A., "Measurements of the Continuum and Atomic Line Radiation from High Temperature Air," *AIAA J.*, Paper No. 67-95, January 1967.

N67-34768

VII. Solid Propellant Engineering

PROPULSION DIVISION

A. Applications Technology Satellite Motor

Development, R. G. Anderson and R. A. Grippi

1. Introduction

In January 1963, JPL initiated a development program to provide a solid propellant apogee motor for a second generation *Syncom* satellite. This program, under the management of the Goddard Space Flight Center, was designated *Advanced Syncom*. It was to result in a spin-stabilized, active repeater communications satellite weighing approximately 750 lb., operating at synchronous altitude (22,300 mi) to handle voice communications, teletype, and monochrome and color television signals.

In January 1964, the *Advanced Syncom* communication program was redirected to include a number of experimental instruments in addition to the original communication instruments. This expanded program is the *Applications Technology Satellite* (ATS) program and will result in a general-purpose satellite capable of operation at synchronous altitude with experimental instruments in the areas of meteorology, communications, radiation, navigation, gravity gradient stabilization, and various engineering experiments. For those satellites to be placed in

synchronous orbit, JPL will provide a solid-propellant rocket motor to provide final required velocity increment at the apogee of the elliptical transfer orbit. This rocket motor is designated the JPL SR-28-1 (steel chamber) or JPL SR-28-3 (titanium chamber). At present, only the JPL SR-28-3 unit is intended for flight use.

Previous reports of progress on the development of this motor have been published in SPS 37-20 to 37-33, Vol. V and SPS 37-34 to 37-44, Vol. IV.

2. Program Status Summary

The motor development program calls for static firing of 4 heavywall motors and 26 flightweight motors, including 2 with flight design titanium chambers, prior to conducting an 8-motor qualification program. To date, the 4 heavywall motors plus 25 flightweight motors have been static fired, 4 of which were under simulated high-altitude conditions at Arnold Engineering Development Center (AEDC), Tullahoma, Tennessee. All of the flightweight motors tested to date have been with type 410 chromium steel chambers, with the exception of Dev. G-8T, G-9T, E-3T, and Q-9T which used titanium chambers. During the past reporting period, one additional development

BLANK PAGE

unit has been tested. The testing of the second storage unit (Dev. F-3), after 24 mo of storage, was performed in May.

The ATS apogee motor qualification phase was conducted at AEDC during July and August 1966. The results are reported in SPS 37-41, Vol. IV.

The first of five *Applications Technology Satellites* (ATS-B) was successfully launched in December 1966. The satellite is presently on station and functioning as planned.

3. ATS Storage Units

Three ATS apogee motors, loaded in September 1965, have been stored at 80°F or ambient temperature after the post-loading requirements were completed in November 1965. The units were processed and loaded to flight-standard procedures. All hardware components are of flight design with the exception of the chamber and the number of layers of chamber insulation. In place of the 6AL-4V titanium chamber, a 410 chromium steel unit was used since the titanium chambers were not available at the time the motors were loaded. The insulation configuration lacks one layer of 0.030-in. material at each end of the motor chamber. This difference in insulation configuration is a result of changes initiated in the flight design after firing the initial titanium motor in November 1965. Either deviation from the flight configuration should not affect the storability of the motor.

These units have been removed at intervals and subjected to various inspections, including weight determinations, visual examination of all components, dimensional checks, and hardware alignment. The last periodic inspection of the storage units was performed in March 1967. During this inspection no additional anomalies were noted on either motor. The inspection results are identical to the November 1966 inspection (SPS 37-43, Vol. IV).

The second storage unit (Dev. F-3) was static tested at the JPL-Edwards Test Station (ETS) facility on May 10, 1967, approximately 20 mo after being cast. Prior to static firing, the unit was subjected to a series of test environments which included booster vibration, booster acceleration, and temperature cycle. These environments simulate, but do not duplicate, the conditions an apogee unit will see during the boost phase into orbit. Visual and radiographic inspection of the unit, after being subjected to the test environments, revealed no anomalies. Table 1 summarizes the weight and measurement data for

Table 1. ATS storage unit dev. F-3 weight and measurement data summary

Item	Post-loading, September 1965	Pre-fire, May 1967
1. Chamber assembly weight, lb (chamber, insulation, propellant, and handling ring)	870.4	870.2
2. Nozzle assembly weight, lb	38.95	38.75
3. Hardware thrust alignment, in./in.	0.00006	0.00003
4. Propellant port diameter alignment, TIR, in.		
Inches from nozzle boss:		
4	0.005	0.005
14	0.007	0.007
24	0.009	0.006
5. Port diameter, in. (60°F)		
Inches from nozzle boss:		
4	10.122	10.167
14	10.127	10.144
24	10.122	10.131
6. Visual inspection (propellant and interfaces)	No discrepancies	Forward end propellant to insulation separation, 1 in. in depth

Dev. F-3. This table includes data taken after the unit was loaded in September 1965, and data recorded 20 mo later, just prior to static testing. All pre-fire data indicated that the apogee unit could be stored for at least 20 mo, after which it could survive a series of simulated launch environments.

The igniters to be used for the storage units were originally assembled in February 1965. Prior to the static test of F-3, a single igniter was disassembled and inspected. No visual changes to the igniter hardware were observed from its long-term ambient storage and subsequent environmental testing.

Dev. F-3 was tested at a grain temperature of 10°F while mounted in the vertical spin stand operating at 150 rev/min. The unit appeared to operate normally during its 45-s burn. A post-fire inspection of the spent motor hardware indicated nominal operation.

An analysis of data related to this second storage unit appeared nominal with the exception of the characteristic velocity value W^* . The measured W^* value of 4903 ft/s is approximately 1% below the average value obtained from development and qualification units. A complete

review of all apogee motor measurement parameters and instrumentation procedures related to storage units F-1 and F-3 is currently in progress. The results of this review will be presented at a later date.

4. Omnidirectional Antenna Tests

Development test J-1 was the fourth and final in a series conducted to evaluate the design and release mechanism of an omnidirectional antenna to be used on the ATS-C spacecraft. The design and fabrication of the antenna were assigned to Hughes Aircraft Co. (HAC) by Goddard Space Flight Center. JPL supported HAC with three apogee motor ignition tests and one full duration (test J-1) apogee motor test.

As shown in Fig. 1, the antenna is located at the apex of a fiberglass dome, which in turn is mounted to the apogee motor's nozzle exit cone. During launch the antenna/dome will be used until apogee motor ignition, at which time it is expelled and no longer needed.

The first three tests that used only the apogee motor's ignition pulse to expell the antenna/dome established

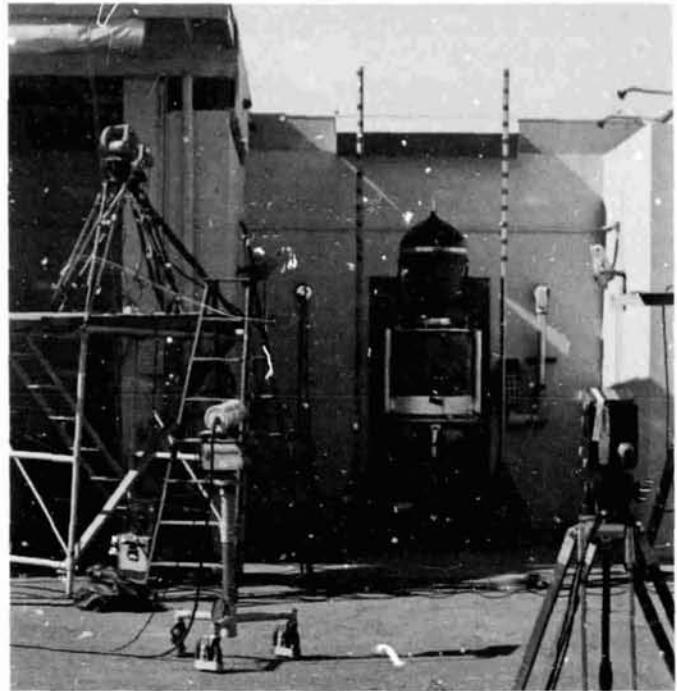


Fig. 2. Pretest installation of test article and high-speed cameras

final design release times, and the flight path of the test article. Test 4 employed a live motor (full duration) as a final confirmation of antenna design and release mechanism.

The test setup for test 4, which was basically the same for all tests, consisted of the equipment pictured in Fig. 2. The motor was mounted on the vertical spin test stand, located in the north test bay of Building E-60 at ETS. During the test, the motor and test article were spinning at 100 rev/min. Four 16mm Fastex cameras, operating at approximately 2,000 frames/s, photographed the release and initial free flight of the antenna/dome combination. A single 16mm Milliken camera, operating at 500 frames/s, was used for over-all test coverage. Fig. 3 shows the five camera positions. Two pressure transducers measured chamber pressure, while a single transducer measured igniter basket pressure. The output of all transducers was recorded on an oscillograph. A special circuit was created to indicate the release of the coaxial cables. The signal indication, which occurs after the antenna has traveled 0.25 in., was also recorded on the oscillograph. A temperature-indicating paint was applied to the antenna stand-off supports. The paint was applied in three colors that indicated temperatures of 500, 700, or 900°F.

The Fastex camera does not have the capability of incorporating a timing mark on the film, therefore a strobe

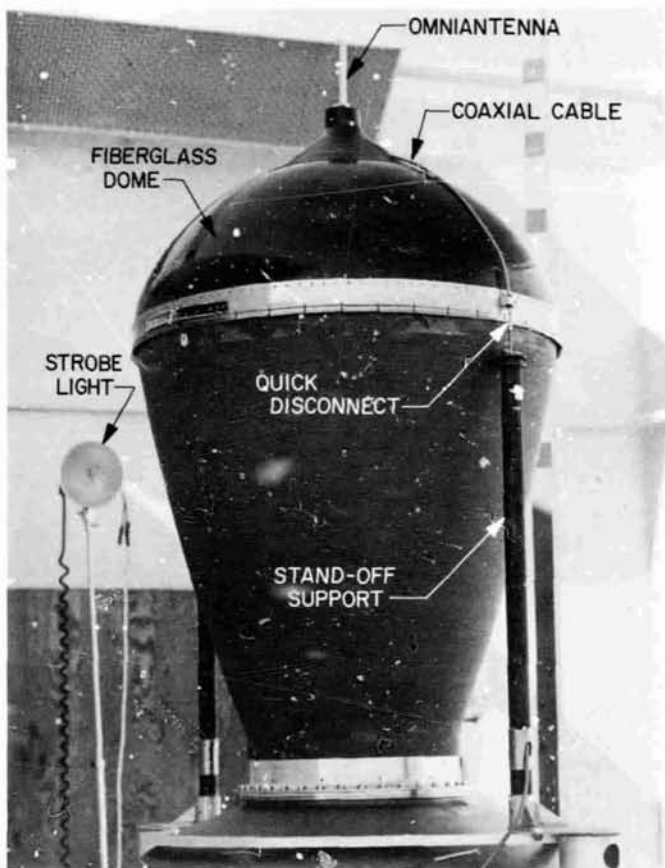


Fig. 1. Omniantenna/dome combination on apogee motor

review of all apogee motor measurement parameters and instrumentation procedures related to storage units F-1 and F-3 is currently in progress. The results of this review will be presented at a later date.

4. Omnidirectional Antenna Tests

Development test J-1 was the fourth and final in a series conducted to evaluate the design and release mechanism of an omnidirectional antenna to be used on the ATS-C spacecraft. The design and fabrication of the antenna were assigned to Hughes Aircraft Co. (HAC) by Goddard Space Flight Center. JPL supported HAC with three apogee motor ignition tests and one full duration (test J-1) apogee motor test.

As shown in Fig. 1, the antenna is located at the apex of a fiberglass dome, which in turn is mounted to the apogee motor's nozzle exit cone. During launch the antenna/dome will be used until apogee motor ignition, at which time it is expelled and no longer needed.

The first three tests that used only the apogee motor's ignition pulse to expell the antenna/dome established

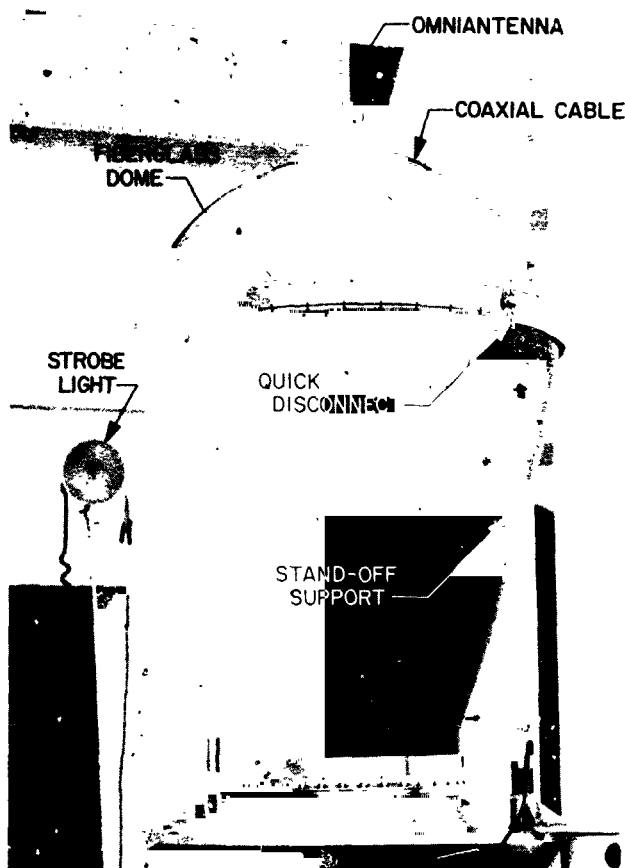


Fig. 1. Omniantenna/dome combination on apogee motor



Fig. 2. Pretest installation of test article and high-speed cameras

final design release times, and the flight path of the test article. Test 4 employed a live motor (full duration) as a final confirmation of antenna design and release mechanism.

The test setup for test 4, which was basically the same for all tests, consisted of the equipment pictured in Fig. 2. The motor was mounted on the vertical spin test stand, located in the north test bay of Building E-60 at ETS. During the test, the motor and test article were spinning at 100 rev/min. Four 16mm Fastex cameras, operating at approximately 2,000 frames/s, photographed the release and initial free flight of the antenna/dome combination. A single 16mm Milliken camera, operating at 500 frames/s, was used for over-all test coverage. Fig. 3 shows the five camera positions. Two pressure transducers measured chamber pressure, while a single transducer measured igniter basket pressure. The output of all transducers was recorded on an oscillograph. A special circuit was created to indicate the release of the coaxial cables. The signal indication, which occurs after the antenna has traveled 0.25 in., was also recorded on the oscillograph. A temperature-indicating paint was applied to the antenna stand-off supports. The paint was applied in three colors that indicated temperatures of 500, 700, or 900°F.

The Fastex camera does not have the capability of incorporating a timing mark on the film, therefore a strobe

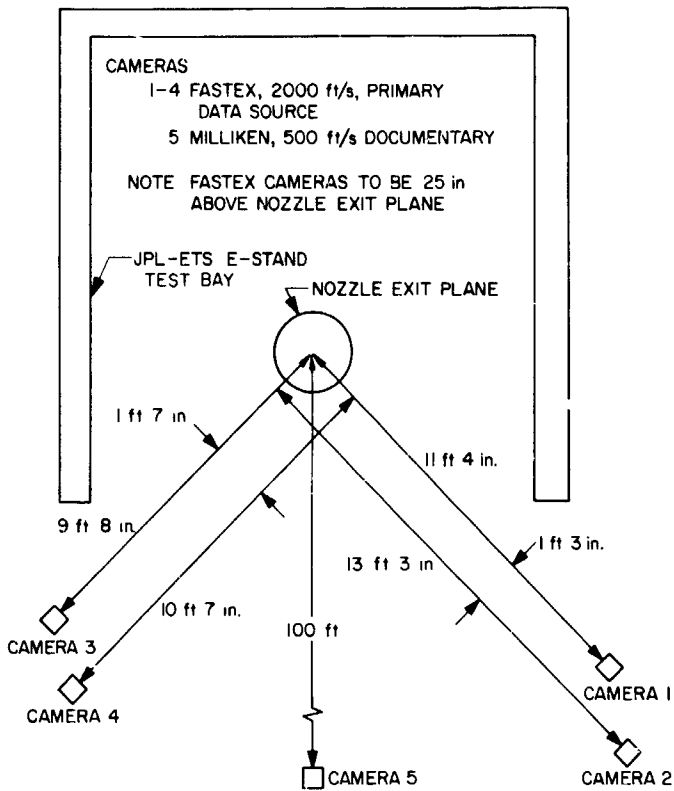


Fig. 3. Omniantenna tests, camera positions

light was placed in view of all Fastex cameras. The strobe light was triggered at the same time as current was supplied to the squib, thus producing on the film a positive indication of ignition sequence start. Fig. 4, using a block diagram, shows the electrical circuits for the high-speed cameras, igniter ignition, and strobe light. As indicated by the figure, the firing of the squib and strobe light and starting of each camera were controlled by a Fastex goose box. The test was initiated by actuating the start switch on each goose box.

Following a dry run which included the testing of all five cameras, test 4 was performed. All data were adequately recorded except for ignition current. A close examination of the oscillograph revealed that it was still possible to correlate the start of the ignition sequence without an ignition current trace. At the time current was applied to the squib circuit, a slight noise signal was generated in all pressure transducer circuits. This noise signal is discernible on all transducer traces recorded on the oscillograph (Fig. 5) and corresponds to zero time (t_0) or first indication of squib current.

The results of the recorded motor chamber and igniter basket pressures are given in Fig. 5. The oscillograph

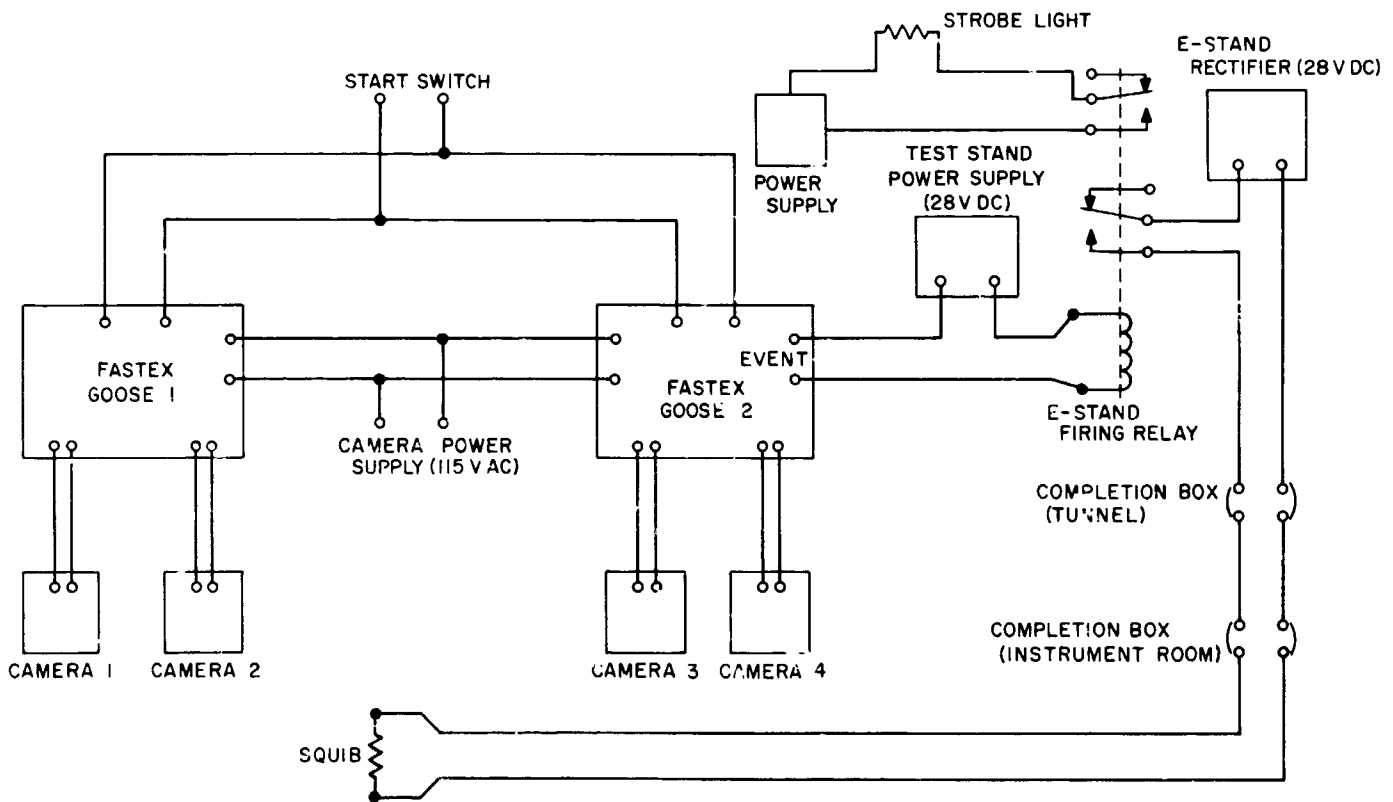


Fig. 4. Electrical diagram of high-speed cameras and igniter ignition circuit

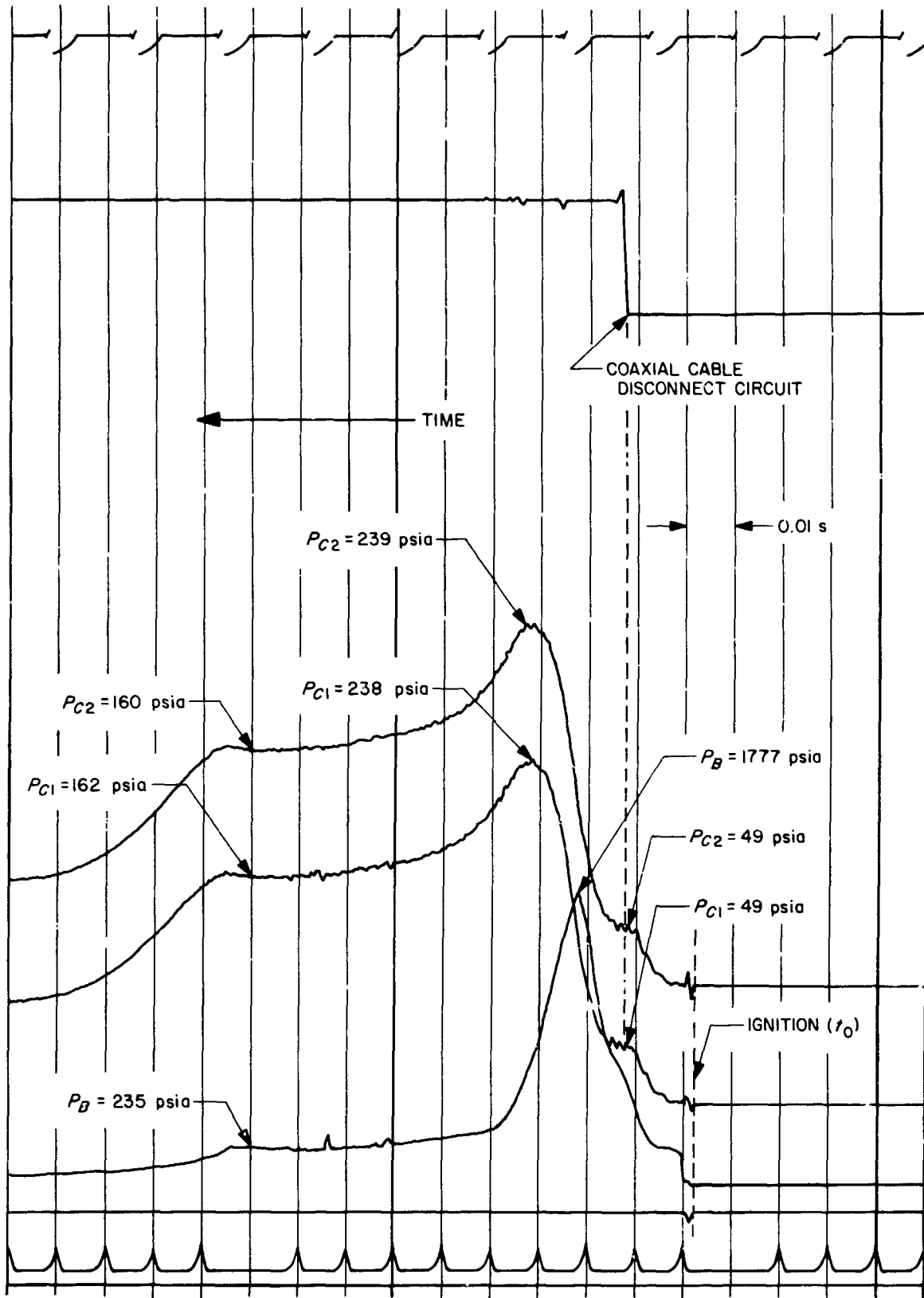
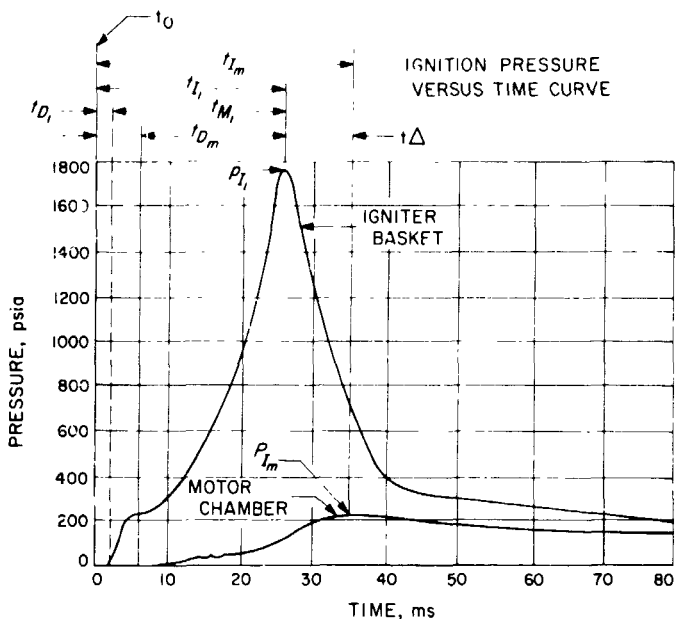


Fig. 5. Motor ignition characteristics, omniantenna test 4



IGNITION PARAMETER DEFINITIONS

- P_{I_i} = PEAK PRESSURE OF IGNITER BASKET DURING IGNITION PHASE
- P_{I_m} = PEAK PRESSURE OF MOTOR CHAMBER DURING IGNITION PHASE
- t_0 = ZERO TIME, OR TIME AT WHICH CURRENT IS APPLIED TO SQUIB
- t_{D_i} = THE DELAY TIME FROM t_0 UNTIL THE FIRST INDICATION OF SQUIB PRESSURE IS SEEN
- t_{D_m} = THE DELAY TIME FROM t_0 UNTIL THE FIRST INDICATION OF MOTOR CHAMBER PRESSURE
- t_I = THE TIME FROM t_0 TILL PEAK IGNITER PRESSURE IS SEEN
- t_{I_m} = THE TIME FROM t_0 TILL PEAK CHAMBER IGNITION PRESSURE IS SEEN; THIS IS NOT THE SAME AS PEAK *R/W* PRESSURE
- t_{Δ} = THE TIME DIFFERENCE BETWEEN PEAK IGNITER BASKET PRESSURE AND PEAK CHAMBER IGNITION PRESSURE
- t_{M_i} = THE TIME FROM INITIAL SQUIB PRESSURE TILL PEAK IGNITER BASKET PRESSURE; THE TOTAL IGNITER REACTION TIME

Fig. 6. ATS apogee motor ignition parameters

trace also shows the results of the antenna disconnect circuit. The ignition parameters on test 4 are nominal when compared to previous apogee motor firings at similar conditions. Fig. 6 and Table 2 summarize the critical ignition phase pressure levels and corresponding times, for the four omniantenna tests. The summary includes the coaxial cable disconnect response time and corresponding chamber pressure.

A visual inspection of the temperature-sensitive paint on the antenna standoff supports and brackets indicated that the temperature was below 500°F during the live motor firing. This result has been documented by color photographs. The antenna standoff brackets, which are bonded to the nozzle exit cone, became unbonded during test 4. This was expected since the nozzle exit cone achieves a temperature, at the bracket interface, of 1100°F, while the bonding adhesive is serviceable to 350°F.

The antenna disconnect circuit showed open (Fig. 5) at 14 ms after the application of squib current. At this time, the antenna had traveled approximately 1/4 in. from its original position. Similarly, the motor chamber pressure was 49 psia which closely corresponds to the nozzle diaphragm rupture pressure. It is felt that the antenna is released from the motor within milliseconds after the nozzle diaphragm ruptures, thus the antenna never sees the peak chamber pressure during the motor's ignition phase.

In summary, the igniter impulse was more than sufficient to separate the antenna/dome from the motor without producing structural damage. Based on visual and photographic coverage, the antenna released and maintained a free-flight path along the motor's centerline well beyond the region of the spacecraft's VHF antennae. A comparison of apogee motor ignition parameters indicates

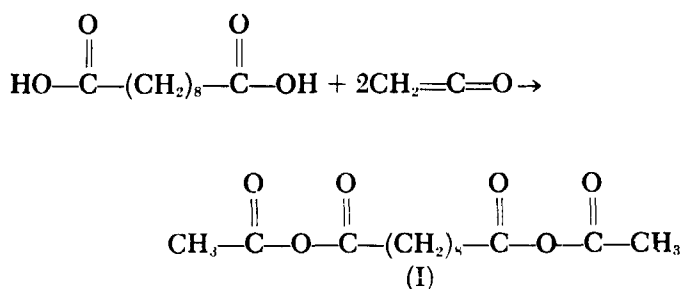
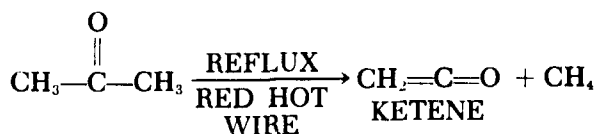
Table 2. Igniter summary, omniantenna tests

Test code	Test date	Temperature, °F	Vacuum start	t_{D_i} , ms	t_{M_i} , ms	t_I , ms	t_{Δ} , ms	t_{I_m} , ms	t_{D_m} , ms	t_{COAX} , ms	P_{I_i} , psia	P_{I_m} , psia	P_{COAX} , psia
0-1	12/15/67	Ambient, 60	No	—	—	39	4	43	17	—	1693	122	—
0-2	2/17/67	Ambient, 60	No	2	28	30	8	38	15	24	1781	127	57
0-3	3/9/67	Ambient, 60	No	2	28	30	6	36	16	25	1863	119	62
J-1	3/10/67	Ambient, 60	No	2	23	25	9	34	5	14	1777	239	49

See Fig. 6 for ignition parameter definitions except t_{COAX} the delay time from t_0 until the indication of coaxial cable disconnect. P_{COAX} motor chamber pressure at the time of coaxial cable disconnect.

Dianhydrides were prepared from dicarboxylic acids and ketene (Ref. 5).

a. Acetic-sebacic acid mixed anhydride (I)



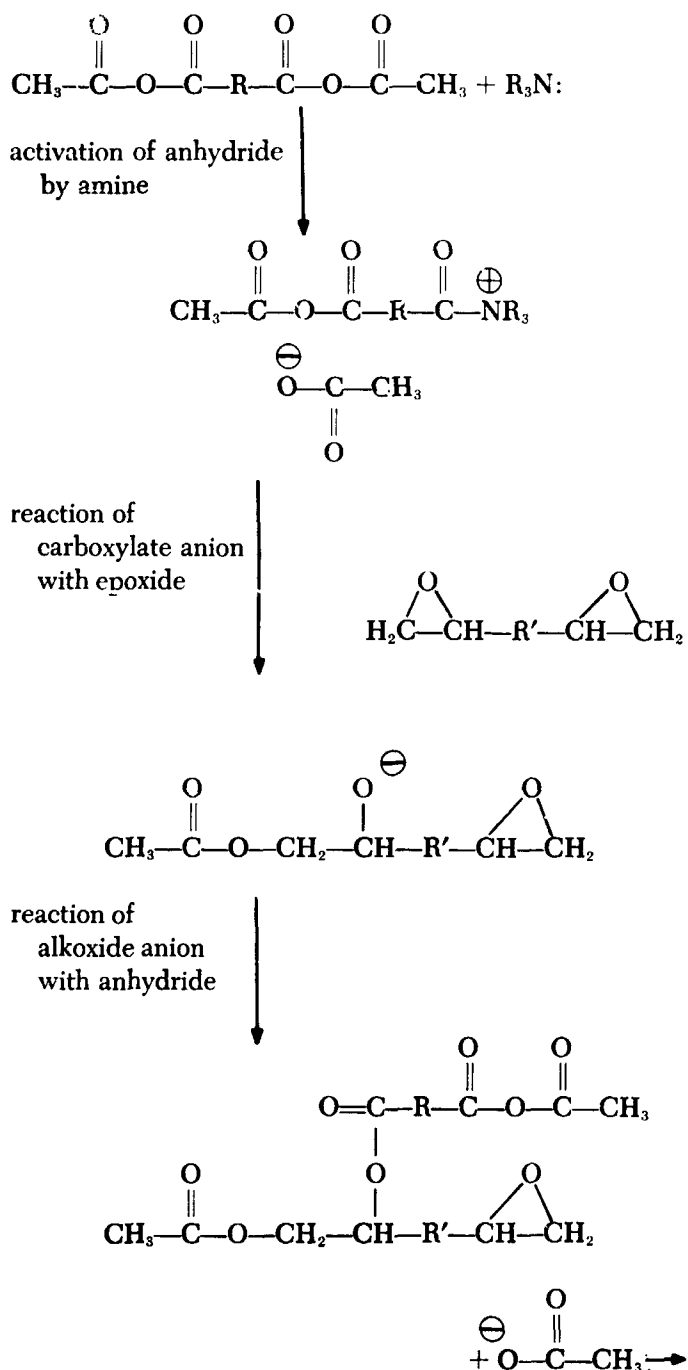
Sebacic acid was partially dissolved in three parts by weight of chromatography tetrahydrofuran. Ketene from a specially constructed ketene generator (Ref. 6) was bubbled through the stirred mixture while holding the temperature at 0°C.

The reaction was continued for 30 min past the point at which all solid sebacic acid had dissolved. Infrared showed the disappearance of the carboxyl peaks at 1710 and 1300 cm⁻¹ and appearance of the anhydride peaks at 1815, 1750, and 1030 cm⁻¹. (If ketene addition went past the point of quantitative reaction, the mixture rapidly became dark brown although no change in the infrared spectrum was observed.) Solvent removal at room temperature, under vacuum, left a colorless oil which solidified at about 20°C.

A series of polymerization mixtures was prepared in the dry box (Table 4). Of the curing agents only the ERL 4221 was distilled before use.

The room temperature reactions were run in vials in the dry box. The 55°C reactions were run with the same samples in an oil bath outside the dry box and the vials were sealed with vacuum grease. The results tend to agree with the literature for cyclic anhydrides. ERL 4221, which is a simple diepoxide (see SPS 37-43, Vol. IV for struc-

tures of curing agents), is inert to the acyclic anhydride unless catalyzed and heated. Tertiary amines are well-known accelerators for anhydride curing of epoxy resins and they have been shown here to have the same effect. The great superiority of pyridine to triethylamine as a catalyst is somewhat surprising in view of its weaker basicity, but is probably due to the lower steric hindrance around the nitrogen and opportunity for charge delocalization in the aromatic ring. The reaction mechanism may be as follows (Ref. 7):



repeating these steps

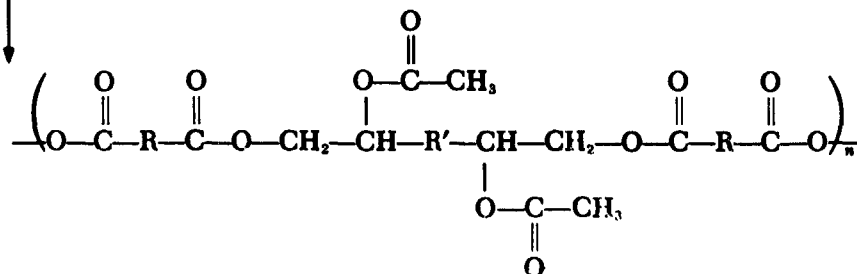


Table 4. Polymerization of sebacic-acetic acid mixed anhydride with epoxides and aziridines

Curing agent	Reaction temperature	ρr	Reaction time	Properties of product	Infrared results
ERL 4221	R.T.	0	25 days	Soft white semisolid	Original anhydride and ester peaks unchanged
ERL 4221 pyridine catalyzed	R.T.	0	25 days	Soft brown semisolid	Ester peak stronger than uncatalyzed case
ERL 4221 triethylamine catalyzed	R.T.	0	25 days	Soft tan semisolid	Ester peak intermediate between above cases
ERL 4221	55°C	0	17 days	Soft white semisolid	Small increase in ester
ERL 4221 pyridine catalyzed	55°C	0	17 days	Very sticky black rubber, can flow at 55°C, soluble in chloroform	Large increase in ester and decrease in anhydride
ERL 4221 triethylamine catalyzed	55°C	0	17 days	Soft tan semisolid	Moderate increase in ester
EPON 801	R.T.	1.0	25 days	Soft yellow semisolid	—
EPON 801 pyridine catalyzed	R.T.	1.0	25 days	Soft yellow solid	Moderate ester peak appeared in addition to anhydride peaks
EPON 801	55°C	1.0	17 days	Soft yellow semisolid	Little change from original small amount of ester
EPON 801 pyridine catalyzed	55°C	1.0	17 days	Brown slightly sticky rubber insoluble in common solvents, decomposes at approximately 300°C rather than melting	Could not be obtained
MAPO	R.T.	1.0	25 days	Soft tan semisolid	Aziridine and anhydride unchanged
MAPO	55°C	1.0	17 days	Brown flowing semisolid	Unchanged
HX 740	R.T.	0	25 days	Soft yellow semisolid	Little change
HX 740	55°C	0	17 days	Yellow-orange slightly sticky rubber, insoluble in common solvents, decomposes with heating more than EPON 801 product, but does not melt	Could not be obtained
ZC 466	R.T.	0	10 min	Large reaction exotherm, product was glass-like solid with large bubbles	—

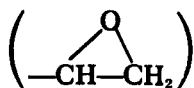
Note: In all cases $\frac{\text{equivalents of curing agent}}{\text{equivalents of anhydride}} = 1.0$

$\rho r = \frac{\text{equivalents of trifunctional curing agent}}{\text{total equivalents of curing agent}}$

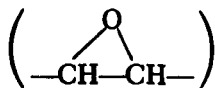
R.T.: room temperature

Obviously, this is oversimplified because the tertiary amine can complex with either carboxyl of the anhydride, and ring attack can take place at either carbon of the epoxide. A linear polyester results in all cases.

The polymers were not the result of epoxide homopolymerization as shown by the appearance of a strong ester peak and significant decrease in anhydride peaks in the infrared. EPON 801 is more reactive and since it is a trifunctional epoxide, catalysis and heating produced a cross-linked polymer. The epoxide groups in EPON 801 are terminal

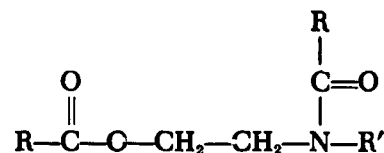
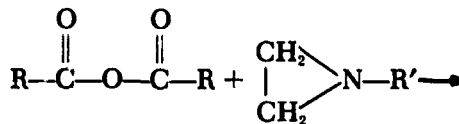


rather than internal



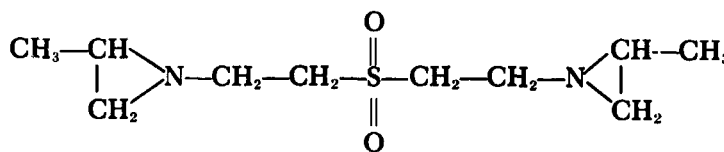
as in ERL 4221.

Catalysis was not used with the aziridines since they themselves contain tertiary nitrogen. MAPC was completely inert. HX 740 was similar at room temperature but when heated, surprisingly (since it is difunctional) gave a product nearly as cross-linked as that from EPON 801. Some reaction other than the predicted one



must be taking place. This is supported by the results with ZC 466. It is a highly active diaziridine because it does not have a carbonyl group adjacent to the nitrogen.

ZC 466



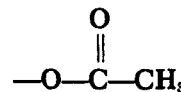
(Thiokol-Elkton)

From these tests it was concluded that the anhydride-epoxide reaction is too unreactive for use as a model system. Anhydride-aziridine is eliminated by unexplained side reactions. However, both showed possibilities for use in binder curing.

b. Acetic-dimer acid mixed anhydride. To investigate this area, hydrogenated, purified dimer acid (SPS 37-43, Vol. IV) was used to represent carboxyl-terminated hydrocarbon binders. Preparation was similar to that of the sebacic acid mixed anhydride. However, since dimer acid is a liquid and completely miscible with tetrahydrofuran, there was no built-in end point indicator to show when ketene addition should be halted. Infrared was inconvenient and rather insensitive for this purpose. Thus, care-

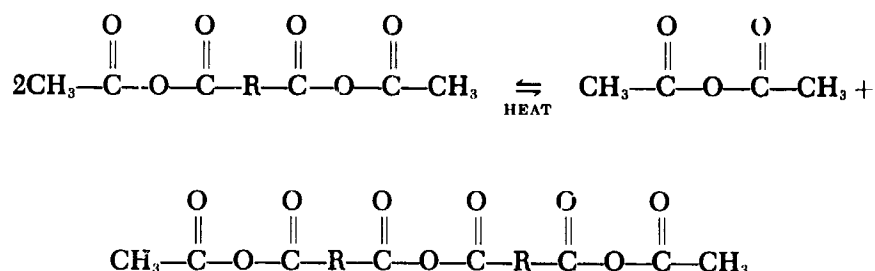
ful observation was necessary to stop the reaction at the first appearance of color due to excess ketene.

A more serious problem arose when it was discovered that the viscosity of the product (originally somewhat less than that of dimer acid) greatly increased as it was rotated under vacuum to remove the last traces of solvent. Infrared showed a corresponding decrease in peaks at 990, 1120, and 1370 cm^{-1} . These belong to the



moiety.

It is well known (Refs. 6 and 8) that unsymmetrical anhydrides can rearrange.



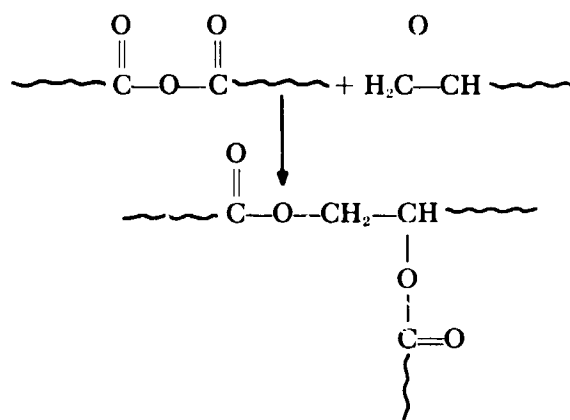
Under vacuum the more volatile acetic anhydride can distill out, leaving a polyanhydride. It was felt that this reaction could be minimized by carrying out all operations at ambient temperature or below and keeping the time under vacuum as short as possible. However, anhydride analysis (using both morpholine and hydrolysis to carboxyl) clearly revealed that these precautions, while improving the product, were not sufficient to completely prevent significant rearrangement. When the mixed anhydride was heated under vacuum (85°C) a very viscous polyanhydride was produced and acetic anhydride was collected in the cold trap. A similar rearrangement probably occurs in the sebacic-acetic acid mixed anhydride, but infrared indicates it to be of much lesser magnitude.

Sensitivity of the acetic-dimer acid mixed anhydride to atmospheric moisture was investigated by infrared analysis (SPS 37-43, Vol. IV). After only one day of exposure the 1370 cm^{-1} peak decreased and the 990 and 1120 cm^{-1} peaks nearly vanished while viscosity increased. Thus, rearrangement occurs even when acetic anhydride only has the opportunity to evaporate at atmospheric pressure. The resulting interchain anhydride linkages are quite stable to hydrolysis and no carboxyl peak appears for approximately 2 wk. After 26 days, a significant amount of anhydride remains. The original mixed anhydride, when stored in a sealed container, does not lose acetic anhydride.

A series of curing mixtures was prepared in the atmosphere using the best acetic-dimer acid mixed anhydride available (about 1/3 of the mixed anhydride groups had rearranged, Table 5). The reaction vials were sealed with vacuum grease and kept at 55°C for 25 days.

The epoxides produced the best cures, although pyridine catalysis was necessary. Both EPON 801 and DER 736, which have terminal epoxide groups, resulted

in essentially complete reaction of anhydride and so the best thermal stability. DER 736 is difunctional yet it yielded an apparently cross-linked product. This can be explained by reaction with the internal anhydride linkages in the rearranged acetic-dimer acid mixed anhydride. Evaporation of acetic anhydride has removed monofunctionality and therefore the effective average functionality of the rearranged anhydride is greater than two.



The resulting branched species is trifunctional, and further such reactions can produce a network structure. (This explanation may also apply to the sebacic acetic anhydride system.)

Of the aziridines, MAPO was nearly inert. HX 740 produced a good rubber but incomplete anhydride reaction resulted in poorer thermal stability. The rubber was somewhat cross-linked for the same reason as that of the DER 736. ZC 466 reacted rapidly and gave the toughest product but its thermal stability was by far the worst. This poor heat resistance has also been observed in ZC 466 curing of carboxyl terminated prepolymers (SPS 37-40, Vol. IV, pp. 98-103). Surprisingly, when mixtures of ZC 466 and EPON 801 or HX 740 were used, curing was incomplete even though these reagents gave good cures when used alone. The original assumption that aziridines

Table 5. Curing of acetic-dimer acid mixed anhydride

Curing agent	ρ_T	Gel time	Properties of product	Infrared results
EPON 801 pyridine catalyzed	1.0	< 3 days	Black, nonsticky rubber easily torn; no softening or bubbling when heated to 350°C; definite decomposition but still somewhat rubbery when cooled to R.T.	Anhydride peaks essentially gone; strong ester peak at 1740 cm^{-1}
DER 736 pyridine catalyzed	0	5 days	Black nonsticky, very weak easily torn rubber; when heated, it softens at 230°C but does not liquefy at 350°C; still rubbery when cooled to R.T.	Anhydride peaks gone; strong ester peak at 1740 cm^{-1}
MAPO pyridine catalyzed	1.0	—	Black fluid	Original MAPO and anhydride peaks almost unchanged
HX 740	0	< 10 days	Light orange, nonsticky rubber; somewhat tougher than above; when heated, it softens and partially liquefies at 250°, badly decomposed and bubbled at 350°, but still mostly solid	Very crude, but apparently some unreacted anhydride along with ester at 1740 and tertiary amide at 1650 cm^{-1}
ZC 466	0	Few hours	Cloudy yellow orange, tough leathery material; somewhat sticky; when heated, turns to liquid, and bubbles appear by 300°C, and by 315°C it is almost entirely molten	Could not be obtained
ZC 466 (50%) HX 740 (50%)	0	< 10 days	Sticky orange rubber	Large amount of unreacted anhydride plus ester at 1740 and tertiary amide at 1650 cm^{-1} ; unexplained peak at 1530
ZC 466 (50%) EPON 801 (50%)	0.5	—	Very viscous orange gum	Large amount of unreacted anhydride plus ester at 1740 and tertiary amide at 1650 cm^{-1} ; very similar to above except for lack of 1530 peak

Note: In all cases:

$$\frac{\text{equivalents of curing agent}}{\text{equivalents of anhydride (based on theoretical pure mixed anhydride)}} = 1.0$$

$$\rho_T = \frac{\text{equivalents of trifunctional curing agent}}{\text{total equivalents of curing agent}}$$

Reaction temperature: 55°C.

Total reaction time: 25 days.

Gel time: time at which the material would no longer flow.

would react analogously to epoxides is supported by infrared peaks at 1740 cm^{-1} (ester) and 1650 cm^{-1} (tertiary amide) in all aziridine cured products.

Curing mixtures were also prepared with 70 wt % ammonium perchlorate loading. Because of the relatively high viscosity of the mixed anhydride (compared with the acid chloride terminated prepolymer), the mixes were not pourable at room temperature even at this low solids level and with the use of lecithin as a wetting agent. The products had poor properties after 10 days at room temperature and 15 days at 55°C. Except for ZC 466 which reacted during mixing and produced a crumbly sand, the results ranged from soap-like (MAPO and HX 740) to brittle plaster (EPON 801 and DER 736).

3. Conclusions

While the anhydride-epoxide and anhydride-aziridine reactions could conceivably be used for binder curing, the problems associated with these systems make them less practical than existing curing reactions. The acid chloride terminated binder (SPS 37-43, Vol. IV, pp. 163-167) appear superior because of its low viscosity and greater room temperature reactivity.

4. Binder Hydrogenation

The work on hydrogenation of unsaturated, carboxyl terminated hydrocarbon binders has been continued. The effect of varying hydrogenation conditions (pressure, temperature), solvents (cyclohexane, hexane, acetic acid), and

catalysts (Pd on carbon, Pd on alumina, PtO_2) was investigated. A 1-gal stirred autoclave has been put into operation to replace the previously used 1-l rocking autoclave.

No better system has been found than Pd on carbon in a hydrocarbon solvent at approximately 2000 psi and 135°C . It has not been found possible to remove the last traces of unsaturation.

To check the possibility that the iodine number is incorrectly indicating unsaturation because of substitution reactions on the carbon adjacent to the carboxyl group, use was made of the tetranitromethane Π complex (Ref. 6). This brightly colored complex is known to form with even highly hindered double bonds. Test mixtures were prepared with a few drops of tetranitromethane per ml of sample at room temperature and reactions were complete in a few minutes (Table 6). Caution is necessary because tetranitromethane is both poisonous and explosive.

Table 6. Test for unsaturation

Compound	Iodine number	Final color, tetranitromethane test
Dimer acid	15	Deep yellow orange
Hydrogenated dimer acid	0.4	Very pale yellow
Hydrogenated telagen S	0.8	Light yellow
Mineral oil	—	Colorless
Acetic acid	—	Colorless

The results show that the test is sensitive to very small amounts of unsaturation and is unaffected by carboxyl groups. It can be made quantitative and used to indicate the number of substituents on the double bond by spectrophotometric determination of the color density (Ref. 9).

C. Pintle Nozzle Thrust Vector Control, L. Strand

A pintle nozzle thrust vector control test program was described in SPS 37-39, Vol. IV, pp. 85-91, the objectives of the program being to: (1) determine if a pivoted pintle nozzle system is capable of producing side thrust of sufficient magnitude for thrust vector control purposes and, (2) determine the criticalness of nozzle pintle position on thrust alignment for thrust magnitude control-thrust termination pintle nozzle systems. Described in SPS 37-39 were the test hardware, instrumentation, test procedure, and its results. A pintle system was incorporated into the gas-flow nozzle test assembly of the JPL flow channel (described in SPS 37-35, Vol. IV, pp. 130-140). Tests were conducted with the pintle canted about its pivot point at angular displacements (θ) from the nozzle centerline, as

illustrated in Fig. 7. Theta values of 0° , $15'$, $30'$, 1° , and $1^\circ 30'$ were used. Test data consisted of the nozzle surface pressure distributions, obtained from 98 nozzle static pressure taps. It was decided at the conception of this program that the additional complexity of attempting to instrument the pintle surface was not warranted.

Since the last report, the test pressure data has been reduced, and, using these results, side force numerical integrations over the nozzle and pintle surface have been performed for the pintle nozzle system in its four canted angle positions. Since the pintle was not instrumented with pressure taps, the pressure at any point on the pintle surface was assumed to be equal to the pressure on the nozzle surface at the point on the same axial station intersected by a radial line drawn through the pintle centerline and the pintle surface point (Fig. 8). This assumption

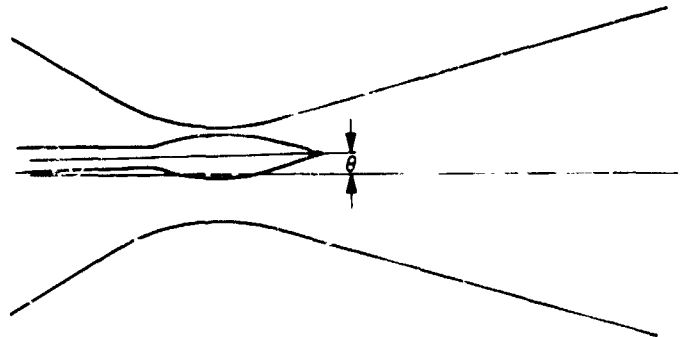


Fig. 7. Canted pintle

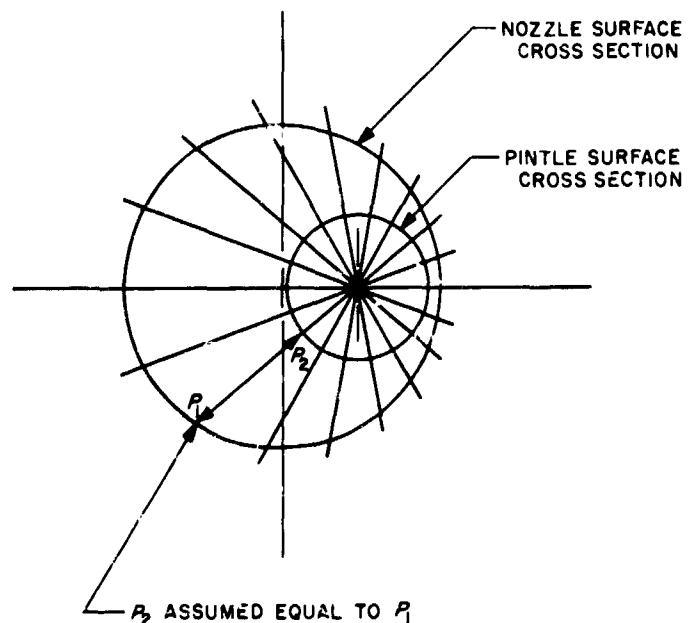


Fig. 8. Pintle surface-pressure determination

should be correct in the plane of the pintle cant and should be a fair approximator in the 180 deg quadrants bounded by these limits. Figure 9 shows plots of the resultant net side force, ratioed by the nozzle supply pressure, normal

to the nozzle centerline and in the plane of the pintle cant summed over the nozzle expansion ratio for the nozzle pintle system and the nozzle alone for the four cant angles. Positive force is in the direction of the pintle cant.

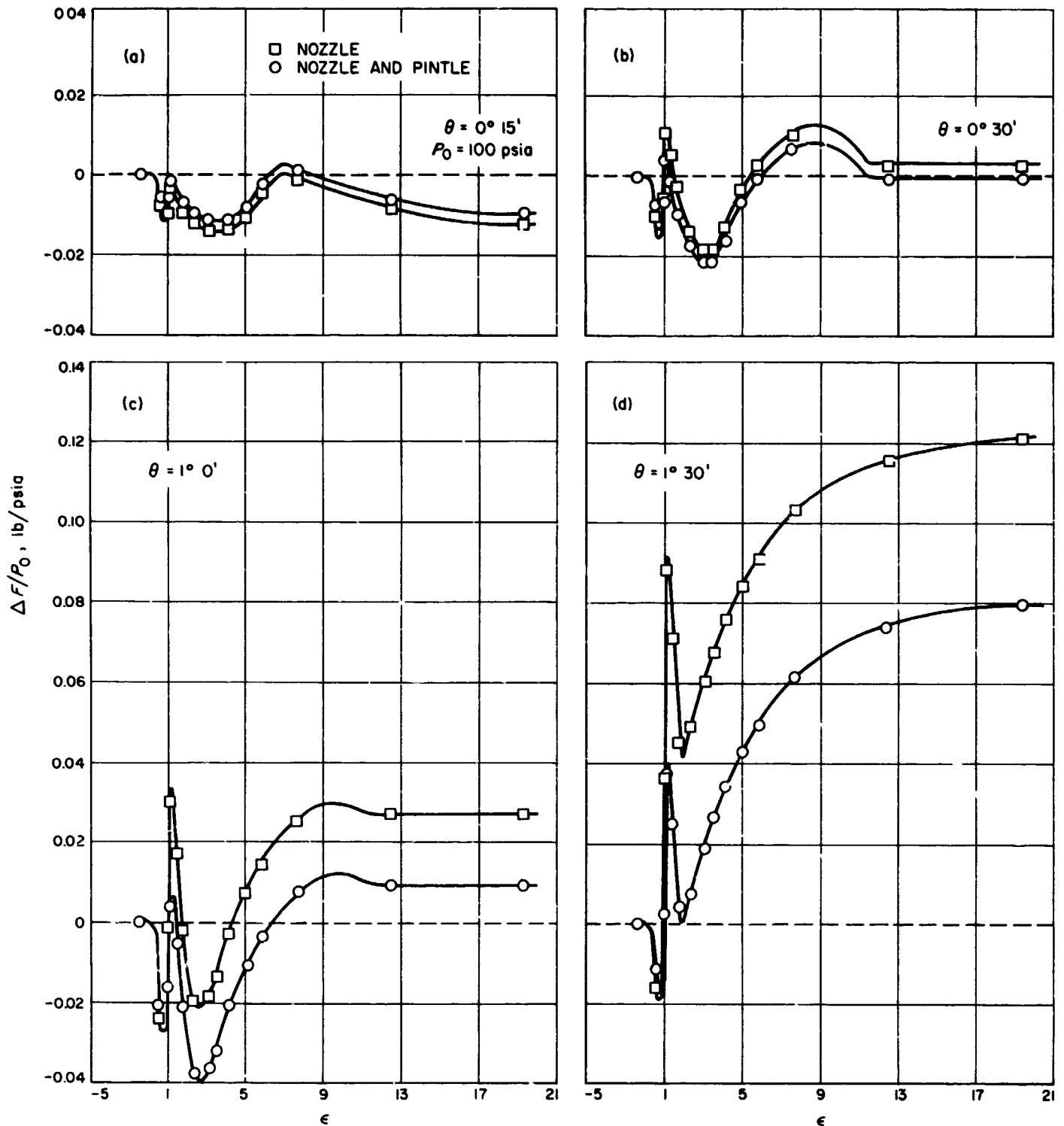


Fig. 9. Sum of net side force/supply pressure ratio versus nozzle expansion ratio

The reversals in side force direction in the nozzle throat region in Fig. 9 ($\epsilon = 1$) are due to the nonsymmetrical flow about the canted pintle. The final jump in side force in the positive direction for each cant angle is due to the shock that emanated from the pintle tip. As was shown in SPS 37-39, and as indicated by the magnitude of the force increases, the shock became progressively greater in strength with increasing cant angle.

For the $1^\circ 30'$ cant, a calculated over-all net side force for the nozzle pintle system of 6% of the nozzle theoretical axial thrust was obtained. As is evident from Fig. 9, this net side force is due solely to the shock wave, the side force due to the nonsymmetrical flow in the nozzle throat completely cancelling itself out.

Figure 10 shows the pintle nozzle over-all net side force/supply pressure ratio plotted versus the pintle cant angle for the four test conditions. Cant angle was arbitrarily chosen as the independent parameter. The abrupt-

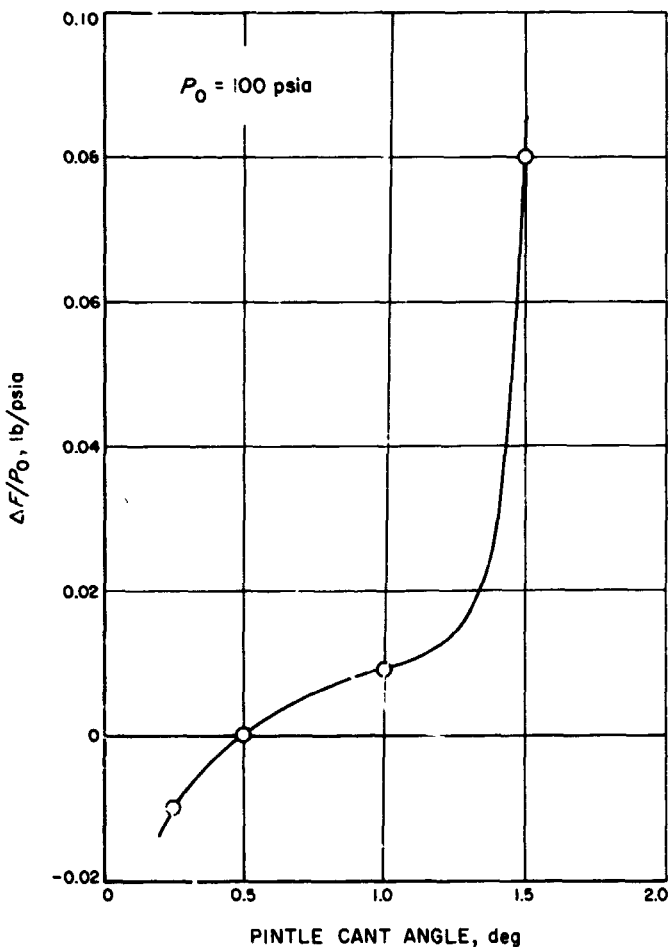


Fig. 10. Over-all net side force/supply pressure ratio versus pintle cant angle

ness of the increase in side force in the positive direction as a result of the pintle tip shock is again illustrated.

Future plans consist of using a recently available method-of-characteristics computer program to make two-dimensional model calculations for comparison with test data, specifically the shock structure, and to compare canted pintle nozzle flow with purely radially translated pintle flow.

D. Low-Pressure Combustion Studies, L. Strand

As was reported in SPS 37-27, Vol. IV, pp. 49-52, in the low-pressure combustion motor tests that have been conducted under this program, the propellant charges were ignited in the stable operating pressure region, burned regressively with decreasing pressure into the unstable pressure region, and ultimately ceased burning (extinguished). For a majority of the test data records, low-frequency low-amplitude oscillations in pressure occurred prior to extinction of combustion. The results of measurements of the negative slope of the last pressure oscillation (Fig. 11) and the mean chamber pressure at, or immediately prior to, the onset of extinction for test runs with JPL 540 propellant and its modification formulations were reported (Fig. 12) in SPS 37-41, Vol. IV, pp. 85-91. Although the data had a great amount of scatter to it, a definite correlation between the rate of depressurization (dP/dt)_e and the mean chamber pressure prior to extinction was found for each propellant whose test data was analyzed.

Data were presented in SPS 37-27 and 37-22, Vol. V, pp. 13-15 (Confidential) showing that, under low-frequency instability conditions, a correlation exists between the frequency of pressure oscillations and the mean chamber pressure at combustion extinction (Fig. 13). In order to assess the importance of the pressure oscillation

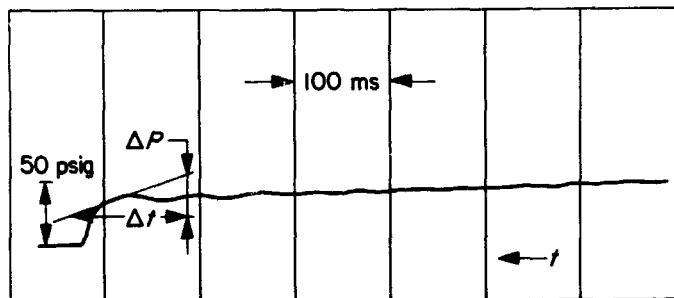


Fig. 11. Pressure-time trace for run 1437, JPL 540-Mod B propellant

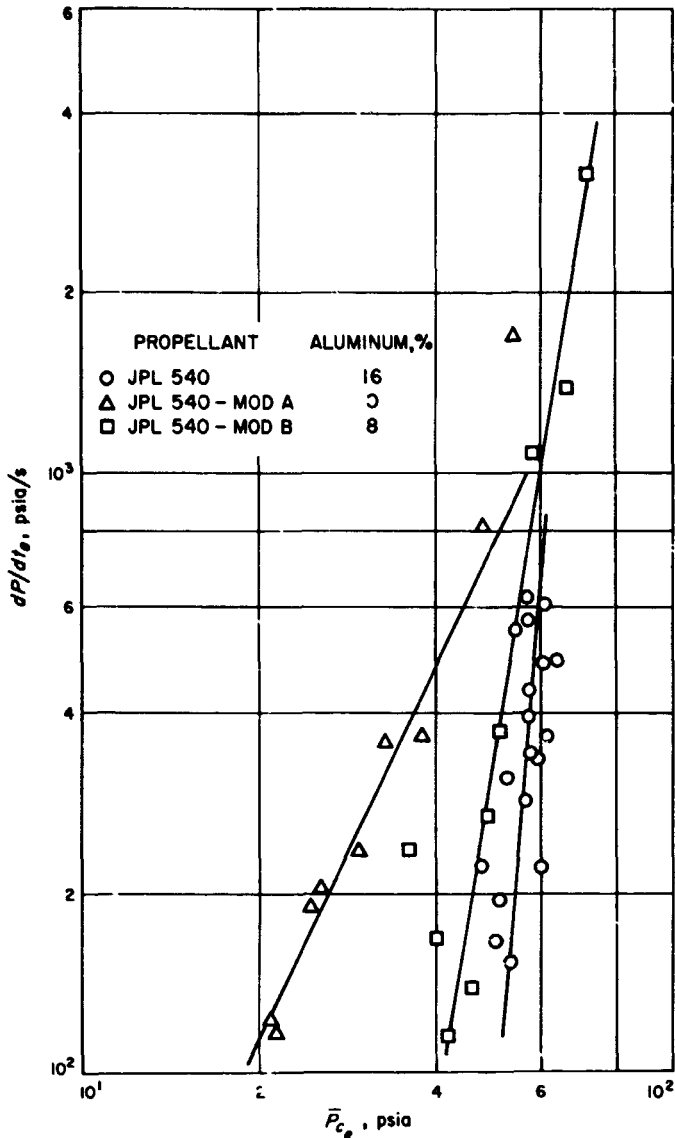


Fig. 12. Rate of chamber depressurization versus mean chamber pressure at combustion extinction

rate of depressurization on low-pressure combustion extinction, it was deemed necessary to determine if the rate-of-depressurization-pressure correlation at combustion extinction is significant in itself, or is merely a consequence of the correlation between frequency and pressure.

Further data reduction has therefore been performed on the low-frequency instability and extinguishment data for five propellants. The additional information consists of the mean chamber pressure, motor L^* , frequency of pressure oscillations, and pressure oscillation maximum rate of depressurization at various points on the test oscillograph pressure-time traces prior to the occurrence of extinction.

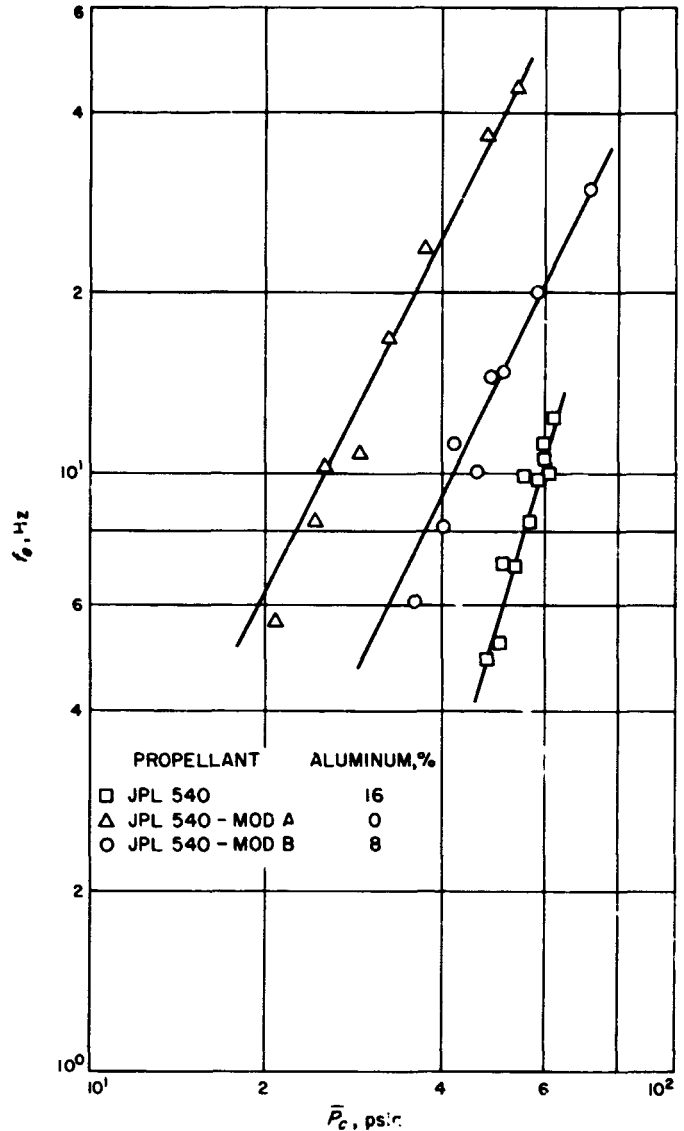


Fig. 13. Pressure oscillation frequency versus mean chamber pressure at combustion extinction

Fig. 14 is a log-log plot of the frequency of pressure oscillations plotted versus the mean chamber pressure for several test firings with a nonaluminized propellant. The frequency data correlates fairly well with pressure, in good agreement in the same pressure region with the results of tests with similar propellants reported by NOTS, China Lake (Ref. 10). Figure 15 shows the maximum rate of depressurization of the pressure oscillations plotted logarithmically versus chamber pressure for the same test runs. Only the extinction depressurization points correlate with pressure. Figures 16-17, 18-19, and 20-21 show the same type of data for 8%, 16%, and 16% (coarser grade) aluminized propellants, respectively. The same results are evident. This difference in the character of

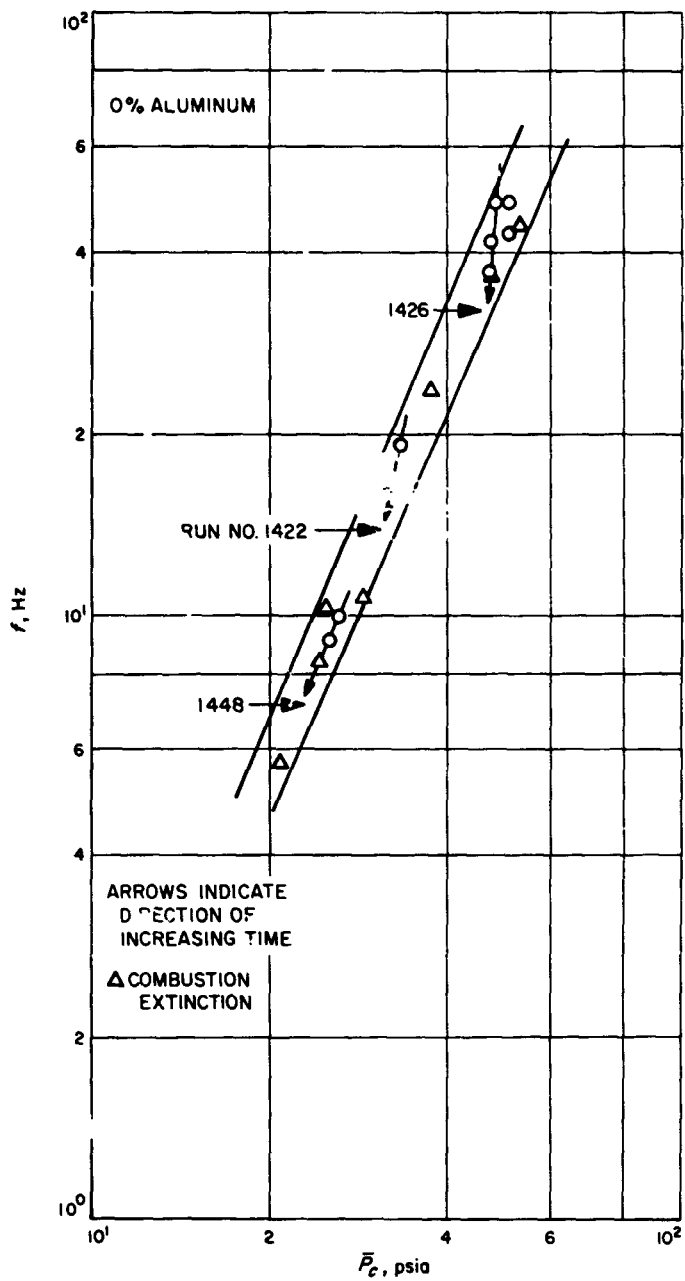


Fig. 14. Pressure oscillation frequency versus mean chamber pressure, JPL 540-Mod A propellant

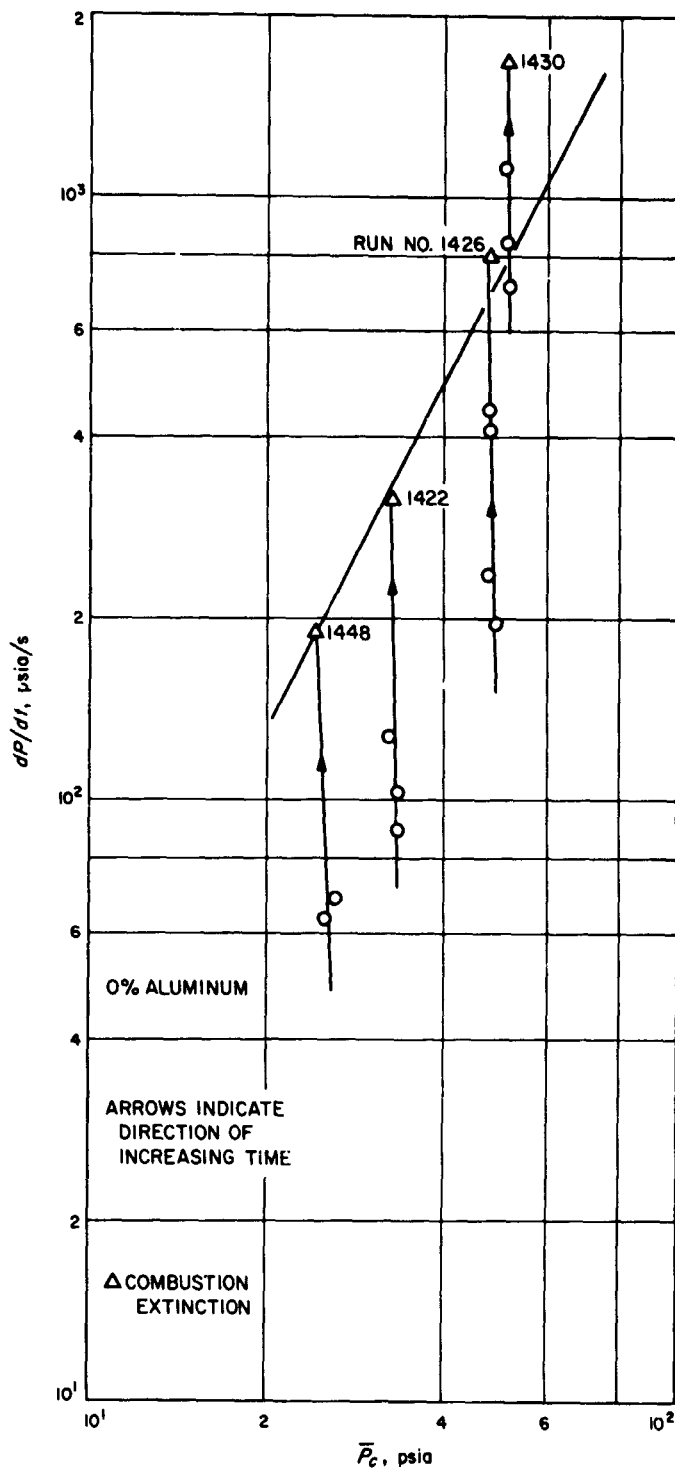


Fig. 15. Pressure oscillation rate of depressurization versus mean chamber pressure, JPL 540-Mod A propellant

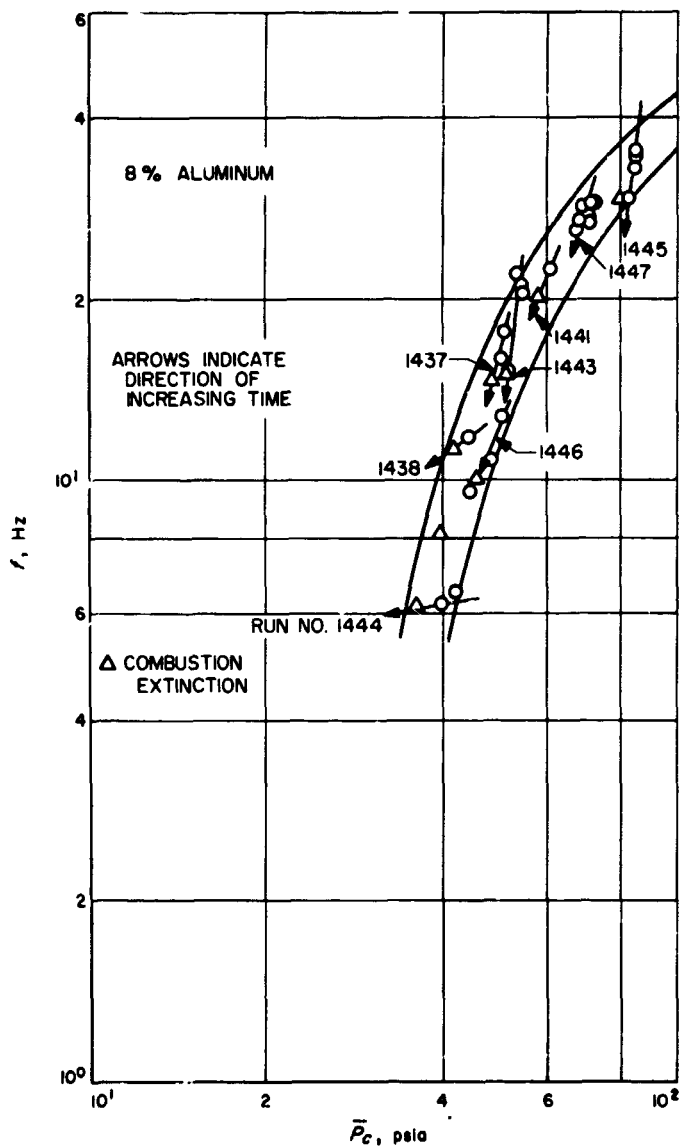


Fig. 16. Pressure oscillation frequency versus mean chamber pressure, JPL 540-Mod B propellant

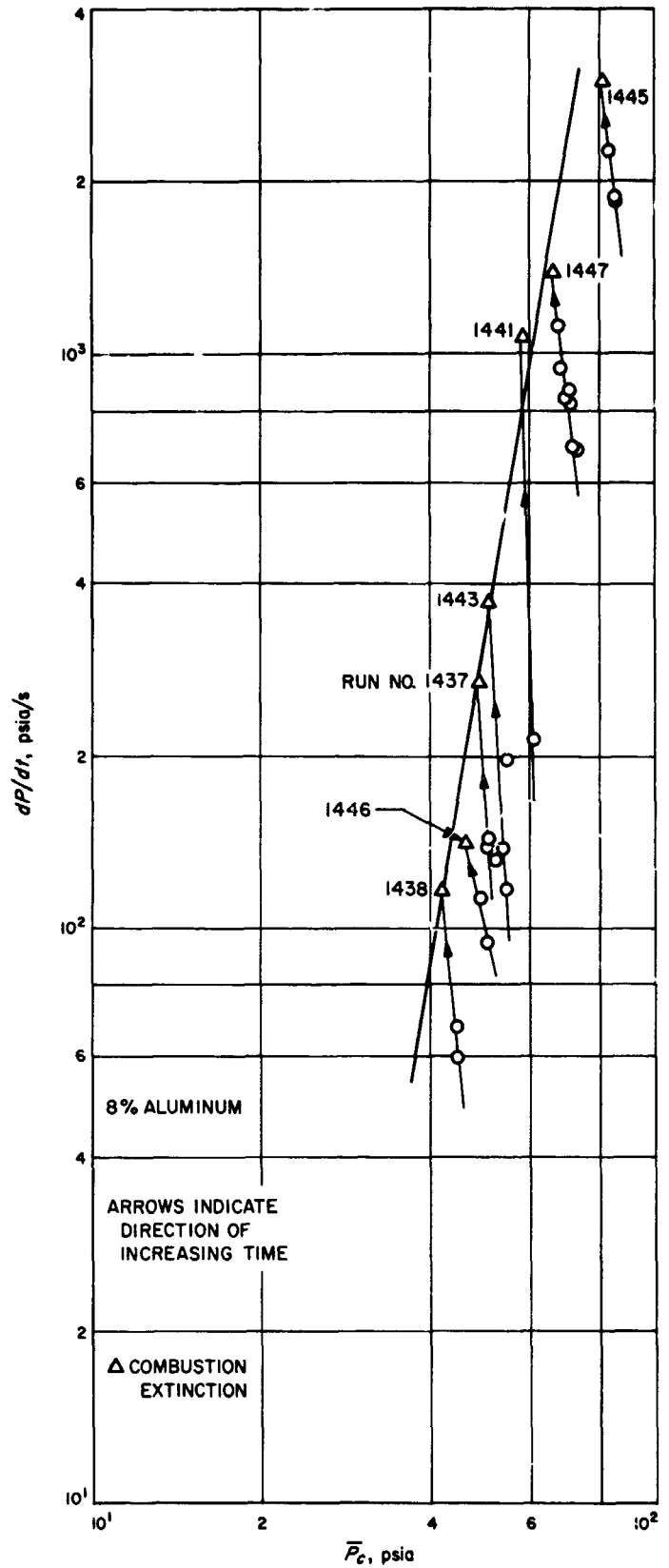


Fig. 17. Pressure oscillation rate of depressurization versus mean chamber pressure, JPL 540-Mod B propellant

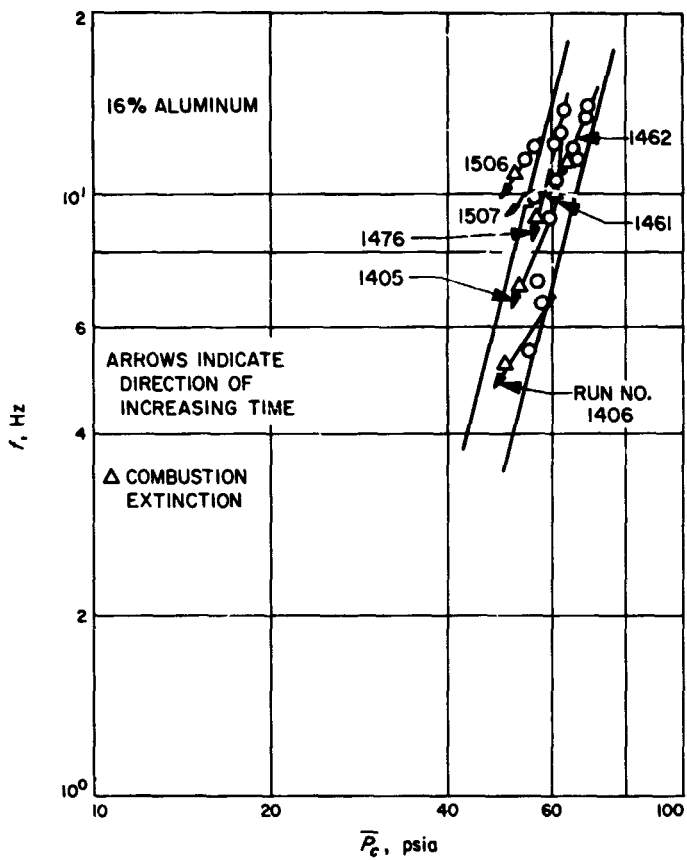


Fig. 18. Pressure oscillation frequency versus mean chamber pressure, JPL 540 propellant

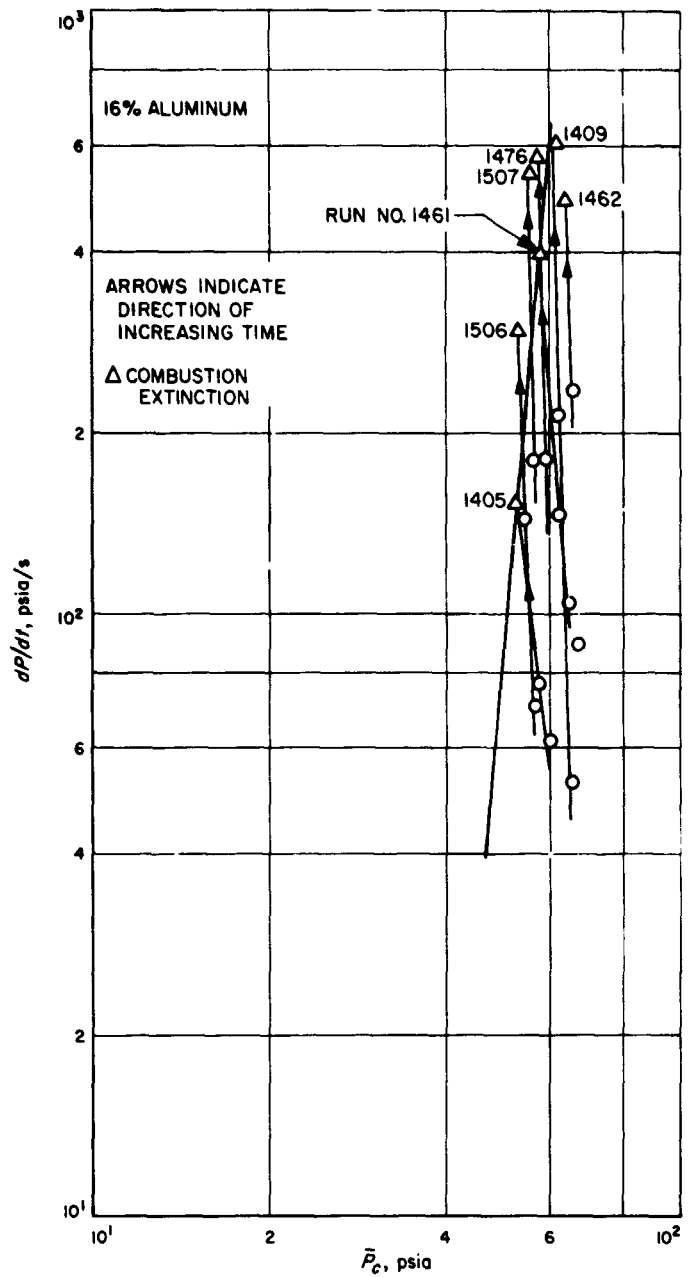


Fig. 19. Pressure oscillation rate of depressurization versus mean chamber pressure, JPL 540 propellant

the frequency and depressurization rate correlations with pressure seems to substantiate the significance of the pressure oscillation rate-of-depressurization-pressure correlation at extinction itself.

The possible significance of pressure perturbations on solid propellant combustion extinction has been noted earlier by Cohen (Ref. 11) and others. Also, the ability of

very rapid chamber venting (rapid depressurization) to quench solid propellant combustion at high chamber pressure operating conditions is well recognized (Ref. 12). The results of the additional data analysis presented here certainly make plausible a postulation that similar mechanisms are controlling rapid depressurization and low-pressure combustion extinction.

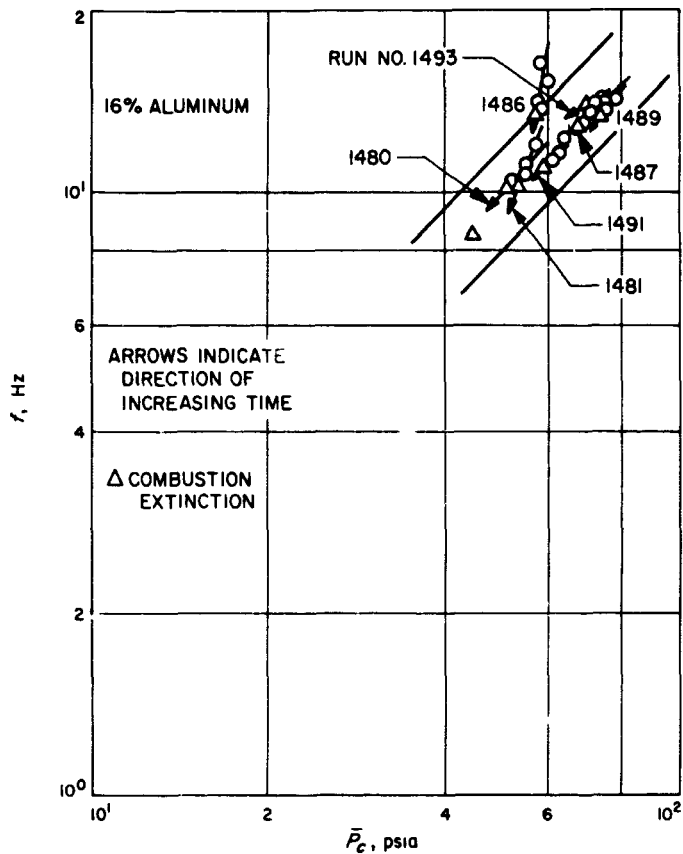


Fig. 20. Pressure oscillation frequency versus mean chamber pressure, JPL 540-Mod 1 propellant

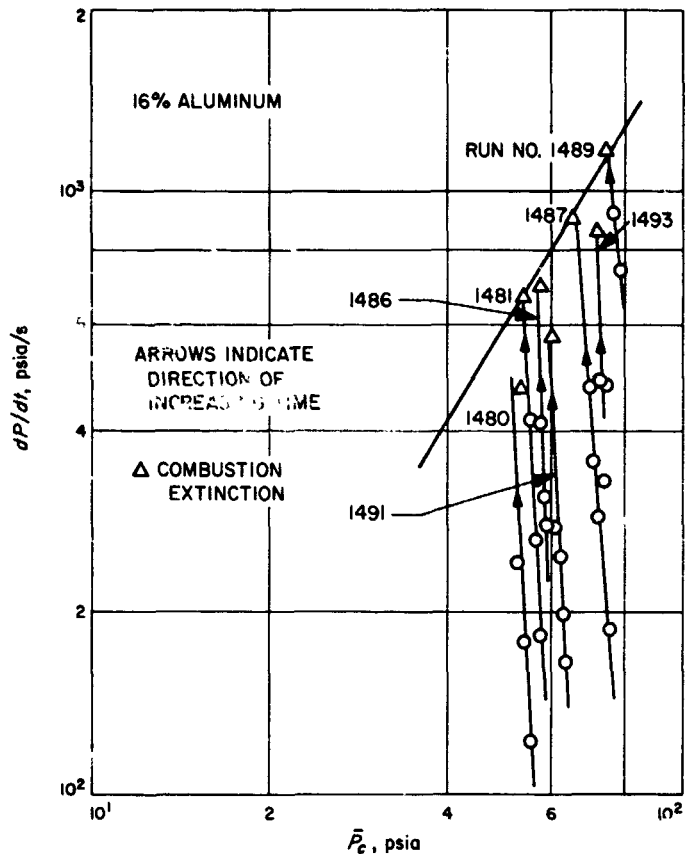


Fig. 21. Pressure oscillation rate of depressurization versus mean chamber pressure, JPL 540-Mod 1 propellant

References

1. Lee, H., and Neville, K., "Epoxy Resins." McGraw-Hill Book Co., New York, 1957.
2. Skeist, I., "Epoxy Resins." Reinhold Publishing Corp., New York, 1958.

References (contd)

3. Dearborn, E. C., Fuoss, R. M., and White, A. F., *J. Polym. Sci.*, Vol. 16, p. 201, 1955.
4. Fisch, W., Hofmann, W., and Koskikallio, J., *J. Appl. Chem.*, Vol. 6, p. 429, 1956.
5. Williams, J. W., and Krynitsky, J. A., "Organic Syntheses," Collective Vol. 3, p. 164. John Wiley & Sons, Inc., London, 1955.
6. Fieser, L., and Fieser, M., "Advanced Organic Chemistry." Reinhold Publishing Corp., New York, 1961.
7. Fischer, R. F., *J. Polym. Sci.*, Vol. 44, p. 155, 1960.
8. Sorenson, W. R., and Campbell, T. W., "Preparative Methods of Polymer Chemistry." Interscience Pub. Inc., New York, 1961.
9. Heilbronner, E., *Helv. Chim. Acta*, Vol. 36, p. 1121, 1953.
10. Price, E. W., Rice, D. W., and Crump, J. E., "Low-Frequency Combustion Instability of Solid Rocket Propellants, 1 May 1963 to 31 May 1964," TPR 360, NOTS TP 3524. U. S. Naval Ordnance Test Station, China Lake, Calif., July 1964.
11. Cohen, N. S., "A Theory of Solid Propellant Extinguishment by Pressure Perturbation," Interagency Chemical Rocket Propulsion Group, 2nd Combustion Conference, CPIA Publication No. 105, pp. 677-696, May 1966.
12. Overall, R. E., and Sawyer, T. T., *Design, Development, and Demonstration of On-Off-On Device for Solid Propellant Rocket Motors*, Final Report on Contract NAS 3-2563. Thiokol Chemical Corporation, Huntsville Division, Huntsville, Alabama, Dec. 4, 1964.

N67-34769

VIII. Polymer Research
PROPULSION DIVISION

A. Characterization Studies on Polyurethane
Elastomers, R. F. Fedors and R. F. Landel

1. Introduction

In an effort to develop a reservoir of standard polymer samples, considerable work has been carried out on a crosslinked polyurethane elastomer prepared by reacting castor oil with a prepolymer prepared by allowing castor oil to react with two equivalents of toluene diisocyanate (Ref. 1). During the initial investigation, several elastomers which differed in the ratio of prepolymer to curing agent were synthesized and were subsequently characterized for mechanical behavior response in both static and dynamic test modes. As part of the mechanical behavior characterization work, the rupture properties were determined in uniaxial tension as a function of test rate and test temperature (Ref. 2).

Since the failure envelope data were available, it was of interest to ascertain if the envelopes representing presumably elastomers of varying network chain concentrations could be superposed in the normal manner (SPS 37-36, Vol. IV, p. 137). Since no data were available on network chain concentration, we undertook to evaluate this parameter from the measured response in uniaxial compression on specimens swollen to equilibrium in several solvents.

2. Experimental Part

a. *Materials.* Since for the two-part polyurethane system, the properties of the resulting products normally depend on the ratio of prepolymer to curing agent, several elastomers were synthesized such that the volume ratio of prepolymer to curing agent was allowed to vary from a 50/50 ratio to an 80/20 ratio. The formulations studied are listed in Table 1. Curing was accomplished by heating the mixtures at 145°C for 2 h (Ref. 3).

Table 1. Composition of polyurethanes studied

Volume ratio of prepolymer/curing agent	NCO equivalents per cm ³ of polymer × 10 ³	OH equivalents per cm ³ of polymer × 10 ³	NCO+OH equivalents per cm ³ of polymer × 10 ³
50/50	1.36	1.39	2.75
55/45	1.49	1.25	2.74
60/40	1.63	1.11	2.74
65/35	1.76	0.97	2.73
70/30	1.90	0.83	2.73
75/25	2.03	0.70	2.73
80/20	2.17	0.56	2.73

BLANK PAGE

Based on the manufacturer's specifications, the prepolymer is reported to have an equivalent weight of 397 g and a density of 1.075 g/cm³. These numbers yield 369 cm³ per equivalent on a volume basis. For the castor oil curing agent, the equivalent weight will be taken as 345 g and using a density value of 0.96 g/cm³, the volume per equivalent is 360 cm³. Employing these numbers, the equivalents per cm³ of mixture for both the hydroxyl (OH) and isocyanate (NCO) groups have been calculated and these are listed in Table 1. It is interesting to observe that although the NCO value increases and the OH value decreases, the total equivalence of reactive functional groups, i.e., the sum of the NCO and OH values, remains effectively constant. This is, of course, a reflection of the fact that the volume per equivalent for both the prepolymer and the curing agent are very nearly the same.

The structural formula for the prepolymer can be represented as shown in Fig. 1, while that for the castor oil curing agent can be represented as shown in Fig. 2. An

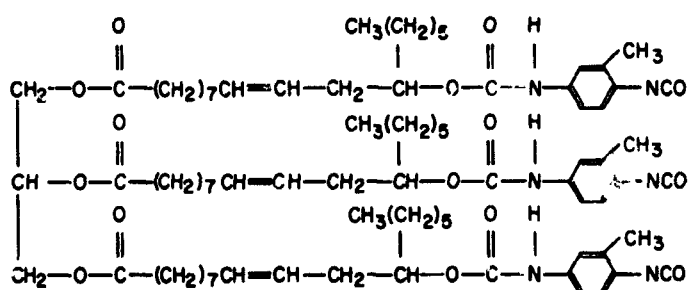


Fig. 1. Structure of prepolymer

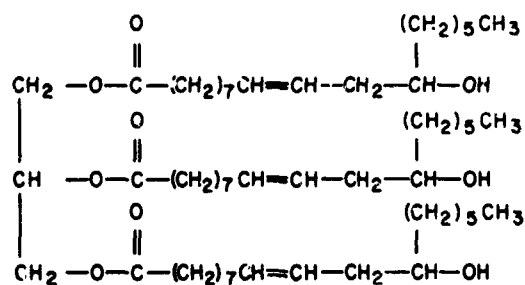


Fig. 2. Structure of curing agent

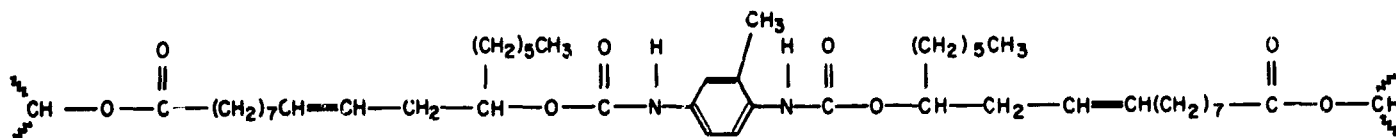


Fig. 3. Network chain

interesting feature of this system is that except for the urethane linkage of the prepolymer, the chemical structures of both the prepolymer and curing agent are identical. Further, if reaction were limited to the addition of the OH group of the curing agent to the isocyanate group of the prepolymer, a network chain so formed would be essentially symmetrical about the urethane linkage and would contain 34 atoms plus the aromatic ring in the main chain. The molecular weight of such a network chain, shown in Fig. 3, is 791 g/mole.

b. Procedures. The method of estimating ν_e which depends on the measurement of the stress-strain behavior of swollen elastomers has already been adequately described (SPS 37-40, Vol. IV, p. 80). The data were obtained on an Instron testing machine using a cross-head speed of 0.02 in./min. The apparent ν_e values were calculated by means of the following equation (SPS 37-43, Vol. IV, p. 177):

$$\nu_e = \frac{mh}{3ART} = \frac{2C_1}{RT} + \frac{2C_2''}{RT} v_2^{1/3} \quad (1)$$

where m is the slope of the load deflection curve, h is the height and A the original undeformed area of the specimen before swelling, R is the gas constant, T is the absolute temperature, ν_2 is the volume fraction of rubber in the swollen gel, $2C_1/RT$ is the value of ν_e at infinite swelling, and $2C_2''$ is related to the $2C_2$ term which appears in the Mooney-Rivlin (Ref. 4) stress-strain equation. When $\nu_2 = 1$, then $2C_2'' = 2C_2$. It is important to notice that for $C_2'' \neq 0$, ν_e as defined by Eq. (1) will depend on ν_2 . On the other hand, for $C_2'' = 0$, ν_e will be independent of ν_2 .

3. Results

a. Equilibrium swelling. The extent of equilibrium swelling in five solvents, benzene, ethylene dichloride, cyclohexane, heptane, and isooctane, is listed in Table 2 along with the ν_e values calculated from the uniaxial compression data on the swollen specimens according to Eq. (1). Examination of the data indicates that for a given solvent, there occurs a marked and monotonic

Table 2. Swelling behavior and apparent chain concentration for polyurethane elastomers

Volume ratio of prepolymer/curing agent	Solvent									
	Benzene		Ethylene dichloride		Cyclohexane		Heptane		Isooctane	
	v_2	ν_e , moles/cm ³ × 10 ⁻⁴	v_2	ν_e , moles/cm ³ × 10 ⁻⁴	v_2	ν_e , moles/cm ³ × 10 ⁻⁴	v_2	ν_e , moles/cm ³ × 10 ⁻⁴	v_2	ν_e , moles/cm ³ × 10 ⁻⁴
50/50	0.353	370	0.380	340	0.660	450	0.771	390	0.794	420
55/45	0.398	390	0.418	390	0.667	480	0.798	—	0.813	—
60/40	0.438	440	0.457	390	0.692	470	0.813	—	0.836	—
65/35	0.462	—	0.481	440	0.706	460	0.816	380	0.863	430
70/30	0.492	350	0.510	400	0.721	440	0.827	—	0.848	—
75/25	0.510	430	0.527	350	0.733	400	0.833	380	0.868	480
80/20	0.527	—	0.542	450	0.745	420	0.839	370	0.943	370

increase in v_2 as the prepolymer volume is increased. Normally, such an increase in v_2 would be ascribed to an increase in the network chain concentration but the results of the compression tests indicate that within the estimated experimental error, the ν_e values are essentially independent of the prepolymer to curing agent ratio. Furthermore, this behavior is observed for all five solvents employed.

In addition, the ν_e data indicate that this parameter is almost independent of v_2 and this fact can be seen more clearly in Fig. 4 where the data are plotted in accordance with Eq. (1). It can be seen that the dependence of ν_e on v_2 is very slight indeed, which implies that C_2'' is very nearly zero. This signifies that the stress-strain data for the dry rubber when plotted in Mooney-Rivlin fashion should have a slope or C_1 value also very close to zero (SPS 37-43).

Since ν_e is essentially independent of the prepolymer/curing agent ratio, the fact that v_2 varies with this ratio can be taken as an implication that the chemical nature of the network chains but not their number depends on this ratio.

Data which bears on this point will now be presented.

b. Dependence of the failure envelope on prepolymer ratio. It has been shown that the failure envelopes for many gum elastomers can be represented by a stress-strain law proposed by Treloar (Ref. 4):

$$\sigma_b = \frac{\nu_e RT n^{1/2}}{3} \left(x - \frac{y}{\lambda_b^{3/2}} \right) \quad (2)$$

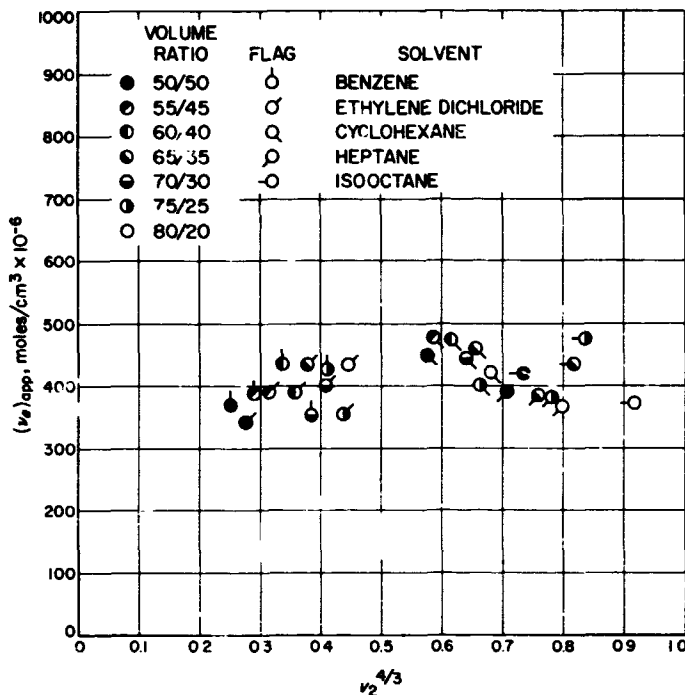


Fig. 4. Dependence of apparent chain concentration, $(\nu_e)_{app}$, on $v_2^{4/3}$

where

$$x \equiv \coth \left(\frac{\lambda_b}{n^{1/2}} \right) - \frac{n^{1/2}}{\lambda_b} \quad (3)$$

and

$$y \equiv \coth \left(\frac{1}{\lambda_b^{1/2} n^{1/2}} \right) - \lambda_b^{1/2} n^{1/2} \quad (4)$$

where σ_b and λ_b are the stress and extension ratios at break respectively, and n is the number of statistical segments per network chain. By plotting

$$\log \left(\frac{3\sigma_b}{\nu_e RT n^{1/2}} \right) \text{ versus } \log \left(\frac{\lambda_b}{n^{1/2}} \right)$$

for several values of n , a family of failure envelopes is obtained which can then be used to obtain approximate values for both ν_e and n from failure envelope data obtained experimentally. In practice, the experimental data plotted in the form $\log (\sigma_b T_0/T)$ versus $\log \lambda_b$ are shifted in order to superpose the experimental data to a theoretical curve. Since the shape of the envelope depends strongly on the n values, this matching or superposition is done on the basis of curve shape and as such is readily accomplished. The distance along the abscissa needed for the shift or fit is equal to $\log n^{1/2}$ while the distance along the ordinate is equal to $\log (3/\nu_e RT_0 n^{1/2})$. Thus, estimates for both n and ν_e can be calculated from the shift distances.

Typical plots of the experimentally obtained failure envelope and that predicted on the basis of Eq. (2) are shown in Fig. 5 for the 50/50 and 55/45 ratios. Inspection of the Figure makes it evident that the shapes of the experimental failure envelopes and those predicted by Eq. (2) are in excellent agreement. Similar results were obtained for the remaining elastomers and the data for ν_e and n evaluated by this procedure are tabulated in Table 3.

These results also demonstrate that ν_e is indeed essentially independent of the ratio of prepolymer/curing

agent; the small differences observed are well within the estimated error involved in the superposition procedure. Furthermore, it is apparent that the magnitude of ν_e

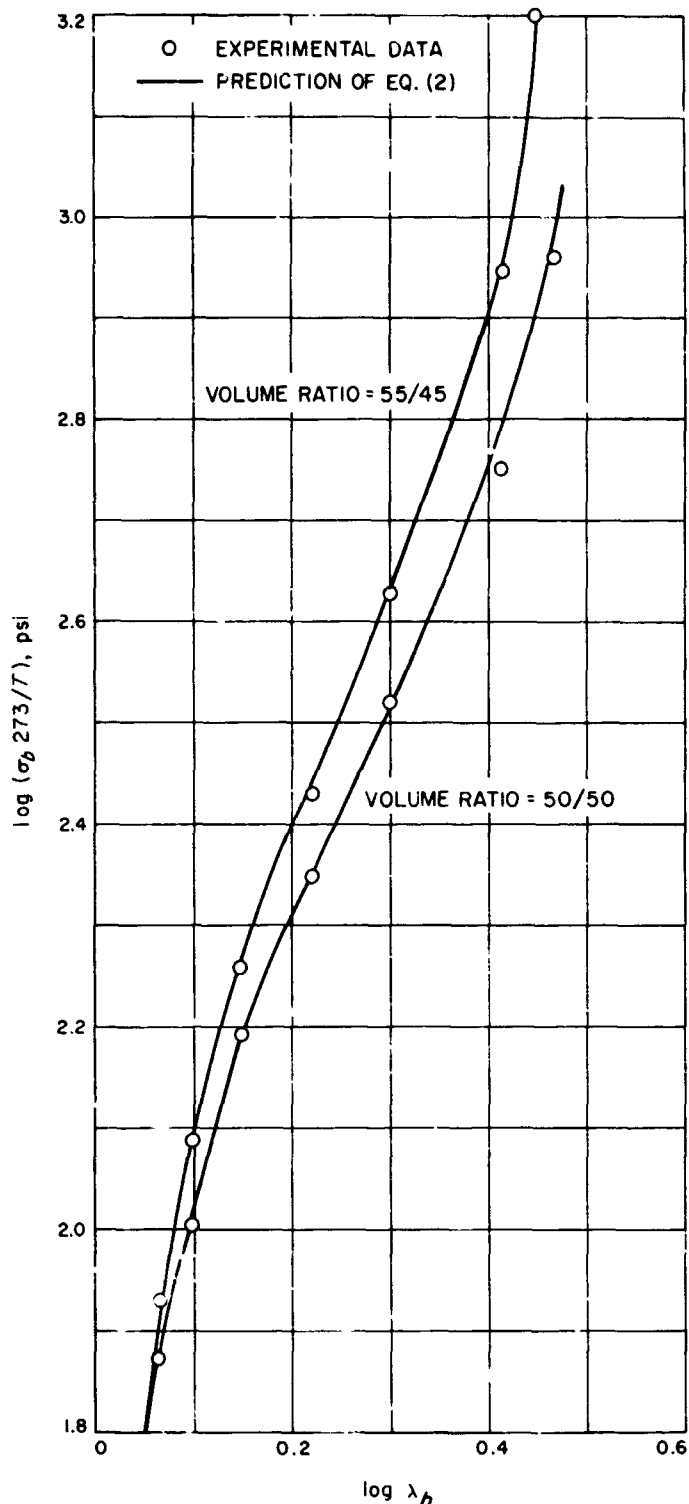


Fig. 5. Failure envelopes for 50/50 and 55/45 volume ratios

Table 3. Estimates of ν_e and n from failure envelopes

Volume ratio of prepolymer / curing agent	ν_e , moles/cm ² × 10 ⁻⁴	n , segments/chain
50/50	410	12
55/45	460	10
60/40	440	7.2
65/35	470	6.6
70/30	490	4.8
75/25	460	4.2
80/20	460	4.2

obtained in this manner is in essential agreement with ν_e determined from the compression measurements on swollen samples. The average value of ν_e obtained from the failure envelope results is 460×10^{-6} compared to 420×10^{-6} moles/cm³ estimated from the compression results.

If it is assumed that all network chains are effective, then the average value of $\nu_e \approx 440 \times 10^{-6}$ moles/cm³ can be used to obtain an estimate for the maximum value of the average molecular weight of a network chain, M_c , since for the present castor oil system, chain entanglements are expected to be absent. Using the relationship $M_c = \rho/\nu_e$ where ρ is the polymer density, $M_c \approx 2300$ g/mole. For the real network, M_c is expected to have a somewhat smaller value, since not all of the chains in the gel are effective and hence capable of supporting an equilibrium load. In principle, the fraction of "active" network capable of permanent elastic deformation can be estimated if the functionality of the reactants, the extent of reaction, and the initial ratio of active groups are known. The value of the fraction of "active" network will be a maximum when this ratio is unity if all other parameters are held constant. On the other hand, this fraction will be markedly reduced if the ratio differs appreciably from unity. This will occur in practice if the "purity" of the reactants is low, i.e., if either the prepolymer or the curing agent contains appreciable amounts of monofunctional or difunctional molecules.

A minimum value for M_c can be estimated by assuming that all the network chains are effective and, further, that they correspond to the structure shown in Fig. 3. This yields $M_c = 790$ g/mole. The true M_c will have a value between the two extremes.

The interesting feature of Table 3 is the n values which decrease monotonically with increase in the prepolymer content of the elastomer. A decrease in n signifies that chain flexibility decreases; i.e., the network chains become more rigid as the prepolymer content increases. Such a change implies a change in the chemical structure of the network chains. However, since the main chains

are of the same type, castor oil (as shown in Figs. 1-3), the only variables would seem to be the chemical nature and functionality of the crosslink.

It is known that the reaction between an OH group and an NCO group is relatively rapid. However, the resulting urethane linkage contains an active hydrogen which is capable of reacting, although at a much slower rate, with additional NCO to generate an allophanate according to the scheme shown in Fig. 6 (Ref. 6). It is important to notice that in this reaction, the active hydrogen is regenerated and is thus available for further reaction. For example, the reaction producing the allophanate group might lead to the formation of a network chain; the reaction of a second isocyanate group would lead to a trifunctional branch point; the reaction of a third, to a tetrafunctional branch point; etc. The reaction of an isocyanate with a urethane could explain, in part, the fact that ν_e is independent of the prepolymer/curing agent ratio while the n values decrease with increase in the prepolymer content—this in spite of the fact the NCO and OH contents were varied as shown in Table 1. On the assumption that the reaction of two functional groups increases the number of network chains by one, then ν_e should be independent of prepolymer content since Table 1 shows that the concentration of reactive groups is independent of prepolymer content.

In addition, as the prepolymer content increases, the OH content decreases and hence both the number of allophanate groups and the extent of branching will increase. Since the allophanate group contains more polar groups than does a urethane group (Fig. 6), the allophanate must confer added rigidity to a network chain which in turn implies that n will decrease. Thus, on this basis, the decrease in the n value is a reflection of the increase in the allophanate content.

c. Interaction parameters. According to the usual approximations (Ref. 7), the relationship between the extent of equilibrium swelling and the chain concentration de-

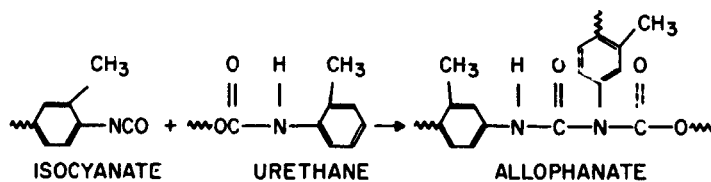


Fig. 6. Reaction of isocyanate with urethane

pends primarily on the molar volume of solvent, V_1 , and the polymer-solvent interaction parameter χ_1 . The explicit dependence is given by (Ref. 8):

$$\nu_e = -\frac{1}{V_1} \frac{\left\{ \ln(1 - \nu_2) + \nu_2 + \nu_2^2 \left[\chi_1 - (1 - \nu_2) \frac{d\chi_1}{d\nu_2} \right] \right\}}{\left(\nu_2^{1/3} g^{2/3} - \frac{\nu_2}{f} \right)} \quad (5)$$

where g is the gel fraction and f is the crosslink functionality which is here taken to be 3. Since ν_e has been estimated by an independent method, Eq. (5) can be used to evaluate the interaction parameter χ_1 . Thus, Eq. (5) can be rearranged to yield:

$$\frac{\nu_e V_1 \left(\nu_2^{1/3} g^{2/3} - \frac{\nu_2}{3} \right) + \ln(1 - \nu_2) + \nu_2}{\nu_2} = \chi_1 - (1 - \nu_2) \frac{d\chi_1}{d\nu_2} \quad (6)$$

Furthermore, the dependence of χ_1 on ν_2 is generally of the form:

$$\chi_1 = a + b\nu_2 \quad (7)$$

where a and b are constants. Assuming Eq. (7) to be valid, the right-hand side of Eq. (6) becomes $(a - b) + 2b\nu_2$; thus, a plot of the left-hand side of the equation [$\equiv (\chi_1)_{app}$] versus ν_2 should be linear with slope $2b$ and intercept $(a - b)$. These results are shown in Fig. 7, where it may be seen that the plots are indeed linear for all the solvents investigated. This in turn justifies the assumed linear dependence of χ_1 on ν_2 , i.e., Eq. (7). From the slope and intercept, values of a and b were obtained and these are

Table 4. Polymer-solvent interaction parameters

Solvent	V_1	δ_s (cal/cm ³) ^{1/2}	χ_1
Benzene	86.9	9.22	0.69 + 0.63 ν_2
Ethylene dichloride	78.8	9.80	0.70 + 0.60 ν_2
Cyclohexane	108	8.25	0.58 + 0.99 ν_2
Heptane	146.5	7.45	0.16 + 1.8 ν_2
Isooctane	165.1	6.90	0.01 + 2.0 ν_2

listed in Table 4. These χ_1 values may be used along with Eq. (5) to estimate ν_e values from measurements of ν_2 .

If it is further assumed that the variations in the chemical structure of the network chain do not influence χ_1 in the limit when $\nu_2 \rightarrow 1$, i.e., for the undiluted polymers, then the χ_1 values listed in Table 4 may be used to obtain a rough estimate for the cohesive energy density, δ_p , of the polymer. It has been shown that χ_1 is related to the cohesive energy density of the solvent and the polymer by means of (Ref. 9)

$$\chi_1 = A + \frac{V_1}{RT} (\delta_s - \delta_p)^2 \quad (8)$$

where A is a constant for a given solvent and the subscripts s and p refer to the solvent and the polymer, respectively. Since A is presumed independent of ν_2 , differentiation of Eq. (8) with respect to ν_2 yields

$$\frac{d\chi_1}{d\nu_2} = -\frac{2V_1}{RT} (\delta_s - \delta_p) \frac{d\delta_p}{d\nu_2} \quad (9)$$

Further, in the limit as $\nu_2 \rightarrow 1$, $d\delta_p/d\nu_2$ should be, to a good approximation, independent of the solvent. Thus, Eq. (9) can be written as

$$\frac{RTb}{2V_1} = -B\delta_s + \delta_p B \quad (10)$$

where $B \equiv d\delta_p/d\nu_2$ and $b \equiv d\chi_1/d\nu_2$. A plot of $RTb/2V_1$ versus δ_s is predicted to be linear with slope of $-B$ and intercept $B\delta_p$. Figure 8 shows the data plotted in this manner using the δ_s values listed in Table 4 (Ref. 10). Although the scatter is relatively great, the data do seem to conform to Eq. (10), and δ_p is calculated from the slope and intercept to be 11.6 (cal/cm³)^{1/2}.

4. Summary

Polyurethane elastomers based on castor oil have been characterized for network chain concentration, chain flexibility, and polymer solvent interaction parameters. It has been found that ν_e is essentially independent of the prepolymer content, but that the chain flexibility decreased as the prepolymer content increased. The polymer-solvent interaction parameter has been determined in benzene, ethylene dichloride, cyclohexane, heptane, and isooctane.

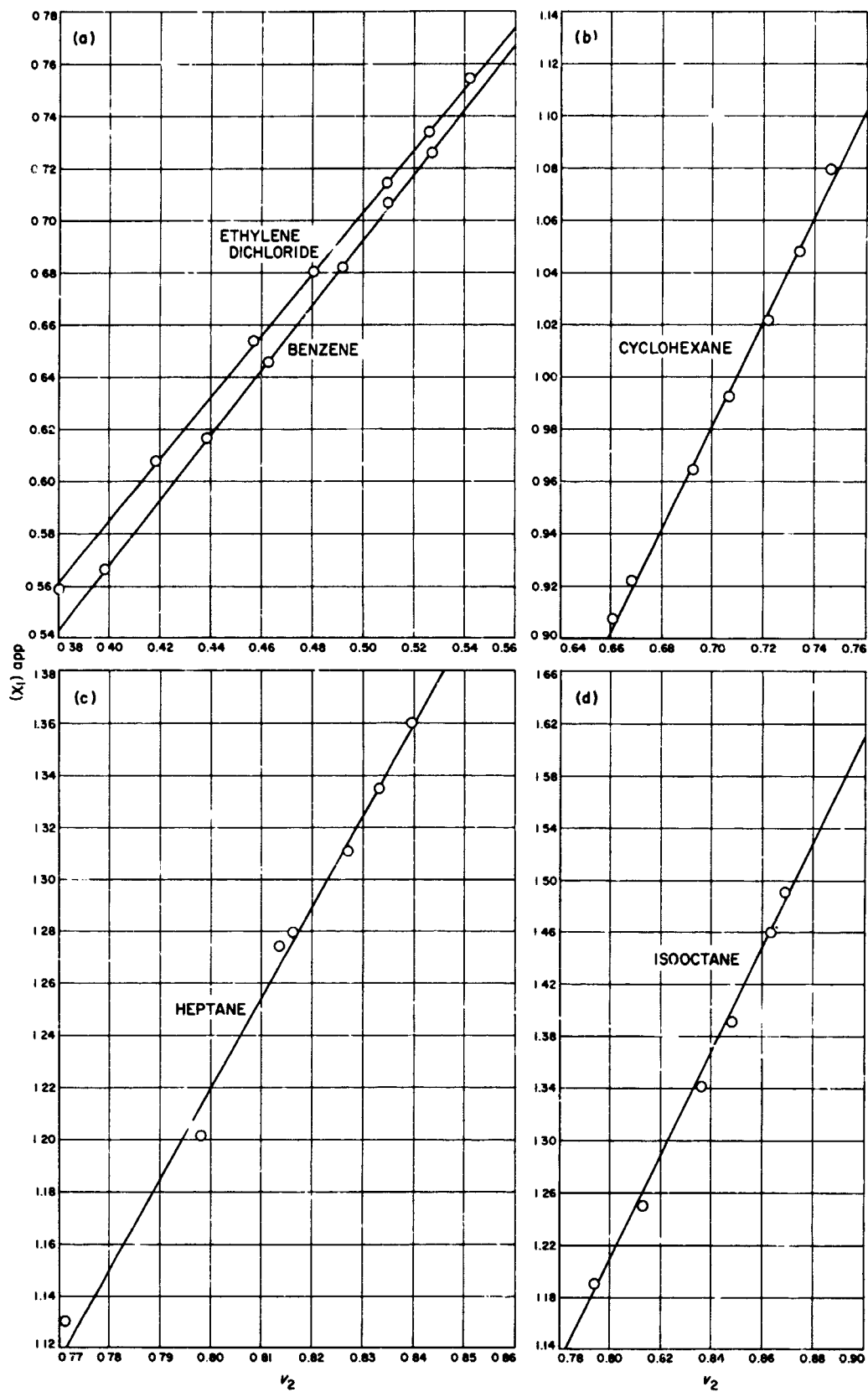


Fig. 7. Dependence of $(X_1)_{app}$ on v_2

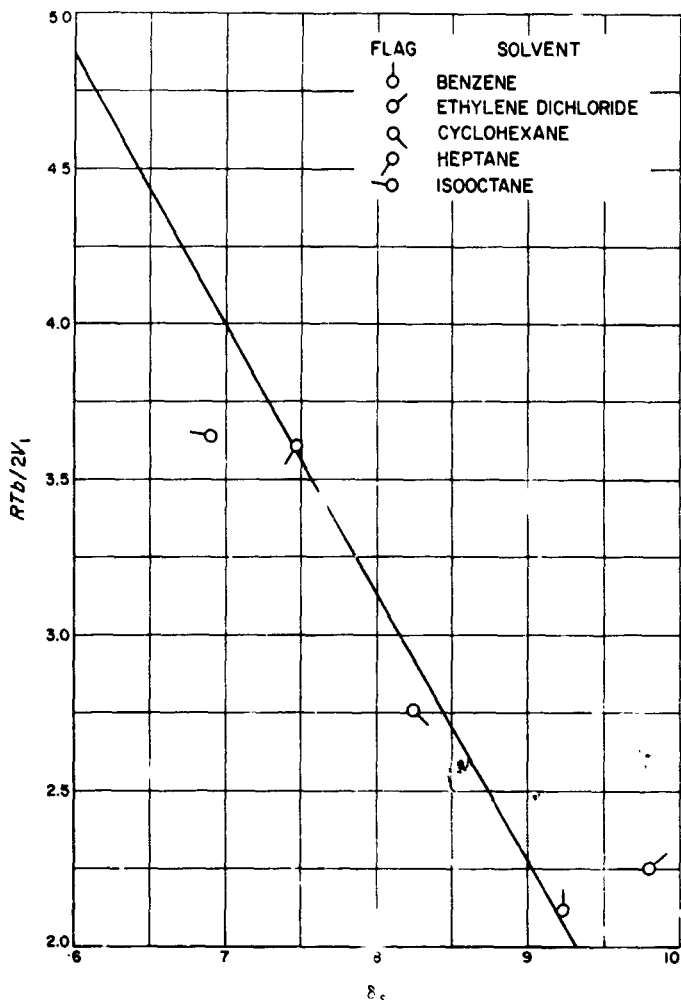


Fig. 8. Dependence of $RTb/2V_1$ on δ_s .

B. Structure-Property Relationships for Polymers. Part I: Influence of the Chemical Nature of an Elastomer on Stress-Strain Response, R. F. Fedors and R. F. Landel

1. Introduction

According to the kinetic theory of rubber elasticity, the uniaxial stress-strain response of an elastomer under sensibly equilibrium conditions, e.g., slow deformation rates at temperatures far removed from the glass temperature, is given by (Ref. 4):

$$\sigma = \nu_e RT \left(\lambda - \frac{1}{\lambda^2} \right) \quad (1)$$

where σ is the stress based on the initial cross-sectional area, ν_e is the number of effective network chains per unit volume of rubber, R is the gas constant, T is the absolute

temperature, and λ is the extension ratio. Numerous studies have demonstrated that this equation is applicable for λ values less than about 2. Moreover, the equation predicts that the response of an elastomer depends only on the number of network chains; thus, the precise chemical nature, per se, of an elastomer does not influence stress-strain behavior.

Recent work has indicated that at higher λ values including the rupture point, Eq. (1) no longer describes the experimental data adequately but that another, more appropriate stress-strain law, which does depend on chemical structure, can be used as an adequate description of the stress-strain behavior and also of the failure envelope (Ref. 5). In what follows, the attempt will be made to demonstrate how chemical structure of a polymer chain can influence this behavior.

2. Discussion

a. Stress-strain behavior at large deformation. As might be anticipated, the region of strain for which the simple kinetic theory is valid is small, generally less than about 100%. For higher strains, it has been found that both the uniaxial stress-strain behavior and the failure envelope (Ref. 5) can be represented by an equation first proposed by Treloar (Ref. 4):

$$\sigma = \frac{\nu_e RT n^{1/2}}{3} \left[x - \frac{y}{\lambda^{3/2}} \right] \quad (2)$$

where

$$x \equiv \coth \left(\frac{\lambda}{n^{1/2}} \right) - \frac{n^{1/2}}{\lambda} \quad (3)$$

and

$$y \equiv \coth \left(\frac{1}{\lambda^{1/2} n^{1/2}} \right) - \lambda^{1/2} n^{1/2} \quad (4)$$

where n represents the number of statistical segments per network chain and the other quantities have their usual significance. Thus, in addition to ν_e , an adequate description of behavior requires the introduction of a second parameter, n . As an example of the utility of Eq. (2), Fig. 9 shows failure envelopes constructed from data reported in the literature (Refs. 11 and 12) for several elastomers. The solid curves are the prediction of Eq. (2). The values of ν_e and n required for fit are shown along with ν_e values calculated using an independent measurement such as the equilibrium modulus. In all cases, the agreement between the ν_e values is excellent. The general behavior of Eq. (2) is worthwhile

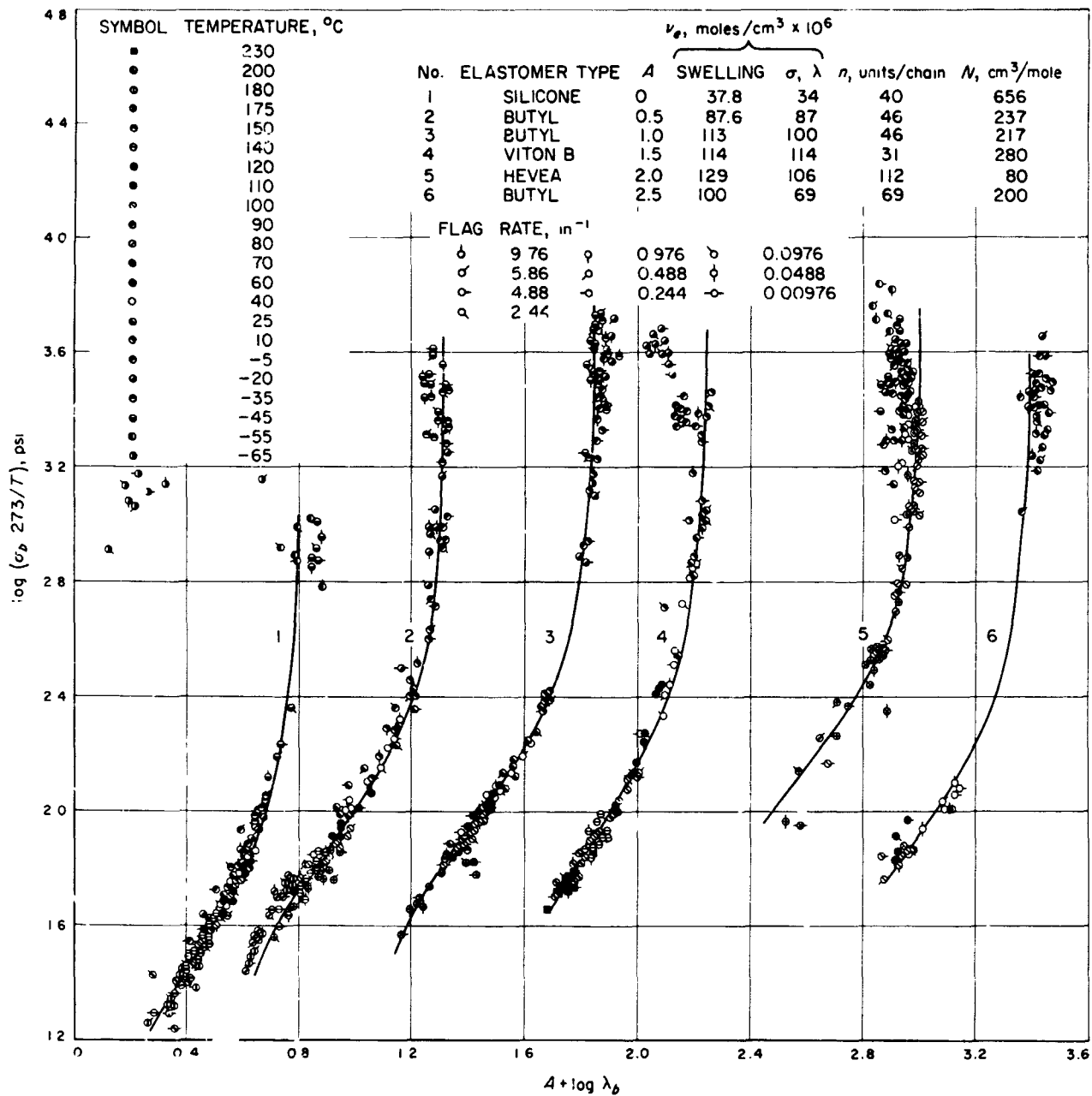


Fig. 9. Comparison of Eq. (2) with experimental failure data for several elastomers

describing. First of all it reduces to the kinetic theory prediction, Eq. (1), at small strains; i.e., the dependence on the parameter n is evident only at relatively high strains. This behavior can be seen more vividly in Fig. 10, which shows the stress-strain behavior at several values of n as the full curves and the kinetic theory prediction as the dashed curve. Secondly, at a fixed value of ν_e , the extensibility of the network increases with increase in n . Moreover, it can easily be shown that the maximum value which λ can assume is given by:

$$(\lambda)_{\max} = n^{1/2} \quad (5)$$

since, according to Eq. (2) $\sigma \rightarrow \infty$ as $\lambda \rightarrow n^{1/2}$ and thus all real λ values must be $\leq n^{1/2}$. Equation (5) has been shown to be consistent with the available data (Ref. 13 and SPS 37-37, Vol. IV, p. 139). Thus, the n value determines, in effect, the maximum strain capability of an elastomeric network.

A relationship between n and ν_e can be written as

$$n = \frac{fg}{\nu_e N_0} = \frac{fgM_x}{N_0} \quad (6)$$

where

$$\nu_e = \frac{1}{xM_x} \quad (7)$$

where f is the fraction of the network which is capable of supporting an equilibrium load, g is the gel fraction, N_0 is the molar volume of a statistical unit, x is the num-

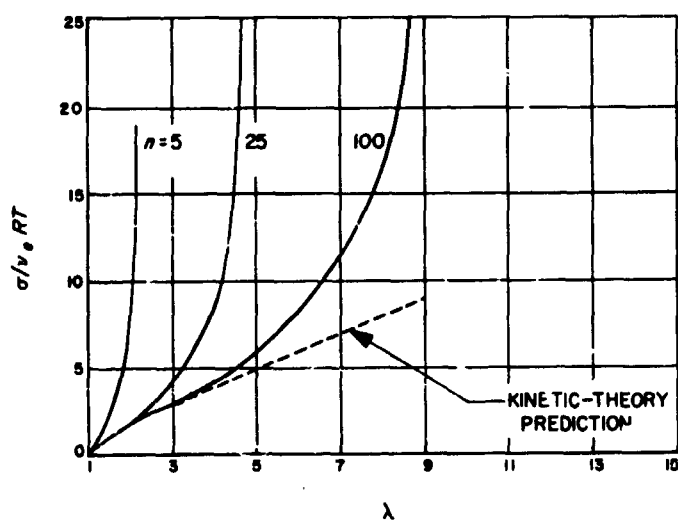


Fig. 10. Dependence of the reduced stress, $\sigma/\nu_e RT$, on λ for several values of n according to Eq. (2)

ber of atoms in the network chain, and M_x is the average molecular volume of a main chain atom. For example, in the case of polystyrene, x is twice the number of monomer units in the chain and M_x is one-half the monomer molecular volume. In what follows, it will be assumed that both f and g are unity since both of these parameters depend on details of the crosslinking process which are not of concern here. This assumption in no way detracts from the results presented below and a subsequent paper in this series will delve into this question in more detail.

For a given elastomer, N_0 is constant and therefore, n and ν_e cannot both be independent variables. Once ν_e is fixed by the number of crosslinks introduced into the system, a knowledge of the N_0 value permits n to be calculated. However, when a series of different elastomers which differ in chemical structure is considered, then both n and ν_e can be taken as independent variables since N_0 is no longer constrained. Thus, according to Eq. (6), at constant ν_e , n can be increased by varying the chemical structure of the polymer such that N_0 is decreased, i.e., by making the polymeric chains more flexible. On the other hand for a given elastomer (N_0 constant) n can be increased by decreasing the number of crosslinks introduced into the system, i.e., by decreasing ν_e . Since in many instances, the value of ν_e may be restricted to a small range in order to achieve a useful modulus level for the elastomer, it is of great interest to consider the dependence of N_0 on chemical structure.

b. Dependence of N_0 on chemical structure. The dimension of a polymer molecule is normally expressed in terms of the mean-square end-to-end distance \bar{r}^2 , which has been shown to depend on n and the effective segment length l by (Ref. 4):

$$\bar{r}^2 = nl^2 \quad (8)$$

Since \bar{r}^2 depends directly on chain flexibility through the value n , measurement of the chain flexibility can be used to calculate n , which in turn can be used to evaluate N_0 .

Chain flexibility is controlled by the nature and extent of potential barriers to rotation about main chain bonds and as such is influenced or affected by short range intramolecular interactions and by long range intermolecular interactions, both of which depend strongly on the precise chemical nature of the polymer chain.

In the case of polymers which are normally classed as elastomeric, the molecules are essentially nonpolar in nature and, thus, the long range interactions are expected

to be small. This is not a fundamental distinction however, since polymers not normally considered elastomeric can be made so by suitably reducing long range interaction, a prime example here being the case of poly(vinyl chloride). In the pure state, poly(vinyl chloride) is not an elastomer; however on adding sufficient amounts of a suitable plasticizer, which presumably disrupts long range effects, the material behaves as an elastomer. To the extent that the short range and long range interactions are temperature dependent, then the chain flexibility and n values will also be temperature dependent. Experimental data, at least for hydrocarbon chains, would indicate that the temperature variation of n is small. For example, the results in Fig. 9 show that, provided the test temperatures are sufficiently above T_g , then a single value of both n and ν_e can be used to describe the failure envelope generated by breaking specimens at different test rate and test temperatures.

If a polymer chain were capable of completely unrestricted rotation as well as having unrestricted bond angles about each bond in the main chain, and, further, if intermolecular interaction were negligible, then n would simply be equal to the number of main chain bonds, i.e., to x in Eq. (6). However, since real chains do have barriers to free rotation, n will always be less than x and in principle if the heights of the barriers were known, then the n could be calculated. Generally, however, sufficient information on the barriers is not available and thus recourse must be had to experimental evaluations of n .

Since n determines the size of the polymer coil, then in principle the measurement of a property which is dependent on polymer coil size can be utilized to estimate n . Properties which depend on size in this way include the scattering of light, the magnitude of the second virial coefficient, and the intrinsic viscosity. Of these, the intrinsic viscosity at the θ temperature, i.e., the temperature at which the dimension of the coil becomes independent of the solvent, is probably the most convenient experimental technique used to estimate n . This method provides a measure of the chain dimension in terms of the ratio of \bar{r}^2 to the chain molecular weight (Ref. 7), i.e., in terms of (\bar{r}^2/M) . For an ideal chain containing no barriers to rotation, a theoretical value of the ratio (\bar{r}_0^2/M) where \bar{r}_0^2 is the mean-square end-to-end chain length in the absence of potential barriers, can be computed. For the ideal chain \bar{r}_0^2 can be written as

$$\bar{r}_0^2 = n_0 l_0^2 \quad (9)$$

where the subscript 0 refers to the ideal chain. If it is specified that the fully extended length of both the real and the ideal chain of equivalent molecular weight be the same, i.e., that

$$nl = n_0 l_0 \quad (10)$$

then this condition ensures that unique n and l values can be obtained. Thus, employing Eqs. (8-10), the relationship between n and n_0 can be written as

$$n = n_0 (\bar{r}_0^2 / \bar{r}^2) \quad (11)$$

Furthermore, N_0 is obtained from

$$N_0 = M_x (\bar{r}_0^2 / \bar{r}^2) \quad (12)$$

and likewise the relationship between n and x can be expressed by

$$n = x (\bar{r}_0^2 / \bar{r}^2) \quad (13)$$

Using these results, ν_e can be expressed as

$$\nu_e = \frac{1}{nM_x} (\bar{r}_0^2 / \bar{r}^2) \quad (14)$$

In order to facilitate comparisons between polymers of different chemical structure, a short compilation of data on several of the more common polymers is presented in Table 5. The data listed are the glass transition temperature, T_g , the density, ρ , the average molecular volume per main chain atom, M_x ; the ratio $(\bar{r}^2 / \bar{r}_0^2)^{1/2}$; the corresponding temperature at which the \bar{r}^2 value (Ref. 14) was measured and finally the calculated values for the molecular volume of a statistical segment.

Unfortunately, there is at present no way to estimate $(\bar{r}^2 / \bar{r}_0^2)^{1/2}$ values from a knowledge of the polymer structure alone, and thus a calculation of n and N_0 values depends on a prior experimental evaluation of $(\bar{r}^2 / \bar{r}_0^2)^{1/2}$.

In the interests of clarity, the entries in the table have been arbitrarily grouped into 5 sets. In set A, are listed several common vinyl polymers which are entirely hydrocarbon in nature. In set B, data for several of the more common polymers which are normally classed as elas-

Table 5. Characteristics of common polymers

Polymer	$T_g, ^\circ\text{C}$	$\rho, \text{g/cm}^3$	$M_w, \text{cm}^3/\text{mole}$	$(\bar{r}^2/\bar{r}_0^2)^{1/2}$	$T, ^\circ\text{C}$	$N_e, \text{cm}^3/\text{mole}$
Set A: vinyl polymers entirely hydrocarbon in nature						
Poly(ethylene)	-125	0.826	15.8	1.61	145	41
Poly(1-butene)	-24	0.868	32.3	1.82	~ 70	110
Poly(isobutene)	-73	0.915	30.6	1.80	24	100
Poly(1-pentene)	-40	0.850	41.2	2.2	~ 31	200
Poly(styrene)	100	1.04	50.0	2.22	~ 30	240
Poly(2-vinyl naphthalene)	<162	1.12	75.6	3.1	30.2	660
Set B: polymers normally classed as elastomeric						
Poly(butadiene) 98% cis	-95	0.91	14.8	1.61	20.5	39
Poly(butadiene) 98% trans	-83	0.91	14.8	1.07	40	17
Poly(chloroprene) 85% trans	-45	1.27	17.4	1.40	25	34
Poly(isoprene) 100% cis	-73	0.91	18.7	1.67	20	52
Poly(isoprene) 100% trans	-60	0.91	18.7	1.38	60	36
Poly(dimethylsiloxane)	-123	0.98	37.7	1.39	~ 20	71
Poly(trifluoro-nitrosomethane-cotetrafluoroethylene): nitroso rubber	-51	1.93	25.9	1.68	35	73
Set C: polyether polymers						
Poly(formaldehyde)	-85	1.25	12.0	2.1	~ 25	53
Poly(ethylene oxide)	-67	1.13	13.0	1.38	~ 20	25
Poly(propylene oxide)	-75	1.01	19.2	1.59	25	49
Poly(tetrahydrofuran)	-79	1.09	13.2	1.55	30	32
Set D: methacrylate polymers with side chain length varied						
Poly(methyl methacrylate)	105	1.20	41.6	2.08	25	180
Poly(ethyl methacrylate)	65	1.10	51.8	1.96	23	200
Poly(n-butyl methacrylate)	20	1.05	67.6	1.98	23	270
Poly(n-hexyl methacrylate)	-5	1.05	80.8	2.25	30	410
Poly(n-octyl methacrylate)	20	1.0	99.0	2.19	20	480
Poly(n-lauryl methacrylate)	-65	1.0	127.0	2.59	~ 25	850
Set E: polyester polymers						
Poly(hexamethylene fumarate)	—	1.1	15.0	1.47	20	33
Poly(hexamethylene maleate)	—	1.1	15.0	1.55	20	36
Poly(hexamethylene succinate)	—	1.1	15.3	1.70	20	44
Poly(hexamethylene sebacate)	—	1.1	14.4	1.62	20	44
Poly(hexamethylene adipate)	57	1.05	15.4	1.65	25	42
Poly(decamethylene adipate)	—	1.1	14.4	1.33	25	27
Poly(decamethylene sebacate)	—	1.1	14.0	1.65	25	40
Poly(ω -oxyundecanoate)	—	1.05	15.9	1.60	20	38

tomeric are given. In set C, data on several interesting polyethers are given. In set D are listed data for a series of methacrylate polymers where the length of the side chain is varied. Finally in set E are provided data for several polyester polymers.

According to both Eqs. (12) and (14), a key molecular parameter is M_x , which for the examples listed in Table 5 varies from a low value of about 12 for poly(formaldehyde) to a high value of 127 for the *n*-lauryl methacrylate polymer; i.e., it takes about ten times more volume of the polymer in the case of the methacrylate in order to provide on the average one main chain atom. The reason for this is clear, for in the methacrylate case, the long lauryl side chain does not contribute to rubberlike elasticity directly, but it does contribute to the mass of the polymer chain. Considered in this context, the M_x can be related to "network chain efficiency" in that the lower the M_x number, the greater will be the fraction of material present as main chain atoms and thus a unit volume of polymer will contain a larger number of network chains capable of supporting a load. As a numerical example, according to Eq. (13), at constant ν_e , i.e., at constant small strain modulus, n for poly(formaldehyde) is about 22 times greater than for the methacrylate, and on this basis, a formaldehyde network in the rubbery state is expected to have a maximum strain capability about 5 times greater.

Also from the data in Table 5, the more subtle influence of isomeric structures can be seen. For example, in set B, the data indicate that the *trans*-isomer for both poly(butadiene) and poly(isoprene) provides a more flexible chain than does the *cis*-isomer. Unfortunately, there are no data available for the 1,2 or 3,4 isomers. However, these chains should even be less flexible than chains based on the *cis*-isomer. In the case of a polymer which might be suitable for application as a solid propellant binder, which is typically present to only about 30 vol %, it is obviously desirable to have the binder contain as many network chains as possible; i.e., the polymer should have a small M_x value.

In order to have a network with a high strain capability, it was indicated that N_0 , the molar volume of a statistical segment, should be as small as possible. Equation (12) shows that N_0 is directly proportional to both M_x and the ratio $(\bar{r}^2/\bar{r}_0^2)^{1/2}$. Thus, other things being equal, a high M_x value contributes to a high N_0 value. Again, the poly(*n*-lauryl methacrylate) has a very large value of $N_0 = 660 \text{ cm}^3/\text{mole}$ and this is a reflection of both the

very high value of $M_x = 127 \text{ cm}^3/\text{mole}$ as well as a relatively high value of $(\bar{r}^2/\bar{r}_0^2)^{1/2} = 2.59$. Poly(2-vinyl naphthalene), set A, has an N_0 value of $660 \text{ cm}^3/\text{mole}$ and this large value also reflects both a high $M_x = 75.6 \text{ cm}^3/\text{mole}$ and a high $(\bar{r}^2/\bar{r}_0^2)^{1/2} = 3.1$.

Table 5 brings out several interesting features. For example, the set B which contains the elastomeric materials, except for poly(isobutene) which is shown in set A, all have low N_0 values, the highest value being $100 \text{ cm}^3/\text{mole}$ for the poly(isobutene). In addition, this set is characterized by both low M_x values and low values of the ratio $(\bar{r}^2/\bar{r}_0^2)^{1/2}$. The relatively low $M_x = 25.9 \text{ cm}^3/\text{mole}$ for the nitroso rubber is a reflection of the fact that the density is high, $\rho = 1.93 \text{ g/cm}^3$. Using these observations as criteria, one can predict that poly(ethylene) should be a good elastomer. However, in this case, the structure is so regular and uniform that the material is normally crystalline to a large extent. However, above the melting point, poly(ethylene) is elastomeric.

The polyethers of set C and the polyesters of set E have M_x and N_0 values which compare favorably with those of the elastomers in set B. However, for materials such as poly(formaldehyde) and poly(hexamethylene adipate), the molecular structures are so regular that either extensive crystallization occurs, or the intermolecular interactions are strong enough so that the T_g value is above room temperature. However, if crystallization can be eliminated and T_g reduced (this can often be accomplished by decreasing chain regularity) then both the polyethers and the polyesters do provide elastomeric materials.

Set D was included in the table to demonstrate the effect on T_g , on M_x and on N_0 of increasing the length of the side chain. It is evident from the N_0 values that long side chains are undesirable in elastomers which are intended to exhibit a high strain capability.

3. Summary

The dependence of the maximum strain capability on the chemical structure of a polymer has been discussed. It was pointed out that the controlling parameter is the chain flexibility which can be conveniently expressed in terms of N_0 , the molecular volume of a statistical chain segment. In subsequent parts of this series, the connection between polymer structure and dynamic behavior will also be discussed.

C. The Suitability of Thermoplastic Rubbers as Binders for Composite Solid Propellants, Interim Report II, B. G. Moser and R. F. Landel

1. Introduction

This article presents results of a continuing study of the application of thermoplastic rubber as a solid propellant binder (SPS 37-41, Vol. IV, pp. 107-109 and SPS 37-43, Vol. IV, pp. 184-189). The burning rate of the propellants made from this binder was found to be low, and plasticizing them with non-polar mineral oil did not yield the increase in burning rate which should have resulted from the poorer oxidizer dispersion in the mineral oil system. It was thought that anti-oxidants in the binders were responsible for the failure of the mineral oil to produce higher burning rates; however, this failure will be discussed from a different viewpoint below.

Ring specimens for tensile studies were determined to be unsuitable for highly loaded thermoplastic rubbers, and strip specimens were substituted. It was shown that the thermoplastic rubbers loaded to both 80 and 85 wt % with ammonium perchlorate dewetted in a plane normal to the principal stress axis. This localized dewetting was considered to constitute failure, and it occurred at elongations of <1%. In the case of the ring specimens, dewetting took place during the straightening of the ring in the Instron jig before it was stressed appreciably. Naturally, this low strain at failure renders the propellant totally unsuitable for any practical application. It was thought that poor binder-to-oxidizer bonding was responsible for the inadequate mechanical properties of the propellant. Consequently, steps were taken to modify the backbone molecules of the binder to increase the adhesive bond between the filler and the rubber. The experimental details and tensile results of one of the modifications are presented here.

2. Experimental Procedure

The backbone of the thermoplastic molecule was chemically modified with three different materials: thioacetic acid, thioglycolic acid, and monothioethylene glycol (2-mercaptoethanol). These modifications result in pendent ester, hydroxy, and carboxyl groups, respectively. Figures 11 and 12 illustrate the rubber molecule and the three different modifications. Two lots of each of the modified rubbers were prepared, so both 1% and 10% of the equivalent double bonds in the butadiene segment were reacted.

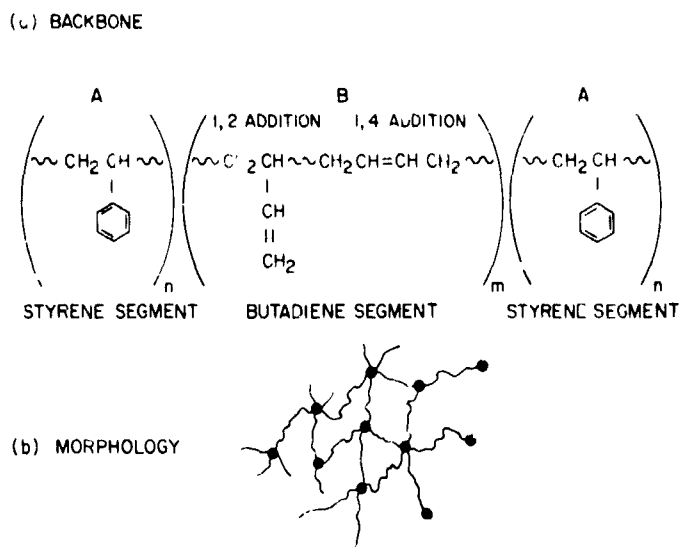


Fig. 11. Structure of Shell polymer

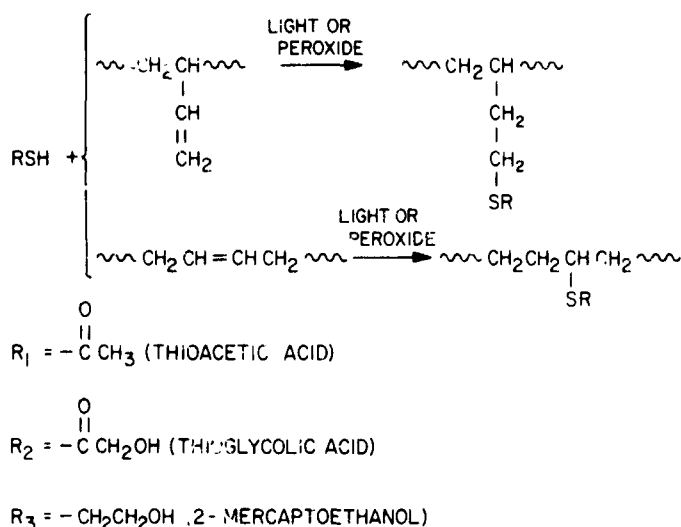


Fig. 12. Chemical modification of Shell thermoplastic rubber

The theory behind the modifications was quite simple and straightforward. It was thought that the pendent groups could chemisorb, or at least hydrogen-bond, to the surface of the ionic filler. This is a standard method of enhancing the bond strength of adhesives and is thought to be partly responsible for the relatively good binder-filler bond in the castable, curable propellants.

However, there is a slightly different viewpoint that could be taken (SPS 37-44, Vol. IV, pp. 108-115). Namely, one may consider the styrene or "hard" part of the rubber to be acting as a filler. This is a reasonable assumption,

since the styrene is well below its glass transition temperature, and its modulus is about 1000 times higher than that of the butadiene or "soft" component of the triblock. This concept of the morphology is schematically represented in Fig. 11(b), where the filled circles represent the domains or droplets of styrene that physically tie the butadiene molecules into a network. According to Fedors' (SPS 37-44) calculations, these droplets are approximately 300 Å in diameter and, as such, are comparable to some of the very fine carbon blacks used as reinforcing agents in rubber goods. The volume fraction of the copolymer ϕ_s is given by:

$$\phi_s = \frac{M_s/\rho_s}{M_s/\rho_s + M_b/\rho_b}$$

where M and ρ are the molecular weight and density, respectively, and the subscripts indicate the components styrene and butadiene. If the density of polystyrene is taken to be 1.04 and that of butadiene is taken to be 0.90, then the above calculation shows that the binder is already approximately 22% filled with "hard" styrene before the 80 wt % oxidizer is added (this oxidizer representing about 65 vol %). Clearly, the final system is approximately 79 vol % filled. This total ϕ can be calculated exactly as follows:

$$\phi_{\text{total}} = \phi_{\text{oxidizer}} + \phi_s(1 - \phi_{\text{oxidizer}})$$

It has been shown in other studies (Ref. 15) that the maximum loading ϕ_m for systems similar to the one under consideration is approximately 0.80 vol % without the use of an effective surfactant, and about 0.88 vol % with the use of a surfactant. If the concept of considering the styrene as a filler is true, then it is not surprising that the mechanical properties of the propellant are poor; the rubber is at ϕ_m !

To test this concept, a series of inert propellants with ammonium sulfate as the filler was employed. The ammonium sulfate ground to 12 and 100 μ was blended into a bimodal mixture of 30%-small/70%-large particles by weight. This is the same particle size and particle size distribution that was used in the propellant employing ammonium perchlorate as the filler. Three different loadings, employing Kraton 101 (Shell Chemical Company) as a binder, were prepared: 40, 50, and 80 wt % ammonium sulfate. The results are discussed below.

3. Results

The three types of Shell thermoplastic rubbers being studied—Kraton 101, Kraton 102, and Thermolastic 125—were chemically modified as described above. Only the thioacetic-acid-modified rubber has been tested to date.

The three rubbers (1% and 10% thioacetic-acid-modified) and the control specimen were loaded with 80 wt % ammonium perchlorate, and rod-like tensile specimens were molded. The results were exactly as reported earlier for the propellant employing the unmodified binder and flat specimens from molded sheets. Very local dewetting, i.e., failure, occurred at <1% strain in all cases. This is illustrated by the typical Instron trace of force versus crosshead travel shown in Fig. 13(a).

To test the second concept, that the styrene or "hard" component of the rubber should be treated as a filler and that the 80 vol % oxidized propellant is too close to ϕ_m , a series of dummy propellants using ammonium sulfate was prepared. The ammonium sulfate was ground to the sizes described above, and Kraton 101 was loaded to 40 and 50 wt %, corresponding to 0.245 and 0.350 vol %, respectively. In addition, the thioacetic-acid-modified Kraton 101, both 1% and 10% double-bond-substituted, was prepared at 40 wt % loading. The results are presented in Table 6. Quite clearly, the 40 and 50 wt % loaded systems are behaving more like a conventional propellant, without the local dewetting observed in the 80 wt % loaded systems.

A quick examination of Table 6 reveals a considerable batch-to-batch variation in the Shore hardness and, consequently, in the modulus. This variation is not reflected in the maximum stress, however. The chemically unmodified and the 10% double-bond-substituted materials exhibit identical properties, whereas the rubber with 1% substitution has considerably reduced σ_m and modulus, but about the same ϵ_m and strain. We have no explanation at present for this behavior. A series of photographs of the tensile test on the 40 wt % sample is given in Fig. 14. A similar series of photographs depicting the line dewetting of the 80 wt % loaded system was presented in SPS 37-43.

A typical Instron curve showing the behavior of the 40 and 50 wt % loaded systems is given in Fig. 13(b). When one compares this curve of Fig. 13(b) with Fig. 13(a), it can be seen that the dewetting takes place more gradually; i.e., there is less of a rapid downturn in the load after the maximum stress is reached. To go one

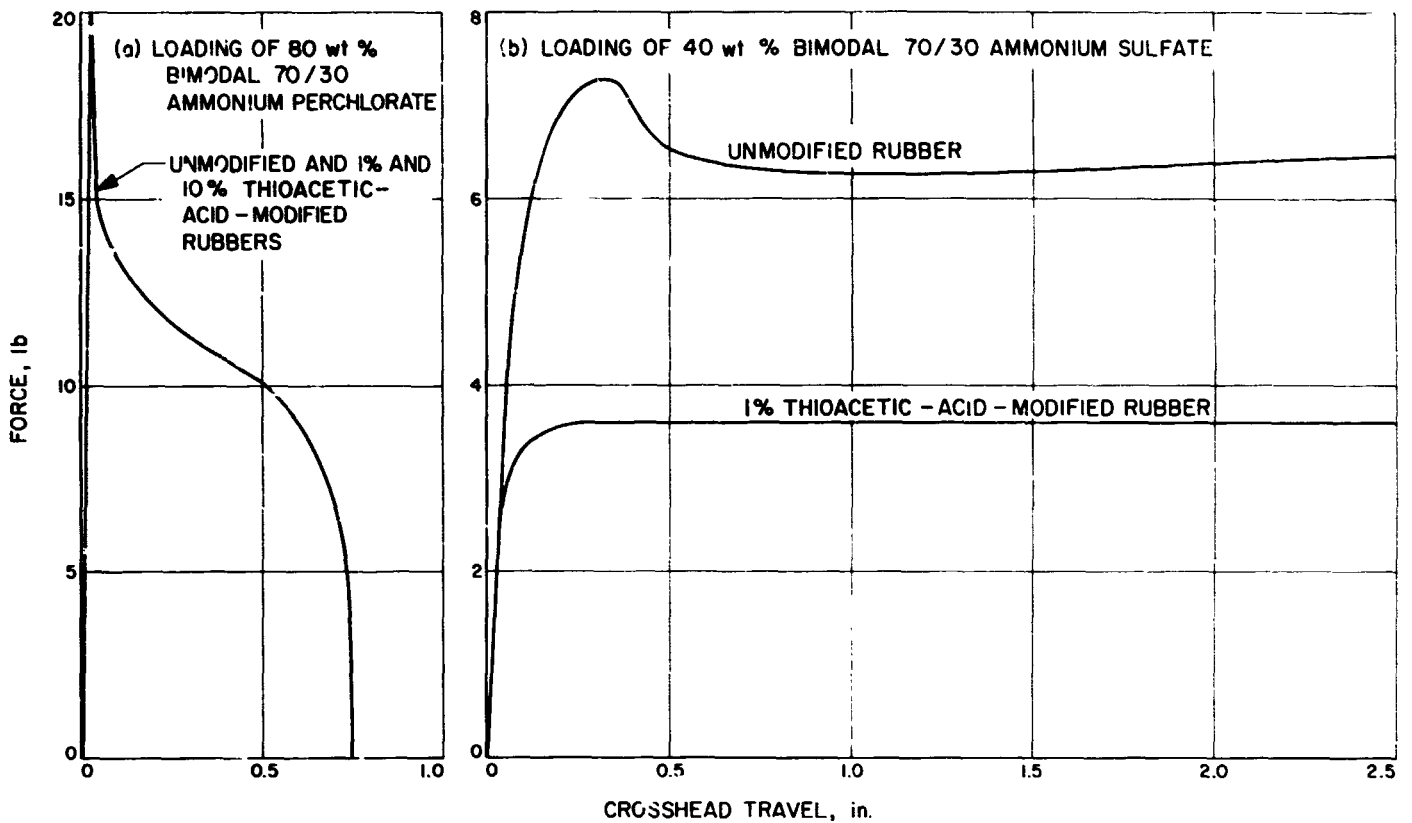


Fig. 13. Typical Instron curves of crosshead travel vs force for modified and unmodified Kraton 101 thermoplastic rubbers (strain rate = 1 in./min)

Table 6. Test results for modified and unmodified Kraton 101

Loading of filler (ammonium sulfate), wt %	Percent of double bonds substituted (thioacetic acid)	σ_m , psi	ϵ_m , %	Average Shore hardness	Average modulus from Shore hardness	Loading of filler (ammonium sulfate), wt %	Percent of double bonds substituted (thioacetic acid)	σ_m , psi	ϵ_m , %	Average Shore hardness	Average modulus from Shore hardness
40	0	256	9.8	78	1900	40	0	264	12.6	81	2100
40	0	265	8.8	78	1900	40	0	248	14.0	81	2100
40	0	293	8.7	78	1900	40	0	—	—	81	2100
40	0	—	—	78	1900	40	1	176	—	71	1100
50	0	282	10.3	84	3000	40	1	189	10.4	71	1100
50	0	286	12.1	84	3000	40	1	186	12.8	71	1100
50	0	292	10.2	84	3000	40	1	184	—	71	1100
80	0	106	<1	>93	>20,000	40	10	261	—	81	2100
80	0	142	<1	>93	>20,000	40	10	251	—	81	2100
80	0	142	<1	>93	>20,000	40	10	251	13	81	2100
40	0	257	—	81	2100	40	10	—	—	81	2100

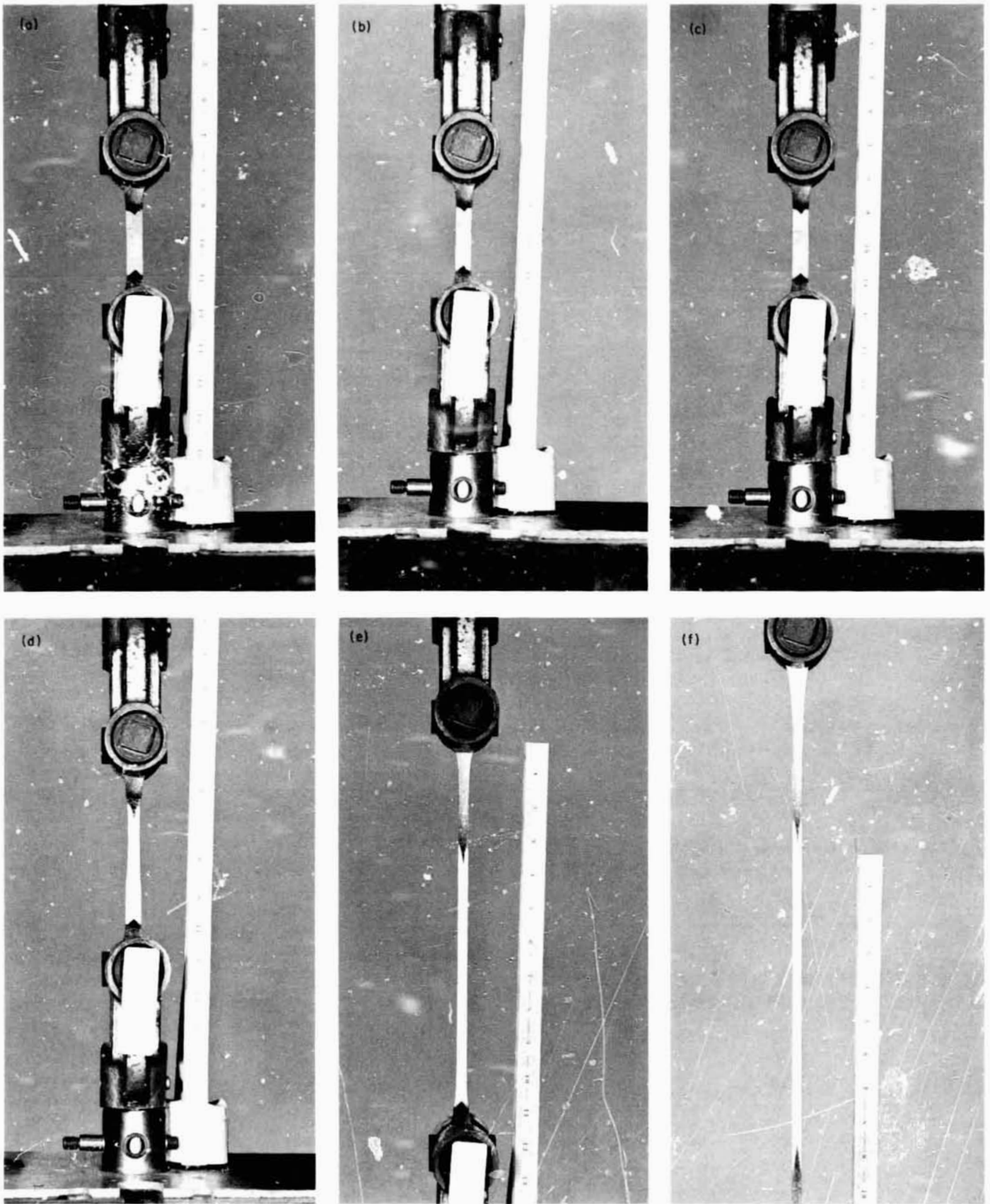


Fig. 14. Tensile test of 40 wt % sample

step further, Fig. 13(b) also depicts the typical Instron curve for the 40 wt % loaded, thioacetic-acid-modified system, where there is no downturn after the maximum load is reached. This appears to show that indeed a tighter bond between binder and filler was achieved, in spite of the decreased stress at maximum in the 1% double-bond-substituted system. It would seem that this decreased value of σ_m may be due to an inherent change in the stress level of the binder and is independent of the binder-filler bond. Unfortunately, our supply of the modified rubber was too limited to test the unfilled rubber. This omission will be rectified on all future lots of chemically modified rubber.

4. Burning Rates

There now seems to be an explanation for the anomalous burning rates reported in SPS 37-41. It is apparent that the addition of mineral oil to the 80 wt % loaded systems cannot result in increased burning rate as a result of decreased dispersion, since, as a matter of fact, the 80 wt % systems are already above ϕ_m . The addition of an agglomerating agent cannot decrease dispersion, because the systems are initially as poorly dispersed as they can be. On the other hand, mineral oil used as a direct substitute for the rubber (already 22 vol % styrene-filled) can have the effect of bringing the vol % loading of the system under ϕ_m . This results in *better* dispersion and a consequent *decrease* in the burning rate, as was observed on one of the systems (SPS 37-43).

5. Interim Conclusions and Future Work

The commercial Shell Chemical Company rubbers Kraton 101, Kraton 102, and Thermolastic 125 are unsuitable as solid propellant binders because the styrene or glassy component of the rubber must be considered to be acting as a filler. Hence, the propellant is loaded above ϕ_m when sufficient oxidizer is added to bring the system near stoichiometry. This fact explains the anomalous burning rate data reported earlier. That is, adding non-polar mineral oil cannot decrease the dispersion of a system that is already above ϕ_m ; in fact, by substituting unfilled mineral oil for an effectively filled (with glassy styrene) rubber, it is conceivable that the dispersion might be improved with an attendant *increased* burning rate.

Chemical modification of the butadiene backbone by reacting 1% and 10% of the double-bond sites with thioacetic acid results in no change in the properties of 80 wt % loaded propellant. In the case of a 40 wt % loaded system, there is a profound change; however,

much of it seems to be in the binder, rather than at the binder-filler bond, which appears to show minor change.

Future work will follow two approaches: First, physical tests will be concluded on the chemically modified commercial rubbers; second, the rubber structure will be modified according to Fedors' theory.

D. The Relationship Between Stress and Strain in Multiaxial Deformations of Elastomers,

W. V. Hutchinson

In theories concerning the finite deformation of elastomers, much discussion has centered around the use of the invariants of the deformation tensor of the elastomers in the evaluation of the stored energy functions of these materials (Refs. 16-23). Also, much thought (Refs. 24-35) has been devoted to the physical interpretation of the gradients of the stored energy functions with respect to these invariants so that the dependence of the stored energy upon these invariants could be derived in a physical theory. Besides being unwieldy coordinates to use in describing the deformations of these materials, physical interpretations of the meanings of the gradients have been unsatisfactory, and physical theories predicting the involvement of all these invariants are unavailable.

Examination of a well-known molecular model enables one to choose, in a straightforward manner, a proper set of coordinates to facilitate the evaluation of the stored energy of an elastomer under a deformation of any axiality. The model chosen is equivalent to that of Kuhn and Gr \ddot{u} n (Ref. 36), which leads to the well-known Langevin function first derived by Langevin in his theory of the magnetic saturation of dipoles (Refs. 37 and 38).

Let us imagine that the bonds of a polymer chain, not subjected to any force, are randomly oriented. Thus, the vectors describing the bond directions will be uniformly distributed over all directions in space. Let us now consider the imposition of a force F_1 along one direction, making an angle θ with one of the bonds of length L (Fig. 15). The force F_1 will tend to align this bond along the direction of the force. The potential energy of a bond in such a force F_1 is $-F_1 L \cos \theta$. Assuming that only thermal energy is tending to offset the alignment of the bond vectors along the direction of the force, the distribution of directions of the bond vectors will be given by

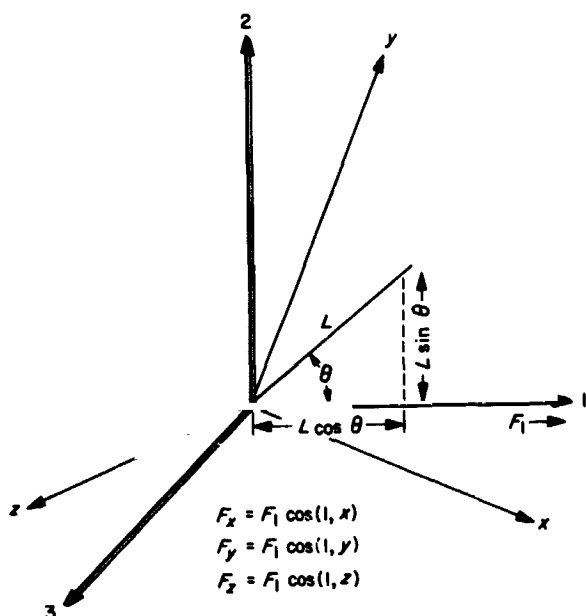


Fig. 15. Geometry defining force F_1 imposed on bond

a Maxwell-Boltzmann distribution such that

$$dN = \exp(-W/kt) dW = \exp[(F_1 L \cos \theta)/kt] \\ \times d(F_1 L \cos \theta) \\ = - \exp[(F_1 L \cos \theta)/kT] F_1 L \sin \theta d\theta$$

The total number of bonds N is given by

$$N = \int_0^\pi dN = - \int_0^\pi \exp[(F_1 L \cos \theta)/kT] F_1 L \sin \theta d\theta$$

From Fig. 15, the projection of one bond of length L along the axis 1 is $L \cos \theta$. Taking \bar{L}_1 to be the average value of this projection on axis 1, along which a force F_1 is imposed, then

$$\bar{L}_1 N = - \int_0^\pi L \cos \theta \exp[(F_1 L \cos \theta)/kT] F_1 L \sin \theta d\theta$$

Substituting for N from above, we obtain

$$\bar{L}_1 = \frac{\int_0^\pi - F_1 L^2 \exp[(F_1 L \cos \theta)/kT] \sin \theta \cos \theta d\theta}{\int_0^\pi - F_1 L \exp[(F_1 L \cos \theta)/kT] \sin \theta d\theta}$$

This integral yields the well-known Langevin function such that

$$\frac{\bar{L}_1}{L} = \coth(F_1 L/kT) - kT/F_1 L$$

If the exponential term in the numerator of the integral above had been first expanded in a power series before evaluation of the integral, it would have been seen that the value of \bar{L}_1 tends toward zero as the force F_1 vanishes. Therefore, it is seen that the effect of the force F_1 is to produce a non-zero average projection of the bond length in the direction of the force. Thus, \bar{L}_1/L is actually $\Delta\bar{L}_1/L$ due to the force F_1 .

If, instead of evaluating the average net displacement of the bond projection upon the direction of the force F_1 , we decide to determine the component at right angles to the force, say along axis 2, the component of the bond projection in this direction will be $L \sin \theta$. Proceeding as before, we obtain the average value of this component:

$$\bar{L}_2 = \frac{\int_0^\pi L \sin \theta dN}{\int_0^\pi dN}$$

For the limits of this integration, we need be concerned only with those bonds having values of θ between 0 and $\pi/2$, since the average value of this projection between these limits is the same as that between 0 and π .

$$\bar{L}_2 = \frac{\int_0^{\pi/2} - L \sin \theta \exp[(F_1 L \cos \theta)/kT] F_1 L \sin \theta d\theta}{\int_0^{\pi/2} - \exp[(F_1 L \cos \theta)/kT] \sin \theta d\theta}$$

The denominator may be evaluated in a straightforward manner. The numerator may best be evaluated by first expanding the exponential in a MacLaurin series and then integrating term-by-term. Therefore, since in the absence of the force F_1 the average value of this component is $\pi/4$, the net displacement due to the force is given by:

$$\frac{\Delta\bar{L}_2}{L} = - \left[\frac{\frac{1}{4}\pi - \frac{1}{3}\left(\frac{F_1 L}{kT}\right) + \frac{\pi}{32}\left(\frac{F_1 L}{kT}\right)^2 + \frac{2}{90}\left(\frac{F_1 L}{kT}\right)^3 + \dots}{1 - \exp(-F_1 L/kT)} \right] - \frac{\pi}{4}$$

It is seen that a force along one direction can, according to this model, produce a net component of displacement of the bond direction in a direction perpendicular to it. This displacement is seen to be negative, as is observed in cases of uniaxial deformations. Also, by symmetry, an equal displacement would be produced along axis 3. The total displacement of the bond vector in space due to the force F_1 is, therefore,

$$\left| \frac{\Delta \bar{L}_T}{L} \right| = \left\{ \left(\frac{\Delta \bar{L}_1}{L} \right)^2 + \left(\frac{\Delta \bar{L}_2}{L} \right)^2 + \left(\frac{\Delta \bar{L}_3}{L} \right)^2 \right\}^{1/2}$$

Let us look now at the force F_1 . We may take this force F_1 to be the resultant of three other forces whose components, measured along a set of orthogonal axes, x , y , and z having the same origin as axes 1, 2, and 3, are F_x , F_y , and F_z . Therefore, we have

$$F_1 = \{F_x^2 + F_y^2 + F_z^2\}^{1/2}$$

The displacement components along the axes 1, 2, and 3 will have components along the axes x , y , and z such that

$$\begin{aligned} \frac{\Delta \bar{L}_1}{L} &= \left\{ \left(\frac{\Delta \bar{L}_1}{L} \right)^2 + \left(\frac{\Delta \bar{L}_2}{L} \right)^2 + \left(\frac{\Delta \bar{L}_3}{L} \right)^2 \right\}^{1/2} \\ &= \left\{ \left(\frac{\Delta \bar{L}_x}{L} \right)^2 + \left(\frac{\Delta \bar{L}_y}{L} \right)^2 + \left(\frac{\Delta \bar{L}_z}{L} \right)^2 \right\}^{1/2} \end{aligned}$$

It may therefore be seen that, under conditions of multi-axial deformation where we may have stresses along any orthogonal axes, the only force felt by the individual bond segments is the vector sum of the components. The over-all displacement will be the vector sum of displacements along any three mutually perpendicular directions. According to this analysis, it would be expected that stress-strain data for any axiality could be related by plotting the vector sums of all forces against the vector sums of all displacements. The quantities $\Delta \bar{L}_i/L$ may be related to the strains $\epsilon_i = \Delta l_i/l_0$ by a proportionality factor. Since, according to the model, the forces concerned are those felt by the individual bond segments, and the density of bond segments per unit area is not likely to change appreciably upon deformation, the forces may be related to the true stresses in the mutually perpendicular directions, i.e., the stresses upon the true cross-sectional area. Therefore, the model considered suggests that stress-strain data of any axiality can be combined into one stress-strain curve by plotting the vector sum of the strains versus the vector sum of the true stresses.

Figures 16-18 are plots of uniaxial and biaxial stress-strain data for two similar natural rubber formulations and one formulation of a polydimethyl siloxane (Silastic 950U) containing 28 wt % of a filler suspected to be a "Cabosil." The data in Fig. 16 are those of Rivlin and Saunders, as calculated from Tables 1, 2, and 6 of Ref. 21. The formulation of this natural rubber is also given in Ref. 21. The data plotted in Figs. 17 and 18 are data obtained at JPL using a stress relaxometer designed by Becker and Landel (Ref. 39). The Becker-Landel stress relaxometer is designed such that the ratio ϵ_x/ϵ_y is given by the quantity $\tan \alpha$. Those experimental points designated as "stripl axial" are from experiments such that ϵ_x is held fixed at zero while ϵ_y is varied. The formulation of the natural rubber in this instance was:

Material	Parts by weight
RSS #1	100
Sulfur	1.0
MBTS	1.25
Thionex	0.25
ZnO	5.0
Stearic acid	2.0
A2246	2.0

This material was cured for 20 min at 143.3°C. The Silastic 950U was a commercial formulation which was cured using a 0.6% benzoyl peroxide catalyst for 5 min at 127°C.

Figures 16-18 show that there is no effect upon the stress-strain curve of the axiality of the stress field if plotted using the suggested coordinates. Further, the energy expended in deformation is simply the integral under the indicated stress-strain curve up to the limit of the vector sum of the stress considered, multiplied by the cosine of the angle between the force and displacement vectors. The cosine of this angle, say ϕ , between the force and displacement vectors is given by:

$$\begin{aligned} \cos \phi &= \cos(\epsilon, 1) \cos(\sigma, 1) + \cos(\epsilon, 2) \\ &\quad \times \cos(\sigma, 2) + \cos(\epsilon, 3) \cos(\sigma, 3) \end{aligned}$$

This equation reduces to

$$\cos \phi = \cos(\epsilon, 1)$$

when the stress is uniaxial along the direction of axis 1.

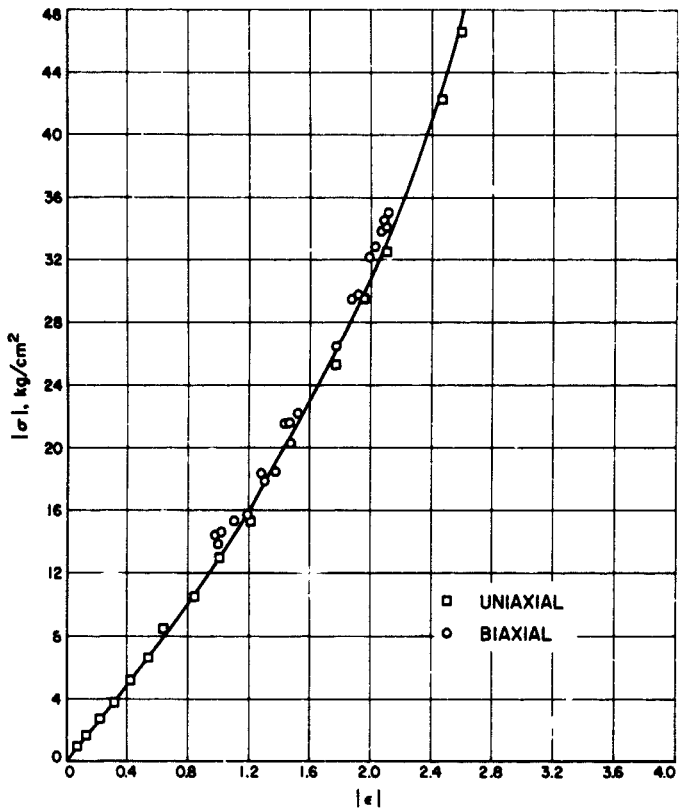


Fig. 16. Uniaxial and biaxial stress-strain data of Rivlin and Saunders (Ref. 21) for a natural rubber formulation

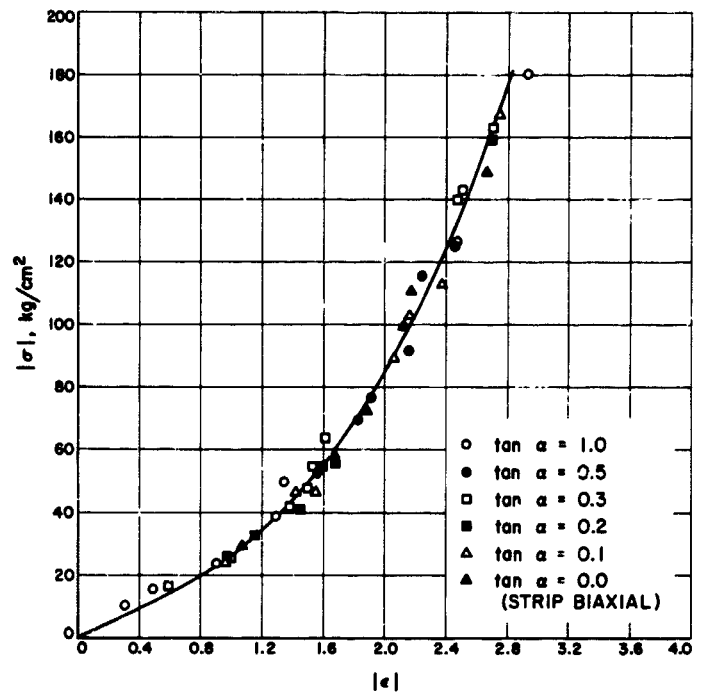
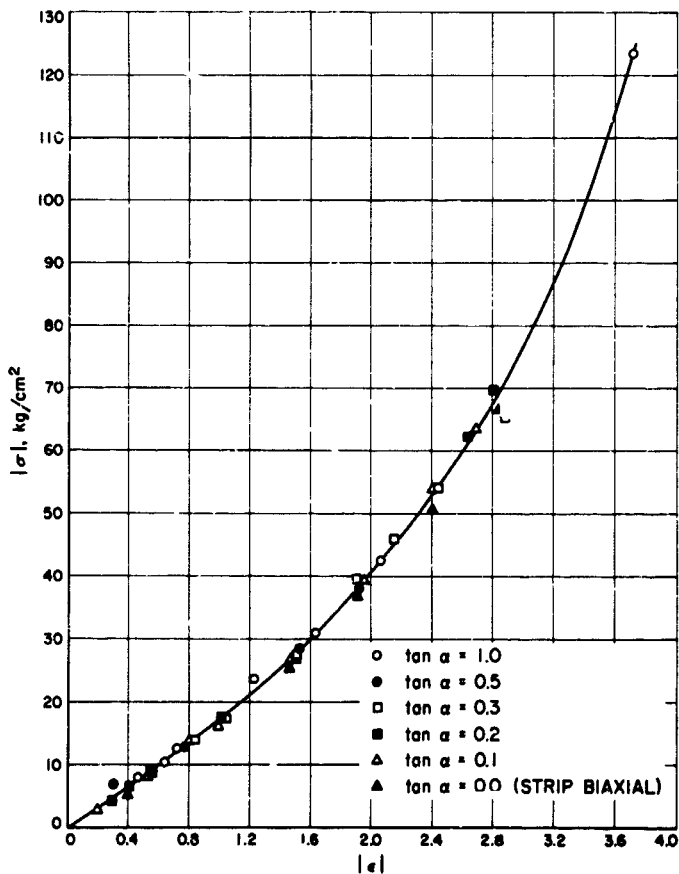


Fig. 18. Uniaxial and biaxial stress-strain data of Hutchinson, Becker, and Landel (Ref. 40) for Silastic 950U

Fig. 17. Uniaxial and biaxial stress-strain data of Hutchinson, Becker, and Landel (Ref. 40) for a natural rubber formulation

The apparent linearity of these three stress-strain curves at small deformations indicates how Hookean behavior is approached at small extensions.

These results suggest that it is unnecessary to use the invariants of the strain tensor defining the deformation of an elastomer in relating the behavior of these materials in multiaxial stress fields to their behavior in a uniaxial stress. Indeed, it appears that one need only take the vector sum of the strains in any three mutually perpendicular directions and correlate that with the vector sum of the true stresses measured along any three mutually perpendicular directions. Also, it appears that, to define the form of the stored energy function of such an elastomer, one need only determine minimally the uniaxial stress-strain behavior, which, when plotted in the coordinates suggested here, may be fit with a power series or perhaps an analytic expression. Since the stress and strain, i.e., the force and displacement, are not colinear, the area under the stress-strain curve must be multiplied by the cosine of the angle between the force and displacement vectors. The angle between these vectors appears to be independent of the axiality of the deformation.

No data are available on the crosslink densities of either the Rivlin and Saunders or the Hutchinson, Becker, and Landel natural rubbers. It is probable, however, that the differences in the original slopes of the stress-strain curves of Figs. 16 and 17 must be manifestations of differences in crosslink densities.

E. Poly(isobutylene) Prepolymers, J. D. Ingham

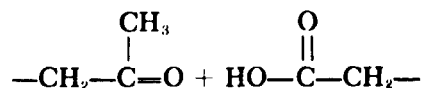
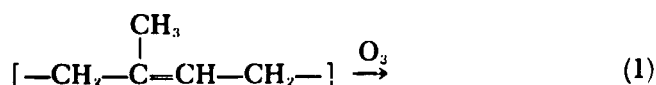
1. Introduction

There is considerable interest in obtaining polymers for solid propellant binders with good elastomeric properties and improved thermal and chemical stability. Although several available polymers are adequate for many specific applications, none possess the features of an ultimately ideal system for composite propellants. Among the most important characteristics of such polymeric systems are minimum chemical reactivity with other propellant ingredients; maximum prepolymer average molecular weight; low viscosity of the binder before curing; and relatively temperature-independent, invariably good mechanical properties of the finally cured, highly filled solid propellant. A maximum prepolymer average molecular weight is required to reduce the concentration of reacting functional groups during cure. This concentration must be reduced to minimize the

exotherm and temperature- and specific-volume changes which can lead to high frozen stress concentrations and other imperfections, particularly for case-bonded applications. This condition is increasingly aggravated as the motor size and angularity of the cross section of the internal perforation increases. For most purposes, the binder should have a maximum ratio of hydrogen atoms to atoms X of higher atomic weight, such as C, N, O, and most metals. A high ratio can be more easily obtained from a higher-molecular-weight saturated hydrocarbon prepolymer, since most modes of chain extension and crosslinking involve linkages with low H/X ratios.

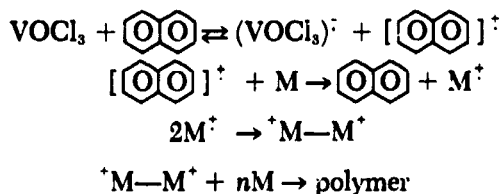
In many respects, poly(isobutylene) containing appropriate terminal groups is an ideal prepolymer; however, its bulk viscosity is higher than most other prepolymers, and it is difficult to prepare difunctional poly(isobutylene). Isobutylene does not respond to polymerization catalysis by free radicals and radical-anions; thus, it must be polymerized by cationic catalysts, which generally produce monofunctional chains containing a maximum of one terminal double bond per molecule.

Rehner and Gray (Refs. 41 and 42) obtained convincing evidence that butyl rubbers (isobutylene-isoprene copolymers) containing small concentrations of isoprene units are oxidatively cleaved by ozone to give carbonyl and carboxyl groups; i.e.,

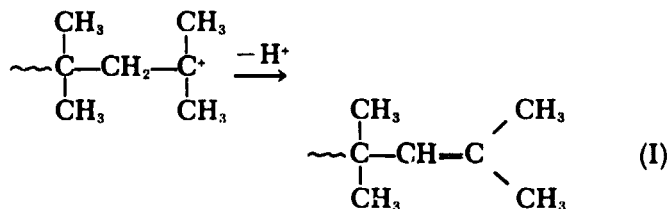


Thus, nominally difunctional poly(isobutylene) can be prepared by degradation of isobutylene-diene copolymers in which the diene is spaced randomly at intervals corresponding to the desired prepolymer molecular weight. For example, Marvel and Jones (Ref. 43) have ozonized butyl rubber of molecular weight 800,000 containing 2 mol % of isoprene units and reduced the product with lithium aluminum hydride to obtain α,ω -diols with number-average molecular weights close to the theoretical value of 2850. It was concluded from end-group analysis and molecular-weight determinations by vapor-phase osmometry that the functionality was slightly greater than two. Presumably, the excess groups were obtained from an occasional 1,2-polymerized isoprene unit in the initial butyl rubber (Ref. 44).

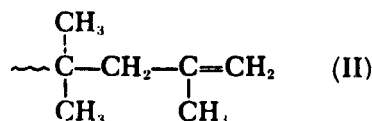
Yamada, Shimada, and Hayashi (Ref. 45) have polymerized isobutylene with the cationic catalyst vanadium oxytrichloride (VOCl_3) in the presence of activators such as naphthalene and butadiene. Although convincing evidence for a dication was not presented, they postulated the following mechanism:



If this mechanism is correct, the predominant terminal groups would be expected to be double bonds formed by transfer reactions involving elimination of a proton from the growing carbonium ion at each end; i.e.,



or



This report is primarily concerned with current efforts to obtain useful poly(isobutylenes) by VOCl_3 catalysis and to determine whether the above mechanism is correct. These proposed castable, low-shrinkage poly(isobutylene) systems should also be applicable as encapsulants, coatings, and sealants.

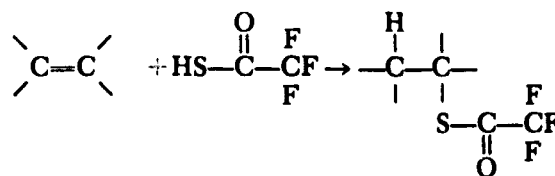
2. Results and Discussion

An unusual feature of activator/ VOCl_3 polymerization, when compared with other cationic polymerizations of isobutylene, is that quite high molecular weights can be obtained at relatively high temperatures. At 0°C with an activator/ VOCl_3 ratio of 0.5, 5 mM of VOCl_3 , and 20 ml of isobutylene in heptane, poly(isobutylene) of $[\eta] = 0.46$ dl/g was obtained (Ref. 45). This corresponds to a molecular weight of $>30,000$, which is too high for consideration as a prepolymer.

Therefore, a polymer was prepared, under conditions of much higher catalyst concentration, to obtain a poly-

mer of molecular weight <2500 . The activator/ VOCl_3 ratio was ~ 0.05 . The catalyst was prepared by dissolving 0.1 g of naphthalene in 5 ml of hexane, followed by distillation of 1 ml of VOCl_3 into the flask attached to the vacuum system. The catalyst was exposed to isobutylene vapor for 30 days. When the isobutylene cylinder was closed from the system, there was a measurable rate of pressure decrease, reflecting reaction of the isobutylene. About 8 g of liquid polymer was obtained after washing and drying. Its bulk viscosity was not measured, but it appeared to be greater than currently used poly(propylene oxide) and less than some current saturated poly(butadienes). The intrinsic viscosity was 0.042 g/dl in CCl_4 at 25°C , which corresponds to an estimated number-average molecular weight, M_n , of ~ 900 . This value is only approximate, primarily because the $[\eta]$ -molecular-weight relationship was extrapolated to molecular weights below $\sim 5,000$. In any case, a polymer of somewhat higher viscosity (and molecular weight) than this product would probably be fluid enough for castable formulations, depending on the end groups and curing system employed.

To obtain information about the nature and concentration of the end groups, a small sample of the polymer was reacted with trifluorothioacetic acid (thioacid) for F^{19} nuclear-magnetic-resonance (NMR) measurements. From the increase in weight, it was determined that the amount of thioacid reacted corresponded to 2 equivalents per 848 in molecular-weight units. The thioacid adds to double bonds as follows:



As determined previously (SPS 37-44, Vol. IV, pp. 115-120), the position of the fluorine resonances depends on the chemical structure of the alkene. Two resonance signals in the area ratio 3/1, corresponding to two types of unsaturation, were observed, as indicated schematically in Fig. 19. Comparison of the area ratio of the sum of these signals to the internal standard, $\text{BrCF}_2\text{CF}_2\text{Br}$, indicated addition of 2 equivalents of thioacid per 924 in molecular-weight units. The larger signal probably corresponds to unsaturation of the type indicated by structure (II) and the smaller, to that indicated by structure (I) above, since it is known that acidic dimerization of isobutylene gives the corresponding structures in the ratio of $\sim 4/1$ (Ref. 46).

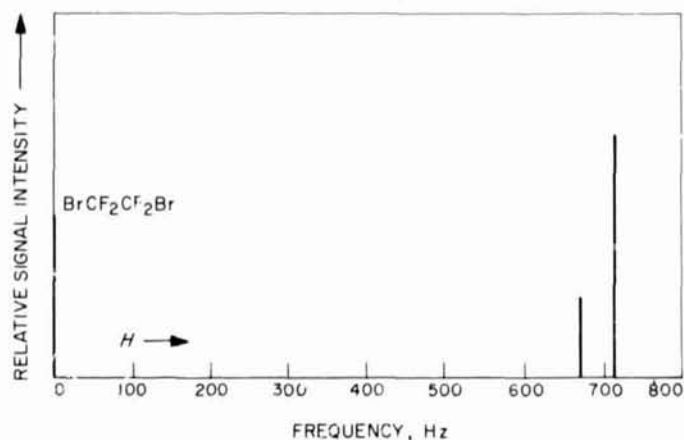


Fig. 19. Schematic F^{19} NMR spectrum of the trifluoro-thioacetic acid adduct of poly(isobutylene) at 56.4 MHz in benzene

Furthermore, these assignments are in qualitative agreement with the known chemical shifts of similar derivatives of 1, 2 and 1, 4 unsaturated groups of poly(isobutadienes) (SPS 37-44). Bromine absorption measurements indicated two unsaturations per 874 in molecular-weight units. Thus, all of these measurements indicate that the poly(isobutylene) prepared by $VOCl_3$ /initiator catalysis is difunctionally unsaturated, with an M_n of ~ 900 , in agreement with the proposed polymerization mechanism. However, one measurement of M_n by vapor pressure osmometry gave a value of ~ 660 for this polymer. Since earlier measurements for a similar poly(isobutylene) by this method gave erratic results, further work will be required to definitely determine M_n . If it is established that this polymer is difunctional, a polymer with slightly higher molecular weight will be prepared for potential chain-extension and crosslinking studies in an attempt to develop a practical castable poly(isobutylene) elastomer system.

F. Method for Measuring the Internal Gas Pressure of Rigid Closed-Cell Foam, E. F. Cuddihy and J. Moacanin

Our study of the rate at which gas is removed from foams under vacuum showed that the diffusion of gases (SPS 37-34 through -37, -39, and -44, Vol. IV) through rigid, closed-cell polymeric foam obeys Fick's Law, and that the necessary diffusion coefficient D could be estimated from equations developed for a simplified model. For foam encapsulant applications in spacecraft, the prime concern would be the time-dependence of the

internal gas pressure, rather than the time-dependence of the outgassing. The internal pressure should also be predictable from Fick's Law and sample geometry, but no experimental verification has been available.

Toward this end, we developed a compact pressure-transducer system which allows direct determination of the internal gas pressure within a foam. A series of transducers buried at various depths within a foam sample being exposed to a vacuum permits direct measurement of the time-dependence of the gas pressure distribution and, hence, a confirmation of Fick's Law behavior and the diffusion coefficient D obtained from the outgassing experiments. By employing this technique for burying the pressure transducers, it also becomes possible to measure the gas pressure internal to the foam during the curing and formation steps, a measurement which has never before been obtained. During the encapsulation of sensitive equipment, the gas pressure acting on the equipment may pose more of a problem than any stresses produced by the final rigid foam. In fact, since most self-foaming systems are highly exothermic, temperatures above 100°C are not uncommon; this, coupled with a high gas pressure, could lead to disastrous results during the encapsulation of certain highly sensitive equipment.

The pressure-transducer systems and the test mold are shown in Figs. 20-23. The transducer systems are constructed in a key-shaped configuration, with the tiny pressure transducer housed in the hollow open-ended top portion of the key (Fig. 20) and the connecting electrical wires running through the shaft (Fig. 21). The entire length of the shaft is filled with an epoxy sealant to prevent a leak between the ambient atmosphere and the



Fig. 20. View of transducer system showing pressure pickup in hollow end

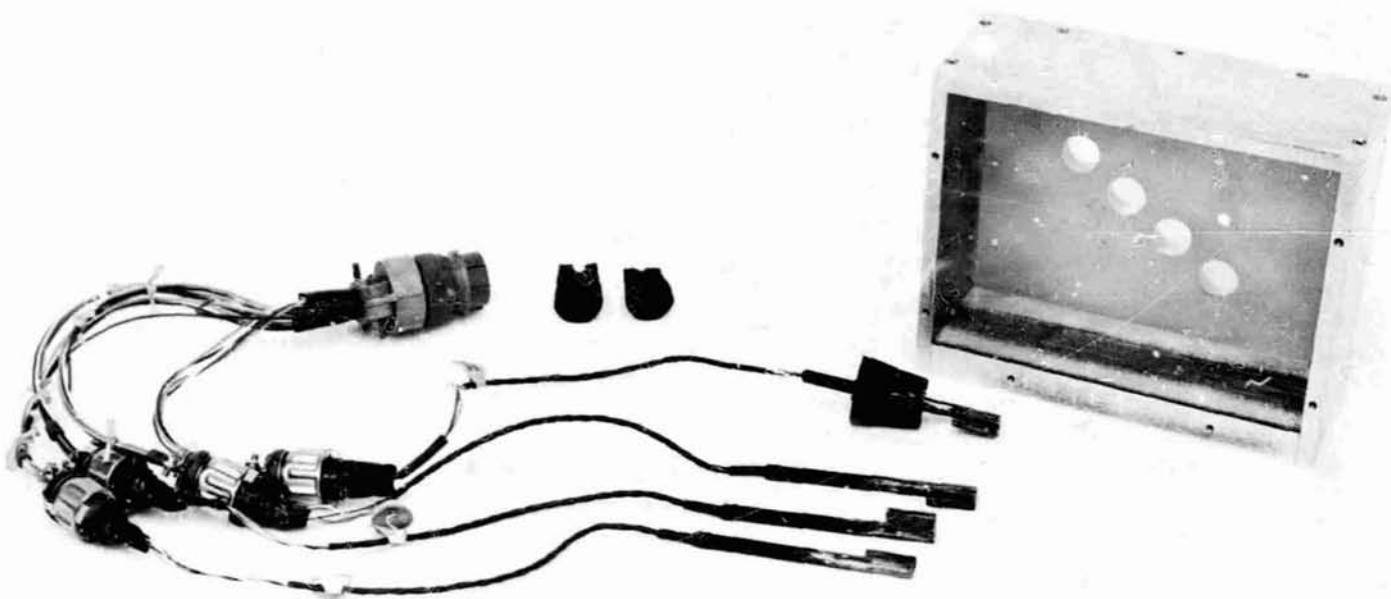


Fig. 21. Transducer systems and test mold unassembled prior to foam blowing

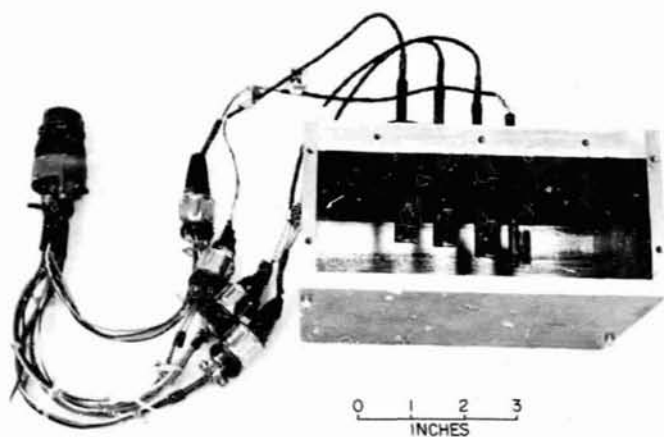


Fig. 22. Assembled unit ready for vacuum test after foam blowing (top panel removed, side panel added)

hollow transducer housing, as well as to reduce the volume of ambient atmosphere trapped in the hollow when the system becomes buried in the foam sample. The units were developed and built by Micro-Systems, Incorporated, of Pasadena, California. The miniaturized pressure transducers are Model PR 1017-0008, while the

entire key assembly has been designated as Model PR 1017-0019.

The test mold is an aluminum "take-apart" box which is 5.5 in. long, 3 in. wide, and 2 in. deep. Four tapered holes in the bottom permit the insertion of the transducer units into the mold. The transducer units are then positioned and locked in place by split rubber corks pressed into the tapered holes. The transducers extend a distance of 1 in. into the mold.

In practice, the liquid foaming material is poured into the mold and allowed to rise, completely surrounding and burying the transducers. As the material foams and rises, it is simultaneously curing and becoming more viscous. Thus, too little foaming material will not flow over the top of the transducers and properly bury the units, whereas too much foaming material will plug the hollow of the key and result in an erroneous output from the pressure pickup. By trial and error for each foaming system, the optimum amount of material can be found which will flow just over the tops of the units, have sufficient "life" left to continue rising to completely bury the units, and not flow inside the hollow of the key to touch or disturb the pressure pickup.

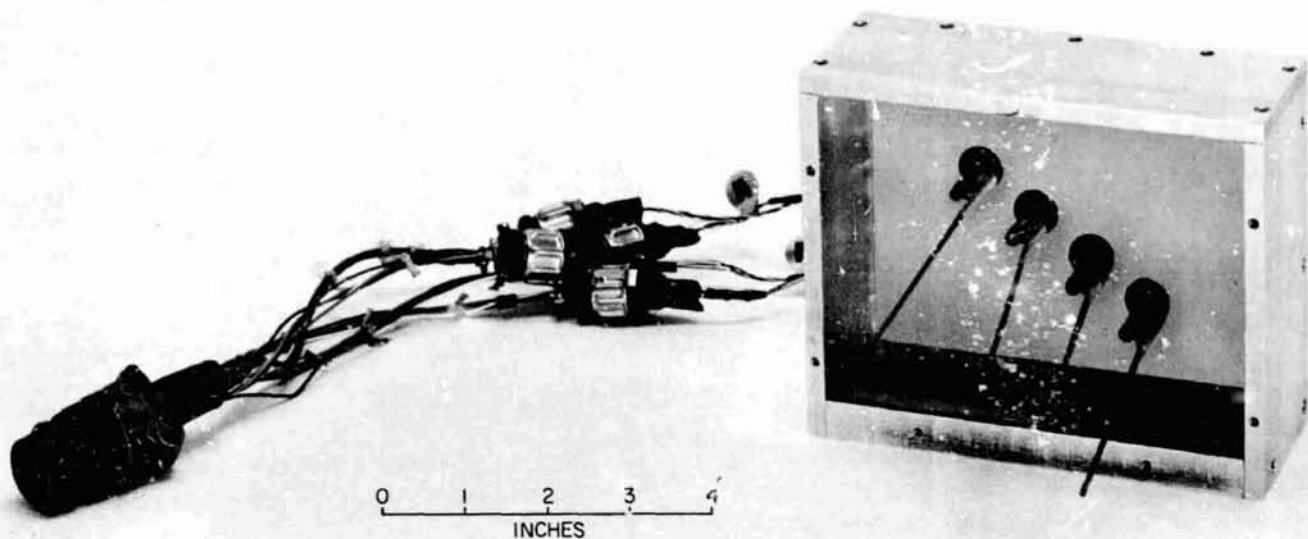


Fig. 23. Vent arrangement for calibrating temperature-dependence of transducer outputs at constant pressure

After foam blowing, the excess foam which has risen above the top of the mold is cut off, the top wall removed, and a panel placed on what was the top of the mold during foaming. The final test arrangement for the vacuum experiment is shown in Fig. 22.

The initial experiments with the pressure transducers were concentrated on measuring the internal gas pressure during foam formation. Two cases were investigated: (1) where the foam was allowed to rise freely, filling and rising above the top of the mold; and (2) where the mold was covered and the same amount of foam material was confined within the mold. The latter case was studied because it was recognized that confinement may have an effect on the internal gas pressure during foaming.

Since the foaming reaction is exothermic, calibration had to include a determination of the temperature-dependence of the transducers at constant pressure. This was done by inserting thin hollow tubes into the transducers (Fig. 23) to act as vents for the foam blown around the units. This procedure yielded the output variation due exclusively to temperature under the actual test conditions. The transducers were then placed inside a temperature-controlled pressure vessel, and the pressure-dependence of the output was obtained as a function of temperature. The results for four transducers are shown in Fig. 24. Thus, the procedure was to simultaneously record

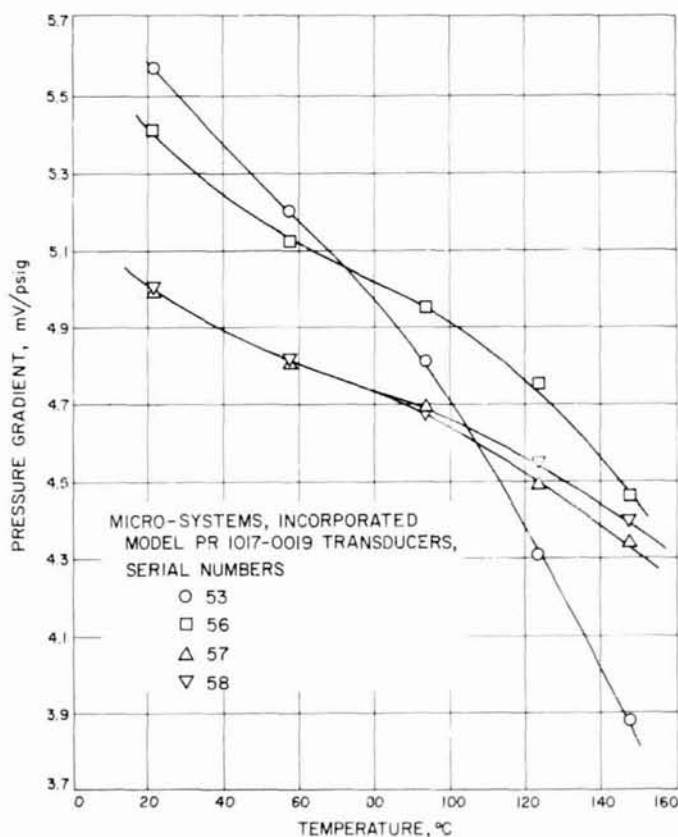


Fig. 24. Calibrations for four transducers

the temperature and transducer outputs during foaming, subtract the temperature-dependence, and then convert to pressure using the calibrations given in Fig. 24.

The internal pressures and temperatures for the unrestricted (open-mold) and confined (closed-mold) foaming conditions are shown plotted against time in Fig. 25. For both cases, the temperature peaked near 120°C, but large differences in peak gas pressures and the follow-up rates of pressure decrease were noted. The unrestricted rise had a peak gas pressure just above 3 psig, which decreased to atmospheric pressure within a few hours. This was a very important, gratifying observation for, in all previous outgassing studies, it was assumed that a foam blown unrestricted contained an atmosphere of pressure.

For confined foaming, the peak pressure exceeded 10 psig—over a three-fold increase when compared with that for unrestricted foaming. This unexpectedly higher value of the internal pressure definitely indicates the need for care when encapsulating sensitive equipment under conditions where foaming confinement can occur. Further, this increase in gas pressure represents a very large effect when compared to the change in foam den-

sity, which only increased from 4.5 lb/ft³ for the unrestricted case to 6.4 lb/ft³ for the confined case. Finally, the rate of decrease of gas pressure for the confined case was considerably lower than that for the unrestricted case; this, though partially the result of a lower diffusion rate caused by the increased foam density, was primarily the result of the very thick skin of solid polymers formed on the surface of the foam. A previous report (SPS 37-39) has detailed the dramatic reduction in outgassing rates which is expected from foams covered with a solid polymer coating.

With this preliminary, but informative work completed, these transducers will next be used to measure the internal pressure decreases during vacuum exposure.

G. Dielectric Strength of Rigid Urethane Foam,

J. Moacanin, J. Farrar, and I. N. Einhorn¹

1. Introduction

Previous results on some electrical properties of foams (SPS 37-39 through -41, Vol. 7) and the diffusion

¹Wayne State University, Detroit, Mich.

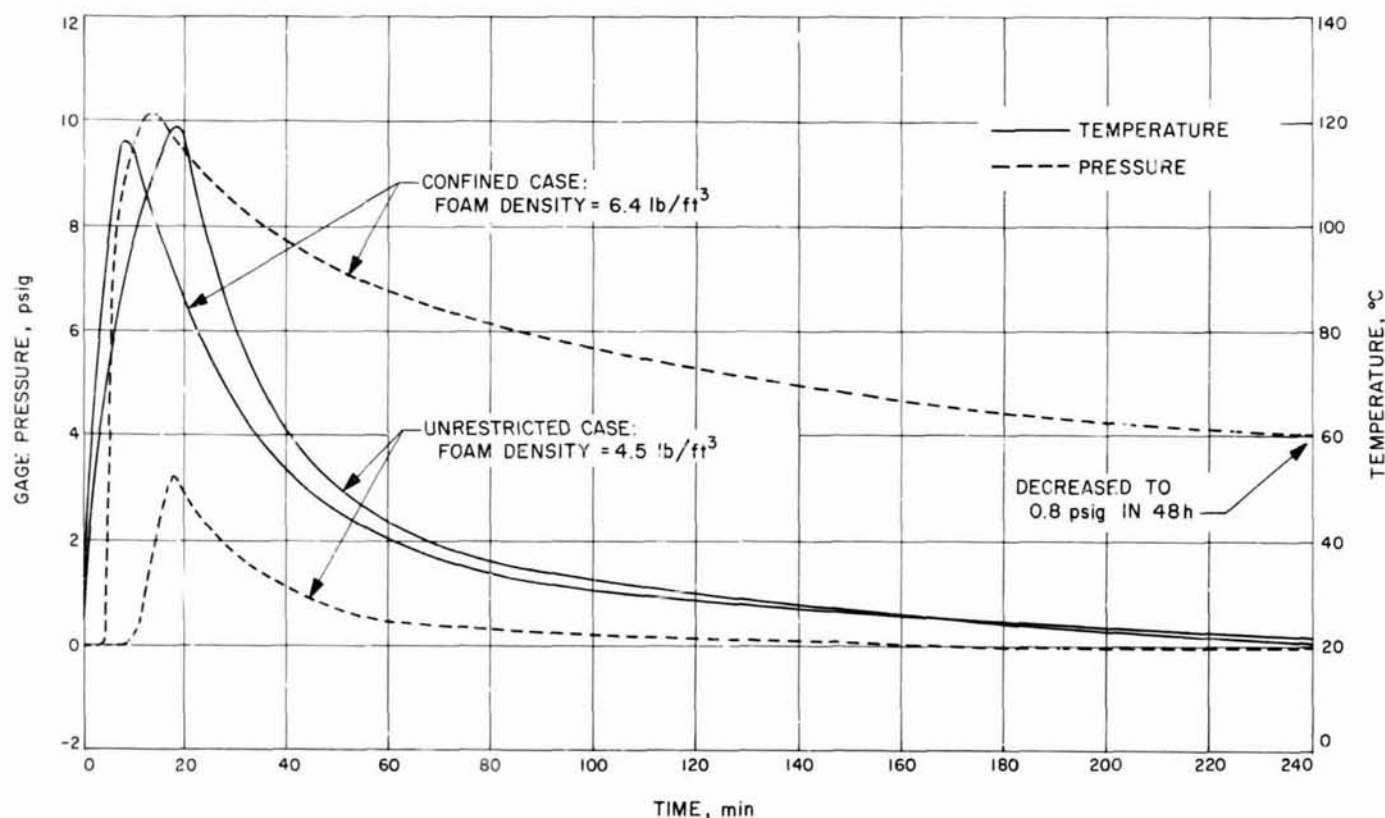


Fig. 25. Internal pressures and temperatures in a rising foam

behavior of the blowing gas (Refs. 47 and 48) have been reported. These efforts were in support of a feasibility study of using foams as lightweight encapsulants. A more detailed investigation of the effect of the geometry of foam structure on the dielectric strength is discussed here.

2. Experiments and Results

For this study, measurements were made with a Dielectric Strength Test Set, Model PDA-1 (Industrial Instruments, Inc.), using the 60-cycle mode. (This tester meets ASTM D149-61 specifications.) Cylindrical 0.25-in. brass electrodes with rounded edges were used. To ascertain the stability of the tester, the breakdown voltage of air was checked periodically; the breakdown voltage for a 1-in. air gap was 17 ± 1 kV. The foam specimen size was at least 4×4 in. to avoid flashover. The thickness varied from 0.25 to 1.00 in.; the optimum value was dictated by the 50-kV (rms) limit of the instrument.

a. Dependence of dielectric strength on thickness. For this study, sheets of 2.5- and 6-lb/ft³ Eccofoam SH (Emerson and Cuming, Inc.) were used. Thickness was varied from approximately 0.15 to 2 in. Plots of the test results for both foam densities (Fig. 26) yield good straight lines. The slope for the 2.5-lb/ft³ foam is about 0.6, and that for the 6-lb/ft³ foam is about 0.5. The value of 0.5 is also characteristic of a solid. Inasmuch as a density of 1.8-lb/ft³ is the practical lower limit for rigid urethane foams, one concludes that the 0.5 value should represent the behavior of foams of all densities of interest.

Seven flexible foams were received from Scott Paper Company (courtesy of Dr. E. A. Blair). The cell size varied by a factor of ten; in all samples, the content of broken cell windows was high. The results are tabulated in Table 7.

Table 7. Dielectric strength^a of flexible urethane foam^b

Number of cells/in.	Thickness, in.	E_b , kV/in.
10	0.41	36.5 ± 1.2
20	0.45	33.3 ± 0.0
30	0.44	35.4 ± 1.2
45	0.51	32.8 ± 1.2
60	0.46	32.3 ± 1.2
80	0.50	30.5 ± 0.5
100	0.45	34.7 ± 1.0

^a Average of five tests.

^b Manufactured by Scott Paper Company; foam density = 2 lb/ft³.

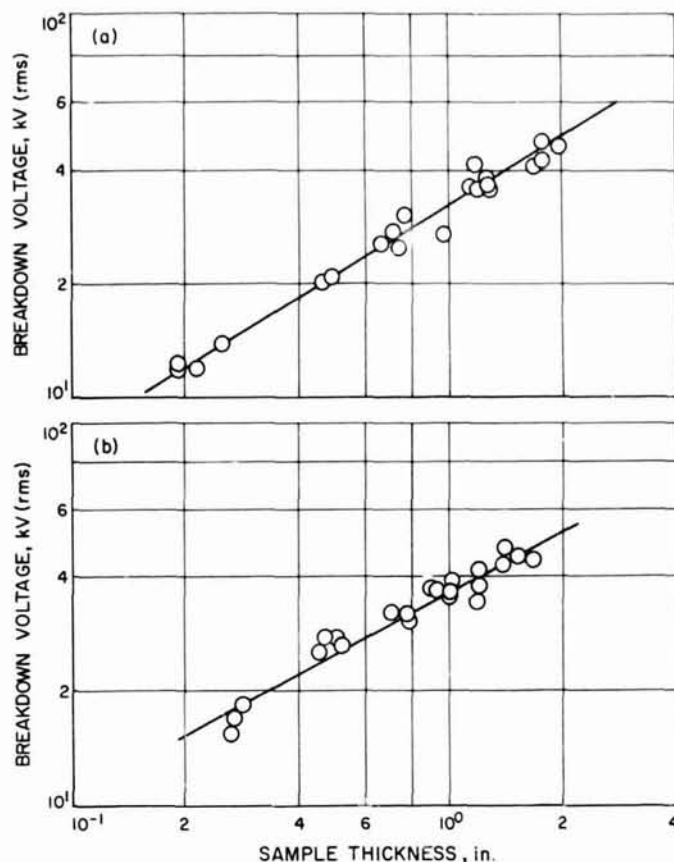


Fig. 26. Dependence of breakdown voltage on sample thickness for foams having densities of (a) 2.5 lb/ft³ and (b) 6 lb/ft³

b. Effect of polymer composition on breakdown. All the fluorocarbon blown foams were prepared at Wayne State University, using a Martin-Sweets Company laboratory model foam machine. The foaming apparatus consisted of a three-component positive-displacement metering and mixing machine, having a maximum capacity of 2 lb/min. Core samples selected for testing were cut out from buns approximately $4 \times 9 \times 4$ in.

A series of foams varying in composition was prepared (Table 8). These samples were tested without regard to the direction of foam rise. It was near the end of the measurements that we discovered the strong directional effects. For all subsequent tests, the orientation of the test specimen was recorded. Because of the neglect of directional effects, these results in terms of the effect of formulation on the breakdown strength E_b are inconclusive, although it appears that increasing the crosslinking density in the polymer increases E_b (Formulations 3057 and 3024). This problem did not arise with Eccofoam specimens, which were furnished as 1-in.-thick

Item	Formulation						
	3079-10	3079-13	3079-17	3079-18	3079-32	3079-33	3079-34
Component, parts by weight							
Polyol A ^a	83.4	83.4	56.0	56.0	55.0	55.0	55.0
Polyol B ^b	—	—	—	—	—	—	—
Polyol C ^c	—	—	—	—	—	—	—
Polyol A-TDI prepolymer	100.0	100.0	100.0	100.0	83.0	83.0	83.0
PAPI	—	—	—	—	—	—	—
Freon R-11	28.0	40.0	22.0	28.0	27.0	21.0	33.0
Silicone oil SF-1079	1.0	1.0	1.0	1.0	1.0	1.0	1.0
Silicone oil DC-201	—	—	—	—	—	—	—
Triethylenediamine	0.15	0.15	0.2	0.2	0.08	0.08	0.08
THANCAT DME ^d	1.2	1.2	1.2	1.2	1.2	1.2	1.2
Dibutyltin dilaurate	—	—	—	—	—	—	—
Phosgard C-22R ^e	—	31.0	—	—	—	—	—
Fyrol 6 ^f	—	—	31.0	31.0	—	—	—
Viral 82 ^g	—	—	—	—	30.0	30.0	30.0
Bulk density, lb/ft ³	1.95	1.68	1.94	1.84	1.95	2.51	1.63
E _b , kV/in. (unknown orientation)	72.0 ± 10	63.6 ± 10	72.2 ± 6	88.0 ± 18	80.5 ± 6	84.0 ± 8	85.4 ± 12
Thickness, in.	0.45 ± 0.2	0.47 ± 0.15	0.46 ± 0.10	0.30 ± 0.10	0.46 ± 0.10	0.30 ± 0.68	0.48 ± 0.10
Number of tests	10	9	10	10	8	10	10
E _b , kV/in. (1 to foam rise)	—	—	—	—	—	—	—
Thickness, in.	—	—	—	—	—	—	—
Number of tests	—	—	—	—	—	—	—
E _b , kV/in. (11 to foam rise)	—	—	—	—	—	—	—
Thickness, in.	—	—	—	—	—	—	—
Number of tests	—	—	—	—	—	—	—
^a Propylene oxide adduct of sorbitol; molecular weight = 700. ^b Propoxylated Mannich reaction product from phenol-diethanolamine-formaldehyde (molar ratio = 1:3:3); equivalent weight = 350. ^c Same as b, but equivalent weight = 650. ^d Jefferson Chemical Company. ^e Monsanto Chemical Company. ^f Victor Chemical Division, Stauffer Chemical Company. ^g Mobil Chemical Company.							

Table 8. Composition and properties of fluorocarbon blown urethane foams

Formulation								
3079-48	3079-30	3111-2	3111-3	3111-4	3111-5	3057-36-2	3024-17-35	3024-28-4
78.0	—	65.0	78.0	65.0	78.0	—	—	—
—	—	—	—	—	—	17.15	36.6	33.4
—	—	—	—	—	—	17.15	—	—
—	—	—	—	—	—	47.1	47.9	48.7
100.0	—	99.0	100.0	99.0	100.0	—	—	—
31.0	—	28.0	33.0	28.0	36.0	13.0	15.0	12.5
1.1	—	1.0	1.2	1.0	1.1	—	—	—
—	—	—	—	—	—	0.6	0.5	0.5
0.6	—	0.6	1.0	0.8	0.4	—	—	—
—	—	—	—	—	—	—	—	—
—	—	—	—	—	—	—	0.03	0.006
13.2	—	—	30.0	—	—	—	—	—
—	—	13.0	—	13.0	—	5.0	—	4.9
—	—	—	—	—	—	—	—	—
2.11	—	2.08	2.18	2.03	1.72	1.95	1.75	2.08
93.9 ± 15	84.7 ± 5	96.0 ± 14	98.8 ± 12	93.9 ± 19	106.4 ± 9	158.6 ± 13	144.1 ± 17	133.6 ± 29
32 ± 0.01	0.46 ± 0.08	0.35 ± 0.02	0.35 ± 0.02	0.26 ± 0.06	0.32 ± 0.02	0.25 ± 0.02	0.18 ± 0.08	0.24 ± 0.04
5	10	5	4	6	7	6	9	9
—	—	—	—	—	—	153.5 ± 10	152.8 ± 2	146.7 ± 2
—	—	—	—	—	—	0.26 ± 0.01	0.24 ± 0.01	0.26 ± 0.01
—	—	—	—	—	—	3	2	2
109.4	—	—	—	—	—	106.9 ± 10	147.2 ± 2	98.8 ± 1
0.265	—	—	—	—	—	0.25 ± 0.02	0.26 ± 0.01	0.26 ± 0.00
1	—	—	—	—	—	3	2	2

slabs and thus, by necessity, were tested only in the direction of foam rise.

c. Effect of density and cell size. Two representative formulations were selected from Table 8: 3111-5 (low crosslink) and 3024-17-35 (high crosslink). For each, the fluorocarbon content was varied in order to vary the density. In addition, the longest dimension of the foam cell was measured in each direction, i.e., with (\parallel) and across (\perp) the direction of foam rise. The diameter of the strut was also recorded. These measurements were made with a binocular microscope at $\times 34$ magnification ($\times 10$ eyepiece, $\times 3.4$ objective). The eyepiece scale was calibrated with a reference slide (52 divisions = 1.0 mm).

Table 9 summarizes results for Formulations 3111-5 and 3024-17-35. These data demonstrate the strong correlation between E_b and the cell dimension in the direction of the electric field.

Currently, we are carrying out a study on the correlation of cell structure with E_b . Figure 27 illustrates the variety of cells one encounters. It is apparent that features such as the distribution of polymer between struts and windows, uniformity in cell size, and structural integrity of windows depend strongly on the formulation.

3. Discussion

From a cursory inspection of the results, it becomes apparent that, with respect to breakdown, foams behave

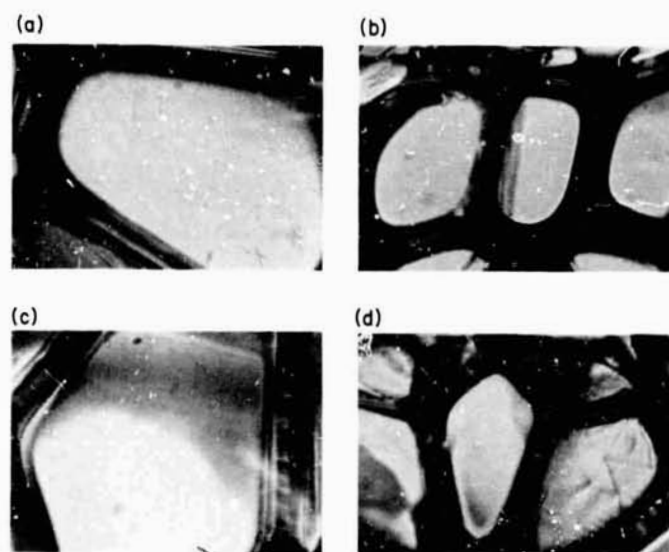


Fig. 27. Examples of cell structure ($\times 80$ magnification): (a) DL-3, (b) DL-6, (c) IE-10, (d) IE-7

more like a solid than a gas. For example, E_b varies as the square-root of the thickness (Fig. 26) in analogy to solids, whereas for a gas E_b is nearly constant. Furthermore, as the blowing gas is removed, the decrease in E_b of the foam is considerably less than that for the pure gas. However, there is strong presumptive evidence that breakdown is discharge-initiated. If intrinsic breakdown were important, one would not expect E_b to be rate-dependent (SPS 37-41, Vol. IV, pp. 109-111). In view of these observations, it appears reasonable to formally consider a foam as a solid in which breakdown is controlled by discharges in voids or flaws

It has become accepted in recent years that gaseous discharges frequently limit the application of many plastics with good dielectric properties. This type of breakdown is produced by electrical discharges occurring in gas-filled cavities in the body of the material, or at the edges of electrodes adjacent to the material. The cavities arise from imperfections in the manufacture of insulated components. As pointed out above, E_b for a gas does not depend on the thickness of the layer. However, when the layer becomes very thin, E_b starts to increase and, for about 0.2 mil, becomes comparable to that of a solid dielectric (Fig. 28). When an electric stress is applied to a solid having a gas-filled space in series with it, local

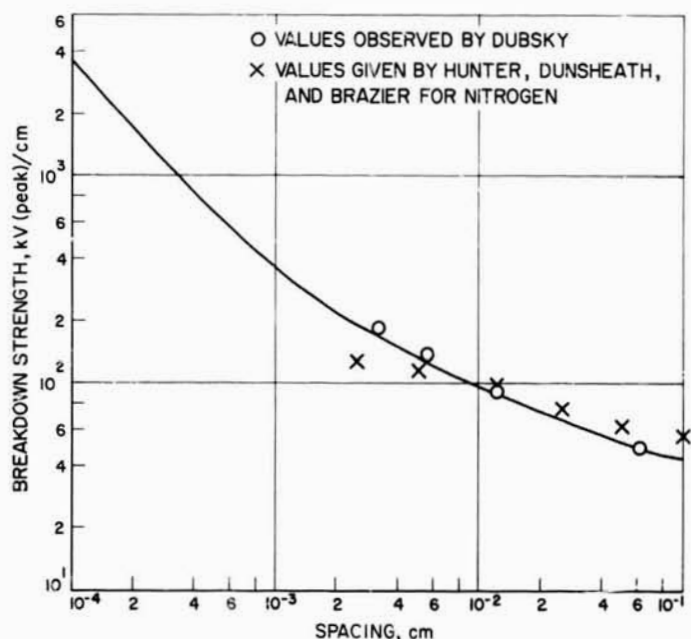


Fig. 28. Variation of breakdown strength with layer thickness for air at 20°C and 760 torr (data from Ref. 50 by permission of D. Van Nostrand Company, Inc.)

Table 9. Effect of varying density and cell size on the properties of Formulations 3111-5 and 3024-17-35

Number	Density, lb/ft ³	F11 content		Measurement direction						Strut thickness, mm	Length ratio (H/L)	E _b ratio (L/H)
				Parallel to rise			Perpendicular to rise					
		Parts by weight	%	Cell length, mm	Thickness, in.	E _b , kV/in.	Cell length, mm	Thickness, in.	E _b , kV/in.			
Formulation 3111-5, Series DL												
1	2.14	37	16.2	1.60	0.25 ±0.04	82.8 ±7.3	1.20	0.23 ±0.03	123.1 ±11.0	0.11 ±0.01	1.33	1.48
2	2.28	30	14.4	—	0.25 ±0.01	90.2 ±24.0	—	0.25 ±0.01	123.7 ±13	—	—	—
3	3.0	25	12.2	1.28	0.25 ±0.02	106.6 ±10.0	0.96	0.24 ±0.01	140.5 ±15	0.07 ±0.01	1.33	1.37
4	3.43	20	10.0	1.26	0.25 ±0.01	116.3 ±6.0	0.90	0.24 ±0.01	135.1 ±18.0	0.07 ±0.01	1.40	1.17
5	4.72	15	7.7	1.09	0.26 ±0.02	126.3 ±5.0	0.90	0.24 ±0.005	140.2 ±8	0.050 ±0.01	1.21	1.11
6	8.19	10	5.3	0.70	0.26 ±0.02	131.1 ±11.0	0.62	0.24 ±0.004	141.4 ±0.242	0.09 ±0.01	1.13	1.08
7	15.4	5	2.7	0.56	0.26 ±0.03	121.3	0.36	—	—	0.09 ±0.01	1.56	—
Formulation 3024-17-35, Series IE^a												
1	2.29	15.0	14.9	0.96	0.233 ±0.005	104.9 ±12.0	0.70	0.236 ±0.008	153.6 ±5.5	0.035 ±0.01	1.37	1.57
2	2.52	13.0	13.3	1.16	0.221 ±0.004	97.3 ±17.0	0.72	0.237 ±0.003	156.4 ±5.2	0.05 ±0.01	1.55	1.56
3	2.57	11.0	11.5	0.92	0.259 ±0.015	104.4 ±11.0	0.74	0.244 ±0.008	153.1 ±3.6	0.04 ±0.01	1.24	1.47
4	3.48	9.0	9.6	0.87	0.249 ±0.010	94.5 ±32	0.48	—	—	0.035 ±0.01	1.85	—
5	12.0	7.0	7.7	—	0.272 ±0.011	53.7 ±9.7	—	Poor sample		0.07 ±0.01	—	—
7	3.28	10.0	10.6	0.78	0.243 ±0.004	100.2 ±15.2	0.60	0.246 ±0.012	139.9 ±16.0	0.07 ±0.01	1.30	1.39
8	8.0	8.0	8.7	—	0.248 ±0.011	83.3 ±8.3	—	Very poor sample		0.065 ±0.01	—	—
9	1.67	—	—	1.6	0.234 ±0.01	67.1 ±22	1.03	0.254 ±0.01	106.2 ±41	0.06 ±0.01	1.55	1.34
10	1.84	—	—	2.15	0.251 ±0.02	63.5 ±14.0	1.20	0.265 ±0.02	147.5 ±16	0.04 ±0.01	1.80	2.33
11	1.45	26.2	23.6	0.92	0.232 ±0.02	61.8 ±3.0	0.73	0.228 ±0.02	130.9 ±13.1	—	1.26	2.11

^a No data available for Series IE, Number 6.

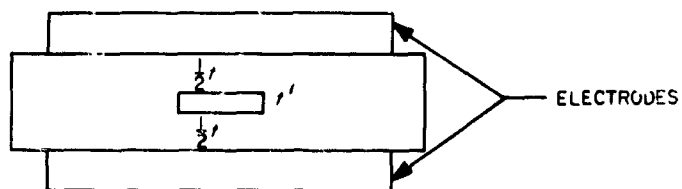


Fig. 29. An idealized void in a solid (reprinted from Ref. 50 by permission of D. Van Nostrand Company, Inc.)

breakdown of the gas will occur before the solid dielectric is overstressed. For structures of this type (Fig. 29), the voltage V_i at which discharges start is approximately given by (Ref. 51):

$$V_i = E_i (t + \epsilon t') / \epsilon \quad (1)$$

where E_b refers to the gas-filled gap of thickness t' , and ϵ is the permittivity of the dielectric of thickness t . Breakdown will occur at some $V > V_i$; it is therefore essential to maximize V_i . For V_i to be high, ϵ of the medium surrounding the cavity must be low, and the cavity depth t' must be as small as possible. These discharge phenomena produce deleterious effects on plastic insulation.

For our purpose, we consider a foam to consist of an array of gas-filled cavities. If breakdown in solids can be controlled by discharges in the relatively few ever-present cavities, then, in a foam with an over-abundance of cavities, the same mechanism must be a virtual certainty. Since for a foam, in general, $t'/t \ll 1$, Eq. (1) becomes

$$V_i/t \cong E_i = E_t/\epsilon \quad (2)$$

Since ϵ for a foam is always smaller than that for a solid, this equation implies for a foam a somewhat higher E_i for a given cavity size. This factor which involves an average property, ϵ , affects the total foam in the same way. The breakdown strength of the gas entrapped in the cell, E_t , depends on the nature of the gas, the pressure, and the size and geometry of the cell. In general, E_t increases with decreasing t' (Fig. 28); hence, the fluctuation in E_t for cavities within a volume element will be determined by the fluctuation in cell size. This means that, when the electric stress is increased gradually, discharges will initiate preferentially in larger foam cavities, with a concurrent degradation of the walls of these cavities. The eventual failure of a wall will lead to the formation of a larger cavity and, hence, a further decrease in E_t . The continuation of this process will lead rapidly to

further increase in the size of the cavity, and ultimately failure of the form will occur. In summary, it is the size of the cavity, i.e., the cell, that will determine the breakdown strength of a foam. Discharge initiation will be favored in the relatively few larger-than-average cells. We refer to such cells as flaws in a foam (Fig. 30).

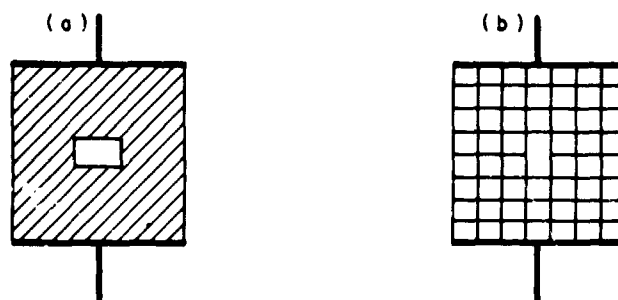


Fig. 30. A void or flaw in (a) a solid dielectric and (b) a closed-cell foam

The correlation between the difference in breakdown strength and the anisotropy of foam structure provided the first striking demonstration of the importance of cell size. Microscopic examination showed that, in general, cells are elongated in the direction of cell rise (Tables 8 and 9). Thus, when the foam is tested parallel to the direction of rise, the applied electric field sees cell gaps which are greater than those in the perpendicular direction. For example, E_b versus density plots for the DL series of fluorocarbon blown foams (Fig. 31) yield two distinct curves. The higher strength corresponds to the perpendicular direction, i.e., the smaller cell gap. Both curves level off for densities exceeding about 4 lb/ft³.

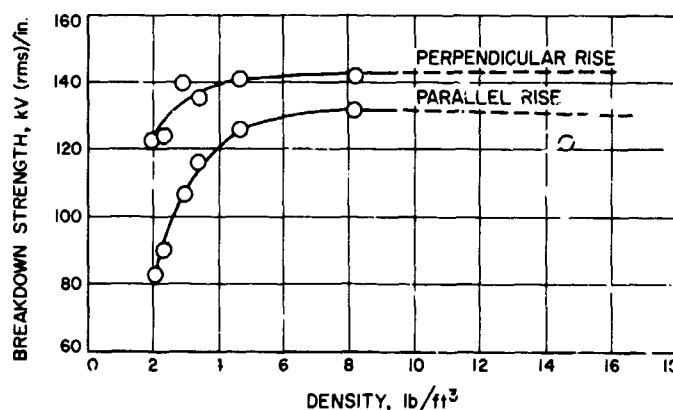


Fig. 31. Difference in breakdown strength with direction of foam rise

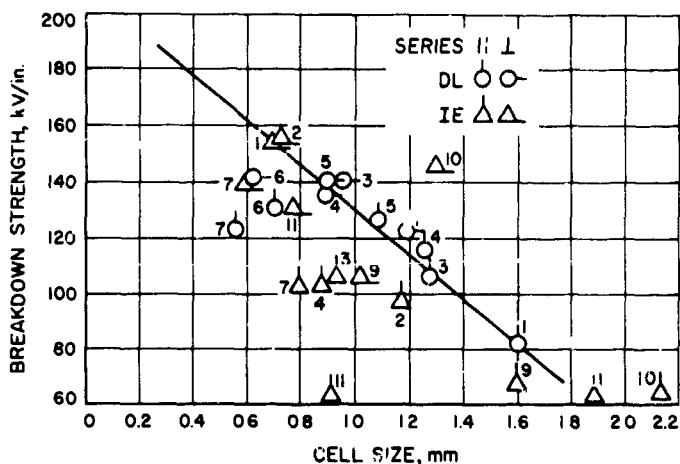


Fig. 32. Variation of breakdown strength with cell size

However, when the E_b values are plotted versus cell size, a good correlation is obtained (Fig. 32). Incidentally, the straight line extrapolates to a value of about 200 kV/in. for zero cell size, a reasonable value for the bulk polymer. In the drawing of the straight line, less weight was given to the low points (i.e., left from the line), because, in most cases, these correspond to irregular microscopic structures. It is seen in Fig. 33 that, of the four structures shown in Fig. 28, two have flaws and fall below the line. An additional demonstration of the trend for a proportionality relationship between E_b and

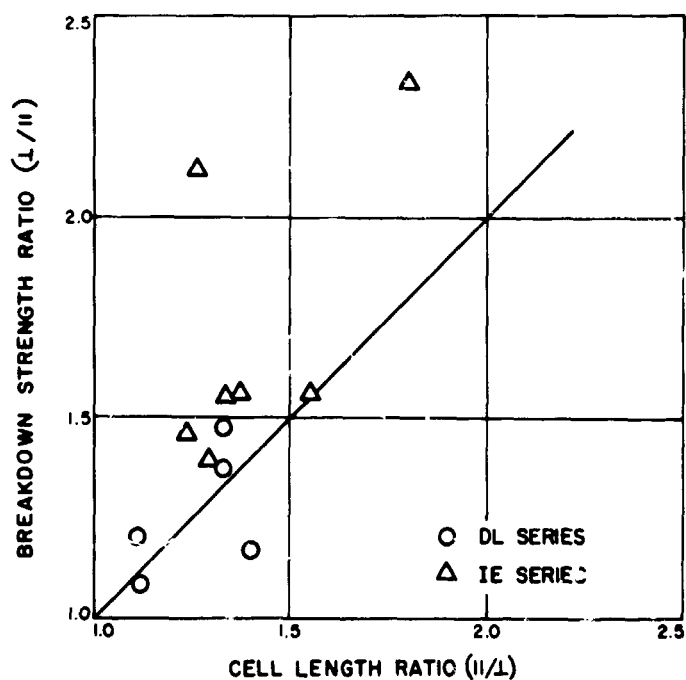


Fig. 33. Correlation between breakdown strength and cell-size anisotropy

cell size is given in Fig. 33. Here, the E_b and the cell-length ratios correspond to the two directions of a given foam; the straight line was drawn with unit slope. One should add that Eq. (1) applies strictly to the idealized geometry shown in Fig. 29, whereas the geometry of foam cells is more complicated. Therefore, no theoretical interpretation can be given at present to the above correlations, although the general trends are clearly indicated.

If the breakdown strength E_b were a function of only the average cell size in the direction of the test, then E_b should be independent of thickness. This is not the case, since the observed slopes in Fig. 26 are not unity but about 0.5. Therefore, it is reasonable to assume that breakdown will depend on the presence of "flaws" in the sense defined above, e.g., multiconnected cells. The distribution of such "flaws" should follow extreme-value statistics; hence, the strength should decrease with increasing volume, i.e., the thickness of the test specimen. [A discussion based on extreme-value statistics was presented by Epstein and Brooks in their study of the breakdown of capacitors (Ref. 52).]

4. Conclusions and Perspectives

The following is a summary, in order of their importance, of the parameters which determine the dielectric strength of a foam:

- (1) *Homogeneity of structure.* Properties of a given foam can be optimized only if the cells are uniform in size and the content of voids or multiconnected cells is kept at a minimum.
- (2) *Cell geometry.* Highly symmetrical cells will minimize the anisotropy of properties; small cell size will improve strength.
- (3) *Gas content and type.* Reducing gas pressure decreases strength. Fluorocarbons lead to much higher strength than carbon dioxide.
- (4) *Polymer distribution in the cell.* It is advantageous to increase the window thickness at the expense of struts. Also, conditions during foaming should minimize the stressing of windows.
- (5) *Density.* The optimum density is 6 to 10 lb/ft³. In this range, the foam has adequate mechanical strengths, and optimization of all the above parameters is easier to achieve. It is difficult to manufacture homogeneous higher-density foams free of voids.

To complete the study discussed here, we are starting determinations of the porosity of cells, cell volume, and thickness and size of windows. These should provide a basis for improved correlations with dielectric strength. More studies are needed on the importance of the composition and pressure. Limited experiments indicated that contamination of Freon II with small amounts of carbon dioxide drastically decreases strength. It is to be expected that the polymer properties should be of considerable importance in determining the resistance to degradation by discharges. Moreover, the polymer should determine, to a large extent, the stability of the foam toward high vacuum, UV, and heat, and its resistance to mechanical damage.

Finally, we must remember that the motivation for this work was to look at the corona and breakdown at low pressures. However, early studies in vacuum showed that the existing knowledge of the electrical properties of foams was insufficient to permit separation of the effects of low gas pressure from other causes for failure.

Now that, as a result of this study, the controlling influence of the cell structural parameters on breakdown has been established, some simple considerations can be used to set a lower limit on the discharge inception voltage V_i . Paschen's Law gives about 320 V as the potential which will initiate discharges under the most unfavorable conditions. Then, for a foam, the corresponding voltage should be at least 320 times the number of cells. For a foam having 1-mm cells, the minimum dielectric strength should thus be about 8 kV/in. Olyphant and Meyer (Ref. 56) noted such an effect in a study of a type of syntactic foams (Scotchcast). Although these foams were highly porous, they observed a strength of 10 kV/in. at 1 torr. Their results are difficult to interpret more precisely, since neither the gas pressure inside the foam nor the porosity were determined. Even so, these results are encouraging. For closed-cell structures, higher values should be expected, for at low pressures the mean free path of a gas molecule cannot exceed the length of the cell. Our results on outgassed urethane foams (SPS 37-39, Vol. IV, pp. 108-111) are consistent with this viewpoint.

References

1. Knauss, W., Clausen, J. F., and Landel, R. F., Report MATSCIT PS 66-1. California Institute of Technology, Pasadena, Calif., Jan. 1966.
2. Blatz, P. J., et al., Report MATSCIT PS 66-6. California Institute of Technology, Pasadena, Calif., May 1966.
3. Report VR-9. Thiokol Chemical Corp., Denville, N. J.
4. Treloar, L. R. G., *The Physics of Rubber Elasticity*. Oxford University Press, 1958.
5. Landel, R. F., and Fedors, R. F., *Rubber Chemistry and Technology* (in press).
6. Saunders, J. H., *Rubber Chemistry and Technology* Vol. 32, p. 337, 1959.
7. Flory, P. J., *Principles of Polymer Chemistry*. Cornell University Press, 1953.
8. Holly, E. D., *J. Polym. Sci.*, Vol. A2, p. 5267, 1964.
9. Huggins, M. L., *Physical Chemistry of High Polymers*. John Wiley & Sons, Inc., New York, 1958.
10. Sheehan, C. J., and Bisio, A. L., *Rubber Chemistry and Technology*, Vol. 39, p. 149, 1966.
11. Smith, T. L., *Technical Documentary Report No. ASD-TDR-62-572*. Wright-Patterson Air Force Base, Ohio, June 1962.

References (cont'd)

12. Smith, T. L., *Technical Documentary Report No. ML-TDR-64-264*. Wright-Patterson Air Force Base, Ohio, Aug. 1964.
13. Landel, R. F., and Fedors, R. F., in *Proceedings of the Fourth International Congress on Rheology*, Brown University, Providence, R. I., Vol. 2, p. 543. Edited by E. H. Lee. 1963.
14. Kurata, M., Iwama, M., and Kamada, K., in *Polymer Handbook*, Chap. IV, p. 1. Edited by J. Brandrup and E. H. Immergut. Interscience Publishers, Inc., New York, 1966.
15. Landel, R. F., Moser, B. G., and Bauman, A. J. "Rheology of Concentrated Suspension: Effect of a Surfactant," in *Proceedings of the Fourth International Congress on Rheology*, Brown University, Providence, R.I., August 26, 1963, Pt. 2. Edited by E. H. Lee. Interscience Publishers, Inc., New York.
16. Rivlin, R. S., *J. Appl. Phys.* Vol. 18, p. 444, 1947.
17. Rivlin, R. S., *Phil. Trans. Roy. Soc. London*, Vol. A240, pp. 459, 491, and 509, 1948.
18. Rivlin, R. S., *Phil. Trans. Roy. Soc. London*, Vol. A241, p. 379, 1949.
19. Rivlin, R. S., *Proc. Roy. Soc. London*, Vol. A125, p. 463, 1949.
20. Rivlin, R. S., *Phil. Trans. Roy. Soc. London*, Vol. A242, p. 173, 1949.
21. Rivlin, R. S., and Saunders, D. W., *Phil. Trans. Roy. Soc. London*, Vol. A243, p. 251, 1951.
22. Rivlin, R. S., "Large Elastic Deformations" in Eirich, F. R., *Rheology, Theory and Applications*, Vol. I, pp. 351-407. Academic Press, Inc., New York, 1956.
23. Mooney, M., *J. Appl. Phys.*, Vol. 11, p. 582, 1940.
24. Gumbrell, S. M., Mullins, L., and Rivlin, R. S., *Trans. Faraday Soc.*, Vol. 49, p. 1495, 1953.
25. Ciferri, A., and Flory, P. J., *J. Appl. Phys.*, Vol. 30, p. 1498, 1959.
26. Ishihara, A., *J. Phys. Soc. Japan*, Vol. 3, p. 289, 1951.
27. Ishihara, A., Hashitsume, N., and Tatibana, M., *J. Chem. Phys.*, Vol. 19, p. 1508, 1951.
28. Flory, P. J., *Trans. Faraday Soc.*, Vol. 57, p. 829, 1961.
29. Thomas, A. G., *Trans. Faraday Soc.*, Vol. 51, p. 569, 1955.
30. Blatz, P. J., and Ko, W., *Trans. Soc. Rheology*, Vol. 6, p. 223, 1961.
31. Treloar, L. R. G., *Trans. Faraday Soc.*, Vol. 42, p. 83, 1946.
32. Treloar, L. R. G., *The Physics of Rubber Elasticity*. Oxford University Press, Oxford, 1956.
33. Krigbaum, W. R., and Kaneko, M., *J. Chem. Phys.*, Vol. 36, p. 99, 1962.
34. Roe, R.-J., and Krigbaum, W. R., *J. Polym. Sci.*, Vol. 61, p. 167, 1962.
35. Scanlan, J., *Trans. Faraday Soc.*, Vol. 57, p. 839, 1961.

References (contd)

36. Kuhn, W., and Grün, F., *Kolloid-Z.*, Vol. 101, p. 248, 1942.
37. Langevin, P., *J. de Phys.*, Vol. 4, p. 678, 1905.
38. Langevin, P., *Ann. Chim. Phys.*, Vol. 5, p. 70, 1905.
39. Becker, G., and Landel, R. F., *J. Macromolecular Phys.* (in press).
40. Hutchinson, W. D., Becker, G. W., and Landel, R. F., *Bull. 4th Meeting ICRPG, Working Group on Mechanical Behavior*, Vol. 1, Oct. 1965.
41. Rehner, J., *Ind. Eng. Chem.*, Vol. 36, pp. 118-124, 1944.
42. Rehner, J., and Gray, P., *Ind. Eng. Chem., Anal. Ed.*, Vol. 17, pp. 367-370, 1945.
43. Marvel, C. S., and Jones, E. B., *J. Polym. Sci., Series A*, Vol. 2, p. 5313, 1964.
44. Stubbs, W. H., Gore, C. R., and Marvel, C. S., *J. Polym. Sci., Series A*, Vol. 4, pp. 447, 448, 1966.
45. Yamada, N., Shimada, K., and Hayashi, T., *J. Polym. Sci., Series B*, Vol. 4, pp. 477-480, 1966.
46. Roberts, J. D., and Caserio, M. C., *Basic Principles of Organic Chemistry*. W. A. Benjamin, Inc., New York, 1965.
47. Cuddihy, E. F., and Moacanin, J., *J. Cell. Plas.*, Vol. 3, No. 2, p. 73, 1967.
48. Norton, F. J., *J. Cell. Plas.*, Vol. 3, No. 2, p. 23, 1967.
49. Mathes, K. N. "Electrical Properties," in *Engineering Design for Plastics*, pp. 441-588. Edited by E. Baer. Reinhold Publishing Co., 1964.
50. Parkman, N., "The Electrical Properties of High Polymers," in *Physics of Plastics*, pp. 285-322. Edited by P. D. Ritchie. D. Van Nostrand Company, Inc. Princeton, N. J., 1965.
51. Epstein, B., *J. Appl. Phys.*, Vol. 19, p. 140, 1948.
52. Epstein, B., and Brooks, H., *J. Appl. Phys.*, Vol. 19, p. 544, 1948.
53. Starr, W., and Endicott, H., *Trans. AIEE Pur. App. and Syst.*, Vol. 80, Pt. III, p. 515, 1961.
54. Moses, G. L., *Trans. AIEE*, Vol. 70, Pt. 1, pp. 763-769, 1951.
55. Moutsinger, V. M., *Trans. AIEE*, Vol. 54, pp. 1300, 1301, 1935.
56. Olyphant, M., Jr., and Meyer, C. L., "Light Weight and Corona Suppressant Encapsulants for Aerospace Industries," paper presented at the NEPCON Convention, Long Beach, Calif., June 1965.

N67-34770

IX. Propulsion Research and Advanced Concepts

PROPULSION DIVISION

A. Liquid MHD Power Conversion, D. G. Elliott,

D. J. Cerini, and L. G. Hays

1. Introduction

The long lifetimes required of electric-propulsion powerplants make systems without rotating parts attractive. A nonrotating Rankine cycle being investigated is the liquid-metal magnetohydrodynamic system wherein lithium is accelerated by cesium vapor in a two-phase nozzle, separated from the cesium, decelerated in a magnetohydrodynamic generator, and returned through a diffuser and heat source to the nozzle.

Fabrication and component testing of the NaK-N₂ conversion system for performance evaluation at room temperature has continued. A test was made with the Haynes Stellite Alloy 25 lithium erosion loop to evaluate the possibility of using that alloy for an 1800°F Cs-Li conversion system.

2. NaK-N₂ Conversion System

Fabrication of the two stator blocks for the 50-kW ac generator to be employed in the conversion system

is in progress. The blocks are 2.50 in. high, 6.50 in. wide, and 8.025 in. long; the width was increased from 6.06 in. (the flow channel width) to permit the addition of O-ring seals between the stators and the copper side plates. The stator slots are tapered to optimize copper and iron utilization as described in Ref. 1.

The stators also employ closed slots, as shown in Fig. 1. It was found in previous generator tests (Ref. 2) that the nonuniform gap field due to open slots increased the fluid *I*²*R* losses. The slots are closed by inserting laminated Hiperco-50 plugs into dovetail grooves machined into the slots. The plugs should eliminate the field nonuniformities and associated power loss while introducing additional iron losses that are much less.

The winding of the first set of coils for the generator is in progress. Each of the 11 traveling-wave coils will consist of 40 turns of 0.045-in.-thick by 0.60-in.-wide copper strip wound on a mandrel with 0.003-in.-thick glass cloth insulation between each turn. As each turn is made, the slot portion of the turn will be placed in a milling machine and the 0.045-in. dimension reduced to 0.030 in. for the first 9 turns and 0.018 in. for the last

BLANK PAGE

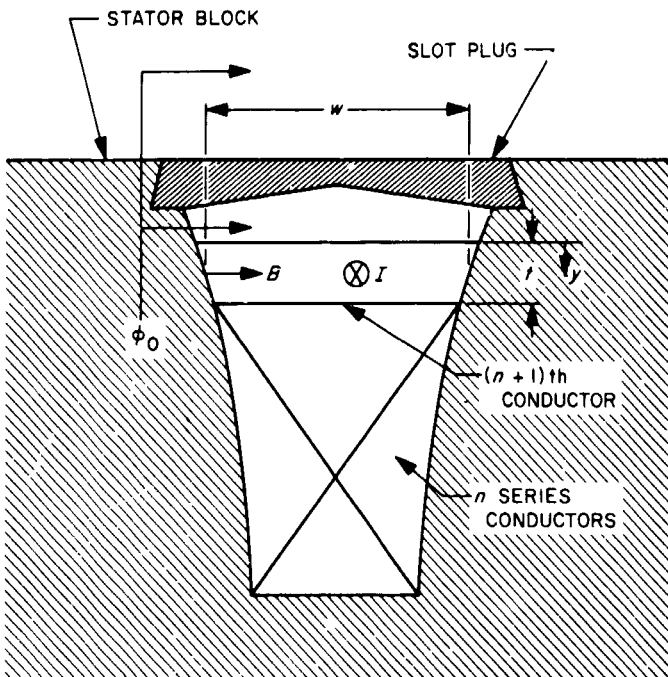


Fig. 1. Slot and winding geometry for MHD generator

10 turns, with three approximately equal intermediate steps in between. After winding, the coil will be epoxy impregnated to achieve interturn bonding. The slot portion of the coil will then be machined to reduce the 0.60-in. width to match the tapered slot shape. Acid etching will then be used to remove the machining burrs. The compensating coils will be fabricated in a similar manner. The thickness and width reductions of the slot portion of the coil produce a constant copper cross-section for each of the turns inside the slot and a fourfold increase in copper cross-section from inside to outside the slot. The coils will be spaced from the slot by 0.5-in.-wide strips of 0.006-in.-thick insulation placed at 1.0-in. intervals along the slot, thus forming twelve 0.006 × 0.5-in. cooling passages, six on each side of the coil. Gaseous nitrogen will be fed from six holes along the bottom of each slot, up along the sides of the coil and then laterally out of the slot through the triangular opening between the coil and the slot plug.

a. Coil ac/dc resistance ratio. At the operating frequency range of the generator, 300 to 600 Hz, the effective resistance of the windings can be significantly higher than the dc value because of nonuniform current distribution caused by the field in the slots. Figure 1 illustrates the geometry of one slot, which carries 40 conductors in the 50-kW generator. The ac/dc resistance ratio is to be found for the $(n + 1)$ th conductor from the bottom, which has thickness t , width w , length L , and conduc-

tivity σ . The conductors each carry a current of rms magnitude I . The field in the $(n + 1)$ th conductor due to the current below it is

$$B = \frac{\mu_0 n I}{w} \quad (1)$$

In the following derivation it will be assumed that n is large so that the additional field due to the current in the $(n + 1)$ th conductor can be neglected.

Figure 2 shows the voltage phasor diagram for the $(n + 1)$ th conductor. The total external flux linking the conductor is ϕ_0 , which includes the gap flux and the slot flux above the conductor. The voltage induced by this flux is $\omega\phi_0$, where ω is the angular frequency, and this voltage leads the current by 90 deg or more. An element

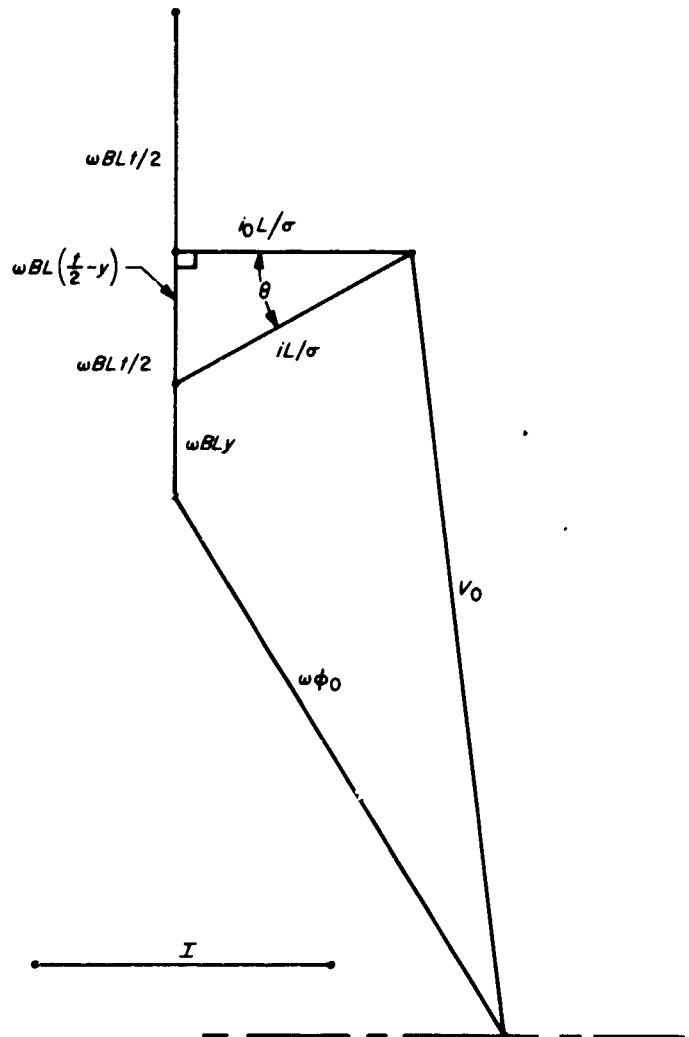


Fig. 2. Voltage phasor diagram for $(n + 1)$ th conductor

of the conductor at distance y from the top is linked by an additional flux of magnitude BLy , and the voltage ωBLy induced by this flux leads the current by 90 deg. The voltage applied to the conductor at the ends of the slot, V_{in} , is the vector sum of the induced voltage at the center of the conductor, $\omega\phi_0 + \omega BLt/2$, and the resistive drop at the center of the conductor i_0L/σ , where i_0 is the current density at the center. The same voltage exists across each element of the conductor; therefore, the current density i at any station y is related to the current density at the center by

$$\left(\frac{iL}{\sigma}\right)^2 = \left(\frac{i_0L}{\sigma}\right)^2 + (\omega BL)^2 (t/2 - y)^2 \quad (2)$$

and also by

$$i = i_0/\cos \theta \quad (3)$$

where θ is the phase difference between i and i_0 .

The net current through the conductor is

$$\begin{aligned} I &= \int_0^t iw \cos \theta dy \\ &= i_0wt \end{aligned} \quad (4)$$

The power dissipated in the conductor is

$$P = \int_0^t \frac{i^2Lw}{\sigma} dy \quad (5)$$

and the ac/dc resistance ratio is

$$\frac{R_{ac}}{R_{dc}} = \frac{P}{I^2 L/wt\sigma} \quad (6)$$

Substituting i from Eq. (2) into Eq. (5), performing the integration, and evaluating i_0 from Eq. (4) and B from Eq. (1), the result (valid for large n) is

$$\frac{R_{ac}}{R_{dc}} = 1 + \frac{(\mu_0 \sigma \omega nt)^2}{12} \quad (7)$$

According to this relation, the ac/dc resistance ratio depends only on the conductor thickness and conductivity, the operating frequency, and the conductor posi-

tion in the slot. Applying this equation to the coil design selected for the generator, it was found that a resistance ratio (for the slot portion) no greater than 2 would be expected. However, there was thought to be a possibility of encountering much higher values in practice, due to deviation of the slot field direction from precise alignment with the conductors, especially near the top of the slot where the gap field would have an influence. Therefore, an experiment was performed to measure the resistance ratio of flat copper strips in approximately the same slot geometry and field environment as in the generator. The test assembly consisted of a C-shaped laminated block with two tapered slots. The assembly (Fig. 3) was installed in a tank which was filled with Freon TF for cooling. The slot on the left was wound with 5 turns of 0.02×0.3 -in. flat copper strip and 23 turns of 0.06-in. diam Litz wire consisting of 600 strands twisted to minimize ac/dc resistance ratio; thus the mean value of n in Eq. (7) for the 5 strips was 25. The other slot was wound with 28 turns of Litz wire. These two coils were excited to produce canceling gap field components. The field coil in the center of the core was used to produce a gap flux that was 90 deg out of phase with, and in the proper ratio to, the slot flux so as to model the ac generator. Measurements were made at 500, 1000, and 1500 Hz, with and without gap flux, and with and without the slot plugs. The 5-turn flat strip coil was then interchanged with 5 turns of Litz wire that had been outside the slot; the strip coil was now outside the slot. The test was

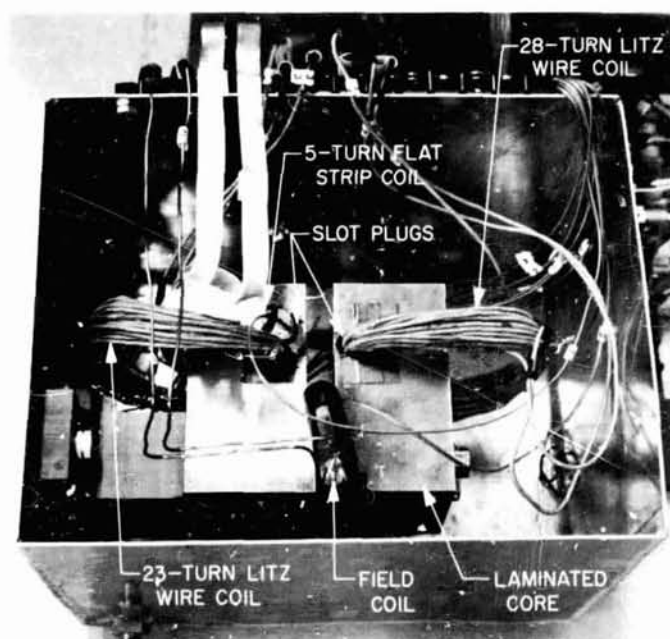


Fig. 3. Test assembly for ac/dc resistance ratio

repeated at the same conditions, and the ac/dc resistance ratio was calculated from the following relation:

$$\frac{R_{ac}}{R_{dc}} = 1 + \frac{\text{change in total power input to the system due to interchanging the strips and the Litz wire}}{I^2 \times \text{dc resistance of 5 slot-lengths of strip}}$$

The ratios obtained with the plugs in place are presented as a function of frequency in Fig. 4 and compared to the theoretical value from Eq. (7), showing the theory to be conservative. The ratios with the plugs removed were several times higher, presumably due to greater distortion of the slot field near the gap.

The ac/dc resistance ratio for the parts of the generator coil outside the slots was also measured, using a 40-turn coil of the same 0.045 × 0.60 in. strip to be employed for the outside turns of the generator. The ratio at 500 Hz was 2. This ratio should be less in the generator, due to the partially canceling fields of the other coils, but even at a ratio of 2 the increase in total winding

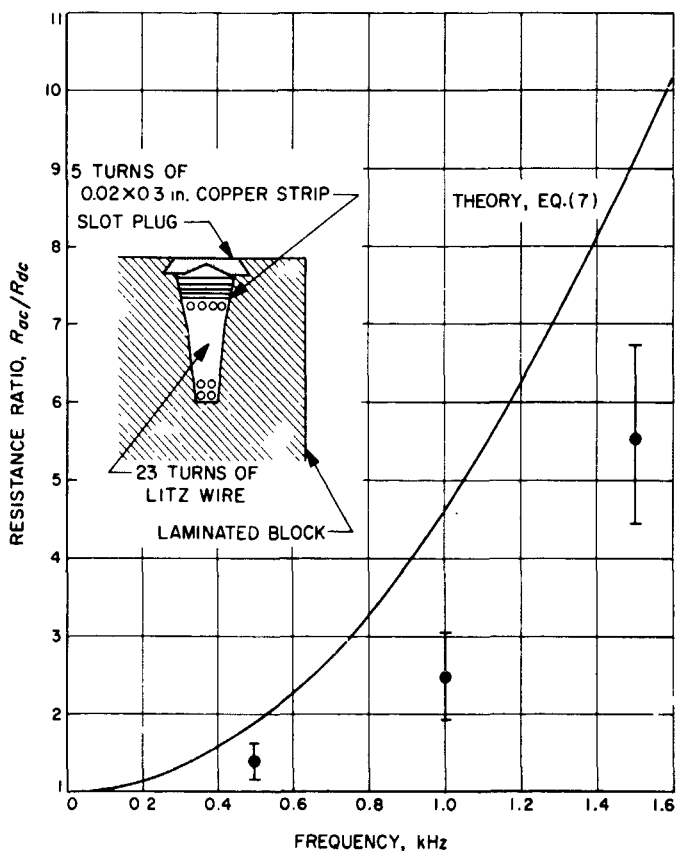


Fig. 4. Measured ac/dc resistance ratio of flat strip conductor

loss would be only 16%, because the dc loss in the large outside conductors is only 16% of the total. It is concluded that Eq. (7) for predicting ac/dc resistance ratio is valid for the ac generator coils with the slot plugs in place and that the generator winding will have an acceptable ac resistance.

b. Single-conductor heat-transfer tests. Tests were also conducted to confirm the design of the ac generator coil-cooling system. Figure 5 shows the test assembly installed in its housing with the cover removed. The aluminum block in the center of the housing has a longitudinal slot of approximately the same cross-section as the slots in the ac generator, including a dovetail groove for the slot plug, which is shown protruding slightly out of both ends of the slot. A bare solid copper bar was installed in the slot with six slot liner strips of 0.006-in.-thick by 0.5-in.-wide Kapton film. The nitrogen flow path was identical to that for the ac generator. The ohmic power loss predicted for the ac generator slots was produced in this test by passing dc current through the copper bar. With twice the predicted power loss for the ac generator, the copper bar temperature could be maintained at 145 to 220°F with 70°F nitrogen flowing at 0.04 to 0.08 lbm/sec, corresponding to an acceptable cooling flow rate of 0.6 to 1.1 lbm/sec for the generator.

Voltage breakdown values between the aluminum block and the copper bar were measured to verify that 0.006 in. of nitrogen gas between the coils and slot in the ac generator would have sufficient dielectric strength at 500 Vac operating voltage. With zero N₂ flow and at ambient temperature, the block to bar resistance was 0.7 MΩ at 500 Vdc and increased only slightly with increasing gas flow or gas temperature. At 1000 Vdc the resistance was constant at 0.6 MΩ until the gas temperature was reduced below 50°F, at which point a breakdown to 2000 Ω occurred, apparently due to water vapor condensation, since the resistance could be restored by elevating the gas temperature. The test demonstrated that the ac generator cooling system is adequate to maintain the coil temperatures below 200°F with approximately 1 lbm/sec total nitrogen flow. Difficulty was encountered in preventing foreign particles from shorting the bar to the slot in the 0.006-in. passage, making it evident that an insulating coating will be necessary for a reliable coil system. Such a coating will raise the coil temperatures approximately 25°F.

c. Hydraulic tests. Water-nitrogen flow calibration tests have begun on the conversion system nozzle-separator

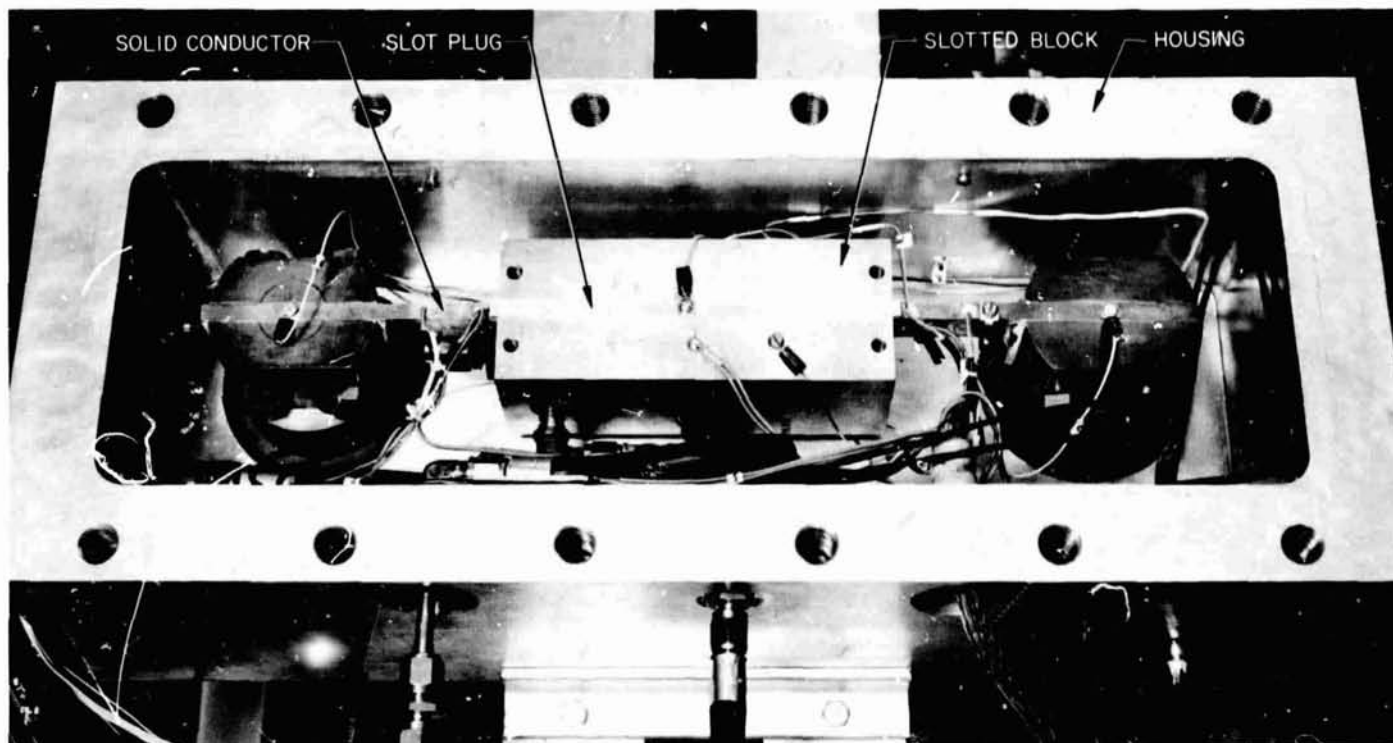


Fig. 5. Winding heat-transfer test assembly

assembly. The test assembly shown in Fig. 6 is installed on a thrust stand.

Initial tests will determine: (1) the percentage of the nozzle liquid flow bypassing the generator capture slot, (2) the percentage of this bypass flow which is recovered from the gas flow by the secondary capture slot, and (3) the flow conditions at the capture slot inlet such as velocity, gas to liquid volume ratio, and stagnation pressure.

Subsequent testing will be on the vaned convergent section following the capture slot to determine vane friction losses and generator inlet flow conditions, followed by testing of dummy stator blocks to determine generator friction losses. The final test assembly will include a diffuser with vaned inlet section to permit determination of diffuser performance; thus verification will be obtained of the fluid power available to the generator for conversion to electrical power.

Test results for the conversion-system separator are shown in Fig. 7 where the separator exit velocity is compared with that of earlier separators which had larger areas than the conversion system separator. The exit velocity is also compared with the theoretical values

from Eq. (10) in SPS 37-27, Vol. IV, p. 77, for nozzle inlet pressures of 230 and 150 psia, and the agreement is within 2%.

The area of the conversion system separator was made smaller than that of the previous separators by increasing the surface inclination from 12 to 18 deg (the optimum angle according to the theory) and by placing the capture slot directly at the final impingement point of the nozzle flow. This reduced the separator surface area by 50% to 102 in.² and increased the separator velocity, as shown in Fig. 7. However, the flow by-passing the primary capture slot and the secondary capture slot was found to be two to three times higher than the flow losses in the previous separators, a loss which is acceptable but will be reduced, if possible, by separator modifications.

3. High-Temperature Tests

The goal of the program beyond the NaK-nitrogen conversion system and cesium-lithium loops is a high-temperature, 300-kWe conversion system using cesium and lithium. The purpose will be to provide full-scale performance and startup data under short-term conditions with a super-alloy containment material. Use of a refractory alloy would allow endurance testing at a later date.

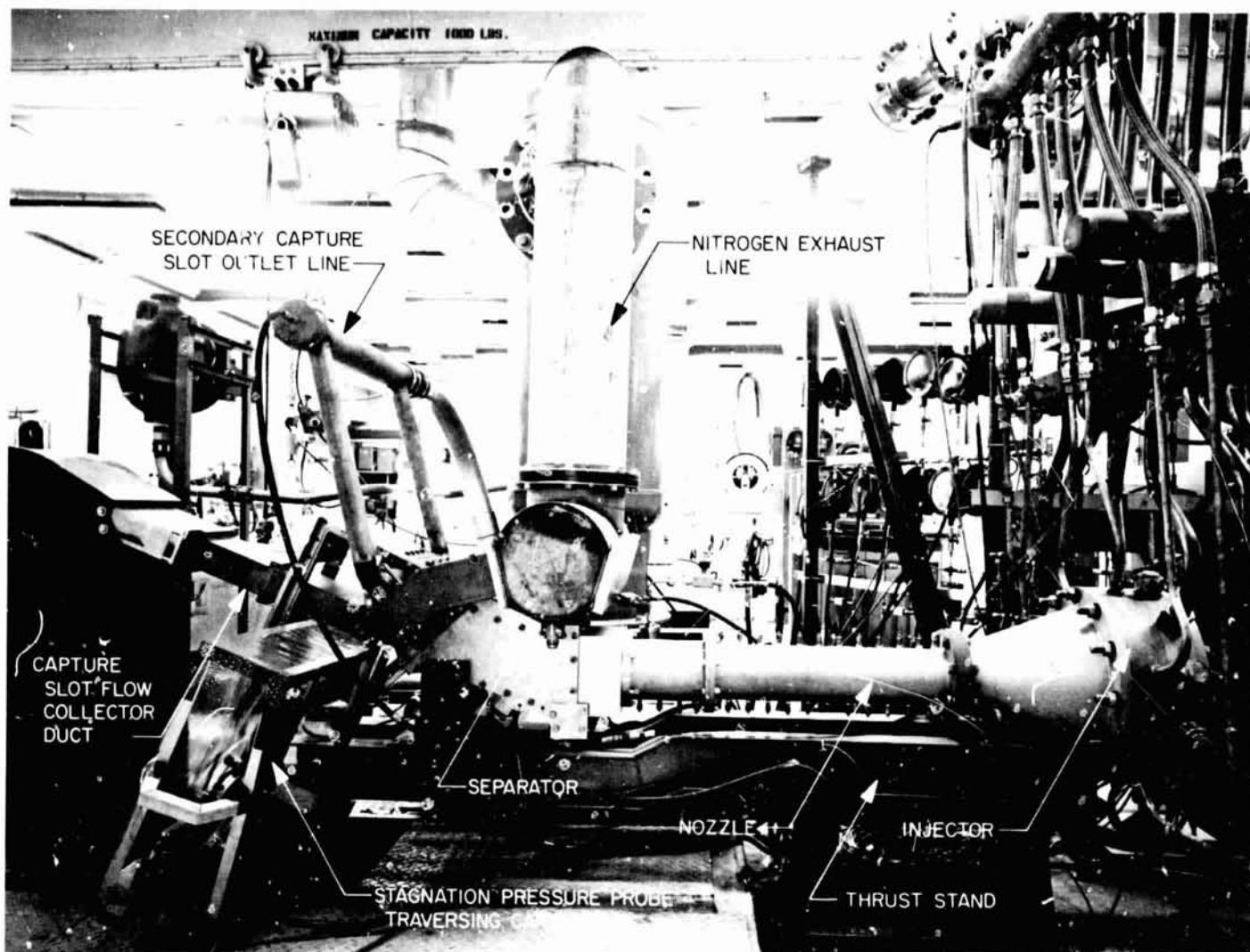


Fig. 6. Nozzle-separator unit installed for water-nitrogen tests

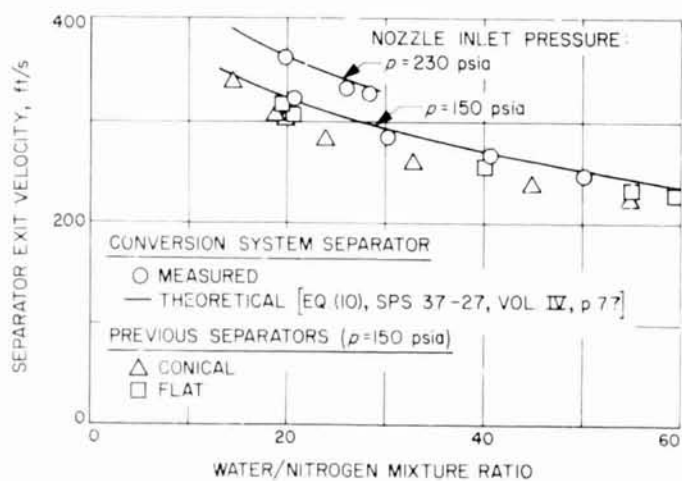


Fig. 7. Separator exit velocity

The maximum temperature for this system will be 1800°F. This value was chosen because cycle performance is comparable to that possible at higher temperatures and because this temperature makes possible the use of materials which are inexpensive relative to the refractory metals required for higher temperatures. Several super-alloys which can be welded and operated in air possess sufficient strength for this application. However, their corrosion rate in high-temperature lithium is either excessive or not well known. One material which has been used with 2000°F lithium vapor and 1800°F liquid lithium for tests of moderate duration¹ (Ref. 3) is Haynes Stellite Alloy 25. The results in these former applications are encouraging but are contradictory to

¹Barker, K., MSA Research Corp., private communication.

other experience with nickel or cobalt alloys exposed to lithium (Ref. 4). To assess the feasibility of using Haynes Stellite Alloy 25 for the 300-kW system, a small loop was constructed of this alloy and operated with 1800°F lithium.

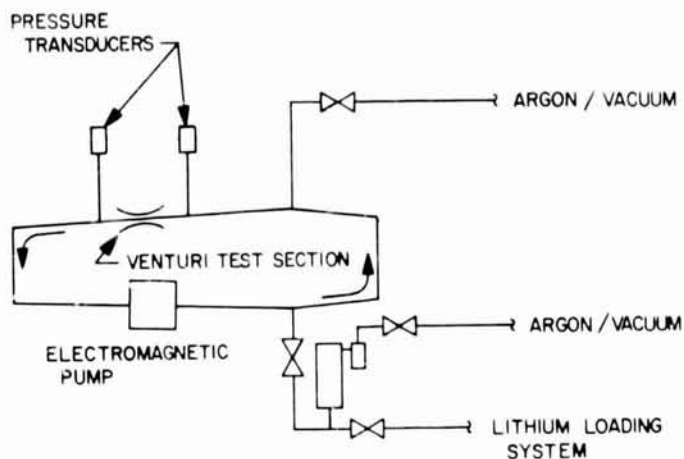


Fig. 8. Piping arrangement of Haynes Stellite Alloy 25 lithium corrosion loop

The loop is shown schematically in Fig. 8. The primary flow circuit and electromagnetic pump duct were constructed of Haynes Stellite Alloy 25. Lithium was circulated by the ac conduction pump. Heat was added by "clam shell" heaters to maintain the temperature at a maximum value of 1800°F. The lithium was accelerated to a velocity of about 210 ft/s in the throat of a venturi. Pressure recovery occurred in the divergent part of the

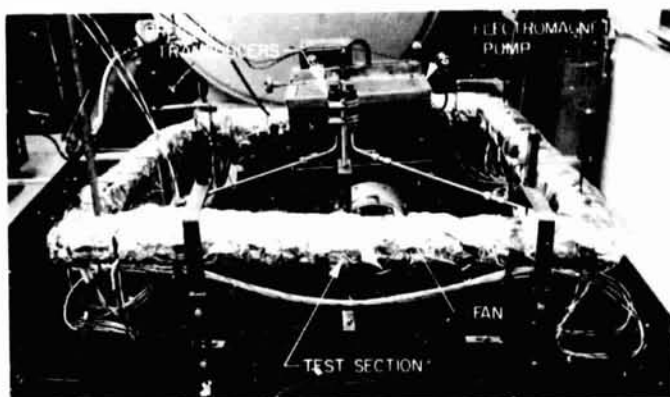


Fig. 9. Haynes Stellite Alloy 25 lithium corrosion loop

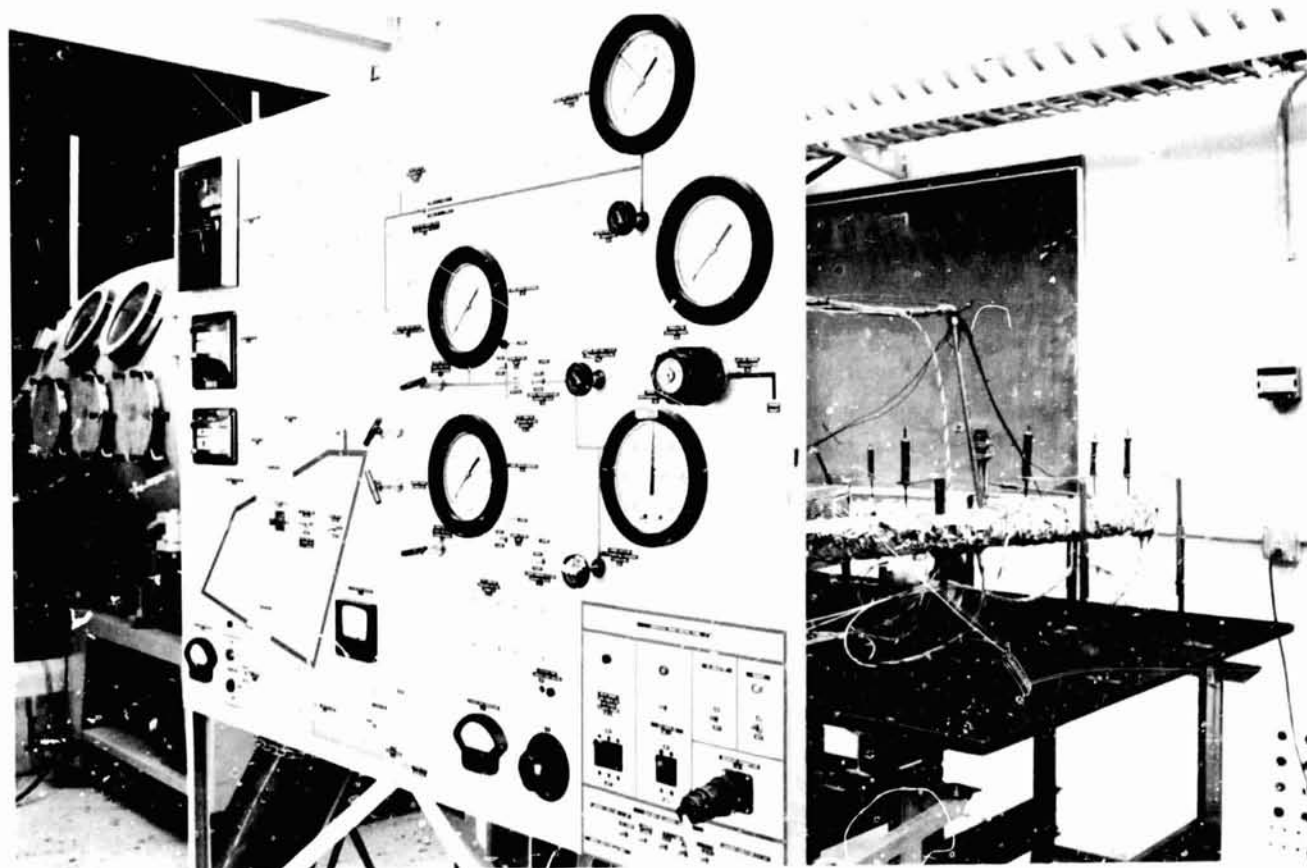


Fig. 10. Control console for Haynes Stellite Alloy 25 loop

venturi and the flow returned to the pump. Figures 9 and 10 are photographs of the main flow circuit and control console. The loop was enclosed within a sheet metal cover during testing to contain any lithium spill that might result from failure of the loop.

The loop was operated with a maximum temperature of 1800°F and a maximum lithium velocity of 210 ft/s. Five cycles from ambient to 1800°F occurred during the test period due to failures of wiring, fans, and other auxiliary components. A total of approximately 93 h of operation above 1000°F and 28 h at 1800°F were realized before the lithium circulation ceased. During the 28-h period the velocity in the venturi throat at 200 V input to the pump gradually decreased from 210 ft/s to zero.

Radiographs of the pump revealed that mass transfer deposits had closed one of the pumping sections. These deposits are shown in Fig. 11 in each of the pumping sections. It is apparent from examining these photographs that the pump bus bars acted as a large heat sink for the flow. The lithium temperature leaving the pump was 140–160°F less than the 1800°F temperature of the test section. The wall temperature at the bus bar locations was probably lower by another 100–200°F. The large temperature difference encountered is not representative of the 300-kW conversion system where the maximum temperature difference in the high-velocity region will be

less than 10°F. However, if the temperature differences in this test were accurately known, the results could be used to estimate mass transfer coefficients which would be applicable to the 300-kW system. It is therefore planned to remove the deposits from the pump, install temperature instrumentation on the pump duct and bus bars, and operate the loop for an additional period to obtain this information.

B. Reactivity Effects From Fuel Displacement in a Small Thermionic Reactor, H. Gronroos and J. P. Davis

1. Introduction

This article reports results of a first-order evaluation of reactivity effects from fuel displacement in a small thermionic reactor. The outer ring of diode-fuel assemblies was displaced either toward the core center or toward the reflector. Figure 12 illustrates the basic configuration used in the calculations.

The purpose of these calculations was to obtain an estimate of the reactivity effect from bowing of fuel elements. There has been interest in such effects in liquid-metal-cooled fast reactors since they were discovered in the EBR² Mark I and Mark II cores (Ref. 5). In these

²EBR = Experimental Breeder Reactor.

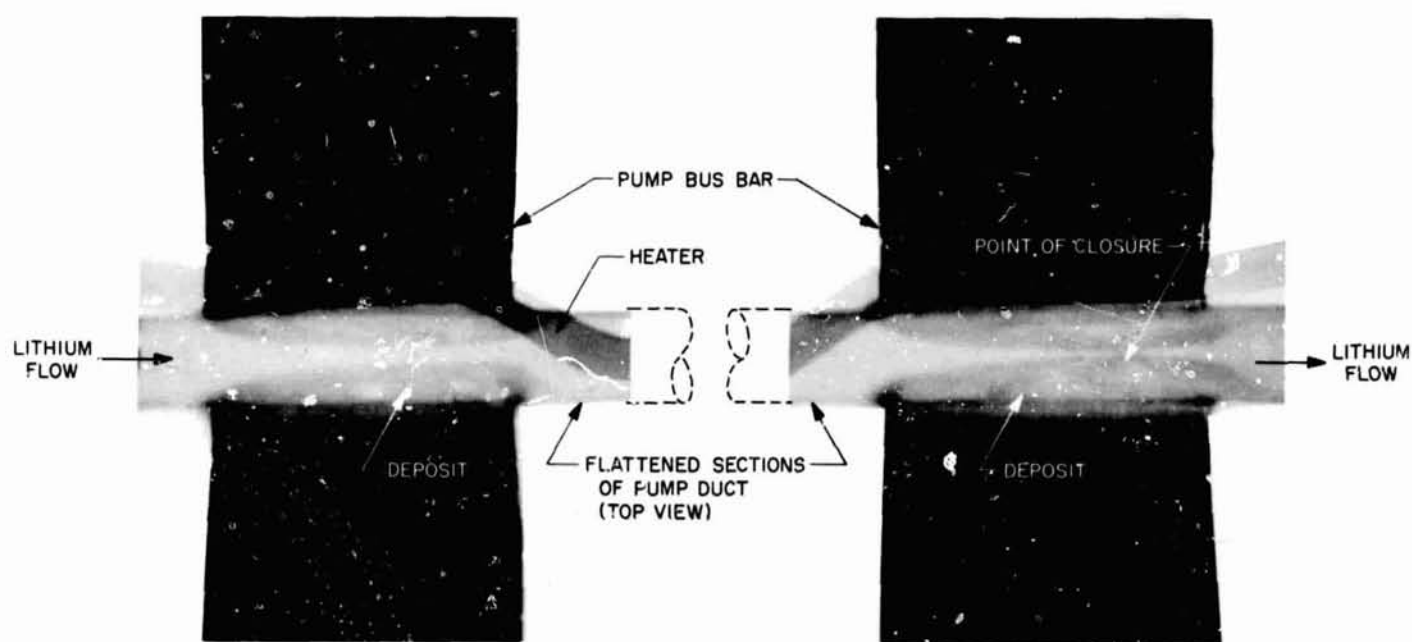


Fig. 11. Mass transfer deposits in Haynes Stellite Alloy 25 pumping sections

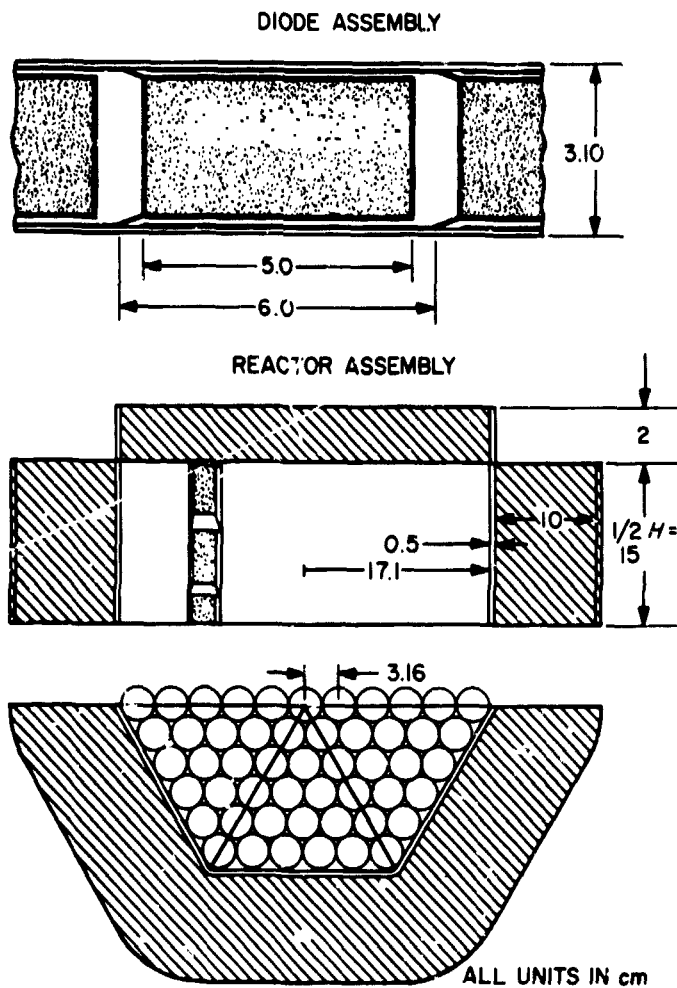


Fig. 12. Thermionic reactor reference design

cores, bowing led to a positive reactivity contribution with ensuing stability problems. The reactivity effects from fuel displacement are unique for each reactor design. Extrapolation of the results in this calculation to other than peripheral diode assemblies, or to other reactor concepts, is not generally valid.

A reactor size applicable for the low power region (50 to 100 kWe) was chosen as a reference design. The reactivity effects decrease with increasing core size and power level, since the optimum diode-fuel assembly becomes smaller.

Several general criticality portrayals applicable to reactors of the type shown in Fig. 12 have been published. They have been obtained by assuming a uniform fuel-structural material mixture in the core and give a first estimate of the critical loading. Figure 13 illustrates the results when data from Ref. 6 are applied. The diode structure and cladding thickness have been used as

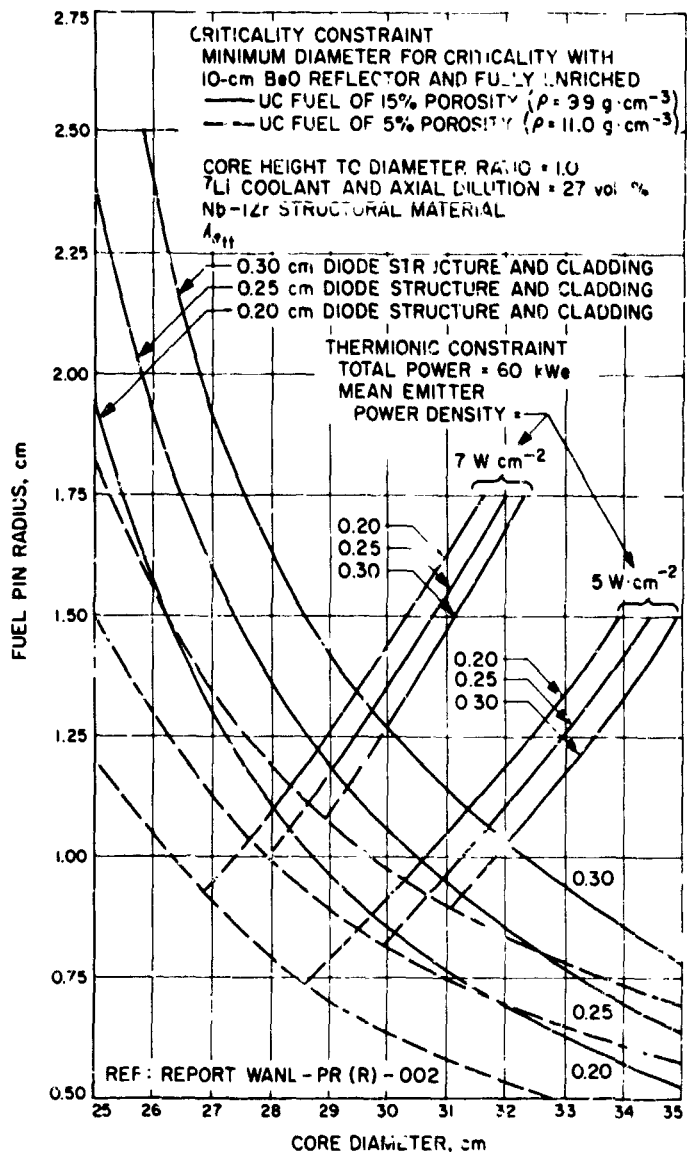


Fig. 13. Criticality portrayal for UC-fueled in-pile thermionic reactors with 10-cm BeO reflectors

parameters. The curves going across Fig. 13 give the minimum diameter necessary for criticality with a 10-cm beryllia reflector. Increasing the reflector thickness beyond 10 cm will give insignificant reduction in fuel pin radius. Superimposed on the criticality limiting curves are the thermionic performance constraints. Power profile flattening requires fuel loading margin, i.e., one must be as much as possible above the criticality constraint curve, thus increasing the fuel pin radius. However, two factors limit the fuel pin size: the generated current and the open-circuit casualty condition. The latter condition, which leads to a large temperature rise in the fuel and emitter, is usually the more serious constraint. The maximum feasible fuel pin radius is therefore about 1.5 cm.

The optimum fuel pin length generally lies between 4 and 7 cm for internally fueled diodes.

2. Reference Design and Calculations

The reference design is illustrated by Fig. 12. For simplicity and computer time economy, a one-dimensional cylindrical geometry was chosen. The calculations were performed for various radial dimensions to cover the expected range of mean radii. Both ${}^7\text{Li}$ and eutectic NaK

were chosen as coolants. A 1-mm coolant annulus was assumed between the core assembly and tank wall. Depending on the thermionic performance, the power output for the reference design will be in the range 50 to 100 kWe.

The effect of fuel displacement was simulated as shown by Figs. 14(a), (b), and (c). The unperturbed core assembly was taken as a homogenous mixture, and the eigenvalue was calculated [Fig. 14(a)]. The outer ring of assemblies was moved 1 mm, which leads either to a compressed or diluted annular core region as illustrated by Figs. 14(b) and 14(c), respectively. The change in eigenvalue measured the reactivity effect. Table 1 gives the material data used in the calculations for the various configurations.

The effect of the tank wall was calculated as well as the effect of power profile flattening by redistribution of fuel.

The one-dimensional radial eigenvalue calculations in cylindrical geometry were performed with the DTF-IV code (Ref. 7). This code solves the neutron transport problem in the S_n approximation. Order $S_n = 4$ was used together with a transverse buckling correction. The standard 16-group Hansen-Roach cross-section set was employed (Ref. 8).

3. Results

Table 2 summarizes the results obtained. The reactivity values were calculated from $(k_p - k)/\beta_d$, where k is the eigenvalue for the unperturbed assembly, k_p the eigenvalue for the perturbed core, and β is the delayed neutron fraction for ${}^{235}\text{U}$ -0.0064.

For comparison a calculation was performed where the whole core was uniformly compressed radially 1 mm and the outer regions correspondingly moved inward without compression. As expected, the reactivity increase is large and over the prompt criticality threshold 100% . In contrast, moving the outer ring of diode-fuel assemblies inward results in a substantial reactivity decrease, between 70 and 85%. Correspondingly, moving the same assemblies outward increases the eigenvalue. These effects are attributable to combined changes in the neutron spectrum and flux level overriding the leakage changes that would cause opposite results.

The effect of the more absorptive NaK coolant is evident from the decreased eigenvalue, but the effect of fuel displacement remains relatively the same as with ${}^7\text{Li}$ coolant.

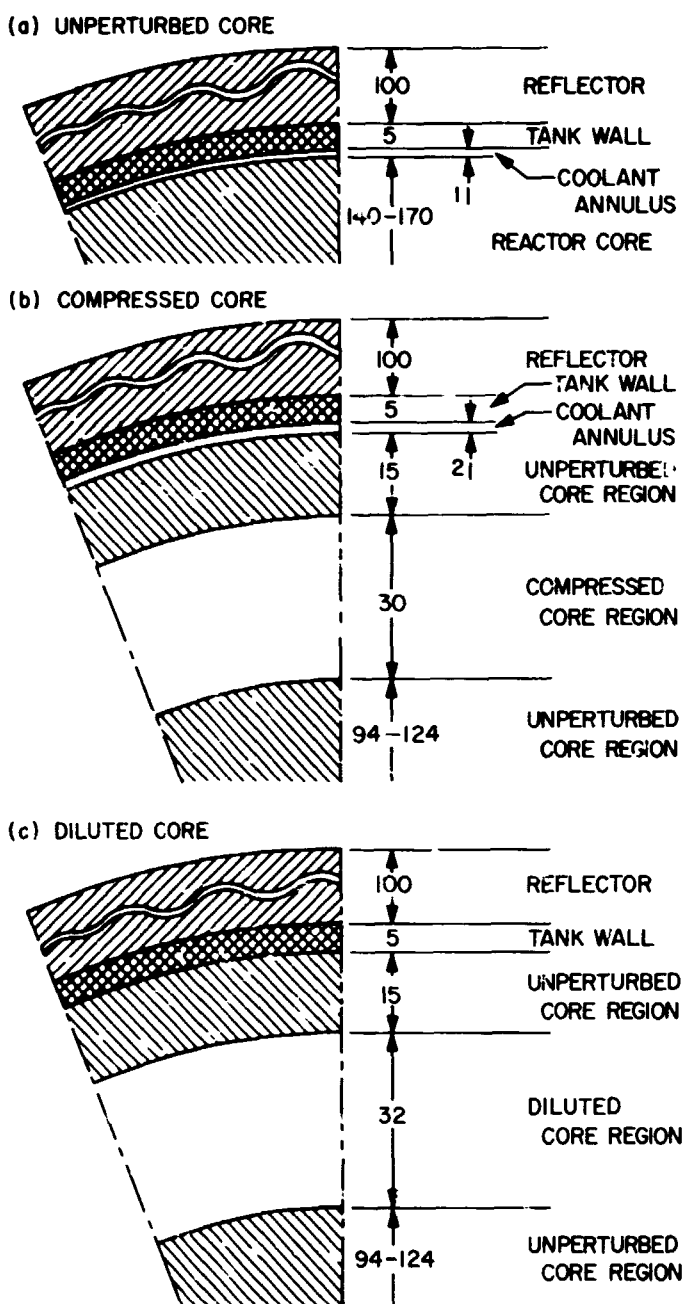


Fig. 14. Radial configurations for criticality calculations

Table 1. Material data for criticality calculations of thermionic reactor

Region	Material	Temperature, °C	Density, g·cm ⁻³	Thickness, cm	Unperturbed core region		Compressed core region		Diluted core region	
					Volume fraction	Atomic densities, at·cm ⁻³ ·10 ²²	Volume fraction	Atomic densities, at·cm ⁻³ ·10 ²²	Volume fraction	Atomic densities, at·cm ⁻³ ·10 ²²
Fuel	UC	1900	9.90	2.50 diam	0.4744	²³⁵ U = 1.0687 ²³⁸ U = 0.0846 C = 1.1788	0.4769	²³⁵ U = 1.0744 ²³⁸ U = 0.08509 C = 1.1850	0.4718	²³⁵ U = 1.0628 ²³⁸ U = 0.08418 C = 1.1723
Emitter	Mo	1800	9.38	0.10	0.1011	0.59618	0.1016	0.59934	0.1005	0.59290
Gap	Vacuum	—	—	0.025	0.0865	—	0.0870	—	0.0860	—
Collector	Nb	1000	8.35	0.10	0.1039	0.56251	0.1044	0.56549	0.1033	0.55941
Insulator	Al ₂ O ₃	975	3.20	0.025	0.0541	Al = 0.20455 O = 0.30682	0.0544	Al = 0.20563 O = 0.30845	0.0539	Al = 0.20342 O = 0.30513
Cladding	Nb	950	8.35	0.050	0.0556	0.30092	0.0559	0.30252	0.0553	0.29927
Coolant	⁷ Li	950	0.455	—	0.1244	0.48585	0.1198	0.46778	0.1292	0.50476
	NaK	950	0.641	—	0.1244	Na = 0.04594 K = 0.09577	0.1198	Na = 0.04423 K = 0.09221	0.1292	Na = 0.04773 K = 0.09950
Coolant	⁷ Li	950	0.455	0-0.2	1.0	3.9059				
Annulus	NaK	950	0.455	0-0.2	1.0	Na = 0.3693 K = 0.7699				
Tank wall	Nb	950	8.35	0.5	1.0	5.4133				
Reflector	BeO	800	2.73	10.0	1.0	Be = 6.5749 O = 6.5749				

Omission of the tank wall yields an increased eigenvalue due to decreased absorption of neutrons thermalized in the reflector.

Power flattening, by decreasing the ²³⁵U enrichment in the central part of the core, does not change appreciably the general effect of fuel displacement, as would be expected.

The above results are summarized in Fig. 15. Figures 16 and 17 show power profiles for the 14.0- and 17.0-cm core calculations, respectively.

A conservative estimate for the reactivity effect from a single displaced peripheral assembly may be obtained by dividing the calculated values with the number of assemblies in the outer ring. For the reference design, a value between +2 and +3¢ for 1-mm outward displacement is calculated.

In a thermionic reactor core, radial fuel displacement would generally not be tolerated, except for that following overall core thermal expansion. However, at the core boundary, and depending on tolerances, the power peaking, power excursions, and open-circuit conditions,

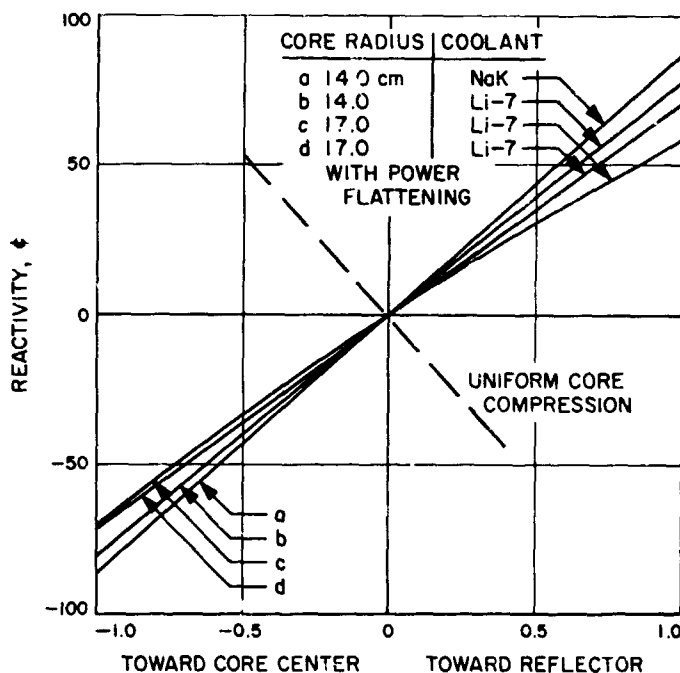


Fig. 15. Reactivity effect from radial displacements of the outer ring of diode assemblies in a small thermionic reactor

Table 2. Results of criticality calculations

Case	Core radius, cm	Coolant	Eigenvalue	Reactivity perturbation, ρ	Comments
Unperturbed core	14.0	⁷ Li	0.96844	0	Reference core
Compressed core region	14.0	⁷ Li	0.96331	- 80	
Diluted core region	14.0	⁷ Li	0.97344	+ 78	
Unperturbed core	14.0	NaK	0.96063	-122	
Uniformly compressed core (1 mm)	14.0	⁷ Li	0.97530 0.98033	+106 +186	
Unperturbed core	14.0	NaK	0.96063	0	Reference core
Compressed core region	14.0	NaK	0.95410	- 86	
Diluted core region	14.0	NaK	0.96617	+ 87	
Unperturbed core	17.0	⁷ Li	1.04400	0	Reference core
Compressed core region	17.0	⁷ Li	1.03957	- 70	
Diluted core region	17.0	⁷ Li	1.04770	+ 58	
Unperturbed core with power flattening	17.0	⁷ Li	1.02201	-344	
Power flattening					Reference core
Unperturbed core	17.0	⁷ Li	1.02201	0	
Compressed core region	17.0	⁷ Li	1.01748	- 71	
Diluted core region	17.0	⁷ Li	1.02653	+ 71	
Unperturbed core with no tank wall	14.0	⁷ Li	0.97990	+179	Δk based on core with tank wall
	17.0	⁷ Li	1.05352	+149	Δk based on core with tank wall

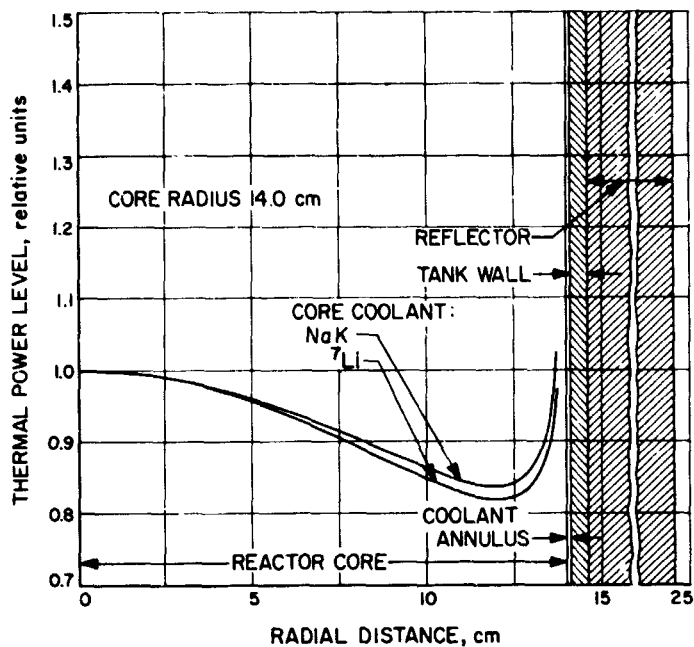


Fig. 16. Power distributions in thermionic liquid-metal-cooled reactors for 14-cm core radius

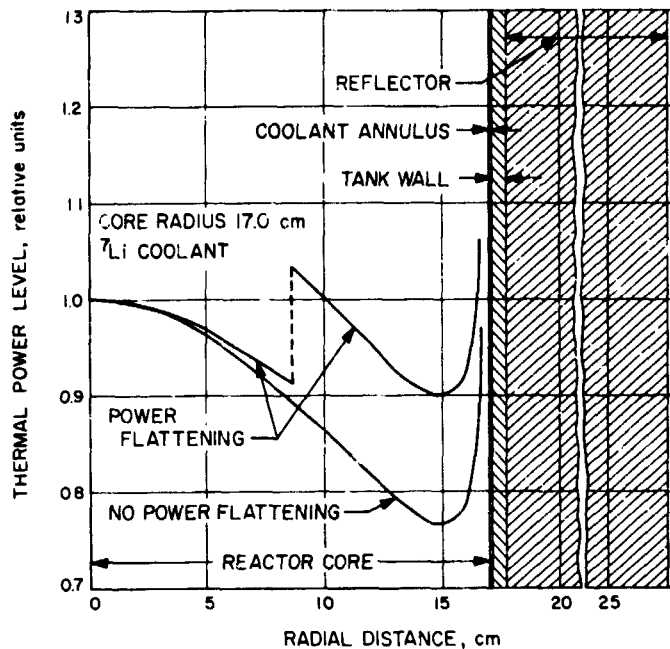


Fig. 17. Power distributions in thermionic liquid-metal-cooled reactors for 17-cm core radius

could conceivably cause some outward bowing. If the effective displacement is limited to a few tenths of a millimeter, the results of this first-order calculation show that the reactivity contribution would be positive and of the order of 10 to 20¢ for the entire outer ring.

C. Comparison of Enthalpy Measurements Obtained in an Internal High-Temperature Flow of Argon as Determined by Conservation of Energy, a Calorimetric Probe, a Flowmeter, and Spectroscopy,

P. F. Massier, L. H. Back, and E. J. Roschke

1. Introduction

A combined experimental and analytical investigation is currently in progress to advance the knowledge of heat-transfer and fluid-dynamic phenomena that occur in ionized gas flows. The investigation was initiated as a consequence of the interest in electrical propulsion and power generation concepts and the use of ionized gas flows in plasma test facilities. Results of convective and radiative heat transfer that have been obtained previously are discussed in SPS 37-22, -23, -24, -36, -37, and -43, Vol. IV. A one-dimensional analysis that applies for isen-

tropic flow of ionized argon appears in Ref. 9, and a boundary layer analysis for laminar flow of an ionized gas with convective heat transfer appears in Ref. 10.

In order to gain an understanding of convective heat transfer from a high-temperature flowing gas, the enthalpy difference between the gas in the main stream and the gas adjacent to the surface must be determined. In addition, measurements are required to establish the heat flux to the wall. With this information the heat-transfer coefficient and other useful parameters can be evaluated. The purpose of this note is to discuss the different methods that have been employed to measure the enthalpy of high-temperature argon flowing through an axisymmetric duct and to compare some of the results.

For equilibrium conditions the enthalpy at a cooled surface can easily be determined from a measurement of the wall temperature; however, the temperature of a steady thermally ionized gas flow is generally too high to be determined directly by use of a simple instrument such as a thermocouple. It therefore becomes necessary to use an instrument that is cooled or one that responds quickly enough so that it can be passed through the gas before it is damaged. Or, optical techniques, such as spectroscopy, which do not come into contact with the

gas stream can be used. Average values of the enthalpy at given axial locations can be determined from energy conservation, which requires knowledge of applied power at the arc heater, heat transfer to the cooled walls and the mass flow rate of the gas. Also, the average enthalpy can be determined by use of an adequately instrumented flowmeter if the mass flow rate of the gas is determined by an independent method.

Experiments have been conducted in which the enthalpy of a steady subsonic flow of high-temperature argon at a Mach no. of about 0.07 has been determined by four methods. They include: conservation of energy, a calorimetric probe as shown in Fig. 18, a flowmeter, and spectroscopy. Results are shown for four tests in which the stagnation pressures were approximately 3.0 and 6.0 psia, and the average stagnation enthalpies at the probe tip location (as determined from the conservation of energy) ranged from about 920 to 1730 Btu/lb. A comparison of the enthalpies by all four methods is made for only the two tests performed at a pressure of about 3.0 psia, because at the higher pressure the gas temperature, and hence the line intensities, caused by de-

excitation were too low to obtain spectroscopic data. The ionization fraction at the arc heater outlet (Fig. 19) ranged up to 0.18; however, by the time the gas flow reached the probe tip the ionization fraction based on the probe measurements was reduced to values less than 0.005 for all tests.

2. Experimental Apparatus

The test apparatus, shown in Fig. 19, consisted of an arc heater followed by a constant-diameter tube with a nozzle attached to the exit of the tube. A 90-deg bend was placed between the arc heater and the tube to shield the tube from the radiation emitted by the arc and to dissipate the vortex motion of the gas introduced upstream of the electrodes. Flow visualization tests using a dye injected into water indicated that this type of a bend is effective for the dissipation of vortex motion. The location of the calorimetric probe which could be traversed radially and the location of the quartz viewport through which spectroscopic data were obtained are also shown in Fig. 19. The walls of the test apparatus contained numerous individual, circumferential coolant passages which were utilized to determine the axial heat transfer distribution by calorimetry. Wall pressure distributions were determined with many pressure taps that were connected to manometers containing oil. These measurements were used as inputs for the complete analysis of the experimental data; however, a discussion of the complete analytical procedure that was used is beyond the scope of this article.

3. Experimental Results

Tabulated results of four tests are given in Tables 3 and 4. Table 3 shows results at the calorimetric probe location. To indicate spectroscopic and flowmeter results at the probe location, the enthalpies at these measuring stations were adjusted by adding the energy per unit mass of argon transferred to the coolant between the probe tip and the respective measuring station. The results at the respective measuring stations are shown in Table 4. Radial distributions of the stagnation enthalpy as determined by the calorimetric probe are shown in Figs. 20 to 23. The methods that were used to obtain the results are described in the subsequent sections.

a. Spectroscopy. The spectroscopic results were acquired by measuring the intensities of eleven atom lines in the range 0.41 to 0.81 μ , using transition probabilities listed by Olsen in Ref. 11. Excitation temperatures were evaluated by the relative line intensity method using a

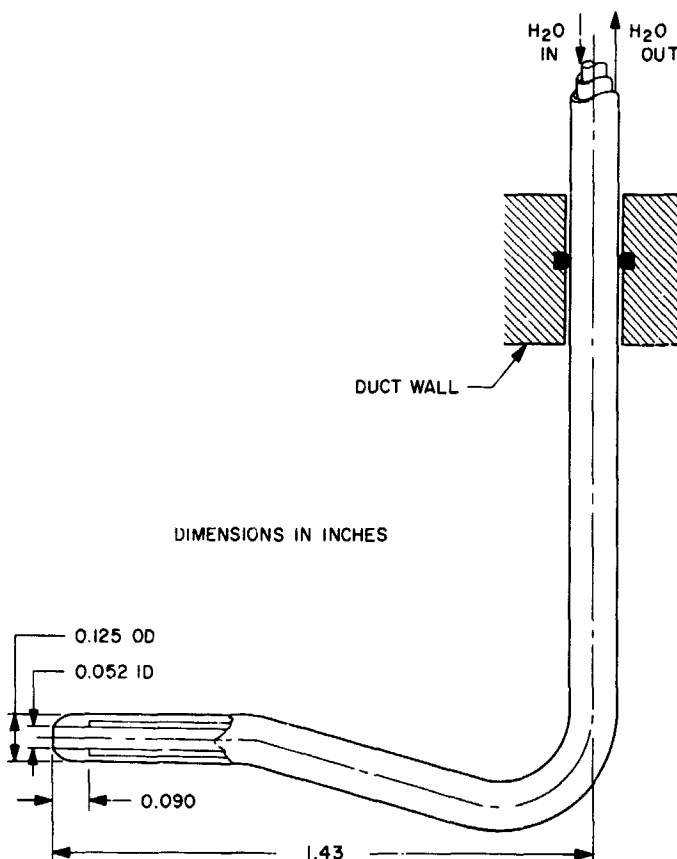


Fig. 18. Calorimetric probe

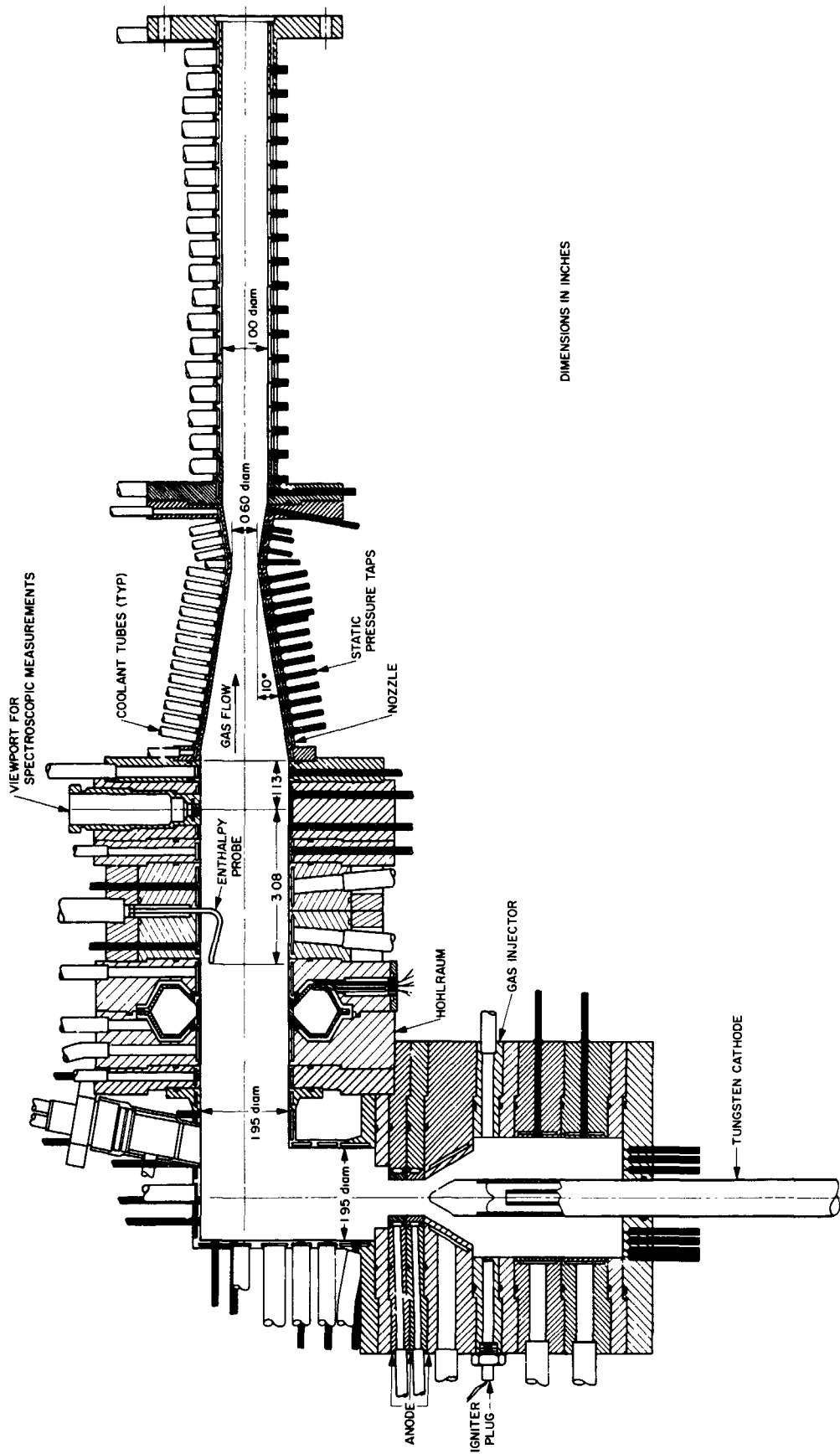


Fig. 19. Ionized gas heat-transfer test apparatus

Table 3. Stagnation enthalpy at probe tip location as determined by various methods

Method of determining enthalpy	Enthalpy, Btu/lb			
	Test 112-40H	Test 112-41H	Test 112-42H	Test 112-44H
Energy balance to probe tip location	1570	1730	1080	920
Average enthalpy as determined from calorimetric probe measurements assuming uniform mass flux distribution	1150	1220	1040	970
Use of measured gas flow rate with nozzle as a choked flowmeter. Enthalpy corrected to probe tip location by taking into account the energy transferred to the coolant between the probe tip and the nozzle throat	1690	1890	1100	920
Spectroscopic measurements of eleven atom lines using relative line intensity method. Enthalpy corrected to probe tip location by adding energy transferred to coolant between the probe tip and the viewport	2320	2470		

Table 4. Stagnation enthalpies at measuring stations and at the arc-heater outlet

Location and method	Stagnation enthalpy, Btu/lb			
	Test 112-40H	Test 112-41H	Test 112-42H	Test 112-44H
At arc-heater outlet as determined by energy balance	5450	6140	2050	1620
Average at probe tip as determined from calorimetric probe measurements	1150	1220	1040	970
At viewport from spectroscopically determined electron temperature	1940	2030		
Average at nozzle throat as determined by using the nozzle as a flowmeter	1000	1080	790	710

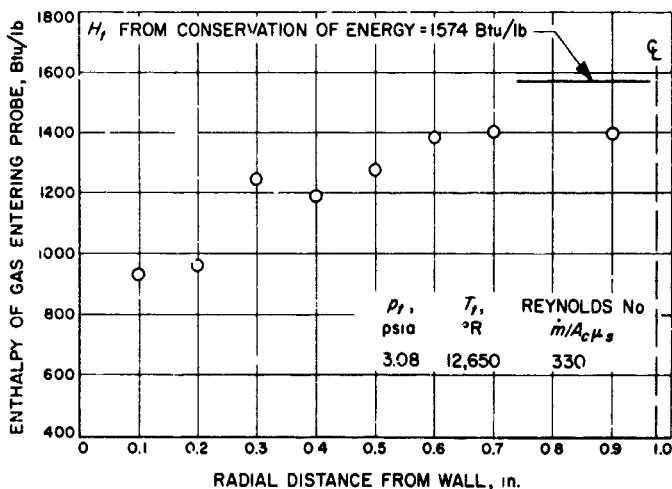


Fig. 20. Calorimetric probe results for Test 112-40H

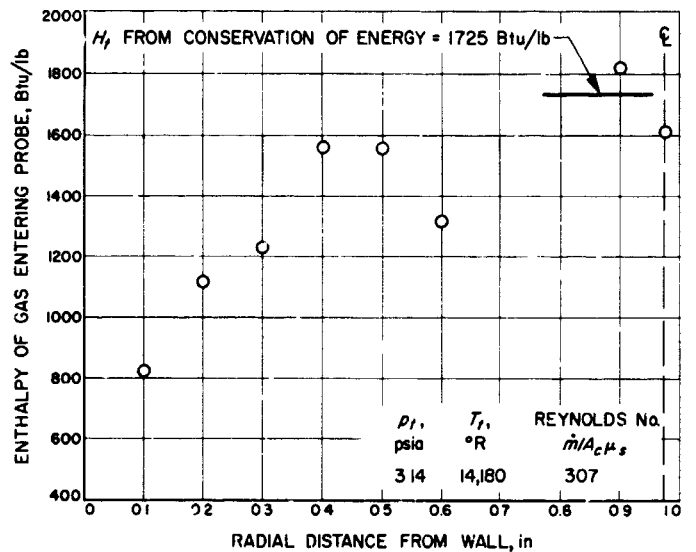


Fig. 21. Calorimetric probe results for Test 112-41H

least-squares straight-line fit through the data (Figs. 24 and 25). The intensity of radiation I , emitted at wavelength λ , in terms of the energy level E , and the excitation temperature T , of the emitters is given by:

$$\log \left(\frac{I\lambda}{gAC} \right) = - \frac{E \log e}{kT} \quad (1)$$

In Eq. (1) g is the statistical weight, A is the transition probability, and k is Boltzmann's constant. C includes an

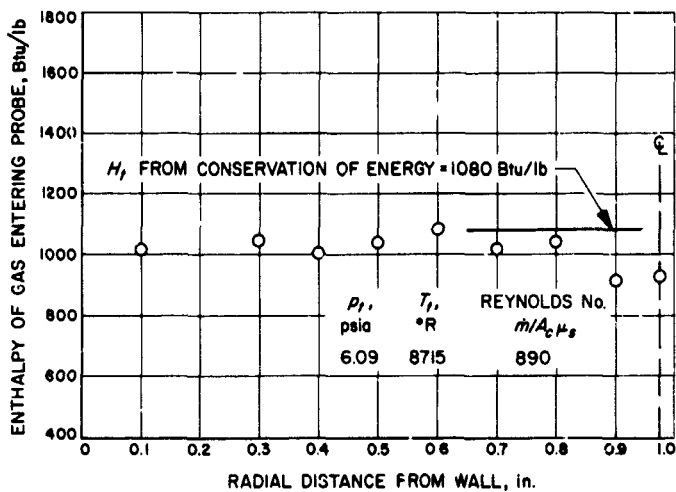


Fig. 22. Calorimetric probe results for Test 112-42H

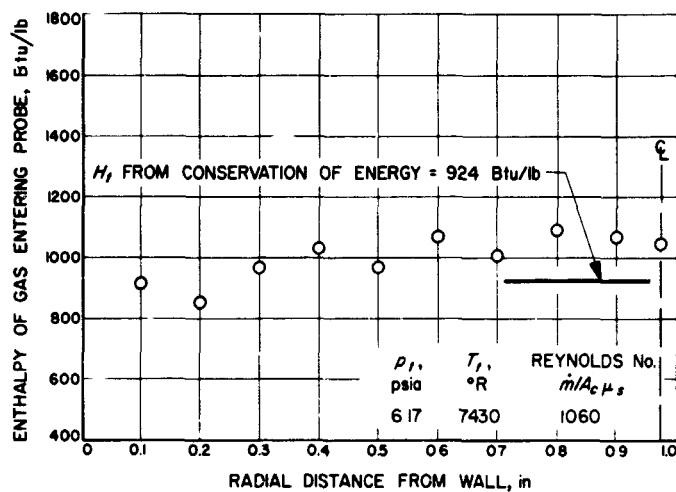


Fig. 23. Calorimetric probe results for Test 112-44H

instrument calibration factor and several physical constants that do not depend on I or λ . Use of Eq. (1) is restricted to an optically thin plasma in which the populations of all excited states at energy level E have Maxwell-Boltzmann distributions. The slope of the line obtained by plotting $\log(I\lambda/gAC)$ versus E established the excitation temperature. The enthalpies were then computed from the temperatures, assuming the gas was in equilibrium. Since the gas velocity was low, static and stagnation enthalpies were nearly the same. The results given in Table 3 show that the enthalpies determined from the spectroscopic measurements assuming thermal equilibrium were higher than those determined by any of the other methods. The line of sight for the spectroscopic measurements was perpendicular to the gas flow direction and through the centerline of the tube as shown

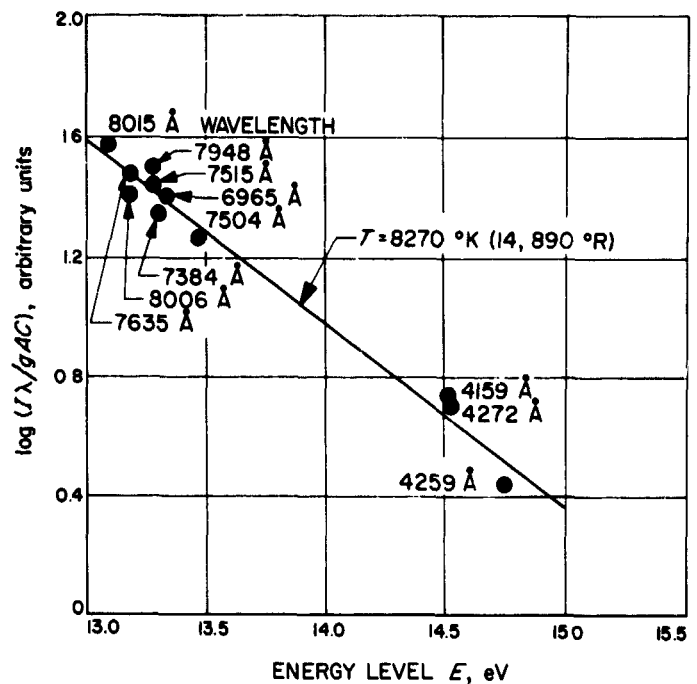


Fig. 24. Excitation temperature as determined from relative intensities of atom lines for Test 112-40H

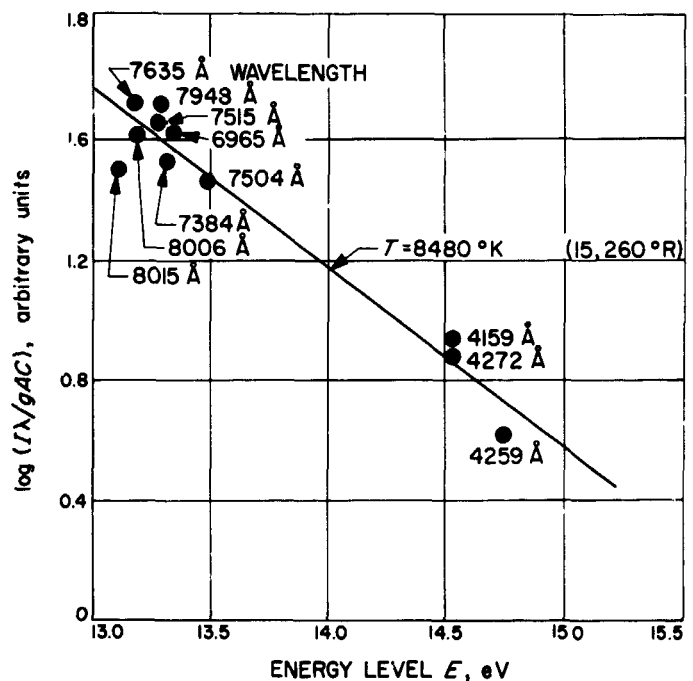


Fig. 25. Excitation temperature as determined from relative intensities of atom lines for Test 112-41H

in Fig. 26. Thus, the relative intensity readings obtained were integrated averages along the line of sight across the duct and not local values. Readings were recorded both with and without a mirror inserted in the view tube

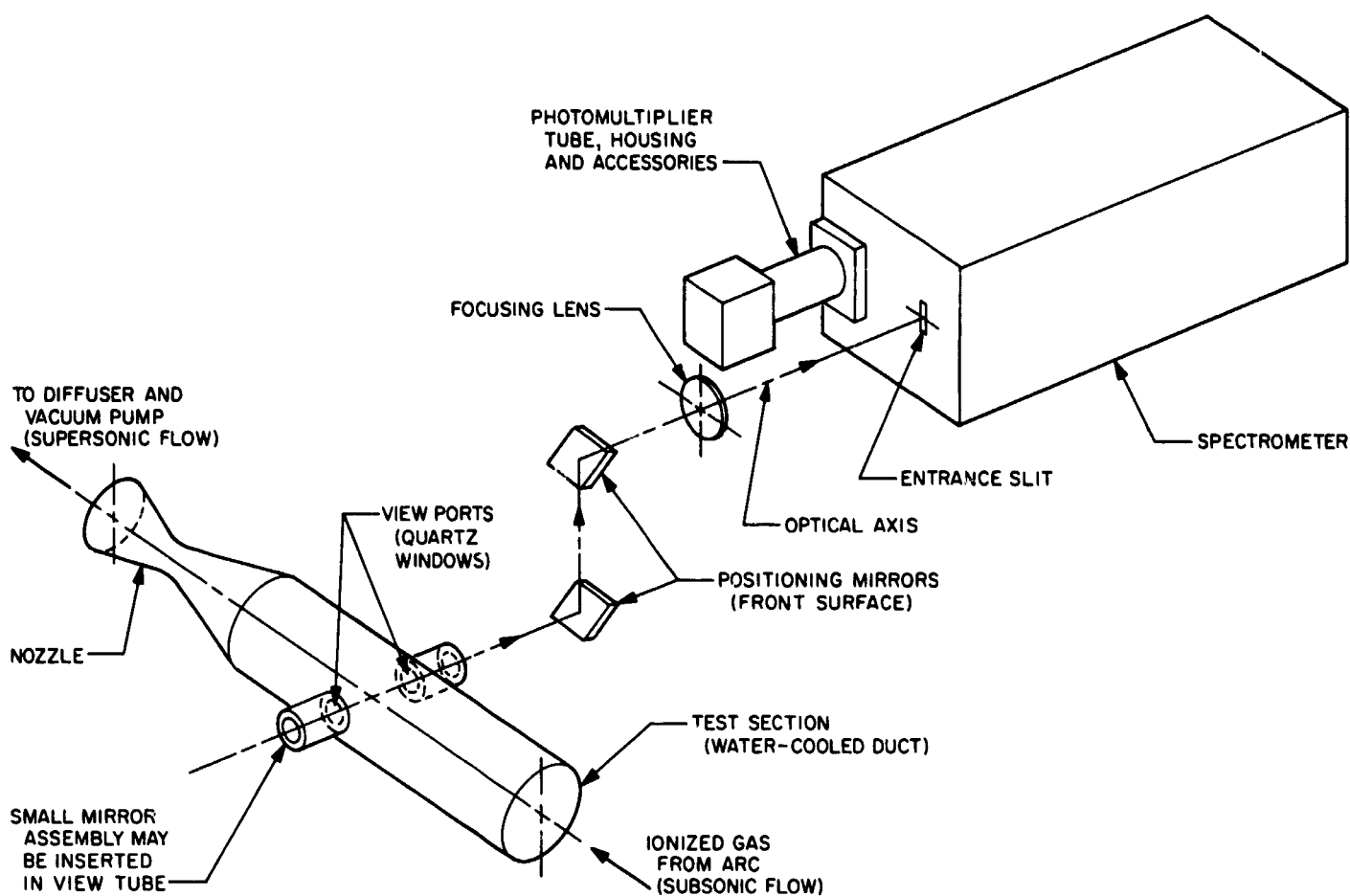


Fig. 26. Arrangement of apparatus for spectroscopic measurements

located in the duct wall opposite the monochromator. Hence it was possible to correct the data approximately for absorption which amounted to a decrease in temperature of only about 5% below uncorrected values. Although the measured intensity of a given line may require a significant correction because of absorption, the effect on temperature is considerably smaller because of the way I and T are related in Eq. (1). For a given line, Eq. (1) may be written:

$$\frac{\Delta T}{T} \approx \left(\frac{kT}{E \log e} \right) \frac{\Delta I}{I}$$

In the present application, $(\Delta T/T) \approx 0.13 (\Delta I/I)$. ΔT and ΔI represent the difference between corrected values and uncorrected values of T and I .

b. Calorimetric probe. The calorimetric probe consisted of three concentric stainless steel tubes properly spaced by longitudinally positioned wires located between the tubes (Fig. 18). At the tip the outer tube was swaged and

welded to the inner tube to form a seal for the water coolant. The outer diameter of the probe was 0.125 in. and the inner diameter 0.052 in. Water entered the inner annulus of the probe at its external extremity, flowed to the probe tip, and then returned through the outer annulus to the discharge pipe. The heat transferred to the coolant was determined by measuring the water flow rate and the water temperature rise. A tare measurement was first obtained without gas flowing through the center tube. Then, with gas flowing through the tube, the flow rate of the bleed gas was measured and the heat transfer determined for this condition. The bleed gas flow rate was measured with a rotameter calibrated with argon at the actual conditions at which the measurements were made. The probe was of sufficient length so that the gas being sampled was cooled to about room temperature at the thermocouple location. With this information it was possible to compute the energy transferred to the coolant by the gas that was being sampled through the center tube, assuming that sampling had no effect on the heat transfer from the main gas flow to the outer tube wall.

This procedure was followed for all tests at each of the radial measuring stations. All tests were conducted at steady-state conditions.

An investigation to determine the influence of sampled flow rate on the measured enthalpy was conducted by Vassallo and is discussed in Ref. 12. He used a Grehrad probe similar in configuration to the one used here but with a slightly larger outer diameter of 0.135 in. For enthalpies in the vicinity of 1000 Btu/lb with the same sampled flow rate as used in Test 112-42H, Vassallo's data would indicate that the measured enthalpy is low by about 8%. This was probably caused by the influence of sampling on the flow field surrounding the probe, which in turn reduced the heat transfer from the gas outside the probe to the coolant in the outer passage. Hence, the tare value was not valid. Vassallo's measurements were conducted in a nitrogen plasma with the probe inserted at the centerline of a jet exhaust. Measurements were made at different sampling flow rates. A linear relationship was found to exist, indicating a trend of decreasing enthalpy with increasing sampling rate. The enthalpy for zero sampling rate was determined by extrapolating a line through the data points. The accuracy of Vassallo's results are dependent to a considerable extent on the accuracy of the temperature measuring instruments that were used. In his experiments at 1000 Btu/lb the coolant temperature rise associated with the sampled flow rate was 0.78°F. This requires not only a calibrated thermocouple with a good readout system, but also proper positioning of the thermocouple in the coolant tube to obtain a true mean temperature. Nevertheless, it appears that definite trends were established by Vassallo's tests. In the investigations reported here the coolant temperature rise associated with the sampled flow rate ranged up to 6°F and was obtained directly by placing the cold junction in the coolant inlet tube, the hot junction in the coolant outlet tube and reading the output on a manually operated potentiometer. For each test the gas flow rate being sampled was maintained constant; however, it was different for different tests. Table 5 is a summary of the sampled gas flow rates and coolant temperature rises associated with the probe. As indicated in Table 3 the weighted average enthalpies (based on an assumed uniform mass flux distribution) as determined from probe measurements deviate approximately 5% from values obtained by the other two methods for the lower energy tests (112-42H and 112-44H). For the higher energy tests, however, (112-40H and 112-41H), the probe values are significantly below the other results, and the deviations are considerably more than would be expected, based on Vassallo's data. One reason for the low average en-

Table 5. Summary of calorimetric probe data

Test No.	Maximum coolant ΔT with gas bleed, °F	Maximum difference in coolant ΔT between bleed flow and zero bleed flow conditions, °F	Minimum difference in coolant ΔT between bleed flow and zero bleed flow conditions, °F	Bleed gas flow rate, lb/sec
112-40H	52.8	3.2	1.4	2.5×10^{-3}
112-41H	60.6	3.6	1.8	2.0×10^{-3}
112-42H	46.2	6.3	4.5	2.5×10^{-3}
112-44H	37.8	4.4	3.6	4.7×10^{-3}

thalpies obtained from the probe measurements could be the assumption of a uniform mass flux distribution, since higher mass flows are likely to have occurred near the center of the duct than near the wall. It should be noted that from the probe measurements the total enthalpy of the gas is determined regardless of whether or not the gas is in equilibrium, providing, of course, that the probe has been properly calibrated for the influence of position and sampling on heat transfer and that the temperature and flow-rate measurements are accurate.

c. Use of the nozzle as a flowmeter. As shown in Fig. 19, a convergent-divergent conical nozzle with half angles of 10 deg was attached to the exit end of the tube which contained the calorimetric probe and the viewport. This nozzle was used as a flowmeter, thereby providing an independent method for determining average values of the stagnation enthalpy. It was necessary to stipulate the contour of the nozzle downstream as far as the throat to perform the calculations. The following procedure was adopted:

First, from experimental values of wall pressures and heat fluxes along the nozzle and prescribed conditions at the nozzle inlet, which were determined from upstream measurements, the flow variables along the nozzle were computed, using the conservation equations of momentum and energy and the equation of state. In this analysis, equilibrium conditions were assumed to exist. The radial distributions of the flow variables were assumed to be uniform; however, since the measured wall pressures were used, the analysis was quasi-two-dimensional. For the purpose of this discussion the significant variable that was computed using the experimental data is the mass flux, ρu . After the initial calculation had been made, this

value of ρu at the nozzle throat was made essentially equal to the mass flux determined from the measured gas flow rate and nozzle throat area, \dot{m}/A_{th} , by adjusting the average enthalpy at the nozzle inlet and iteratively performing the calculations up to the throat on a digital computer until the ratio of the two mass fluxes was within the limits of a 0.995 and 1.005. In previous measurements of nozzle pressure distributions (Fig. 8 of Ref. 13) it was found that even though mass fluxes in conical nozzles deviated from one-dimensional values, the mass flux at the edge of the boundary layer at the throat agreed with the one-dimensional value.

As with the spectroscopic results the enthalpies determined in this manner at the nozzle inlet were then adjusted to obtain values at the probe location by adding the energy per unit mass of argon transferred to the coolant between the probe tip and the nozzle inlet. As may be observed in Table 3, the average enthalpies determined in this manner are about the same as obtained by energy balance for the two low-enthalpy tests and somewhat larger for the other two tests than the values obtained both by the probe and by energy balance.

d. Conservation of energy. The other method that was used for determining the average enthalpy of the gas at the probe tip location was by subtracting the total rate of heat transferred to the coolant (up to the probe tip location) from the applied power to the arc heater and then dividing by the measured gas flow rate. This method is applicable regardless of whether or not the fluid is in equilibrium. The enthalpies determined in this manner appear in Tables 3 and 4 and in Figs. 20 to 23. The significance of this method is that it forms a good basis for comparison with the other methods, because the core flow must have been highly nonadiabatic between any two locations downstream of the bend. This fact was established in several ways, by: (1) the comparatively uniform distributions obtained by the calorimetric probe, (2) the rapid and large growth of the energy thickness which was computed from the measured heat transfer but not reported here, and (3) analyzing the data and computing all flow variables, having imposed different assumptions, one of which included the existence of an adiabatic core beginning at various locations, such as the arc heater outlet and the nozzle inlet. Another assumption was the limiting condition of a decreasing energy in the core along the flow direction equivalent to the energy transferred to the coolant. The water dye studies demonstrated mixing just downstream of the bend, but before the flow arrived at the nozzle the mixing had essentially

ceased for Reynolds numbers that were in the range of the high-temperature argon tests.

4. Discussion of Comparisons

In Table 3 the average enthalpy as determined from the calorimetric probe measurements was obtained by a weighted mean of the product of mass flow rate and local enthalpy, assuming a uniform mass flux distribution across the duct. The enthalpies evaluated from the flowmeter and from the spectroscopic measurements were adjusted, as stated previously and in the table, to account for the relative locations of the nozzle and the viewport with respect to the probe tip. A comparison of the results shows that the methods that agreed best were the energy balance and the flowmeter.

For both Tests 112-40H and 112-41H the spectroscopic values were considerably higher than for all of the other results, even when comparing the downstream unadjusted values of Table 4 with the enthalpies at the probe tip location shown in Table 3. The excitation temperature measured spectroscopically was assumed to be the electron temperature, since it is probable that the free electrons were dominant in determining the excitation of the bound electronic states. Experimental results obtained in Ref. 14 corroborate this viewpoint. Since it is not known whether the apparent high values of excitation temperature were indeed a consequence of a nonequilibrium effect, the spectroscopic values in Tables 3 and 4 are based on an assumed thermal equilibrium in which the heavy particle temperature is taken equal to the measured excitation temperature. Approximate electron number densities and ionization fractions for two tests are listed in Table 6 at the specified temperatures. There are at least two reasons why the values based on electron temperature (Tables 3 and 4) are high compared to the other measurements. Firstly, the spectroscopic data were obtained by viewing through a single port along a diametral

Table 6. Approximate values of electron number density and ionization fraction obtained from the Saha equation at the specified temperature and measured static pressure

Test No.	Based on average gas temperature at location of calorimetric-probe tip		Based on spectroscopic temperature at location of viewport	
	N_e, cm^{-3}	α	N_e, cm^{-3}	α
112-40H	0.13×10^{16}	0.6×10^{-3}	10^{16}	5×10^{-3}
112-41H	0.3×10^{16}	3×10^{-3}	1.4×10^{16}	7×10^{-3}

Table 7. Ratio of the total heat transfer to the applied power

	Test 112-40H	Test 112-41H	Test 112-42H	Test 112-44H
Total heat transferred to coolant obtained by summation for 70 coolant passages divided by applied electrical power at arc heater	1.00	1.00	0.95	0.95

the data and the consequent good agreement achieved, as shown in Table 7, when comparing the overall energy balance of the system determined by adding the energy transfer to each of 70 coolant passages with that of the applied power at the arc heater. In this comparison the difference in temperature between the argon entering and leaving the apparatus was taken into account. The low enthalpies obtained from the probe measurements for the higher energy tests was likely to have been caused by the influence of sampling on the heat transfer from the gas flow surrounding the probe to the outer surface of the tube. The magnitude of this effect is influenced not only by the amount of the sampled flow rate but also by the radial position of the probe. The disturbance of the flow field surrounding the probe is probably largest near the intake (probe tip) and that part of the probe that is parallel to the flow of the main stream. When the probe is at the centerline position of the duct, a large fraction of the total probe length is perpendicular to the main flow direction, and this part is probably not influenced to a great extent by sampling. However, when the probe is closer to the duct wall, a larger fraction of the total probe length exposed to the main stream is parallel to the main flow direction and an additional length extends outside the duct and is not affected at all by the gas stream. Therefore, sampling would then have a greater percentage effect on the total heat transfer from the main gas stream to the outer wall of the probe. This implies that the data points in Figs. 20 and 21 actually would be higher near the wall if the effect of sampling on heat transfer from the main gas stream to the outer probe wall could be taken into account, and would thus form a more uniform enthalpy distribution. Because of the sampling effect on heat transfer from the main stream, a short probe tip should give better results than a long tip. Thus, it is possible to improve the accuracy of the probe beyond that of these tests by a more sophisticated calibration procedure.

5. Summary and Conclusions

The enthalpy of a steady internal flow of weakly ionized argon at a pressure of 3.1 psia and a Mach no. of about 0.07 was determined experimentally by four different methods. At an energy level of approximately 1700 Btu/lb the enthalpies determined from energy balance and by use of a choked flowmeter agreed within 7%. Average calorimetric probe results were considerably lower and spectroscopic values obtained through a small port (assuming thermal equilibrium) were considerably higher than those obtained by the other two methods. Near the centerline of the duct the probe results were the same as the energy balance results for one test and deviated 12% in the other test.

The reasons for the apparent high values of the spectroscopic results are not known; however, two possibilities were exploited. First the data were obtained by viewing through a single port along a diametral line; hence, it is likely that maximum average values of line intensities were observed rather than more realistic lower averages as would be determined from scans of the entire flow field and use of the Abel inversion method. Second, the gas may not have been in thermal equilibrium. Although use of the excitation temperatures to determine equilibrium values of enthalpy gave high results, it was demonstrated that the energy associated with a non-equilibrium condition, if it did exist, was negligibly small.

The apparent low enthalpies determined from the calorimetric probe measurements are likely to have resulted from the influence of gas sampling on the flow field surrounding the probe, which in turn affected the heat transfer from the main gas stream to the outer wall of the probe. The extent of this influence is dependent upon the radial position of the probe.

At a pressure of about 6.1 psia and an enthalpy of approximately 1000 Btu/lb (at which the line intensities were too weak to obtain spectroscopic data) the results of the energy balance, the flowmeter, as well as the probe agreed within 5%. For these conditions the radial distributions of the enthalpy were quite uniform.

Use of a calorimetric probe to obtain enthalpy distributions in a high-temperature gas stream is feasible; however, to obtain good accuracy at high enthalpies the instrument should be calibrated to evaluate the influence of the bleed flow rate and the probe position on the heat transfer from the main stream to the outer wall of the probe. The length of the probe tip should be minimized

both from the standpoint of minimizing the tare measurements, as well as minimizing the influence of the bleed flow rate on the heat transfer from the main stream to the probe outer wall.

Of the four methods that were used to evaluate the enthalpy of the high-temperature internal flow of argon, two apply for nonequilibrium as well as equilibrium flows. These methods are the calorimetric probe and energy balance. The spectroscopic relative line intensity method may be used to determine excitation temperatures for optically thin gases not in thermal equilibrium provided the populations of all excited states at energy level E , have Maxwell-Boltzmann distributions. However, for such a nonequilibrium condition this method does not yield the temperature (or enthalpy) of the heavy species. The temperature and enthalpy of the heavy species can be determined by the relative line intensity method only when the gas is in thermal equilibrium.

A definition of terms used appears at the end of this article.

<i>Definition of terms</i>	
A	transition probability
A_c	cross-sectional area of duct
A_{th}	cross-sectional area at throat of nozzle
C	constant including instrument calibration factor and other physical constants not dependent on I or λ
E	energy level of excited states
g	statistical weight
h	enthalpy per unit volume of gas
$\Delta h_{nonequit}$	increment of enthalpy per unit volume contributed by nonequilibrium effect
h_{tot}	sum of the enthalpies of all species per unit volume including ionization
H_t	stagnation enthalpy per unit mass of gas
I	intensity of radiation for a spectral line
I_0	first ionization potential, for argon, $I_0/k = 3.29 \times 10^5 \text{ }^\circ\text{R}$ $= 1.829 \times 10^5 \text{ }^\circ\text{K}$
k	Boltzmann constant
\dot{m}	mass flow rate
N	particle number density, per unit volume
p_t	stagnation pressure
T	temperature

<i>Definition of terms (contd)</i>	
T_t	stagnation temperature
ΔT	temperature difference
u	gas velocity
α	ionization fraction, $\alpha = N_e/(N_e + N_a)$
λ	wavelength
μ	viscosity
ρ	density
<i>Subscripts</i>	
a	atoms
e	electrons
i	ions
h	heavy particles
g	gas

D. Analog Studies of Thermionic Reactor Dynamics, H. Gronroos

1. Introduction

A past SPS article on thermionic reactor kinetics and stability (SPS 37-41, Vol. IV, pp. 119-124) compared various system models employed in the analysis. Analytical and analog computer simulation methods were used to predict stability criteria, transients, and transfer functions. Recently, a digital computer code was written for transfer function evaluation, but employing linear system equations.

This article gives the equations used for analog simulation in the production calculations and some of the results. The analytical model is consistent with the preliminary study objective, which was to evaluate limited transient behavior and the general stability situation in a small liquid-metal-cooled space thermionic reactor. The simplifications leading to an analytically tractable description of the system are substantial. However, guided by past experiences from dynamics studies of other reactor types, the adopted description is expected to yield an acceptable first evaluation of the system behavior.

Figure 12 in "B. Reactivity Effects From Fuel Displacement in a Small Thermionic Reactor," shows the basic reactor reference design. The system is completed by adding in parallel the electric load and two heat-rejection loops, as shown by Fig. 27. Model expansions currently being pursued will result in a more accurate description

of the thermionic conversion process and will develop the control system simulation.

2. System Equations

The equations below were developed for a lumped parameter model, with the parameters assumed to be temperature independent. The general format is the same as that given in SPS 37-35, Vol. IV, pp. 180-188, but with

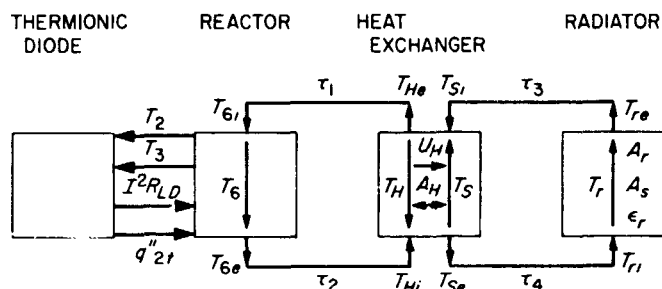


Fig. 27. Thermionic reactor space powerplant model

exceptions as listed. Table 8 gives the parameter values, while Figs. 27 and 28 define the geometry. Figures 29 and 30 show the simulated current-voltage characteristics and thermionic conversion performance. The analog simulation diagram is shown in Fig. 31.

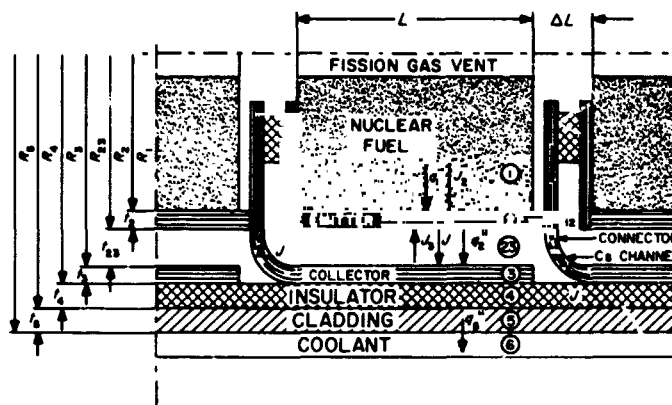


Fig. 28. In-pile thermionic module with series stacked diodes

Table 8. Initial values and parameters of thermionic reactor powerplant simulation model

Neutron kinetics								
Item	Symbol (unit)	Value	Values for delayed neutron groups					
Neutron density	n ($n \cdot \text{cm}^{-3}$)	10.0	$i = 1$	$i = 2$	$i = 3$	$i = 4$	$i = 5$	$i = 6$
Precursor density	C_i ($c_i \cdot \text{cm}^{-3} \cdot \text{s}$)		0.06727	0.9129	13.12	16.18	67.04	29.92
Fraction of delayed neutrons	$\alpha_i = \beta_i / \beta$	$\beta = 0.0064$	0.0261	0.1278	0.4079	0.1877	0.2135	0.0380
Precursor decay constant	λ_i (s^{-1})		3.88	1.40	0.311	0.116	0.0317	0.0127
Reactivity	ρ (β)	Variable						
Reactivity temperature coefficient	α_k ($\delta k / k \cdot ^\circ\text{K}^{-1}$)	Variable						
Conversion factor	γ ($\text{W} \cdot \text{n}^{-1}$)	8.178						
Thermionic diode heat transfer ^a								
Item	Symbol (unit)	Fuel (1)	Emitter (2)	Gap (23)	Collector (3)	Insulator (4)	Cladding (5)	Coolant (6)
Average temperature	T ($^\circ\text{K}$)	2150.00	2050.00		1300.00	1266.00	1232.00	1225.00
Volume	V (cm^3)							
Density	ρ ($\text{g} \cdot \text{cm}^{-3}$)	9.90	18.00		8.30	3.20	8.35	0.44
Heat capacity	c_p ($\text{W} \cdot \text{s} \cdot \text{g}^{-1} \cdot ^\circ\text{K}^{-1}$)	0.268	0.188		0.31	1.19	0.31	4.14
Thermal conductivity	k ($\text{W} \cdot \text{cm}^{-1} \cdot ^\circ\text{K}^{-1}$)	0.23	1.59	0.0165	0.63	0.0347	0.63	6.00
Outer radius	r (cm)	1.50	1.60	1.625	1.725	1.775	1.850	
Thickness	t (cm)		0.10	0.025	0.10	0.05	0.075	
Length	L, L' (cm)	5.00	5.00	5.00	5.00	5.00	6.00	6.00

^a See Fig. 28.

Table 8 (contd)

Thermionics					
Item	Symbol (unit)	Value	Item	Symbol (unit)	Value
Net current density	I ($A \cdot cm^{-2}$)	10.0	Diode electric load	R_{LD} ($\Omega \cdot cm^2$)	0.06
Emitter to collector current	J_2 ($A \cdot cm^{-2}$)	11.0	Collector work function	ϕ_2 (eV)	2.10
Collector back emission	J_3 ($A \cdot cm^{-2}$)	1.0	Boltzmann constant/electron charge	k_B/e (eV \cdot $^\circ K^{-1}$)	$8.616 \cdot 10^{-5}$
Diode voltage	V (V)	0.6	Stefan-Boltzmann constant	σ_{SB} ($W \cdot cm^{-2} \cdot ^\circ K^{-4}$)	$5.67 \cdot 10^{-12}$
Diodes in series	N_{DS}	5.0	Emitter and collector emissivity	ϵ_2, ϵ_3	0.3
Diode assemblies in parallel	N_{DP}	50.0			
Primary coolant loop					
Item	Symbol (unit)	Value	Item	Symbol (unit)	Value
Reactor coolant inlet temperature	T_{ri} ($^\circ K$)	1200.0	Heat exchanger inlet temperature	T_{Hi} ($^\circ K$)	1250.0
Reactor coolant exit temperature	T_{re} ($^\circ K$)	1250.0	Heat exchanger exit temperature	T_{He} ($^\circ K$)	1200.0
Coolant flow rate	w_c ($g \cdot s^{-1}$)	75.3	Heat exchanger median temperature	T_H ($^\circ K$)	1225.0
Coolant transport delay	τ_1, τ_2 (s)	0.1	Heat exchanger primary side mass	M_H (kg)	29.5
Coolant channel velocity	v_c ($cm \cdot s^{-1}$)	117.0	Heat exchanger heat capacity	c_{pH} ($W \cdot s \cdot g^{-1} \cdot ^\circ K^{-1}$)	0.837
Primary coolant loop					
Item	Symbol (unit)	Value	Item	Symbol (unit)	Value
Heat exchanger secondary temperature	T_s ($^\circ K$)	1185.0	Radiator temperature	T_r ($^\circ K$)	1185.0
Heat exchanger secondary inlet temperature	T_{si} ($^\circ K$)	1155.0	Radiator inlet temperature	T_{ri} ($^\circ K$)	1235.0
Heat exchanger secondary outlet temperature	T_{se} ($^\circ K$)	1235.0	Radiator exit temperature	T_{re} ($^\circ K$)	1155.0
Heat exchanger secondary side mass	M_s (kg)	29.5	Radiator pipe length	L_r (cm)	200.0
Heat exchanger heat capacity	c_{ps} ($W \cdot s \cdot g^{-1} \cdot ^\circ K^{-1}$)	0.837	Radiator armor cross-section	A_s (cm^2)	1.26
Total coolant flow rate	w_{LT} ($g \cdot s^{-1}$)	1564.0	Armor density	ρ_r ($g \cdot cm^{-3}$)	8.35
Coolant transport delay	τ_2, τ_1 (s)	0.1	Radiator emissivity	ϵ_r	0.8
Coolant flow rate in radiator pipe	w_r ($g \cdot s^{-1}$)	31.3	Radiation area (one pipe)	A_r (cm^2)	1420.0

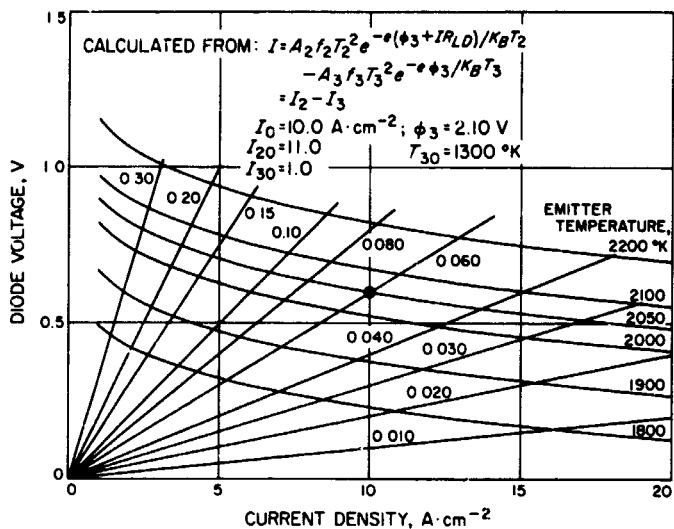


Fig. 29. Diode current-voltage characteristics

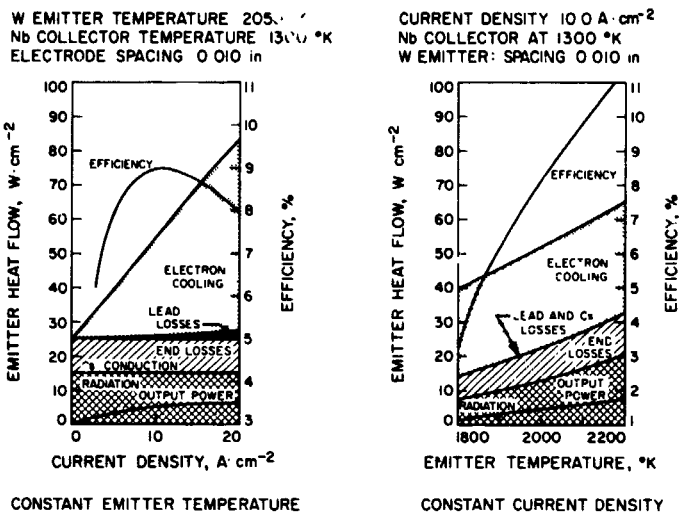


Fig. 30. Emitter heat flow and diode efficiency

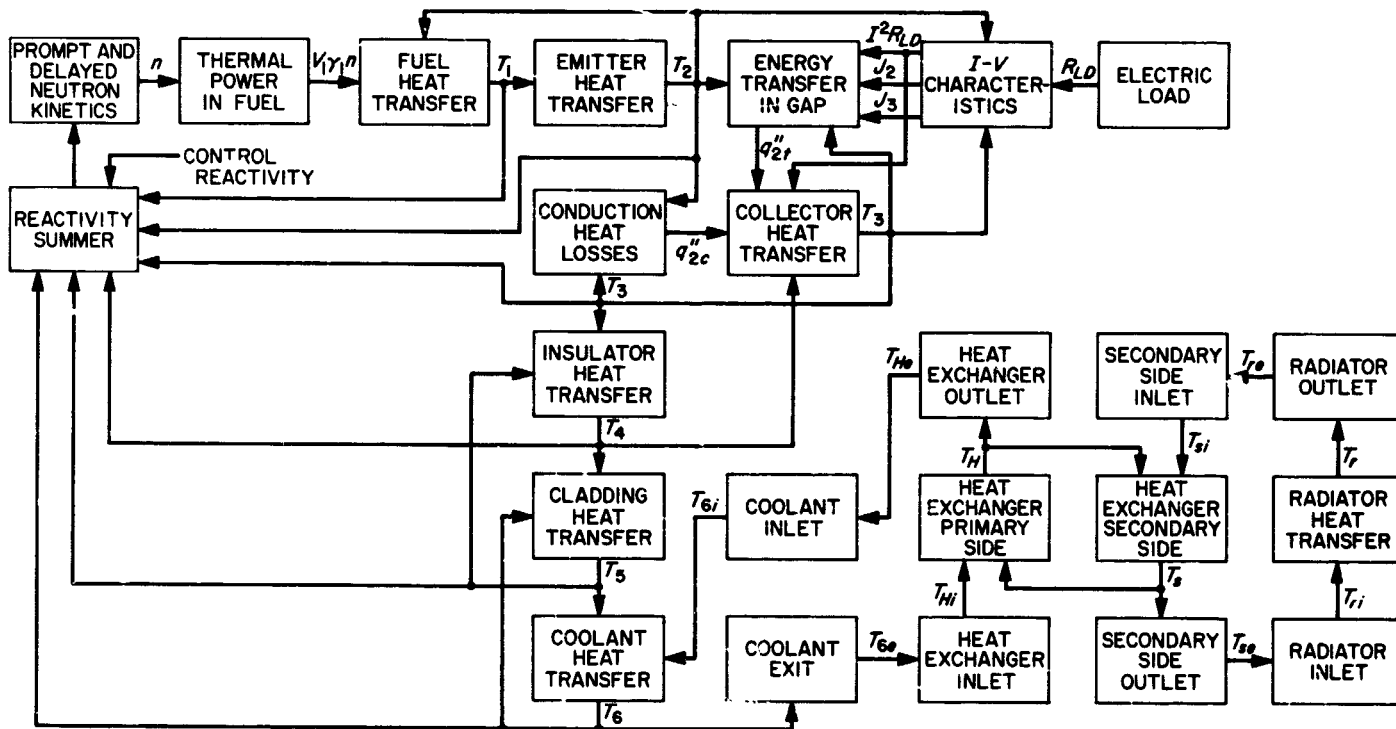


Fig. 31. Analog computer simulation of space thermionic reactor powerplant

The analytical description of the thermionics is the most approximate. If the emitter and collector temperature variations are kept within $\pm 150^\circ\text{K}$ (except for the open-circuit condition), the current density variations within $\pm 7 \text{ A} \cdot \text{cm}^{-2}$, and the cesium temperature variations are less than $\pm 10^\circ\text{K}$, the description gives a reasonable characterization of the thermionic performance.

Other limitations arise from the assumption of constant parameters and lumping the spatial regions. The frequency response above $\sim 1 \text{ Hz}$ is therefore of limited quantitative accuracy. However, the relevant frequency range for the present studies is below the 1 Hz value.

The equations in the analog simulation were:

(a) Neutron kinetics

$$n = \frac{\sum_{i=1}^6 \lambda_i C_i}{1 - \rho} ; C_i = c_i \Lambda \quad (1)$$

$$\frac{dC_i}{dt} = a_i n - \lambda_i C_i \quad (2)$$

$$\rho = \rho_{control} + \sum_k \alpha_k [T_k - T_{k0}] \quad (3)$$

Eq. (1) linearized becomes

$$\delta n = \rho \cdot n_0 + \sum_{i=1}^6 \lambda_i C_i - n_0 \quad (4)$$

(b) Region 1, nuclear fuel

$$V_1 \rho_1 c_{p1} \frac{dT_1}{dt} = V_1 \gamma_1 n - 8 \pi L k_1 (T_1 - T_2) \quad (5)$$

(c) Region 2, emitter

$$V_2 \rho_2 c_{p2} \frac{dT_2}{dt} = 8 \pi L k_1 (T_1 - T_2) - 2 \pi r_2 L q_2'' \quad (6)$$

$$q_2'' = q_2'' + q_2'' = 57.5 \text{ W} \cdot \text{cm}^{-2} \text{ at } t = 0 \quad (7)$$

(d) Region 23, interelectrode gap

$$q_{2t}'' = I(IR_{LD} + \phi_3) + \frac{2 k_B}{e} (J_2 T_2 - J_3 T_3) + \frac{\sigma_{SB}}{\frac{1}{\epsilon_2} + \frac{1}{\epsilon_3} - 1} (T_2^4 - T_3^4) \quad (8)$$

$$q_{2c}'' = h_{23} (T_2 - T_3) \quad (9)$$

(e) Current-voltage characteristics

$$I = A f_2 T_2^2 \exp -e(\phi_3 + IR_{LD})/kT_2 - A f_3 T_3^2 \exp -e\phi_3/kT_3 \quad (10)$$

$$= J_2 - J_3$$

(f) Region 3, collector

$$V_3 \rho_3 c_{p3} \frac{dT_3}{dt} = 2 \pi r_2 L [q_{2t}'' + h_{23} (T_2 - T_3) - I^2 R_{LD}] - 4 \pi r_{23} \frac{k_3}{t_4} (T_3 - T_4) \quad (11)$$

(g) Region 4, insulator

$$V_4 \rho_4 c_{p4} \frac{dT_4}{dt} = 4 \pi r_{34} \frac{k_4}{t_4} (T_3 - T_4) - 4 \pi r_{34} L \frac{k_4}{t_4} (T_4 - T_5) \quad (12)$$

(h) Region 5, cladding

$$V_5 \rho_5 c_{p5} \frac{dT_5}{dt} = 4 \pi r_{34} L \frac{k_4}{t_4} (T_4 - T_5) - 2 \pi r_5 L' h_{56} (T_5 - T_6) \quad (13)$$

(i) Region 6, coolant in reactor

$$N_{DS} V_6 \rho_6 c_{p6} \frac{dT_6}{dt} = N_{DS} h_{56} 2 \pi r_5 L' (T_5 - T_6) - 2 w_6 c_{p6} (T_6 - T_{6i}) \quad (14)$$

$$T_6 = \frac{1}{2} (T_{6e} + T_{6i}) \quad (15)$$

$$\tau_1 \frac{dT_{6i}}{dt} = T_{6i} + T_{H1} - 2 T_{H1} \quad (16)$$

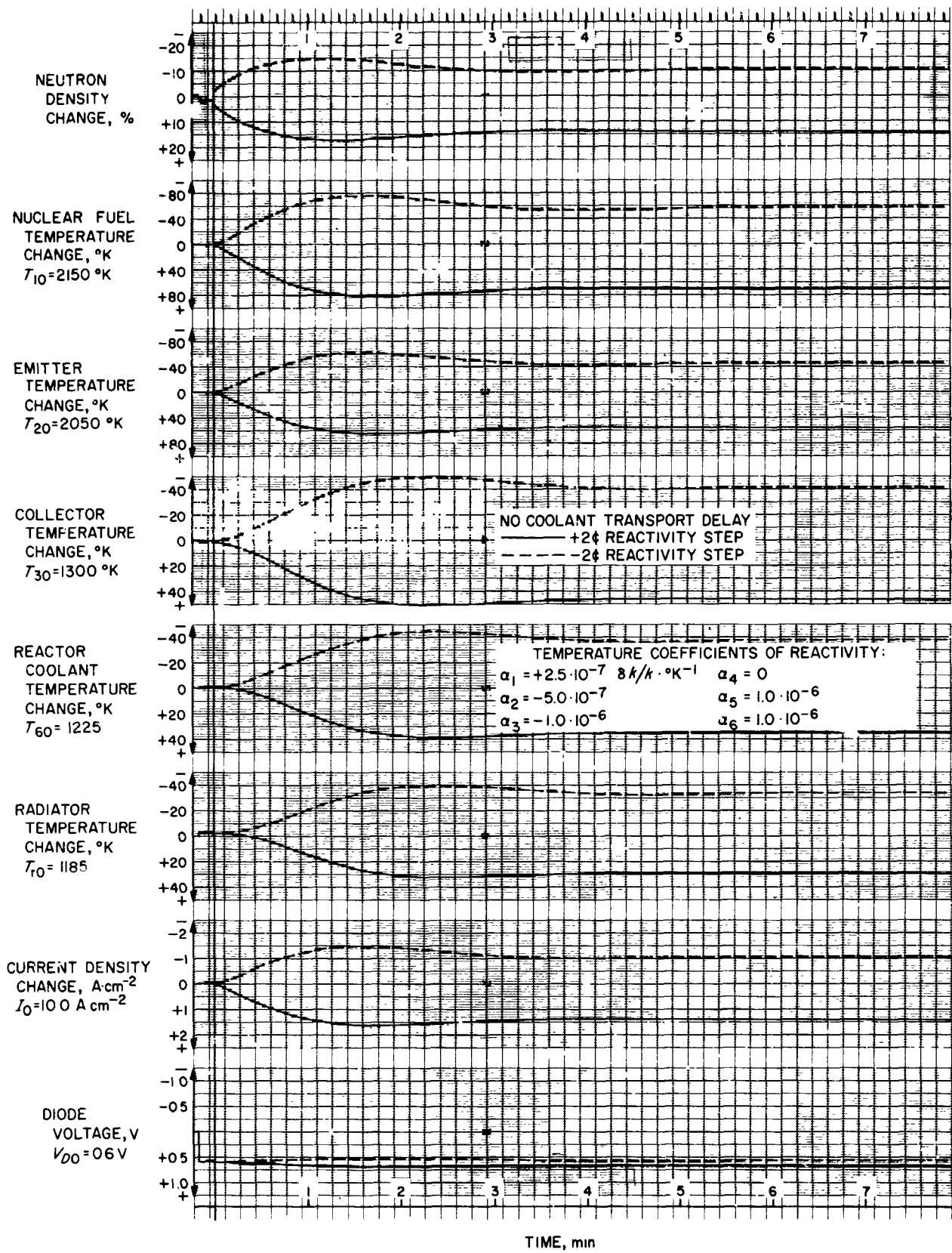


Fig. 32. Response to a 2-c step reactivity perturbation in a space thermionic reactor powerplant

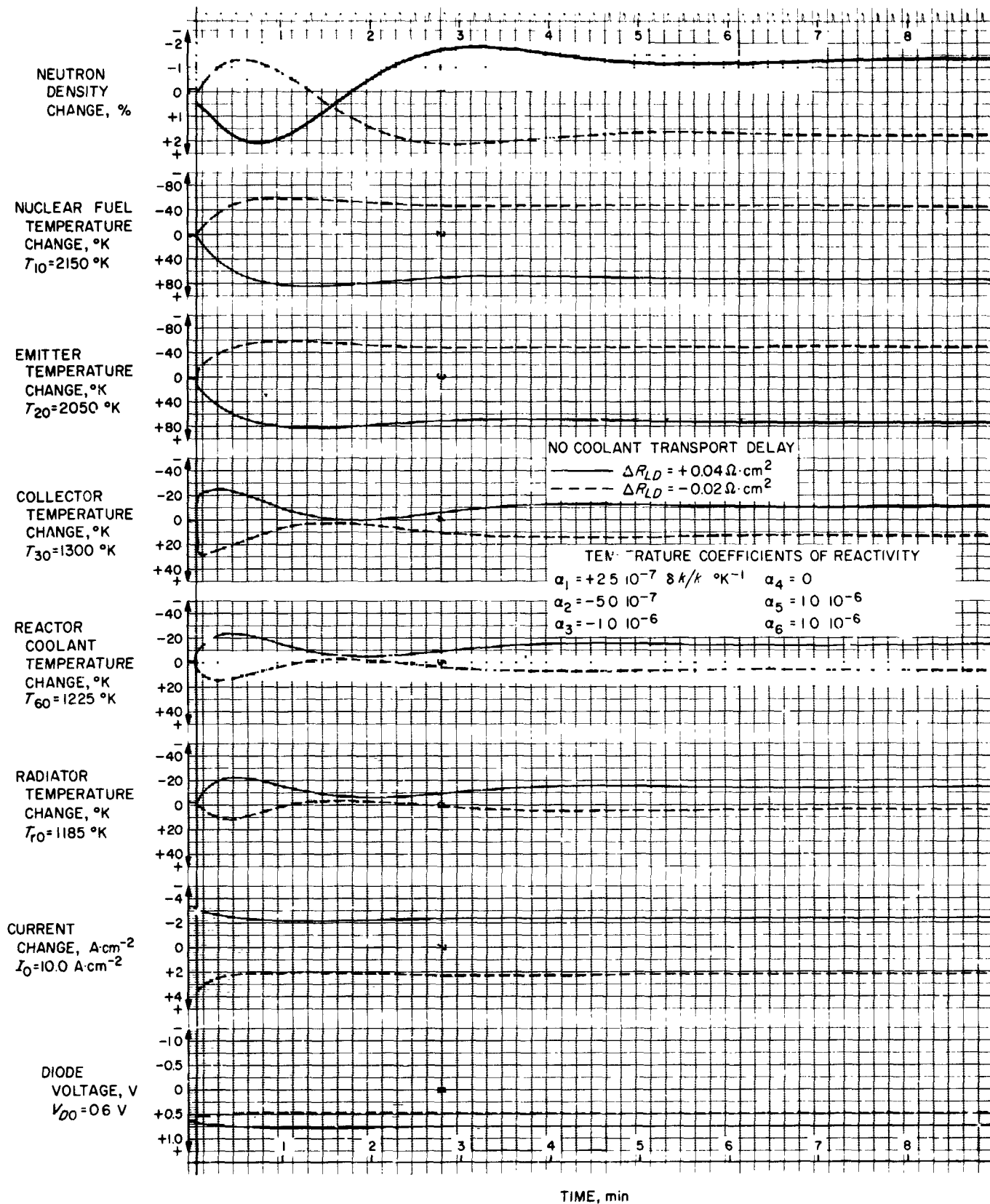


Fig. 33. Response to step electric load perturbations in a space thermionic reactor powerplant

(j) Primary loop

$$\tau_2 \frac{dT_{Hi}}{dt} = T_{Hi} + T_{Hi} - 2T_0 \quad (17)$$

$$T_H = \frac{1}{2} (T_{He} + T_{Hi}) \quad (18)$$

$$M_H c_{pH} \frac{dT_H}{dt} = N_{DP} w_0 c_{p0} 2(T_{Hi} - T_H) - U_H A_H (T_H - T_s) \quad (19)$$

(k) Secondary loop

$$M_s c_{ps} \frac{dT_s}{dt} = U_H A_H (T_H - T_s) - 2 w_{Li} c_{pLi} (T_s - T_{si}) \quad (20)$$

$$\tau_4 \frac{dT_{ri}}{dt} = T_{ri} + T_{si} - 2T_s \quad (21)$$

$$T_r = \frac{1}{2} (T_{re} + T_{ri}) \quad (22)$$

$$\tau_3 \frac{dT_{si}}{dt} = T_{si} + T_{ri} - 2T_r \quad (23)$$

$$L_r A_s \rho_r c_{pr} \frac{dT_r}{dt} = 2 w_{Li} c_{pLi} (T_{ri} - T_r) - \epsilon_r \sigma_{SB} A_r T_r^4 \quad (24)$$

3. Transient Studies

Figures 32 and 33 show representative trajectories for reactivity perturbations and electric load perturbations, respectively. The legends for the various curves are listed on the figures. The chosen set of reactivity feedback coefficients were deemed plausible. However, there is a large uncertainty in these coefficients, as Fig. 34 illustrates for the fuel and emitter doppler coefficients. Because of this, the feedback coefficients were treated as variables, and various combinations were tried to determine stability ranges, as discussed in Sect. 4. In general, for stable combinations and small perturbations, the change in the equilibrium operating point is relatively large because of the small feedback effects. More interesting are the studies on diode and reactor open-circuit casualties. The former type of failure will probably occur frequently. It is therefore important to design the system

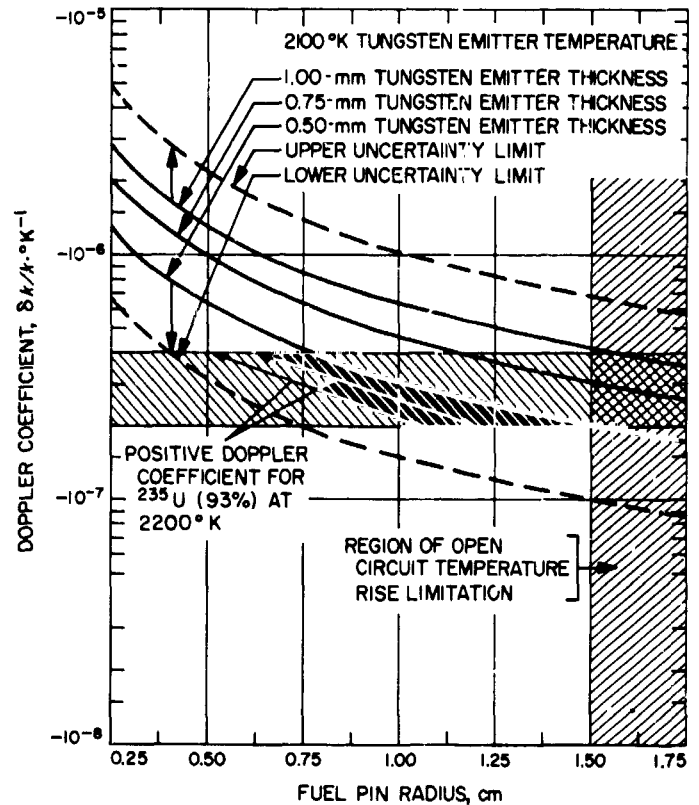


Fig. 34. Doppler coefficient for tungsten emitters as function of fuel pin radius and emitter thickness

to tolerate this. Figure 35 shows the trajectories for these casualties, with expected feedback coefficients.

Trajectories have also been taken with a model where the fuel was divided into six radial regions, instead of lumped into one. With UC fuel, the difference between the models for the change in average fuel temperature is only a few degrees because of the relatively large thermal conductivity. Figure 36 illustrates the temperature profile during an open-circuit transient.

4. Stability

One of the main objectives in the studies was to investigate the stability of the system. Both the analytical evaluations and the analog computer simulations imply that only the zero-frequency point needs to be investigated when determining basic stability. This holds for the expected range of feedback coefficients in a small liquid-metal-cooled system. The zero-frequency asymptotic stability criterion amounts to requiring that the zeroth order term a_n in the general linear equation

$$a_0 \frac{d^n x}{dt} + a_1 \frac{d^{n-1} x}{dt} + \dots + a_{n-1} \frac{dx}{dt} + a_n x = 0$$

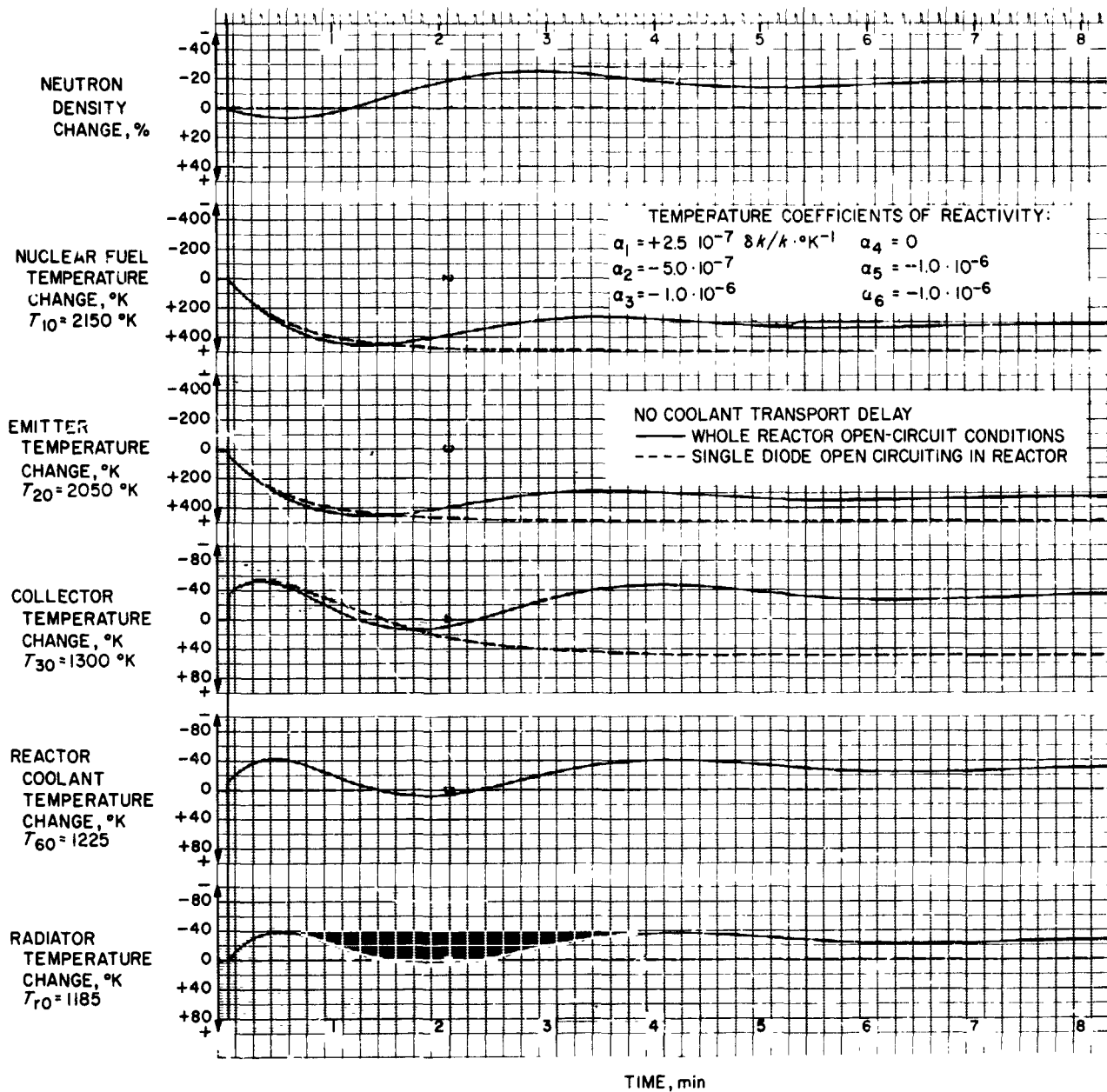


Fig. 35. Open-circuit response in a space thermionic reactor powerplant

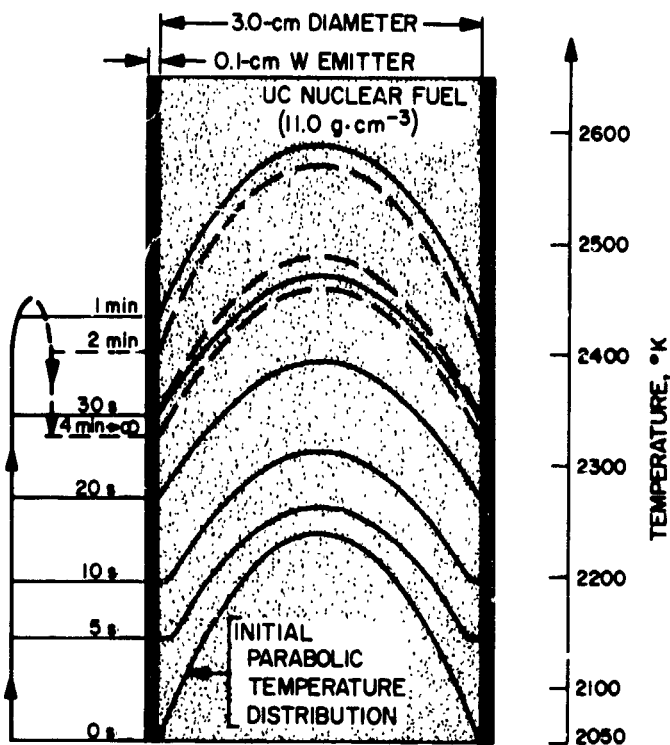


Fig. 36. Reactor open-circuit temperature rise in nuclear fuel and emitter with expected feedback

be larger than zero. The other conditions arising from the Routh-Hurwitz array are neglected. The latter will restrict the stability region, but for the system under study, become important only for unrealistically high positive and negative feedback coefficients. When this was postulated, the analog computer yielded oscillatory trajectories or spirals.

Summarizing in one expression the zero-frequency condition, one obtains

$$n_0 \sum_i \alpha_i \frac{dT_i}{dn} = \frac{n_0}{k} \frac{\delta k}{dn} < 0 \quad (25)$$

where

n_0 = equilibrium neutron density,

T_i = temperature in reactor region i ,

α_i = temperature coefficient of reactivity in reactor region i .

The weighting factors dT_i/dn are calculated from the equilibrium condition ($dT_i/dt = 0$). If the fuel is the only

region with positive feedback, it is of interest to express Eq. (25) in terms of the ratio of the fuel and emitter feedback coefficients thus

$$\frac{\alpha_1}{\alpha_2} \leq \frac{dT_2}{dT_1} + \sum_{i \geq 3} \frac{\alpha_i}{\alpha_2} \frac{dT_i}{dT_1} \quad (26)$$

Further developed in terms of the design parameters for fuel and emitter, one obtains after simplifications

$$\frac{\alpha_1}{\alpha_2} = \frac{1 + \sum_{i \geq 3} \frac{\alpha_i}{\alpha_2} \frac{dT_i}{dT_1}}{\frac{D_2 \theta}{8k_1} + 1} \quad (27)$$

where

D_2 = diameter of fuel-emitter assembly

k_1 = fuel thermal conductivity (k_2 assumed much larger)

θ = measure of heat transfer variations with temperature for the interelectrode gap

= 0.10–0.15

$\sum_{i \geq 3}$ = contributions from regions $i \geq 3$ (generally a small positive number).

A plot of Eq. (27) with $\sum_{i \geq 3} = 0$ as applied to the complete model is shown in Fig. 37. The uncertainties arising from the doppler coefficients are also indicated in Fig. 37. The general shape of the curves in Fig. 37 have been confirmed with the analog computer both for linear and nonlinear models. Computer measured ratios of α_1/α_i are shown in Table 9. The constant coolant inlet temperature model gives the most conservative stability ratio estimate. That the simple expression [Eq. (27)] is not applicable for large values of the feedback coefficients is shown by Fig. 38, which gives the computer-measured stability regions for α_3 versus $(\alpha_1 + \alpha_2)$ for various models. The curve for the complete model shows a knee at $\alpha_3 = -4 \cdot 10^{-6} \delta k/k \cdot ^\circ K^{-1}$. The large radiator mass introduces a thermal time constant leading to a resonance peak at about 0.007 Hz.

5. Conclusions

Within the constraints inherent in the simulation model the following may generally be stated about the dynamics

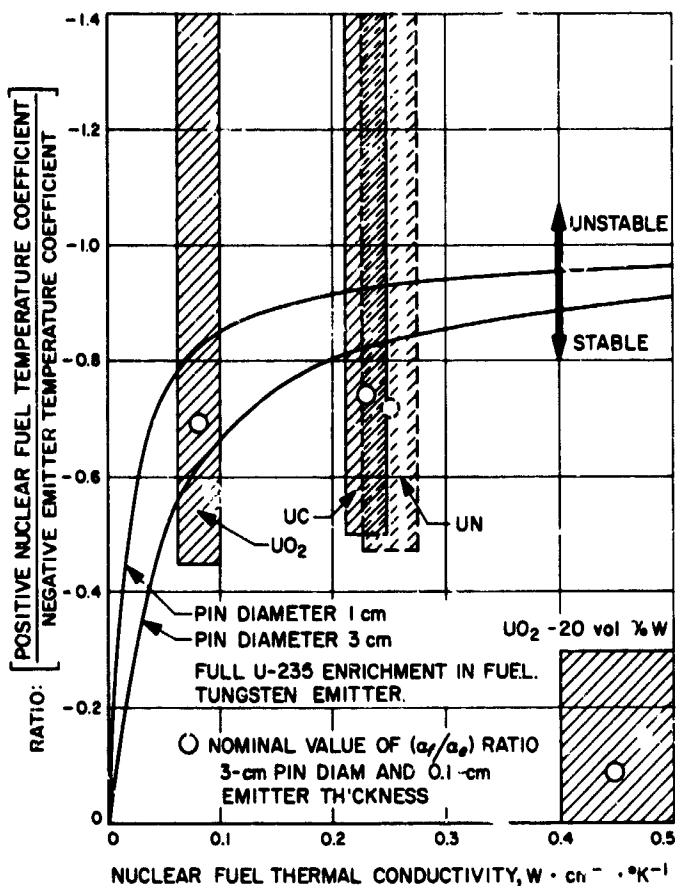


Fig. 37. Ratio of positive nuclear fuel temperature coefficient to negative emitter temperature coefficient for zero-frequency asymptotic stability

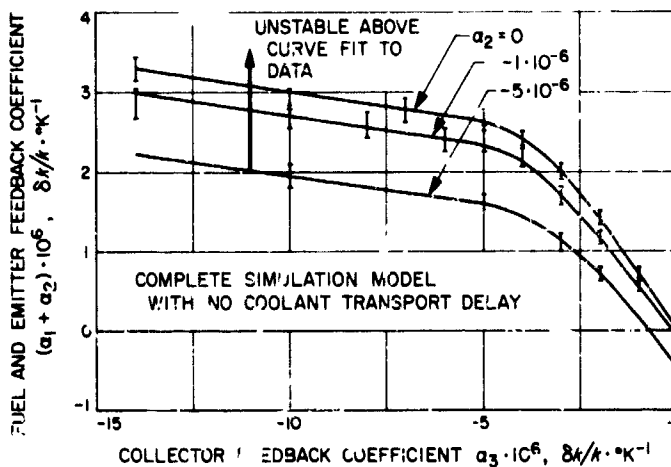


Fig. 38. Stability in space thermionic reactor powerplant as measured on analog simulation

of a small liquid-metal-cooled thermionic space reactor powerplant:

(1) In a stable system the transients from minor electric load and reactivity perturbations are damped

and can be handled by the control system. The generally small feedback leads to a relatively large change in operating point even for minor reactivity perturbations necessitating active control.

(2) In a stable system, open-circuit casualties lead to fast fuel and emitter temperature increases. Should the whole reactor open circuit, the resulting temperature rise appears slow enough to be controllable without damage to the reactor.

(3) The large uncertainties in the doppler coefficients for the fissile isotopes and refractory metals at the present time do not allow a final conclusion with regard to inherent stability. This applies only to highly enriched unalloyed nuclear fuels. However, even pessimistic estimates of doppler magnitudes so far have indicated stable systems for the reactors investigated. The system can tolerate a positive fuel temperature coefficient if stabilizing negative

Table 9. Analog computer measured values of temperature coefficient ratios for zero-frequency asymptotic stability

Region	$\frac{\alpha_1}{\alpha_2} = \frac{\text{Positive fuel temperature coefficient}}{\text{Negative structure region temperature coefficient}}$		
	No coolant transport time delay	Constant reactor coolant inlet temperature	Constant heat exchanger secondary coolant inlet temperature
Emitter	0.92	0.70	0.75
Collector	0.68	0.25	0.30
Insulator	0.62	0.18	0.20
Cladding	0.54	0.17	0.18
Coolant	0.51	0.09	0.11

5 to 10% accuracy on measured data.

contributions are provided from other regions. Various methods to increase the negative feedback are available, and may be required to protect the reactor from prompt criticality accidents.

- (4) The zero-frequency asymptotic stability criterion appears adequate when investigating inherent stability.

E. Flow Visualization Studies Demonstrating the Effects of a Transverse Gas Velocity on a Glow Discharge, J. A. Gardner

1. Introduction

A complete analytical description of the phenomena associated with the fluid dynamics, the energy transfer, and the electrodynamics that occur in an electrical propulsion or power generation device such as an MPD arcjet or an MHD accelerator is difficult to establish realistically. In order to eventually achieve a more comprehensive understanding of the many combinations of processes that occur in the electrical discharge region and at the electrode surfaces of such devices, an investigation has been initiated which first allows visual observation and measurements to be made of some of the influencing factors such as the effect of a transverse gas velocity, pressure, and applied electric field strength on the behavior of the discharge. It is anticipated that these results will then provide a basis for establishing more comprehensive experimental and theoretical methods of investigating the complex interactions of the processes that occur near electrode surfaces, particularly those related to the transfer of energy. The objective of the investigation discussed in this note was to determine in a qualitative sense the influence of a transverse velocity on a glow discharge without applied magnetic fields. In addition, the effects of a change in the static pressure with a constant gas velocity were also observed. Thiene (Ref. 15) and Thiene, Chambers, and von Jaskowsky (Ref. 16) have reported analytical and experimental investigations on the convective flexure of a plasma conductor. Their experiments, however, were conducted at much lower gas velocities, larger currents (about 2 A) and pressures near and above atmospheric.

2. Experimental Apparatus

The apparatus used for this investigation is illustrated in Fig. 39. A pair of copper electrodes with flat parallel surfaces were enclosed in a six-port glass test chamber. A subsonic two-dimensional Lucite nozzle, which is

barely visible in the photograph, was located with its throat adjacent to the left edge of the electrodes. The nozzle, shown in more detail in Fig. 40, had throat dimensions of 0.50×2.00 in. The argon gas flow entered the glass test chamber through the inlet duct and passed between the electrode surfaces after leaving the nozzle. From the electrode region the gas flowed into the exhaust duct and the vacuum system.

The high-voltage direct-current power supply used in these studies consisted of a primary controlled transformer, a full-wave rectifier, and two $4\text{-}\mu\text{F}$ capacitors used as filters. The upper limit of the voltage for this variable power supply was approximately 7,000 V.

3. Experimental Procedure and Results

To provide a basis for comparison, initial investigations were performed in the absence of flow. Tests with argon were conducted at three static pressures inside the glass test chamber: 50, 100, and 200 mmHg. Photographs of the discharge between the electrodes at these pressures with zero gas velocity and a current of 15 mA are shown in Figs. 41(a), (b), and (c). The plasma column appears vertical and perpendicular to the electrode surfaces at the two lower pressures but slightly canted at the highest pressure. It is evident that the visible discharge decreases in diameter as the pressure is increased and that at the highest pressure the diameter increased from the cathode located at the bottom to the anode located at the top. At zero velocity the stability of the discharge was not affected in the 50 to 200 mmHg pressure range. The voltage drop across the gap between the electrodes was approximately 400 V.

The effect of a transverse gas velocity on the configuration of the discharge at a pressure of 100 mmHg and a current of 15 mA is shown in Figs. 42(a), (b), and (c) for gas velocities of 84, 127 and 220 ft/s. Corresponding argon mass flow rates were 0.0084, 0.0125, and 0.0216 lb/s. The velocity distribution across the nozzle exit plane was determined by a pitot tube and was found to be uniform. It is evident that a substantial distortion of the column occurs by the motion of the gas and that the distortion is increased as the gas velocity is increased. With a flowing gas at this pressure the entire column became visible, the column attached to the trailing edge of the anode, and the size of the bright spot on the cathode surface increased but did not appear to be dependent on velocity. Furthermore, a bright region appeared along the trailing surface of the cathode. The thickness of the distorted glow was approximately $\frac{1}{16}$ in. and was essentially planar.

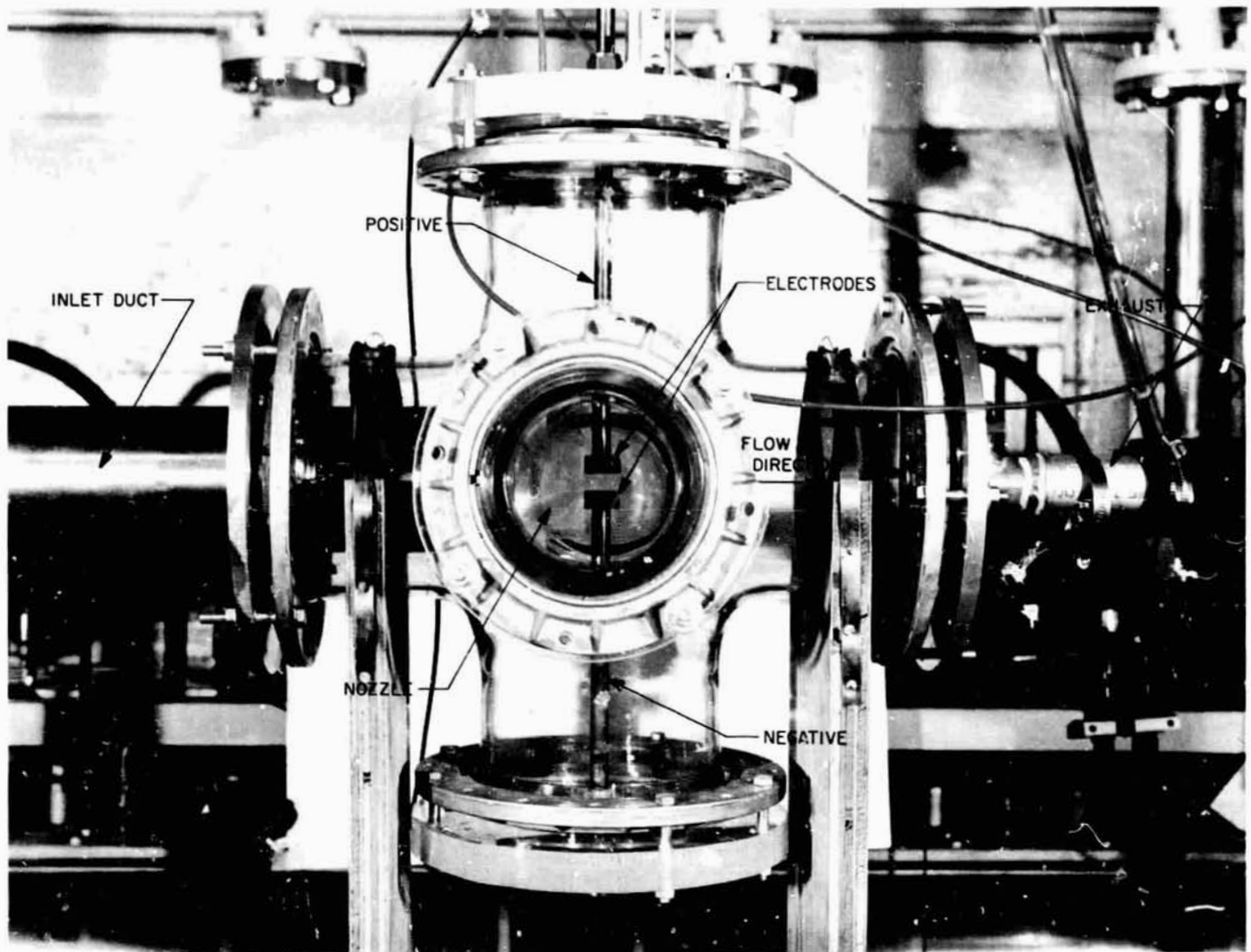


Fig. 39. Experimental apparatus for the study of velocity and pressure effects on glow discharge phenomena

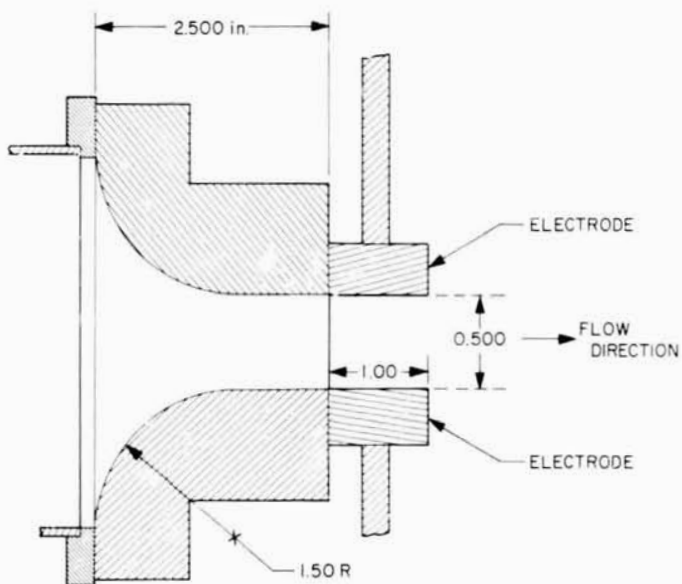


Fig. 40. Two-dimensional subsonic nozzle and electrode configuration

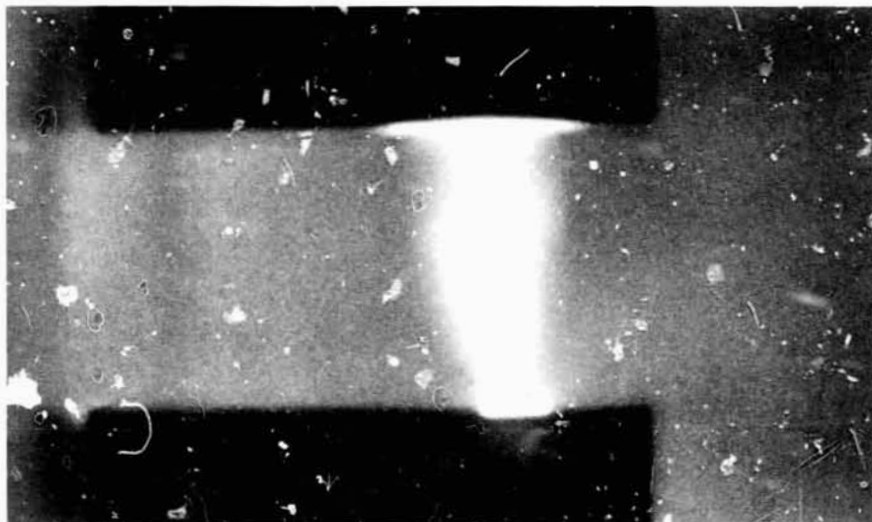
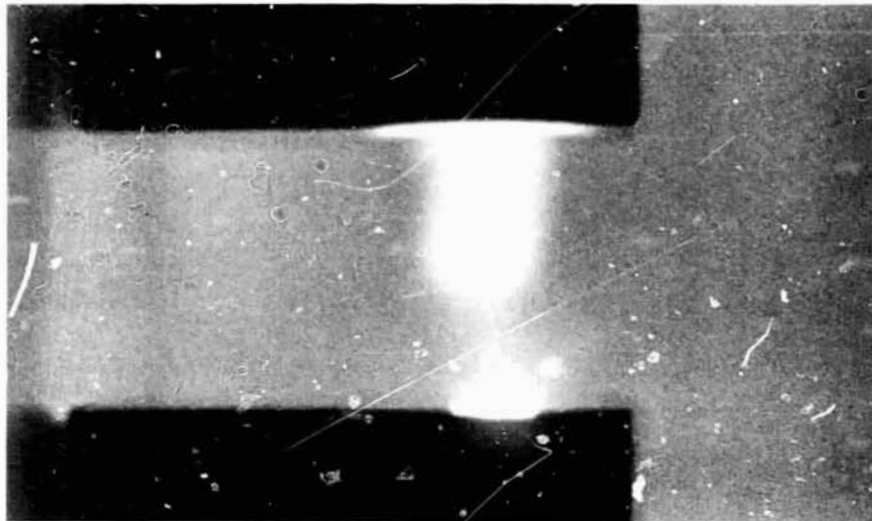
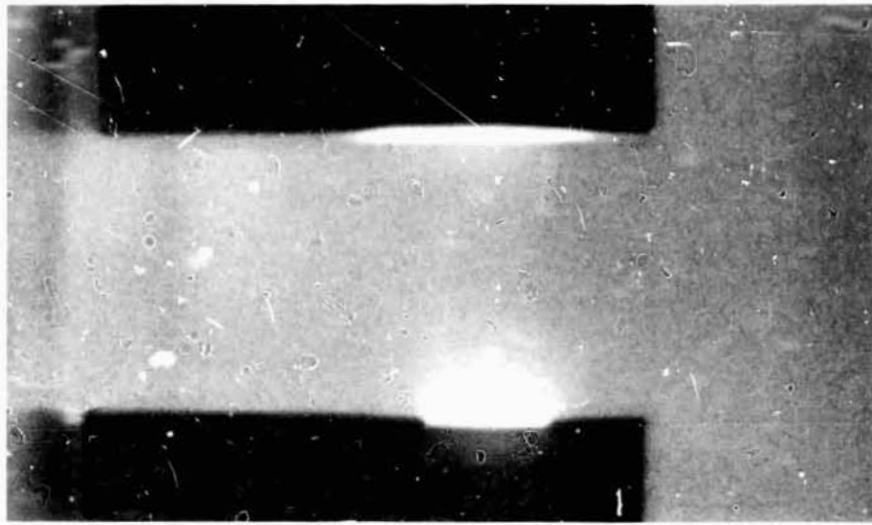


Fig. 41. Glow discharge in the absence of argon gas flow for an electrode separation of 0.500 in. and a discharge current of 15 mA (a) 50 mmHg, (b) 100 mmHg, and (c) 200 mmHg

BLANK PAGE

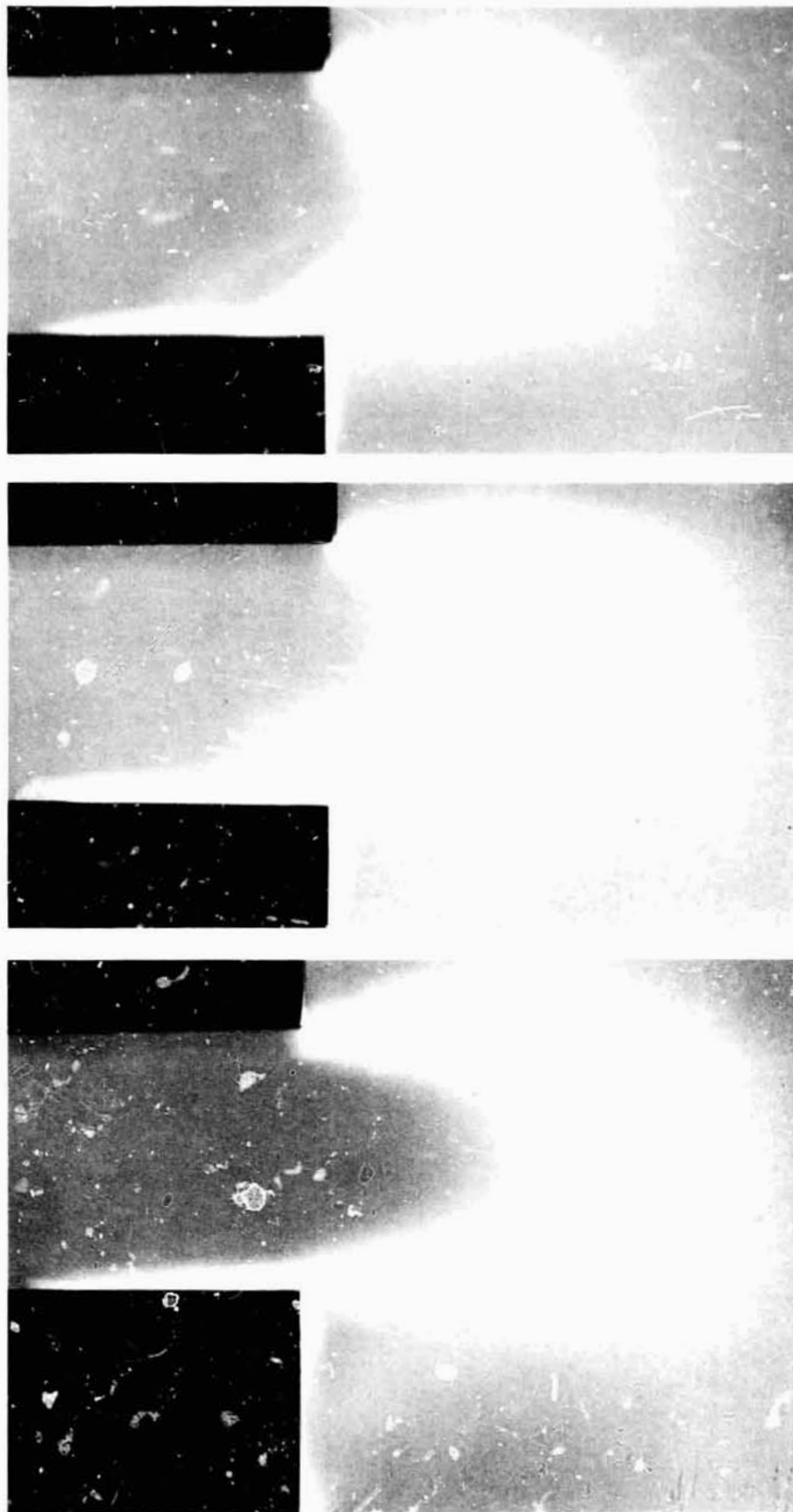


Fig. 42. Glow discharge in the presence of argon gas flow for an electrode separation of 0.500 in., discharge current of 15 mA and static pressure of 100 mmHg. Gas velocities are (a) 84 ft/s, (b) 127 ft/s, and (c) 220 ft/s

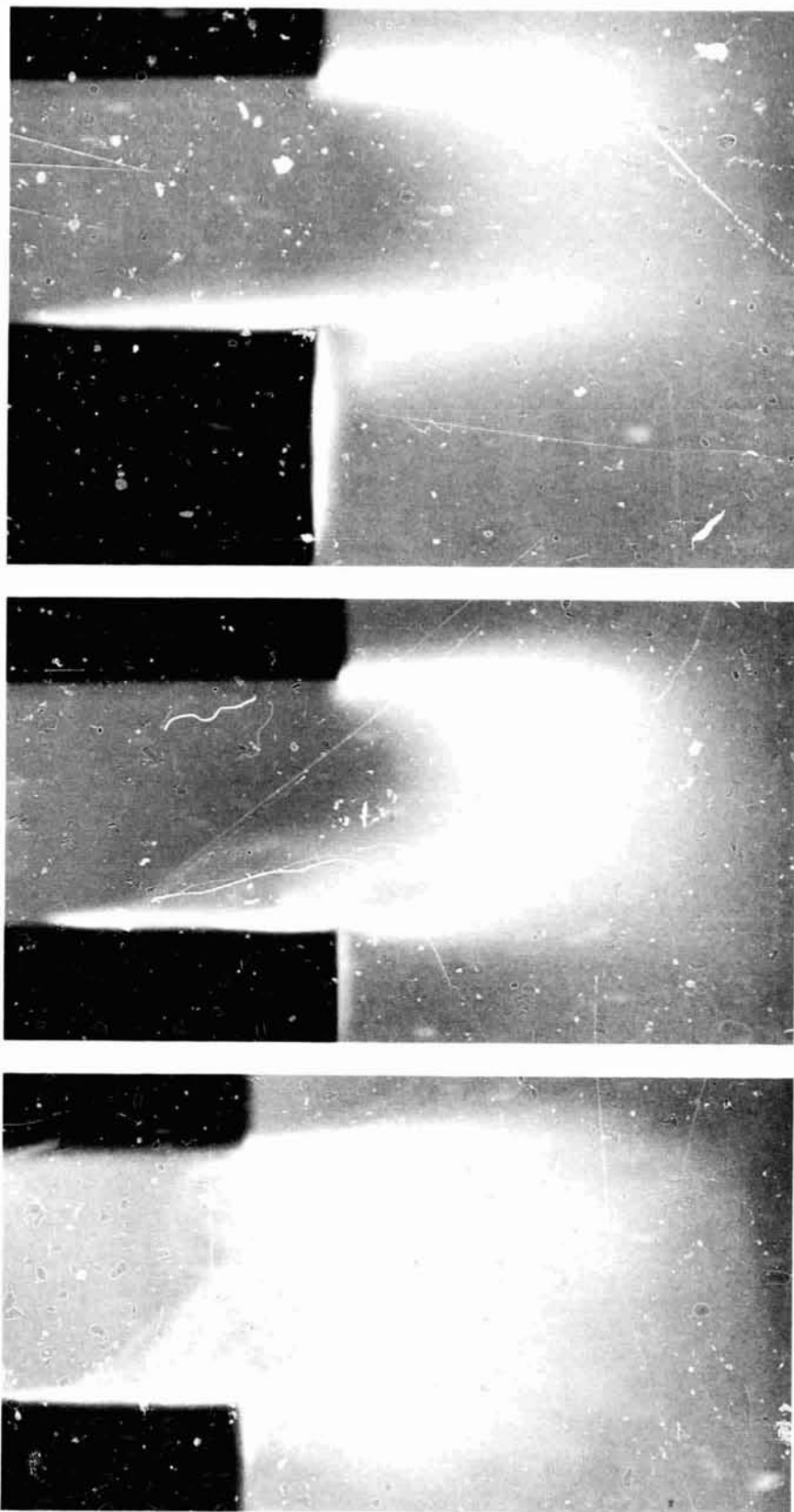


Fig. 43. Glow discharge in the presence of argon gas flow for an electrode separation of 0.500 in., discharge current of 15 mA and gas velocity of 127 ft/s. Static pressures are (a) 50 mmHg, (b) 100 mmHg, and (c) 200 mmHg

The color of the discharge changed as the velocity increased indicating a possible change in excitation. Also, the plasma column fluctuated whenever there was gas flow.

At a gas velocity of 127 ft/s and a discharge current of 15 mA, the effect of pressure is shown in Figs. 43(a), (b), and (c) for pressures of 56,102 and 203 mmHg. It is evident that as the pressure was increased the intensity of the discharge increased and that at the highest pressure the fluctuations were greatest. Also, the extent of the bright region along the trailing surface of the cathode decreased as the pressure was increased.

4. Summary and Conclusions

An elementary experimental investigation of the effects of pressure and a transverse subsonic gas velocity on the structure of a glow discharge between parallel electrode surfaces has shown that the effects are large. Pressures ranged between approximately 50 and 200 mmHg and argon gas velocities ranged between about 80 and 220 ft/s. The transverse flow of gas caused the discharge to distort into a U-shape and attach to the trailing edge of the anode. Also, the cathode bright spot was increased in size and extended around the trailing edge covering at least a portion of the trailing surface. The U-shaped discharge was planar and about $\frac{1}{16}$ in. thick. An increase in pressure without gas flow caused the cathode bright spot and the diameter of the discharge to decrease. At a gas velocity of 127 ft/s an increase in pressure reduced the size of that portion of the cathode bright spot that was visible along the trailing surface and increased the fluctuating motion of the discharge.

F. Influence of Swirl on the Velocity Distribution in a Constant-Diameter Duct When the Swirling Flow Is Injected Perpendicular to the Axis of the Duct, P. F. Massier and E. J. Roschke

1. Introduction

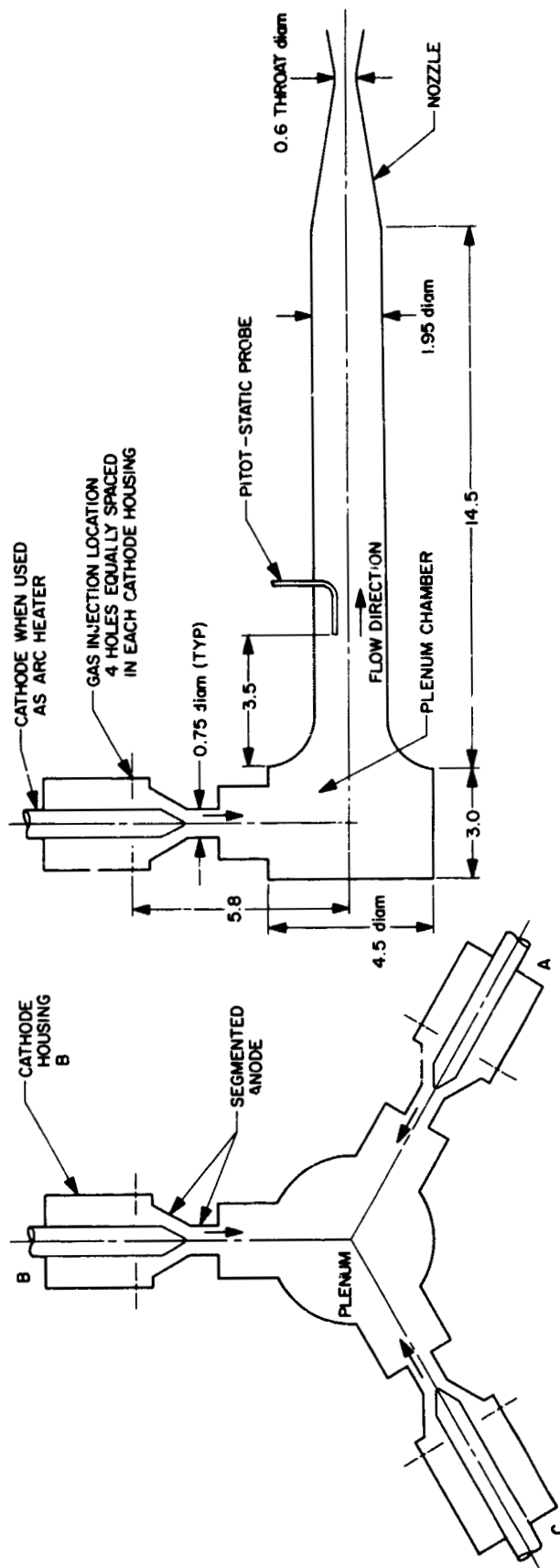
An objective of the current plasma heat-transfer investigations is to determine the influence of ionization on convective heat transfer. In the experiments argon is ionized by means of an electric-arc heater from which the heated gas then flows through the test sections. The upper bound of the mixed gas temperature can be increased and under certain conditions fluctuations in the flow can be reduced by introducing swirl into the flow

before the gas passes through the arc region. However, the swirl component of the velocity causes the convective heat transfer to increase (SPS 37-24, Vol. IV) and introduces fluid dynamic complexities into the flow field that are difficult to analyze. Therefore, it is desirable to somehow provide means for dissipating the swirl after the gas has been heated whenever simpler more uniform flows are to be investigated.

An effective method of causing the injected vortex to dissipate is to force the swirling fluid to negotiate a sharp 90-deg turn. The present discussion pertains to two types of experiments that have been conducted on the influence of sharp turns on swirling fluid motion at approximately room temperature. The first of these experiments is associated with three impinging, swirling jets of argon introduced to a plenum chamber as shown in Fig. 44, with the axis of symmetry of the plenum perpendicular to the axes of the swirling jets. From the plenum the mixed fluid expanded into a constant-diameter duct in which radial traverses were made with pitot-static probes so that velocity distributions could be determined. The average gas velocity in the duct was about 55 ft/s, and the Reynolds numbers were approximately 9,000 and 26,000. The results are compared with those obtained when nonswirling fluid was injected radially into the plenum. The second set of experiments was conducted with dye injected into swirling water and visually observing the flow patterns as the water negotiated a sharp turn. This test apparatus which differed from that of the argon experiments was constructed of Lucite and is shown in Fig. 45.

2. Argon Gas Experiments

To determine the radial distributions of axial velocity in the 1.95-in.-diam duct at the axial location shown in Fig. 44, pitot-static probes were used which were constructed as shown in Fig. 46. The two static pressure holes were connected to a common manifold which was then attached to one end of an inclined manometer containing DC 200 silicone oil. The total pressure tube was connected to the other end of the manometer so that pressure difference was read directly. The density of the argon flowing through the duct was determined from a static pressure measurement on the duct wall and a temperature measurement in the gas feed line near the injectors. Since the gas velocity was only about 55 ft/s, it was permissible to use Bernoulli's incompressible equation to compute the velocities from these measurements. The mass flow rate of the argon was measured with a rotameter; consequently, an average velocity at the probe



DIMENSIONS ARE INTERNAL IN INCHES

END VIEW

Fig. 44. Test apparatus configuration used for gas flow experiments

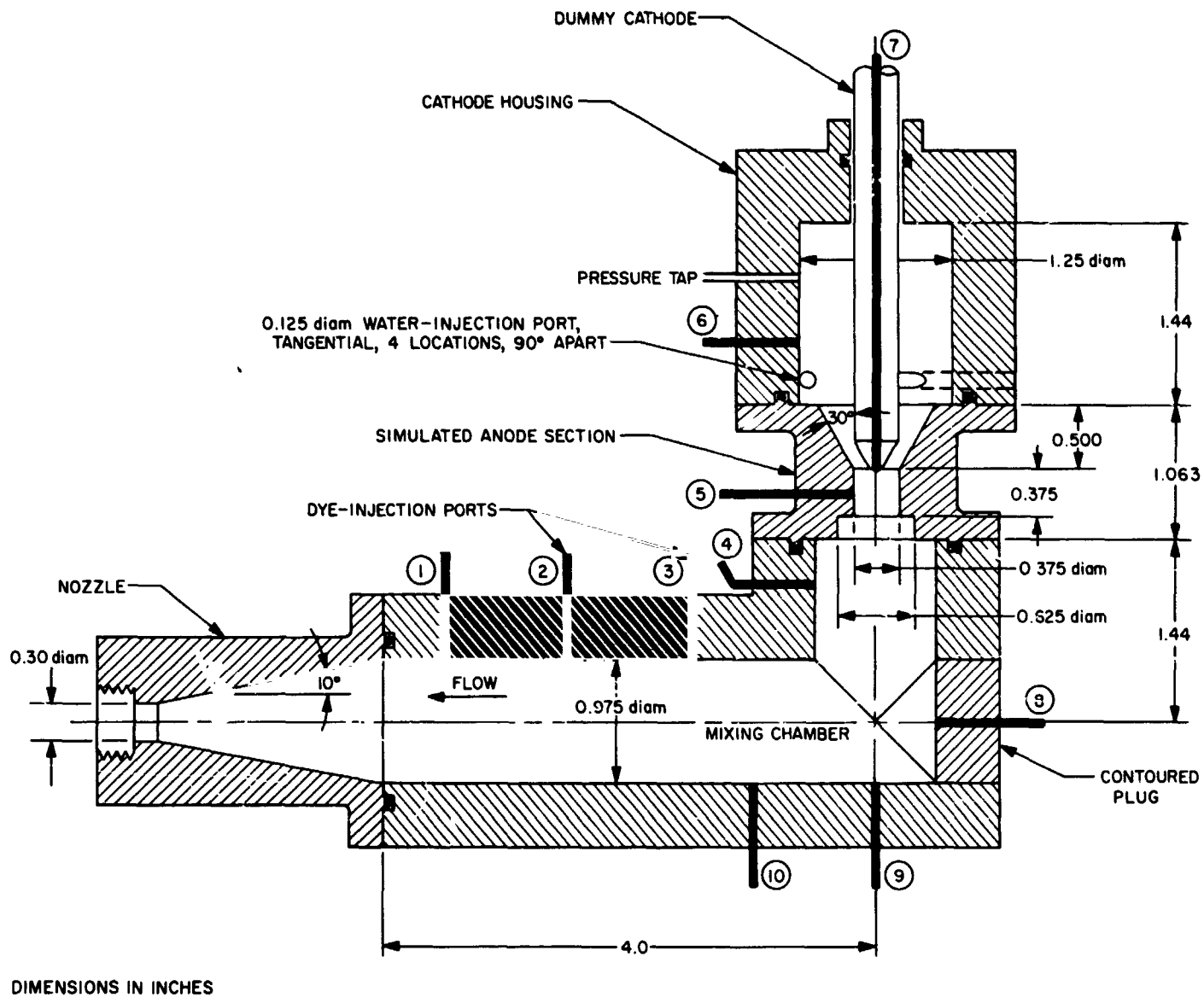


Fig. 45. Cross-sectional view of the flow visualization apparatus

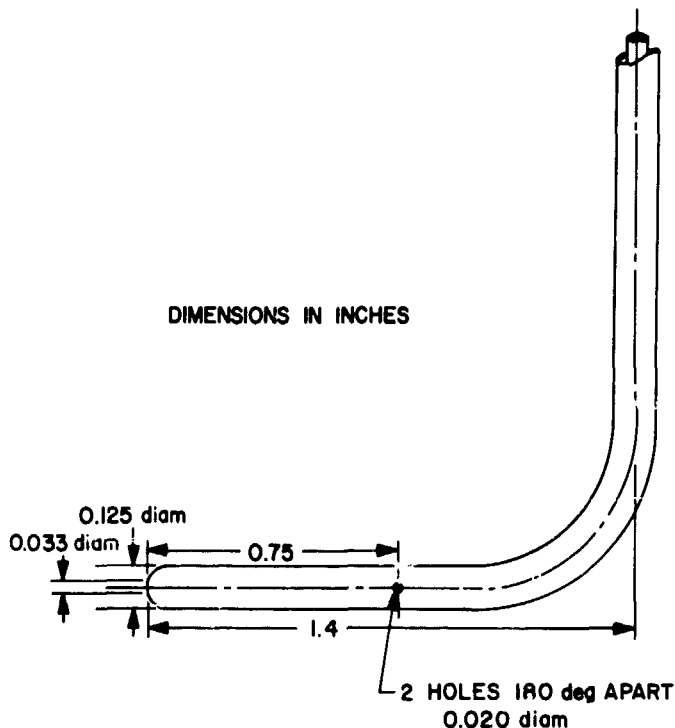


Fig. 46. Pitot-static probe

location could be determined by use of the continuity equation. This provided a comparison for the probe results.

Radial traverses were made with two different probes at circumferential locations X and Y as shown in Figs. 47, 48, 49, and 50. Because of the gradual bend in the probes they could not be traversed across the entire diameter; hence, after obtaining data within the travel distance, the duct segment containing the probes was rotated 90 deg so that data could be obtained along the entire length of a diametral line. Thus Probe A was rotated to position Z and used to obtain data along the original diametral traverse line XZ of Probe B as well as perpendicular to the original diametral line of Probe A. The extent of the traverse was such that there was considerable overlap between the original traverse of Probe B and the traverse of Probe A after the duct segment had been rotated. Radial distributions of axial velocity for pressures of approximately 2 and 6 psia in the 1.95-in.-diam duct are shown in Figs. 47 and 48 for tests in which nonswirling jets were injected into the plenum. The nonswirling flow condition was achieved with radial flow injectors in each of the three housings from which the gas was introduced into the plenum. As shown in the figures the velocity distributions in the free stream, which extends across most of this duct, are quite uniform when this type of

injection was used. Furthermore, the average velocities computed from the measured mass flow rates, which also appear on the figures, agree well with the probe results.

In Figs. 49 and 50 radial distributions of axial velocity are shown for tests in which three swirling jets were injected into the plenum; these tests were conducted at about the same pressures and along the same radial lines as were the nonswirling flow tests. The swirl was induced by tangential injectors that had been substituted for the radial injectors in each of the three housings. It is evident in Figs. 49 and 50 that there was greater deviation from uniform flow with injected swirl than when nonswirling flow was injected. Deviations from an average velocity, however, are not excessive and the swirl present initially in the jets at injection into the plenum chamber appears to have been dissipated quite effectively. Static pressure distributions made along the end wall of the plenum indicated variations across its diameter of less than 5 mm of oil.

Static pressures were also measured along one of the end walls of the three cathode housings. All of these housings contained 0.75-in.-diam centerbodies which are the cathodes when the housings are used as arc heaters for high-temperature flow tests. From these end-wall pressure distributions it was possible to compute the approximate tangential velocity distributions shown in Fig. 51. The upper curve is for an 8-psia test, since end-wall pressures were not recorded at 6 psia. This figure shows that the maximum tangential velocities greatly exceeded the axial velocities in the 1.95-in.-diam duct even at the lower stagnation pressure. The differences in pressures between the inner and the outer radii on this end wall was about 100 mm oil for a 2-psia swirling flow test and about 580 mm oil for a 6-psia swirling flow test. There was essentially no radial pressure difference along this end wall for the nonswirling flow tests.

3. Water Flow Visualization Experiments

Flow visualization experiments were conducted in a special Lucite, half-scale model of an earlier arc-jet heat-transfer apparatus which has been described in SPS 37-43, Vol. IV, pp. 206-216. That apparatus also contained a sharp 90-deg turn and either radial or tangential injectors, as was desired. A schematic view of the flow visualization model with tangential injectors is shown in Fig. 45. Ten dye-injection ports were located as shown from which dye was injected in a radial direction perpendicular to the local wall except for a single port located in the tip of the dummy cathode. All internal flow passages were

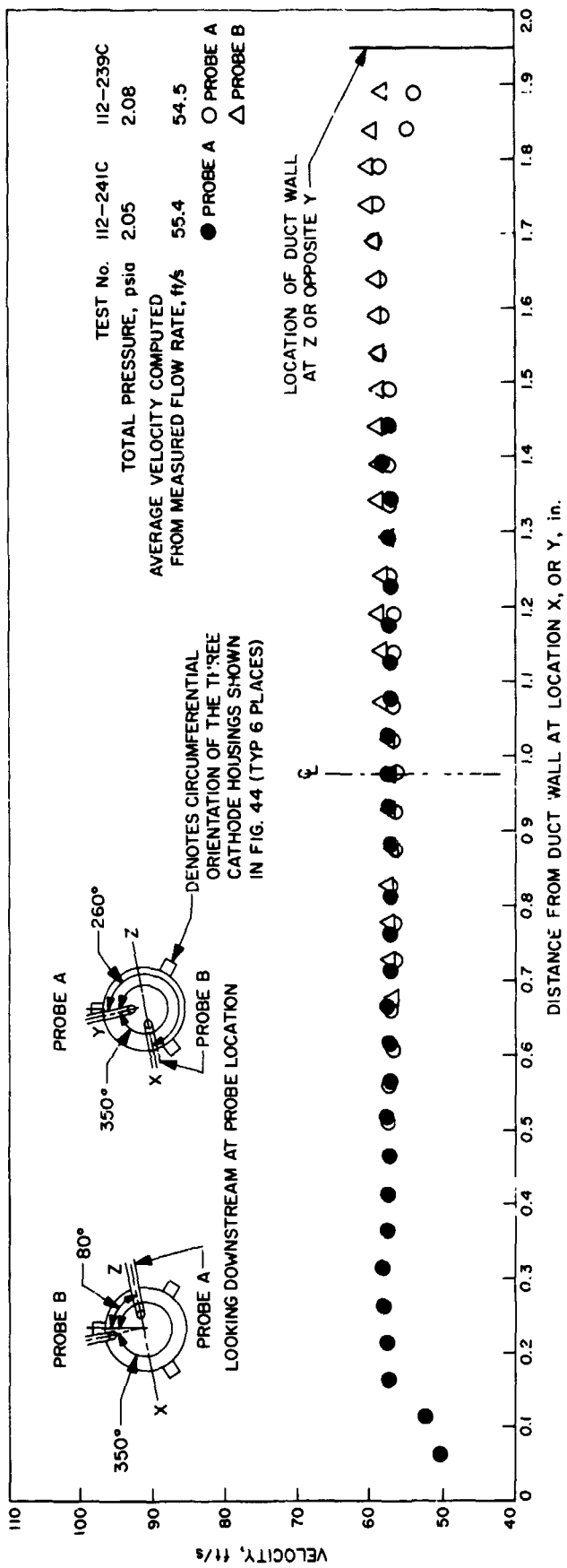


Fig. 47. Axial velocity distribution in the straight duct for radial injection into the cathode housing at a pressure of 2 psia at the probe location

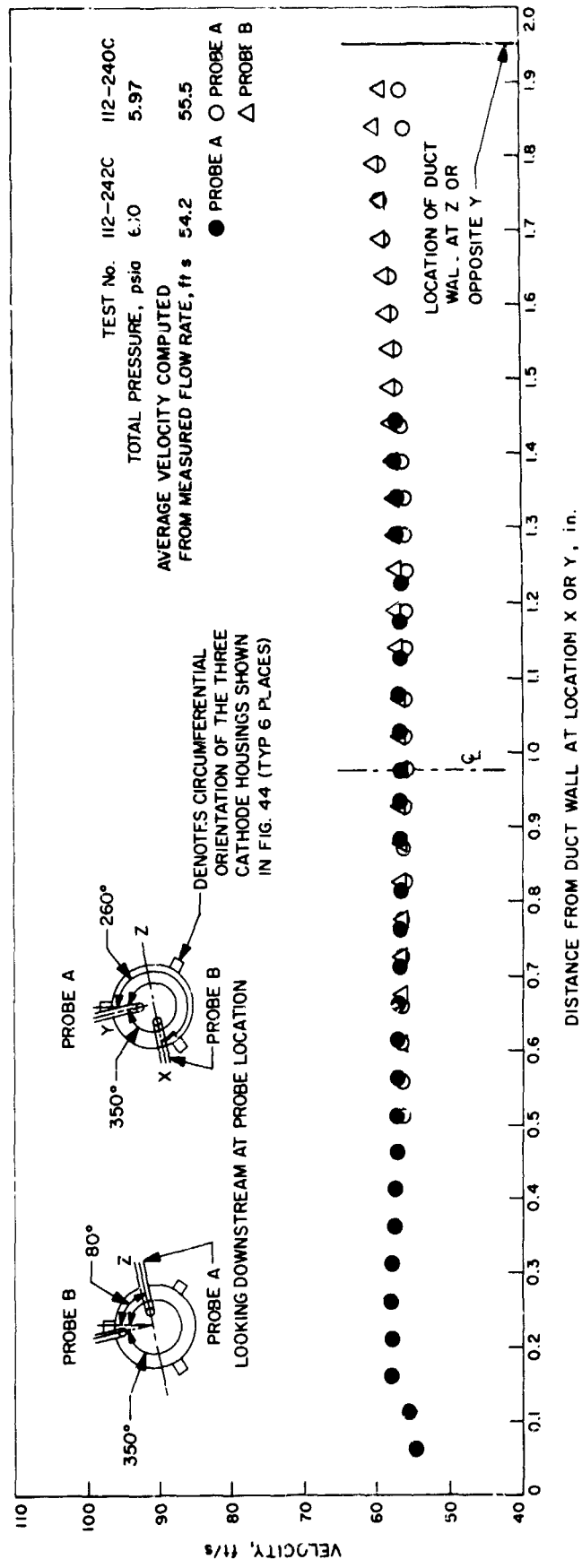


Fig. 48. Axial velocity distribution in the straight duct for radial injection into the cathode housing at a pressure of 6 psia at the probe location

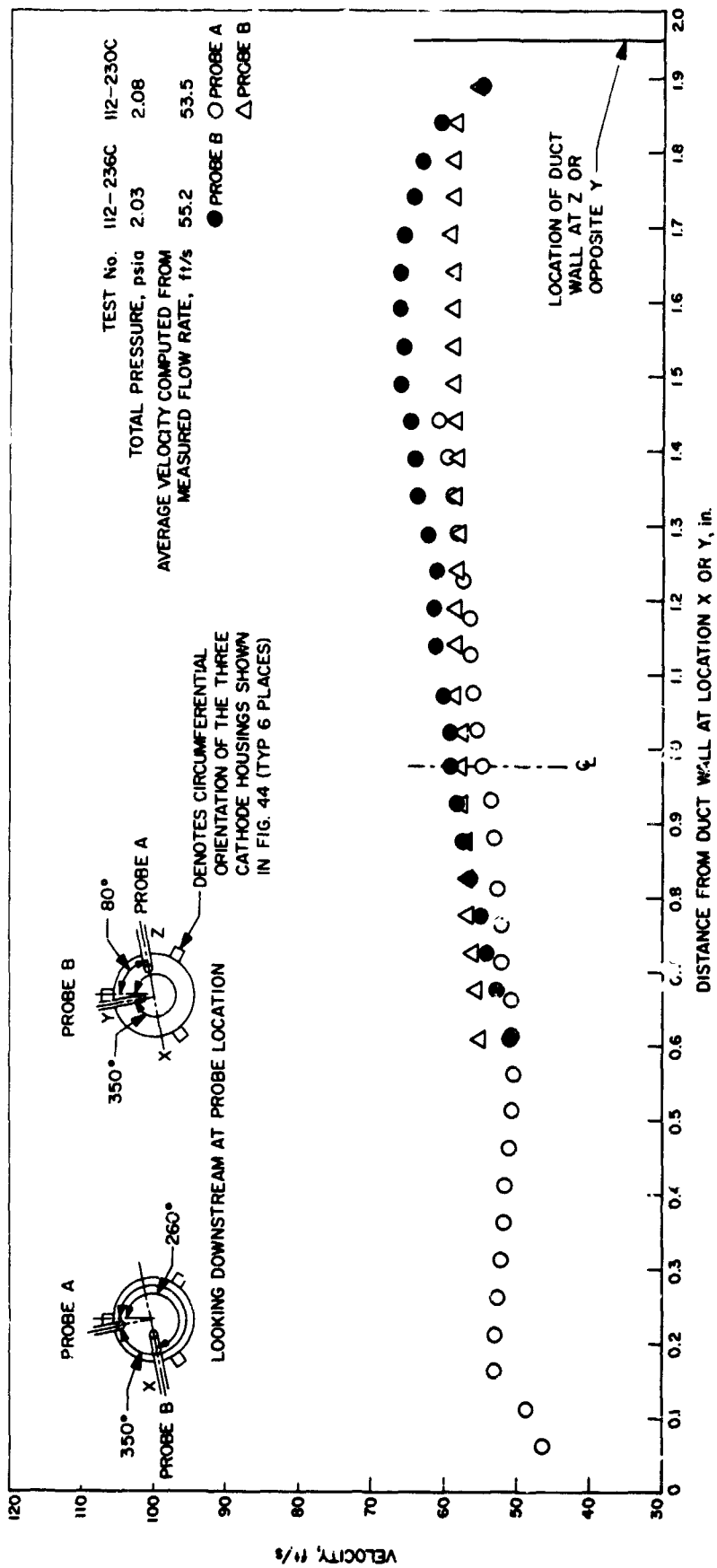


Fig. 49. Axial velocity distribution in the straight duct for tangential injection into the cathode housing at a pressure of 2 psia at the probe location

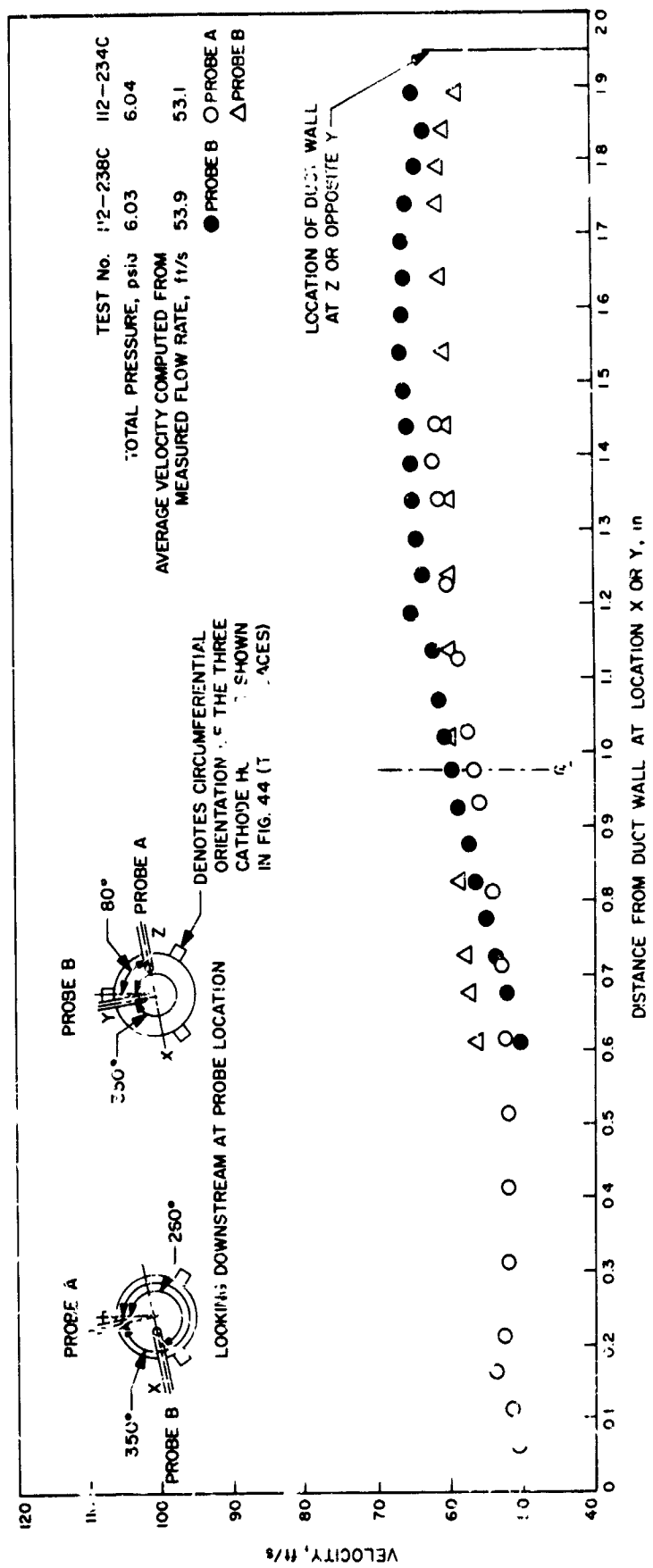


Fig. 50. Axial velocity distribution in the straight duct for tangential injection into the cathode housing at a pressure of 6 psia at the probe location

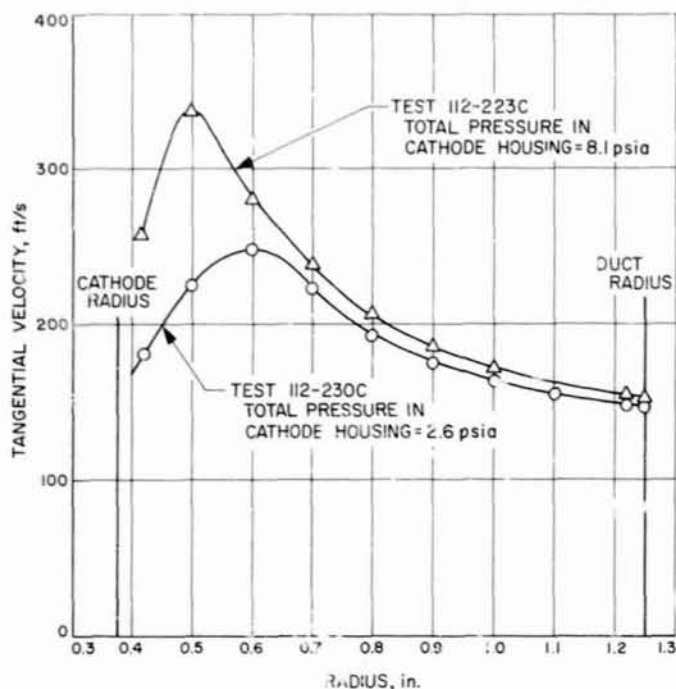


Fig. 51. Tangential velocity distributions in cathode housing B

axisymmetric with respect to their centerlines. For radial injection of water, a different cathode-housing section was used; the axial location of the injection was the same as shown in Fig. 45 but the ports were approximately twice the diameter of the tangential injection ports. Water flow rates were adjusted and measured by means of a calibrated rotameter upstream of the injectors. Mixing chamber Reynolds numbers in the same range as those obtained in the larger, hot-gas apparatus were of interest. The motions of dye filaments were observed visually and photographed.

A typical dye study of the flow with tangential water injection is shown in Fig. 52 for a mixing chamber Reynolds number of about 200. This photograph was taken shortly after injection of dye from Ports 2, 6, 7, and 10 was initiated. Swirl introduced by the injectors is particularly evident in the region of accelerated flow near the cathode tip; the effect of swirl on the dye filament issuing from the tip of the cathode is readily apparent. Although it is not so clear in this photograph, it was determined that flow near the wall of the cathode housing spiraled up the wall, flowed radially inward toward the cathode, then spiraled downward along the surface of the cathode. Flow separation from the inside corner of the 90-deg bend is apparent. Although flow in the mixing chamber appears erratic, the integrity of the dye filaments suggests that it is laminar and that the type of

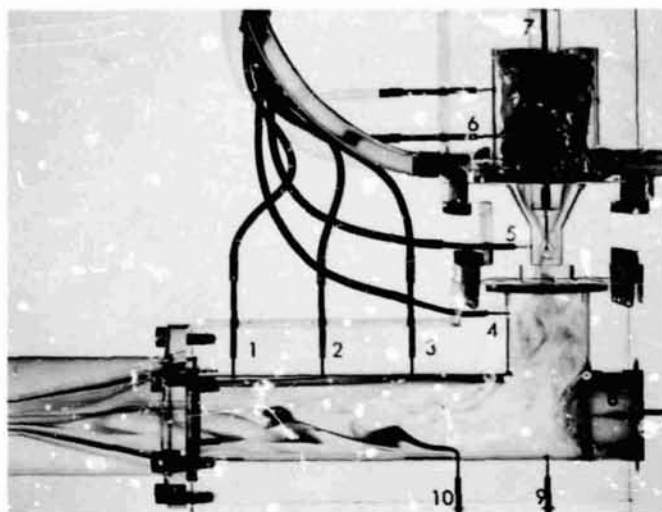


Fig. 52. Dye study in half-scale model of an arc jet with tangential water injection. Mixing chamber Reynolds no. of ≈ 200 . Dye introduced from Ports 2, 6, 7, and 10

effects which would be expected from a pure swirling flow have been removed. Flow just upstream of, and into, the nozzle appears reasonably uniform.

A comparison of flow with tangential and radial injection is shown in Figs. 53(a) and (b), for a mixing chamber Reynolds number of about 200. The effect of swirl at the entrance to the 90-deg bend is very pronounced in Fig. 53(a). Dye injected from Port 5 indicates that swirling flow through the throat of the anode section spreads rapidly in the radial direction at the entrance of the bend. Virtually no spread of this jetlike flow was discerned without swirl as indicated in Fig. 53(b); instead it impinged on the opposite wall of the bend in the vicinity of Port 9. Flow separation regions observed at the entrance of the bend (near Port 4) in the outside corner of the bend (near Ports 8 and 9) and downstream of the inside corner of the bend were much reduced in size by swirl. A comparison of the structure of dye filaments in the mixing chamber, Fig. 53(a) and (b), indicates that the diffusion rate of the dye is lowest for the case of the tangential injector. This may indicate that the flow attained a higher degree of orderliness when swirl was introduced upstream of the elbow.

Because of the higher velocities, and hence much higher rates of diffusion, dye studies of flows at Reynolds numbers of 600 and higher lacked specific detail. However, the overall effects of swirl were similar to those observed at lower Reynolds numbers. In particular, the radial spread of the flow passing from the anode throat

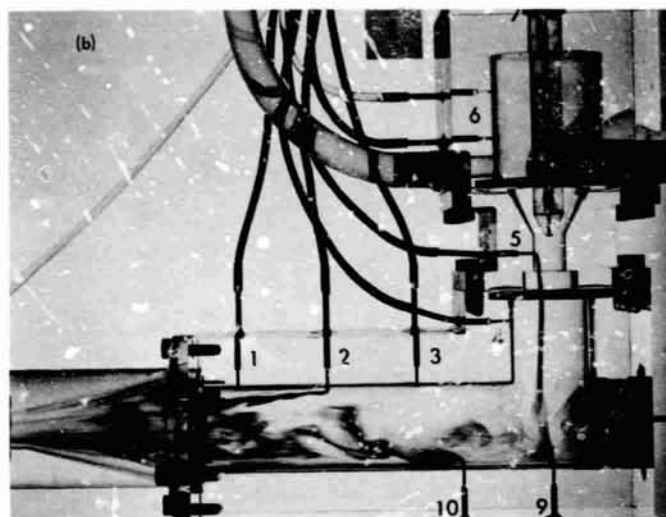
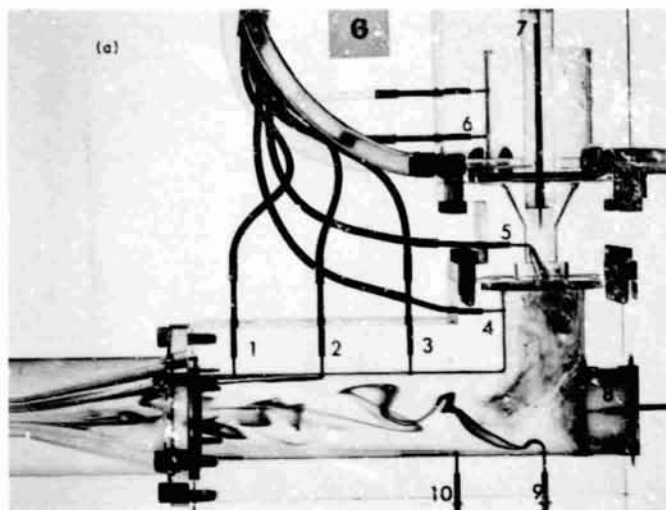


Fig. 53. Dye studies at a mixing chamber Reynolds no. of ≈ 200 : (a) tangential injection, dye introduced from Ports 2, 5, and 9; (b) radial injection, dye introduced from Ports 2, 5, and 10

into the entrance of the bend was significantly greater with swirl than without swirl.

Several general comments concerning these flows are of interest. Firstly, these flows are highly complicated by first undergoing acceleration in the converging annular nozzle formed by the anode wall and the cathode tip, which also produces a wake, passing through the anode throat, and discharging into a rather short entrance region upstream of the bend. These flows are not characteristic of what would occur with long, constant-diameter entrance sections. Less is known concerning

secondary flows in miter bends than in 90-deg elbows of more gentle radius, so that conjectures concerning the influence of swirl on those secondary flows would not be of high value. Admittedly, the interpretation of such complex flows by visualization is somewhat subjective. However, it is thought that introduction of swirl in this particular channel improved the flow by providing more uniform mixing and greatly reducing the stagnation effect in the corner of the bend, and by reducing the size and effect of separation regions in the vicinity of the bend. The bend appeared to be quite effective in removing swirl from the flow. Although there was evidence of some crossflow components at the entrance of the nozzle with both types of injection, even at the lower Reynolds numbers, these effects were no greater when tangential injection was used and were not the result of swirl. That is, there was no evidence of a preferential and consistent swirl component at the entrance to the nozzle when tangential injection was used.

4. Summary and Conclusions

Two types of experiments were conducted to determine the influence of a sharp 90-deg turn on the motion of a swirling fluid. In the first set of experiments three equally spaced impinging jets of swirling argon gas at approximately room temperature were introduced radially inward into a plenum chamber. In the plenum the fluid negotiated a 90-deg turn and then accelerated to an axial velocity of approximately 55 ft/s into a straight constant-diameter duct whose centerline was coincident with that of the plenum. Radial distributions of the axial velocity acquired in the duct with pitot-static probes indicated that the maximum departure from a uniform axial velocity distribution in the free stream was about $\pm 14\%$. For tests in which nonswirling fluid was introduced into the plenum the radial distributions of axial velocity were essentially uniform except near the duct wall.

In the second set of experiments swirling water flows were forced to negotiate a sharp 90-deg turn in a miter elbow which was located downstream of a scale model of a convergent annular arc heater. A constant-diameter duct similar in size to that of the elbow was attached to the downstream end of the elbow. Dye injected through small ports located at numerous places in the duct wall indicated that the swirl was effectively dissipated by the sharp 90-deg bend.

References

1. Elliott, D. C., Cerini, D. J., Hays, L. G., and Weinberg, E., "Theoretical and Experimental Investigation of Liquid-Metal MHD Power Generation," *Electricity from MHD*, Vol. II, pp. 995-1018, International Atomic Energy Agency, Vienna, 1966.
2. Cerini, D. J., and Elliott, D. G., "Performance Characteristics of a Single-Wavelength Liquid-Metal MHD Induction Generator With End-Loss Compensation," Proceedings of Eighth Symposium on Engineering Aspects of Magnetohydrodynamics, pp. 11-27, Stanford University, Stanford, California, March 28-30, 1967.
3. Tepper, F., Udavcak, R., and Zelenak, J., "Determination of the Solubility of Potassium and Cesium in Lithium," Report No. MSAR 64-19, MSA Research Corp., Callery, Penn., April 1964.
4. McKisson, R., et al., "Solubility Studies of Ultra Pure Transition Elements in Ultra Pure Alkali Metals," Report No. AI-65-210, Atomics International, Canoga Park, California, March 1966.
5. Thalgot, F. W., et al., "Stability Studies on EBR-I," Proceedings of the U.N. International Conference on the Peaceful Uses of Atomic Energy, Geneva, 1958, Vol. 12, pp. 242-265, 1958.
6. "High Temperature Liquid-Metal-Cooled Reactor Study," Vol. I, Final Report, Report WANL-PR(R)-002, March 1964, Westinghouse Electric Corp., Astro-nuclear Laboratory.
7. Lathrop, K. G., "DTF-IV, a Fortran IV Program for Solving the Multigroup Transport Equation with Anisotropic Scattering," Report LA-3373, Los Alamos Scientific Laboratory, November 12, 1965.
8. Hansen, G. E., and Roach, W. H., "Six and Sixteen Group Cross-Sections For Fast and Intermediate Critical Assemblies," Report LAMS-2543, Los Alamos Scientific Laboratory, December 6, 1961.
9. Witte, A. B., "Analysis of One-Dimensional Isentropic Flow With Tables for Partially Ionized Argon," Technical Report 32-661, Jet Propulsion Laboratory, Pasadena, California, Sept. 30, 1964.
10. Back, L. H., "Laminar Boundary Layer Heat Transfer From a Partially Ionized Monatomic Gas," *Phys. Fluids*, Vol. 10, No. 4, pp. 807-819, April, 1967.
11. Olsen, H. N., "Measurement of Argon Transition Probabilities Using the Thermal Arc Plasma as a Radiation Source," *J. Quant. Spectros. Rad. Trans.*, Vol. 5, pp. 59-76, 1963.
12. Vassallo, F. A., "Miniature Enthalpy Probes For High Temperature Gas Streams," ARL 66-0115 Aerospace Research Laboratories, Office of Aerospace Research, USAF, Wright-Patterson Air Force Base, Ohio, June 1966.
13. Back, L. H., Massier, P. F., and Gier, H. L., "Comparison of Measured and Predicted Flows Through Conical Supersonic Nozzles, With Emphasis on the Transonic Region," *AIAA Journal*, Vol. 3, No. 9, Sept. 1965, pp. 1606-1614.

References (contd)

14. McGregor, W. K., and Brewer, L. E., "Spectroscopy of Supersonic Plasma: III. Electron Temperature Measurements in Argon Plasma by Two Independent Methods," Report No. AEDC-TR-65-131, Rocket Test Facility, Arnold Engineering Development Center, Air Force Systems Command, Arnold Air Force Station, Tennessee, Nov., 1965.
15. Thiene, P., "Convective Flexure of a Plasma Conductor," *Phys. Fluids*, Vol. 6, p. 1319, 1963.
16. Thiene, P. G., Chambers, J. E., and von Jaskowsky, W., "An Experimental Investigation of the Behavior of an Arc Positive Column in the Presence of Forced Convection," *Plasmadyne*, T-4TN031-334, April 1961.

X. Liquid Propulsion

PROPULSION DIVISION

A. Advanced Liquid Propulsion Systems, L. R. Toth, H. B. Stanford, and W. F. MacGlashan

1. Introduction, L. R. Toth

The advanced liquid propulsion systems program is investigating selected problems generated by spacecraft operational requirements for propulsion systems capable of high inherent reliability, long-term storage in the space environment, multiple start in free fall (zero gravity), and engine throttling. The solutions proposed to satisfy these requirements are coordinated for practical application in a system.

Periodic reports (starting with SPS 37-8, Vol. IV) describe the progress of work on the various parts of a specific system. Recent accomplishments concerned with bladder and component development are outlined below.

These include:

- (1) Composite bladder material testing.
- (2) Fill valve with three different materials of construction.

2. Composite Bladder Material Testing, H. B. Stanford

The structure and testing of composite bladder materials fabricated from Teflon film, Teflon felt, and aluminum foil was discussed in SPS 37-36, Vol. IV. Since then 18-in.-diam hemispherical bladders have been made from this material by Dilectrix Corporation of Farmingdale, Long Island, under contract to JPL. Eight of these bladders were delivered to JPL, where both helium leak and water expulsion tests have been conducted with them.

This material was developed as the result of early attempts to demonstrate a bladder material with some cycle life and improved permeability characteristics to N_2O_4 ; hydrazine; and the pressurant gases, helium and nitrogen. The Teflon films, TFE and FEP, are the basic structural materials for strength and flexibility; the aluminum foil is an intended permeation barrier; and the Teflon felt is to provide a protective, motion damping, cushion for the purpose of preventing the destructive sharp folds and creases detrimental to the aluminum foil. Originally the felt was to serve also as a vehicle for a buffer chemical $Mn(OH)_2$, manganese hydroxide, intended to react with the small quantity of N_2O_4 that would permeate through

inevitable pinholes in the aluminum foil. Although this chemical worked well in swatch testing, its inclusion in the bladder structure was not part of the initial fabrication feasibility effort.

The test procedure called for the bladder to be leak-tested with helium in the as-received condition. Those bladders that were to be expulsion-tested with water were then to be given one complete expulsion test, reinstalled in the steel tank, and leak-tested again with helium to determine the deterioration of the aluminum foil barrier. This alternate expulsion cycle and leak test was then repeated until the helium leak rate exceeded the capability of the detection device. When this excessive helium leak rate was attained, these bladders were expulsion-cycled to major failure or until water leakage occurred. Two bladders with low helium leak rates were selected for long-term desert storage testing with N_2O_4 in one bladder and distilled water in the other. The permeation rate of N_2O_4 is to be determined by a periodic check of the pH factor of the distilled water.

a. Expulsion cycling and slosh testing. The water expulsion testing of the 18-in.-diam hemispherical bladder was conducted in Plexiglas tanks on the slosh and expulsion test equipment described in SPS 37-21 Vol. IV. Expulsion pressure was limited to 30 psi by the Plexiglas tanks. Slosh loads were applied at $\pm 3/4$ in. linear motion, ± 2 deg rotational motion at 128 cycles/min. The composite material



Fig. 1. Folding control pattern of 3/16-in. Teflon rods fused to 18-in. diam hemispherical composite bladder

bladders were run with a companion bladder of ordinary TFE-FEP Teflon laminate structure. Both still and motion pictures were taken as required for an adequate record. Expulsion efficiency was determined by measuring the water before filling the bladder and after expulsion in glass manometers connected to the bladder outlets. The water flow rates were determined by means of turbine-type flow meters in the connecting lines. Water temperature was measured by means of thermocouples inserted into the flow lines and by thermometers suspended within the glass monometers.

The actual laminate arrangement of the material in these bladders was as follows:

TFE	3 mil
FEP	1 mil
Aluminum foil	1/2 mil
FEP	2 mil
Aluminum foil	1/2 mil
FEP	2 mil
Teflon felt	0.090 in.
FEP-TFE	3 mil-1 mil

Total thickness was approximately 0.100 in.

One bladder was made with a pattern of 3/16-in. Teflon rods fused to the outside in an effort to induce folding control. The control pattern is shown in Fig. 1. This device proved completely ineffective on this configuration of bladder due to the fact that the differential stiffness between the bladder wall, the 90-deg intersection of the flat and curved surfaces, and the Teflon rods was insufficient to force the folding mode of the bladder into the desired pattern. At the beginning of the expulsion cycle the Teflon rods exerted some control of the folding mode, but, as expulsion progressed, random folding very similar to that on nonstiffened bladders was obtained (Figs. 2-4).

Once a folding pattern was established, it repeated itself throughout the entire cycle life of the bladder, as much as 120 cycles in some cases. In Table 1 cycle life and failure history are recorded for the bladders tested.

Expulsion efficiency showed some variation between bladders and was found to average 98.7% from a total of 239 tests on three different bladders.

A typical expulsion efficiency curve is shown in Fig. 5. Conventional TFE and FEP bladders of the same hemi-

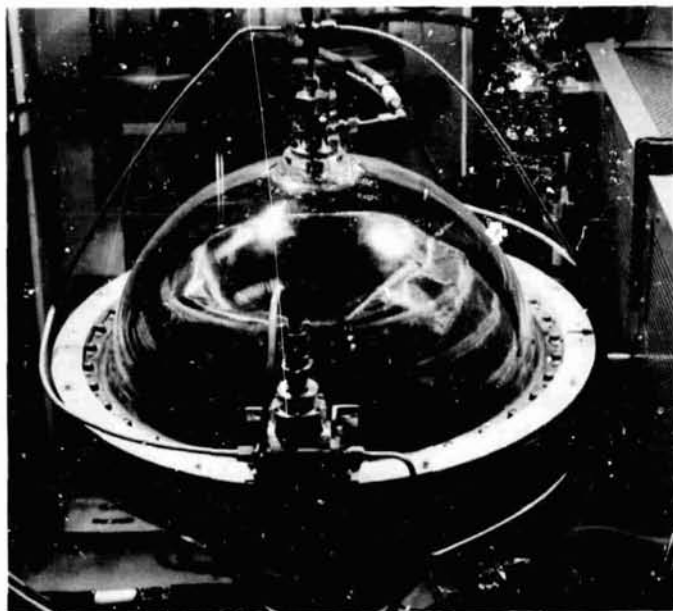


Fig. 2. Hemispherical composite bladder (18-in. diam) with fold control device exhibiting some control of folding mode

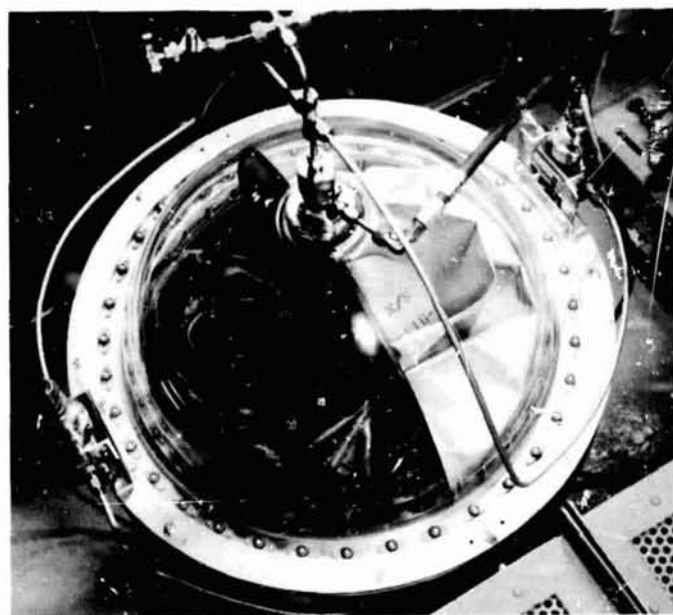


Fig. 3. Hemispherical composite bladder (18-in. diam) with fold control device exhibiting loss of control of folding mode

spherical configuration have averaged 99.8% expulsion efficiency in similar testing.

The relatively low average expulsion efficiency demonstrated by the composite bladders is accounted for by the fact that bladder SN 4-6-95-1213 with 120 expulsions averaged only 97.8% efficient and SN 4-3-95-1213 with 102



Fig. 4. Collapsed 18-in.-diam hemispherical bladder without folding control device

expulsions averaged 99% efficient. These low expulsion efficiencies resulted from both bladders leaking more or less continuously in the neck and flange area. It is believed that this failure at the neck and flange is a fabrication and handling problem and not directly attributable to the composite material structure itself. These bladders were installed several times in different tanks during the helium leak and expulsion cycling test series. This excessive handling, together with a comparatively thin flange, resulted in extensive damage that is not readily repaired.

Throughout the expulsion testing it had been noted that the slosh damping effect of the composite bladder was considerable. To demonstrate this fact further a hemispherical composite bladder together with a Teflon bladder of conventional TFE-FEP sintered material approximately 0.014 in. thick was slosh-tested in a spherical Plexiglas tank. Slosh modes were measured to $\pm 1\frac{1}{2}$ in. linear motion, $\pm 5\%$ rotational motion at a frequency of 225 cycles/min. This amounted to an acceleration of approximately $1\frac{1}{2}g$.

The bladders were installed with the flat sides parallel to the direction of linear motion. During this test the conventional Teflon bladder thrashed violently about, while the motions of the composite bladder were damped to gentle oscillations indicative of almost complete control of the fluid surface. Since this test was conducted at the upper limit of capability of the test machine, incurring the possibility of damage, it was not repeated.

In conclusion it can be said that bladders made from the Teflon film, Teflon felt, and aluminum foil composite

Table 1. Cycle life and failure history of three 18-in.-diam hemispherical composite material expulsion bladders

Test bladder SN	Expulsion No.	Failure area	Result	Repair
4-3-95-1213 avg 99% expulsion efficiency	3	Flange	Leak	} Small patch bonded with Armstrong Adhesive 520 Replaced neck from TFE-FEP bladder. Bonded with Armstrong Adhesive 520 Unable to stop leak. Continued with expulsions Replaced test bladder with SN-4-6-95-1213. Used SN-4-3-95-1213 as companion bladder Unable to repair
	7	Flange	Leak	
	9	Flange	Leak	
	12	Neck	Leak	
	28	Neck	} Approx 25 cm ² leakage per expulsion	
	85	Neck		
102	Flat back	5 fatigue breaks at edge		
4-5-95-1213 avg 99.4% expulsion efficiency	1	Flange	Leak	Replaced neck from TFE-FEP bladder. Bonded with Armstrong Adhesive 520 Unable to repair
	7	Neck	Leak	
4-6-95-1213 avg 98.5% expulsion efficiency	10	Neck	Leak (small)	} With layer of Armstrong Adhesive 520 Bonded with tape (Tuck 90CB) Unable to repair
	40	Neck	Leak	
	62	Neck	Leak	
	80	Neck	Leak	
	115	Neck	Leak	
130	Flat back at points where bladder folds	Approx 8 fatigue points		

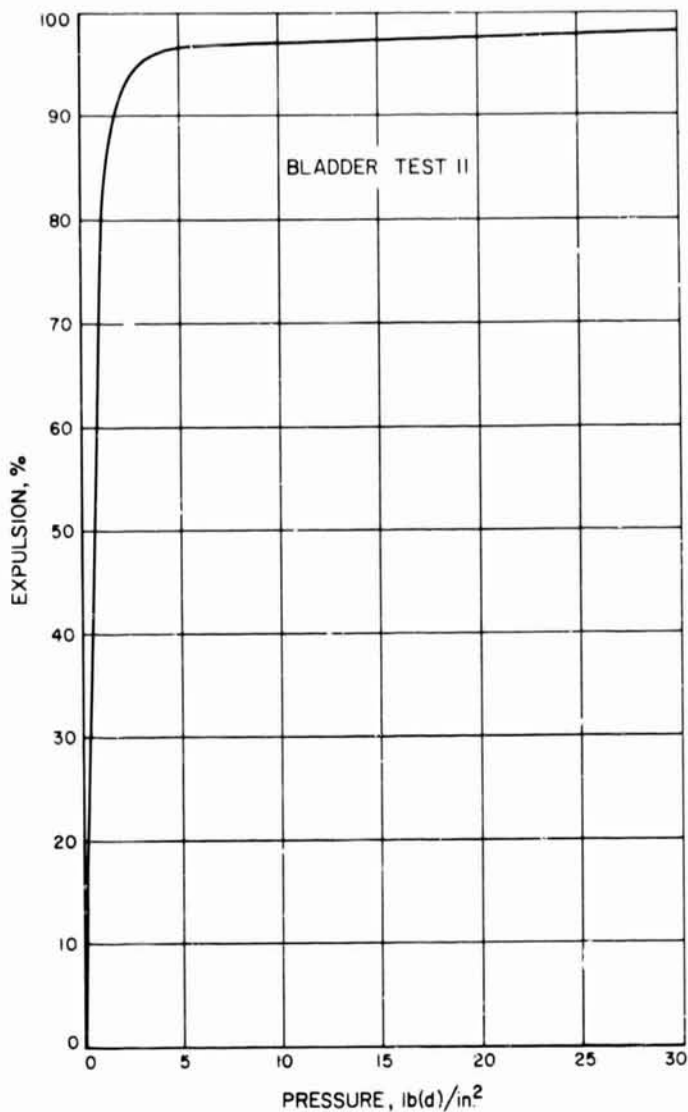


Fig. 5. Expulsion efficiency of 18-in.-diam hemispherical bladder of Teflon film, felt, and aluminum foil laminated material

material can be expected to have a very slightly lower expulsion efficiency than ordinary TFE-FEP bladders, but their cycle life will be longer. Their slosh damping and liquid surface control are a marked improvement over conventional TFE-FEP bladders. Helium leak test information is currently being evaluated and will be presented at a later time.

3. Fill Valve Development, W. F. MacGlashan

In SPS 37-35, Vol. IV a manually operated on-off fill valve, referred to as the type with the headless screw, was briefly described. This fill valve is shown in Fig. 6, a sectioned fill-valve test unit. The test unit consists of the flight

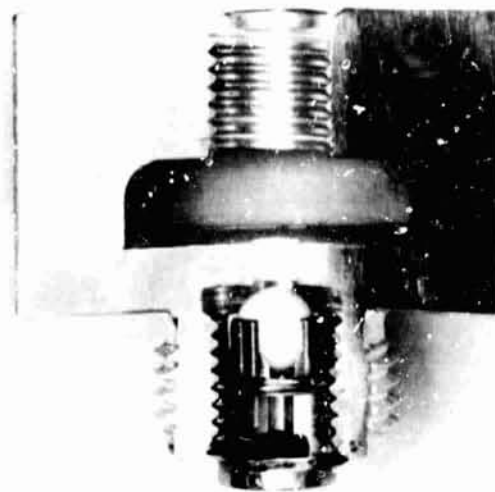


Fig. 6. Sectioned fill-valve test unit

portion fill valve which is electron beam welded to a hollowed hexagonal block so as to simulate a tank with an integral filling valve. Fig. 7 shows a cross-section detail of the electron beam weld and the fill-valve parts.

Three parts comprise the fill-valve flight portion: an internally and externally threaded boss into which the seat is precision lapped; a screw; and a ceramic ball, which is retained in the end of the screw. The screw holds the ball against the seat to form the single seal in the valve when the valve is closed. A ground coupling (not shown) permits the valve to be actuated while under pressure. The seat ball threads are completely relieved of axial load due to line pressure (sealing force only is transmitted by the threads). The ground fitting (not pressure balanced) is retained by engaging external threads on the flight boss. This valve represents the simplest form for the flight portion and is more fully described in JPL Technical Report 32-875 entitled, *Fill-Valve Development for the Advanced Liquid Propulsion System (ALPS)*.

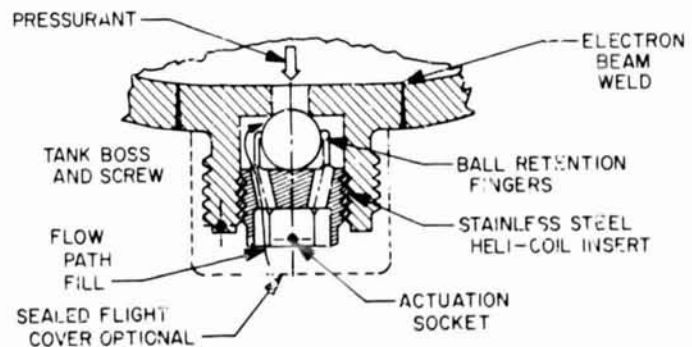


Fig. 7. Fill-valve cross section

A total of 24 fill-valve test units (Fig. 6) have been made. Eight each maximum and minimum tolerance units were fabricated in 6061-T6 aluminum alloy, 17-4PH stainless steel, and 6AL4V titanium. These units will be used for general testing such as

- (1) Thermal cycling while in contact with pressurized gaseous nitrogen, hydrazine, and nitrogen tetroxide.
- (2) Selected type-approval testing.
- (3) Long-term storage while in contact with pressurized fluids.

B. Resonant Combustion, R. M. Clayton

1. Introduction and Background

The resonant combustion (RC) project has been attempting to define, experimentally, the nonsteady fully developed wave phenomena associated with the destructive mode of liquid rocket combustion instability. This work, for the most part, has dealt with two different injector designs which utilize 11-in.-diam chambers, operated at 300 psia combustion pressure with the Corporal and the $N_2O_4 + 50/50$ (UDMH/ N_2H_4) propellant combinations. It has been found (Ref. 1) through high-response pressure measurements on these engines (both on the walls and the internal wall surfaces) that a high-amplitude, steep-fronted pressure disturbance, having many of the essential characteristics of a combustion-driven shock wave (hence, detonation-like):

- (1) Sweeps supersonically about the chamber circumference.
- (2) Has a wave shape, velocity, and amplitude which are relatively unaffected by chamber length changes but are affected by variations in the propellant mass flux distribution in the chamber cross section.
- (3) Has a direction of rotative travel which appears to be related to the orientation of the resonance initiating disturbance, with respect to nonuniformities in the injected propellant distribution.

In order to extend the definition of this combustion mode to a combustor having significantly different design parameters, a third injector was fabricated for an 18-in.-diam engine, having $\frac{1}{2}$ the propellant mass flux (across the chamber cross section) and 100 psia chamber pressure. The $N_2O_4 + 50/50$ propellants were again used.

¹Also SPS 37-30, -36, -41, -42, -43, Vol. IV, pp. 123-130, 163-173, 134-151, 88-103, 224-230, respectively.

Early work with this injector designated RC injector 1, demonstrated that it produced a relatively high combustion performance (SPS 37-30, Vol. IV, pp. 123-130) but that it was plagued with a random roughness under certain operating conditions, which constrained its smooth operation to off-design flow conditions. The addition of face baffles prevented transitions to sustained resonance, even when the engine was bombed, but they had no measurable influence on the roughness (or "popping" as it has come to be known). Thus, since smooth combustion operation was attainable only for nondesign operating conditions (even with baffles), and since the baffles were not wanted for the planned resonance studies, efforts to correct the problem were undertaken so that the experimental technique of scheduled bomb-induced resonance could be used (Ref. 1) without the interference of spontaneous transitions. Recent results of these efforts, which serve to establish the steady state behavior of the combustor as it is to be used during the resonant combustion studies, are presented here.

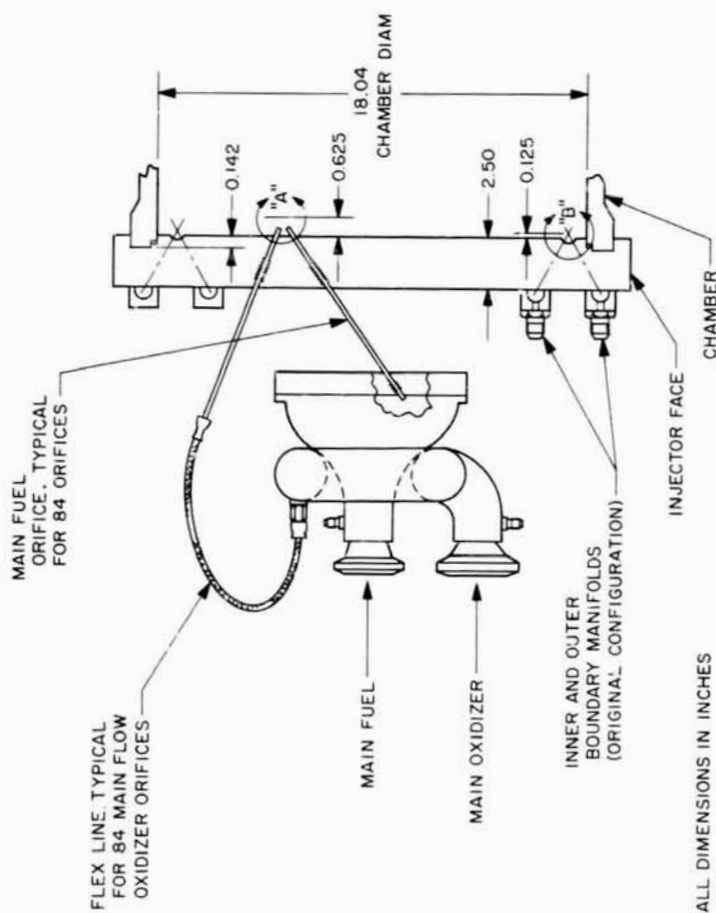
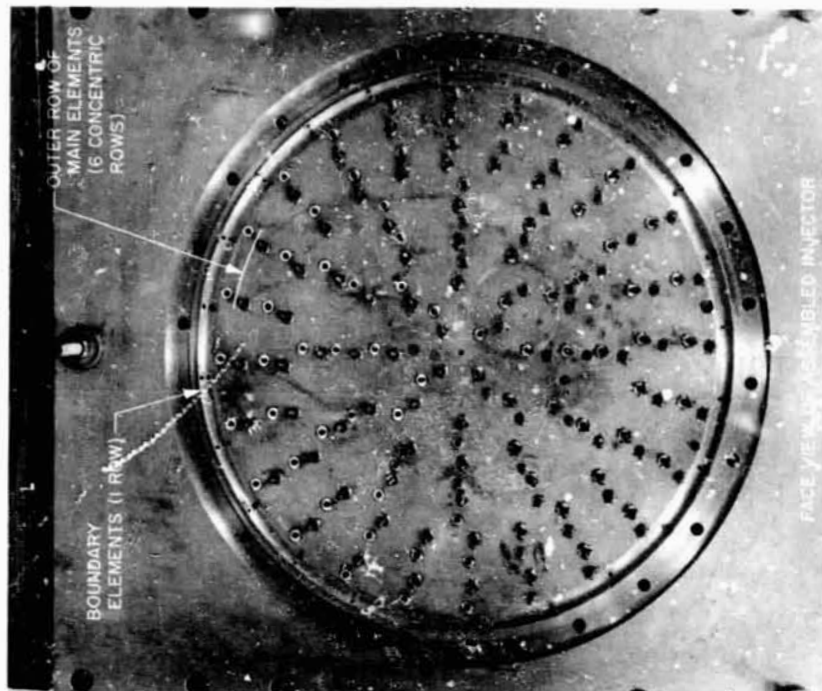
2. Combustion Behavior of the Original Configuration

The total flow rate for RC injector 1 comprises a main (or core) flow and a boundary flow. Injector design conditions are listed in Table 2. Figure 8 depicts the geometry of the respective unlike-impinging doublet injector elements and shows the composite arrangement of these elements in the flat-faced injector.

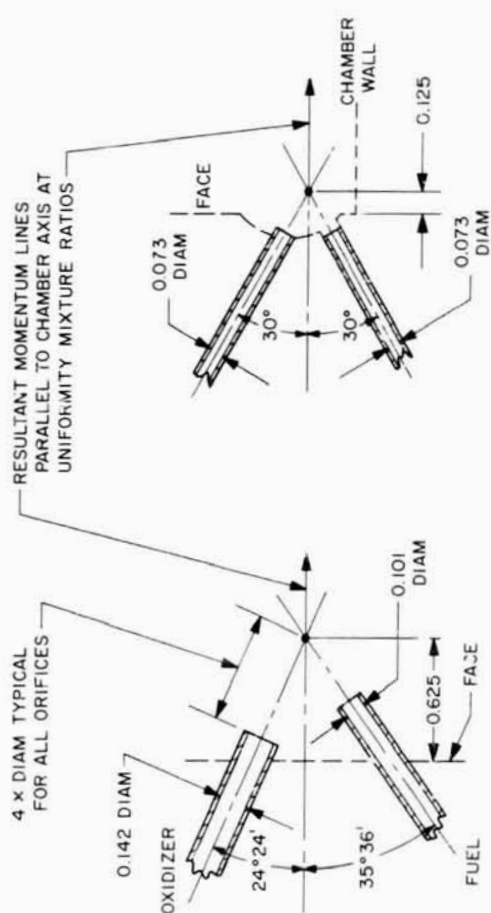
Table 2. Design conditions for the RC Injector 1/18-in. engine

Parameter	Main		Boundary		Overall	
	F ^b	O ^c	F	O	F	O
Flow rate, lbm/s	22.98	48.48	3.48	4.44	26.46	52.92
Injector Δp , psi (manifold to chamber)	129	120	108	96	—	—
Injection velocity, ft/s	86	58	92	68	—	—
Mixture ratio, \dot{m}_o/\dot{m}_f	2.11		1.27		2.00	
Fraction of total flow	0.90		0.10 ^d		100	
Number of injector elements	84		24		108	
Conditions:						
$A_t = 127.7 \text{ in.}^2$						
$p_c = 100 \text{ psia}$						
$\epsilon_r = 2.95$						
$\epsilon_r = 2.00$						
$F_{r,p} \cong 14,700 \text{ lbf}$						
$f^1 = 0.31 \text{ lbm/s-in.}^2$						
^a Propellant mass flux, defined as $\frac{\text{total propellant flow rate}}{\text{chamber cross-section area}}$						
^b Fuel.						
^c Oxidizer.						
^d Defined as Z.						

ALL MAIN ELEMENTS ORIFICE LENGTH $100 L/D$
 BOUNDARY ELEMENTS $30 L/D$



ALL DIMENSIONS IN INCHES



VIEW B
 BOUNDARY ELEMENTS

VIEW A
 MAIN ELEMENTS

Fig. 8. RC injector 1 basic design geometry

The element designs shown in Fig. 8 optimize the mixing uniformity in accordance with Ref. 2, and the element arrangement in the face optimizes the nominal uniformity of axial mass flux. The low mixture ratio boundary flow (Table 2) is meant to provide relatively low-temperature reaction products next to the chamber wall as is common practice for the reduction of heat transfer in many of today's operational engines. Separate manifolds feed the propellants to the main and boundary orifices permitting separate control over the flow conditions for either portion of the injector. Thus, besides having an injection pattern layout, which is representative of current design practice, and thereby enhancing its usefulness in studying nonsteady combustion phenomena plaguing "real" engine development, the engine can be operated over a range of flow conditions so that the influence of these variations on combustion behavior can be evaluated.

In the initial series of firings to characterize this combustion behavior, it was discovered that the engine exhibited the popping phenomenon over a relatively wide range of boundary flow conditions but that the actual range also depended somewhat on the main flow conditions. Eventually, a correlation of the occurrence of this rough combustion mode with the concentration of ox-

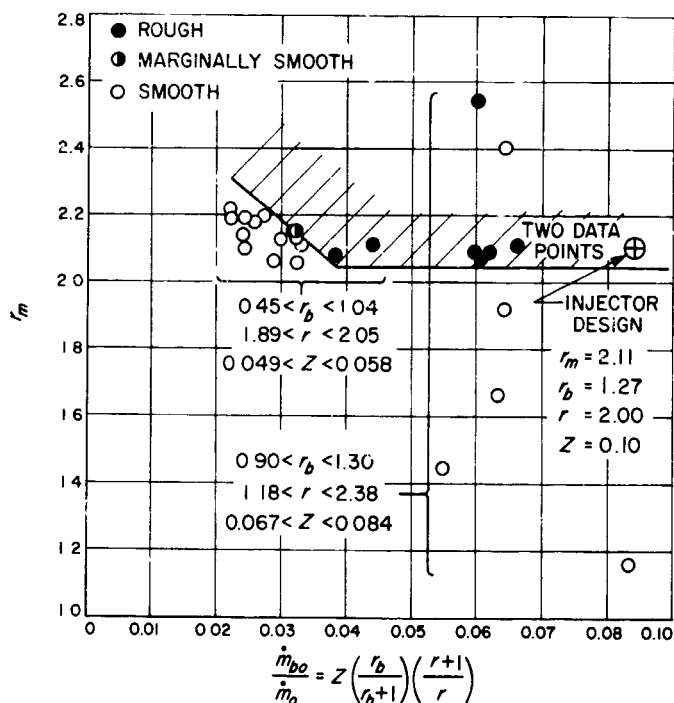


Fig. 9. Correlation of rough mode with concentration of oxidizer near the chamber wall; RC injector 1 with original boundary system

dizer near the chamber wall was obtained and is summarized in Fig. 9. (In these experiments the injector incorporated face baffles which inhibited the initiation of resonant combustion.) Data points representing separate firings are plotted as main flow mixture ratio (r_m) versus the ratio of boundary oxidizer flow to total oxidizer flow (\dot{m}_{b0}/\dot{m}_0). Smooth firings are shown as open circles and rough firings as solid circles. A somewhat arbitrarily positioned line separating these modes of operation is also shown. It is apparent from this figure that smooth combustion was not possible at the injector design point, even though a test stand feed system deficiency precluded operation at precisely that point.

As a result of this behavior, it was concluded that the source of the roughness originated in the region of the chamber boundary and that it was most likely related to processes controllable by the boundary flow injection scheme. However, before attempting to correct the problem through actual injector modifications, it was decided to establish the steady state performance of the engine in its original state by operating under the constraints for smooth combustion depicted in Fig. 9. These results were presented previously in SPS 37-30, Vol. IV, pp. 123-130 but for present purposes are repeated here in Fig. 10 in terms of relative performance (uncorrected for any losses) versus overall mixture ratio (r). The relative performance parameters are defined as

$$\eta_c = \frac{c^*}{c_{th}^*} \times 100$$

$$\eta_n = (C_F/C_{F_{th}})_{vac} \times 100$$

$$\eta = (I_s/I_{s_{th}})_{vac} \times 100$$

Where (see Ref. 3 for details of computational method):

c^* = characteristic velocity computed from the measured flow rates and chamber pressure; nozzle entrance static pressure converted to throat stagnation conditions.

C_F = thrust coefficient computed from measured thrust and chamber pressure; extrapolated to vacuum conditions.

I_s = specific impulse computed from measured thrust and flow rates; extrapolated to vacuum conditions.

The theoretical reference in each case was based on equilibrium flow at the overall mixture ratio for 100 psia

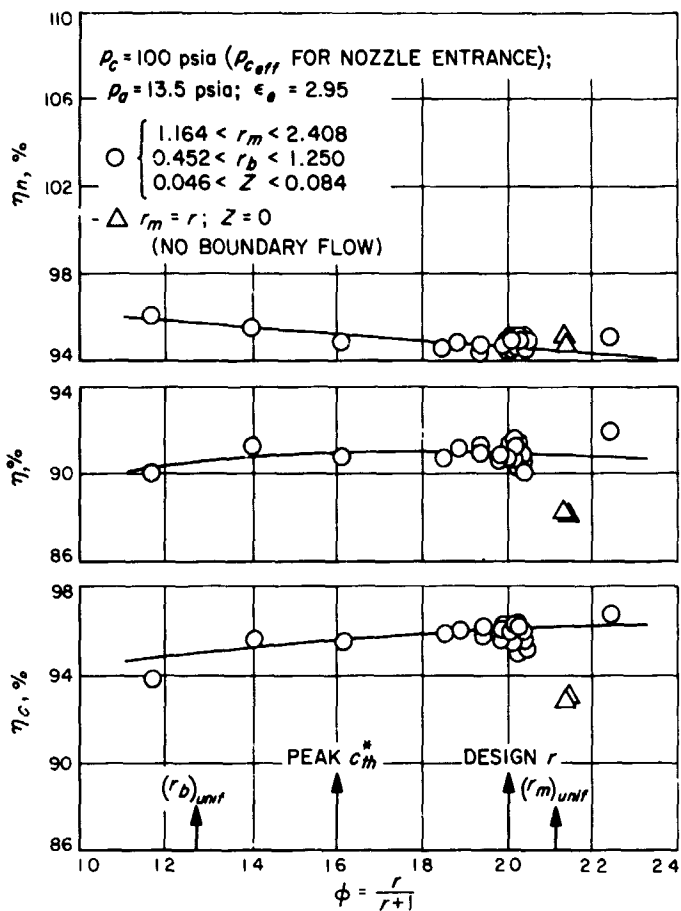


Fig. 10. Experimental relative performance of RC injector 1 with original boundary system; oxidizer near wall (runs B-914-917, -919, -926-939, -941-944)

chamber pressure expanding to a vacuum with an expansion ratio of 2.95. The following heats of formation (in K cal/mole) were used

$$N_2O_4 = -4.676, N_2H_4 = 12.050, UDMH = 12.724$$

Note that 96% of theoretical equilibrium c^* was produced by the engine at near the design r even though the optimum (design) boundary injection conditions could not be used. Note also, however, that a substantial reduction in performance (3%) occurred when no boundary flow was used. This result was attributed to combustion effects in the reacting sprays which separate the impinging propellant streams and reduce liquid phase mixing. For the outermost row of main elements, considering that the oxidizer streams are nearest the wall (cf Fig. 8), stream separation results in an oxidizer-rich region surrounding the core reactants. The net result, of course, a reduction in combustion efficiency by virtue of the in-

creased nonuniformity of overall mixture ratio, since in the absence of the boundary flow injection no fuel is available to counteract the excess oxidizer. It is further noted that the combined flow from the outer row of main elements and the boundary elements constitutes approximately 35% of the total injected flow; hence, even a small mixing degradation in these regions has a relatively large effect on the overall performance of the engine.

3. Combustion Behavior of the Revised Configuration

In view of the pronounced influence of the near-wall flow conditions on the behavior of the engine, as just discussed, an assessment of the boundary flow injection system was undertaken which indicated that modifications to the manifolds and orifice entries were needed to assure hydraulically stable flow conditions at the orifice exits. It was felt that improvements here might curtail the rough combustion mode and, hence, lessen the constraints on operating conditions, allowing the engine to be operated at its design point without employing face baffles.

Thus, it was presumed that if the roughness (or pops) were eliminated, spontaneous transitions to the resonant mode would be eliminated, but not the *artificially induced (bomb)* transitions. Success in accomplishing this would then enhance the control of experimental conditions under which the subsequent resonance studies could be performed. Additionally, it was felt that operation at the complete design mixture ratio condition would produce an increase in performance beyond the 96%, which had already been achieved.

Test stand revisions to correct the previously mentioned feed system deficiencies were also incorporated; but, since they affected only the capability of providing the required flow rates to the boundary manifold inlets, details of the revisions will not be discussed here.

Changes to the manifolds and orifice entries are summarized schematically in Fig. 11. (Note that no changes were made to the original element geometry or to the composite arrangement of the elements in the injector face.) The original three-entry-port semitoroidal manifolds were replaced by the single-port toroidal design as shown. The new design decreased the effective manifold volume (total volume between propellant valves and orifices) by a factor of two which, in itself, improved the starting transient flow control, but the manifold's chief attribute was improved propellant distribution and orifice entry configuration. Photographs of the original and revised injector

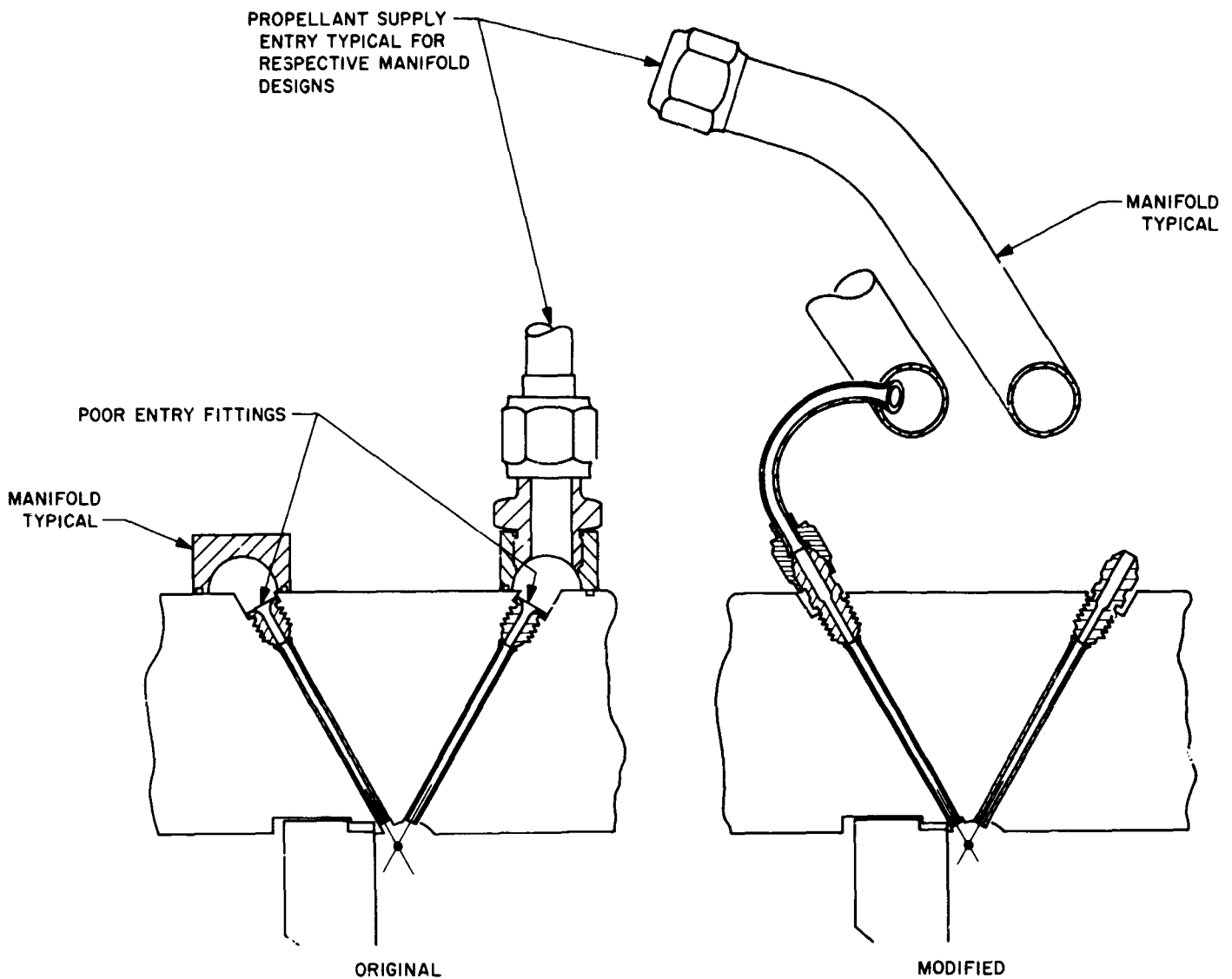


Fig. 11. Comparison of original and modified boundary inlet conditions

assemblies are shown in Fig. 12(a) and (b), respectively. Additional details of the revised manifold are illustrated in Fig. 13, which shows one of the stepped-diameter torus manifolds with its feed tubes supplying the individual orifices.

When the original injector was disassembled for incorporation of the new boundary manifolds, a discrepancy in the orifice inlet fittings (Fig. 11) was also discovered. The fittings were standard Army-Navy (AN) tubing fittings, which had been reworked to provide the contoured entry as well as a bore matching the orifice ID (oversize in relation to AN specifications). Unfortunately, the increased bore thinned the chamfered end of the fitting, which had then been inadvertently deformed during subsequent in-

jector assembly. The entire group of early firings had been made with these poor entry fittings.

This fitting problem was rectified for the revised manifold installation; however, the long entry formed by the feed tube arrangement apparently stabilizes the injected streams even with poor orifice entry fittings. In a cursory examination of these effects, no disruption of a representative stream was obtained when a poor fitting was used with the long-entry configuration. However, stream disruption in the form of increased spreading and directional instability was detected when the long tube entry was not employed. The standard 30-diam-length orifice tube was used in each case.

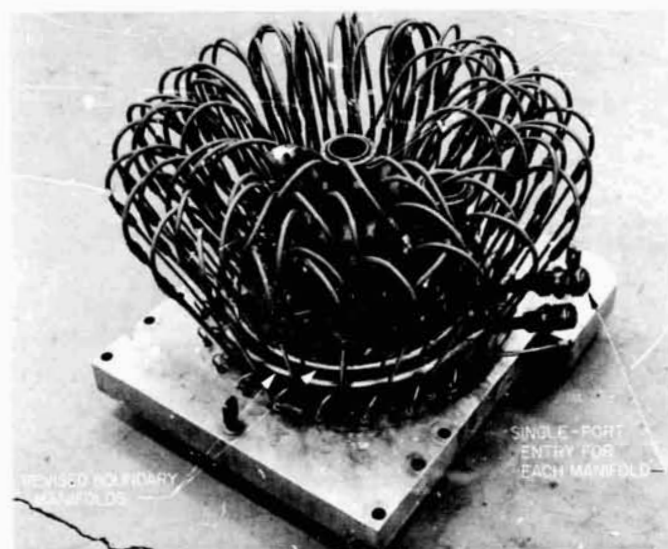
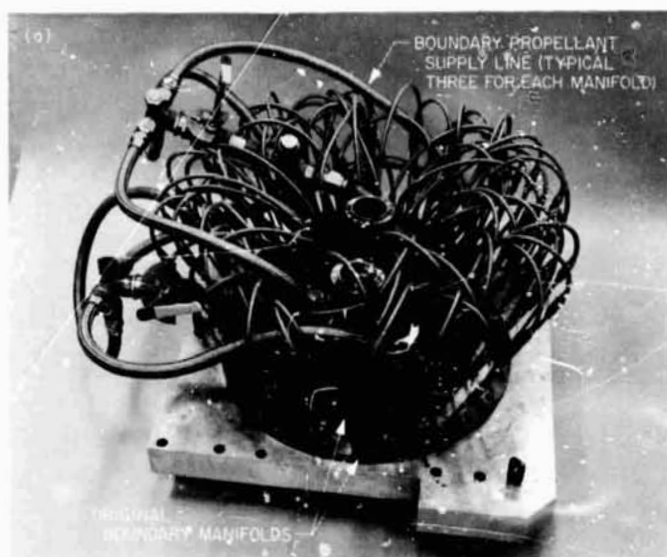


Fig. 12. RC injector 1 assembly: (a) original version; (b) modified version

With the boundary injection system revised as described above and the face baffles removed, evaluation of the combustion characteristics of the engine was extended to cover the range of nominal operating conditions listed in Table 3. Figures 14 and 15 summarize the results for the boundary bipropellant orientations of oxidizer-near-wall and fuel-near-wall, respectively, where relative performance (defined as before) is plotted versus boundary mixture ratio, with the main mixture ratio held nominally constant at its design value.

Except for the lowest value of boundary flow mass fraction ($Z = 0.05$), maximum relative performance was

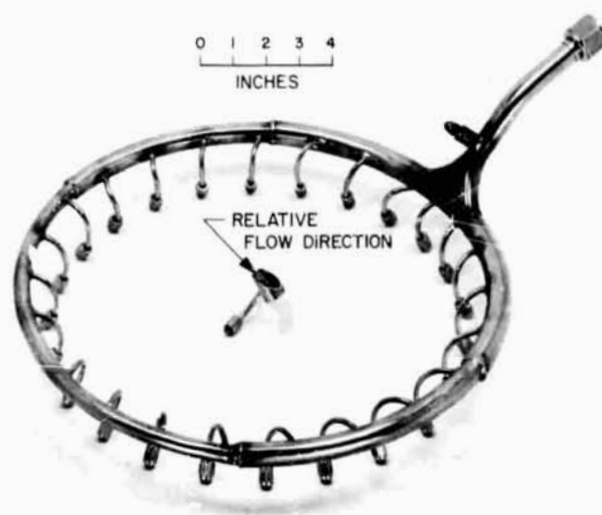


Fig. 13. Toroidal boundary manifold

Table 3. Range of nominal operating conditions used to evaluate the combustion characteristics of the revised RC injector 1/18-in. engine

Operating condition	Range
Main mixture ratio	Constant at design value of 2.11
Bipropellant boundary mixture ratio	0.5-2.11
Ratio of boundary to total propellant flow (Z)	0-0.15
Bipropellant boundary stream orientation (unlike impinging)	(1) Inner fuel; outer oxidizer (design condition) (2) Outer fuel; inner oxidizer
Single-propellant boundary flow (like-on-like impinging)	(1) Both streams fuel (2) Both streams oxidizer

obtained at near the design boundary mixture ratio for both propellant orientations. However, the oxidizer-near-wall condition gives $\sim 1\%$ better performance for all conditions.

For comparison, representative data for the injector with its original boundary manifold configuration are also shown on Fig. 14. From this it can be seen that, for the same operating conditions (i.e., $r_b = 0.6$), the modified boundary manifolding did not change the relative performance. However, the ability to operate at the design point does improve performance by at least 1.0%. A further performance increase to approximately 98% appears possible if the boundary flow mass fraction is increased to 15%.

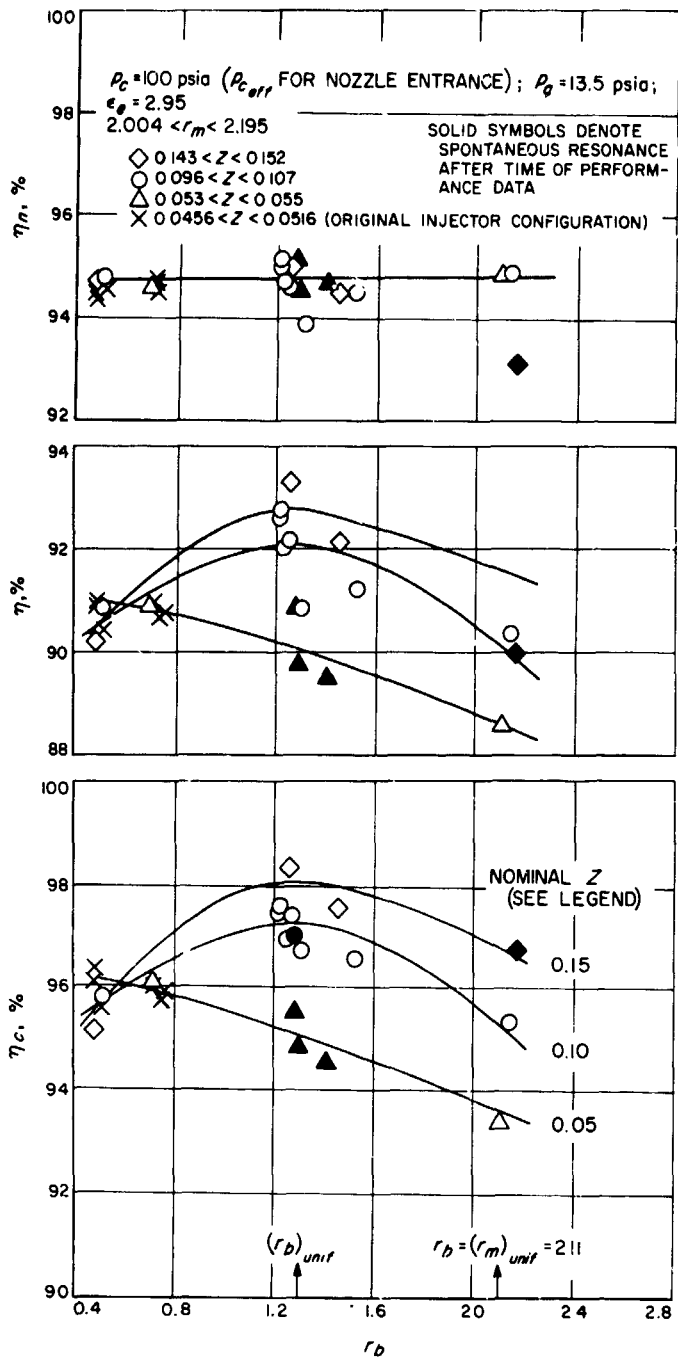


Fig. 14. Experimental relative performance of modified RC injector 1; boundary oxidizer near wall (runs B-1002, -1023, -1024, -1026-1029, -1030-1042)

A more convenient illustration of the effects of varying the boundary flow conditions is shown in Fig. 16, where the experimental η_c curves from Figs. 14 and 15 are compared with certain computed results and to the performance obtained for the single-propellant boundary-flow and no-boundary-flow firings (Table 3). The latter condition produced the same low performance (93%) ob-

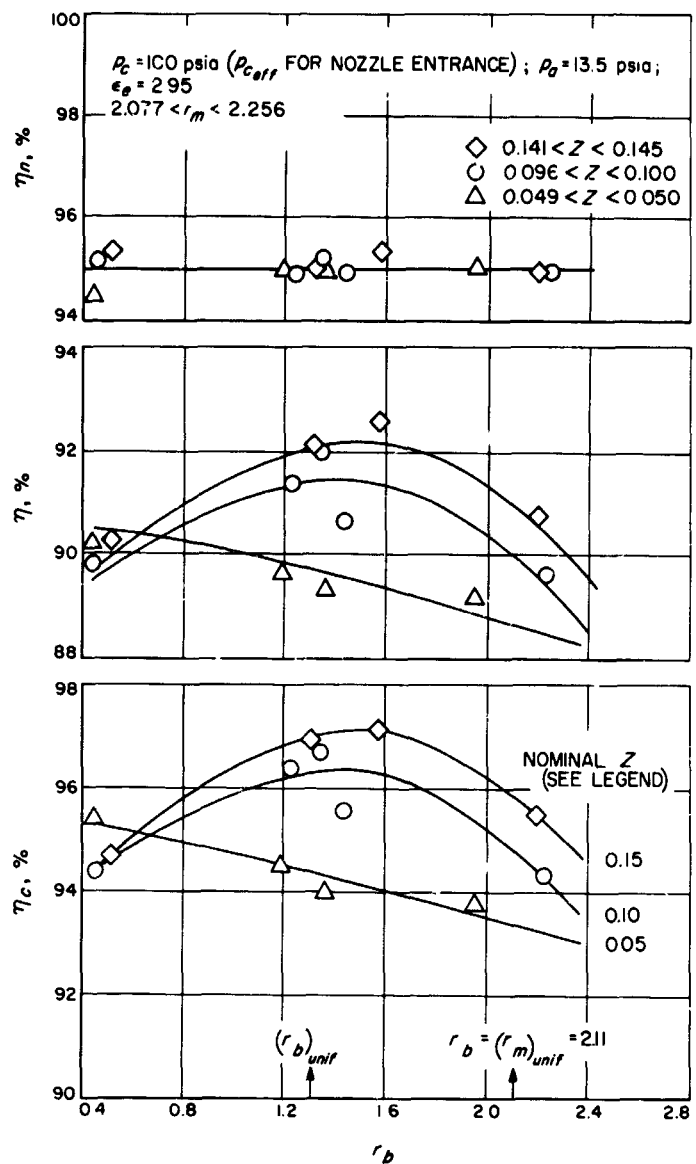


Fig. 15. Experimental relative performance of modified RC injector 1; boundary fuel near wall (runs B-1043, -1044, -1046-1049, -1060-1066)

served in the previous evaluations, while the oxidizer-only condition produced even lower performance. However, combustion efficiency returned to the 95-96% level when fuel-only was injected into the boundary region.

These single-propellant results seem to confirm the earlier conclusion that considerable degradation in mixing occurs in the outer row of the main flow through a stream separation effect and are analogous to results obtained by Johnson (Ref. 4). The introduction of fuel alone into the boundary region complements the oxidizer rich zone and enhances the relative performance. Conversely,

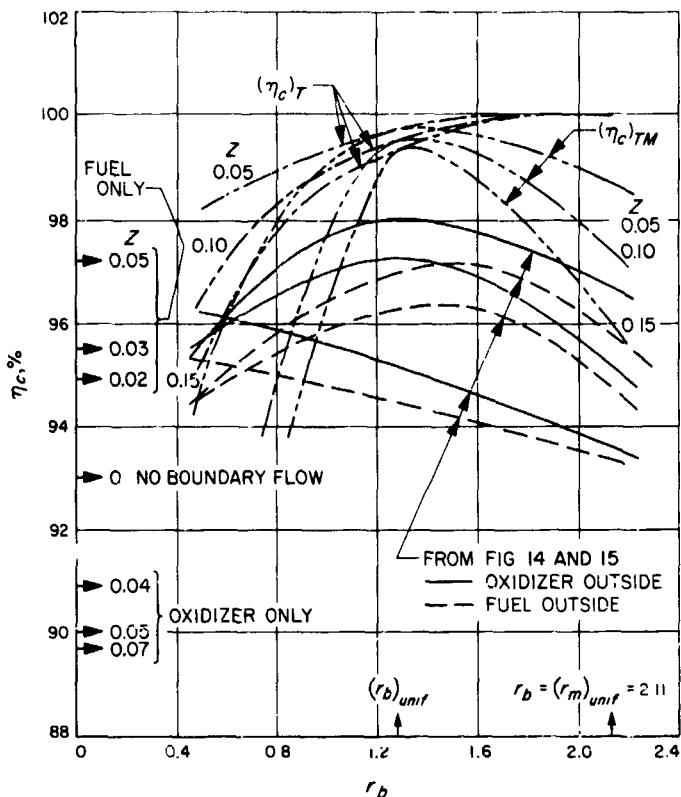


Fig. 16. Comparison of computed and experimental variation in relative combustion performance with boundary flow variation; modified RC injector 1

the injection of additional oxidizer reduces the performance.

On the other hand, bipropellant boundary injection seems to yield a somewhat different influence, at least for the higher fractions of boundary flow ($Z = 0.1$ and 0.15). In view of the forementioned large proportion of total mass flux contained in the outer region of the combustion volume and the consequent sensitivity of overall performance to efficient reaction in this region, it is reasonable to expect that the mixing factor defined by Rupe (Ref. 2) for unlike impinging doublets might explain the trend of the variation in relative performance with variations in boundary flow mixture ratio.

In order to illustrate these effects, a simple computational model was assumed for the engine wherein the main and boundary flows supply propellants to two separate zones of different mixture ratio and/or fraction of total mass flow. Each zone was presumed to react to complete thermal and chemical equilibrium according to its injected composition, with no interaction with each

other. The expected thermochemical performance was then taken to be closely approximated (Ref. 5) by the mass-weighted average theoretical performance of the two zones. Thus, for nonuniform thermochemical effects only

$$c_T^* = Z(c_{th}^*)_b + (1 - Z)(c_{th}^*)_m \quad (1)$$

Where the subscripts T , b , and m refer to thermochemical, boundary, and main, respectively.

To account for degraded spray mixing and subsequent incomplete thermochemistry in the boundary flow zone due to off-design flow conditions, a mixing efficiency was defined as

$$\eta_M = \frac{(E_M)_b}{80} \times 100 \quad (2)$$

where the mixing factor $(E_M)_b$ is a measure of the uniformity of mixture ratio in the resultant spray from a pair of impinging streams. Actual values for $(E_M)_b$ for the appropriate boundary flow mixture ratio are taken from the empirically derived correlation presented in Ref. 2. According to this same correlation, $(E_M)_b$ has a maximum mean value of 80 (for the boundary element design) at the so-called uniformity mixture ratio, which occurs when the product of velocity-pressure and diameter ratios for the doublet streams is unity.

Inserting Eq. (2) into the boundary performance term appropriately and substituting a constant value of 5570 ft/s for $(c_{th}^*)_m$ [since for these experiments $r_m = (r_m)_{unif} = \text{constant}$] modifies Eq. (1) to include variable spray-mixing effects in the boundary flow. Thus,

$$c_{TM}^* = \frac{\eta_M^2 (c_{th}^*)_b}{100} + 5570(1 - Z) \quad (3)$$

where the subscript TM refers to a combination of nonuniform thermochemistry and variable spray mixing effects.

Computed theoretical performance is now defined as either

$$(\eta_c)_T = \frac{c_T^*}{c_{th}^*} \times 100 \quad (4)$$

or

$$(\eta_c)_{TM} = \frac{c_{TM}^*}{c_{th}^*} \times 100 \quad (5)$$

where c_{th}^* is, again, the theoretical equilibrium performance based on overall mixture ratio.

Evaluations of Eqs. (4) and (5) over the range of conditions covered by the experiments are plotted as the uppermost sets of curves in Fig. 16. Comparison of the computed and experimental trends of performance variation with r_b indicates that, indeed, inclusion of the mixing factor variation is required to predict the experimental variation and that relatively little stream separation is occurring with the boundary injection elements, which are roughly half the size scale of the main elements.

Evidence that *some* separation occurs, however, is believed to be manifested in the slightly lower performance potential of the fuel-near-wall orientation, since this orientation would direct any separated boundary oxidizer toward the already oxidizer rich outer periphery of the main-flow reactants. Also, both of the computational methods show performance trends for variable boundary mass fraction, which are opposite to the experimental trends. These facts and the singular performance curve for $Z = 0.05$ are believed to result from zone interactions (e.g., secondary mixing between the main and boundary zones), which were not considered in the computations.

Spontaneous resonant combustion was encountered several times in the course of these experiments, due to the sensitivity of the un baffled injector to chamber pressure disturbances. The solid symbols shown in Fig. 14 indicate those firings in which the transition took place from steady state conditions. This transitional time was characteristic for the oxidizer-near-wall stream orientation. Whether or not the triggering disturbance was typically a random pop is not known (although this is presumed); however, at no time did the grossly rough combustion observed for the original injector appear.

For the fuel-near-wall orientation considerable difficulty was experienced in getting through the starting transient without triggering the resonant mode. However, no firing exhibited a transition once the start was successfully accomplished. For this reason, no resonant runs are indicated on Fig. 15 even though the fuel-near-wall orientation appeared to be the most unstable. Likewise, the fuel-only condition was very susceptible to transitions during the start.

Definitive measurements on the fully developed resonant disturbance exhibited by this engine are the subject of future experiments. Suffice it to say that the limited high response measurements taken here indicate that:

- (1) The sustained resonant wave appears to be the same rotating mode regardless of transitional time.
- (2) No preferential rotation direction was observed.
- (3) Boundary flow conditions did have a significant influence on wave amplitude, velocity, and wave form; for example, absence of boundary flow reduced the amplitude approximately 50%.

4. Conclusions

- (1) The described revisions to the boundary injection system hydraulic configuration resulted in an extension of the smooth combustion regime but apparently did not completely eliminate the popping phenomenon.
- (2) The revisions did not modify the performance of the engine for the same off-design flow conditions, however, a clearly improved performance was obtained at the design condition.
- (3) The engine is dynamically unstable without face baffles.
- (4) The sustained resonant disturbance is significantly affected by the prevailing boundary flow conditions.

C. Injector Development: Stream Separation Experiments, R. W. Riebling

1. Introduction

For most propellant combinations, several primary processes must be efficiently accomplished to ensure good combustion, regardless of the type of injector employed. These are: (1) propellant mixing, (2) atomization and vaporization, and (3) chemical reaction. Normally, chemical reaction rates are quite rapid compared to the rates of mixing and atomization, so that one or both of the latter two physical processes usually controls the overall combustion rate.

For unlike-impinging-jet injectors burning highly reactive hypergolic earth-storables of the nitrogen tetroxide (N_2O_4)/hydrazine (N_2H_4) class, it is well known that performance is degraded as the jet diameters are increased. This is attributed (Ref. 6) to rapid liquid-phase chemical reactions at the interface between the impinging streams of unlike propellants. The gaseous combustion products formed in the impingement region are believed to "blow apart" or separate the two liquid jets to the extent that incompletely mixed and poorly atomized sprays are formed.

The work of Johnson (Ref. 7) and Stanford (SPS 37-31, and -36, Vol. IV, pp. 192 and 173, respectively) showed that these stream separation effects are negligible with jets of small diameter (~ 0.02 in.), become noticeable at intermediate diameters (~ 0.05 in.), and seriously degrade performance with large (~ 0.25 -in.) diameter jets. Thus, it appears that there is some critical stream dimension (for jets it is their diameter) above which disruption of the impingement process, and, therefore, performance degradation can occur.

One way of reducing the dimension of a round jet, hopefully to a value below the critical stream dimension, is to impinge each jet tangentially against a curved deflector surface, where it spreads to form a thin, flat sheet (Fig. 17). Impinging-sheet injectors of this type have been under development at JPL for several years. They are generically similar to impinging-jet devices, but the sheets are quite thin (sheet thickness is typically only 1/8 of jet diameter), so it should be possible to use relatively large jets before the critical stream dimension is exceeded.

In order to verify this contention, single element unlike impinging-sheet injectors with jet diameters of 0.08 and 0.33 in. were built and fired with N_2O_4/N_2H_4 in a series of experiments designed to detect and measure the extent of propellant stream separation. The results of tests made with the 0.08-in. orifice diameter injector were reported

in SPS 37-44, Vol. IV. This report presents the results of experiments with the larger injector and compares them with all previously reported data (for both jets and sheets) in terms of the critical stream dimension.

2. Apparatus and Procedures

The injector is shown in Fig. 18. Each deflector surface had a radius of 2.300 in. and turned the flow through 45 deg, resulting in a 90-deg impingement. Both orifices were 0.325 in. diam, and over 100 diameters in length to assure attainment of fully-developed turbulent flow. The overhang ratio

$$\frac{h}{d} \equiv \frac{R}{d} (1 - \cos \theta) \quad (1)$$

of each deflector/orifice pair was 2.07. Using the correlation developed in Ref. 8, the maximum sheet thickness (at the sheet centerline) was found to be 0.05 in. The devices were mounted to the injector face in such a manner that the spacing between the knife-edges of the deflectors could be varied continuously from 0 to 1 in. A constant spacing of 0.1 in. was used in the present experiments. Under nominal operating conditions (mixture ratio = 1.2, chamber pressure = 150 psia) injection velocities were 72 and 84 ft/s for oxidizer and fuel, respectively. Construction was of type 304 stainless steel.

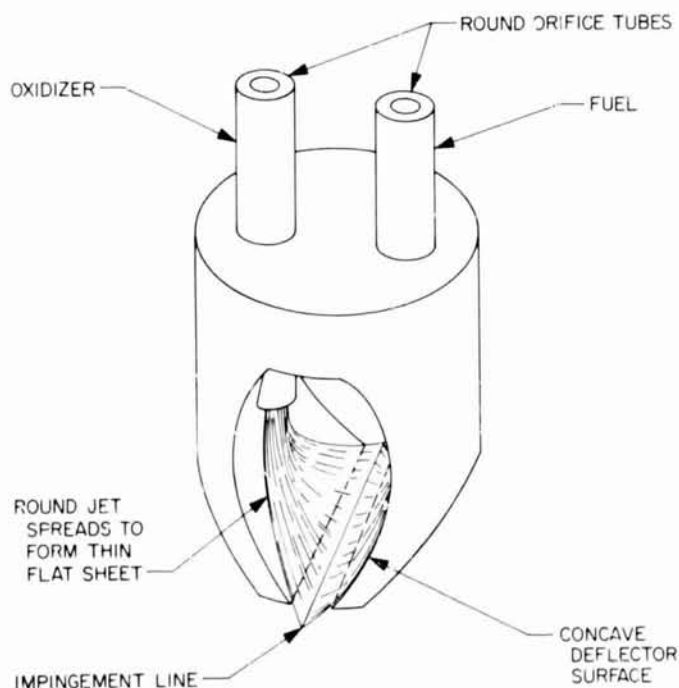


Fig. 17. Typical impinging-sheet injector element

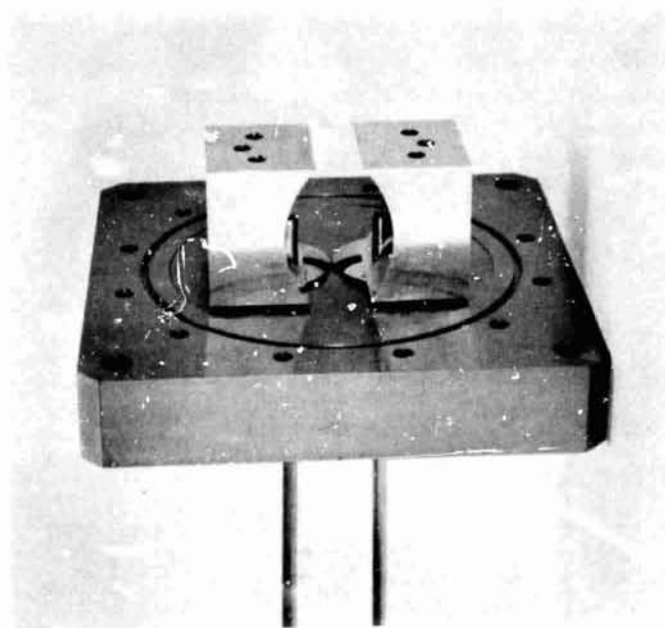


Fig. 18. 2000-lbf thrust single element, impinging-sheet injector

The combustion chamber was illustrated in Ref. 7. It had a characteristic length (L^*) of approximately 110 in. and was divided into two longitudinal channels by a mild steel baffle plate oriented in a plane perpendicular to the injector face. The top of this baffle was situated far enough from the injector to avoid interference with the impingement process, and the plate extended to a point in the convergent portion of the nozzle just upstream of the physical throat. Two full-cone commercial spray nozzles were located in the chamber wall, one on each side of the baffle, and turbulence rings were mounted in the chamber, downstream of the spray nozzles.

The experiments consisted of determining the difference in performance measured when the propellants sprayed from the side nozzles, one spraying fuel and the other oxidizer, were reversed. The concept involved is that if the propellants flowing from the main injector are repelled from each other to form a fuel-rich zone on the fuel orifice side and an oxidizer-rich zone on the oxidizer orifice side of the chamber, the baffle should prevent secondary mixing due to turbulence and diffusion. Thus, one channel should contain an oxidizer-rich flow and the other a fuel-rich flow of gases. Spraying oxidizer into fuel-rich gases and fuel into the oxidizer-rich gases (termed "unlike" propellants henceforth), should increase performance, while spraying fuel into fuel-rich gases and oxidizer into oxidizer-rich gases (termed "like" propellants henceforth) should reduce performance. If the streams from the main injector do not blow apart, and a relatively uniform mixture ratio distribution exists in the chamber, performance should remain relatively unchanged when the propellant sprays are reversed. If the streams penetrate through each other, the fuel-rich and oxidizer-rich channels will be reversed and the performance changes should indicate this condition also.

3. Experimental Results

Eight short-duration (1-3 s) firings were conducted, in which propellants were injected through the main injector plus the side-spray nozzles along the chamber walls. In some tests, "like" propellants were injected at the sides, while in others, "unlike" propellants were injected. In each of these series, the side flows were varied from about eight to nearly thirty weight percent of the total flow rate, while the flow through the main element was held constant. To measure the datum performance level the engine was fired at the design flow rate with no side injection.

The results are summarized in Table 4. Chamber pressures were measured at the entrance to the convergent section of the nozzle and corrected to stagnation values. Performance was evaluated on the basis of the total flow rate of propellants (from both the main element and the side streams) injected into the chamber. Characteristic velocity efficiency η_{c^*} was chosen as the comparative index of performance level, and is the ratio of the measured value of c^* to that theoretically attainable with full shifting equilibrium flow at the experimentally measured values of chamber stagnation pressure and mixture ratio. No corrections were made to the measured values of c^* because the results were to be used primarily for comparative purposes.

4. Discussion of Results

The test results are shown graphically in Fig. 19. From a reference level of 75.9% with no side-stream injection, η_{c^*} dropped steadily as the fraction of propellants injected as "like" side flows was increased. This indicated that the propellant streams had not penetrated each other and that the oxidizer-orifice side of the injector spray was quite oxidizer-rich. Since there was little unreacted fuel on that

Table 4. Results of baffled-chamber firings to determine degree of stream separation of unlike impinging sheets in 2000-lbf injector

Test No.	Kind of side spray	Oxidizer flow, lbm/s		Fuel flow, lbm/s		\dot{w}_t , lbm/s	Spray, wt % side	Overall mixture ratio	Chamber pressure p_c , psia	Characteristic velocity c^* , ft/s	Combustion efficiency η_{c^*} , %
		Main element	Side spray	Main element	Side spray						
1	Like	2.34	0.92	2.05	0.84	6.15	28.6	1.13	129	4095	70.3
2	Like	2.19	0.44	1.92	0.27	4.82	14.5	1.20	105	4230	73.0
3	Like	2.27	0.24	1.94	0.13	4.58	8.1	1.21	101	4297	74.1
4	None	2.29	0	1.77	0	4.06	0	1.30	91	4360	75.9
5	Unlike	2.28	0.24	1.95	0.14	4.61	8.25	1.21	108	4550	78.4
6	Unlike	2.24	0.42	1.93	0.27	4.86	14.2	1.21	117	4685	80.7
7	Unlike	2.34	0.63	2.02	0.52	5.50	20.7	1.17	131	4643	79.8
8	Unlike	2.32	0.90	2.01	0.83	6.06	28.6	1.13	142	4565	78.4

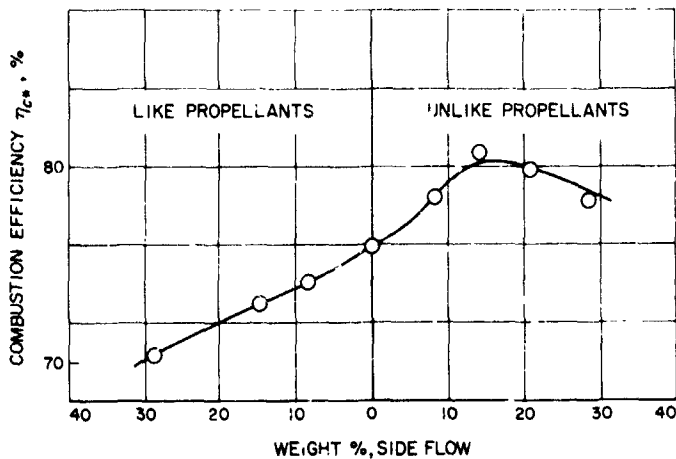


Fig. 19. Variation of combustion efficiency with side flow in baffled chamber experiments with 2000-lbf single element impinging-sheet injector

side of the main element's spray with which the raw oxidizer from the side spray could react, performance was lowered by the amount of heat absorbed by the uncombined oxidizer. Similar arguments apply to the fuel-rich side. On the other hand, when "unlike" propellants were added as side sprays the performance increased to a maximum of about 80% at 20% side flow. From these data it may be concluded that severe stream separation occurred under the conditions of these experiments.

The relative change in η_{cs} , and not its absolute value, is of significance in discussing these results. Disruption of the impingement process can only result in inefficient mixing and poor atomization, both of which reduce the absolute levels of η_{cs} . Introduction of unlike side sprays corrects to some degree for inefficient primary mixing, as shown in Fig. 19, but has little effect on atomization (and, therefore, propellant vaporization rates). Somewhat

greater performance increases might have been possible had some attempt been made at optimizing the side injection apparatus but such efforts were beyond the scope or intent of the program. The primary purpose of the side sprays in this experiment was to detect, rather than remedy, stream separation effects.

The results of all previous stream separation experiments are compared in Table 5. For impinging-jets, the critical stream dimension is taken to be the jet diameter, while for impinging-sheets it is the maximum (centerline) thickness calculated from the general correlation of Ref. 8. It is seen that no appreciable stream separation occurred when the critical stream dimension was about 0.02 in. or less, but that values in excess of about 0.05 in. resulted in separation and concomitant performance degradation. The point of incipient combustion effects must be located somewhere between those two limiting values. At present it is not known whether the onset of stream separation is gradual or sudden as the critical dimension is increased.

Further examination of Table 5 shows that stream separation occurred with the 0.06-in. orifice diameter (100-lbf thrust/element) jet injector, but not with the 100-lbf/element sheet injector, even though the latter device had larger (0.08-in.) orifices. This is attributed to the eight-fold reduction in the critical stream dimension effected by flattening the jets into thin sheets. It would, therefore, be expected that a 2000-lbf single element not susceptible to these combustion effects would be possible, provided that its sheet thickness could be reduced to something on the order of 0.02 in. The general sheet thickness correlation of Ref. 8 indicates that this could be done if the overhang ratio (h/l) of the element were greater than approximately 4. Such an element is presently being designed and will be test-fired to verify this contention.

Table 5. Effect of element scale on stream separation for various single element impinging-stream injectors

Element type	Thrust/element, lbf	Source	Orifice diameter, in.	Maximum sheet thickness, in.	Critical stream dimension, in.	Stream separation?
Impinging jet	2000	Ref. 7	0.24	—	0.24	Yes
Impinging sheet	2000	This report	0.33	0.05	0.05	Yes
Impinging jet	100	SPS 37-31, Vol. IV	0.06	—	0.06	Yes
Impinging sheet	100	SPS 37-44, Vol. IV	0.08	0.01	0.01	No
Impinging jet	10	SPS 37-36, Vol. IV	0.02	—	0.02	No

References

1. Clayton, R. M., and Rogero, R. S., *Experimental Measurements on a Rotating Detonation-Like Wave Observed During Liquid Rocket Resonant Combustion*, Technical Report 32-788, Jet Propulsion Laboratory, Pasadena, Calif., Aug. 15, 1965.
2. Rupe, J. H., "A Correlation Between the Dynamic Properties of a Pair of Impinging Streams and the Uniformity of Mixture Ratio Distribution in the Resulting Spray," Progress Report 20-209, Jet Propulsion Laboratory, Pasadena, California, Mar. 28, 1956.
3. Clayton, R. M., Rupe, J. H., and Gerbracht, F. G., *An Experimental Correlation of the Nonreactive Properties of Injection Schemes and Combustion Effects in a Liquid Propellant Rocket Engine. Part II: Experimental Apparatus and Techniques*, Technical Report 32-255, Jet Propulsion Laboratory, Pasadena, Calif., May 15, 1967.
4. Johnson, B. H., *An Experimental Investigation of the Effects of Combustion on the Mixing of Highly Reactive Liquid Propellants*, Technical Report 32-689, Jet Propulsion Laboratory, Pasadena, Calif., July 15, 1965.
5. Wrobel, J. R., "Some Effects of Gas Stratification on Choked Nozzle Flows," AIAA paper 64-266 (June 29-July 2, 1965).
6. Elverum, G. W., Jr., and Staudhammer, P., *The Effect of Rapid Liquid-Phase Reactions on Injector Design and Combustion in Rocket Motors*, Progress Report 30-4, Jet Propulsion Laboratory, Pasadena, Calif., Aug. 25, 1959.
7. Johnson, B. H., *An Experimental Evaluation of the Effects of Combustion on the Mixing of Highly Reactive Liquid Propellants*, Technical Report 32-689, Jet Propulsion Laboratory, Pasadena, Calif., July 15, 1965.
8. Riebling, R. W., *The Formation and Properties of Liquid Sheets Suitable for Use in Rocket Engine Injectors*, Technical Report 32-1112, Jet Propulsion Laboratory, Pasadena, Calif., June 15, 1967.

N67-34772

XI. Lunar and Planetary Instruments

SPACE SCIENCES DIVISION

A. Development of Wet Chemical Process Control Circuitry, J. R. Clark

1. Introduction

Wet-chemistry experiments in earth orbit or on a planetary surface require control circuitry for the many processes and setup steps needed to obtain specific chemical reactions. These reactions may be involved with the analysis of urine and blood for specific compounds that are important in determining man's physical condition. On a planetary surface the reactions might be used for the detection of the basic compounds found in living organisms. Some typical processes and setup steps are pump cycling, valve positioning, filling or emptying a test cell of fluid, proportioning fluids, mixing fluids, and extracting a representative test sample from a larger volume of fluid. Processes of this type are discussed here.

Normally, the control circuitry will consist of (1) integrated circuits to perform the logic functions, and (2) discrete components to buffer the integrated circuits and

to act as drivers or current amplifiers for the prime movers. The circuitry should be designed to operate on level changes rather than pulses, and the use of monostable and bistable multivibrators should be held to a minimum since they are sensitive to false triggering.

2. Discussion

The following circuits have been constructed and are currently under evaluation.

a. Waste pump cycle control (Fig. 1). With this circuitry the pump must operate through one cycle for each positive-going level change at the input. When the input to gate 1 goes positive (logical 1 to logical 0 change—negative logic), transistor Q3 is turned off via gates 4 and 5. The toggle made up of gates 2 and 3 is also set so that the second input to gate 4 is at ground potential (logical 1). The off condition of Q3 turns on Q2 and places approximately +3 Vdc across the motor. The motor now drives the pump and the cam as shown. The switch then "rides off" the cam lobe and applies +3 Vdc

BLANK PAGE

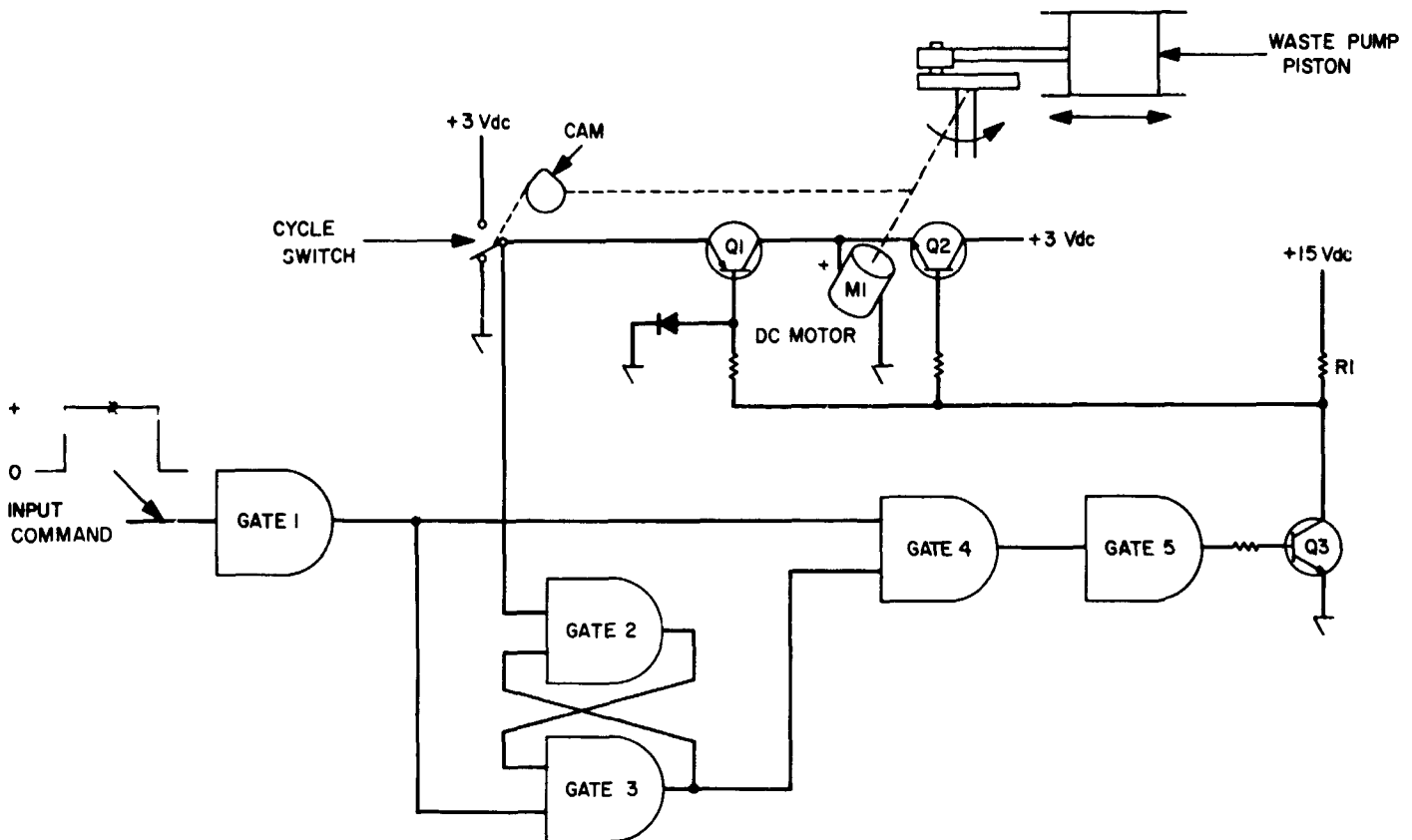


Fig. 1. Waste pump cycle control

to the input of gate 2. This toggles the flip-flop so as to turn on transistor Q3 via gates 4 and 5, and switches control of the pump from the input command to the cycle switch. Transistor Q2 now turns off. The base of transistor Q1 is grounded, but its emitter is tied to +3 Vdc through the cycle switch, thus forward-biasing its base-emitter junction and turning it on. Transistor Q1 now supplies motor current, and the pump continues to drive until the cam lobe again reverses the switch so as to ground the emitter of Q1, terminating the pump cycle and dynamically braking the motor to minimize coasting effects.

b. Valve position control. This control requires that any one of the four valve positions shown in Fig. 2 may be selected so that the correct fluid can be utilized. To rotate the valve from position 4 to position 1, a current is supplied to turn on transistor Q1 and provide a ground return for the dc motor. The metal disk of the rotary switch mounted on the end of the valve now rotates until the notch in the disk interrupts the motor return or the collector circuit of transistor Q1. When this happens, the disk voltage rises. This change is fed to the input of

gate 1 which triggers the monostable multivibrator. This in turn momentarily energizes the dynamic braking relay through gate 2. The motor stops as soon as the motor return is broken, and both switch and valve position are synchronized.

c. Test cell plunger control. Here the requirement is to fill or empty a test cell of solutions by means of the plunger (Fig. 3). The plunger is pulled backward or pushed forward by means of a lead screw, motor combination, as shown in the figure. By connecting the motor in a bridge circuit through a full limit switch and an empty limit switch, the dc motor can be controlled to go both directions to either fill or empty the test cell. Energizing transistors Q3 and Q4 will cause the motor to fill; energizing transistors Q7 and Q8 will cause the test cell to empty. Connecting the limit switches as shown allows the plunger to be driven out of the limit when the test cell is either full or empty. To fill the test cell, a fill command is applied to one input of gate 1 to turn on transistor Q1 through gate 2. This will turn on transistors Q3 and Q4 and cause the motor to rotate in the fill direction. Removing the fill command will stop the motor.

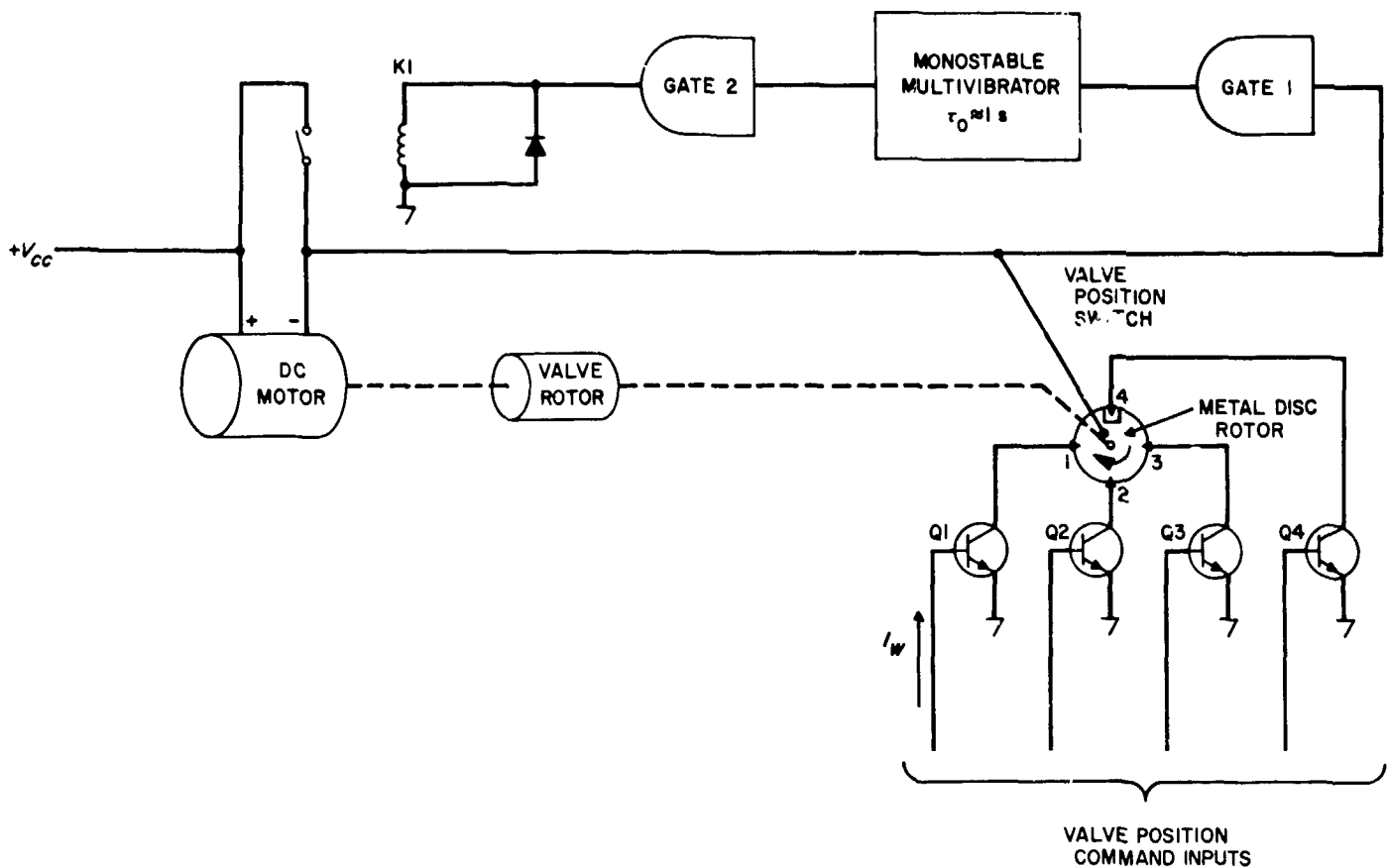


Fig. 2. Valve position control

In a like manner, an empty command can be applied to gate 5 to turn on transistor Q5 through gate 6. This will reverse the motor direction and cause the test cell plunger to empty the test cell.

To accomplish the mixing operation, full and empty limit switch actuations are sensed and used to reverse the drive inputs to either Q1 or Q5. This is done by connecting the normally closed contacts of the full and empty limit switches to the toggle that is made up of gates 7 and 8. First, the mix inhibit is released. The flip-flop output to gate 4 remains at ground potential. The output of gate 4 is then at a positive potential, thereby turning on transistor Q5 via gates 5 and 6. This causes the plunger to drive in a direction so as to empty the test cell. When the empty limit switch is actuated, the flip-flop is toggled via the normally closed contact of the empty limit switch, since transistor Q7 is still on. Transistor Q5 is then turned off and the input from the flip-flop to gate 3 is now at ground potential. The output of gate 3 turns on transistor Q1 via gates 1 and 2 as well as

transistors Q3 and Q4, causing the motor to drive in a direction such that the test cell fills again.

This oscillatory action can be carried on as long as needed to complete a mixing process. To terminate the mixing process, the mix-inhibit gate is reapplied to preset the flip-flop made up of gates 7 and 8 and to block further commands to gates 3 and 4. The mix process will normally be terminated upon conclusion of an integral number of full limit switch actuations.

d. Revolutions counting for metering of fluids into the test cell. The test-cell plunger must be pulled back a specified number of lead-screw drive-gear revolutions so that various reagents may be metered into the test cell. This is done by counting the number of revolutions made by the drive gear of the test-cell plunger, as shown in Fig. 4. A revolutions count switch is actuated through a crack pin and lever. The output of the revolutions count switch toggles the flip-flop made up of gates 1 and 2 so as

NC-NORMALLY CLOSED
NO-NORMALLY OPEN

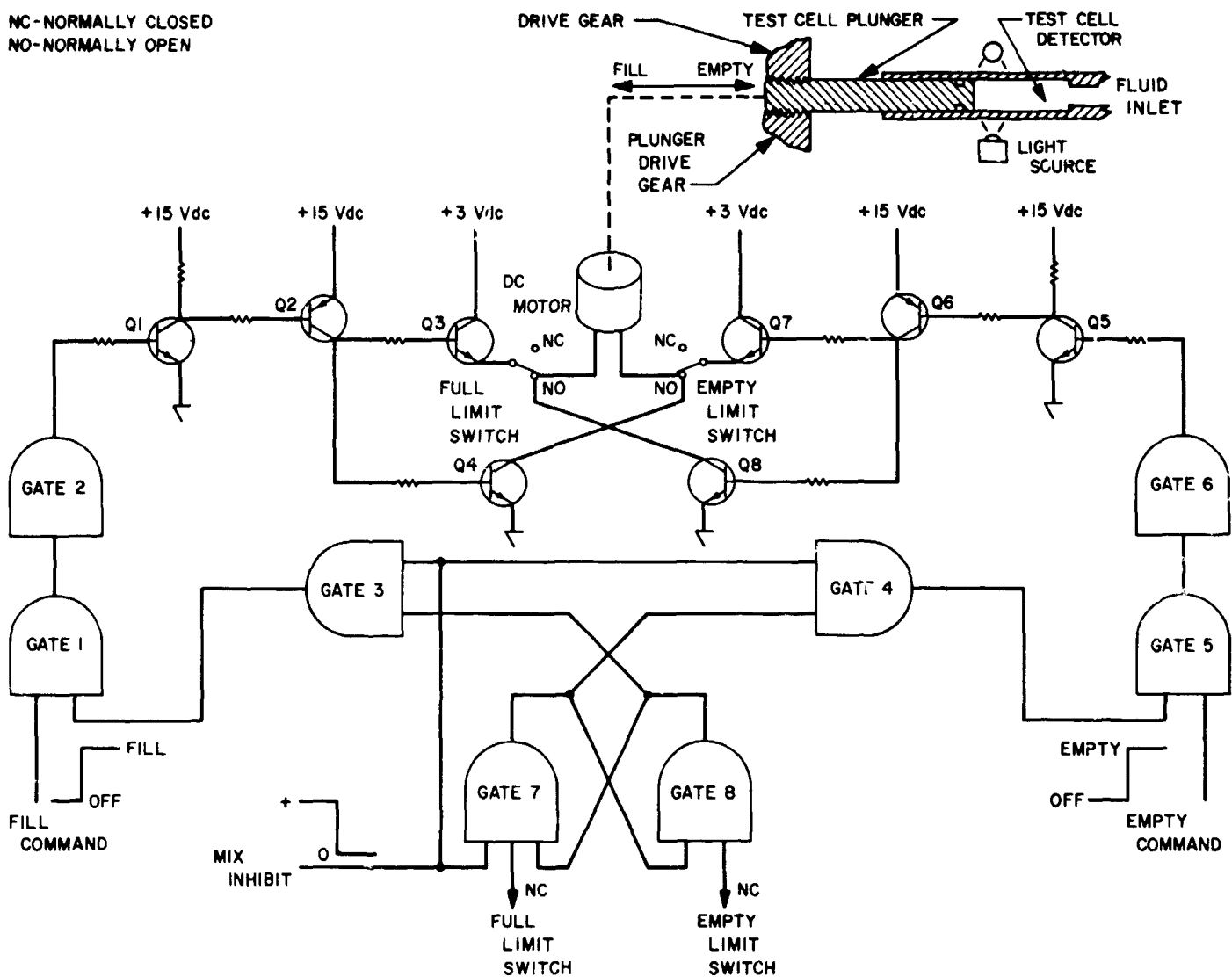


Fig. 3. Test cell plunger control

to generate a noise-free level change which is counted by the counters (B0, B1, and B2). Gate 3 is used to detect a specific count in the counter that corresponds to a specified number of revolutions. The output of gate 3 will go positive when the specific count or number of revolutions has been reached.

e. Fluid sample control (Fig. 5). A discrete sample must be obtained from the liquid passing by the inlet; the accumulated sample is then discharged upon command. The mechanism used for filling or emptying is similar to the test cell plunger control discussed above. With the same transistor bridge arrangement, the motor will fill or empty the accumulator upon command. If Q1 is energized or turned on, the accumulator will fill; if Q5 is turned on, the accumulator will empty.

A sample sequence is initiated by applying a positive voltage on the sample command line; this toggles the flip-flop made up of gates 1 and 2 so that the second input to gate 3 is at ground potential. This activates the system and also allows for fluid transport lags so that the sample taken is representative of what is passing by the inlet. When the sample command goes back to ground potential, the output of gate 3 goes positive and turns on transistor Q1 via gates 4 and 5 causing the accumulator piston to begin pulling back. When the cam rotates to the point where the switch is moved off the lobe, the common terminal of the switch is at a plus voltage. The plus voltage then toggles the flip-flop made up of gates 1 and 2 so that the second input to gate 3 is at plus potential, blocking any further sample commands that might occur.

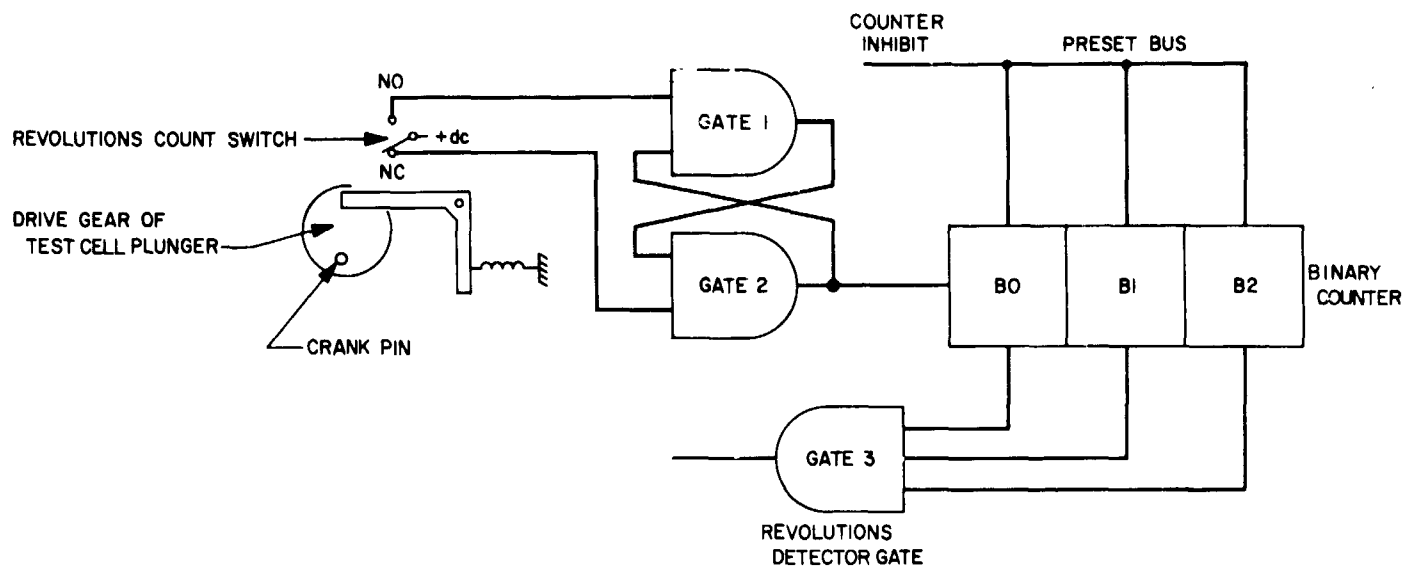


Fig. 4. Revolution counting for metering of fluids

The common line is also fed from the switch to a second input of gate 4 so that control of the accumulator is switched from the sample command line to the cycle switch. When the cam makes one full revolution, the common line is driven back to ground potential. This will ground the second input of gate 4, turning off transistor Q1 and stopping the sample process. When Q1 turns off, the monostable multivibrator is energized via gates 6 and 9. The monostable multivibrator produces a 1-s pulse which is used to energize the relay K1 and thus provide dynamic braking on the motor.

After a number of samples have been taken, a dump command can be applied to empty the accumulator and deliver the accumulated samples to the analyzer. This dump command inhibits gate 5 so transistor Q1 cannot be turned on, and also presets the flip-flop made up of gates 1 and 2 to preclude the possibility of toggling by a sample command at an incorrect time. Transistor Q5 is then turned on via gates 7 and 8 by the dump command. When the accumulator is completely empty, the

empty limit switch is actuated, interrupting the motor current. Ganged to this limit switch is an accumulator empty sense switch (S2B) which also is actuated. The accumulator empty sense switch is used to inhibit the dump command so that it need not be removed the instant the accumulator is empty. Application of the accumulator empty sense signal drives the output of gate 8 to ground potential, thus energizing the monostable multivibrator via gates 6 and 9, which in turn energizes the relay through gate 10 to again provide dynamic braking.

3. Conclusion

The circuits described have been constructed and are currently under evaluation. The logic functions are performed by the Texas Instrument SN51 series of logic elements. Future work will continue with development of control circuits for such processes and mechanisms as phase separation, filtration, centrifuging, and linear motors.

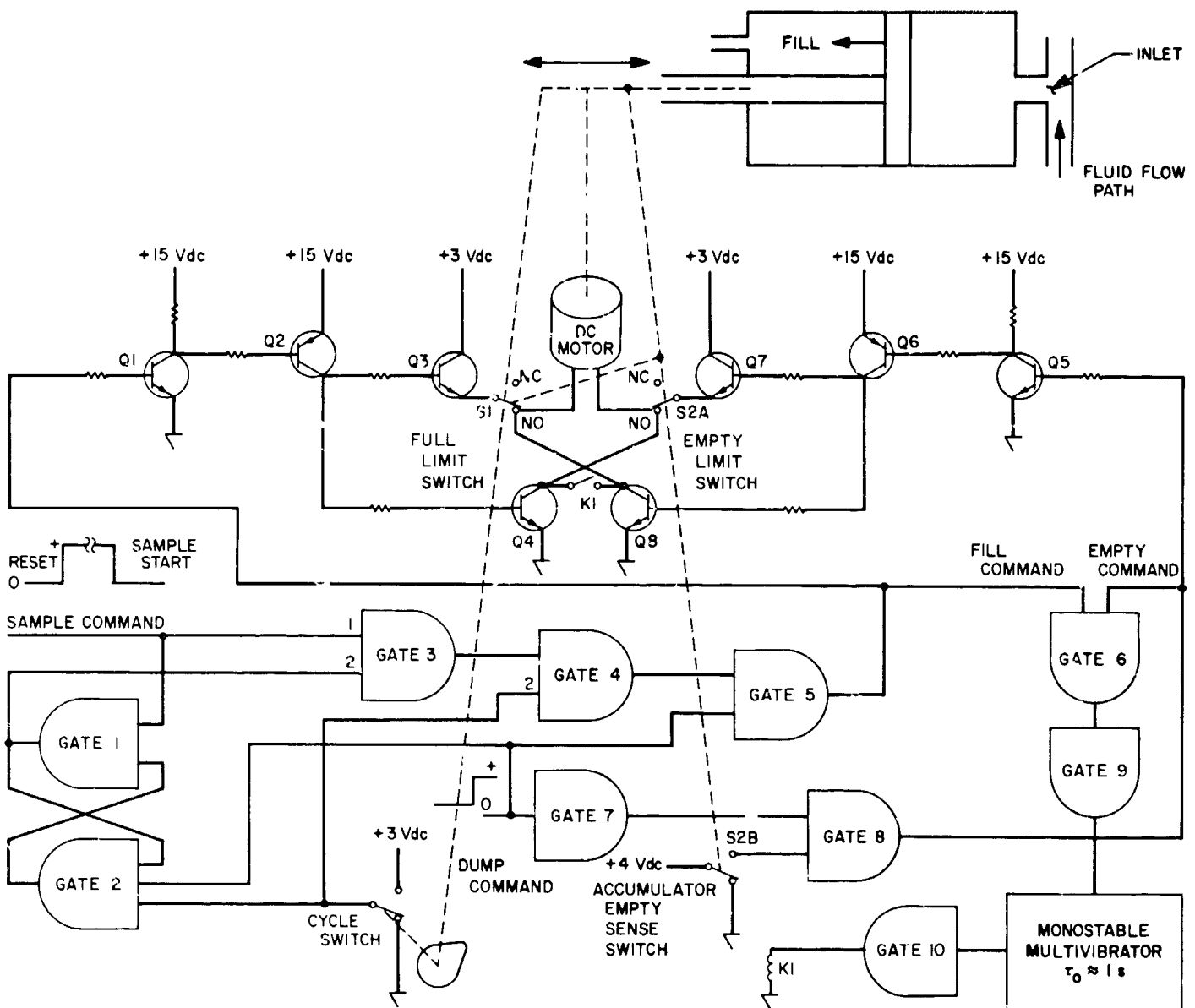


Fig. 5. Fluid sample control

N67-34773

XII. Space Instruments

SPACE SCIENCES DIVISION

A. Surface Temperature of Mars, J. H. Shaw¹ and P. W. Schaper

1. Introduction

Although it is known that CO₂ is the principal infrared absorbing gas in the atmosphere of Mars, and some estimates of the variation of surface temperature with geographic location, time of day, and season are available, no measurements have been made of the vertical atmospheric temperature profile or its dependence on surface temperature, etc. It has been shown (Ref. 1) that significant information about the temperature profile up to the 1-mb level in the Martian atmosphere can be obtained. This requires an instrument having a spectral resolving power of about 100 to measure the outgoing radiation from Mars near 2300 cm⁻¹, where a strong band of CO₂ occurs.

A small, fast, fixed-grating, multidetector spectrometer capable of measuring radiation from 1000 to 10,000 cm⁻¹ (but specifically designed to measure the low spectral steradiancies expected for the Martian atmosphere near 2300 cm⁻¹), with the required resolving power, has been constructed (see SPS 37-43, Vol. IV, pp. 239-248).

¹Ohio State University, Department of Physics, Columbus, Ohio.

The radiation chopping frequency is 300 Hz, and the PbSe detectors are chosen to have high D^* values in this spectral region when operated at the expected temperatures of between 200 and 240°K. The D^* values of these detectors decrease rapidly at frequencies below 2000 cm⁻¹, and no suitable detector is available for the region below 1700 cm⁻¹. In addition to the detectors placed to receive radiation between 2200 and 2500 cm⁻¹ which give information about the Martian atmosphere temperature profile, other detectors can also be included to measure surface temperatures. It is the purpose of this report to suggest the most suitable location for such detectors and to discuss the factors that determine the minimum temperatures which can be accurately measured with the present instrument.

To determine the absolute temperature of the Martian surface by measuring its emitted thermal radiation, the following requirements must be met:

- (1) Know the relation between the spectral steradiancy of the surface and its temperature.
- (2) Know the response of the measuring instrument to incoming radiation.

BLANK PAGE

- (3) Correct for additional radiation entering the instrument; e.g., solar radiation scattered from the planet or thermal radiation from an overlying atmosphere.
- (4) Correct for absorption occurring between the surface and the instrument; e.g., by an overlying atmosphere.

Each of these factors is discussed below.

2. Mars as a Radiation Source

a. Thermal radiation from the surface. The spectral steradiance of the Martian surface due to thermal emission can be written as

$$B_\nu(T) = e_\nu 2h\nu^3 c^2 [\exp(hc\nu/kT) - 1]^{-1} \quad (1)$$

where T is the surface temperature and e_ν is the emissivity. Earth-based observations indicate temperatures that vary from 300°K to less than 200°K. As on earth, these temperatures are related to the amount of solar radiation received. Although no measurements of the emissivity in the spectral region of interest are currently available, it appears unlikely that it is less than 0.8.

For temperatures of 300°K or less and for frequencies higher than 1700 cm^{-1} , $B_\nu(T)$ decreases very rapidly with both increasing frequency and decreasing temperature as shown in Fig. 1. Thus, at any frequency there is some minimum surface temperature for which $B_\nu(T)$ can be accurately measured with the present instrument. (These minimum temperatures are evaluated later in the report.)

If only one detector is used, it must have a wide dynamic range (10^4) because of the strong dependence of $B_\nu(T)$ on T and the wide range of surface temperatures expected. It may be more useful to consider using two or more detectors with different dynamic ranges in different spectral regions.

Since the emissivity is unknown, it is necessary either to determine this quantity or to assume a value, if T is to be evaluated from measurements of B_ν . An order-of-magnitude estimate of the error involved by assuming the emissivity to be unity can be obtained if a blackbody at 240°K radiating at 2000 cm^{-1} is considered. Its spectral steradiance can be reduced 25% by either reducing the temperature by 5°K or reducing the emissivity from 1.0 to 0.75. Similar calculations for other temperatures and frequencies in the range of interest indicate that the assumption of perfect emissivity will introduce an error

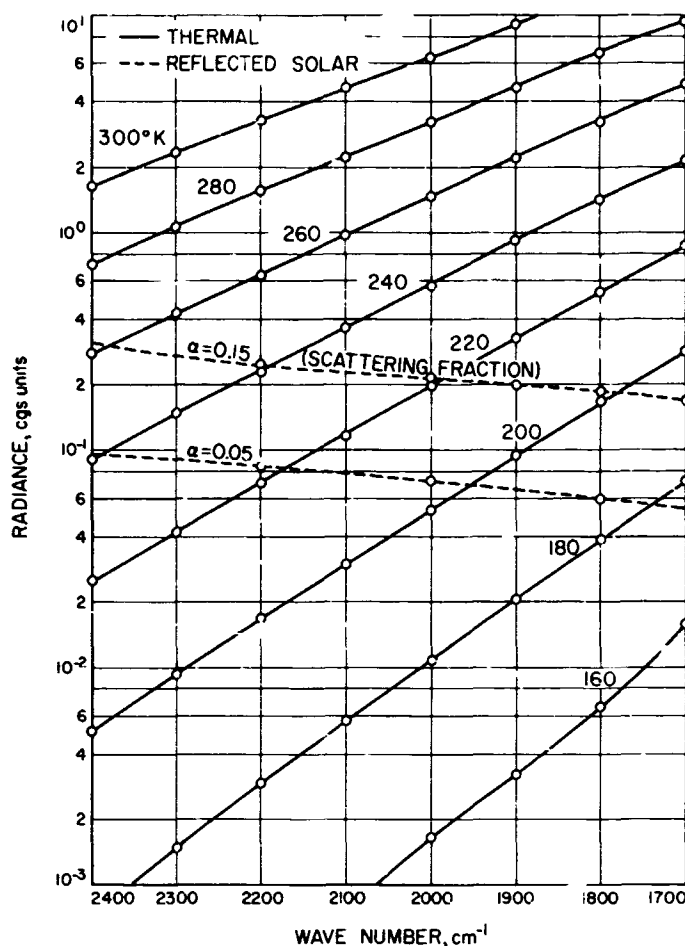


Fig. 1. Blackbody steradiance and reflected solar radiance

of less than 5°K. At lower frequencies, the change in spectral steradiance of a blackbody with temperature is less rapid. For example, at 1000 cm^{-1} the increase in spectral steradiance of a blackbody whose temperature is increased from 235 to 240°K is 13%; hence, the uncertainty in the emissivity in this region results in a larger uncertainty in temperature than that obtained at 2000 cm^{-1} .

It is shown that the emissivity may be determined when scattered solar radiation can be observed. This is possible near 2000 cm^{-1} , but more difficult at 1060 cm^{-1} .

b. Scattered solar radiation. Incident solar radiation may be scattered by the Martian surface and by molecules and particles in the atmosphere. Rayleigh scattering by molecules in the Martian atmosphere can be ignored for the frequency interval considered here. No estimates of the scattering characteristics in the infrared by Martian cloud particles are available. Such scattering should be small over areas where the surface can be seen in the visible.

Thus, effects of atmospheric scattering and absorption are neglected in this section.

Scattering from the Martian surface can occur. At the subsolar point, the irradiance of the surface is

$$I_v = \pi (r/R)^2 \tau B_v^s \cos z \quad (2)$$

where

B_v^s = spectral steradiance of the sun

r = solar radius, 695,000 km

R = mean Mars-sun distance, 2.28×10^8 km

$\tau = 1$ = transmittance of Martian atmosphere

z = angle between incoming solar radiation and the local vertical

To a reasonable approximation, B_v^s is given by Eq. (1) where $T_{sun} = 6000^\circ\text{K}$.

If the surface acts as a Lambert diffuser scattering a fraction α of the incident radiation, where $\alpha = 1 - e$ (e is the surface emissivity), then the spectral steradiance of the surface due to scattered solar radiation is

$$B_{v_s} = \frac{\alpha}{\pi} (I_v) = 9.3 \times 10^{-6} \alpha B_v^s \cos z$$

If it is assumed that $\alpha = 0.05$,

$$B_{v_s} = 4.65 \times 10^{-8} B_v^s \cos z \quad (3)$$

The variation of B_{v_s} with frequency is shown in Fig. 1 for $\alpha = 0.05$, $\alpha = 0.15$, and $z = 0$. The observed spectral steradiance of the daylight side of the planet is then

$$B_{v_s} = B_{v_s} + e_v B_v(T)$$

For points on the surface away from the subsolar point, B_{v_s} will depend on z and may be significant compared with $e_v B_v(T)$. If the surface temperature is calculated from Eq. (1) assuming $B_{v_s} = e_v B_v(T)$ and $e_v = 1$, the surface temperature will be estimated as $T + \Delta T$ where T is the true surface temperature. If B_{v_s} is given by Eq. (3), then at any frequency a surface temperature can be found for which $\Delta T = 5^\circ\text{K}$. The dependence of this temperature on frequency is shown in Fig. 2. At any frequency the error will be larger than 5°K if the surface temperature is less than that shown. Since these temperatures are of

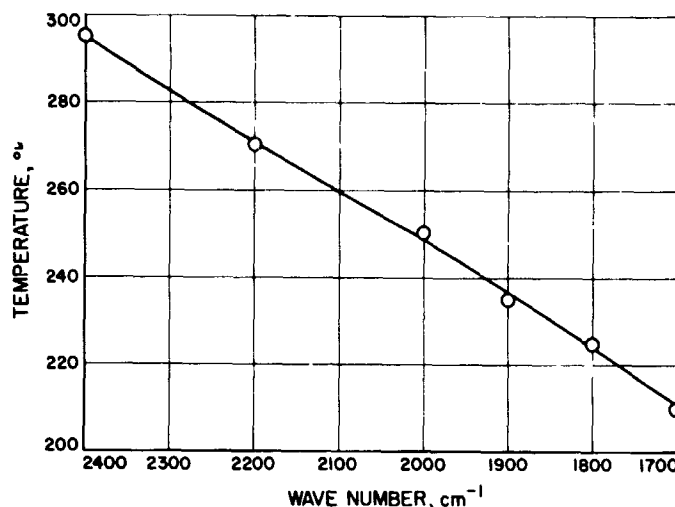


Fig. 2. Martian surface temperatures for which reflected solar radiation ($\alpha = 0.05$) gives a reading too high by 5°K

the same order as those of the surface, some method of estimating B_{v_s} and e_v is required if accurate surface temperatures are to be determined.

This may be done by placing detectors to receive radiation at frequencies ν_1 and ν_2 which lie between 1700 and 2200 cm^{-1} . Then the observed spectral steradiancies B_1 and B_2 at ν_1 and ν_2 , respectively, can be written

$$B_1 = e_1 B_1(T) + 9.3 \times 10^{-6} \alpha_1 B_1^s \cos z \quad (4)$$

and

$$B_2 = e_2 B_2(T) + 9.3 \times 10^{-6} \alpha_2 B_2^s \cos z \quad (5)$$

Approximate solutions to these equations can be found, assuming that the surface radiates as an ideal blackbody and that the scattering coefficient is the same at both frequencies. Therefore,

$$e_1 = e_2 = 1$$

and

$$\alpha_1 = \alpha_2 = \alpha$$

Then

$$B_1 = B_1(T) + \alpha I_1 \quad (6)$$

$$B_2 = B_2(T) + \alpha I_2 \quad (7)$$

where

$$I_1 = 9.3 \times 10^{-6} B_{\nu_1}^* \cos z$$

and

$$I_2 = 9.3 \times 10^{-6} B_{\nu_2}^* \cos z$$

Hence.

$$B_2 - \left(\frac{I_2}{I_1}\right) B_1 = B_2(T) - \left(\frac{I_2}{I_1}\right) B_1(T) \quad (8)$$

Since B_1 and B_2 can be measured and I_2/I_1 and z are known, both T and α can be calculated. Equation (8) allows temperatures to be estimated to $\pm 1^\circ\text{K}$ for most surface temperatures and solar radiancy.

Consider the following example:

If

$$T = 240^\circ\text{K}$$

$$e_1 = e_2 = 0.95$$

$$\alpha_1 = \alpha_2 = (1 - e) = 0.05$$

$$\nu_1 = 2000 \text{ cm}^{-1}$$

$$\nu_2 = 2200 \text{ cm}^{-1}$$

then

$$B_{1_0} = 0.635 \text{ ergs s}^{-1} \text{ cm}^{-2} \text{ sr}^{-1} (\text{cm}^{-1})^{-1}$$

and

$$B_{2_0} = 0.311 \text{ ergs s}^{-1} \text{ cm}^{-2} \text{ sr}^{-1} (\text{cm}^{-1})^{-1}$$

Substituting these values and $I_2/I_1 = 1.14$ into Eq. (8) gives

$$1.14 B_1(T) - B_2(T) = 0.413 \quad (9)$$

The results obtained are given in Table 1. Comparison of these results with Eq. (9) shows that this equation is satisfied when $T = 240 \pm 1^\circ\text{K}$. This is in good agreement with the initial assumption.

Table 1. Sample temperature calculation

$T, ^\circ\text{K}$	B_1	$1.14 B_1$	B_2	$1.14 B_1 - B_2$
235	0.458	0.522	0.179	0.343
240	0.592	0.672	0.237	0.435
245	0.756	0.860	0.311	0.549

This result may be compared with the surface temperatures calculated from Eqs. (4) and (5):

$$T = 246^\circ\text{K at } 2000 \text{ cm}^{-1}$$

and

$$T = 254^\circ\text{K at } 2200 \text{ cm}^{-1}$$

Once T has been determined, it is possible to calculate α and to perform the calculations again using Eq. (5) with $e_\nu = (1 - \alpha)$. This will not significantly improve T , but will enable reasonable values for α and e_ν to be calculated, provided that α_1 and α_2 are nearly the same.

c. Absorption and emission by the Martian atmosphere.

One of the principal constituents of the Martian atmosphere is CO_2 . The spectrum (Ref. 2) of 10 atm-m at 300°K and 100-torr pressure is shown in Fig. 3. This should approximate the transmission of one air mass of the Martian atmosphere in the spectral region of interest. Although some absorption (and consequently emission) occurs throughout the region from 1900 to 2400 cm^{-1} , these are both small at 1970 cm^{-1} (5.2μ) and 2160 cm^{-1} (4.65μ). If there are no other constituents that absorb in this spectral region, detectors placed at either of these

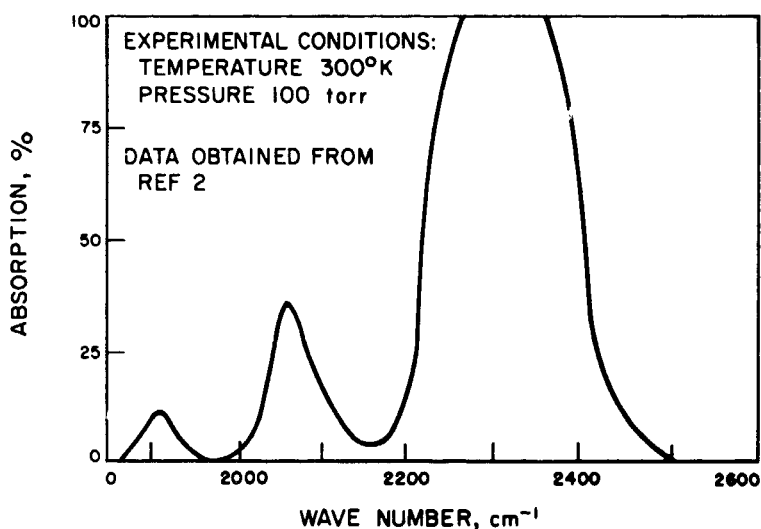


Fig. 3. Spectrum of 10.4 atm-m CO_2

locations will give information requiring minimal corrections for atmospheric effects.

A quantitative estimate of atmospheric absorption in this region requires additional information of the CO₂ spectrum, the pressure and temperature variation with height in the Martian atmosphere, and the CO₂ mixing ratio.

d. SNR expected for spectrometer for blackbody sources. To a reasonable approximation, the radiation flux through the multidetector spectrometer from a source of spectral steradiancy B_ν is

$$F_\nu = B_\nu g A_s (A_g/f^2) \Delta\nu$$

where

g = spectrometer transmission = 0.20 (estimated)

A_g = area of grating = 60 cm²

A_s = area of entrance slit or PbSe detector optics = 0.45 cm²

f = focal length of Ebert mirror = 25.4 cm

$\Delta\nu$ = spectral bandpass of instrument at frequency ν

Hence,

$$F_\nu = 5.5 \times 10^{-3} B_\nu \Delta\nu, W$$

If the detector is the only source of noise, then the SNR expected is

$$S/N = D^* F_\nu / (A \Delta f)^{1/2}$$

where

D^* = spectral detectivity of detectors, cm (Hz)^{1/2} W⁻¹

A = area of detector element = 0.01 cm²

Δf = bandpass of electrical system = $\frac{1}{4} \tau$

τ = time constant of electrical system = 2.0 s

Hence,

$$S/N = 0.155 B_\nu \Delta\nu D^* \quad (10)$$

3. D^* of PbSe Detectors

The PbSe detectors in the present instrument were manufactured by the Santa Barbara Research Corporation. The 1966 catalog of this company gives curves

showing the variation of D^* with wavelength for detectors operated at 77, 193, and 295°K. For a fixed operating temperature and wavelength, the D^* values of individual detectors can vary by an order of magnitude. Additional curves for intermediate temperatures can be estimated from the curves for the maximum D^* value. Two curves showing the estimated variation of D^* with frequency for operating temperatures of 220 and 240°K are shown in Fig. 4. These temperatures are typical of those expected for a Mars flyby or orbiter instrument. Both curves show a rapid decrease of D^* for frequencies lower than 2000 cm⁻¹.

4. Spectral Slit Width

The multidetector instrument is designed to give a resolving power of 100 at 2300 cm⁻¹ if a 3-mm-wide entrance slit is used. The resolving power will be somewhat larger than this at lower frequencies if the width of the detector optics in the spectral plane is maintained at 3 mm. However, in this report it is assumed that $R = \nu/\Delta\nu = 100$ at all frequencies. Thus, $\Delta\nu$ varies from 17 cm⁻¹ at 1700 cm⁻¹, to 24 cm⁻¹ at 2400 cm⁻¹.

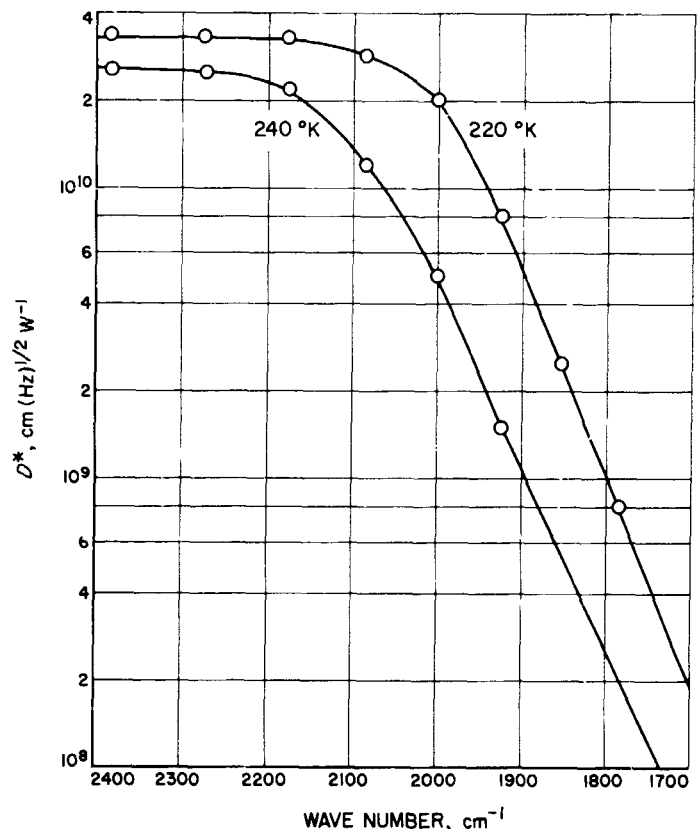


Fig. 4. D^* of PbSe detectors at temperatures indicated

5. SNR Calculation

In the previous section, the variations of $\Delta\nu$ and D^* with frequency have been discussed. If these values are substituted into Eq. (10), then the SNR to be expected from the multidetector instrument for various blackbody sources can be calculated. The results of these calculations are shown in Fig. 5 for a detector temperature of 220°K. Also shown in this figure is the SNR expected for scattered solar radiation alone, assuming that $\alpha = 0.05$ and that the sun is vertically overhead.

From this figure, it is possible to estimate the blackbody temperatures for which an SNR of 10 is obtained. This ratio is about the minimum required to obtain useful data. The minimum detectable temperatures obtained in this manner are shown in Fig. 6.

6. Uncertainties in Chopper Steradiancy

The output of the instrument is a measure of the difference between the spectral steradiancy of the planet

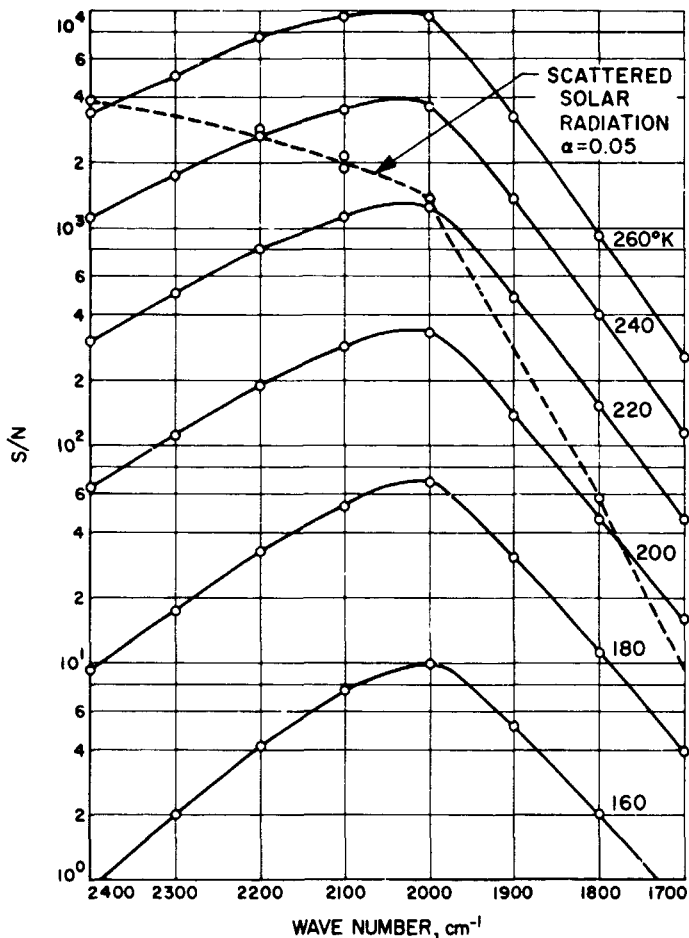


Fig. 5. PbSe SNRs for varying blackbody temperatures

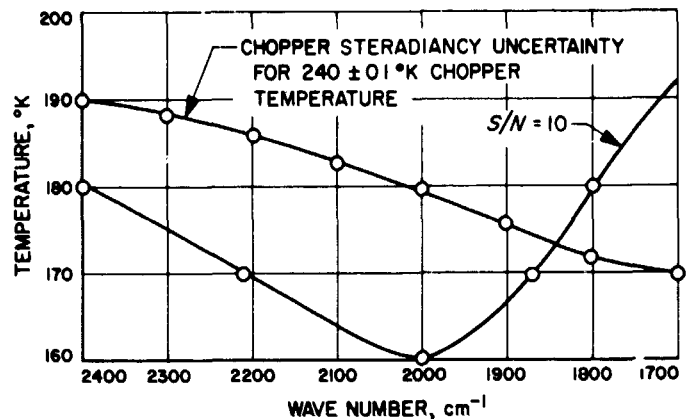


Fig. 6. Minimum detectable temperatures for instrument conditions stated

and the chopper. It is expected that the chopper temperature will be maintained near 240°K and that its temperature can be measured to $\pm 0.1^\circ\text{K}$. The surface of the chopper will be coated to have an emissivity near unity.

During flight an estimate of the chopper temperature and emissivity will be obtained periodically both by inserting another blackbody source in front of the chopper and by allowing the spectrometer to view space. The experience obtained with the instrument to date suggests that these calibration techniques will allow the effective blackbody temperature of the chopper to be determined to an accuracy of about 0.1°K .

The output of the spectrometer is a measure of the difference in steradiancy of the chopper and the source. If there is an uncertainty ΔB_c in the chopper steradiancy, then there is the same uncertainty in the source steradiancy. Hence, from Eq. (1) and assuming $\exp(hc\nu/kT) \gg 1$,

$$B_\nu(T) = 2 h \nu^3 c^2 \exp\left(-\frac{h\nu c}{kT}\right)$$

$$\frac{dB_\nu(T)}{dT} = \frac{2h^2 \nu^4 c^3}{kT^2} \exp\left(-\frac{h\nu c}{kT}\right)$$

If the chopper is at T_1 and the source at T_2 , and ΔT_1 and ΔT_2 are the uncertainties in their temperatures, then since $\Delta B_1 = \Delta B_2$, and

$$\left(\frac{1}{T_1}\right) \exp\left(-\frac{h\nu c}{kT_1}\right) \Delta T_1 = \left(\frac{1}{T_2}\right) \exp\left(-\frac{h\nu c}{kT_2}\right) \Delta T_2$$

one obtains

$$\Delta T_2 = \left(\frac{T_1}{T_2}\right)^2 \exp\left[\frac{h\nu c}{k}\left(\frac{1}{T_1} - \frac{1}{T_2}\right)\right] \Delta T_1$$

Thus, ΔT_2 can be found as a function of frequency. Alternatively, if it is assumed that $\Delta T_2 \leq 5^\circ\text{K}$ is a criterion of satisfactory measurements of T_2 , the corresponding value of T_2 can be determined. In this manner, the second curve in Fig. 6 was obtained using values of $T_1 = 240^\circ\text{K}$ and $\Delta T_1 = 0.1^\circ\text{K}$.

7. Conclusions

From the data presented above, the following conclusions can be made:

- (1) Ideally, the spectrometer is sufficiently sensitive to determine surface temperatures as low as 160°K to an accuracy of 5°K provided the spectral steradiancy is measured near 2000 cm^{-1} .
- (2) If the calibration of the instrument allows the chopper temperature to be determined only to within 0.1°K , the minimum temperature that can be measured, 5°K is closer to 180°K .
- (3) If the effects of absorption and thermal emission by CO_2 in the Mars atmosphere are to be minimized, detectors should be placed near 1970 and 2160 cm^{-1} . The lowest temperatures that can be determined by these detectors are 161 and 167°K at 1970 and 2160 cm^{-1} , respectively. The chopper calibration uncertainty will increase these respective temperatures to 178 and 185°K .
- (4) At these frequencies, scattered solar radiation may be appreciable compared with the thermal emission during the daytime. If daytime surface temperatures are to be determined, to eliminate the effects of scattered solar radiation it will be necessary to use at least two detectors and to use a method similar to that described earlier.
- (5) Further investigations of the absorption by CO_2 between 1700 and 2300 cm^{-1} for the conditions expected in the Martian atmosphere are required to determine the influence of this gas on the observations.
- (6) Two detectors should be placed near 1970 cm^{-1} and two near 2160 cm^{-1} to obtain the necessary dynamic range.

- (7) The detectors to be used for surface temperature measurement will not interfere with temperature sounding detectors.

It is concluded that with the available instrumentation, Martian surface temperatures above 180°K can be determined to 5°K . This accuracy can be improved to 1°K if surface temperatures above 200°K are encountered.

B. Complete Error Analysis of Relative and Absolute Orientation in Extraterrestrial Stereophotogrammetric Mapping Techniques, M. Benes

1. Introduction

The primary objective of spacecraft imaging systems is to derive reliable topographical data about an extraterrestrial scene. Both photometric and stereophotogrammetric methods have been considered for this purpose (see Refs. 3-7).

This study will concentrate primarily on the stereophotogrammetric method, with the intent to:

- (1) Identify and characterize major error sources.
- (2) Determine and evaluate the complete law of propagation of errors.
- (3) Establish imaging constraints influencing the accuracy of stereo mapping techniques.

The final goal, however, is to compare the stereophotogrammetric method with the photometric (which is being treated and tested separately), and to:

- (1) Determine the applicability and accuracy criteria.
- (2) Establish the constraints each method places upon a television system.
- (3) Design an optimum approach guaranteeing best possible topographical results of future space missions.

The progress that has been made with respect to stereophotogrammetric mapping procedures is described here.

2. Practical Tests

The first stage of the present research work consisted of practical evaluations of given photogrammetric stereopairs. These pictures were generated mathematically and showed a cone under different illumination conditions. This approach was chosen as it offered possibilities for comparison of both methods.

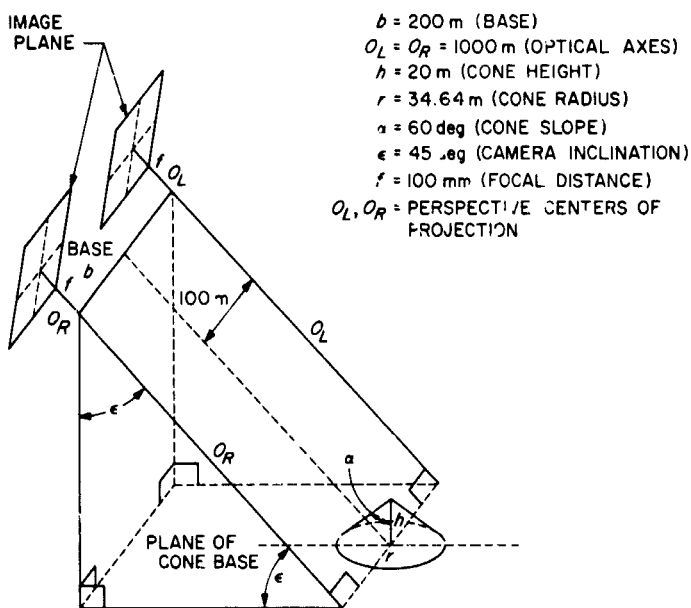


Fig. 7. Camera setup and parameters

The camera setup and parameters are shown schematically in Fig. 7. It is evident that, in this special hypothetical case, the direct solution described in SPS 37-28, Vol. VI, pp. 52-56, can be applied.

The model coordinates in the inclined camera coordinate system can be computed from relations (1-3):

$$Y = \frac{bf}{p_x} \quad (1)$$

$$X = Y \frac{x'}{f} \quad (2)$$

$$Z = Y \frac{z'}{f} \quad (3)$$

where p_x is the observed horizontal parallax and x', z' are observed image coordinates.

These computed model coordinates can be simply rotated into the horizontal ground system.

$$\begin{bmatrix} X^T \\ Y^T \\ Z^T \end{bmatrix} = \begin{bmatrix} 1 & 0 & 0 \\ 0 & \cos \epsilon & \sin \epsilon \\ 0 & -\sin \epsilon & \cos \epsilon \end{bmatrix} \cdot \begin{bmatrix} X \\ Y \\ Z \end{bmatrix} \quad (4)$$

Using these relations for several points on the cone base and apex, four different models were observed and computed.

Two stereopairs were in the form of approximately 10-times enlarged prints; the other two were on approximately 7-times enlarged glass plates. Consequently, the image coordinates were observed either with an accurate scale or on the Mann monocomparator. The results obtained were very good and are defined by the following average deviations:

(1) Photographic prints:

$$\left. \begin{aligned} \sigma_{xT} &= \pm 0.1 \text{ m} \\ \sigma_{yT} &= \pm 0.3 \text{ m} \\ \sigma_{zT} &= \pm 0.3 \text{ m} \end{aligned} \right\} \text{ for the cone apex}$$

$$\sigma_r = \pm 0.8 \text{ m for the cone radius}$$

$$\sigma_{zT} = \pm 0.95 \text{ m for the cone base}$$

(2) Glass plates:

$$\left. \begin{aligned} \sigma_{xT} &= \pm 0.2 \text{ m} \\ \sigma_{yT} &= \pm 0.1 \text{ m} \\ \sigma_{zT} &= \pm 0.15 \text{ m} \end{aligned} \right\} \text{ for the cone apex}$$

$$\sigma_r = \pm 0.45 \text{ m for the cone radius}$$

$$\sigma_{zT} = \pm 0.7 \text{ m for the cone base}$$

These results correspond to 8- to 12- μ observational precision and may lead to premature optimistic conclusions. To avoid this possibility, encountered difficulties must be listed and analyzed.

a. Encountered difficulties

Point identification. Exactly the same point must be observed in both pictures, which is very problematic in brightly illuminated areas. Because of misidentification, some points had to be rejected as blunders; however, in a real case—such as lunar photography—there will always be an adequate number of good points from which to choose.

Fiducial marks. To get good results the observed image coordinates must be refined; i.e., corrected for image shrinkage, lens distortion, atmospheric refraction, and ground curvature, and then finally reduced to the principal point of origin. From the mathematical point of view, this is no great problem; however, if the fiducial marks are not well defined, as was the case of the hypothetical photographs, very little can be done. The fiducial marks here are represented by sample marks, which cannot be considered sufficiently accurate for analytical

photogrammetric purposes. In fact, to find the optimum position of the fiducial marks, and thus the relatively good results shown above, required several attempts. However, for future applications it will be necessary to calibrate the camera system with respect to these parameters. The same, of course, applies also to the reseau marks used in TV vidicon systems.

Resolution. In some cases, point resolution was very low; however, this is due to the televised transmission techniques, and quality pictures such as in conventional photogrammetry cannot be expected.

The direct terrestrial solution described above will find only a limited use in extraterrestrial mapping problems (with the possible exception of missions similar to *Surveyor*); therefore the general solution, including relative and absolute orientation, was applied to the same cone stereopairs. This was done when major difficulties arose, because for some reason the iterative process in relative orientation failed to converge, and consequently no, or absolutely unrealistic, results were obtained. These results gave rise to some pessimistic conclusions. However, after a thorough mathematical analysis, the following explanations and conclusions were set forth.

b. Explanation and conclusions

- (1) The hypothetical mathematical model used (shown in Fig. 7) is unrealistic; i.e., with the given 0.2 base-to-height ratio and the small (12.5 mm) vidicon image format, there will never be an image overlap and consequently no stereo evaluation.
- (2) The image of the cone is so small that the six points used for relative orientation least-squares adjustment are so close to each other that even very small differential changes in observed coordinates cause the system to diverge; i.e., the system is so sensitive to differential errors that it practically becomes unsolvable.

These undesirable results have shown the necessity of further research devoted to derivation and evaluation of the complete error analysis of the general stereophotogrammetric case applied to extraterrestrial mapping techniques. A brief treatment of these problems follows.

3. Theoretical Analysis

The general solution of a photogrammetric stereopair consists of two steps; namely, relative and absolute orientation.

a. Relative orientation. Although several approaches to the solution of the relative orientation problem exist, the approach based on the principle of collinearity has been chosen here because it seems to offer the most convenient way of solving the many required differentiations.

The entire concept of this procedure is shown schematically in Fig. 8. The left camera system remains fixed; only the right system is rotated (ω'' , ϕ'' , κ'') and translated (Y_0'' , Z_0'') until all corresponding rays intersect at a proper elevation and without any model y -parallaxes. The x -component of the base X_0'' is deliberately chosen as equal to 1, because in relative orientation scaling is of no interest. This leaves five unknowns to be determined.

The following symbols were used:

- X_0'', Y_0'', Z_0'' base components in the left camera system
- x', y', x'', y'' observed image coordinates
- z', z'' focal distances of the left and right camera
- x''^*, y''^* image coordinates of the right plate rotated into a system parallel with the model system
- z''^* focal distance of the right camera rotated into the same system
- A three-dimensional orthogonal rotational matrix going from "ground" into "photo"
- X, Y, Z model coordinates of an observed point

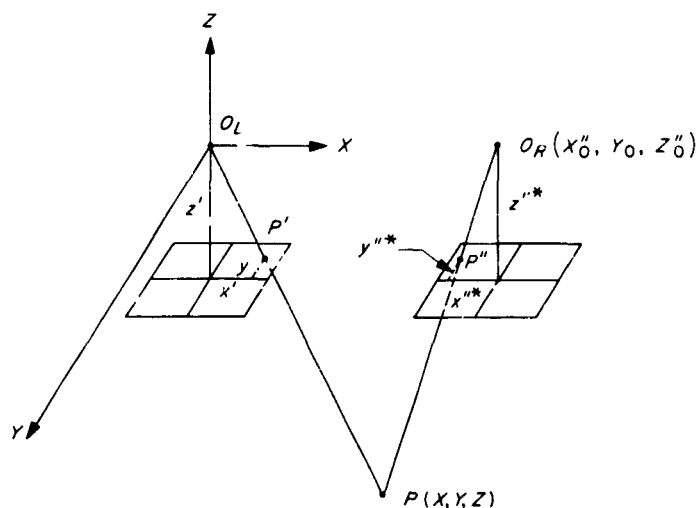


Fig. 8. Relative orientation of a stereopair based on the principle of collinearity

If the right camera is properly oriented (i.e., rotated and translated with respect to the left camera), model coordinates of any measured point can be computed:

$$Z = \frac{Z_0'' x''^* - z''^*}{x''^* - \frac{x'}{z'} z''^*} \quad (5)$$

$$X = \frac{x'}{z'} Z \quad (6)$$

$$Y = \frac{y'}{z'} Z \quad (7)$$

However, the three rotational and two translational elements must first be determined. To do this, the collinearity equations in a compact determinant form are used:

$$F_x = \begin{vmatrix} x'' & z'' \\ A_1 B & A_3 B \end{vmatrix} = 0 \quad (8)$$

$$F_y = \begin{vmatrix} y'' & z'' \\ A_2 B & A_3 B \end{vmatrix} = 0 \quad (9)$$

where A_1, A_2, A_3 are rows of the A-matrix, and

$$B = \begin{bmatrix} X - X_0'' \\ Y - Y_0'' \\ Z - Z_0'' \end{bmatrix}$$

The computational process is iterative and is based on the principle of the least-squares method.

In the first step, using $\omega'' = \phi'' = \kappa'' = Y_0'' = Z_0'' = 0$, approximate X, Y, Z coordinates are computed from Eqs. (5-7). Then relations (8) and (9) are linearized; in this way, two observation equations are obtained for each point (usually six points are used).

$$F_x = 0 = F_x^{approx} + dF_x$$

$$F_y = 0 = F_y^{approx} + dF_y$$

or

$$v_x = l_{11} + l_{12} d\omega'' + l_{13} d\phi'' + l_{14} d\kappa'' + l_{15} dY_0'' + l_{16} dZ_0'' \quad (8a)$$

$$v_y = l_{21} + l_{22} d\omega'' + l_{23} d\phi'' + l_{24} d\kappa'' + l_{25} dY_0'' + l_{26} dZ_0'' \quad (9a)$$

The coefficients l_{ij} ($i = 1, 2; j = 1, \dots, 6$) are quite complicated and therefore are not given explicitly in this report. However, Eqs. (8a) and (9a) are changed into a system of normal equations; then corrections $d\omega'', d\phi'', d\kappa'', dY_0''$, and dZ_0'' are computed. Consequently, new improved model coordinates X, Y, Z can be determined and used for the second iteration. A proper stopping criterion must be established (usually three to five steps are required to satisfy it).

The question now arises as to the accuracy of the final adjusted model coordinates. For terrestrial mapping purposes this is relatively unimportant because model coordinates are always transformed into a ground system, and the available ground control points supply sufficient and reliable accuracy criteria. For this reason, little attention has been given to these problems thus far. However, in extraterrestrial cases this is of utmost importance because of the absence of any ground control.

For the purpose of the following error analysis, relations (5-7) can be conveniently rewritten as

$$Z = \frac{u_1}{u_2} \quad (5a)$$

$$X = u_3 Z \quad (6a)$$

$$Y = u_4 Z \quad (7a)$$

These equations now enable a relatively simple differentiation:

$$dZ = d \frac{u_1}{u_2} = \frac{1}{u_2} (du_1 - Z du_2) \quad (10)$$

or, after substitution for du_1 and du_2 (all unmarked parameters pertain to the right camera system),

$$dZ = \frac{1}{u_2} \left[x^* dZ_0 - (Z - Z_0) dx^* + (X - 1) dz^* + \frac{z^*}{z'} Z dx' - \frac{z^*}{z'} dz' \right] \quad (10a)$$

However, since

$$\begin{bmatrix} x^* \\ y^* \\ z^* \end{bmatrix} = A^T \begin{bmatrix} x'' \\ y'' \\ z'' \end{bmatrix} = A^T C$$

Eq. (10a) can be further adapted to

$$dZ = \frac{1}{u_2} [T_1 d\omega + T_2 d\phi + T_3 d\kappa + T_4 dZ_0 + T_5 dx' + T_6 dz' + T_7 dx'' + T_8 dy'' + T_9 dz''] \quad (11)$$

where

$$T_1 = \begin{vmatrix} (X-1) & (Z-Z_0) \\ \frac{\partial A_1^r}{\partial \omega} C & \frac{\partial A_3^r}{\partial \omega} C \end{vmatrix} \quad T_2 = \begin{vmatrix} (X-1) & (Z-Z_0) \\ \frac{\partial A_1^r}{\partial \phi} C & \frac{\partial A_3^r}{\partial \phi} C \end{vmatrix}$$

$$T_3 = \begin{vmatrix} (X-1) & (Z-Z_0) \\ \frac{\partial A_1^r}{\partial \kappa} C & \frac{\partial A_3^r}{\partial \kappa} C \end{vmatrix} \quad T_4 = x^* = A_1^r C$$

$$T_5 = \frac{z^*}{z'} Z \quad T_6 = -\frac{z^*}{z'} X$$

$$T_7 = \begin{vmatrix} (X-1) & (Z-Z_0) \\ a_{11}^r & a_{31}^r \end{vmatrix} \quad T_8 = \begin{vmatrix} (X-1) & (Z-Z_0) \\ a_{12}^r & a_{32}^r \end{vmatrix}$$

$$T_9 = \begin{vmatrix} (X-1) & (Z-Z_0) \\ a_{13}^r & a_{33}^r \end{vmatrix}$$

Formula (11) could be considered as sufficient for most cases; however, to complete the analysis, one more influence must be anticipated; namely, the uncertainty of the principal point position with respect to the image center defined by fiducial marks.

It is evident from Fig. 9 that real image coordinates must be written as

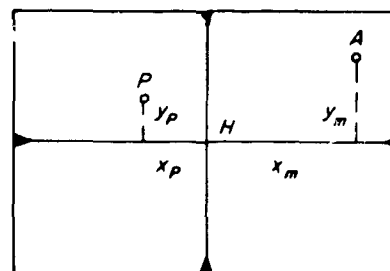
$$x = x_m - x_p \quad (12)$$

$$y = y_m - y_p \quad (13)$$

where x_m, y_m are the measured (observed) image coordinates and x_p, y_p are displacements of the principal point P with respect to the image center H .

Relations (12) and (13) can be simply differentiated and, after substitution into (11), the final formula is obtained:

$$\begin{aligned} dZ = & S_1 d\omega + S_2 d\phi + S_3 d\kappa + S_4 dZ_0 + S_5 dx'_m \\ & - S_5 dx'_p + 0 dy'_m + 0 dy'_p + S_6 dz' + S_7 dx''_m \\ & - S_7 dx''_p + S_8 dy''_m - S_8 dy''_p + S_9 dz'' \quad (14) \end{aligned}$$



P = PRINCIPAL POINT
 H = IMAGE CENTER
 A = OBSERVED POINT

Fig. 9. Displacement of the principal point with respect to the image center

where

$$S_i = \frac{1}{u_2} T_i \quad \text{for } i = 1, 2, \dots, 9$$

Following the same thought and differentiating Eqs. (6a) and (7a), the following relations can be obtained for dX and dY :

$$\begin{aligned} dX = & u_3 S_1 d\omega + u_3 S_2 d\phi + u_3 S_3 d\kappa + u_3 S_4 dZ_0 + (u_3 S_5 + S_{10}) dx'_m \\ & - (u_3 S_5 + S_{10}) dx'_p + 0 dy'_m + 0 dy'_p + u_3 (S_6 - S_{10}) dz' \\ & + u_3 S_7 dx''_m - u_3 S_7 dx''_p + u_3 S_8 dy''_m - u_3 S_8 dy''_p + u_3 S_9 dz'' \end{aligned} \quad (15)$$

$$\begin{aligned} dY = & u_4 S_1 d\omega + u_4 S_2 d\phi + u_4 S_3 d\kappa + u_4 S_4 dZ_0 + u_4 S_5 dx'_m - u_4 S_5 dx'_p \\ & + S_{10} dy'_m - S_{10} dy'_p + u_4 (S_6 - S_{10}) dz' + u_4 S_7 dx''_m - u_4 S_7 dx''_p \\ & + u_4 S_8 dy''_m - u_4 S_8 dy''_p + u_4 S_9 dz'' \end{aligned} \quad (16)$$

where

$$S_{10} = \frac{Z}{z}$$

Equations (14-16) can be rewritten in a compact matrix form

$$dX = S_X D \quad (15a)$$

$$dY = S_Y D \quad (16a)$$

$$dZ = S_Z D \quad (14a)$$

and the standard errors can be computed from

$$\begin{bmatrix} m_X^2 & m_{XY} & m_{XZ} \\ m_{XY} & m_Y^2 & m_{YZ} \\ m_{XZ} & m_{YZ} & m_Z^2 \end{bmatrix} = \mu^2 S Q S^T = M^2 \quad (17)$$

where μ is the standard error of unit weight, Q is the variance-covariance matrix of the 14 parameters, and

$$S^T = [S_X \ S_Y \ S_Z]$$

The preceding derivations were based on the assumption that the cameras were different; however, if the same camera is used for both exposures, certain simplifications are possible. Namely, it is evident that

$$z' = z'' = z, \quad x'_p = x''_p = x_p, \quad y'_p = y''_p = y_p$$

and, after differentiation and substitution into Eqs. (14), (15), and (16), the following relations are received:

$$dZ = S_1 d\omega + S_2 d\phi + S_3 d\kappa + S_4 dZ_0 + S_5 dx'_m + 0 dy'_m + S_7 dx''_m + S_8 dy''_m - (S_5 + S_7)dx_P - S_8 dy_P + (S_6 + S_9)dz \quad (18)$$

$$dX = u_3 S_1 d\omega + u_3 S_2 d\phi + u_3 S_3 d\kappa + u_3 S_4 dZ_0 + (u_3 S_5 + S_{10})dx'_m + 0 dy'_m + u_3 S_7 dx''_m + u_3 S_8 dy''_m - [u_3 (S_5 + S_7) + S_{10}]dx_P - u_3 S_8 dy_P + u_3 (S_6 + S_9 - S_{10})dz \quad (19)$$

$$dY = u_4 S_1 d\omega + u_4 S_2 d\phi + u_4 S_3 d\kappa + u_4 S_4 dZ_0 + u_4 S_5 dx'_m + S_{10} dy'_m + u_4 dx''_m + u_4 S_8 dy''_m - u_4 (S_5 + S_7)dx_P - (u_4 S_8 + S_{10})dy_P + u_4 (S_6 + S_9 - S_{10})dz \quad (20)$$

Similarly, as before, one can write

$$dX = R_X D_{red} \quad (19a)$$

$$dY = R_Y D_{red} \quad (20a)$$

$$dZ = R_Z D_{red} \quad (18a)$$

and also

$$M^2 = \mu^2 R Q_{red} R^T \quad (21)$$

where Q_{red} is the reduced variance-covariance matrix of 11 parameters only, and

$$R^T = [R_X R_Y R_Z]$$

b. Absolute orientation. After the relative orientation is achieved, the entire model must be translated, rotated, and scaled until it fits the required ground system. This transformation, of course, is an additional source of errors that influence the accuracy of the final result. For extraterrestrial mapping purposes where no ground control points are available, it is especially important to determine and analyze this influence, as this is the only way that an accuracy estimate can be obtained.

The transformation can be written in a compact matrix form:

$$X = sA^T x + B \quad (22)$$

where

$$X = \begin{bmatrix} X_G \\ Y_G \\ Z_G \end{bmatrix}, \quad x = \begin{bmatrix} X_M \\ Y_M \\ Z_M \end{bmatrix}, \quad B = \begin{bmatrix} b_X \\ b_Y \\ b_Z \end{bmatrix}$$

s = scale factor

A^T = rotational matrix going from "model" into "ground"

Therefore, there are ten parameters involved in the error analysis: three rotations (ω, ϕ, κ), one scale factor (s), three translations (b_x, b_y, b_z), and three model coordinates (X_M, Y_M, Z_M).

The necessary differentiation of formula (22) is relatively easy:

$$\begin{aligned}
 dX &= s \frac{\partial A^T}{\partial \omega} x d\omega + s \frac{\partial A^T}{\partial \phi} x d\phi + s \frac{\partial A^T}{\partial \kappa} x d\kappa + A^T x ds \\
 &+ \frac{\partial B}{\partial b_x} db_x + \frac{\partial B}{\partial b_y} db_y + \frac{\partial B}{\partial b_z} db_z + s A^T \frac{\partial x}{\partial X_M} dX_M \\
 &+ s A^T \frac{\partial x}{\partial Y_M} dY_M + s A^T \frac{\partial x}{\partial Z_M} dZ_M
 \end{aligned} \tag{23}$$

or, in a simplified matrix form,

$$dX = PU \tag{23a}$$

where

$$dX = \begin{bmatrix} dX_G \\ dY_G \\ dZ_G \end{bmatrix}, \quad P = [P_1 P_2 \cdots P_{10}]$$

$$U^T = [d\omega \ d\phi \ d\kappa \ ds \ db_x \ db_y \ db_z \ dX_M \ dY_M \ dZ_M]$$

and also

$$P_1 = s \begin{bmatrix} 0 & 0 & 0 \\ -a_{13} & -a_{23} & -a_{33} \\ a_{12} & a_{22} & a_{32} \end{bmatrix} x$$

$$P_2 = s \begin{bmatrix} (-\sin \phi \ \cos \kappa) & (\sin \phi \ \sin \kappa) & (\cos \phi) \\ (\sin \omega \ \cos \phi \ \cos \kappa) & (-\sin \omega \ \cos \phi \ \sin \kappa) & (\sin \omega \ \sin \phi) \\ (-\cos \omega \ \cos \phi \ \cos \kappa) & (\cos \omega \ \cos \phi \ \sin \kappa) & (-\cos \omega \ \sin \phi) \end{bmatrix} x$$

$$P_3 = s \begin{bmatrix} a_{21} & -a_{11} & 0 \\ a_{22} & -a_{12} & 0 \\ a_{23} & -a_{13} & 0 \end{bmatrix} x \quad P_4 = A^T x$$

$$P_5 = \begin{bmatrix} 1 \\ 0 \\ 0 \end{bmatrix} \quad P_6 = \begin{bmatrix} 0 \\ 1 \\ 0 \end{bmatrix} \quad P_7 = \begin{bmatrix} 0 \\ 0 \\ 1 \end{bmatrix}$$

$$P_8 = s \begin{bmatrix} a_{11} \\ a_{12} \\ a_{13} \end{bmatrix} \quad P_9 = s \begin{bmatrix} a_{21} \\ a_{22} \\ a_{23} \end{bmatrix} \quad P_{10} = s \begin{bmatrix} a_{31} \\ a_{32} \\ a_{33} \end{bmatrix}$$

Finally, as in the case of relative orientation, standard errors can be computed:

$$m_x^2 = PQ P^T \mu^2 \quad (24)$$

where μ is the standard error of unit weight and Q is the variance-covariance matrix of the ten parameters involved.

4. Statistical Results

To prove the correctness of the theoretical analysis described in Section 3 and to obtain a reliable picture of the practical applicability of extraterrestrial mapping techniques, four hypothetical stereo models were constructed:

- (1) Image format 20×20 cm, focal distance = 100 mm.
- (2) Vidicon format, focal distance = 25 mm.
- (3) Vidicon format, focal distance = 50 mm.
- (4) Vidicon format, focal distance = 100 mm.

The flight height chosen was 1000 m and only the base was changed, so that the base-to-height ratio corresponded to a longitudinal overlap from 8 to 97.5%. For the large format, the base-to-height ratio was kept within normal limits; however, because of the small vidicon format (approximately 12.5×12.5 mm) it did not exceed 0.4 for the best case. This, of course, represents the first great problem of vidicon stereophotography.

For each overlap, six evenly distributed points were computed, as is the standard procedure of relative orientation. In the first stage of the statistical analysis, no errors in absolute orientation were anticipated; therefore all interest could be focused on the relative orientation itself. Each model was then computed four times:

- (1) Observed image coordinates of the right picture only were changed; no camera calibration errors were assumed.
- (2) Same as (1), except that calibration errors were set equal to 10μ .
- (3) Both pictures changed; no calibration errors.
- (4) Same as (3), except that calibration errors = 10μ .

This design guarantees enough statistical data to make reliable initial conclusions. Figures 10-12 show the important relation between the focal distance of the camera

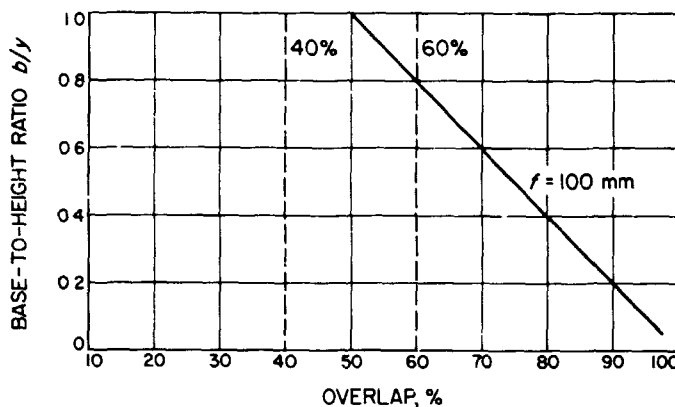


Fig. 10. Relation between base-to-height ratio, focal distance, and overlap for the large format

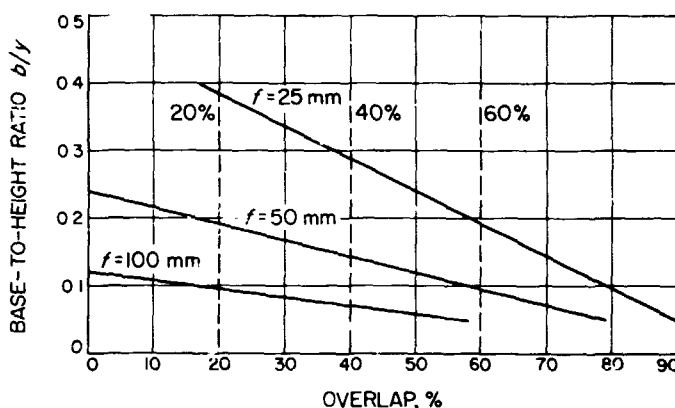


Fig. 11. Relation between base-to-height ratio, focal distance, and overlap for the vidicon format

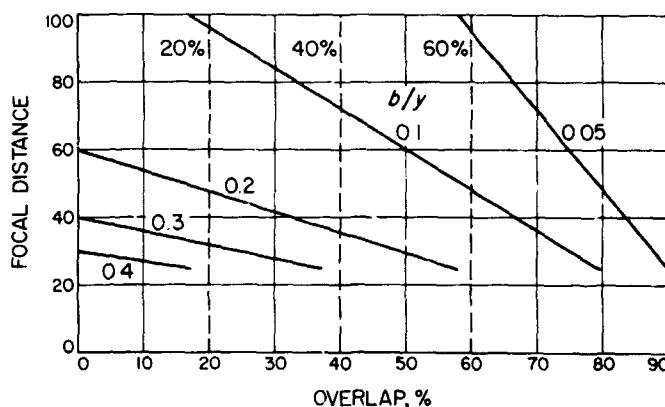


Fig. 12. Relation between focal distance, base-to-height ratio, and overlap for the vidicon format

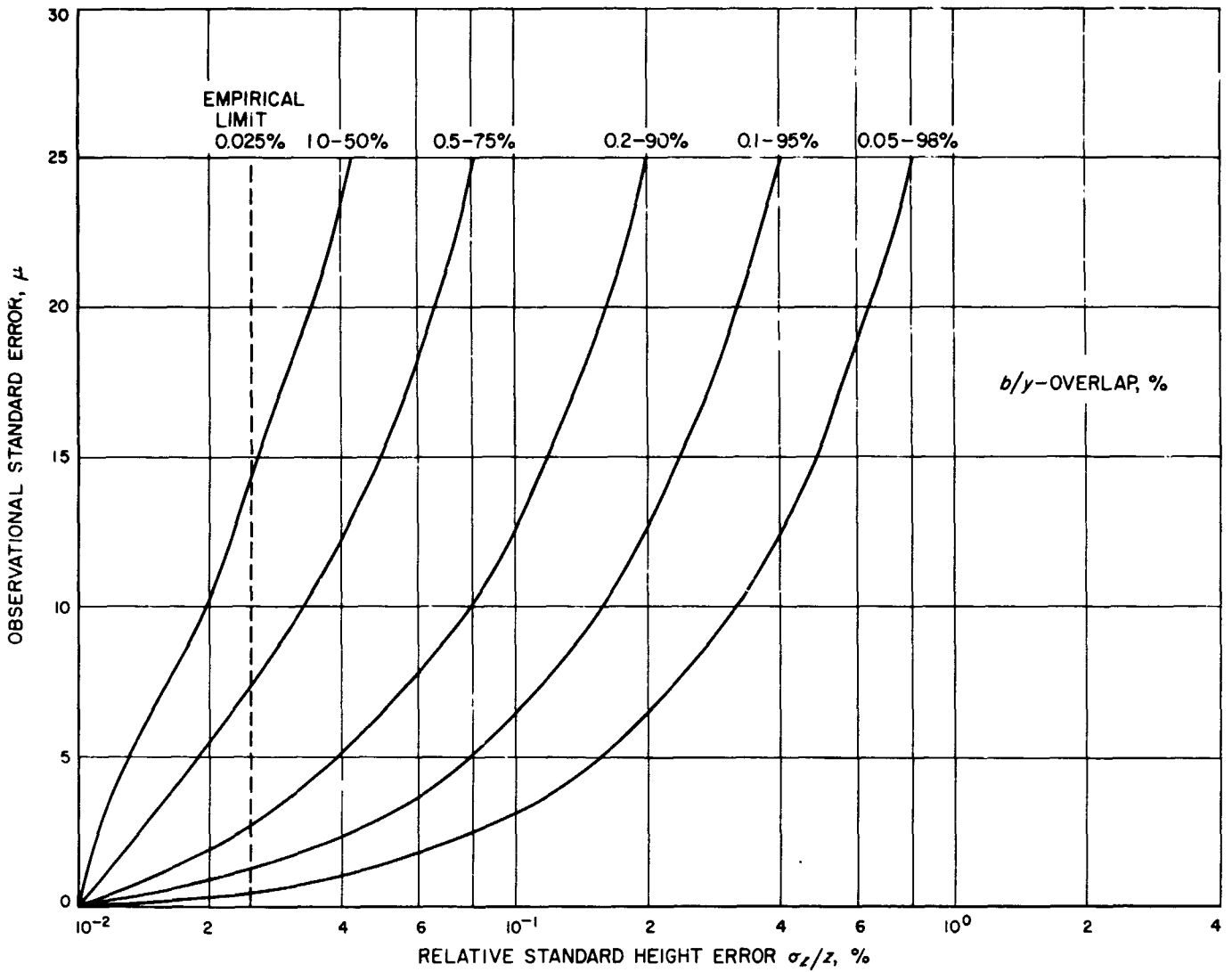


Fig. 13. Relation between observational errors, base-to-height ratio (overlap), and relative height errors: large format, $f = 100$ mm

system, the base-to-height ratio, and the overlap percentage. Figures 13-15 give the actual results of the performed statistical analysis; i.e., relative standard height errors σ_z/Z of computed model points (positional standard errors σ_x and σ_y are not so important because they are correlated with σ_z and are usually smaller, or at least of the same order). It is also interesting to notice that the influence of the assumed $10\text{-}\mu$ calibration errors was practically insignificant, and therefore only these cases are shown.

The results for the large format, $f = 100$ mm (Fig. 13), agree very well with empirical limits known from conventional stereophotogrammetry. This is a good indirect proof for the correctness of the presented theoretical analysis. The results for the vidicon format, $f = 25$ mm (Fig. 14), all lie outside the empirical limit, which is 0.025%, and the curves are also much steeper than they were in Fig. 13. This clearly indicates the difficulties of extraterrestrial mapping problems. The results for the vidicon format, $f = 50$ mm (Fig. 15), show a slightly smaller

influence of calibration errors than in the previous case; otherwise the curves are steeper and less favorable.

Although several models were computed for the vidicon format, $f = 100$ mm, it would be of little value to show the results graphically since in most of these tests the iterative process failed to converge, or—if it did—absolutely unrealistic coordinates with excessively large standard errors were obtained. The reasons for this, together with important statistical conclusions and some practical suggestions, are briefly summarized.

5. Conclusions and Suggestions

Considering the importance of these problems, it would be rather premature to make some definite and final conclusions. However, the performed statistical analysis was sufficiently complete to give a clear general picture about the applicability of stereophotogrammetry to extraterrestrial mapping problems and to show its advantages and pitfalls.

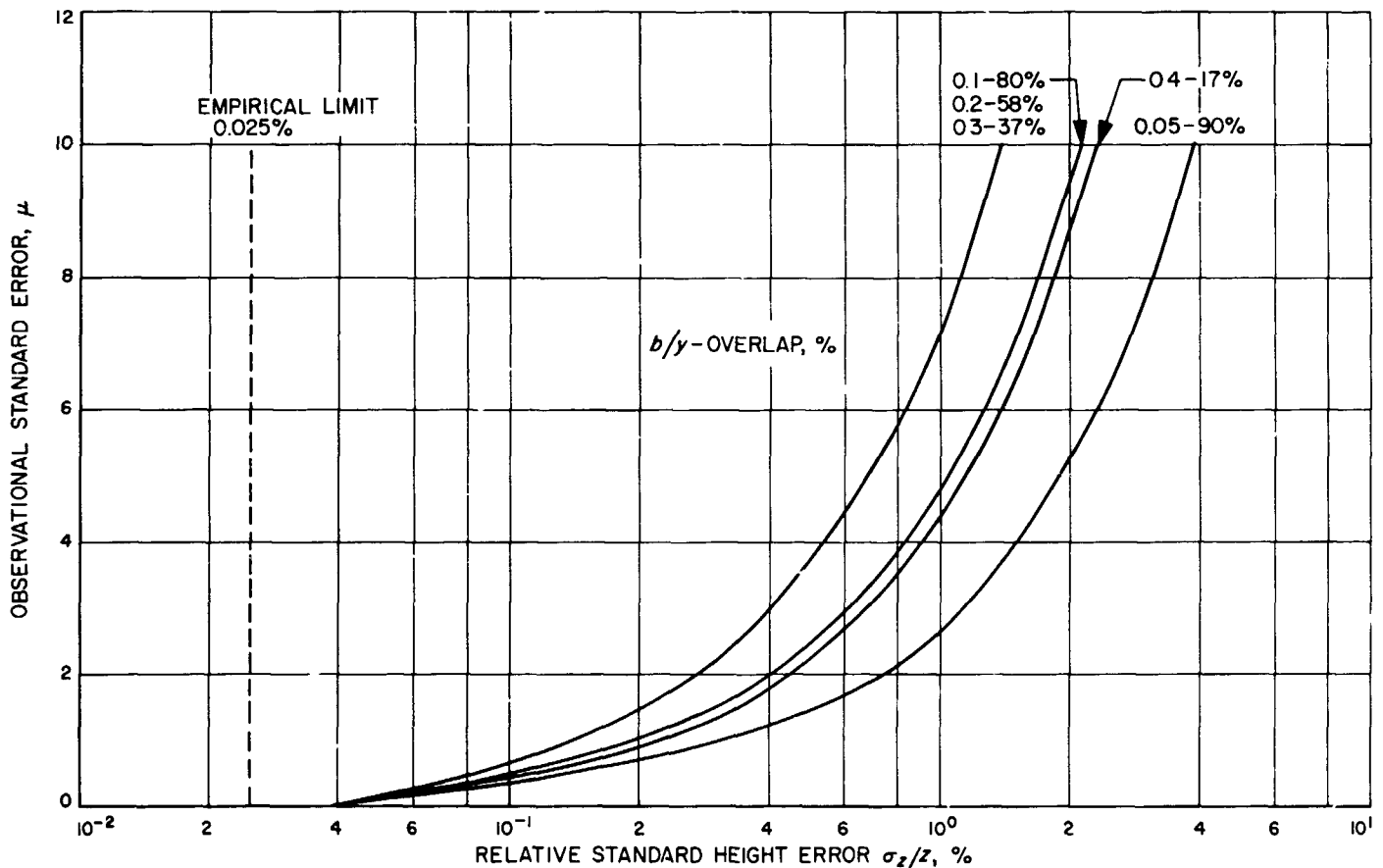


Fig. 14. Relation between observational errors, base-to-height ratio (overlap), and relative height errors: vidicon format, $f = 25$ mm

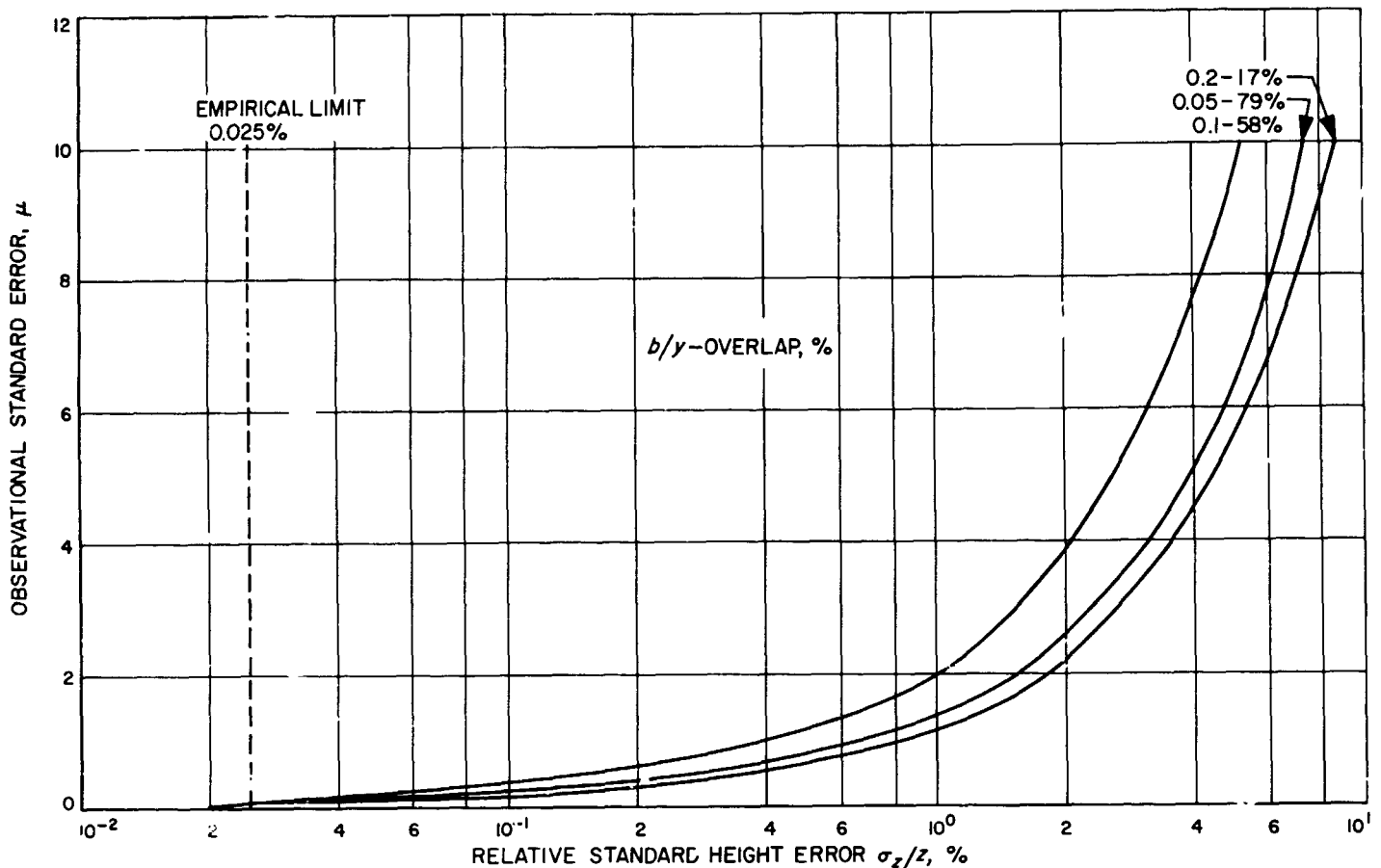


Fig. 15. Relation between observational errors, base-to-height ratio (overlap), and relative height errors: vidicon format, $f = 50$ mm

Some of the important conclusions are:

- (1) The derived theoretical analysis is correct and represents completely the law of propagation of errors.
- (2) Because of the extremely small format of the vidicon camera system (approximate 12.5×12.5 mm), the system of normal equations required for the solution of relative orientation may become very ill-conditioned. (This can be proven by M , N , and P numbers used in numerical analysis.) This means that even very small changes in coefficients—i.e., in observed image coordinates—result in considerable changes in computed parameters, and consequently the standard errors become very large. Sometimes, especially for $f = 100$ mm, the system may even fail to converge (compare Figs. 13-15).
- (3) In some cases the computed model coordinates seemed to be influenced by certain quasi-systematic errors; however, after the standard errors were

determined, to rely upon such results and to introduce a proper scale factor only appeared very doubtful.

- (4) It was interesting to notice the influence of the focal distance, which differs completely from terrestrial cases. It was shown that the focal distance must be considered in close correlation with overlap and base-to-height ratio, and—most important—the smaller it becomes, the better results are obtained (i.e., in case of the vidicon format).

These and other factors seem to indicate that stereophotogrammetric techniques should not be used for certain specified purposes. This, of course, is not true. However, there are certain limitations; to discover and define these in full detail, the following suggestions have been made:

- (1) Instead of trying to solve the relative orientation of a photogrammetric stereopair, external orientation data should be used. The derived theoretical

error analysis can be used profitably for the determination of all necessary constraints and accuracy criteria.

- (2) Another possible approach would be to use a larger vidicon format. This poses an interesting research problem, the solution of which could be based on the same theoretical error analysis. It is realized that certain state-of-the-art limitations should also be considered.
- (3) In the practical part of this report, relative orientation problems were investigated; these proved to be of a critical nature. However, to complete the analysis, further statistical tests dealing with absolute orientation should also be performed.
- (4) Since the law of propagation of errors differs completely for terrestrial photogrammetry cases, research should also be done in this field. These techniques will surely be used for *Surveyor*-type photography and similar purposes, and might prove to be very convenient, because in this case the size of the vidicon format is not critical.
- (5) The importance of highly accurate measurements for all image coordinates is clearly shown. This problem is closely related to the problem of the image quality and the calibration parameters of the camera system. Research efforts devoted to these problems would prove most rewarding.
- (6) The possibility of convergent photography enabling a very high base-to-height ratio should also be investigated.

Generally speaking, the applicability of stereophotogrammetric techniques to extraterrestrial mapping problems is somewhat limited under present conditions. However, the method itself looks very promising, and there is no doubt that after all constraints and parameter accuracy criteria are discovered and determined, it will become very effective and reliable.

References

1. McClatchey, R. A., *The Use of the 4.3-Micron Band to Sound the Temperature of a Planetary Atmosphere*, paper presented at the Symposium on Electromagnetic Sensing of the Earth From Satellites, November 22-24, 1965, Coral Gables, Fla. (sponsored by the American Meteorological Society and the American Geophysical Union).
2. Howard, J. N., Burch, D. E., and Williams, D., *Near Infrared Transmission Through Synthetic Atmospheres*, Geophysical Research Paper 40, Air Force Cambridge Research Laboratories, Cambridge, Mass., 1955.
3. Kirhofer, W. E., and Willingham, D. E., *Ranger VII Photographic Parameters*, Technical Report 32-964. Jet Propulsion Laboratory, Pasadena, Calif., Nov. 1966.
4. Rindfleisch, T., "Photometric Method for Lunar Topography," *Photogrammetric Engineering*, Vol. XXXII, No. 2, March 1966.
5. *Manual of Photogrammetry*, Third Edition. American Society of Photogrammetry, Washington, D.C., 1966.
6. Harpe, R. W., *Experiments With Minimum to Optimum Base-Height Ratios*, TR 55. Army Map Service, Washington, D. C., Feb. 1966.
7. Hedden, R. T., *Lunar Charting Experiments Utilizing Ranger VIII Materials in the AS-IIA Analytical Plotter*, ACIC TP-20. Aeronautical Chart and Information Service, St. Louis, Mo., Sept. 1965.

N67-31774

XIII. Science Data Systems

SPACE SCIENCES DIVISION

A. Video Film Converter, R. D. Brandt

1. General

The work discussed here is a continuation of the digital video data processing efforts reported in SPS 37-31, Vol. IV, pp. 22-35, and SPS 37-22, Vol. IV, pp. 68-71. This paper discusses the video film converter (VFC) presently being used for video data processing.

The VFC (Fig. 1) is a device that either exposes or reads 35- or 70-mm film with the highest fidelity possible (less than 1 m, 1 spot) by means of a flying spot scanner. This reading or recording is done by producing on the face of the cathode ray tube (CRT) an analog or digital raster whose size, position, and rotation are completely variable and dialed-in by the VFC operator. The positioning, focus, and intensity accuracies achieved include those produced by electronic pincushion correction, dynamic focus, and a CRT intensity closed loop. The VFC has the capability to interface with a general-purpose computer to produce processed images and readable symbols.

2. Controls

The VFC is controlled by its operator through three control panels as well as via the computer simulator interface unit (see Fig. 2). The implementation of controlling the VFC from an IBM 360/44 computer is presently in the engineering stage and should be completed within the next six months. On the operational control panel, the operator has the selection of the control of the VFC which can be STANDBY, COMPUTER, or INTERNAL.

When the control selection is COMPUTER, the computer chooses the mode, e.g., *sequential-digital-read* or *random-sequential-record*, etc., and provides camera advance commands and the synchronizing pulses and data for intensity, positioning, and character selection. The VFC uses these data within the constraints set on the format control panel and the exposure control panel by the operator. When INTERNAL control is selected, the operator chooses the mode and initiates the rasters and camera advances from the operation control panel.

BLANK PAGE

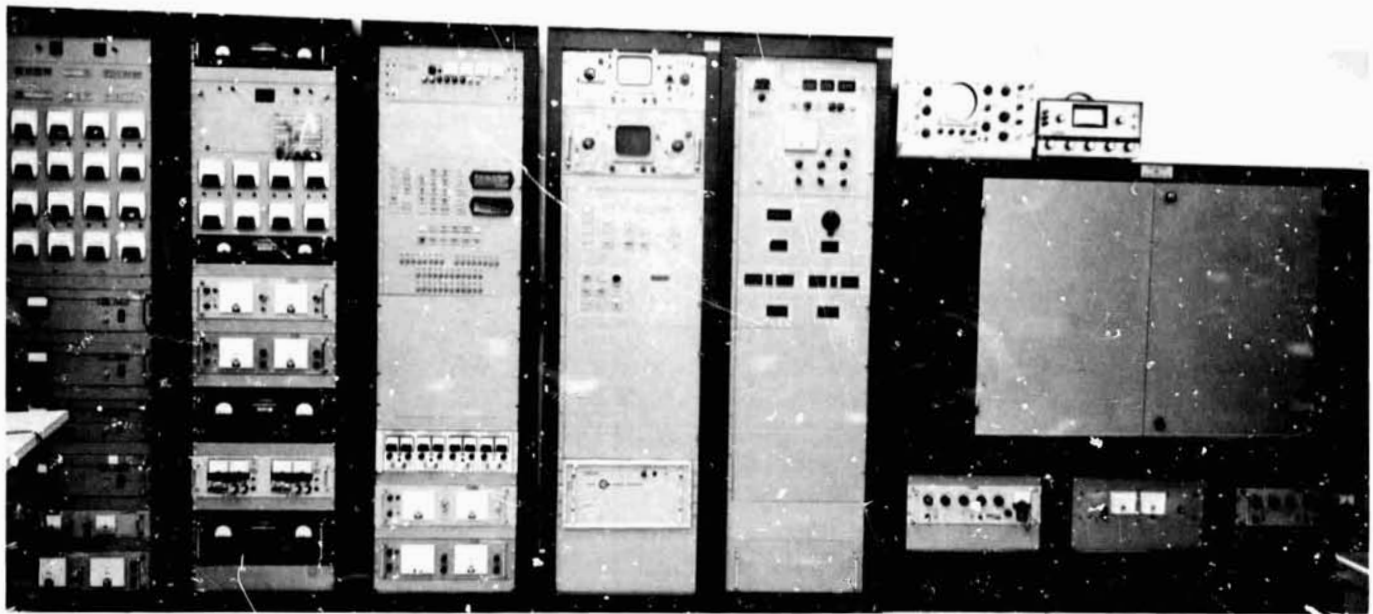


Fig. 1. The video film converter

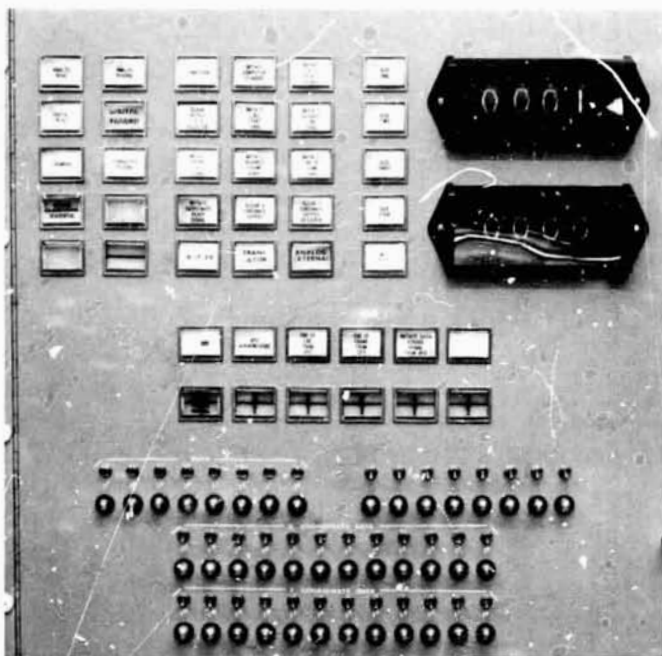


Fig. 2. Computer simulator interface

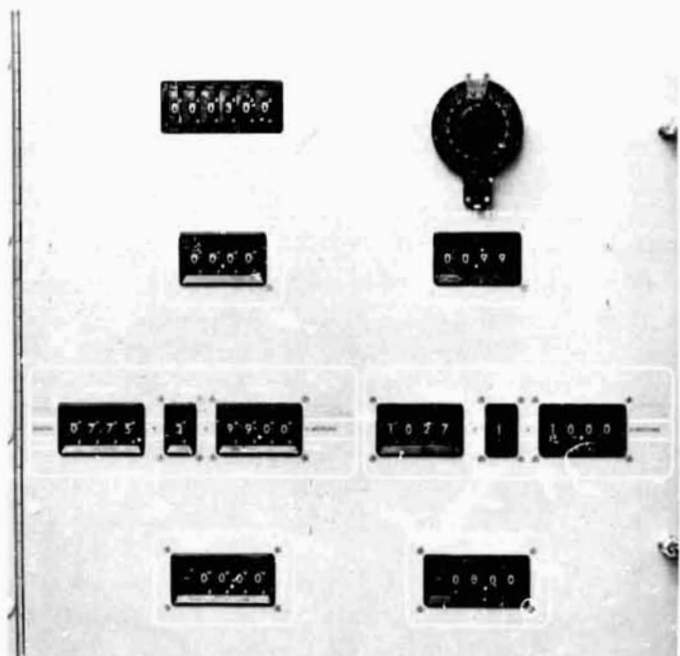


Fig. 3. Format control panel

3. Format Generation

The format is produced by the following groups:

(1) The format control panel (see Fig. 3) sets the size, offsets, and rotation of the raster; the time of the analog sweeps; and offsets of the symbols.

(2) The format logic correlates the modes and syncs in order to properly control the deflection generation groups and the intensity unblank group.

(3) The analog deflection generator produces an analog sweep ramp synchronous with commands from the format logic control; the ramp times are

controlled by the settings on the format control panel. The maximum number of horizontal scan lines per frame is 3999. The vertical size of the raster is controlled by the line spacing (10.00 to 100.00 μ) and the number of lines per frame. The horizontal time per line (300 to 500,000 μ sec) and the horizontal sizing (10.00 to 50.00 mm) are independently controlled.

- (4) The digital deflection generator produces incremental deflection for line and element spacing synchronous with the format logic control commands. At the number of lines and elements corresponding to the settings on the format control panel, those generators will reset and notify the format logic control. The maximum number of horizontal scan lines per frame is 3999. Each line may contain up to 3999 elements. The element spacing and line spacing are independently controlled (10.00 to 100.00 μ). This allows for various size rasters to be generated within the constraints of the 35- or 70-mm film format.

4. Deflection

The deflection scaling groups develop scaled composite sweeps from the outputs of the deflection generator groups, the Straza symbol generator, and offsets. This scaling group controls the size of the rasters via the sizing controls on the format control panel. These composite signals consist of both horizontal and vertical sweeps with reference to the raster itself. The sweeps are then put into the rotation potentiometer where the sine and cosine parts of the horizontal and vertical sweeps are produced. These sine and cosine components are then combined to form X and Y components of the rotated raster, where X and Y relate to the coordinates on the film. The X and Y sweep signals are then put into the deflection drivers to drive the CRT deflection coils.

The pincushion group is used to electronically generate correction signals to eliminate geometrical pincushion distortion on a flat faced CRT. Pincushion correction signals, when properly adjusted, will correct X and Y sweeps at the deflection drivers in order to allow a square raster to be displayed on the CRT face.

The protection group senses sweep losses and protects the CRT by intensity blanking.

5. Focus

Static control of the spot size of the beam at the face of the CRT is provided by the static focus driver and coil.

In addition, the focus is controlled as a function of sweep position by the dynamic focus group, driver, and coil. This dynamic focusing is required because of the beam length difference in reaching the flat CRT face when the electron beam is deflected through varying angles during sweeps.

6. Intensity

The CRT intensity closed loop corrects for phosphor variations on the face of the CRT and linearizes the video input-CRT intensity output transfer function. The feedback element in the loop is a photomultiplier whose gain is controlled by the exposure control panel (see Fig. 4). For greater closed loop linearity and frequency response, a nonlinear amplifier network is inserted in the forward loop to compensate for the nonlinear characteristic of the CRT intensity transfer function. A grid switch is inserted at the input to the grid to allow blanking control for format and protection as well as a special fast unblanking for symbol dot writing.

The cathode bias control provides the CRT cathode bias and protects the CRT against supply drift or failure and accidental system shutdown.

The input video control group provides selectable scaling, offset, and polarity of the signal to the CRT closed loop from internal sources or from the external analog or digital intensity inputs. The digital intensity inputs to the VFC are in the form of 6- or 8-bit characters.

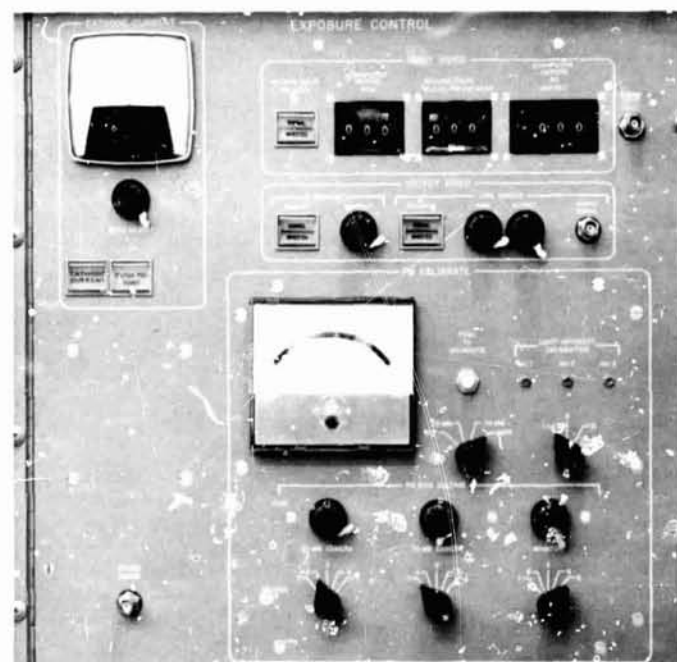


Fig. 4. Exposure control panel

The 6- or 8-bit characters are converted (D/A) within the VFC, and the resulting analog signal is used to amplitude-modulate the beam current of the high resolution CRT within the VFC. In addition to accepting either 6- or 8-bit characters, one or several of the bits may be inhibited by switches on the computer simulator interface. This provides a means for data compression analysis.

The output video control group converts the output of the readout photomultipliers to signals of proper polarity, offset, and magnitude that are compatible with the external intensity A/D requirements and the intensity control of the monitor oscilloscope.

7. Camera Control

The camera control group provides correlation of the 35- and 70-mm camera advancements either by operator or computer request, or automatically at the end of each frame of information scanned on the film.

B. Cycle Length Versus Initial State for Linear Feedback Shift Registers, M. Peilman

The matrix method provides information about the behavior of the entire linear feedback shift register (FSR)

in terms of cycle lengths (see SPS 37-44, Vol. IV, pp. 200-216). The generating function provides information about the behavior of each memory element of a linear FSR. Therefore the generating function may be used to relate an initial internal state to the length of the cycle in which it is contained (Ref. 1).

The generating function is defined as

$$G(x) = \sum_{n=0}^{\infty} a_n x^n \quad (1)$$

where

$$a_n = \sum_{i=1}^r C_{r-i} a_{n-i} \quad (2)$$

or

$$a_n = 1 + \sum_{i=1}^r C_{r-i} a_{n-i} \quad (3)$$

Rules of modulo 2 arithmetic are used in all summations. The linear recurrence relationships in Eqs. (2) and (3) correspond to the case where $e = 0$ and $e = 1$, respectively, in Fig. 5.

CASE 1. Where $e = 0$:

$$\begin{aligned} G(x) &= \sum_{n=0}^{\infty} \left(\sum_{i=1}^r C_{r-i} a_{n-i} \right) x^n \\ &= \sum_{i=1}^r C_{r-i} x^i \sum_{n=0}^{\infty} a_{n-i} x^{n-i} \\ &= \sum_{i=1}^r C_{r-i} x^i \left(a_{-i} x^{-i} + a_{-i+1} x^{-i+1} + \dots + a_{-1} x^{-1} + \sum_{n=0}^{\infty} a_n x^n \right) \\ &= \sum_{i=1}^r C_{r-i} x^i \left[a_{-i} x^{-i} + a_{-i+1} x^{-i+1} + \dots + a_{-1} x^{-1} + G(x) \right] \\ G(x) \left(1 + \sum_{i=1}^r C_{r-i} x^i \right) &= \sum_{i=1}^r C_{r-i} x^i \left(a_{-i} x^{-i} + a_{-i+1} x^{-i+1} + a_{-1} x^{-1} \right) \\ G(x) &= \frac{\sum_{i=1}^r C_{r-i} x^i \left(a_{-i} x^{-i} + a_{-i+1} x^{-i+1} + \dots + a_{-1} x^{-1} \right)}{1 + \sum_{i=1}^r C_{r-i} x^i} \quad (4) \end{aligned}$$

The denominator of Eq. (4) is the reciprocal polynomial of the characteristic polynomial of the associated matrix characterizing the behavior of an r -stage FSR with linear feedback where $e = 0$. That is,

$$\phi(x) = x^r + \sum_{i=1}^r C_{r-i} x^{i-1} \quad (5)$$

where the indeterminate λ has been replaced by x . The reciprocal polynomial of Eq. (5),

$$x^r \phi\left(\frac{1}{x}\right) = 1 + \sum_{i=1}^r C_{r-i} x^i$$

is the denominator of Eq. (4). The indeterminate x has no real significance.

In general, $G(x)$ is a function of the initial internal state $a_{-1} a_{-2} \dots a_{-r}$ and the feedback connections $C_{r-1}, C_{r-2}, \dots, C_0$. (Recall that $C_{r-r} = C_r$ is always 1.) $G(x)$ is the ratio of two polynomials with module 2 coefficients. The initial state for which $a_{-1} = a_{-2} = \dots = a_{-r+1} = 0$, and $a_{-r} = 1$, yields

$$G(x) = \frac{1}{1 + \sum_{i=1}^r C_{r-i} x^i} \quad (6)$$

In general,

$$\begin{aligned} \frac{1}{1 + \sum_{i=1}^r C_{r-i} x^i} &= a_0 + a_1 x + \dots + a_{k-1} x^{k-1} \\ &+ x^k (a_0 + a_1 x + \dots + a_{k-1} x^{k-1}) \\ &+ x^{2k} (a_0 + a_1 x + \dots + a_{k-1} x^{k-1}) \\ &+ \dots \\ &= \frac{a_0 + a_1 x + \dots + a_{k-1} x^{k-1}}{1 + x^k} \end{aligned} \quad (7)$$

Thus, for the initial state $(00 \dots 01)$, the denominator of $G(x)$ as expressed in Eq. (4) divides $x^k + 1$ where k is the period of the sequence. This initial state results in the longest period. This corresponds to the matrix characterization of a linear FSR where $\phi(\lambda)$, as well as its reciprocal, $\lambda^r \phi(1/\lambda)$ divide $\lambda^k + 1$, where the smallest value of k for which this is true is the length of the longest cycle.

When the numerator and denominator of $G(x)$ as expressed in Eq. (4) have a common factor, a sequence is generated with a period less than k which divides k .

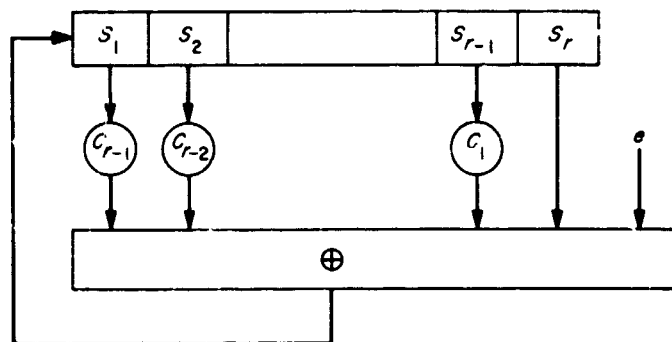


Fig. 5. Generalized r -stage FSR with linear feedback

EXAMPLE 1:

Given $a_n = a_{n-1} \oplus a_{n-5}$

$$\phi(x) = x^5 + x^4 + 1$$

then

$$\begin{aligned} x^5 \phi\left(\frac{1}{x}\right) &= 1 + x + x^5 \\ &= (1 + x + x^2) (1 + x^2 + x^3) \end{aligned}$$

The period associated with $x^5 \phi(1/x)$, as well as with $\phi(x)$, is the least common multiple of 3 and 7, which equals $3 \times 7 = 21$. This period results when the initial state is $00 \dots 01$, and has the generating function

$$G(x) = \frac{1}{1 + x + x^5}$$

From Eq. (4) the initial state can be determined, which yields

$$G(x) = \frac{1 + x + x^2}{(1 + x + x^2) (1 + x^2 + x^3)} = \frac{1}{1 + x^2 + x^3}$$

associated with a period of length 7. Note that $C_{r-i} = 1$ for $i = 1, 4$:

$$\begin{aligned} &a_{-1} \\ &\frac{a_{-3} + C_{-4} x + a_{-5} x^2 + a_{-2} x^3 + a_{-1} x^4}{1 + x^2 + x^3} \\ &a_{-1} = 0 \qquad a_{-4} = 1 \\ &a_{-2} = 0 \qquad a_{-5} = 1 \\ &a_{-3} = 1 \end{aligned}$$

Note that $a_{-1} + a_{-5} = 0 + a_{-5} = 1$.

The initial state 00111 yields a period of 7. Similarly, the initial state 01101 yields a period of 3. The trivial period of 1 results with the initial state of 00000 where $G(x) = 0$ (thus giving $0 + 0x + 0x^2 + \dots$). As shown in Eq. (4), $G(x)$ is extremely useful in determining a state of a minor cycle, especially when r is large.

CASE II. Where $e = 1$.

$$G(x) = \sum_{n=0}^{\infty} \left(1 + \sum_{i=1}^r C_{r-i} a_{n-i} \right) x^n$$

$$= \sum_{n=0}^{\infty} x^n + \sum_{n=0}^{\infty} \left(\sum_{i=1}^r C_{r-i} a_{n-i} \right) x^n$$

The second term on the right was evaluated for case I. Therefore,

$$G(x) = \frac{1}{1+x} + \sum_{i=1}^r C_{r-i} x^i \left[a_{-i} x^{-i} + a_{-i+1} x^{-i+1} + \dots + a_{-1} x^{-1} + G(x) \right]$$

$$G(x) \left(1 + \sum_{i=1}^r C_{r-i} x^i \right) = \frac{1 + (1+x) \sum_{i=1}^r C_{r-i} x^i (a_{-i} x^{-i} + a_{-i+1} x^{-i+1} + \dots + a_{-1} x^{-1})}{1+x}$$

$$G(x) = \frac{1 + (1+x) \sum_{i=1}^r C_{r-i} x^i (a_{-i} x^{-i} + a_{-i+1} x^{-i+1} + \dots + a_{-1} x^{-1})}{(1+x) \left(1 + \sum_{i=1}^r C_{r-i} x^i \right)} \quad (8)$$

The initial state $00 \dots 0$ where $a_{-1} = a_{-2} = \dots = a_{-r} = 0$ yields

$$G(x) = \frac{1}{(1+x) \left(1 + \sum_{i=1}^r C_{r-i} x^i \right)} \quad (9)$$

This characterizes the sequence with the longest period. It also characterizes the *longest sequence of an $(r+1)$ -stage linear FSR where $e = 0$* (Fig. 5). The characteristic polynomial of the $(r+1)$ -stage FSR has a reciprocal polynomial which is identical to the denominator of Eqs. (8) and (9). (Note that the factors of $x^n \phi(1/x)$ are the reciprocals of the factors of $\phi(x)$. The polynomial $x+1$ is a self-reciprocal.)

EXAMPLE 2:

$$a_n = 1 \oplus a_{n-1} \oplus a_{n-2} \oplus a_{n-4}$$

For the initial state 0000,

$$G(x) = \frac{1}{(1+x)(1+x+x^2+x^4)}$$

$$= \frac{1}{1+x^3+x^4+x^5}$$

$$= 1 + x^3 + x^4 + x^5 + x^6 + x^8 + x^9 + x^{14} + x^{17} + \dots$$

$$= 1 + x^3 + x^4 + x^7 + x^8 + x^9 + x^{14} (1 + x^3 + \dots)$$

$$\{a_n\} \begin{matrix} a_0 & a_1 & a_2 & a_3 & a_4 & a_5 & a_6 & a_7 & a_8 & a_9 & a_{10} & a_{11} & a_{12} & a_{13} & a_{14} & a_{15} & a_{16} & a_{17} & \dots \\ 1 & 0 & 0 & 1 & 1 & 1 & 1 & 0 & 1 & 1 & 0 & 0 & 0 & 0 & 1 & 0 & 0 & 1 & 0 & \dots \end{matrix}$$

A five-stage FSR with the linear recurrence relationship

$$a_n = a_{n-3} \oplus a_{n-4} \oplus a_{n-5}$$

has the same $G(x)$ for the initial state 00001. Since both FSRs generate the same sequence, successive states of the four-stage FSR must agree with successive states appearing in the four leftmost stages of the five-stage FSR. Furthermore, it may be shown that if the five-stage FSR were initialized with 10000, successive states of the four rightmost stages correspond to successive states of the four-stage FSR. The $G(x)$ for the initial state 10000 is

$$G(x) = \frac{x}{1 + x^3 + x^4 + x^5}$$

The x in the numerator corresponds to a cyclic shift of one digit period in the sequence. The state contained in a minor cycle of

$$a_n = 1 \oplus a_{n-1} \oplus a_{n-2} \oplus a_{n-4}$$

may be found by determining the state which reduces $G(x)$ of Eq. (8) to

$$G(x) = \frac{1 + x^2 + x^3}{(1 + x^2)(1 + x^2 + x^3)} = \frac{1}{1 + x^2}$$

Note that

$$\begin{aligned} (1 + x)(1 + x + x^2 + x^4) &= (1 + x)^2(1 + x^2 + x^3) \\ &= (1 + x^2)(1 + x^2 + x^3) \end{aligned}$$

and $C_{r-i} = 1$ for $i = 1, 2, 3$:

$$\frac{\begin{matrix} a_{-1} \\ a_{-2} + a_{-1}x \\ a_{-4} + a_{-1}x + a_{-2}x^2 + a_{-1}x^3 \end{matrix}}{1 + (1+x)[(a_{-1} + a_{-2} + a_{-4}) + (a_{-1} + a_{-3})x + a_{-2}x^2 + a_{-1}x^3]}$$

Multiplying and adding terms of like power will yield

$$\begin{aligned} 1 + (a_{-1} + a_{-2} + a_{-4}) + (a_{-2} + a_{-3} + a_{-4})x \\ + (a_{-1} + a_{-2} + a_{-3})x^2 + (a_{-1} + a_{-2})x^3 \\ a_{-1} + a_{-2} &= 1 \\ a_{-1} + a_{-2} + a_{-3} &= 1 \\ a_{-2} + a_{-3} + a_{-4} &= 0 \\ a_{-1} + a_{-2} + a_{-4} &= 0 \end{aligned}$$

The simultaneous solution of these equations results in $a_{-1} = 0, a_{-2} = 1, a_{-3} = 0$, and $a_{-4} = 1$.

The initial state 0101 for $a_{-1} a_{-2} a_{-3} a_{-4}$ yields a period of 2. The same results could have been derived more systematically from

$$a_n = a_{n-3} \oplus a_{n-4} \oplus a_{n-5}$$

by applying Eq. (4) and finding $a_{-1} a_{-2} a_{-3} a_{-4} (a_{-5})$ which reduces the numerator to $1 + x^2 + x^3$.

$C_{r-i} = 1$ for $i = 3, 4, 5$:

$$\begin{aligned} a_{-3} + a_{-2}x + a_{-1}x^2 \\ a_{-4} + a_{-3}x + a_{-2}x^2 + a_{-1}x^3 \\ \frac{a_{-5} + a_{-4}x + a_{-3}x^2 + a_{-2}x^3 + a_{-1}x^4}{1 + x^2 + x^3} \\ a_{-1} = 0 \\ a_{-1} + a_{-2} = 1, \quad a_{-2} = 1 \\ a_{-1} + a_{-2} + a_{-3} = 1, \quad a_{-3} = 0 \\ a_{-2} + a_{-3} + a_{-4} = 1, \quad a_{-4} = 1 \end{aligned}$$

The initial states of the leftmost four stages gives the desired initial state $a_{-1} a_{-2} a_{-3} a_{-4}$ of 0101.

C. Spacecraft Woven Plated Wire Memory,

W. J. Rousey

1. Introduction

Science mission requirements for a low-power, non-destructive readout (NDRO) memory motivated a development program which is being conducted, under contract, by the Librascope Group of General Precision, Inc. This effort will result in the delivery of a flight-qualified engineering model (Fig. 6) by the end of FY 1968. To achieve this, an electrically scaled-down bread-board version of the engineering model (Fig. 7) has been developed and delivered. In addition to the normal design goals for flight hardware, emphasis is being given to establishing the feasibility of memory sterilization.

2. General Characteristics

The electrical and mechanical characteristics of the memory are given in Table 1. The memory capacity is 1024 words, 20 bits each, all of which are randomly accessible (a bit can be obtained in 600 ns). The information is processed bit-serially, in and out, and the memory operates in the NDRO mode. New information is simply written over the old. The memory is also inherently nonvolatile. Standby power is less than 40 mW, and when clocking the memory at a 100-kHz rate, the read or write

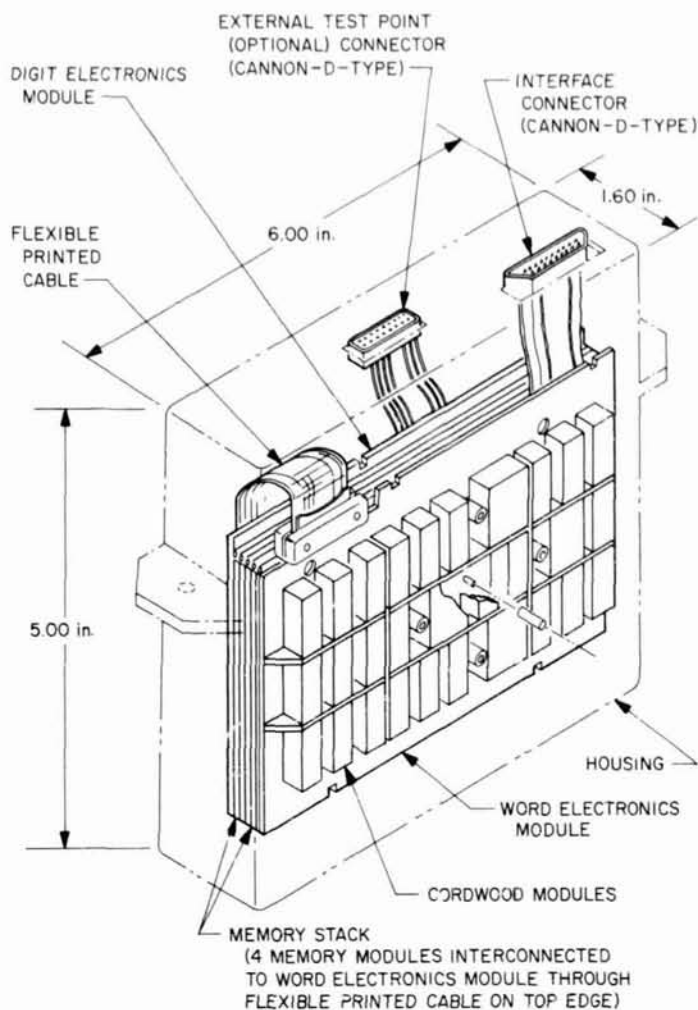


Fig. 6. Engineering model memory system package

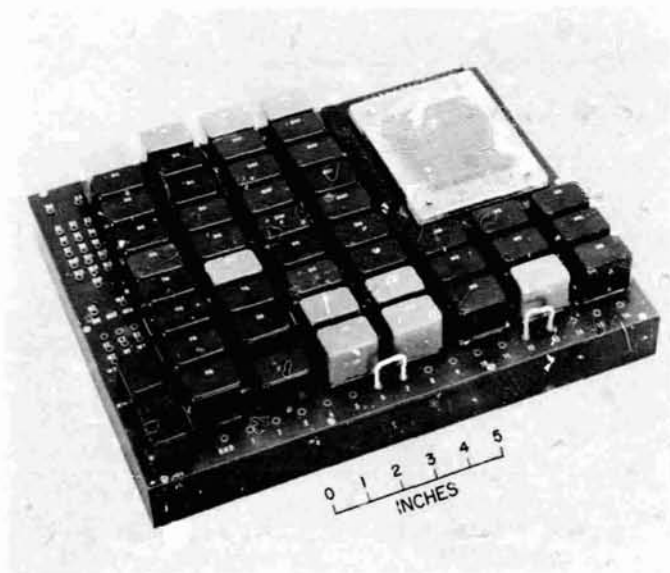


Fig. 7. NDRO readboard memory system

Table 1. Engineering model memory system

Parameter	Characteristics
Capacity	1024 words, 20 bits each; 20,480-bits total
Storage means	Magnetic, on thin film of permalloy plated on copper alloy wire substrate
Electronics	Integrated circuits and silicon semiconductors
Volatility	Nonvolatile
Data transfer mode	Bit-serial read and write
Addressing	Random by word
Data transfer rate	0 to 100,000 bits/s
Signal interface	Compatible with all common TTL and DTL integrated circuit families
Input signals	Clear, address, read or write, data, clock
Output signals	Data, bit markers
Readout mode	Nondestructive
Data alteration	New data written over old; no erase operation required
Power consumption	40mW on standby; 240mW when writing at 100-kHz clock rate
Power supply tolerance	$\pm 10\%$
Weight	4 lb
Volume	48 in ³

power consumption is less than 250 mW. Integrated circuits are used wherever practical, with discrete components comprising the remainder of the system. The input/output circuits are compatible with most diode-transistor logic (DTL) and transistor-transistor logic (TTL) forms of integrated circuit logic elements.

3. Woven Plated Wire Memory (WPWM)

a. Array. Information is stored in a woven plated wire matrix which is a cloth-like array of fine copper wires (Fig. 8). The wires are woven on a large automatic loom, with the insulated word lines serving as the warp and the digit line inserted as the woof.

b. Plating. Conductive wires are coated with a thin-film magnetic material in a multibath, continuous-flow plating operation (Fig. 9). During this operation, the wire is cleaned, polished, plated, tested, and cut into lengths.

c. Weaving. In the weaving process, the desired number of strands of wire (word lines) are held parallel to each other in the loom. Alternate strands are raised, and a magnetically plated wire is inserted by the automatic loom orthogonally to the insulated wires.

d. Storage medium. The memory element is a small-diameter (8 mil) conductive wire plated with magnetic material that has controlled magnetic qualities. During fabrication, the direction of magnetization is constrained to lie circumferentially in the absence of an applied magnetic field, making this the "easy" axis of magnetiza-

tion. A magnetization vector H_s (Fig. 10) represents a binary digit by resting in either of the easy directions (which are 180 deg apart). The magnetic coating is sufficiently thin that flux reversal within the memory element takes place by coherent domain rotation. It is interesting to note that this switching mode is much faster than the wall-motion mode of conventional ferrite cores and is less sensitive to temperature variation.

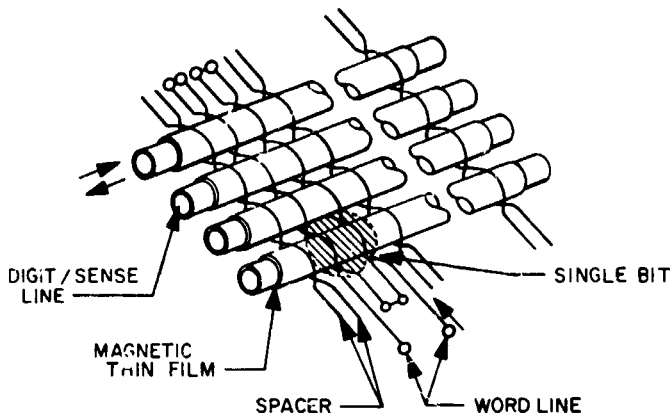


Fig. 8. Basic memory matrix and location of a stored bit

The memory element features a closed magnetic path around the circumferential (easy) axis. Since self-demagnetization fields are not present, the coating can be thicker than planar magnetic films, thus generating higher output voltages. Coupling of the coating to the copper substrate is also improved, further increasing output voltage and decreasing digit drive requirements. The closed magnetic path also decreases susceptibility to external magnetic fields. The magnetically plated wires (Fig. 8) form the digit/sense lines, while the insulated wires are interconnected to form the word coils of the woven array. A memory element is formed at each looped position along the plated wire. Although the magnetic coating is continuous, only those sections in proximity to

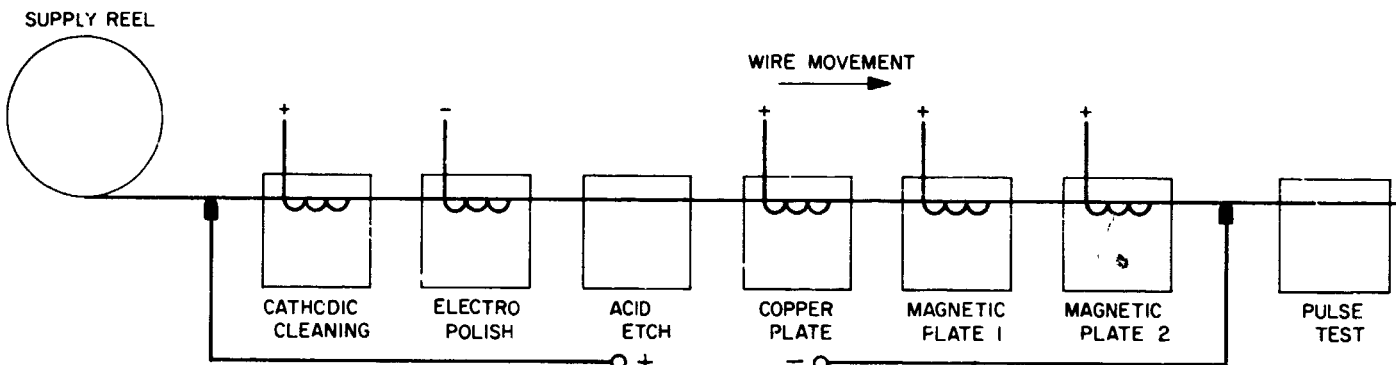


Fig. 9. Plating line schematic diagram

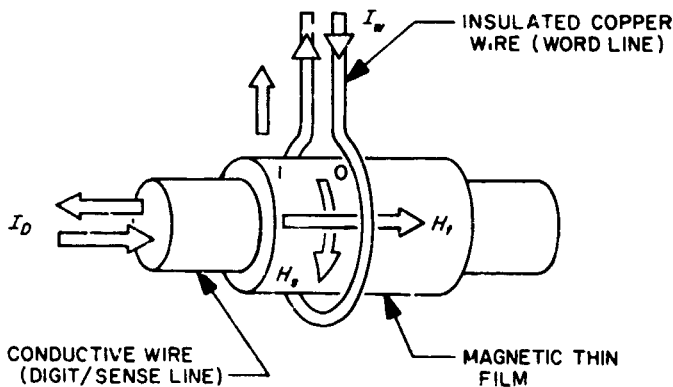


Fig. 10. Binary digit

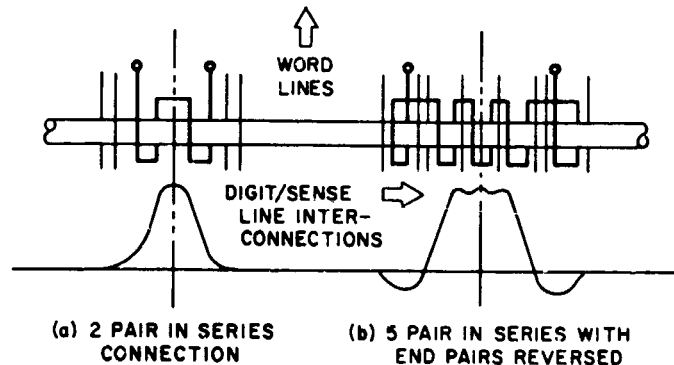


Fig. 11. "Shaped" drive fields

the word coils contribute to memory operation. Thus, a single plated wire is divided into many memory elements; suitable spacing of the word coils avoids interaction between elements. The weaving technique is mechanized such that multiturn coils can be produced; the advantage of this configuration is shown in Fig. 11. To produce these "shaped" drive fields, an automatic loom is used. Preselected word lines are interconnected to make word coils, or left unconnected to provide spacing between word coils. Thus, bit interaction along the magnetically plated digit/sense lines is avoided, so that repetitive reading, writing, or rewriting with the same polarity will not cause spreading of magnetization. External magnetic fields of 0.5 Oe or less will not affect memory operation. The use of multiturn coils also permits the use of lower word-drive currents in writing and reading. The weaving process results in close coupling between word and digit wires, and thus in still lower word currents.

e. Reading from memory. Interrogation of the memory element is accomplished by pulsing the word line with current I_w (Figs. 10 and 12). The induced magnetic field rotates the plated wire's magnetization vector from its quiescent position in the easy (circumferential) axis H_s toward the hard (axial) axis H_l . This, in turn, induces a voltage in the conductive substrate wire, which now serves as the sense line. Its polarity depends on the

direction of the magnetization vector in its quiescent state. On removal of the word current, the vector returns to its *original* quiescent state, again inducing a voltage of opposite polarity in the digit/sense line. Hence, the readout process is inherently nondestructive; i.e., no re-writing or "restore" function is required. Full cycle time for NDRO operation is on the order of 100 ns. Information may be reused repeatedly in NDRO without fear of alteration. However, stored information may be altered by the write process.

f. Writing into memory. Writing into the memory element is accomplished by passing word current I_w (Fig. 10) through the insulated wire word line. This in turn applies a relatively large word field to the conductive digit/sense wire, thus rotating the magnetization vector H_s from the easy axis into the hard axis H_l of the magnetic film. A relatively small digit drive current I_D (Figs. 10 and 13) in the plated wire then tilts the magnetization vector away from the hard direction. When the word current is removed, the magnetization vector rotates to the easy axis in the *one* or *zero* direction as determined by the polarity of the digit drive current.

4. System Description

a. Memory organization. The engineering model (EM) memory is internally organized around a memory stack

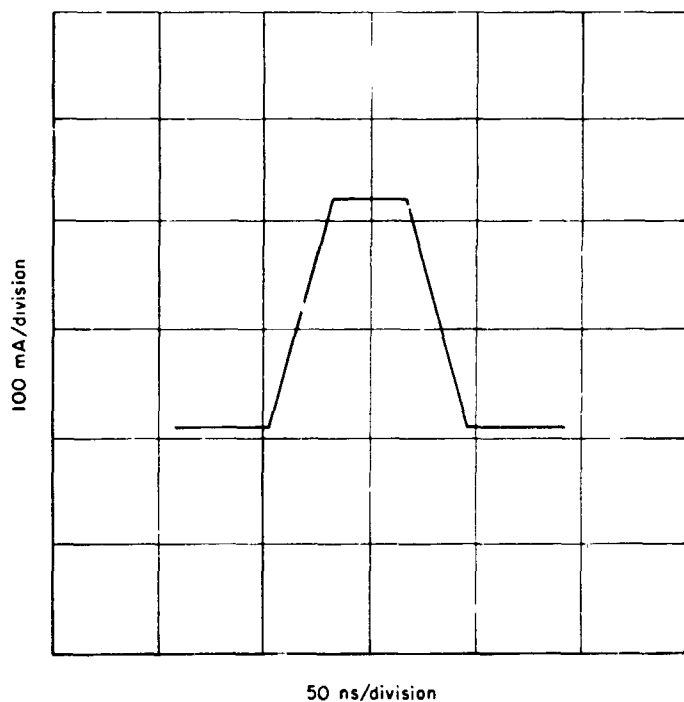


Fig. 12. Word drive current (read or write cycle)

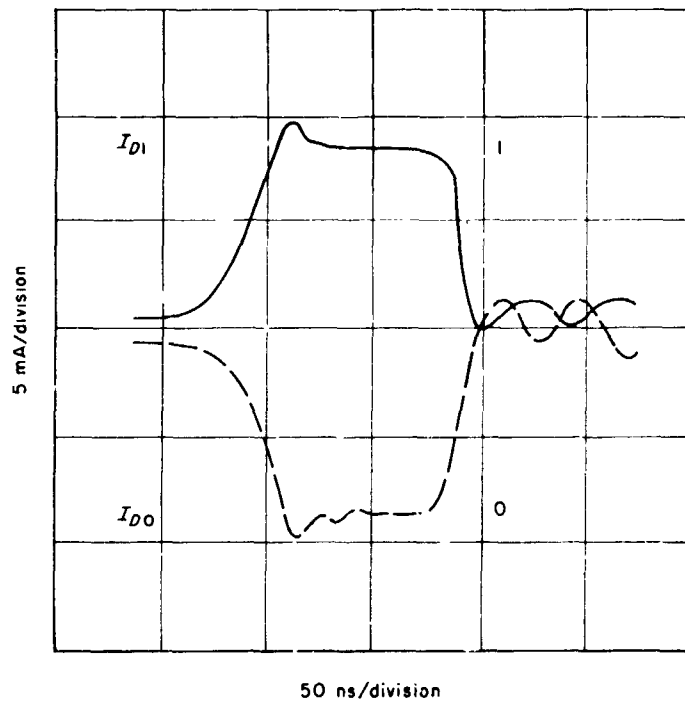


Fig. 13. Digit current (write cycle only)

of 256 words of 80 bits each, which are electrically organized to store 1024 "system" words of 20 bits each. The EM memory unit is a random-word-access, bit-serial memory, and is shown in the simplest block diagram form in Fig. 14. Operating in true bit-serial mode, the memory shares a single read amplifier and single digit driver over all digit lines.

b. Sequence of operation. Refer to Fig. 15. After application of power, the sequence begins with a clear input

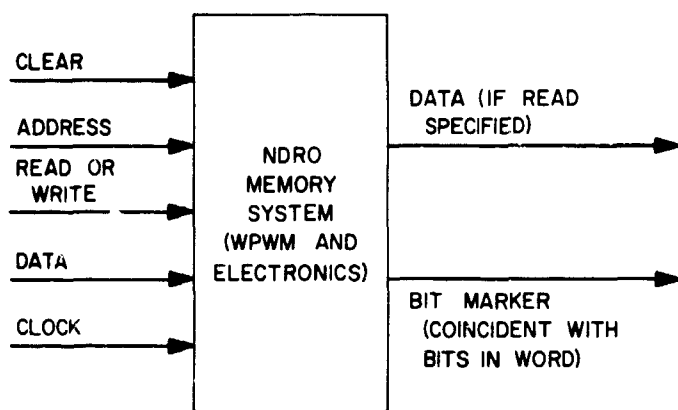


Fig. 14. Functional block diagram for engineering model NDRO memory system

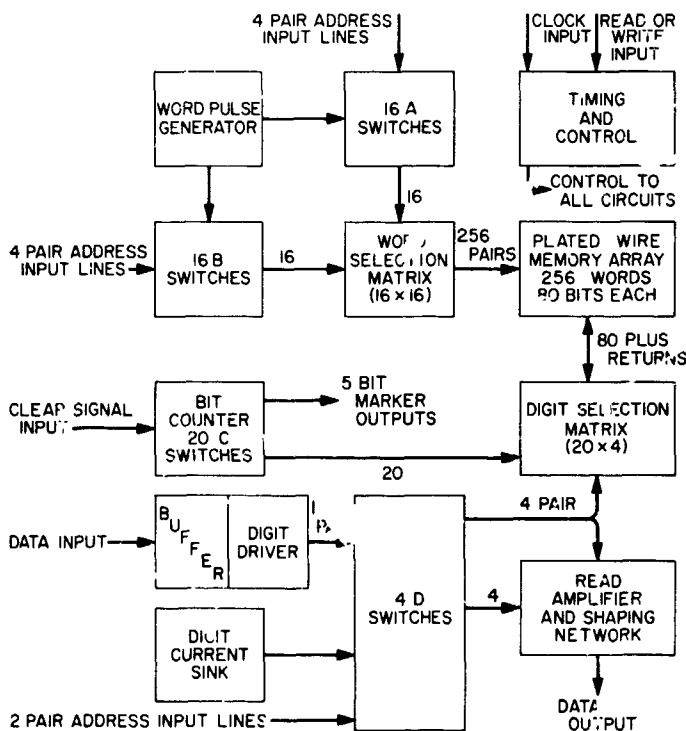


Fig. 15. Engineering model memory system block diagram

signal. The clear signal will set the first flip-flop in the bit counter to a standby-ready state. After establishing the desired address and specifying read or write, the detection of a clock pulse initiates the operating cycle. The leading edge of the clock pulse activates the appropriate timing generators (Fig. 15) and the following signals appear¹:

- (1) A 1- μ s power and address timing pulse (ADT) from the voltage regulator switch to word switches A and B and to digit switch D.
- (2) Initial delay timing (IDT) which is a 500-ns delay interval (provided to allow all switches to settle).
- (3) A 1.6- μ s marker pulse timing (MPT) which operates the bit counter control circuit to provide high current output drive capability through the bit counter flip-flop that is in the ready state.

On the trailing edge of IDT, a 270-ns word pulse timing (WPT) signal is started (Figs. 16 and 17). This, in turn, triggers a word pulse generator (WPG) which yields a current pulse 200 mA in amplitude and 270 ns in duration. The WPG signal is necessary to drive the appropriate word line through the selected word switches A and B (Fig. 15). The system is now ready for read or write (R/W) operation.

Read operation. Assuming the R/W line is at the correct level, a read gate in the selected D switch (Fig. 18) is activated to forward-bias diodes in the digit selection transformer matrix (D1 or D2), thus opening a transmission path between a digit line and the read amplifier. The timing network generates a strobe pulse (Figs. 16 and 17) for the shaping network amplifier coincident with the arrival of the readback signal from the plated digit wire. (This readout voltage is a result of current in the word line which induced a voltage in the plated wire.) If signal polarity at strobe time indicates a *one*, a 1- μ s data output pulse is immediately started. No data output pulse is generated for a *zero*. The entire read operation has required less than 1 μ s, and shortly after the termination of WPT, power is removed from the A, B, and D switches. The bit counter advances on the trailing edge of the MPT and all circuits return to standby condition. When the leading edge of the next clock pulse is detected, the read cycle is repeated.

Write operation. When write is specified by the R/W line, the memory responds exactly as it does in the read

¹Waveforms shown on Fig. 17.

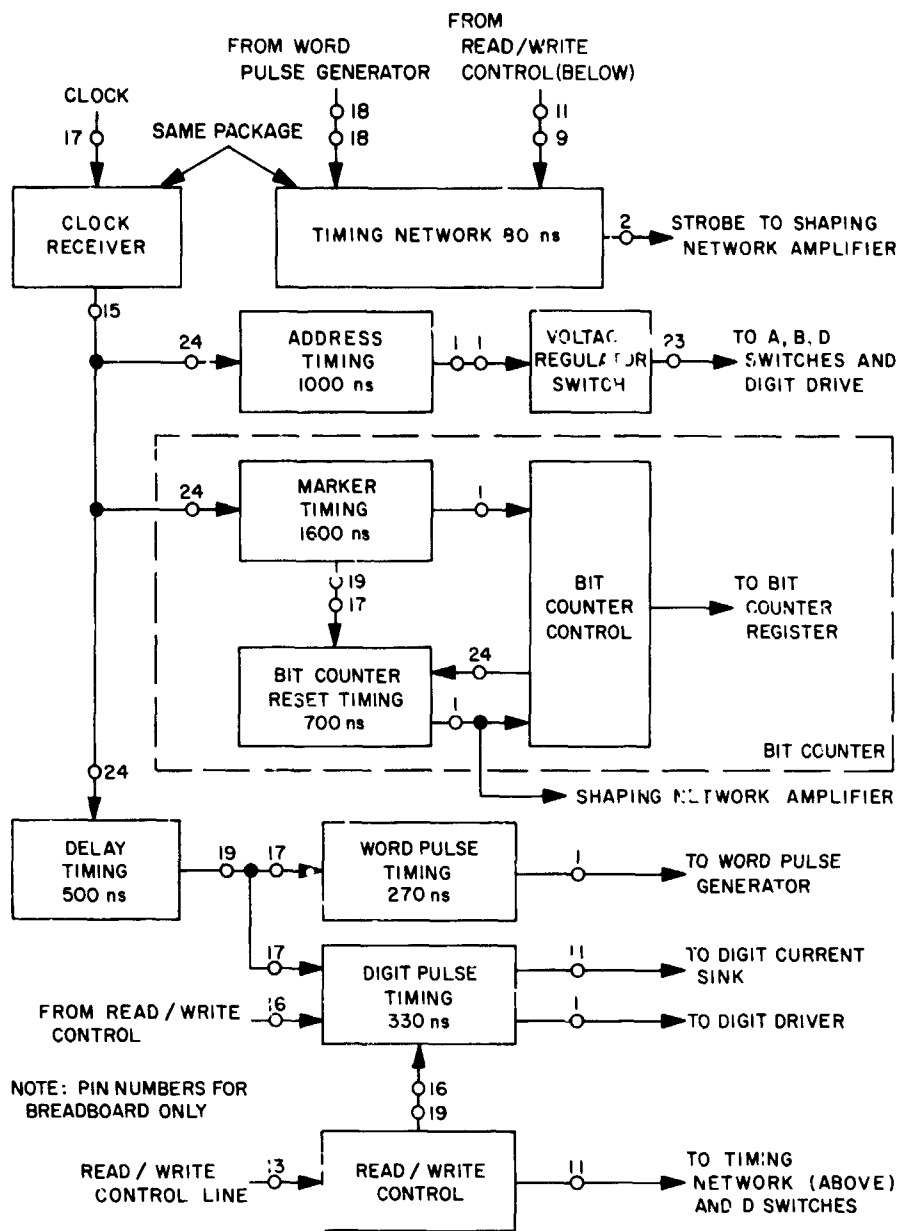


Fig. 16. Timing block diagram

mode, with one exception. A 330-ns digit current pulse (DWT) (Figs. 16 and 17) is generated coincident with the word current pulse. Polarity of digit current is determined by the sense of the binary bit to be stored, and this sense is a function of the voltage level on the input data line. A buffer stage transfers the incoming data to the digit driver (Fig. 15). The digit driver will drive the current pulse through the selected D switch, then to the digit matrix transformer and through the appropriate plated digit wire. After termination of word and digit current, power is removed as in read operation. The bit counter advances as in read operation; all circuits return to standby and await the next clock pulse.

5. Breadboard Test Results

a. Environmental. Proper electrical operation was verified over the temperature range of -10 to $+85^{\circ}\text{C}$. Shock and vibration testing of the memory planes was performed (planes in nonoperating condition), and the results were satisfactory.

b. Sterilization. The Polymer Research Section (382) of JPL conducted sterilization testing.² A memory plane

²JPL Specification VOL-505G3-ETS was used as the defining document.

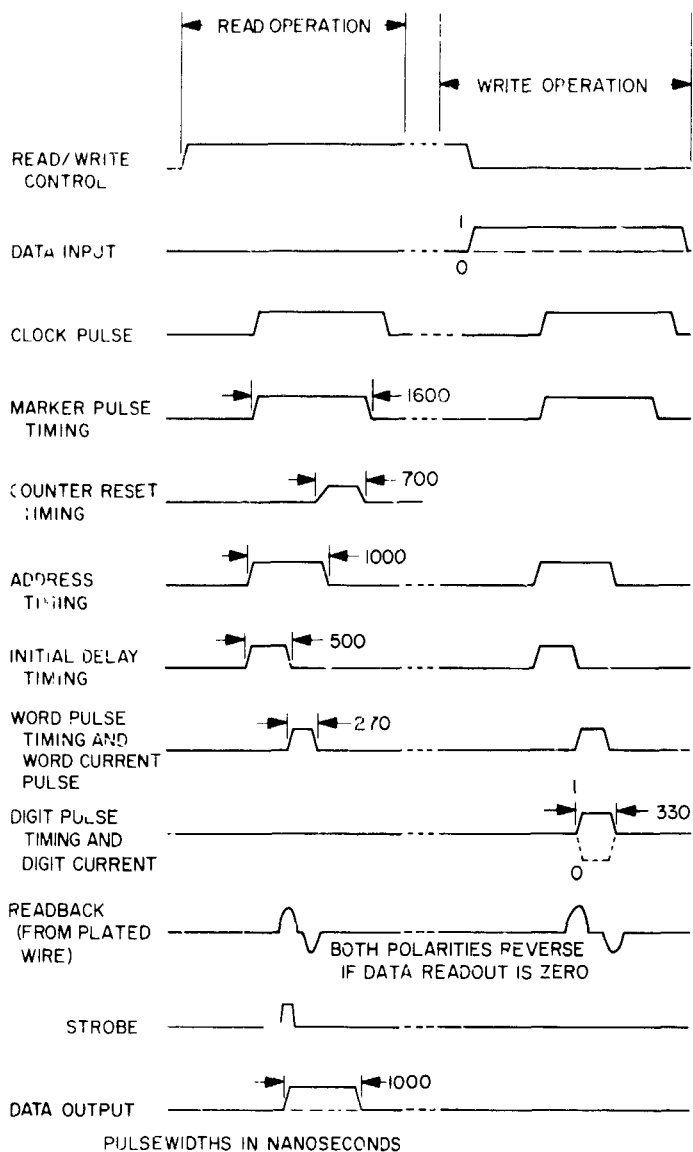


Fig. 17. System timing diagram

was tested in accordance with the type approval requirements. Basically, the test consisted of subjecting the plane to ethylene oxide (ETO) decontamination environment; this was followed by a period of storage in a dry heat sterilization chamber. Post-test evaluation revealed the RTV-615 silicone rubber potting compound (encapsulant for memory planes) to be extremely degraded, with essentially no adhesion to the substrate (printed circuit board). Degradation of the RTV-615 was advanced

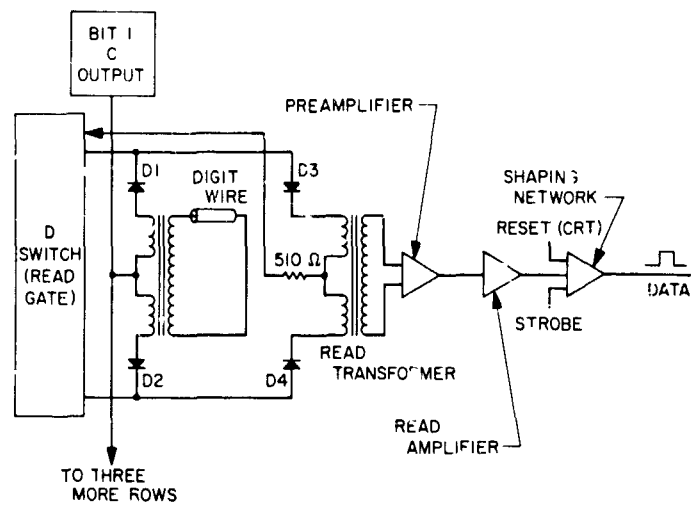


Fig. 18. Simplified read signal selection diagram

to the point of zero tensile strength and elongation. However, there was no electrical degradation.

It was later revealed that primer SS-4101 was used on the printed circuit board when SS-4120 should have been used. The wrong primer accounted for loss of adhesion to the substrate. Processing errors during encapsulation probably accounted for the degradation in tensile strength and elongation. New dummy potted samples of the memory plane were made using the correct primer and carefully controlled processing techniques. These specimens were then subjected to the same ETO and dry-heat sterilization tests. Post-test examination revealed none of the original problems; indeed, microscopic examination failed to show any flaws in the exposed boards or castings.

6. Future Activity

The engineering model memory will be developed and qualified during the 1967 calendar year, with delivery scheduled for January 1968. This development is the second phase of a two-part contract, the first of which yielded a working breadboard model. The technology impartation from the breadboard to the engineering model is expected to result in the creation of a memory capable of meeting *Mariner Mars* or *Voyager*-type mission requirements.

Reference

1. Golomb, S. W., *Sequences With Randomness Properties*, Engineering Report 6193, The Martin Co., Engineering Laboratory, Baltimore, Md., June 14, 1955.

N67-34775

XIV. Lunar and Planetary Sciences

SPACE SCIENCES DIVISION

A. Spectral Reflectance of Silicate Rock Powders, J. B. Adams and A. L. Filice

This study was undertaken to provide an experimental basis for the geologic interpretation of spectral reflectance measurements of planetary surfaces. The search for an understanding of the spectral reflectance properties of large areas of terrain has led to an investigation of silicate rocks in granular to powdered form. The deserts of the earth, when viewed from an aircraft or from space, typically are seen to be mantled with soil, alluvium, talus, and other types of particulate debris, rather than vast expanses of fresh, solid rock. *Surveyors* and *Lunar Orbiters* have confirmed earlier predictions that much, if not all, of the surface of the moon is covered with particulate material ranging in size from huge blocks to fine powder. Also, the dust storms on Mars suggest a surface mantled by particulate rock material.

In this laboratory study of particulate rocks, changes in the wavelength distribution of reflected light were measured as functions of rock composition and mineralogy, particle size, particle shape, particle packing, and angle of illumination. The experimental results show that silicate rocks in powdered form can be classified as

belonging to the broad categories of rock glasses, crystalline acidic rocks, or crystalline basic-ultrabasic rocks, on the basis of spectral reflectance properties in the 0.4- to 2.0- μ wavelength region. Distinguishing characteristics are the ratio of reflected light at 0.7 μ to that at 0.4 μ (here termed R/B), the change in R/B with albedo, the maximum albedo of a rock powder, and the occurrence of broad absorption bands in the reflectance spectra between 0.8 and 2.0 μ . Spectral reflectance properties depend strongly on particle opacity, which in turn is controlled by chemical composition, mineralogy, and particle size; however, reflectance is also affected in a regular way by particle packing, particle shape, and illumination geometry.

The broad classes of rock types can be distinguished most readily if the particle size can be estimated. This is facilitated in the case of unsorted pulverized rock (e.g., associated with impact craters) because of the preponderance of small (< 100 μ) particles that coat the surfaces of the large particles, thereby imparting the properties of the small particles alone. On the other hand, if rock composition is known, an estimate of particle size can be made from the spectral reflectance data.

BLANK PAGE

It is concluded that under most geologic conditions a combination of several spectral reflectance properties is capable of giving some gross-composition information on silicate rock powders; in view of its potential usefulness, especially in planetary exploration, this approach warrants further development.

A more complete account of the results of this study will appear in a forthcoming issue of the *Journal of Geophysical Research*.

B. Cloud-Top Pressure and Abundance of Hydrogen in the Atmosphere of Jupiter,

J. E. Beckman

The widths of methane absorption lines were measured to half-intensity from spectra taken with the A-camera coude spectrograph of the 82-in. Struve telescope at the McDonald Observatory. These careful determinations in the 6200-A high overtone band enabled the cloud-top pressure for Jupiter of 2.3 ± 0.3 atm to be found. If predictions of more detailed scattering models are considered, this is a high limit. In any case, it precludes a hydrogen abundance of 250 km-amagat obtained by Rank, et al. (Ref. 1), which would produce a cloud-top pressure of 6 atm even without the inclusion of other atmospheric constituents. A new hydrogen abundance of 68 ± 15 km-amagat, derived from previous data of the author (Ref. 2), is suggested. The data of Rank, et al., are reinterpreted to produce a result lying between 63 and 72 km-amagat, which is in very good agreement with the author's new result. From the total pressure and the hydrogen and methane abundances, new numerical abundance ratios for H:He:C:Ne are derived for the upper atmosphere of the planet.

A more detailed account of this work will appear in the August 1967 issue of the *Astrophysical Journal*.

C. Use of the Visible and Near-IR Spectrum in Analysis of the Lunar Surface, A. L. Filice

1. Introduction

The visible and near-IR spectrum of solar energy returned from the surface of the moon has been analyzed by four principal methods:

- (1) Photometry.
- (2) Polarimetry.
- (3) Luminescence.
- (4) Spectrophotometry.

These four techniques and their application to the analysis of the nature of the lunar surface are discussed.

2. Photometry

Lunar photometry consists of measuring intensity and angular dependence of the visible spectrum of light returned from the moon. This parameter can be measured at various phase angles and in different locations on the lunar surface. The variation of reflectivity with lighting and viewing angle is expressed mathematically as a photometric function. Photometric studies have shown the moon to be a target that has no limb darkening, and has a photometric function characterized by a rapid increase in reflectivity or backscatter at or near 0-deg phase angle¹ which is independent of the lunar latitude at which it is measured (Fig. 1). Average albedo values for the lunar surface range from 0.070 for the maria to 0.115 for the highlands, where that value is the fraction of the incident light which is reflected. Minimum values of around 0.04 are recorded for certain flooded craters (Billy, Grimaldi) and maximum values around 0.15 for the large, bright, rayed craters (Tycho, Copernicus). Small, bright craters on the maria with albedos as high as 0.30 have been observed.²

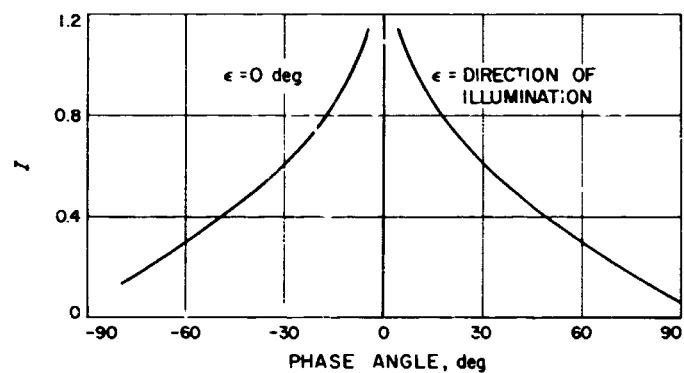


Fig. 1. Brightness (van Diggelen)

Interpretation of the photometric properties of the lunar surface has been difficult because, until recently, no terrestrial analogs could be found that would successfully reproduce the lunar characteristics. These are:

- (1) Very low albedo.
- (2) Strong backscatter at 0-deg phase angle.
- (3) Independence of brightness functions with latitude.

¹This occurs when the direction of illumination and observation coincide. The full moon observed from earth approximates this geometry.

²Z. Kopal, personal communication.

The early investigators Orlova (Ref. 3), van Diggelen (Ref. 4), and others, were able to match the albedo of the moon with various materials such as volcanic ash and cinders, but they could not reproduce the strong backscatter (Fig. 1). Van Diggelen (Ref. 4) was the first to reproduce the complete curve when, in the course of investigating many kinds of materials, he used a dark sponge-like lichen.

Hapke (Ref. 5) subsequently reproduced the lunar photometric curve by working with fine powders sifted into a very porous configuration, which he termed "fairy castle" structure. The important observation here is that in order to match the lunar photometric function, one must use a porous sample; a porous structure has many light traps and exhibits about the same amount of reflecting surfaces for any viewing direction. The photometric properties are independent of the chemical or mineralogical composition of the surface, because lichen (a very unlikely material on the moon), as well as a basalt powder, can adequately reproduce the photometric curve of the moon.

Because of Hapke's work it has been assumed by many that a fine ($\geq 40\mu$) porous surface layer must exist on the moon in order to account for the lunar photometric characteristics. *Rangers VII, VIII, and IX*, as well as *Luna IX* and *Surveyor I* have only provided additional information over which to debate the existence of a dust layer on the moon. However, *Surveyor I* has shown many particles $\geq 500\mu$, the resolution limit of its camera system.

Recently, Oetking (Ref. 6) has shown that the strong backscatter near 0-deg phase angle is not peculiar to the lunar surface. It is exhibited by most terrestrial substances, including standard diffusing surfaces, when observed with an instrument of small aperture.

Halajian (Ref. 7) has now removed the necessity that the lunar surface *must* be fine grained, less than 40μ . By employing a photometer approximately 10 m high, he was able to enlarge his sample area to approximately 7.5 cm in diameter, as opposed to Hapke's photometer which would only sample an area approximately 1.3 cm in diameter. Halajian verified that *any* porous surface will reproduce the lunar photometric function if the albedo is low. This includes furnace slag, coarse-grained volcanic cinder (1 mm to 2 cm), scoria, sea coral painted black, and metallic meteorites. Sea coral painted black actually exceeds the backscatter of the lunar surface, possibly placing an upper limit on the lunar roughness.

A value of 70% porosity and a low albedo were found to be the criteria necessary to reproduce the lunar photometric curve according to Halajian. It now becomes obvious from the multitude of materials which reproduce the lunar photometric function that the following *cannot* be uniquely inferred from earth-based photometric analysis:

- (1) Chemical composition.
- (2) Particle size.
- (3) Surface roughness (macrostructure).
- (4) Structural homogeneity.
- (5) Interparticle cohesion.
- (6) Depth of surface layer.
- (7) Bearing strength.

3. Polarimetry

The measurement of the polarization properties of the lunar surface has been pursued by many investigators, but the first precise work was done by Lyot (Ref. 8) with a highly sensitive polarimeter of his own design. He examined the whole disk and showed that the light returned from the lunar surface is linearly polarized, and that the directions of polarization maxima are always exactly perpendicular or parallel to the plane of observation. (No elliptical polarization has been detected for the moon.)

Intensity of polarization is defined as $P = (I_1 - I_2) / (I_1 + I_2)$ or the ratio of polarized light to total light, where I_1 is the intensity of the horizontal vibration component and I_2 is the intensity of the perpendicular vibration component. Polarization is phase-dependent (Fig. 2). At 0- and

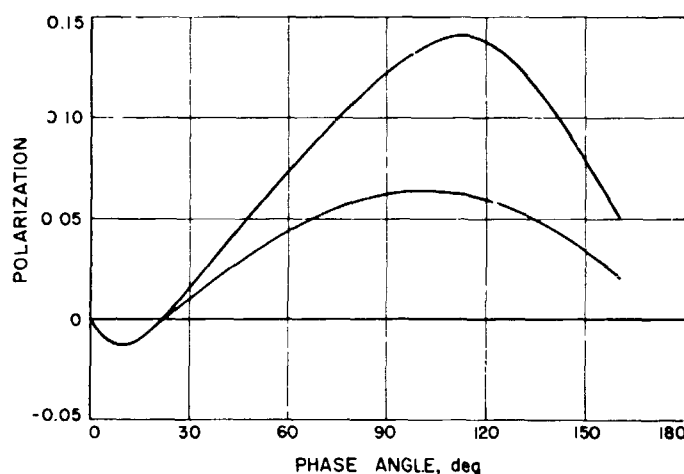


Fig. 2. Polarization (Wright, Dollfus)

23-deg phase angle there is no polarization. Negative polarization (parallel to the plane of vision) occurs between 0 and 23 deg with a maximum of 0.012 at 11 deg. Positive polarization (perpendicular to the plane of vision) occurs between 23 deg and the limit of observation at approximately 160 deg, with a maximum which is variable in intensity and phase angle from 0.066 to 0.088 deg and from 95 to 110 deg.

Polarization is observed to be inversely proportional to the albedo of a particular region, the continents giving rather consistent minimum values and the maria giving more variable maximum values. Also, polarization at a given phase angle is independent of position on the lunar surface in areas of similar albedo.

Laboratory investigations of polarimetric properties of materials were carried out by Lyot (Ref. 8), but Dollfus' work (Ref. 9) is more recent and complete. Dollfus found that neither specularly reflecting nor roughened diffusing surfaces would reproduce the peculiar polarization curve of the moon. As a specular surface he used quartz sandstone, and for the diffusing surface he used coarse volcanic fragments. In all cases, the positive polarization was too high and the negative polarization too low. Also, the inversion point as well as the maximum and minimum points failed to coincide with the lunar curve.

Both Lyot and Dollfus found that finely powdered opaque substances will reproduce the polarimetric curve of the moon. Volcanic ash of the proper albedo can duplicate the curve almost exactly. Dollfus stated that it is the intricate nature of the surface structure that allows the volcanic powder to produce the observed polarization, and he stated that the fine grain size is a key factor in obtaining this structure. He concluded that the moon must be covered with ash, lighter in the highlands and darker in the maria.

It appears that the interpretation of polarimetric phenomena is subject to the same pitfalls that obstruct the interpretation of photometric data. Since both polarization and photometric measurements are apparently governed by the same sample parameters, it would seem likely that the polarization data of the moon will parallel photometric data in that they offer no unique information in the study of the characteristics of the lunar surface.

From recent polarimetric and spectrophotometric observations of the moon, Gehrels, et al. (Ref. 10), have drawn some interesting conclusions as to the nature of the lunar surface. They observed an opposition effect, or a

brightness surge, for extremely small phase angles and a "reddening" (increased red versus blue wavelength energy return) at large phase angles. The near-zero phase measurements were made during an eclipse. The maximum polarization values at near-zero phase are 0.13 and 0.27 for the maria and the highlands, respectively. Their polarization curves agree with those of Lyot for wavelengths near 0.54μ , but polarization is greater for wavelengths near 0.36μ and less for wavelengths near 0.94μ .

By applying Hapke's photometric function to their data, Gehrels, et al., postulate a tenuous ionic surface cloud of volume density 0.05 with a thickness of 0.06 mm, composed of particles with a radius of 0.8μ and separated from each other by 10μ . They stated that this model explains all photometric and polarimetric properties of the moon and asteroids. A serious drawback to this hypothesis, however, is that particles of the hypothesized surface layer must have a refractive index of ~ 1.3 , which is too low for any rocks and would require an ice surface.

Recent experimental and theoretical work by Halajian (1965) and Hapke (1963) has shown that the model of Gehrels, et al., does not reproduce the photometric function of the moon. Furthermore, Halajian's work with slag, sea coral, etc., has shown that all the photometric observations of Gehrels, et al., can be duplicated without calling upon a tenuous cloud of any sort. It remains to be seen whether the tenuous cloud is needed to explain polarimetric data.

4. Luminescence

The feasibility of detecting and measuring luminescent energy from the lunar surface has been investigated by Nash (Ref. 11), Greenman, et al. (Ref. 12), and others.

Laboratory results on different rock samples lead these authors to the following conclusions:

- (1) In general, most of the luminescence occurs at the visible and near-ultraviolet wavelengths.
- (2) The acidic igneous rocks (granitic) show the greatest luminescence efficiency, and the basic (basaltic) rocks the least.
- (3) Luminescence spectra of samples are generally broadband and featureless, and intensity generally decreases with decreasing grain size.

- (4) Excitation efficiencies of X-ray, electron and proton induced luminescence are so low ($< 5 \times 10^{-5}$) as to preclude their use in any luminescence measurements for the moon.
- (5) UV-energy is the only stimulus with excitation efficiency ($\sim 1\%$) sufficient to produce detectable luminescence with present instrumentation for lunar observation.

Greenman, et al. (Ref. 12), state that on the sunlit side a measurable signal must be detected against a high background (visible reflected light), whereas on the dark side a very small signal (due to low incident radiation energies) must be detected against essentially no background.

The observational data concerning lunar luminescence have been reviewed by Ney, et al. (Ref. 13), who conclude that only the spectroscopic evidence can be taken to support the reality of luminescence. They offer alternative explanations for the anomalous albedo variations of certain craters (van Diggelen, Ref. 14) and the interference filter photography work of Kopal and Rackham (Ref. 15).

The most thorough spectrometric observations of the moon to date have been made by McCord (Ref. 16), who measured variations in the depths of the H and K Fraunhofer lines. The measurements were conducted over a six-month period and under a wide variety of lighting conditions at different locations on the moon.

McCord states that no line depth variations corresponding to greater than 5% increase in nonsolar radiation were detected, and variations of 2% were only infrequently detected. Variations of 0.5 to 2% occurred more frequently and varied with time and location on the lunar surface. The author concludes that the variations in line depths resulted from visible emission occurring on or near the lunar surface. Also, the author states that the more frequent variations (0.5-2%) of intensity may have two possible explanations:

- (1) Solid mineral luminescence caused by compositional differences with lunar area, or
- (2) Several different line-filling phenomena occurring on or near the lunar surface.

5. Spectrophotometry

As early as 1911, Miethe and Seegert (Ref. 17) reported and recorded lunar color differences as well as color

changes with phase angle. Unfortunately, much work in spectrophotometry has been only semiquantitative. Almost every investigator has used his own approach as to what parts of the lunar surface should be measured. Consequently, one cannot utilize fully the previous spectrophotometric investigations because of the nonsystematic method of data acquisition. A wide variety of observing conditions, instruments, and systems further complicate the intercomparison of lunar color data. Much controversy over the redness and blueness of a particular lunar area has arisen because of the above-mentioned difficulties in previous spectrophotometry. Standard wavelengths of measurement as well as narrow $\Delta\lambda$ intervals would be of great value in improving the usefulness of lunar color data.

Several interesting properties, however, have been detected by observers using photographic and photoelectric techniques to measure various parts of the lunar visible spectrum. (Although these differences are small, they are real as evidenced by similar results of many investigators.) A summary of the lunar data discussed by Adams (Ref. 18) is given below:

- (1) Visible spectral response is a broad continuum with red wavelengths ($\sim 0.7 \mu$) reflecting stronger than blue ($\sim 0.04 \mu$) wavelengths.
- (2) Radlova (Ref. 19), Barabashev, et al. (Ref. 20), and Teifel' (Ref. 21) have all confirmed that, in general, the brighter (higher albedo) lunar areas are the redder.
- (3) Gehrels, et al. (Ref. 10), found a systematic linear increase of redness with increase in phase angle to about 40-45 deg.
- (4) Tull (Ref. 22) gives a spectral curve from 0.91 to 1.54 μ of Mare Tranquillitatis, and Moroz (Ref. 23) gives curves from 0.35 to 2.2 μ of maria and highlands. They all show minimums around 1.0 μ .

Recent laboratory investigations in the visible and near-IR spectrum by Adams and Filice (Ref. 24) have duplicated the observed spectrophotometric properties mentioned above by using basic and ultrabasic samples of varying particle size. The albedo range ($\sim 0.07-0.30$) as well as the albedo-redness relationship and the minimum at 1.0 μ are reproduced in the samples used. Other rock types (granites, rhyolites, tuffs, tektites, pumice, obsidian, etc.) failed to meet one or more of the criteria listed for the moon. Other parameters such as packing and particle shape were examined, but particle size was found to be the critical parameter that affects spectral response of powders of a given composition.

Adams, comparing the data of Adams and Filice with similar data for the moon, has concluded that the whole visible portion of the moon is compatible with a basic-ultrabasic composition. He suggests that the albedo difference between the maria and highlands may be due to a different mean particle size, the maria being younger, darker, and coarser; the highlands being older, brighter, and of finer particle size.

D. Linear Martian Features on *Mariner IV* Frames 3 and 11, J. Negus deWys

Present knowledge of the Martian surface is strongly dependent upon what is gleaned from *Mariner IV* photographs. Only frames 3 and 11 are considered here. Frame 3 (Figs. 3a and 3b) is between 5 and 15°N lat in the Amazonis desert area; frame 11 (Figs. 4a and 4b) is between 30 and 35°S lat in a semi-dark area. In addition to the dense cratering, several types of linear markings are apparent:

(1) A gross northwest-southeast and northeast-southwest pattern of fairly straight lineations is

present in frame 11. Picture elements represent ~ 1.2 km. Thus these larger features are ~ 1 to 5 km in width and may be traced across the entire frame. These could be tectonic features with accompanying volcanics in the northeastern quadrant of the frame.

(2) A finer linear pattern in the same directions is visible with both dark and light components. These are ~ 1.2 km wide and average ~ 6 to 7 km long. Both the gross and fine patterns cut across craters and appear on the floors, rims, and surrounding terrain.

(3) A third type of linear pattern appears to meander. Examples are well exhibited in the northwest corner of frame 3 and in the northwest corner of frame 11. In the former, a dendritic pattern is also exemplified. The three main natural materials which show gross meandering patterns on earth are glaciers, water, and lava (where following a previously shaped valley); combination of rock or particles with one of the foregoing is also possible. At the presently accepted Martian surface pressure

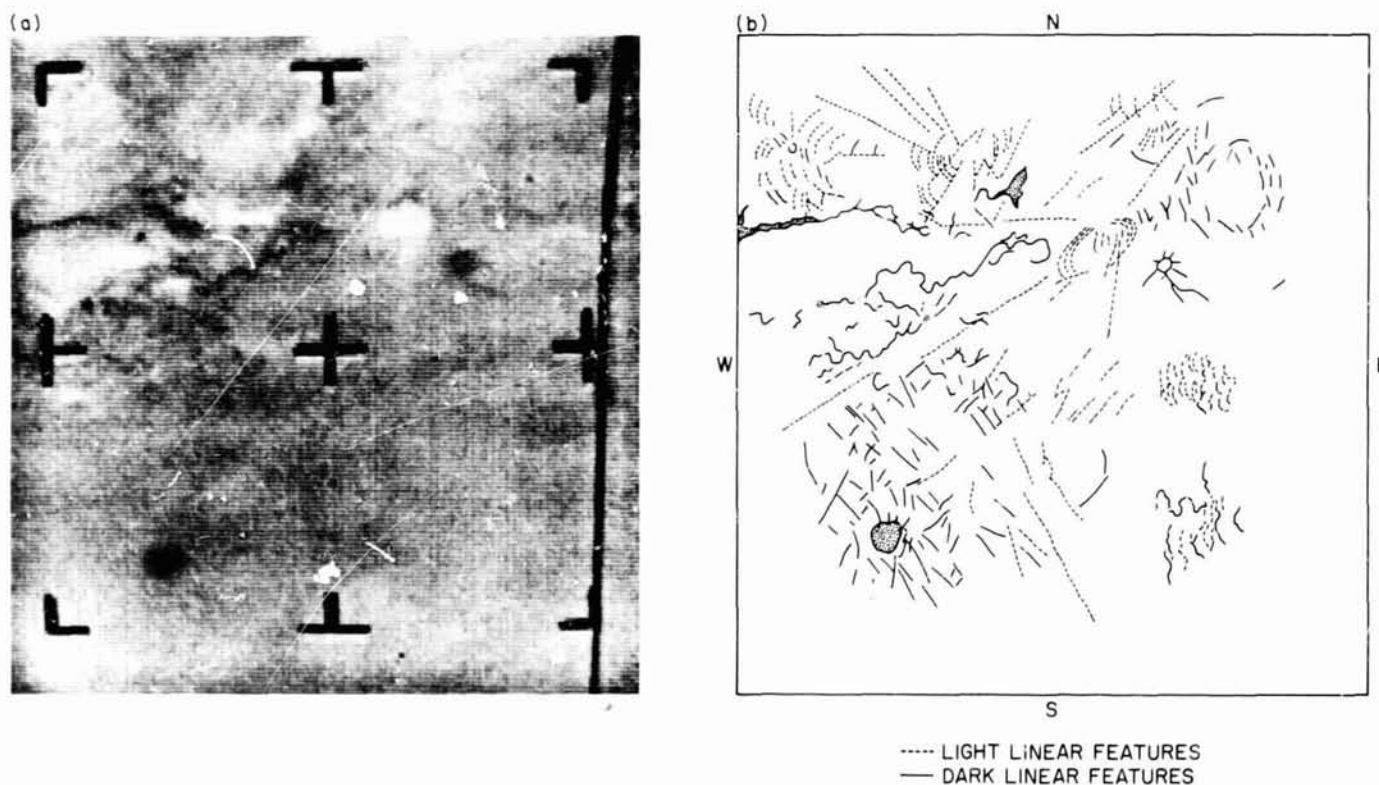


Fig. 3. *Mariner IV* frame 3: (a) ~ 5–15°N lat over Amazonis desert area; one picture element ~ 1.2 km; sun angle 14 deg from zenith; (b) tracing of some visible linear features

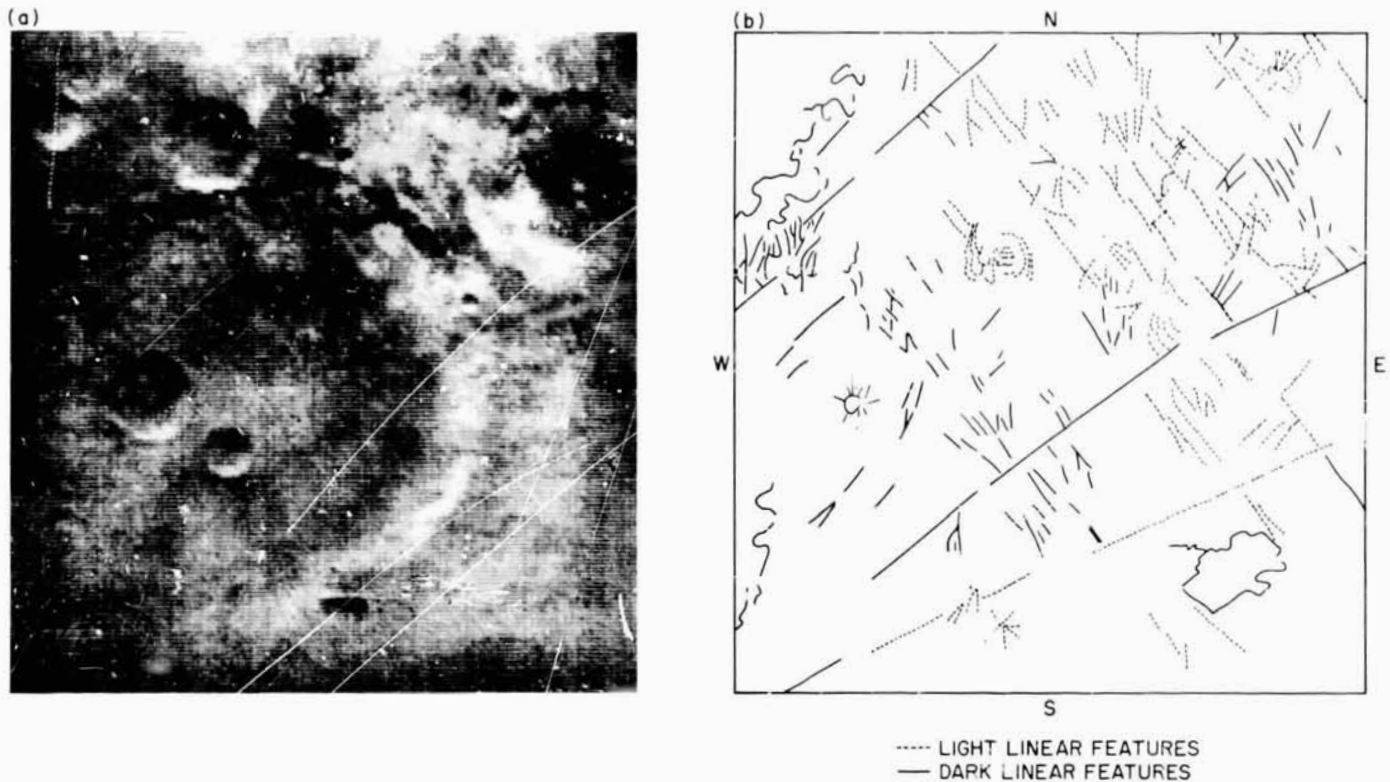


Fig. 4. *Mariner IV* frame 11: (a) $\sim 30\text{--}35^\circ\text{S}$ lat over semidark area; one picture element ~ 1.2 km; sun angle 47 deg from zenith from north; (b) tracing of some visible linear features

of 9 ± 4 mb, liquid water is not possible. It is possible to form a simulated meander pattern with overlapping crater rims.

- (4) Radial lines around white patches are seen in frame 11. Frequently white areas occur with dark central dots (1.2 km). This partly white area in frame 11 in the northeast corner may be frost. Frame 3 also shows radial lines with concentric rings in the northwest corner.
- (5) Arcuate light markings are observed in the extreme northwest of frame 3. As this is in the so-called desert area, these features may represent large dune configurations.

- (6) Unusual or combination effects might be another category.

Linear features shown in Figs. 3b and 4b are examples only, and are not intended to represent complete tracings of linear features. Further interpretation is not proposed at this time. This is a very preliminary representation of a study of linear features on *Mariner IV* photographs. Dr. H. T. U. Smith³ is collaborating in this work; independent tracings are being used to verify features.

³Chairman of geology at University of Massachusetts, Amherst, Mass., and specialist in geomorphology and photogeology.

References

1. Rank, D. H., Fink, U., and Wiggins, T., "Measurements on Spectra of Gases of Planetary Interest: Part II—H₂, CO₂, NH₃, and CH₄," *Astrophys. J.*, Vol. 143, pp. 980-988, March 1966.
2. Beckman, J. E., "Planetary Abundances Measured Using an Image Intensifier," *Planet. Space Sci.*, Vol. 15, 1967 (in press).
3. Orlova, N. S., *Uch. Zap. Univ. Leningrad*, No. 153, 1952.
4. van Diggelen, J., *Reach. Obs. Utrecht*, Vol. 14, No. 2, 1959.
5. Hapke, B. W., "A Theoretical Photometric Function for the Lunar Surface," *J. Geophys. Res.*, Vol. 68, No. 15, pp. 4571-4586, Aug. 7, 1963.
6. Oetking, P., "Photometric Studies of Diffusely Reflecting Surfaces With Applications to the Brightness of the Moon," *J. Geophys. Res.*, Vol. 71, No. 10, pp. 2505-2513, May 15, 1966.
7. Halajian, J. D., *Photometric Measurements of Simulated Lunar Surfaces*, Report RE-219. Grumman Aircraft Engineering Corporation, Research Dept., Bethpage, N. Y., July 1965.
8. Lyot, B., *CR Acad. Sci.*, Paris, Vol. 179, p. 1733, 1924.
9. Dollfus, A., "Recherche d'une Atmosphere Autour de la Lune," *Ann. Astrophys.*, Vol. 19, No. 71, 1956.
10. Gebel's, T., Coffeen, T., and Owings, D., "Wavelength Dependence of Polarization," *Astron. J.*, Vol. 69, No. 10, pp. 826-852, 1964.
11. Nash, D. B., "Proton-Excited Luminescence of Silicates—Experimental Results and Lunar Implications," *J. Geophys. Res.*, Vol. 71, No. 10, pp. 2517-2534, May 15, 1966.
12. Greenman, N., et al., *Feasibility Study of the Ultraviolet Spectral Analysis of the Lunar Surface*, Report SM 48529. Douglas Aircraft Co., Inc., Santa Monica, Calif., March 1965.
13. Nye, E. F., Woolf, N. J., and Collins, R. J., "Mechanisms for Lunar Luminescence," *J. Geophys. Res.*, Vol. 71, No. 7, pp. 1787-1793, 1966.
14. van Diggelen, J., "The Radiance of Lunar Objects Near Opposition," *Planet. Space Sci.*, Vol. 13, pp. 271-279, April 1965.
15. Kopal, Z., and Rackham, T., "Excitation of Lunar Luminescence by Solar Activity," *Icarus*, Vol. 2, pp. 481-500, 1963.
16. McCord, T., "Observational Study of Lunar Visible Emission," *J. Geophys. Res.*, Vol. 72, No. 8, pp. 2087-2097, 1967.
17. Fiethe, A., and Seegert, B., "Über Qualitative Verschiedenheiten des von den Einzelnen Teilen der Mondoberfläche Reflektierten Lichtes," *Astron. Nach.*, Vol. 188, pp. 239-246, 1911.
18. Adams, J. B., "Lunar Surface Composition and Particle Size; Implications From Laboratory and Lunar Spectral Reflectance Data," *J. Geophys. Res.*, Vol. 72, 1967 (in press).

References (contd)

19. Radlova, L. N., "Photographic Colorimetry of the Moon," *Astron. Zh.*, Vol. 20, No. 1, 1943.
20. Barabashev, N. P., Ezerskii, V. I., and Fedoretz, V. A., "Color Contrasts of the Lunar Surface," *Sov. Astron.—AJ*, Vol. 3, pp. 484–489, 1959.
21. Teifel', V. G., "On Normal Color Indexes and the Color-Brightness Relation for Portions of the Lunar Surface," *Sov. Astron.—AJ*, Vol. 3, pp. 955–959, 1959.
22. Tull, R. G., "The Reflectivity Spectrum of Mars," *Icarus*, Vol. 5, pp. 505–514, 1966.
23. Moroz, V. I., "Infrared Spectrophotometry of the Moon and the Galilean Satellites of Jupiter," *Sov. Astron.—AJ*, Vol. 6, No. 9, pp. 999–1006, 1966.
24. Adams, J. B., and Filice, A. L., "Spectral Reflectance 0.4μ to 2.0μ of Silicate Rock Powders," *J. Geophys. Res.*, Vol. 72, 1967 (in press).

N67-34776

XV. Fluid Physics

SPACE SCIENCES DIVISION

A. The Density Disturbance Ahead of a Sphere in Rarefied Supersonic Flow, D. A. Russell

The nature of the flow upstream of a blunt body in a supersonic stream is strongly dependent upon the ratio of inertial to viscous forces; i.e., the Reynolds number Re . For large Re , the disturbance is characterized by a discontinuous shock wave standing close to the body (inviscid solution), while for small Re the shock wave is replaced by a smooth disturbance which extends far upstream (free-molecular solution). The transition of the flow between these two limiting solutions is the subject of the present experimental study.

The experiment is shown schematically in Fig. 1. Spherical models are sting-mounted in either a $M = 4.2$

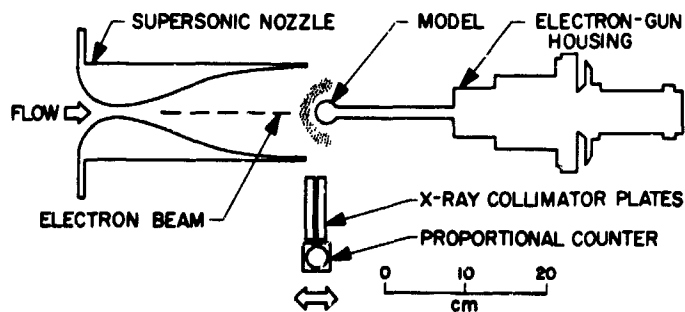


Fig. 1. Schematic of the experiment

(nominal Mach number) nitrogen stream, or a $M = 3.8$ argon stream. Re (based on free-stream properties and body radius) is varied by changing both the model size and the total pressure of the flow. A 15-kV, 10- to 100- μ A electron beam passes through the sting and discharges through a $\frac{1}{2}$ -mm orifice at the body nose. The beam electrons produce a small amount of X-radiation through collisions with the flowing gas atoms. This radiation is measured along the axis in front of the body by traversing a proportional counter equipped with collimating plates. At each position, the total number of photons with energies between 2 and 15 kV is counted over a preset time interval. Calibrations have shown that this output is linearly related to the local gas density for the conditions encountered in the experiments, and that the magnitude of the X-ray flux agrees with theoretical predictions.

Some early results are shown in Fig. 2, where stagnation-streamline data are presented for a $\frac{1}{2}$ -in. radius sphere operated in nitrogen with $Re = 100$. Data were taken with the body water-cooled (body temperature $T_b =$ flow total temperature T_0), and with the body liquid-nitrogen-cooled ($T_b = 0.26 T_0$). The ordinate was obtained by counting X-rays for a time interval sufficient to give at least 1000 counts when the detector was looking at the undisturbed stream (10–40 s). The background noise of the detector system, 1 to $\frac{1}{2}$ counts/s, is significant only for the longer

BLANK PAGE

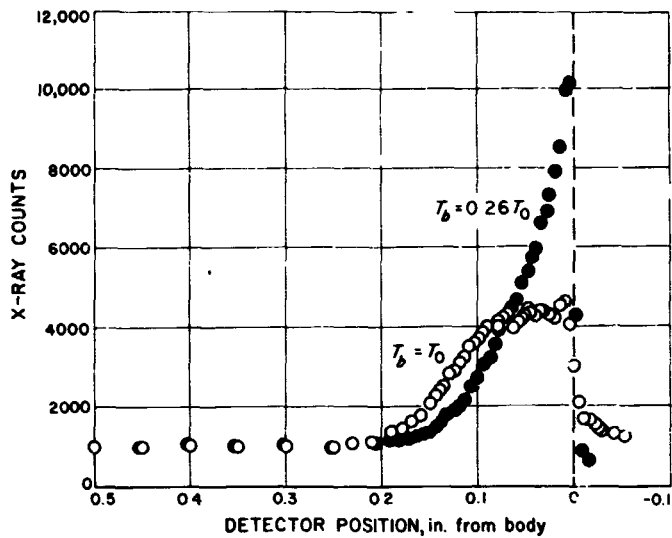


Fig. 2. Stagnation streamline data for a sphere in nitrogen: $Re = 100$; $M = 4.4$; $R = \frac{1}{2}$ in.

time intervals. The location of the model nose is given by the midpoint of the signal cutoff on the data profiles (this was verified by observing the X-ray signal from a 0.001-in. wire taped over the model orifice). The cooled model data of Fig. 2 were obtained with a 0.1-mm

collimator spacing, while the uncooled points were for a 0.25-mm spacing. The uncooled data exhibit a somewhat broader cutoff, and thus poorer resolution; however, the resolution was still sufficient to ensure an undistorted upstream profile.

All of the profiles exhibit a small residual signal for locations behind the model nose, such as may be seen in Fig. 2. Experiments have shown that this is attributable to backscattering off the model surface, and it should have no effect on the measurements in front of the model. A check on the effect of the beam orifice was provided by drilling the orifice out to either a 1- or 1.5-mm diameter. The X-ray profiles were altered only at stations closer than one orifice diameter from the model surface; consequently, data points closer than one orifice diameter are not used for the final profiles.

Results for nitrogen are collected in Figs. 3 and 4. The $Re = 30, 50,$ and 200 profiles were taken with a $\frac{1}{4}$ -in.-radius model, and the 100 and 400 with a $\frac{1}{2}$ -in. model. The background noise has been subtracted from each count and the number divided by the mean upstream count to give the density ratio ρ/ρ_∞ . The continuum solution ($Re = \infty$) and the free-molecular solution ($Re = 0$) are

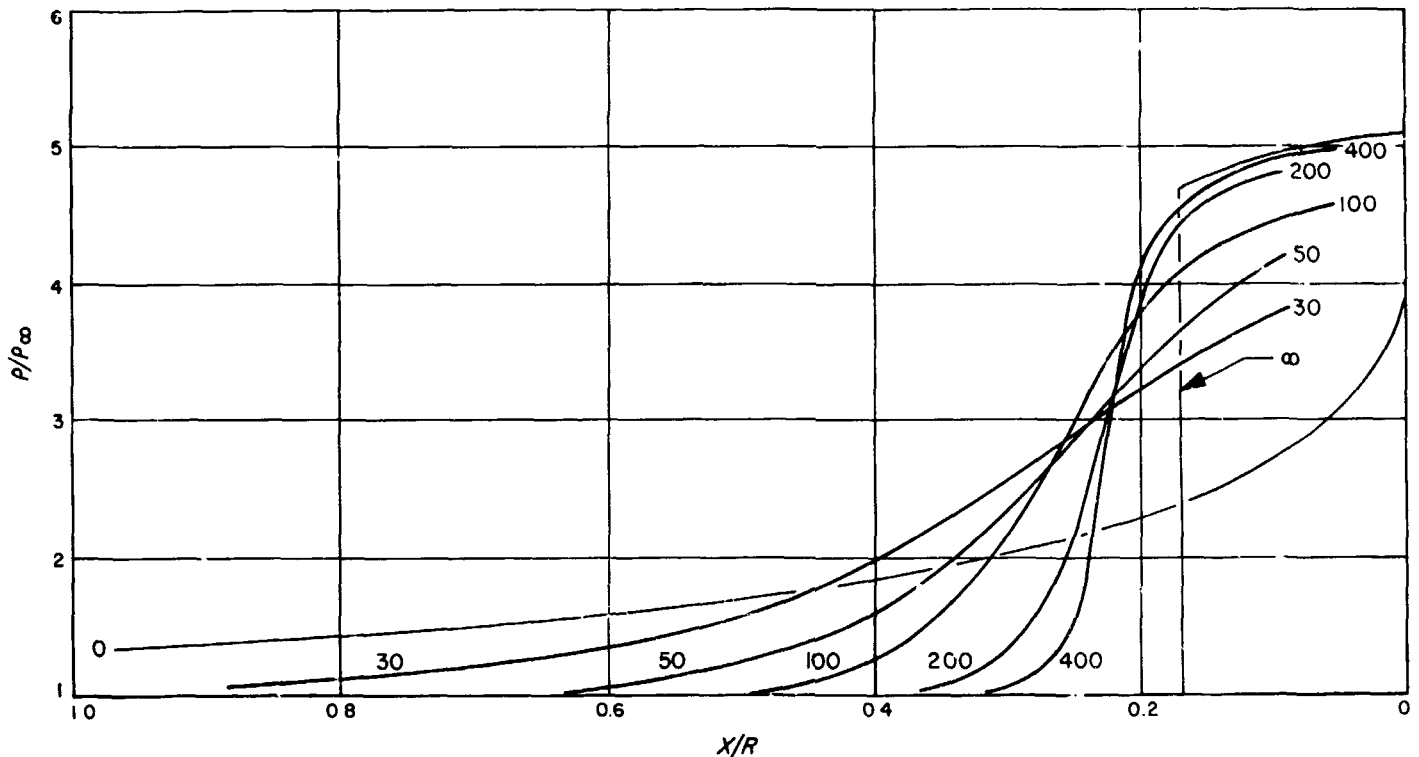


Fig. 3. Density distribution along the stagnation streamline of spheres for various Re in nitrogen: $T_b = T_0$; $M = 4.2$ ($Re = 0$ and $Re = \infty$ curves are calculated)

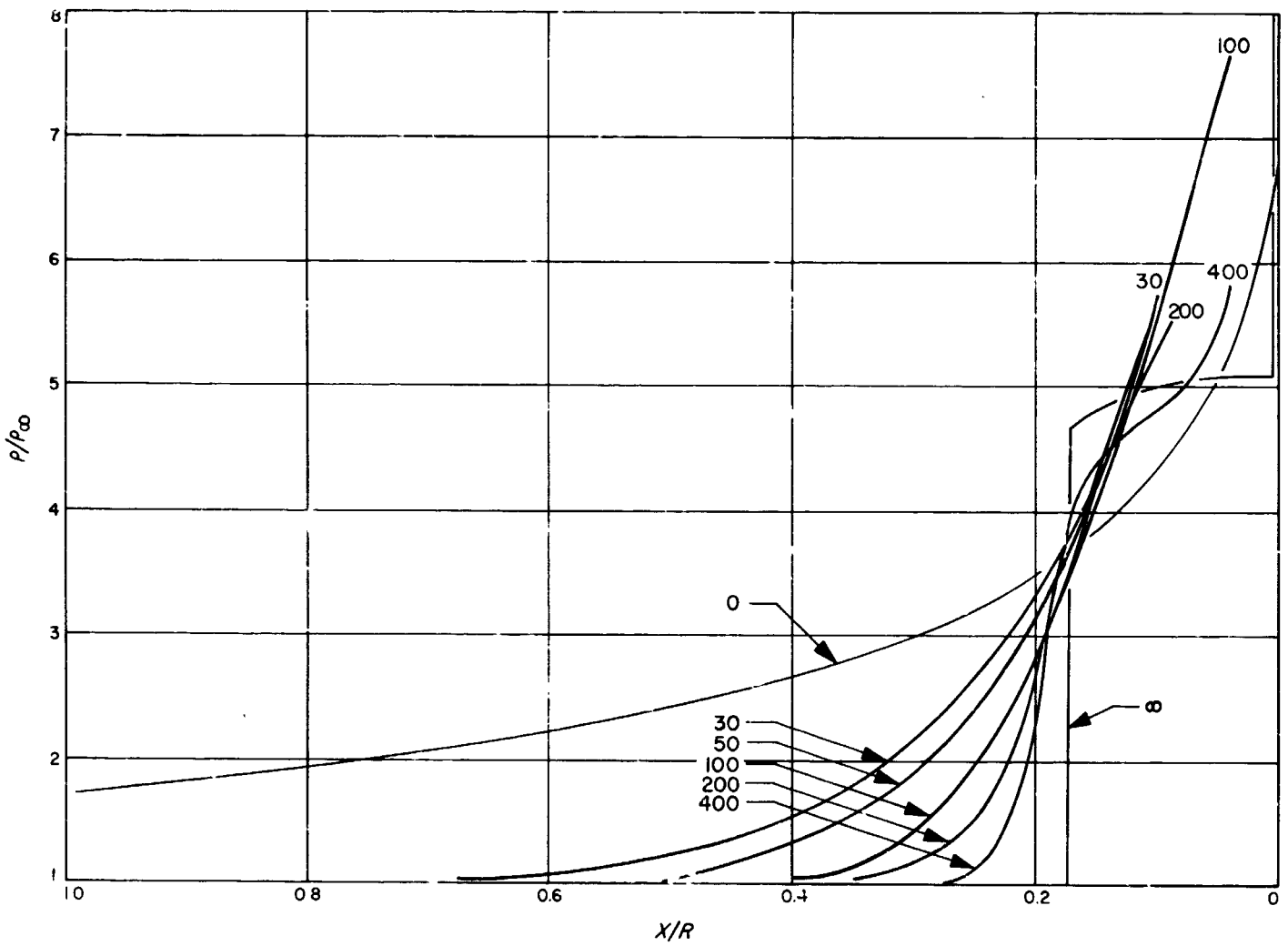


Fig. 4. Density distribution along the stagnation streamline of cooled spheres for various Re in nitrogen:
 $T_b = 0.26 T_0$; $M = 4.2$ ($Re = 0$ and $Re = \infty$ curves are calculated)

shown for comparison. It is seen that the measurements cover a range of Re that includes features of both limiting solutions.

Similar measurements are now being completed in argon. Various ways of correlating the data are being explored; however, the experimental profiles will be used principally as a definitive check on the theoretical models. Present plans are to compare the results with two different numerical solutions, one based on a Monte Carlo model (Ref. 1) and the other on approximation to the Navier-Stokes equations (Ref. 2).

B. The Stability of Viscous Three-Dimensional Disturbances in the Laminar Compressible Boundary Layer. Part I, L. M. Mack

In SPS 37-43, Vol. IV, pp. 277-281, a detailed derivation was given of the viscous stability equations for a three-dimensional disturbance, or more precisely, an oblique plane-wave disturbance, in a two-dimensional mean flow. It was shown that in a rotated coordinate system (called the tilde system) where the x -axis is parallel to the wave normal, the equations of motion are almost identical to the equations for a two-dimensional disturbance in a two-dimensional mean flow. Only the components of the free-stream Mach number and Reynolds number in the x -direction appear in the transformed equations, which differ from the two-dimensional equations only in having two additional dissipation terms in the energy equation. One of these terms can easily be included in the two-dimensional equations, but the inclusion of the other term increases the order of the equations from six to eight.

If it can be demonstrated that the neglected dissipation term has little influence on the results for a certain range of Mach and Reynolds numbers, then the sixth-order system can be used for three-dimensional calculations in this range without the complication of going to the eighth-order system. The dissipation terms, in the tilde coordinates and with the reference velocity the free-stream velocity in the x -direction, are

$$D = \gamma(\gamma-1) \frac{\tilde{M}_1^2}{\tilde{R}_0} \left[2\mu \frac{du}{dy} \left(\frac{\partial \tilde{u}'}{\partial y} + \frac{\partial v'}{\partial x} \right) + \frac{d\mu}{dT} \left(\frac{du}{dy} \right)^2 \frac{T'}{\cos^2 \psi} - 2\mu \frac{du}{dy} \tan \psi \frac{\partial \tilde{w}'}{\partial y} \right]$$

It is the last term that must be dropped in the sixth-order system because it requires the use of the z -momentum equation for \tilde{w}' .

Dunn (Ref. 3) has presented an argument that establishes orders of magnitudes for the various terms of the stability equations. In his view, all disturbances other than v' are of the same order of magnitude, with y -derivatives of disturbances one order of magnitude larger than the disturbances themselves and x -derivatives of disturbances. Consequently, the last dissipation term is of the same order as $2\mu(du/dy)(\partial \tilde{u}'/\partial y)$, the dominant term of the other three. However, according to the inviscid theory \tilde{u}' and \tilde{w}' have different behaviors both near the wall and near the critical layer. At the wall, $\tilde{u}' \neq 0$ and $\tilde{w}' = 0$, while at the critical point \tilde{w}' has a stronger singularity than \tilde{u}' . Consequently, in the viscous theory one can expect the $\partial \tilde{w}'/\partial y$ term to be dominant near the critical point, and the $\partial \tilde{u}'/\partial y$ term to be dominant near the wall.

The order-of-magnitude arguments are more suggestive than exact, and the only way to be sure of the effect of an individual term on the eigenvalues is through actual calculation. Two types of calculation were made in an attempt to assess the importance of the missing dissipation term. In the first, the effect of all the dissipation terms other than the $\partial \tilde{w}'/\partial y$ term was obtained by setting $D = 0$. In the second, an estimate of the $\partial \tilde{w}'/\partial y$ term itself was obtained by replacing \tilde{w}' with its inviscid form, an approximation that is useful only under those circumstances where the inviscid solution is close to the viscous solution throughout most of the boundary layer.

The results obtained with $D = 0$ made quantitative the well-known fact that dissipation has a small effect at low Mach numbers and high Reynolds numbers, and a large effect at high Mach numbers and low Reynolds numbers. At $R = 1000$, where R is the square root of the x -Reynolds number, the change in the maximum amplification rate with $D = 0$ is 10% at $M_1 = 3.0$ and 25% at $M_1 = 4.5$. The results with the inviscid form of \tilde{w}' showed the $\partial \tilde{w}'/\partial y$ term to have a large effect at both low and high Mach numbers, with a minimum effect of about 9% at $M_1 = 3.0$. The large effect at the lower Mach numbers can be disregarded because in this range, for the Reynolds numbers of interest, the viscous solution is far from the inviscid solution. A tentative conclusion can be drawn that results obtained from the sixth-order system are adequate for Reynolds numbers greater than 1000 and Mach numbers less than 3.

On the basis of this finding, the sixth-order system was used to calculate the time rate of amplification as a function of wave number, wave angle, Reynolds number, and Mach number in the indicated Mach and Reynolds

number range. First, the maximum amplification rate was established as a function of wave number and angle at a fixed Mach number and Reynolds number. Then, with the wave angle fixed at the angle of maximum amplification, the amplification rate was computed as a function of wave number at several Reynolds numbers to establish what can be called the overall maximum amplification rate at a given Mach number. Actually, the latter computation should be done for several wave angles, because the wave angle for maximum amplification is itself a function of Reynolds number. However, in view of the approximate nature of the calculations this refinement was omitted.

These results are summarized in Figs. 5 and 6. In Fig. 5, the ratio of the maximum three-dimensional amplification rate to the maximum two-dimensional amplification rate is plotted as a function of wave angle for $R = 1500$ and $M_1 = 1.6, 2.2,$ and 3.0 . The large value of this ratio at $M_1 = 2.2$ and 3.0 is a reflection of the low two-dimensional amplification rate rather than any important change in the three-dimensional amplification rate. In Fig. 6, the ratio of the maximum amplification rate for the most unstable wave angle at $R = 1500$ to the maximum inviscid

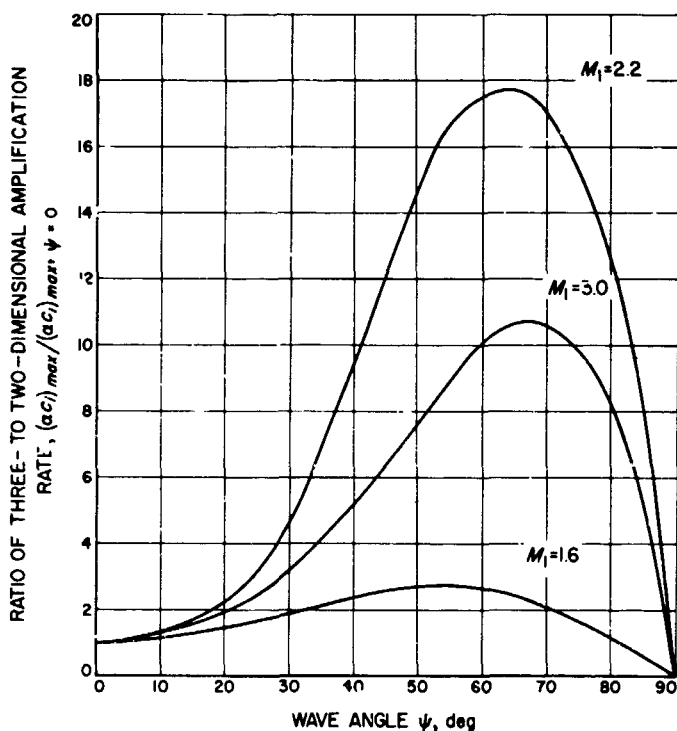


Fig. 5. Effect of wave angle on the amplification rate of first-mode three-dimensional disturbances at $R = 1500$

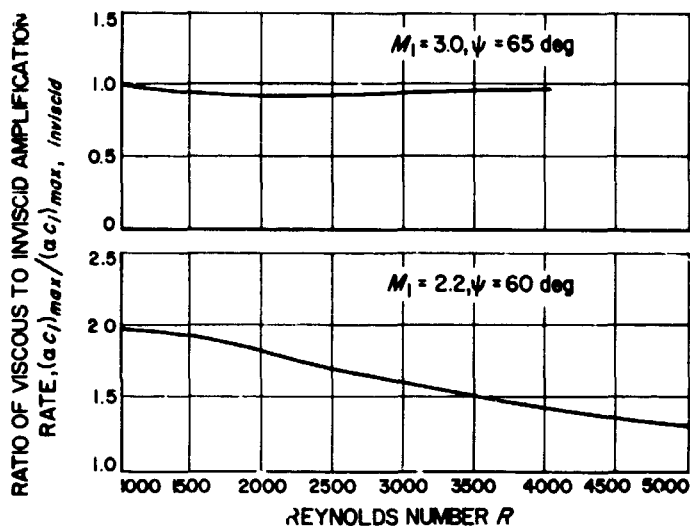


Fig. 6. Effect of Reynolds number on the maximum amplification rate of first-mode three-dimensional disturbances

amplification rate is plotted as a function of Reynolds number for $M_1 = 2.2$ and 3.0 . At $M_1 = 3.0$, the maximum amplification rate is almost independent of Reynolds number, while at $M_1 = 2.2$ the low Reynolds number maximum amplification rate is double the inviscid value. In contrast, a two-dimensional disturbance at low Reynolds numbers has over eight times the inviscid amplification rate.

Now if the overall maximum amplification rate itself, and not a ratio, is plotted against Mach number, it is found that from $M_1 = 1.5$ to $M_1 = 3.0$ the amplification rate is virtually independent of Mach number and equal to about one-half of its value at $M_1 = 0$. The portion of this curve up to $M_1 = 2.2$ has already been given in approximately correct form in SPS 37-42, Vol. IV.

The above results should be in error by no more than 10% according to the estimates described previously. However, the limitation of the sixth-order system to $M_1 < 3$ and $R > 1000$ is serious. In particular, the restriction to $R > 1000$ does not permit the important calculation to be made at any Mach number of the overall growth of a fixed-frequency disturbance as it passes through the unstable region. To correct these deficiencies, as well as to obtain exactly the importance of the \tilde{w}' dissipation term, there is no alternative but to use the eighth-order system of equations. These equations require the computer program to be changed, so that instead of integrating three linearly independent solutions, each solution consisting of a six-component vector,

and satisfying three boundary conditions at the wall, it will integrate four solutions, each solution consisting of an eight-component vector, and satisfy four boundary conditions at the wall. The changes required in the program as it is described in Ref. 4 are briefly presented below.

The number of changes required can be kept to a minimum by using the stability equations in the tilde form. The eight dependent variables are

$$\begin{aligned} \tilde{Z}_1 &= \tilde{f} & \tilde{Z}_2 &= \tilde{f}' & \tilde{Z}_3 &= \tilde{\phi} & \tilde{Z}_4 &= \frac{\pi}{\gamma \tilde{M}_1^2} \\ \tilde{Z}_5 &= \theta & \tilde{Z}_6 &= \theta' & \tilde{Z}_7 &= \tilde{h} & \tilde{Z}_8 &= \tilde{h}' \end{aligned}$$

where \tilde{f} , $\tilde{\phi}$, and \tilde{h} are the complex amplitude functions of the velocity fluctuations \tilde{u}' , \tilde{v}' , \tilde{w}' , and π and θ are the amplitude functions of the pressure and temperature fluctuations. The first four equations and the sixth equation are unchanged from the sixth-order system (Ref. 4). The fifth equation has a changed term and a new term. These two terms are

$$\begin{aligned} \tilde{Z}'_5 &= - \left[\sigma(\gamma-1) \tilde{M}_1^2 \frac{1}{\mu} \frac{d\mu}{dT} \left(\frac{du}{d\eta} \right)^2 \frac{1}{\cos^2 \psi} \right] \tilde{Z}_5 \\ &+ \left[2\sigma(\gamma-1) \tilde{M}_1^2 \tan \psi \frac{du}{d\eta} \right] \tilde{Z}_8 + \dots \end{aligned}$$

The independent variable is $\eta = y\sqrt{R_e}/x$, the Blasius variable. The two new equations are

$$\begin{aligned} \tilde{Z}'_7 &= \tilde{Z}_8 \\ \tilde{Z}'_8 &= - \left(\frac{\tilde{\alpha} \tilde{R}}{\mu} \frac{1}{T} \frac{du}{d\eta} \tan \psi \right) \tilde{Z}_3 + \left(\frac{1}{\mu} \frac{d\mu}{dT} \frac{d^2 u}{d\eta^2} \tan \psi \right) \tilde{Z}_5 \\ &+ \left(\tilde{\alpha}^2 + \frac{i \tilde{\alpha} \tilde{R}}{\mu} \frac{u-c}{T} \right) \tilde{Z}_7 + \left(\frac{1}{\mu} \frac{d\mu}{dT} \frac{dT}{d\eta} \right) \tilde{Z}_8 \end{aligned}$$

The notation is that of Ref. 4.

In the free stream, the first six equations are the same as with $\tilde{w}' = 0$, and the two new equations do not involve \tilde{Z}_1 through \tilde{Z}_6 . Therefore, three of the four linearly independent solutions are unchanged from the sixth-order

system. The fourth solution can be written by inspection, and is

$$\begin{aligned} \tilde{Z}_7^{(4)} &= \tilde{Z}_7^{(4)}(\eta_s) \exp \{ - [\tilde{\alpha}^2 + i \tilde{\alpha} \tilde{R} (1-c)]^{1/2} (\eta - \eta_s) \} \\ \tilde{Z}_8^{(4)} &= - [\tilde{\alpha}^2 + i \tilde{\alpha} \tilde{R} (1-c)]^{1/2} \tilde{Z}_7^{(4)}(\eta_s) \\ &\times \exp \{ - [\tilde{\alpha}^2 + i \tilde{\alpha} \tilde{R} (1-c)]^{1/2} (\eta - \eta_s) \} \end{aligned}$$

The other six components of the fourth solution are zero. The characteristic value $-[\tilde{\alpha}^2 + i \tilde{\alpha} \tilde{R} (1-c)]^{1/2}$ is identical to the already computed characteristic value of the velocity viscous solution. Because the original three solutions are unchanged, the subroutine VALVEC which computes the characteristic values and characteristic vectors can be left unchanged. The fourth solution is added in subroutine SETDI, where the initial derivatives and differences are computed, and the numbering is changed to account for having four eight-component vectors instead of three six-component vectors.

The derivatives are calculated by multiplying the coefficient matrix by the solution vector. In the subroutine AMAT, which computes the matrix components, the additional components are added and the numbering is changed. The matrix multiplication subroutine MMULT requires only a change of subscript limit from 6 to 8. The integration subroutine also requires only subscript changes. The subroutine ZERO, which satisfies the two velocity boundary conditions at the wall, must now satisfy three velocity boundary conditions. A renumbering of the previous components, addition of the proper components of the fourth solution, and changes of subscript limits to solve four instead of three linear algebraic equations are required. The logic of the main program is unchanged, as the eigenvalues are still found by a linear perturbation scheme based on the boundary condition for the temperature fluctuation, $Z_5(0) = 0$. Only subscript limits must be changed. Finally, the program was revised in such a way that either the sixth-order or eighth-order system of equations can be used simply by specifying an input quantity to be either 36 or 48. This option is important, because to use the eighth-order system for two-dimensional problems would mean an unnecessary waste of machine time. Numerical results from the eighth-order system will be presented in a future issue of this volume.

References

1. Bird, G. A., "Aerodynamic Properties of Some Simple Bodies in the Hypersonic Transition Regime," *AIAA J.*, Vol. 4, No. 1, pp. 55-60, January 1966.
2. Levinsky, E. S., and Yoshihara, H., "Rarefied Hypersonic Flow Over a Sphere," in *Hypersonic Flow Research*, pp. 81-106. Edited by F. R. Riddell. Academic Press, New York, 1962.
3. Dunn, D. W., *On the Stability of the Laminar Boundary Layer in a Compressible Fluid*, Ph.D. Thesis. Massachusetts Institute of Technology, Cambridge, Mass., 1953.
4. Mack, L. M., "Computation of the Stability of the Laminar Compressible Boundary Layer," in *Methods in Computational Physics : Volume 4*, pp. 247-299. Academic Press, New York, 1965.

XVI. Physics

SPACE SCIENCES DIVISION

A. The Polar Substorm—Flow of Magnetic Flux Tubes and Auroral Effects, G. Atkinson

Satellite results of the last few years have made it increasingly clear that the magnetosphere (Fig. 1a) may be considered as being composed of two types of magnetic field lines:

- (1) Field lines that close in the vicinity of the earth (see Fig. 1b). These occupy a region that can be approximated by a toroid, and tend to have a dipole configuration.
- (2) Field lines in the geomagnetic tail (Fig. 1c). These do not close in the vicinity of the earth, but are extended to great distances by the solar wind, forming two semicircular cylinders of oppositely directed magnetic flux, separated by a sheet of plasma called the neutral sheet.

A knowledge of the transport processes for field lines between the two regions is necessary in understanding many of the observed occurrences in the magnetosphere.

Two mechanisms by which the solar wind transfers field lines from the region of closed field lines into the tail are commonly discussed in the literature.

- (1) Viscous mechanisms. The flow of solar wind around the sides of the magnetosphere causes a frictional or viscous-like drag on flux tubes near the boundary, and stretches these into the tail.
- (2) Combination with the interplanetary field. It has been suggested by Dungey (Ref. 1) that an oppositely aligned interplanetary field line can connect with a field line at the front of the magnetosphere and drag it into the tail (see Fig. 2).

The return flow of field lines from the tail to the region of closed field lines probably occurs by recombination across the neutral sheet. The theory that this recombination occurs impulsively, with each impulse causing a polar substorm, has been independently suggested by Axford (Ref. 2), Dungey (Ref. 3), and Atkinson (Ref. 4).

BLANK PAGE

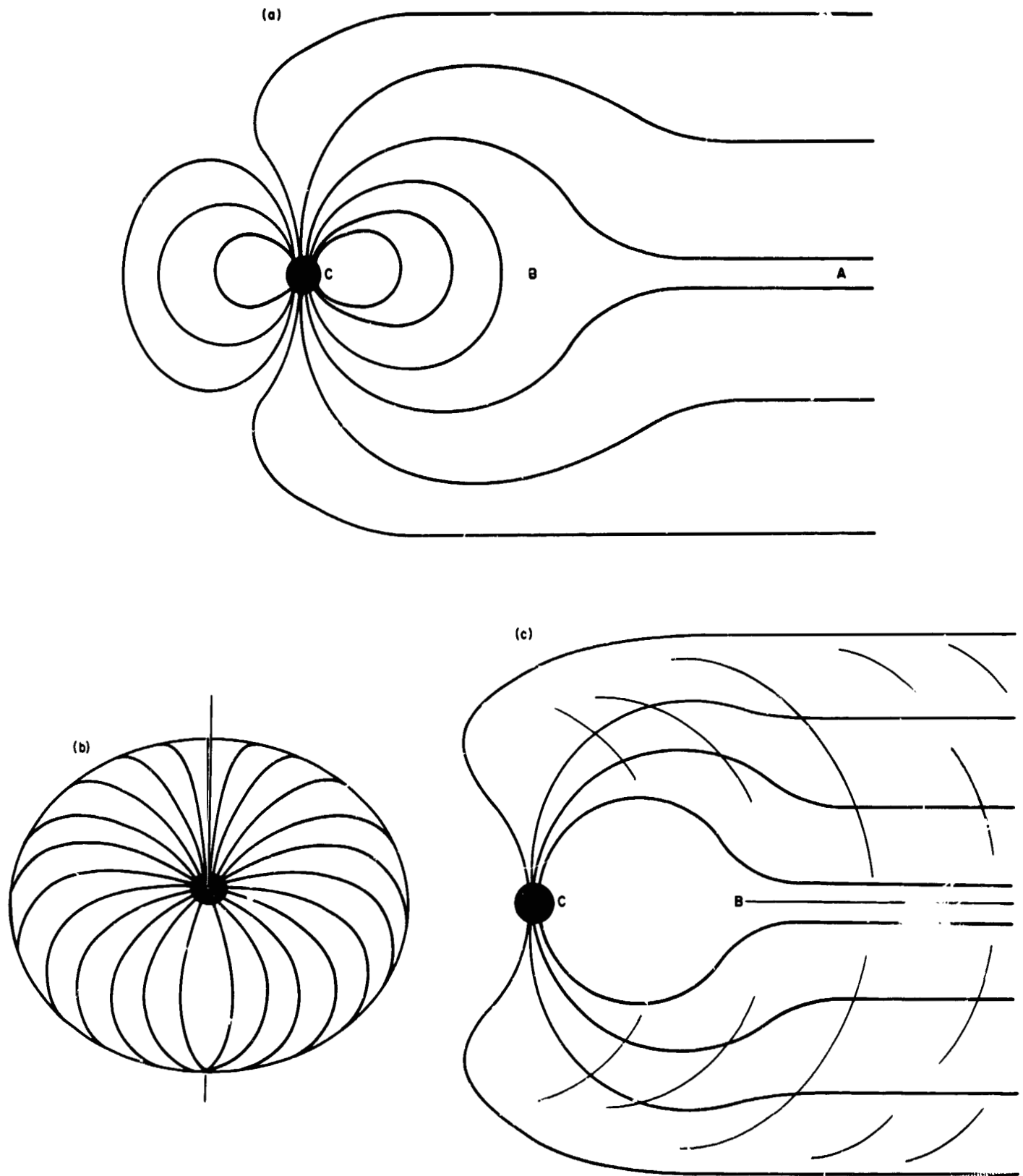


Fig. 1. The magnetosphere: (a) section through moon-midnight meridian; (b) oblique view of region of closed field lines; (c) tail field lines

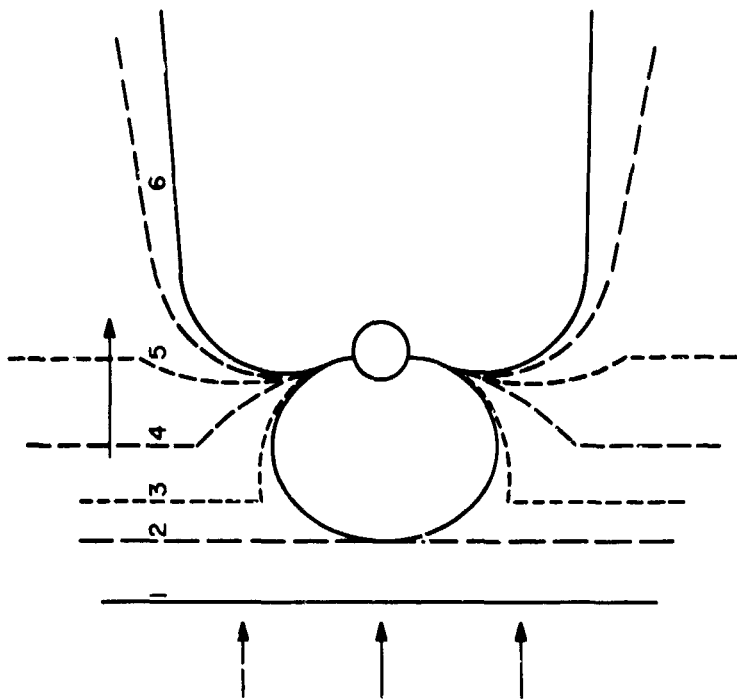


Fig. 2. Flow of field lines into tail by combination with interplanetary field

The polar substorm is an event that occurs every few hours and has a duration of about an hour. The two major effects associated with it are intense auroral activity and large geomagnetic disturbance, particularly at high latitudes. Both of these have a well-defined morphology that depends on local time. There are a number of other manifestations of the substorm such as X-ray activity under bright aurora, enhancement of ionospheric ionization, and magnetic micropulsations. In recent years, there have been added to the above a number of satellite observations, including a rapid large-scale injection of plasma into the nightside of the magnetosphere, and changes in magnetic field strength at some places within the magnetosphere simultaneous with the polar substorm.

The model of polar substorms as proposed by Atkinson (Ref. 4) is essentially a flow sequence as follows:

First stage. The solar wind drags magnetic field lines into the tail with a resulting increase in the total magnetic flux in the tail and a storage of potential energy.

Second stage. The polar substorm begins when field lines start to recombine at the neutral sheet. Once a normal component is established across the neutral sheet,

the curvature in the field lines pulls the plasma out of the recombination region, allowing the recombination rate to increase. Thus, there is an implosion of field lines into the neutral sheet. The energetics of the substorm leads to the conclusion that about 10^8 Wb of magnetic flux recombine during the substorm. Much of the energy of the magnetic field that is annihilated is given to the particles. This implies that particles receive energies of several keV in agreement with the observed auroral electron energies. The bulge width during the first 10 min implies that the recombination is confined to a slot 6 or 7 earth radii wide (in the east-west direction). It is proposed by Atkinson (Ref. 5) that the west edge of this slot propagates westward during the course of the substorm causing the westward traveling surge.

Third stage. The recombined field lines and plasma flow onto the nightside of the region of closed field lines. This initial flow and adjustment is controlled by hydromagnetic waves and consequent velocities. The extent of this flow is limited by the fact that these flux tubes have their "feet" in a conducting sheet (the ionosphere), which restricts this initial rapid flow and retains a bulge on the nightside of the closed region. Thus, the closed region resembles a toroidal coil with an excess of turns on the midnight section, and the outward bulge in the equatorial plane maps along field lines as a northward bulge into the polar cap, or more precisely, into the region inside the auroral oval. (The auroral arcs trace out an oval believed to contain the feet of the tail field lines.) The auroral arcs are observed to form such a northward bulge near midnight during a polar substorm.

Fourth stage. The fourth stage in the flow is the flow of flux tubes around the magnetosphere as the bulge attempts to subside. (The actual growth or decay at any time depends upon the relative speeds of the third and fourth stages.) This motion is relatively slow because it involves the flow of flux tube feet through the conducting ionosphere; i.e., the $\mathbf{E} = -\mathbf{v} \times \mathbf{B}$ fields necessary for such flows produce dissipative currents in the ionosphere. It was proposed in Ref. 6 that these currents in the high conductivity strips at the foot of the auroral arcs were the westward electrojet—the source of intense high latitude magnetic disturbance.

In Ref. 5, an approximate flow equation was developed and applied to the growth and decay of the bulge. The bulge was assumed symmetric in the east-west direction, and the curvature of the system was neglected. The two solutions to this problem shown in Figs. 3 and 4 are for flows at the feet of flux tubes. To translate to a point

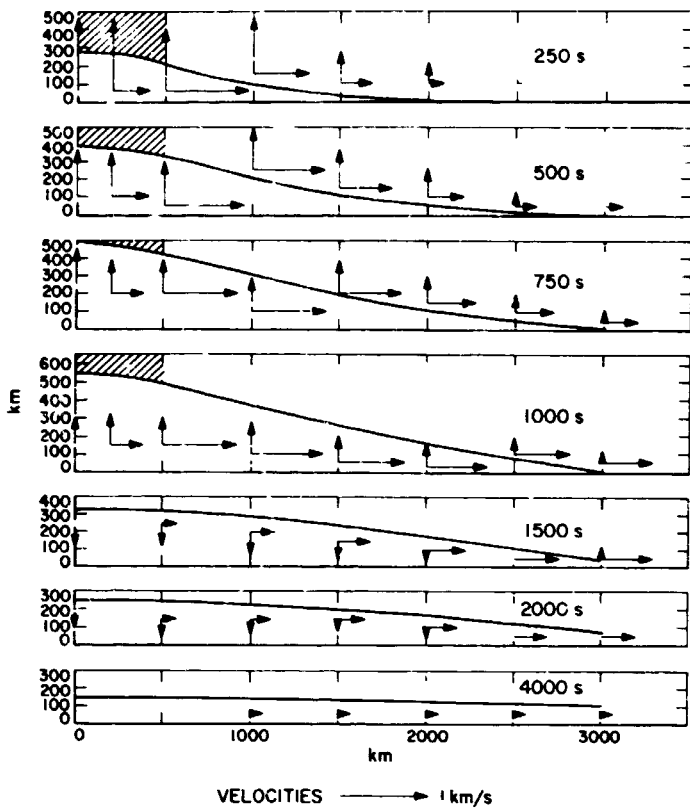


Fig. 3. Computed time development of substorm bulge

elsewhere on a flux tube, velocities and distances are multiplied by the square root of the ratio of the magnetic field strengths. The solution in Fig. 3 is a linearized approximation, and is probably the least accurate as it involves an incorrect boundary condition. However, it has the advantage that a source term can be included to study the growth and subsidence of the bulge. The arrows show the predicted easterly flow velocities of flux tubes south of the oval, and the north-south velocity of the auroral arcs (the bulge). The shading indicates where fluid is being added to the bulge, and the shape is shown at different times in the substorm.

The solution in Fig. 4 is an analog model solution and shows the flow (and flow velocities in m/s) during the subsidence of the bulge. The velocities are a factor of 1.5 to 2 lower than observation indicates. In view of the uncertainty in the parameters used (in particular the conductivity of the ionosphere) as well as the approximate nature of the equations, the observations fall well within the probable error of the prediction.

The observed growth and decay of the auroral bulge is shown in Fig. 5 (after Akasofu, Ref. 7). This shows the north polar cap of the earth and the location of auroral

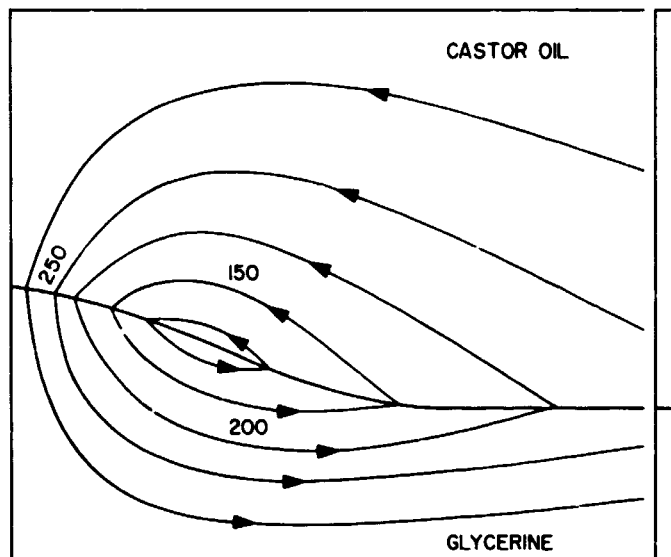


Fig. 4. Analog model solution for flow

arcs. The initial growth of the bulge northward at velocities of 1 km/s is followed by a slower subsidence and east-west spreading at velocities of several hundred meters per second, in agreement with the predictions. An asymmetry can be seen to develop with the formation of a wave-like feature (the westward traveling surge) propagating to the west. Atkinson (Ref. 5) suggested that this represents further recombination of flux tubes as the west boundary of the recombination slot in the tail propagates westward. The general auroral activity inside the bulge is indicative that these flux tubes have just recombined, and contain energetic particles, some of which precipitate as auroral particles. These auroral patches thus provide a tracer for following the flow of a particular flux tube. From this the east-west observations of flow velocity are obtained.

An independent method of observing magnetic flux tube velocities (using whistlers to obtain velocities in the outer magnetosphere) has been used by Carpenter and Stone (Ref. 8). Southward velocities of 700 m/s were observed in the bulge during a substorm. Figure 3 predicts southward velocities in the range 1000 to 2000 m/s during the expansive phase of the bulge (the rate of addition of fluid, 2000 m/s, minus the northward velocity of the arc), in reasonable agreement with the whistler observation.

Thus, it can be seen that the model accounts in some detail for the auroral effects of a polar substorm. The auroral forms; the auroral bulge shape, growth, and subsidence rates; the velocity of auroral patches; the

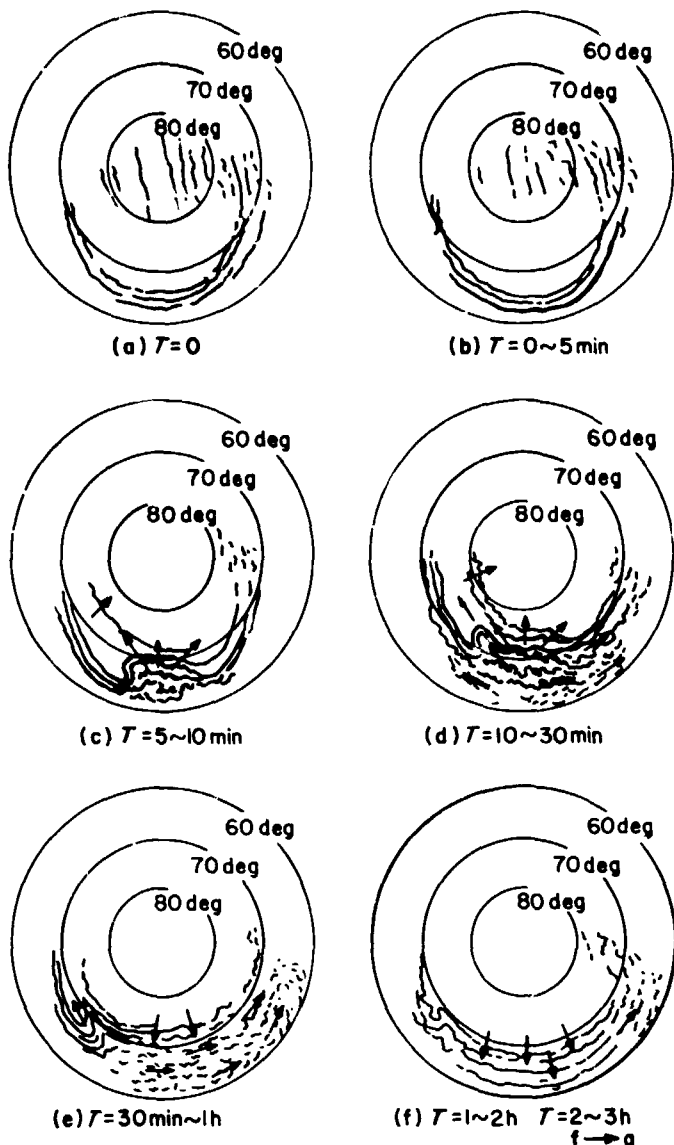


Fig. 5. Observed time development of substorm bulge (after Akasofu, 1964)

auroral particle energy; and the total energy of the substorm are in agreement with the model. A further paper (Ref. 9) shows that there is agreement with the observed magnetic fluctuations over a wide range of latitudes and longitudes.

B. The Dynamitron Accelerator as a Source of Thermal Neutrons, R. H. Parker, E. L. Haines, A. B. Whitehead, and W. F. Wegst

Versatility is an important consideration in the design of a basic research facility. The emphasis of the effort may be expected to change many times over the useful

life of the facility. Thus, the Nuclear Physics Research Group at JPL selected as its main research instrument an accelerator capable of directly accelerating electrons and a variety of positive ions. In addition, by use of a suitable ion beam and target, neutrons can be produced, expanding the scope of the possible experiments. If these neutrons are slowed in a moderator, the accelerator becomes a source of thermal neutrons, similar to a small reactor. This summary discusses how the dynamitron accelerator at JPL is used as a source of thermal neutrons.

The three elements for producing thermal neutrons by this method are the accelerator, the target, and the moderator. The dynamitron accelerates deuterons to an energy of 2.5 MeV, with currents up to 1.5 mA. The beam current is greater than that produced by most accelerators. The neutrons are produced when this energetic beam of deuterons strikes a beryllium target, causing beryllium nuclei to undergo nuclear transformation to boron and release a high velocity neutron. These neutrons emerge into a large tank of distilled water which slows them down to thermal velocities. These thermal neutrons are then available for nuclear or radiation experiments.

The high-current capability of the accelerator presented some special problems in the design of the target. It was mounted on the end of the evacuated beam tube which protruded into the center of the water tank, and formed the membrane between the vacuum and the water. The target had to withstand the intense heat produced by power densities as high as 20 kW/cm² from the deuteron beam. It was found, first by calculation and then by experiment, that this heat could best be dissipated into the water if the target backing was a copper disk 30 mils thick. Beryllium metal 3 mils thick was evaporated onto the copper prior to its placement at the end of the beam tube (Ref. 10).

Tests were performed to determine the yield of thermal neutrons and their angular distribution. The accelerator was operated at energies between 2 and 2.5 MeV, with beam currents of about 1.0 mA. Thermal neutrons were detected by the gold-foil activation technique. The gold activity was measured, using an end-window proportional counter, during a two-week interval. Identification of the half-life established that the activity was due solely to the activation of gold. These activities were used to calculate the flux of thermal neutrons at the gold foil. Corrections were made for the perturbation of the foil and for the background due to high energy neutrons and other sources of activation.

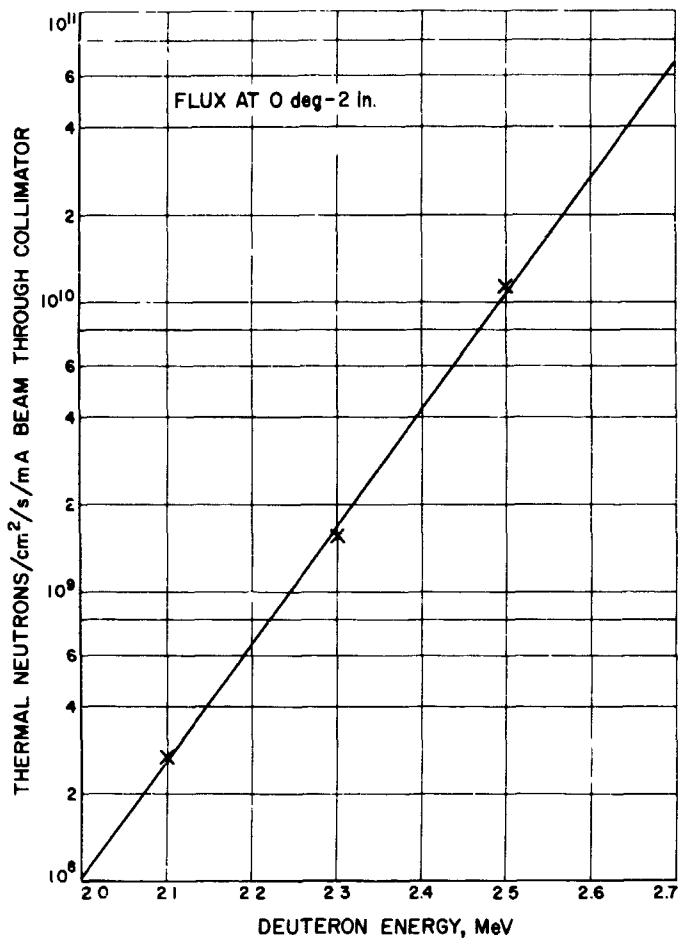


Fig. 6. Thermal neutron production/cm²/s/mA of deuteron beam versus deuteron energy

The results are summarized in Figs. 6 and 7. Figure 6 shows the optimum flux of thermal neutrons as a function of the energy of the deuterium ions. It is this flux that is available to an experimenter. The graph of flux rises very rapidly with energy, indicating that small increases in the available energy will substantially increase the neutron yield. Modifications to the accelerator are scheduled that will permit it to operate at 3 MeV. An increase of an order of magnitude in the available neutron flux may be realistically anticipated. Figure 7 shows contours of thermal neutron flux as a function of position in the moderator. It is noted that the optimum position for experiment location is immediately behind the target and approximately 2 in. away.

These thermal neutrons will be used in experiments which require large numbers of energetic heavy ions. The neutrons will produce fission fragments in a thin uranium plate. The neutrons will also be used for activation experiments and radiation effect experiments.

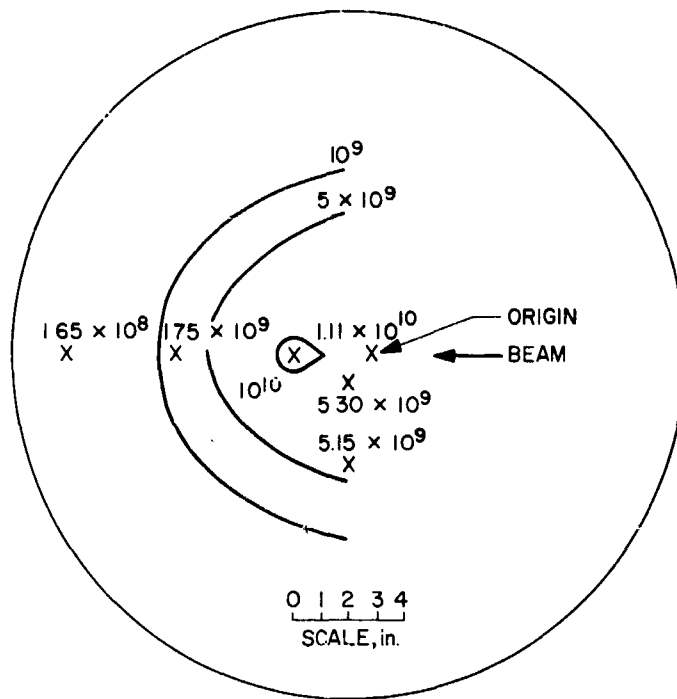


Fig. 7. Thermal neutron production contours in moderator tank at 2.5-MeV deuteron energy

C. The Algebra of Fermi-Dirac Operators and Its Application to the Many-Body Problem, M. M. Saffren

One method used in the problem of determining the approximate eigenstates of a many-body system is the so-called "equation-of-motion method" (Ref. 11). This method can be described in many ways, but the one most useful utilizes the quantized wave field $\psi(\mathbf{r})$. If we limit ourselves to a particular many-body problem — that of the electron gas — this field is the electron field. It is still more convenient to use this field in its momentum space representation

$$C(\mathbf{k}) = \int \frac{e^{-i\mathbf{k}\cdot\mathbf{r}}}{\sqrt{V}} \psi(\mathbf{r}) d\mathbf{r}$$

(where V denotes the quantization volume, and the integral is performed over this volume), and in this representation the field obeys the Fermi-Dirac anticommutation relation

$$C(\mathbf{k}) C^+(\mathbf{k}') + C^+(\mathbf{k}') C(\mathbf{k}) = \delta_{\mathbf{k}\mathbf{k}'}$$

where $\delta_{\mathbf{k}\mathbf{k}'}$ is the Kronecker delta.

In the equation-of-motion method, we seek operators of the form

$$\gamma(\mathbf{k}) = C(\mathbf{k}) + \sum A_{\mathbf{pqr}} C^+(\mathbf{p}) C(\mathbf{q}) C(\mathbf{r}) + \dots$$

to represent the electron-like excitations of the electron gas. We do this by requiring that

$$[H, \gamma(\mathbf{k})] \cong \omega_{\mathbf{k}} \gamma(\mathbf{k})$$

which is to say that the operators $\gamma(\mathbf{k})$ are eigenoperators of the Hamiltonian H in some approximate sense. For the free-electron Hamiltonian, for example, the $\gamma(\mathbf{k})$ are the $C(\mathbf{k})$ themselves, and are exact eigenoperators. For the plasma-like excitations, which exist only in the interacting electron gas, we seek operators of the form

$$b(\mathbf{k}) = \sum A_{\mathbf{pq}} C^+(\mathbf{p}) C(\mathbf{q}) + \sum B_{\mathbf{pqrs}} C^+(\mathbf{p}) C^+(\mathbf{q}) C(\mathbf{r}) C(\mathbf{s}) + \dots$$

and require that, for these,

$$[H, b(\mathbf{k})] \cong \Omega_{\mathbf{k}} b(\mathbf{k})$$

Thus far this method, the equation-of-motion method, has been applied successfully only to the electron gas in the limit of high density (Ref. 11). However, the density of electrons in actual metals is comparatively low. We seek to extend the equation-of-motion method, therefore, to this more interesting range of density.

In this method, one has always dealt with products of operators of the form

$$C^+(\mathbf{p}) C^+(\mathbf{q}) \dots C(\mathbf{r}) C(\mathbf{s})$$

These operators are in the so-called normally ordered form. Since these operators do not commute, calculations involving such products can become quite involved. In an attempt to simplify the computational difficulties, we have studied the algebra of such products in some detail. Although this study is reported in detail in Ref. 12, some of the results are mentioned here.

We show explicitly that the algebra of N Fermi-Dirac operators is equivalent to a simple matrix algebra of order 2^{2N} . We point out that the operators in this algebra have a dual role as operators and as states. Most importantly, we find a basis for the Fermi-Dirac algebra more convenient than normally ordered products. We choose as the basis the operators

$$C^+(\mathbf{p}) \dots C^+(\mathbf{q})(0) C(\mathbf{r}) \dots C(\mathbf{s})$$

These are very nearly normally ordered, except for the term (0) which denotes the expression

$$\prod_{\mathbf{p}} C(\mathbf{p}) C^+(\mathbf{p})$$

where the product is taken over all \mathbf{p} . For operators in this basis we have a very simple form for products

$$[C^+(\mathbf{p}) \dots C^+(\mathbf{q})(0) C(\mathbf{r}) \dots C(\mathbf{s})] \times [C^+(\mathbf{p}') \dots C^+(\mathbf{q}')(0) C(\mathbf{r}') \dots C(\mathbf{s}')] = \delta_{\mathbf{rp}'} \dots \delta_{\mathbf{sq}'} C^+(\mathbf{p}) \dots C^+(\mathbf{q})(0) C(\mathbf{r}') \dots C(\mathbf{s}')$$

This expression for the product is simpler than that obtained for normally ordered operators. This basis also proves quite convenient when expressing the Fermi-Dirac algebra as the Lie algebra $U(2^N)$. The relation of Fermi-Dirac algebras to Clifford algebras and the relation of the Fermi-Dirac algebra to the spin-representations of the orthogonal groups are also discussed in Ref. 12.

References

1. Dungey, J. W., *Cosmic Electrodynamics*. Cambridge University Press, New York, 1958.
2. Axford, W. I., "Magnetic Storm Effects Associated With the Tail of the Magnetosphere," paper presented at the ESRO Conference on the Magnetosphere, Stockholm, Nov. 1965.

References (contd)

3. Dungey, J. W., "The Reconnection Model of the Geomagnetic Tail," preprint, Imperial College, Department of Physics, London, 1966.
4. Atkinson, G., "A Theory of Polar Substorms," *J. Geophys. Res.*, Vol. 71, pp. 5157-5164, 1966.
5. Atkinson, G., "An Approximate Flow Equation for Geomagnetic Flux Tubes and Its Application to Polar Substorms," *J. Geophys. Res.*, Vol. 72, 1967 (submitted for publication).
6. Atkinson, G., "Polar Magnetic Substorms," *J. Geophys. Res.*, Vol. 72, pp. 1491-1494, 1967.
7. Akasofu, S. I., "The Development of the Auroral Substorm," *Planet. Space Sci.*, Vol. 12, pp. 273-282, 1967.
8. Carpenter, D. L., and Stone, K., "Direct Detection by a Whistler Method of the Magnetospheric Electric Field Associated With a Polar Substorm," *Planet. Space Sci.*, Vol. 15, pp. 395-397, 1967.
9. Atkinson, G., "The Current System of Geomagnetic Bays," *J. Geophys. Res.*, Vol. 72, 1967 (submitted for publication).
10. Parker, R. H., and Frazer, R., "A Simple Beryllium Target for Thermal Neutron Production," *Nucl. Instrum. Methods*, 1967 (submitted for publication).
11. Pines, D., and Nozieres, P., *The Theory of Quantum Liquids: Volume I*. W. A. Benjamin, Inc., New York, 1966.
12. Saffren, M. M. *Algebra of Fermi-Dirac Operators and Their Application*, Technical Report 32-1169, Jet Propulsion Laboratory, Pasadena, Calif. (to be published).

XVII. Communications Systems Research
 TELECOMMUNICATIONS DIVISION

A. Block Coding and Synchronization Study,
J. Stiffler and A. Balakrishnan

1. Optimum Tracking PSK Modulated Carriers, J. Stiffler

a. Introduction. The received signal in a phase-shift-keyed (PSK) communication system typically has the form $y_l(t) = (2)^{1/2} A \sin(\omega_c t + \theta_j + \phi_0(t)) + n(t)$, $lT_s < t < (l+1)T_s$, where $n(t)$ is white, Gaussian noise, T_s is the symbol period, $\theta_j = 2\pi j/n$ is one of the n possible symbol phases, and $\phi_0(t)$ is a random carrier phase shift. Efficient demodulation of such a signal necessitates the capability of tracking this carrier phase deviation. In this article we propose a method for doing this based on the maximum-likelihood method of phase estimation. We assume the symbol timing is already known.

The principle is as follows: We first determine the probability density $p(y_l(t)|\phi)$. It is well known that

$$E \left\{ \frac{\partial \log p(y_l(t)|\phi)}{\partial \phi} \right\} = 0$$

for $\phi = \phi_0$ and that

$$E \left\{ \frac{\partial^2 \log p(y(t)|\phi)}{\partial \phi^2} \right\} = - E \left\{ \left(\frac{\partial \log p(y(t)|\phi)}{\partial \phi} \right)^2 \right\}$$

also for $\phi = \phi_0$. Thus, the expected value of the derivative

$$\frac{\partial \log p(y_l(t)|\phi)}{\partial \phi} \equiv f(\phi)$$

is a monotonically decreasing function of ϕ in the vicinity of its true value, positive for $\phi < \phi_0$ and negative for $\phi > \phi_0$. This function can therefore be filtered and used to control the frequency of the oscillator producing the local replica of the carrier. Once the local and received carriers are "in-lock," the filtered signal $f(\phi)$ should enable the local oscillator to track the received carrier as in an ordinary phase-locked loop. The optimum filter can be determined by the same methods used for ordinary loops.

We will refer to the resulting phase tracking loops as "optimum" tracking devices. They are optimum in the same sense that a phase-locked loop is optimum. If the received carrier phase were constant, the optimum loop filter would weigh all the past equally. The loop would thus be forced to satisfy the equation

$$\frac{\partial \log p(y(t)|\phi)}{\partial \phi} = \sum_l \frac{\partial \log p(y_l(t)|\phi)}{\partial \phi} = 0$$

BLANK PAGE

Accordingly, it would be asymptotically unbiased and efficient (Ref. 1). If ϕ can change with time, the only remaining possibility is to choose the filter preceding the oscillator so as to weigh the past in an optimal manner in determining the present phase-estimate. This is precisely what is done in the determination of the optimum phase-locked loop filter. At first glance, it might appear meaningless to attempt to track $\phi_0/\phi_0(t)$ when θ_j is also a random variable. But if the local phase reference were perfect, ϕ_0 would be zero and θ_j could assume only one of n precisely known values. The imperfect phase reference causes a discrepancy between the values θ_j is known to be able to have and the values it apparently does assume. In other words, $\phi_0(t)$ simply causes a bias in the observed phases. If $\phi_0(t)$ can be assumed to vary slowly with time, remaining relatively constant over a number of T_s second intervals, this bias can be estimated and removed.

b. The tracking loops and their performance. It is not difficult to show that the function $p(y_l(t)|\phi)$ can be expressed in the form

$$p(y_l(t)|\phi) = \frac{1}{n} \sum_{j=1}^n \exp \{2R(a_l(\phi) \cos \theta_j + b_l(\phi) \sin \theta_j)\} \quad (1)$$

where $R = A^2 T_s / N_0$, N_0 is the single-sided noise spectral density,

$$a_l(\phi) = \frac{1}{AT_s} \int_{lT_s}^{(l+1)T_s} y(t) (2)^{1/2} \sin(\omega_c t + \phi) dt$$

and

$$b_l(\phi) = \frac{1}{AT_s} \int_{lT_s}^{(l+1)T_s} y(t) (2)^{1/2} \cos(\omega_c t + \phi) dt$$

The maximum-likelihood estimate of the phase ϕ , on the basis of the signal $y_l(t)$, $lT_s < t < (l+1)T_s$, is a solution of the equation

$$\frac{\partial \log p(y_l(t)|\phi)}{\partial \phi} = 0 \quad (2)$$

We contend, however, that any $\phi = \hat{\phi}$ satisfying the equation

$$\frac{\partial}{\partial \phi} \sum_{j=1}^n [a_l(\phi) \cos \theta_j + b_l(\phi) \sin \theta_j]^n = 0 \quad (3)$$

will also be a solution to Eq. (2).

To prove this statement, we expand the exponential of Eq. (1) in a power series, take the logarithm of the resulting expressions, and differentiate with respect to ϕ , obtaining

$$\frac{\partial \log p(y_l(t)|\phi)}{\partial \phi} = \frac{\sum_{v=0}^{\infty} \frac{1}{v!} \frac{\partial}{\partial \phi} \sum_{j=1}^n [2R(a_l(\phi) \cos \theta_j + b_l(\phi) \sin \theta_j)]^v}{\sum_{v=0}^{\infty} \frac{1}{v!} \sum_{j=1}^n [2R(a_l(\phi) \cos \theta_j + b_l(\phi) \sin \theta_j)]^v} \quad (4)$$

We next observe that, for any set of functions $f_j(\phi)$, with $f'_j(\phi) \equiv \partial f_j / \partial \phi$

$$\begin{aligned} \frac{1}{v} \frac{\partial}{\partial \phi} \sum_{j=1}^n f_j^v(\phi) &= \sum_{j=1}^n f_j^{v-1}(\phi) f'_j(\phi) = \sum_{i=1}^n f_i(\phi) \sum_{j=1}^n f_j^{v-2}(\phi) f'_j(\phi) - \sum_{i=1}^n \sum_{j=i+1}^n f_i(\phi) f_j(\phi) \sum_{k=1}^n f_k^{v-3}(\phi) f'_k(\phi) \\ &+ \sum_{i=1}^n \sum_{j=i+1}^n \sum_{k=j+1}^n f_i(\phi) f_j(\phi) f_k(\phi) \sum_{l=1}^n f_l^{v-4}(\phi) f'_l(\phi) + \cdots + (-1)^{n-1} f_1(\phi) f_2(\phi) \cdots f_n(\phi) \sum_{j=1}^n f_j^{v-n-1}(\phi) f'_j(\phi) \end{aligned} \quad (5)$$

As a final manipulation needed in the proof of the significance of Eq. (3), we rewrite the function

$$a_l(\phi) \cos \theta_j + b_l(\phi) \sin \theta_j$$

in the form

$$\alpha_l \cos(\theta_j + \phi) + \beta_l \sin(\theta_j + \phi) \quad (6)$$

where

$$\alpha_l = \frac{1}{AT_s} \int_{lT_s}^{(l+1)T_s} y(t) (2)^{1/2} \sin \omega_c t dt$$

and

$$\beta_l = \frac{1}{AT_s} \int_{lT_s}^{(l+1)T_s} y(t) (2)^{1/2} \cos \omega_c t dt$$

are both independent of ϕ . The summation

$$\sum_{j=1}^n (a_l(\phi) \cos \theta_j + b_l(\phi) \sin \theta_j)^v = \sum_{j=1}^n (\alpha_l \cos(\theta_j + \phi) + \beta_l \sin(\theta_j + \phi))^v \quad (7)$$

can then be written

$$\sum_{j=1}^n (k_0 + k_{s1} \sin(\theta_j + \phi) + k_{c1} \cos(\theta_j + \phi) + k_{s2} \sin 2(\theta_j + \phi) + k_{c2} \cos 2(\theta_j + \phi) + \dots + k_{sv} \sin v(\theta_j + \phi) + k_{cv} \cos v(\theta_j + \phi)) \quad (8)$$

and is independent of ϕ for all $v < n$. This follows because

$$\sum_{j=1}^n \sin \mu(\theta_j + \phi) = \sum_{j=1}^n \cos \mu(\theta_j + \phi) = 0$$

for all integers μ , $0 < \mu < n$, when $\theta_j = 2\pi j/n$. Consequently, equating $f_j(\phi)$ and $a_l(\phi) \cos \theta_j + b_l(\phi) \sin \theta_j$, we have established the following:

(1) $\partial/\partial\phi \sum_j f_j^v(\phi) = 0$ for $v = 0, 1, \dots, n-1$.

(2) If $\partial/\partial\phi \sum_j f_j^n(\phi) = 0$ for $\phi = \hat{\phi}$, then by recursion, using Eq. (5), $\partial/\partial\phi \sum_j f_j^v(\phi) = 0$ for $\phi = \hat{\phi}$, for all v .

(3) Thus, Eq. (2) is identically zero for any $\phi = \hat{\phi}$, satisfying Eq. (3), as was to be shown.

Equation (3) can be expressed in a more convenient form by making the substitution

$$c_l(\phi) = \frac{a_l(\phi) - ib_l(\phi)}{2}$$

which yields

$$\frac{\partial}{\partial\phi} \sum_{j=1}^n (c_l(\phi) e^{i\theta_j} + c_l^*(\phi) e^{-i\theta_j})^n \quad (9)$$

with $c_l^*(\phi)$ the complex conjugate of $c_l(\phi)$. Expanding the summand in a binomial series and interchanging the order of summation, we obtain the function

$$-in^3 (c_l(\phi))^n - (c_l^*(\phi))^n =$$

$$\frac{n^3}{2^{n-1}} \sum_{\substack{v=1 \\ \text{odd } v}}^n \binom{n}{v} a_l^{n-v}(\phi) b_l^v(\phi) (-1)^{(v-1)/2} \quad (10)$$

If $y_l(t) = (2)^{1/2} AT_s \sin(\omega_c t + \theta_r + \phi_0) + n(t)$ is the signal received over the interval $lT_s < t < (l+1)T_s$, then

$$a_l(\phi) = \cos \phi' + n_1$$

$$b_l(\phi) = \sin \phi' + n_2 \quad (ii)$$

where

$$\phi' = \phi_0 - \phi + \theta_r \equiv \phi_r + \theta_r$$

$$n_1 = \frac{1}{AT_s} \int_{lT_s}^{(l+1)T_s} n(t) (2)^{1/2} \sin(\omega_c t + \phi) dt$$

and

$$n_2 = \frac{1}{AT_s} \int_{tT_s}^{(l+1)T_s} n(t) (2)^{1/2} \cos(\omega_c t + \phi) dt$$

Thus,

$$c_l(\phi) = \frac{e^{i\phi'}}{2} + m_1, c_l^*(\phi) = \frac{e^{-i\phi'}}{2} + m_2$$

where

$$m_1 = \frac{n_1 + in_2}{2}, m_2 = m_1^*$$

and

$$-in^3 E \{c_l^n(\phi) - (c_l^*(\phi))^n\} = \frac{n^3}{2^{n-1}} \sin n\phi' = \frac{n^3}{2^{n-1}} \sin n\phi_e \quad (12)$$

Moreover,

$$E \left\{ \frac{\partial^2}{\partial \phi^2} \sum_{j=1}^n (c_l(\phi) e^{i\theta_j} + c_l^*(\phi) e^{-i\theta_j})^n \right\} = -n^4 E \{c_l^n(\phi) + c_l^*(\phi)^n\} = -\frac{n^4}{2^{n-1}} \cos n\phi_e \quad (13)$$

From Eq. (12) we conclude that one of the roots of the function (3) is indeed an unbiased estimate of ϕ_0 . In addition, from Eq. (13) the sign of the expected value of this function will be positive when the estimate ϕ of ϕ_0 is less than ϕ_0 and negative when ϕ exceeds ϕ_0 so long as $|\phi_0 - \phi| \leq \pi/n$. Accordingly, if this function itself after suitable filtering is used as the input to a voltage-controlled oscillator (VCO), the resulting device will be able to track the received carrier phase. These PSK carrier tracking loops are shown in Fig. 1 for $n = 2, 3$, and 4.

There are, of course, $2n - 1$ other values of ϕ_0 for which the expected values of Eq. (3) are zero. The expected value of the second derivative is negative for $n - 1$ of these solutions, indicating a total of n possible lock-in points. This would also be the situation if the actual maximum-likelihood estimator were used, since, as we have already observed, any solution to Eq. (3) is also a solution to the maximum-likelihood equation. Indeed, the inevitability of this n -fold ambiguity is apparent from the very nature of the problem.

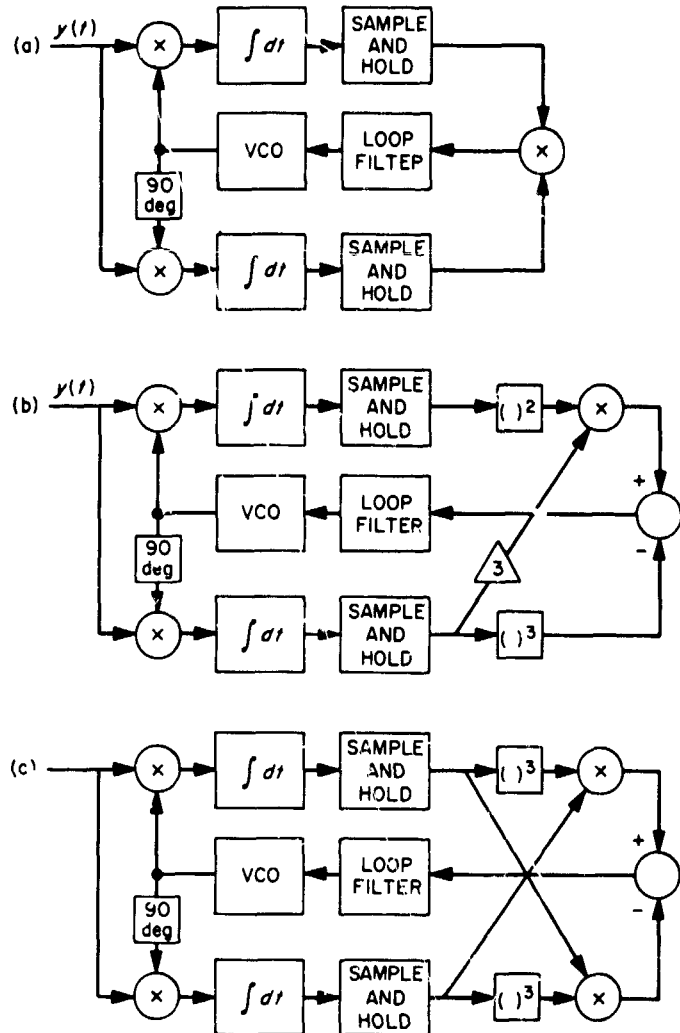


Fig. 1. PSK carrier tracking loops: (a) $n = 2$, (b) $n = 3$, (c) $n = 4$

These carrier tracking loops are suboptimum only because the expected values of the derivatives of Eqs. (2) and (3) are not necessarily equal. The true maximum-likelihood estimate might, therefore, have a smaller variance. Nevertheless, when the signal-to-noise ratio R is small, the expansion (4) is well approximated by retaining only the first non-zero terms in both the numerator and denominator. In this case, thus, the two estimators are identical. The estimator based on the function (3) is therefore asymptotically optimum as $R \rightarrow 0$. Moreover, as we shall see, this same estimator is also asymptotically optimum at the other extreme when $R \rightarrow \infty$.

To analyze the performance of these loops we needed only observe that, when the bandwidth of the combined filter-integrator portion of the tracking loop is narrow relative to $1/T_s$, the following conditions hold:

- (1) The noise consists of a sequence of independent noise pulses of width T_s . Thus, the noise spectrum at the loop filter input is of the form

$$S_n(\omega) = \sigma_n^2 T_s \left(\frac{\sin \frac{\omega_c T_s}{2}}{\frac{\omega_c T_s}{2}} \right)^2 \quad (14)$$

where σ_n^2 is the variance of the noise pulse amplitude. So far as the loop is concerned, the noise is white, therefore, with the two-sided spectral density $S_n(0) = \sigma_n^2 T_s$.

- (2) The signal at the loop input, when the tracking error is small, is approximately

$$A' \phi_e(t) \equiv \frac{n^4}{2^{n-1}} \phi_e(t) \quad (15)$$

and is linear in $\phi_e(t)$.

- (3) Since many noise pulses determine the VCO phase $\phi_1(t)$, the signal $\phi_e(t) = \phi_0(t) - \phi_1(t)$ is essentially independent of any one of these noise pulses.

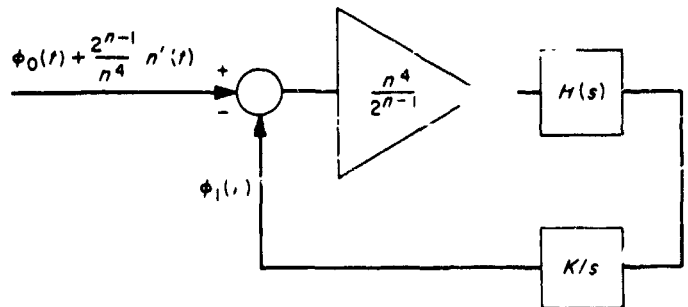


Fig. 2. Linear model of PSK carrier tracking loops

Thus, the tracking loops are equivalent to the linear model of Fig. 2. This is, of course, also the linear model of an ordinary phase-locked loop when the received signal has the amplitude $n^4/2^{n-1}$ and the noise is white with the spectral density σ_n^2 . Thus, we immediately conclude that the phase error variance is

$$\sigma_\phi^2 = \frac{2\sigma_n^2 B_L T_s}{(n^4/2^{n-1})^2} \quad (16)$$

The noise variance σ_n^2 can be shown to be, after some manipulation,

$$\sigma_n^2 = -n^6 [E \{c_l^n(\phi) - (c_l^*(\phi))^n\}^2 + E^2 \{c_l^n(\phi) - (c_l^*(\phi))^n\}] = \frac{n^6}{2^{2n-3}} \sum_{k=1}^n \binom{n}{k}^2 k! \frac{1}{R^k} \quad (17)$$

Thus,

$$\sigma_\phi^2 = \frac{B_L T_s}{n^2} \sum_{k=1}^n \binom{n}{k}^2 k! \frac{1}{R^k} \quad (18)$$

when $R = A^2 T_s / N_0$ is large,

$$\sigma_\phi^2 \sim \frac{B_L N_0}{A^2} \quad (19)$$

Since this would be the phase variance in the absence of any modulation whatsoever, it clearly represents the optimum performance obtainable from any carrier phase tracking device. This validates the statement made above that the loops described here are asymptotical optimum

as $R \rightarrow \infty$. They are also optimum when R is small compared to unity, in which case

$$\sigma_\phi^2 \sim B_L T_s \frac{n!}{n^2 R^n} \quad (20)$$

Evidently, then such loops will be practical only for small values of n , unless R is also relatively large.

2. Signal Design for a Class of Clutter Channels,

A. Balakrishnan¹

The problem of signal design (or optimal selection of signals for transmission over a given channel) has for the

¹Member of the staff of the Engineering Department, the University of California at Los Angeles. Research prepared under contract to the Jet Propulsion Laboratory.

most part (Refs. 2, 3, and 4) been studied for channels with additive noise independent of signal parameters. In this article we consider such a problem for channels characterized by the presence of an additive noise component dependent multiplicatively on the signal in such a way that increasing the signal energy increases the noise power. Such a noise component is usually referred to as clutter or a reverberation component, and occurs in many applications such as sonar, and recently also in signal transmission from a spacecraft in the vicinity of a planet. The fact that an increase in signal power need not result in improvement, especially when the ambient or temperature limited noise is small, makes signal design essential in these applications. In our analysis we have assumed a model in which the clutter or reverberation component is stationary Gaussian with a covariance function which is a product of the covariance function characterizing the medium and the covariance function of the signal.

The general method for the signal design problem is the same as before; we first optimize the receiver regardless of the signal to be transmitted, and then seek the optimal signals that minimize the error, the receiver being always optimum for the signals chosen. In this article we consider a binary system, the receiver being optimized for minimum probability of error.

For our purposes, the basic detection problem can be stated as follows:

Null hypothesis H_0 :

$$x(t) = n(t) \quad 0 \leq t \leq T$$

Alternate hypothesis H_1 :

$$x(t) = s(t) + n(t) \quad 0 \leq t \leq T$$

where (the functions are allowed to be complex) $s(t)$ is a known (sure) signal, and $n(t)$ is the "clutter" noise, a stationary Gaussian process with covariance function $R(t)$,

$$R(t) = R_c(t) R_s(t) + \phi \delta(t)$$

where

$$R_s(t) = \int_{-\infty}^{\infty} (\exp 2\pi i f t) |\psi_s(f)|^2 df$$

$$\psi_s(f) = \int_0^T (\exp i f t) s(t) dt$$

and $R_c(t)$ is a given covariance function.

As is well known, the optimal receiver is obtained by setting a suitable threshold for

$$\int_0^T x(t) \overline{g(t)} dt \quad (1)$$

where

$$\int_0^T R(t-s) g(s) ds = s(t) \quad 0 \leq t \leq T \quad (2)$$

The corresponding probability of detection (whether in radar or communications) is a monotone function of the signal-to-noise ratio:

$$\int_0^T \overline{g(t)} s(t) dt \quad (3)$$

The signal design problem is that of choosing the optimal signal $s(\cdot)$ which maximizes the probability of detection, or equivalently the signal-to-noise ratio, subject to energy or bandwidth constraints.

We shall first consider the problem under the constraint that:

$$\int_0^T |s(t)|^2 dt = E \quad (4)$$

It is convenient at this point to use operator theory. Thus let H denote the space $L_2(0, T)$, and for each element $s(\cdot)$ in H , let us introduce the linear transformation $R(s)$, mapping H into H , by:

$$R(s)f = q; \quad \int_0^T R_c(t-\sigma) R_s(t-\sigma) f(\sigma) d\sigma = q(t) \quad 0 \leq t \leq T$$

Then Eq. (3) can be written, using the inner product in H as:

$$[(\phi I + R(s))^{-1} s, s] = [q, s] \quad (5)$$

where it is noted that I is the identity, and since $R(s)$ is non-negative definite, $[\phi I + R(s)]$ has a linear-bounded

inverse. The problem of signal design is thus one of maximizing Eq. (5) subject to

$$[s, s] = E$$

Now it is readily verified that the functional defined by Eq. (5) is sufficiently smooth on H so that the maximum is actually attained by an element s_0 , say. Moreover, the

constraint set being defined by a continuous convex function, we may employ the Lagrange parameter method, and use the fact that s_0 must maximize

$$[(\phi I + R(s))^{-1} s, s] + \gamma [s, s] \quad (6)$$

The functions being Frechet differentiable, the gradient of Eq. (6) must vanish at $s = s_0$. Thus for arbitrary h in H ,

$$\frac{d}{d\lambda} \{[(\phi I + R(s_0 + \lambda h))^{-1} (s_0 + \lambda h), s_0 + \lambda h] + [s_0 + \lambda h, s_0 + \lambda h]\} |_{\lambda=0} = 0$$

Now

$$\frac{d}{d\lambda} [\phi I + R(s_0 + \lambda h)]^{-1} |_{\lambda=0} = [I + R(s_0)]^{-1} \left[\frac{d}{d\lambda} R(s_0 + \lambda h) \Big|_{\lambda=0} \right] [I + R(s_0)]^{-1}$$

and a direct calculation shows that the gradient is given by:

$$\int_0^T \int_0^T \overline{g_0(t)} g_0(t') R_c(t-t') [s_0(\sigma + t - t') + \overline{s_0(\sigma + t' - t)}] dt dt' + (\gamma s_0(\sigma) + \gamma \overline{s_0(\sigma)}) - (g_0(\sigma) + \overline{g_0(\sigma)}) \quad 0 \leq \sigma \leq T \quad (7)$$

where

$$g_0 = (\phi I + R(s_0))^{-1} s_0 \quad (8)$$

Hence it is necessary that the optimal signal satisfy the nonlinear integral equation that results by setting Eq. (7) to be zero, the constant γ being so chosen as to yield the energy E . The problem of finding an analytical solution of the equation would appear to be a difficult one; it is of course possible to give a computational algorithm based on steepest descent using Eq. (7).

In order to get some analytical results, albeit approximate, we now consider the special case where the time-bandwidth products involved are large enough to allow us to essentially make the time interval T infinite in Eqs. (2) and (3), so that we may work equivalently in the frequency domain. We have then that the functional Eq. (5) to be maximized can be expressed:

$$\int_{-\infty}^{\infty} \frac{|\psi_s(f)|^2}{\phi + P_r(f)} df \quad (9)$$

where

$$P_r(f) = \int_{-\infty}^{\infty} K(f-f') |\psi_s(f')|^2 df';$$

$$K(f) = \int_{-\infty}^{\infty} e^{2\pi i f t} R_c(t) dt \quad (10)$$

This is an immediate consequence of the fact that if T is infinite in Eq. (2), the Fourier transform of $R(\cdot)$ and Eq. (3) is equal to

$$\int_{-\infty}^{\infty} \psi_g(f) \overline{\psi_s(f)} df$$

where $\psi_g(f)$ is the Fourier transform of $g(\cdot)$. We note that Eq. (9) depends only on the signal "spectral density" $|\psi_s(f)|^2$, and hence we denote the latter by $P(f)$, and Eq. (9) is thus to be maximized over the class of positive functions $P(\cdot)$ subject to

$$\int_{-\infty}^{\infty} P(f) df = E$$

Actually we shall consider a slightly more general problem in this setting. Thus we shall consider the problem of choosing the optimal signal of energy E from the class of signals band limited to $(-B, B)$ in the sense that we add an additional constraint:

$$P(f) = 0 \quad |f| > B$$

We can now use the Lagrange parameter method and seek to maximize:

$$\int_{-B}^B \frac{P(f) df}{\phi + P_r(f)} + \gamma \int_{-B}^B P(f) df \quad (11)$$

where

$$P_r(f) = \int_{-B}^B K(f-f') P(f') df'$$

over the class of positive functions in $L_1(-B, B)$. The maximum is again attained by some function $P(\cdot)$, and denoting it by $P_0(\cdot)$, and the functional in Eq. (11) by $r(\cdot)$, if $h(\cdot)$ is any positive function in $L_1(-B, B)$, and for sufficiently small λ ,

$$P_0(f) + \lambda h(f) \geq 0 \quad -B \leq f \leq B$$

we have that:

$$\frac{d}{d\lambda} r(P_0 + \lambda h)|_{\lambda=0} =$$

$$\int_{-B}^B \left(\frac{1}{q_0(f)} - \int_{-B}^B \frac{K(f-f') P_0(f')}{q_0(f)^2} df' \right) h(f) df + \int_{-B}^B \gamma h(f) df$$

where

$$q_0(f) = \phi + \int_{-B}^B K(f-f') P_0(f') df' \quad (12)$$

It follows from this that the optimal signal spectrum must satisfy:

$$\frac{1}{q_0(f)} - \int_{-B}^B \frac{K(f-f') P_0(f') df'}{q_0(f)^2} + \gamma = 0 \quad -B \leq f \leq B \quad (13)$$

We note that this result could also be obtained from Eq. (7) by taking the Fourier transform of Eq. (7) under the assumption of infinite T . As before, γ is again to be determined to satisfy the energy constraint. Multiplying Eq. (13) by $P_0(f)$ and integrating, we obtain:

$$\phi \int_{-B}^B \frac{P_0(f)}{q_0(f)^2} df + \gamma E = 0$$

and hence we may rewrite Eq. (13) as:

$$\frac{1}{q_0(f)} - \int_{-B}^B \frac{\tilde{K}(f-f') P_0(f') df'}{q_0(f)^2} = 0 \quad (14)$$

where

$$\tilde{K}(f-f') = \frac{\phi}{E} + K(f-f') \quad -B \leq f, f' \leq B$$

and in place of Eq. (12) we can write equivalently:

$$q_0(f) = \int_{-B}^B \tilde{K}(f-f') P_0(f') df'$$

Equations (13) and (14) are nonlinear integral equations but have a simple solution if we can find $P(\cdot)$ such that

$$\int_{-B}^B K(f-f') P(f') df' = c \quad -B \leq f \leq B \quad (15)$$

where $P(\cdot)$ is positive and in $L_1(-B, B)$. For in this case Eq. (13) becomes:

$$\frac{1}{c} - \frac{(c-\phi)}{c^2} + \gamma = 0$$

or

$$\phi + \gamma c^2 = 0$$

and of course γ can always be chosen to satisfy this, so that we have obtained a solution of Eq. (13). Also, the functional Eq. (3) itself has the maximum value:

$$\frac{E}{\phi + c} \quad \text{if} \quad \int_{-B}^B P(f) df = E \quad (16)$$

If we consider the special case where

$$K(f) = k \quad -L \leq f \leq L$$

$$= 0 \quad |f| > L \quad (17)$$

it is readily verified that if $2B \leq L$, then Eq. (15) has the solution

$$P(f) = \text{constant} \quad -B \leq f \leq B$$

and thus we can take:

$$P_0(f) = \frac{E}{2B} \quad -B \leq f \leq B \quad (18)$$

then we have for the corresponding maximal signal-to-noise ratio:

$$\frac{E}{\phi + kE} \quad (19)$$

In particular, if $\phi = 0$, we note that the maximal signal-to-noise ratio is $(1/k)$ and is independent of the signal energy. The bandwidth can also be chosen as small as desired, and increasing it up to L brings no improvement. For $2B > L$, we do not know the solution of Eq. (13). However, it is easy to calculate the signal-to-noise ratio for signal spectrum given by Eq. (18), and since it sheds some light on the general nature of the results, we shall indicate it here. We have

Case 1: $L \leq 2B \leq 2L$

Signal-to-noise ratio

$$= \left(\frac{2E}{2B}\right) \left\{ \left(\frac{L-B}{\phi + kE}\right) + \frac{2B}{kE} \log \left(\frac{\phi + kE}{\phi + \frac{kE}{2} + \frac{kE}{2B}(L-B)} \right) \right\}$$

Case 2: $L \leq B$

Signal-to-noise ratio

$$= (2E) \left\{ \frac{B-L}{2B + 2kLE} + \left(\frac{1}{kE}\right) \log \left(\frac{2B\phi + 2kEL}{2B\phi + kEL} \right) \right\}$$

This is

$$\geq \frac{E}{\phi + \left(\frac{LkE}{B}\right)} \rightarrow \frac{E}{\phi} \quad \text{as } B \rightarrow \infty \quad (20)$$

and of course E/ϕ cannot obviously be exceeded.

If there is no constraint on the bandwidth, then for any arbitrary $K(\cdot)$, we note that the choice, Eq. (18), yields

$$\text{Signal-to-noise ratio} \geq \frac{E}{\phi + k_B E}$$

where

$$k_B = \sup_f \frac{1}{2B} \int_{-B}^B K(f-f') df'$$

But k_B clearly goes to zero as B tends to infinity, and we get Eq. (20) in general as well.

B. Combinatorial Communication, H. Rumsey, Jr., and L. Baumert

1. A Multiplier Theorem For Difference Sets

a. Introduction. The equivalence of difference sets with the binary two-level autocorrelation sequences of space communications (Ref. 5) has led to extensive investigations of difference set existence problems. For certain values of the difference set parameters v, k, λ , the existence question is extremely difficult. In particular, the usual methods of handling these problems are frequently ineffectual when $n = k - \lambda$ divides v . We present a theorem which is most useful under just these circumstances. A weak form of this theorem is indicated in Ref. 6, but it is not made clear there whether the stronger result was known. In any case, we know of no published proof of this result.

b. Preliminaries. A difference set $D = \{d_1, \dots, d_k\}$ is a collection of k residues modulo v , which possesses the property that every non-zero residue α of v can be expressed as a difference of elements of D in precisely λ ways. Thus the parameters v, k, λ are related by the equation $k(k-1) = \lambda(v-1)$. With each difference set we associate a polynomial $\theta(x) = x^{d_1} + \dots + x^{d_k}$, called the *Hall polynomial* of the set. This polynomial then satisfies

$$\theta(x)\theta(x^{-1}) \equiv k - \lambda + \lambda(1 + x + \dots + x^{v-1}) \pmod{x^v - 1}$$

If t is an integer prime to v , the set $tD = \{td_1, \dots, td_k\}$ taken modulo v is also a difference set with the same parameters v, k, λ as D . If $tD = \{d_1 + s, \dots, d_k + s\}$ modulo v , then t is said to be a *multiplier* of the difference set D . (Note that for t not prime to v , tD is not even a difference set.) If t is a multiplier of D and $\theta(x)$ is the associated Hall polynomial, then

$$\theta(x^t) \equiv x^t \theta(x) \pmod{x^v - 1}$$

Consider the Hall polynomial of a difference set reduced modulo $x^w - 1$, where w divides v . That is, consider

$$\theta_w(x) = \sum_{i=0}^{w-1} C(i) x^i \equiv \theta(x) \pmod{x^w - 1}$$

Define a *w-multiplier* of the difference set to be any integer t , for which there exists a non-negative integer s satisfying

$$\theta_w(x^t) \equiv x^s \theta_w(x) \pmod{x^w - 1}$$

Clearly, a w -multiplier is a w_1 -multiplier for all w_1 dividing w . Thus an ordinary multiplier is a w -multiplier for every w dividing v .

Multipliers are extremely useful for deciding whether or not a difference set exists. The principal means of guaranteeing that a hypothetical difference set D possesses a multiplier is the following theorem of Marshall Hall (Ref. 6).

Multiplier theorem. Let D be a difference set and let n_1 divide n , $(n_1, v) = 1$, and $n_1 > \lambda$. If for every prime p dividing n_1 , there is a j such that $p^j \equiv t \pmod{v}$, then t is a multiplier of D .

In the case which concerns us, n divides v ; thus, Hall's multiplier theorem cannot help. However, under certain conditions we can guarantee the existence of a w -multiplier for some divisor w of v , and frequently this enables us to solve the existence problem.

c. The existence of w -multipliers. By reasoning completely analogous to that used by Hall (Ref. 6) in the proof of his multiplier theorem, one can conclude the following:

Theorem. Let D be a difference set and let n_1 divide n , $(n_1, w) = 1$, and $n_1 > \lambda v/w$, where w is a divisor of v . If for every prime p dividing n_1 , there is a j such that $p^j \equiv t \pmod{w}$, then t is a w -multiplier.

Unfortunately, the condition $n_1 > \lambda v/w$ is rarely satisfied; thus this theorem is not often of use. Our main result is more satisfactory:

Theorem. Let w divide v and suppose that for every prime p dividing n there is an integer j such that $p^j \equiv t \pmod{w}$. Then t is a w -multiplier of every cyclic difference set with these parameters n, v .

Proof. It follows from the difference set property that

$$\theta_w(x) \theta_w(x^{-1}) \equiv n + \frac{\lambda v}{w} T_w(x) \pmod{x^w - 1} \quad (1)$$

where $T_w(x)$ is defined to be $1 + x + \dots + x^{w-1}$. Thus

$$\theta_w(x) \theta_w(x^{-1}) \equiv n \pmod{f_i(x)}$$

when $f_i(x)$ is any one of the distinct irreducible factors of $T_w(x)$ over the rational field K . Let $\zeta = e^{2\pi i j/w}$ be that root of $f_i(x)$ for which j is least positive; then we have a factorization of n in the field $K(\zeta)$ given by $\theta_w(\zeta) \theta_w(\zeta^{-1}) = n$. Since $K(\zeta)$ is a cyclotomic field, the hypothesis of our theorem implies that every prime ideal divisor of n (hence every prime ideal divisor of $\theta_w(\zeta)$) is fixed under the field automorphism $\zeta \rightarrow \zeta^t$. (Ref. 7 provides all required algebraic number theory.) Thus the principal ideals $(\theta_w(\zeta^t))$ and $(\theta_w(\zeta))$ are the same. This means that $\theta_w(\zeta^t) = \mu \theta_w(\zeta)$ where μ is a unit of $K(\zeta)$. As $1, \zeta, \dots, \zeta^{m-1}$ form an integral basis for this field (here m is the degree of $f_i(x)$), we may express μ as a polynomial in ζ with rational integral coefficients. Say $\mu = S_i(\zeta)$. Thus $\theta_w(\zeta^t) \theta_w(\zeta^{-1}) = n S_i(\zeta)$, which implies

$$\theta_w(x^t) \theta_w(x^{-1}) \equiv n S_i(x) \pmod{f_i(x)} \quad (2)$$

There will be such a congruence for each irreducible factor $f_i(x)$ of $T_w(x)$. We wish to deduce a similar congruence modulo $T_w(x) = f_1(x) f_2(x) \dots f_r(x)$. Suppose

$$\theta_w(x^t) \theta_w(x^{-1}) = n R_j(x) + A(x) F_j(x) \quad (3)$$

where $F_j(x) = f_1(x) \dots f_j(x)$. This is immediate for $j = 1$ from Eq. (2). Assuming Eq. (3) holds for j , we ask

about $j + 1$. Now $f_{j+1}(x)$ and $F_j(x)$ have no common factors. Thus their resultant z is a non-zero rational integer, and there exist integral polynomials $C(x)$ and $D(x)$ such that

$$C(x)F_j(x) + D(x)f_{j+1}(x) = z \quad (4)$$

(Ref. 8 contains proofs of all the relevant resultant theory.) But z can be expressed as a product of factors $\alpha - \beta$ where α is a root of $F_j(x)$ and β is a root of $f_{j+1}(x)$. Thus α and β are different w th roots of unity, and if η is a primitive w th root of unity, we have $\alpha - \beta = \eta^y(\eta^l - 1)$ for appropriate exponents y, l . Now η^y is a unit and $\eta^l - 1$ is a root of

$$\frac{[(x+1)^w - 1]}{x} = x^{w-1} + \dots + w = 0$$

thus $\eta^l - 1$ divides w . Hence z will divide an appropriate power of w , and, since $(n, w) = 1$ is implied by the hypothesis, we also have $(n, z) = 1$. From Eq. (2), with $i = j + 1$, we have

$$C(x)F_j(x)\theta_w(x^t)(x^{-1}) = nC(x)F_j(x)S_{j+1}(x) + C(x)B(x)F_{j+1}(x) \quad (5)$$

Multiplying Eq. (3) by $D(x)f_{j+1}(x)$ and adding the result to Eq. (5) gives

$$z\theta_w(x^t)\theta_w(x^{-1}) = nS(x) + G(x)F_{j+1}(x)$$

This can be combined with the trivial relation

$$n\theta(x^t)\theta(x^{-1}) = nH(x)$$

to yield (since n and z are relatively prime)

$$\theta_w(x^t)\theta_w(x^{-1}) = nR_{j+1}(x) + A(x)F_{j+1}(x)$$

Continuing in this manner, we find

$$\theta_w(x^t)\theta_w(x^{-1}) = nR(x) + A(x)T_w(x) \quad (6)$$

as desired.

Since $A(x)T_w(x) \equiv A(1)T_w(x)$ modulo $x^w - 1$, Eq. (6) yields the congruence

$$\theta_w(x^t)\theta_w(x^{-1}) \equiv nR(x) + A(1)T_w(x) \pmod{x^w - 1}$$

Here, with $x = 1$, we get $k^2 = nR(1) + A(1)w$. Since we know that $k^2 = n + \lambda v$ and $(n, w) = 1$, this implies that $A(1) \equiv \lambda v/w$ modulo n . Thus, by altering $R(x)$ if necessary, we get

$$\theta_w(x^t)\theta_w(x^{-1}) \equiv nR(x) + \frac{\lambda v}{w}T_w(x) \pmod{x^w - 1} \quad (7)$$

From this (at $x = 1$ again) we deduce

$$R(1) = 1 \quad (8)$$

Since $(t, w) = 1$, we know that

$$\theta_w(x^t)\theta_w(x^{-t}) \equiv \theta_w(x)\theta_w(x^{-1}) \equiv n + \frac{\lambda v}{w}T_w(x) \pmod{x^w - 1}$$

Thus $\theta_w(x^t)\theta_w(x^{-t})\theta_w(x)\theta_w(x^{-1}) \equiv [n + (\lambda v/w)T_w(x)]^2$ modulo $x^w - 1$, while from Eq. (7) we get the value

$$\left[nR(x) + \frac{\lambda v}{w}T_w(x) \right] \left[nR(x^{-1}) + \frac{\lambda v}{w}T_w(x) \right]$$

Since $R(x)T_w(x) \equiv R(1)T_w(x)$ modulo $x^w - 1$, a comparison of these two yields

$$R(x)R(x^{-1}) \equiv 1 \pmod{x^w - 1}$$

But $R(x)$ has integer coefficients; thus $R(x) = \pm x^s$. As $R(1) = 1$, we see $R(x) = x^s$. Thus Eq. (7) takes the form

$$\theta_w(x^t)\theta_w(x^{-1}) \equiv nx^s + \frac{\lambda v}{w}T_w(x) \pmod{x^w - 1} \quad (9)$$

Multiply Eq. (9) through by $\theta_w(x)$ and use Eq. (1). After simplifying, this becomes

$$\theta_w(x^t) \equiv x^s \theta_w(x) \pmod{x^w - 1}$$

That is, t is a w -multiplier of every difference set with parameters n, v as was to be shown.

d. Some examples. We restrict ourselves to examples which pass the various parameter inequalities of Yamamoto and others (Ref. 9); that is, to cases where it is meaningful to apply our theorem.

Assume a difference set exists with parameters $v, k, \lambda, n = 2325, 84, 3, 81$. Then our theorem implies that 3 is a 31-multiplier. Since $(3 - 1, 31) = 1$, there is a shift $D + s \equiv d_1 + s, \dots, d_{n_4} + s$ of the hypothetical difference set which is fixed modulo $x^{31} - 1$ under the multiplier. That is,

$$\theta_{31}(x^3) \equiv \theta_{31}(x) \pmod{x^{31} - 1}$$

for this shift. Since 3 is a primitive root of 31, this implies that

$$\theta_{31}(x) \equiv b_0 + b_1(x + \dots + x^{30}) \pmod{x^{31} - 1}$$

Thus

$$\theta_{31}(1) = 84 = b_0 + 30b_1 \quad b_0, b_1 \geq 0$$

while the constant coefficient of Eq. (1) above is

$$b_0^2 + 30b_1^2 = 306$$

These last two equations have no integral solutions b_0, b_1 . Thus our hypothetical difference set does not exist.

Assume a difference set exists with parameters $v, k, \lambda, n = 276, 100, 36, 64$. Then 2 is a 69-multiplier by our theorem. As before, 2 fixes some shift of D modulo $x^{69} - 1$; thus also modulo $x^3 - 1$. This implies that 2 is a 3-multiplier for the same fixed shift modulo $x^3 - 1$. From this we conclude (as before) that $\theta_3(x) \equiv b_0 + b_1(x + x^2)$ and that

$$b_0 + 2b_1 = 100$$

$$b_0^2 + 2b_1^2 = 3376$$

These imply that $b_0 = 28$ and $b_1 = 36$.

If we now consider 2 as a 69-multiplier, we see that those residues i ($i, 69) = 3$ fall into two sets of 11 elements each plus the singleton 0. Thus $b_0 = 28 = c_0 + 11(c_1 + c_2)$

with $0 \leq c_0, c_1, c_2 \leq (276/69) = 4$. But this equation has no such integral solutions c_1 . Thus no difference set exists for these parameter values.

C. Propagation Studies, P. Reichley

1. The Effect of Atmospheric Variations on High-Precision Tracking

a. Summary. For high-precision tracking accuracy, it is necessary to have a good model of the atmosphere in order that the effects on range, doppler, and elevation angle can be accounted for. The time variation of the atmospheric parameters, such as scale height and refractivity, determine over how long of a period of time estimates of such atmospheric parameters can be used.

In order to study these atmospheric variations, ground and balloon weather data for 1966 was obtained from the U. S. Air Force at Edwards Air Force Base in the Mojave Desert. The climate at Edwards is very similar to the climate at the Goldstone Tracking Station and thus presented a good study case.

We present in this article the results of that study, and the effects of these variations on range, doppler, and elevation angle.

b. Introduction. The atmosphere was assumed to have a spherically symmetric exponential index of refraction n where

$$n(r) = 1 + \alpha e^{-(r-r_0)/h} \quad (1)$$

where $\alpha = N_0 \times 10^{-6}$, $N_0 =$ ground level refractivity, $h =$ scale height, and $r_0 =$ ground level radius vector.

The weather data obtained from Edwards Air Force Base was in two forms. The first form consisted of hourly readings of pressure, temperature, and relative humidity at ground level. The second form consisted of balloon readings of pressure, temperature, and relative humidity taken at 1,000-ft intervals from the ground. The balloons were released at irregular intervals during the day.

To compute the refractivity the following formula (Ref. 10) was used:

$$N = \frac{77.6}{T} \left(p + \frac{4810e}{T} \right) \quad (2)$$

where T = temperature, °K; p = pressure, mbar; and e = vapor pressure, mbar. Since the data contained relative humidity rather than vapor pressure, it was necessary to convert. Relative humidity R is defined as

$$R = \frac{e}{e_s} \times 100 \quad (3)$$

where e_s is the saturation vapor pressure. The saturation vapor pressure is defined (Ref. 11) by

$$e_s = 6.10 \times 10^{\frac{7.4475t}{234.7 + t}} \quad (4)$$

where t is the temperature in degrees centigrade.

Hence, using Eqs. (2), (3), and (4), the hourly readings of pressure, temperature, and relative humidity were converted to refractivity readings.

To compute the scale heights the balloon readings were used. Following Bean (Ref. 12), the scale height is defined by

$$\frac{1}{h} = \ln \frac{N_0}{N_1} \quad (5)$$

where N_1 is the refractivity at 1-km elevation. The pressure, temperature, and relative humidity at 1-km elevation were obtained from the balloon data, and then Eqs. (2), (3), and (4) were utilized to compute N_1 . Hence, from Eq. (5), the balloon readings were converted to scale heights.

c. Refractivity and scale height variations. The refractivity during the year 1966 varied from a minimum of 251 to a maximum of 331 which, interestingly, both occurred during the month of September. The distribution of the refractivity is shown in Fig. 3. The average refractivity for the year was 281 with a standard deviation of 12.

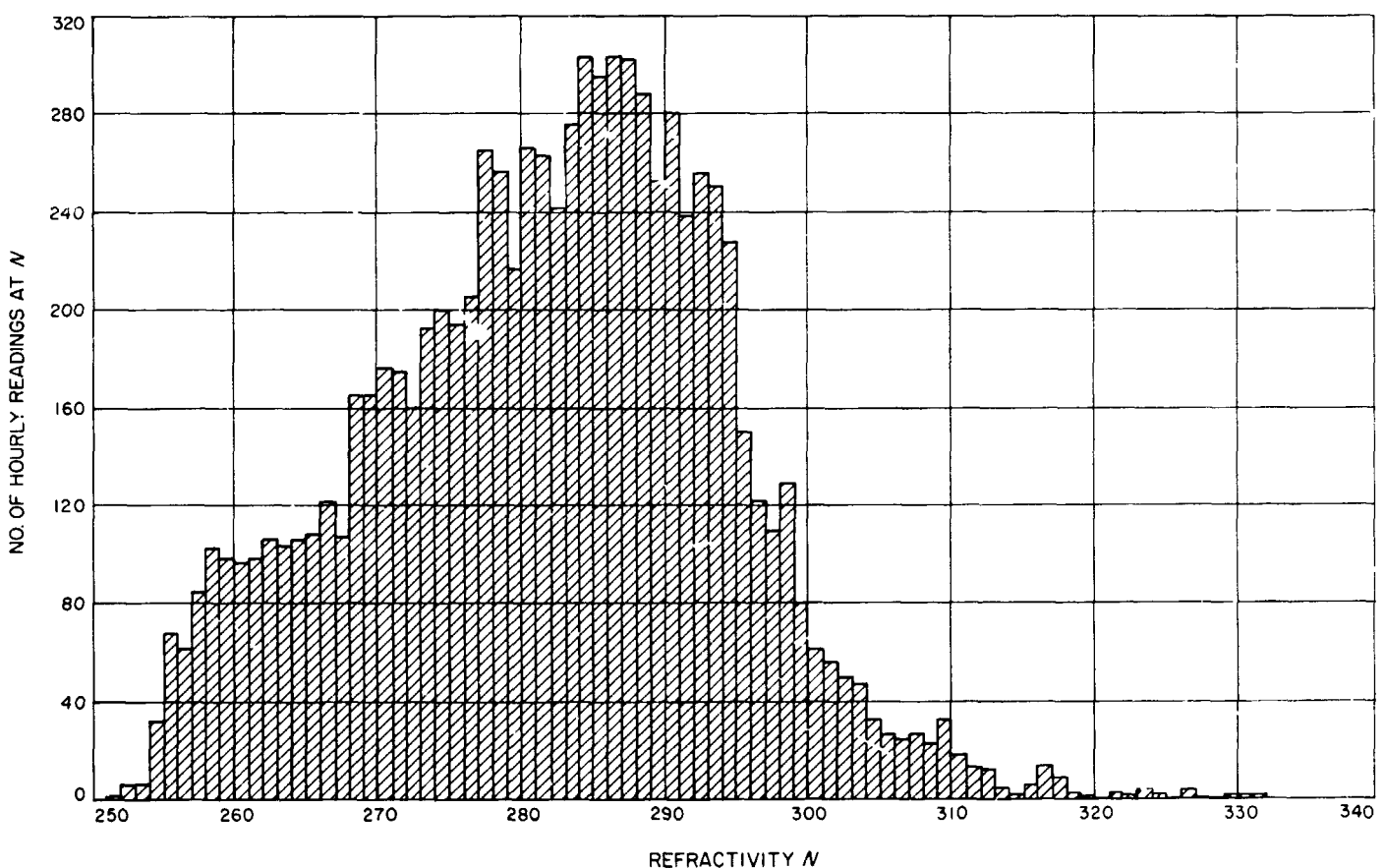


Fig. 3. Refractivity distribution for 1966

The variation in refractivity during each day and from day to day during the month of September is illustrated in Fig. 4. The month of September was chosen because of the wide variations during the month. The mean daily variation in refractivity for the year was 24.2 with a maximum daily variation of 45.

Since balloon data was not taken at regularly spaced intervals, the scale height data was not in a form to yield a complete analysis as was the refractivity data. The scale height during the year varied from a minimum of 3.83 km to a maximum of 25.05 km. In several cases, the expo-

ponential model for the index of refraction was not applicable. In these cases, the refractivity profile was parabolic rather than exponential as shown in Fig. 5.

d. Effects on high-precision ranging. In SPS 37-43, Vol. IV, pp 314-321, we presented formulas yielding corrections to range, doppler, and elevation angle for a signal passing through the earth's atmosphere. The range correction formula is

$$R_c = \alpha \left(\frac{\pi}{\beta} \right)^{1/2} \frac{e^{\beta(1-b_0)}}{(1+b_0)^{1/2}} \operatorname{erfc}((\beta(1-b_0))^{1/2}) \quad (6)$$

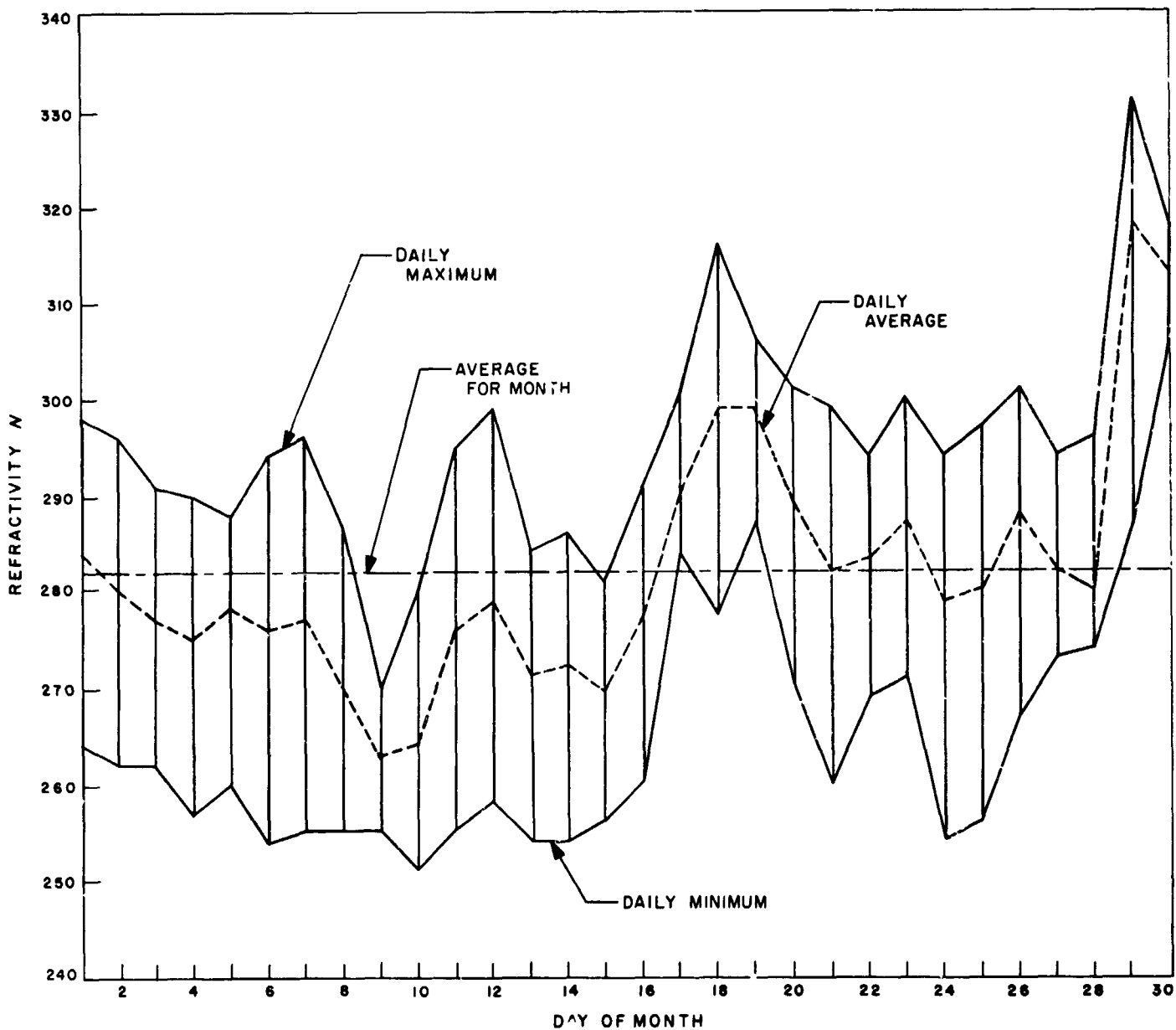


Fig. 4. Variations in refractivity for September 1966

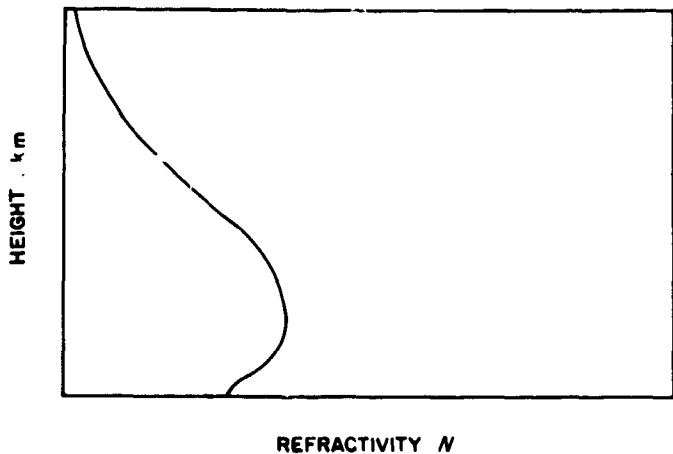


Fig. 5. Example of parabolic refractivity profile

the doppler correction formula (range rate) is

$$\dot{R}_c = \frac{2\alpha(r_1^2 - b_0^2)^{1/2}}{(r_1^2 - b_0^2)^{1/2} - (1 - b_0^2)^{1/2}} \left(\dot{\theta} - \frac{b_0 \dot{r}_1}{(r_1^2 - b_0^2)^{1/2} r_1} \right) \times (1 - (\beta\pi(1 - b_0))^{1/2} e^{\beta(1-b_0)} \operatorname{erfc}((\beta(1 - b_0))^{1/2})) \quad (7)$$

and the elevation angle correction formula is

$$e_s = \frac{\alpha}{(r_1^2 - b_0^2)^{1/2} - (1 - b_0^2)^{1/2}} \times \left[\left(\frac{\beta\pi(r_1^2 - b_0^2)^{1/2}}{1 + b_0} \right)^{1/2} e^{\beta(1-b_0)} \operatorname{erfc}((\beta(1 - b_0))^{1/2}) - 1 \right] \quad (8)$$

In the above formulas $\beta = 1/h$, $b_0 =$ straight line impact parameter

$$\frac{r_1 \sin \theta}{(1 + r_1^2 - 2r_1 \cos \theta)^{1/2}}$$

$r_1 =$ straight line range to spacecraft, $\dot{r}_1 =$ straight line range rate to spacecraft, $\dot{\theta} =$ rate of change of spacecraft-center of earth-station angle, $\operatorname{erfc}(x) =$ complementary error function of x , and all lengths are measured in earth radii.

We wish now to look at the effects that maximum variations in scale height and refractivity have on range,

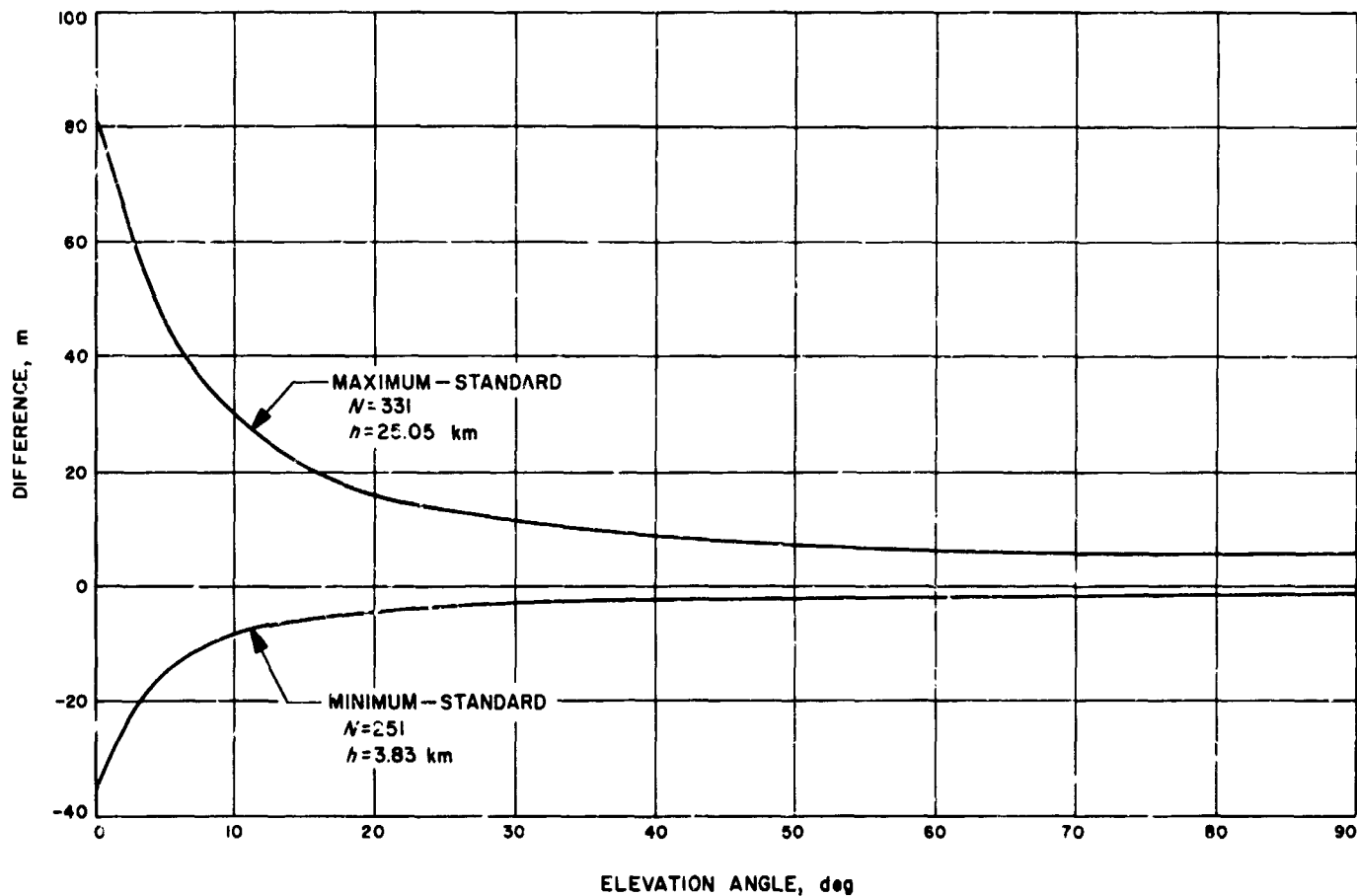


Fig. 6. Difference between maximum and minimum range corrections and standard range correction

doppler, and elevation angle. We shall assume that $r_1 = 10^4$ km, $\dot{r}_1 = 3$ km/sec, and $\dot{\theta} = 7.3 \times 10^{-5}$ rad/sec (rotation rate of the earth). The range correction, Eq. (6), and the doppler correction, Eq. (7), are minimum when scale height and refractivity are minimum; and they are maximum when scale height and refractivity are maximum. The elevation angle correction, Eq. (8), is minimum when scale height is maximum and refractivity is minimum; and the elevation angle correction is maximum when the conditions are reversed.

If we assume a standard atmosphere for the year based on the average refractivity and average scale height, then we can compare the maximum and minimum variations in range, doppler, and elevation angle corrections with this standard model. The average scale height was 9 km, but this figure is not as reliable as the average refractivity since the data was taken at irregular intervals.

Assuming an S-band frequency of 2388 MHz, we have plotted the results of this comparison in Figs. 6, 7, and 8.

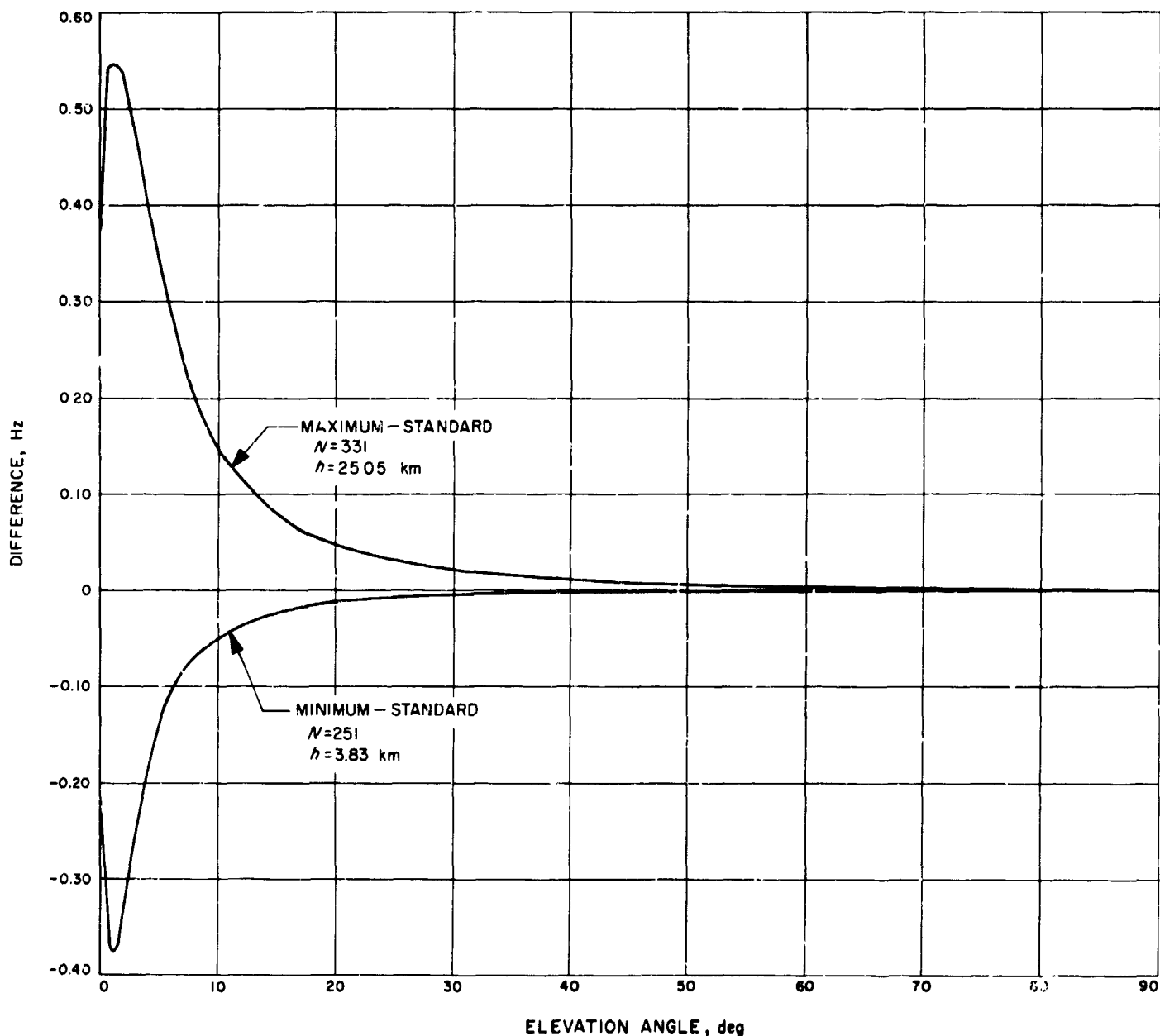


Fig. 7. Difference between maximum and minimum doppler corrections and standard doppler correction

The largest variation from the standard in each figure is seen to occur for the maximum correction. The non-exponential character of the range and doppler correction curves is due to the different rates at which the maximum and minimum corrections decrease with respect to the standard correction. The actual correction curves themselves decrease exponentially.

e. Conclusions. If we examine Figs. 6, 7, and 8, especially at low elevation angles, we see then the variation

from the standard correction can be quite sizable. The variation between the maximum and standard range corrections can be sizable even at quite high elevation angles.

These results all point up to the fact that if higher tracking accuracies are to be realized, then atmospheric parameters for range, doppler, and elevation angle corrections will have to be obtained on a real-time basis. We realize that we have chosen to compare maximum and minimum conditions for the entire year with the standard, but these

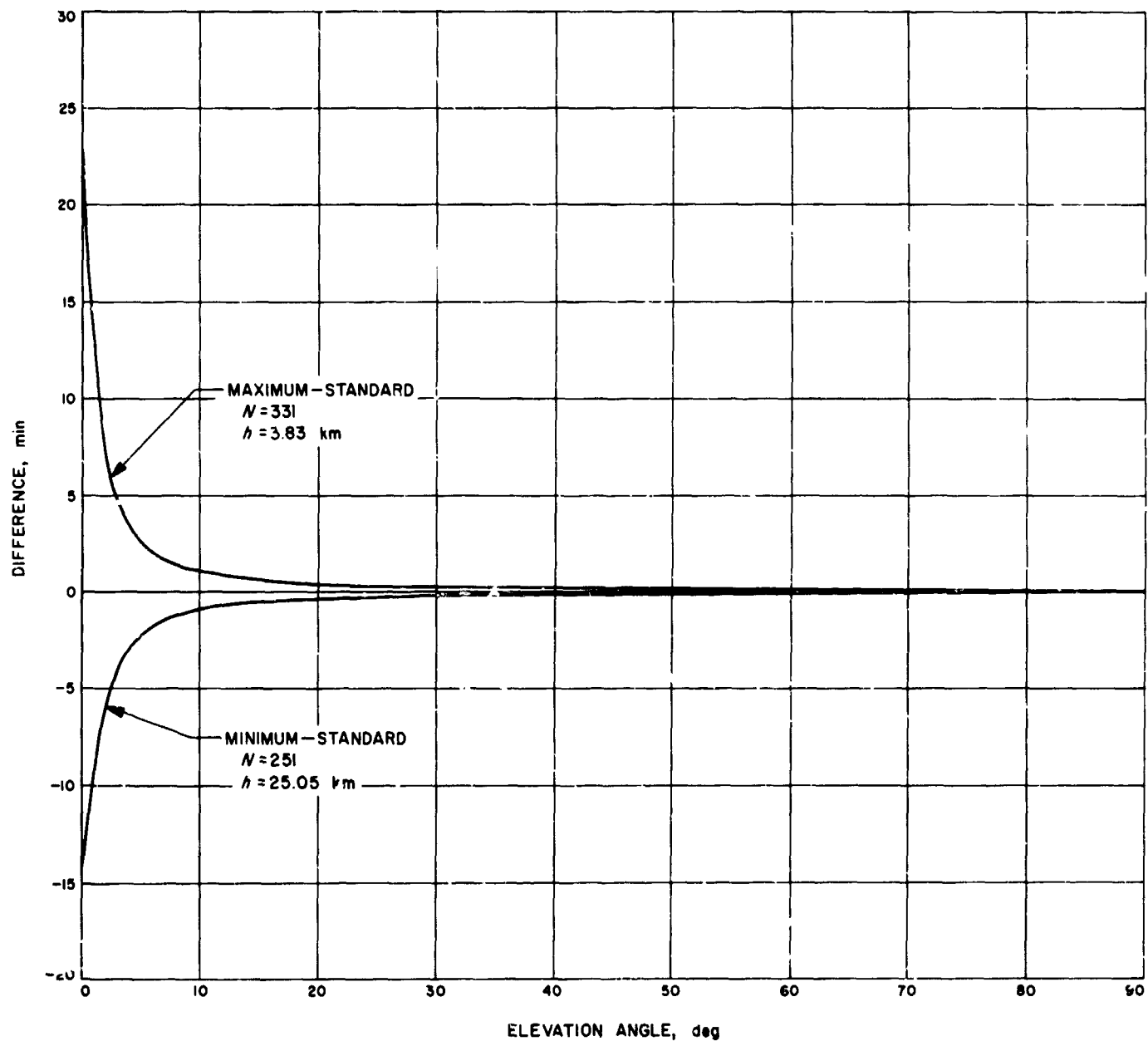


Fig. 8. Difference between maximum and minimum elevation angle corrections and standard elevation angle correction

are conditions that will occur. Also, as was pointed out earlier, the exponential model for the index of refraction did not fit in some cases. This is a problem that still needs to be resolved.

If obtaining real-time atmospheric parameters proves impractical, then we must decide, on a statistical basis, how much of the time, for a given length of time, a local model will hold within error limits. This, however, may not be possible, since weather is not predictable with the same accuracy as the tracking accuracies involved.

D. Communication Systems Development,

W. C. Lindsey and A. J. Viterbi

1. Error Rates in Phase Coherent Systems With Bandpass Limiters, W. C. Lindsey

a. Introduction. Recently, considerable interest has developed in attempting to understand how a bandpass limiter affects the performance of one-way locked, coherent (phase-shift keyed, PSK) and differentially coherent (DPSK) data demodulators. Such demodulators are typical of the *Mariner*- and *Pioneer*-type transmission-data detection systems. The subject of this article is, therefore, to develop mathematical models for overall system performance as a function of well-defined system parameters. These parameters are defined such that measurements taken from various passes of the spacecraft may be used to evaluate and predict system performance at various times after launch. The results are also useful in predicting system performance prior to launch, and in evaluating the performance of a particular laboratory simulation. *To avoid discrepancies in practice versus theory, it is necessary that the parameters in the test set-up (or spacecraft-to-DSIF link) be compatible, in definition, with those which follow.* This frequent error is the prime motivation behind this article.

b. System model. Briefly, the transmitter emits a low-index phase-modulated wave such that, out of the total radiated power of P watts, P_c watts remain in the carrier component for purposes of tracking, and S watts is allocated to the data signal. The total transmitter power is, therefore,

$$P = P_c + S + P_l \quad (1)$$

where P_l is any loss which may occur due to the modulation process.

If the signaling states are assumed to occur with equal probability and the data signals are negatively correlated

and contain equal energies, the conditional bit-error probability, conditioned upon a fixed RF carrier-loop phase error ϕ , of a PSK system, may be shown (Ref. 13) to be given by

$$P_E(\phi) = \frac{1}{(2\pi)^{1/2}} \int_{(2R)^{1/2} \cos \phi}^{\infty} \exp\left[-\frac{x^2}{2}\right] dx; \quad (\text{PSK}) \quad (2)$$

where

$$R = \frac{ST_b}{N_0} \quad (3)$$

with S = signal power, $N_0 = kT^\circ$ = single-sided spectral density of the channel noise, k = Boltzmann's constant, T° = system temperature in $^\circ\text{K}$, and T_b = duration of the data bits. The average bit-error probability is easily obtained by averaging over the probability distribution $p(\phi)$ of the phase error. This distribution has been characterized in Ref. 14 and we shall define it in a later section.

In the case of detecting DPSK signals, the conditional bit-error probability is easily shown (Refs. 15, 16) to be given by

$$P_E(\phi) = \frac{1}{2} \exp[-R \cos^2 \phi]; \quad (\text{DPSK}) \quad (4)$$

where the parameter R is defined in Eq. (3).

The average bit-error probability becomes

$$P_E = \int_{-\pi}^{\pi} p(\phi) P_E(\phi) d\phi \quad (5)$$

where substitution of Eq. (2) for $P_E(\phi)$ into Eq. (5) yields the average performance of a PSK system, while substitution of Eq. (4) into Eq. (5) yields the average performance of a DPSK system.

c. Probability distribution model for $p(\phi)$. The characterization of the distribution $p(\phi)$ requires considerable elaboration (beyond the scope of this article) on the response (signal plus noise) of a phase-locked loop when preceded by a bandpass limiter. Suffice it to say, however, that the distribution may be modeled on the basis of experimental and theoretical evidence given in Refs. 14,

17, 18, and 19. Calling upon this body of theory, the distribution for $p(\phi)$ is well approximated by

$$p(\phi) = \frac{\exp[\rho_L \cos \phi]}{2\pi I_0(\rho_L)}; \quad |\phi| < \pi \quad (6)$$

where

$$\rho_L = \frac{2P_c}{N_0 \omega_{L0}} \cdot \frac{1}{\Gamma} \left(\frac{1+r_0}{1+\frac{r_0}{\mu}} \right) \quad (7)$$

and the parameters ω_{L0} , r_0 , and μ are defined from the closed-loop transfer function $H(s)$ of the carrier tracking loop, i.e.,

$$H(s) = \frac{1 + \left(\frac{r_0 + 1}{2\omega_{L0}} \right) s}{1 + \left(\frac{r_0 + 1}{2\omega_{L0}} \right) s + \frac{\mu}{r_0} \left(\frac{r_0 + 1}{2\omega_{L0}} \right)^2 s^2} \quad (8)$$

Here μ is taken to be the ratio of the limiter suppression factor α_0 at the loop's "design-point" (usually referred to as threshold) to the limiter suppression, say α , at any other point, i.e., $\mu = \alpha_0/\alpha$. This, of course, assumes that the filter in the carrier tracking loop is of the form

$$F(s) = \frac{1 + \tau_1 s}{1 + \tau_2 s} \quad (9)$$

in which case

$$r_0 = \alpha_0 K \frac{\tau_2^2}{\tau_1} \quad (10)$$

where K is the equivalent simple-loop gain (Ref. 17). The subscripts "0" refer to the values of the parameters at the loop "design-point." The parameter ω_{L0} is defined by

$$\omega_{L0} = \frac{1 + r_0}{2\tau_2 \left(1 + \frac{\tau_2}{r_0 \tau_1} \right)} \quad (11)$$

It is convenient to define the loop bandwidths ω_L and b_L through the relationship

$$\omega_L = 2b_L = \frac{1}{2\pi f} \int_{-\infty}^{+\infty} |H(s)|^2 ds \quad (12)$$

Substitution of Eq. (8) into Eq. (12) yields

$$\omega_L = \omega_{L0} \left[\frac{1 + \frac{r_0}{\mu}}{1 + r_0} \right] = 2b_L \quad (13)$$

Analogously, one may define $\omega_{L0} = 2b_{L0}$ in which case Eq. (13) becomes

$$2b_L = (2b_{L0}) \left[\frac{1 + \frac{r_0}{\mu}}{1 + r_0} \right] \quad (14)$$

This is the usual definition of loop bandwidth. Here we use lower-case letters to denote these bandwidths so as to conform to the standard set by Tausworthe (Ref. 17). The factor Γ is well approximated (Ref. 17) by

$$\Gamma = \frac{1 + 0.345 \rho_H}{0.862 + 0.690 \rho_H} \quad (15)$$

where ρ_H is the signal-to-noise ratio at the output of the receiver's IF amplifier, i.e.,

$$\rho_H = \frac{2P_c}{N_0 \omega_H} \quad (16)$$

The parameter ω_H is the two-sided bandwidth of the second IF amplifier in the double-heterodyne receiver. In one-sided bandwidth notation, $\omega_H = 2b_H$ and

$$\rho_H = \frac{P_c}{N_0 b_H} \quad (17)$$

The parameter ρ_H is also the signal-to-noise ratio at the input to the bandpass limiter.

The remaining parameter to define is the factor $\mu = \alpha_0/\alpha$. It may be shown that limiter suppression α is given by

$$\alpha = \left(\frac{\pi}{2} \right)^{1/2} \left(\frac{\rho_H}{2} \right)^{1/2} \exp \left[-\frac{\rho_H}{2} \right] \left\{ I_0 \left(\frac{\rho_H}{2} \right) + I_1 \left(\frac{\rho_H}{2} \right) \right\} \quad (18)$$

where $I_k(z)$, $k = 1, 2$, is the modified Bessel function of argument z and order. To specify α_0 we rewrite the

parameter ρ_H as follows, viz,

$$\rho_H = \frac{P_c}{N_0 b_H} \cdot \frac{b_{L0}}{b_{L0}} = \frac{P_c}{N_0 b_{L0}} \cdot \frac{b_{L0}}{b_H} = zy \quad (19)$$

where

$$z = \frac{P_c}{N_0 b_{L0}}; \quad y = \frac{b_{L0}}{b_H} \quad (20)$$

In practice, the parameters of the carrier tracking loop are specified at a point which we have referred to as the loop "design-point" (sometimes called threshold). If we define the design point as $z_0 = Y_0 = \text{constant}$, then the parameter α_0 is given by

$$\alpha_0 = \left(\frac{\pi}{2}\right)^{1/2} \left(\frac{Y_0 y}{2}\right)^{1/2} \exp\left[-\frac{Y_0 y}{2}\right] \left\{ I_0\left(\frac{Y_0 y}{2}\right) + I_1\left(\frac{Y_0 y}{2}\right) \right\} \quad (21)$$

From Eq. (21) it is, therefore, clear that system performance, namely P_E , depends upon the choice of Y_0 . In the DSN this choice is usually taken to be $Y_0 = 2$ so that

$$z_0 = \frac{P_{c0}}{(kT_0)(b_{L0})} = 2 \quad (22)$$

or, equivalently,

$$\frac{P_{c0}}{(kT_0)_0 (2b_{L0})} = 1$$

at the design point. In the next section we explore the dependence of P_E upon z , and R for the case where $Y_0 = 1$ and $Y_0 = 2$, $r_0 = 2$, and $y = 1/200$.

The variance of the distribution $p(\phi)$ is given by

$$\sigma_\phi^2 = \int_{-\pi}^{\pi} \phi^2 p(\phi) d\phi \quad (23)$$

Substitution of Eq. (6) into Eq. (23) and carrying out the integration yields

$$\sigma_\phi^2 = \frac{\pi^2}{3} + \frac{4}{I_0(\rho_L)} \cdot \sum_{k=1}^{\infty} \frac{(-1)^k I_k(\rho_L)}{k^2} \quad (24)$$

where the functions $I_k(u)$ are imaginary Bessel functions. The variance of the phase error is plotted in Fig. 9 for

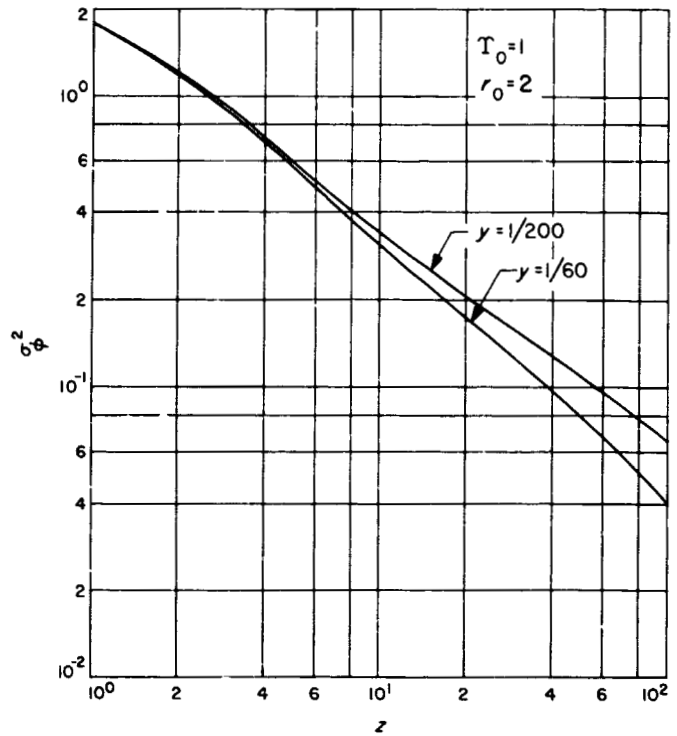


Fig. 9. Phase error variance σ_ϕ^2 vs signal-to-noise ratio z in the carrier tracking loop

various values of z with $r_0 = 2$, $Y_0 = 1$ and $y = 1/200$, $y = 1/60$. This variance is in close agreement with the variance predicted from Tausworthe's linear spectral method (Ref. 17).

d. Error rates in PSK and DPSK detectors. Assuming that $r_0 = 2$ (corresponds to a damping factor of 0.707 in the loop as determined from linear phase-locked loop theory), the error probability for PSK systems is easily determined from the material and definitions given in previous sections, viz,

$$P_E = \int_0^\pi \frac{\exp(\rho_L \cos \phi)}{\pi I_0(\rho_L)} \operatorname{erfc}[(2R)^{1/2} \cos \phi] d\phi \quad (25)$$

where

$$\operatorname{erfc}(\beta) = \int_\beta^\infty \frac{1}{(2\pi)^{1/2}} \exp\left(-\frac{z^2}{2}\right) dz \quad (26)$$

$$\rho_L = \frac{3z}{\Gamma\left(1 + \frac{2}{\mu}\right)}; \quad R = \frac{ST_b}{N_0} \quad (27)$$

$$\Gamma = \frac{1 + 0.345 zy}{0.862 + 0.690 zy} \quad (28)$$

$$z = \frac{P_c}{N_0 b_{L0}}; \quad y = \frac{b_{L0}}{b_H} \quad (29)$$

$$\mu = \frac{(Y_0)^{1/2} \exp\left(-\frac{Y_0 y}{2}\right) \left[I_0\left(\frac{Y_0 y}{2}\right) + I_1\left(\frac{Y_0 y}{2}\right) \right]}{(z)^{1/2} \exp\left(-\frac{zy}{2}\right) \left[I_0\left(\frac{zy}{2}\right) + I_1\left(\frac{zy}{2}\right) \right]} \quad (30)$$

$$Y_0 = \frac{P_{c0}}{N_0 b_{L0}} \quad (31)$$

The integration in Eq. (25) may be carried out (Ref. 13); however, the resulting infinite series of Bessel functions does not shed appreciable light upon its behavior as a

function of x and R . To illustrate this behavior, Eq. (25) has been evaluated numerically on a digital computer for various values of the parameters R , $x = z/2$ for $Y_0 = 1$ and $Y_0 = 2$ with $r_0 = 2$, $y = 1/400$. These results are given in Figs. 10 and 11.

Similarly, the performance of DPSK systems is given by

$$P_E = \int_0^\pi \frac{\exp(\rho_L \cos \phi - N \cos^2 \phi)}{2\pi I_0(\rho_L)} d\phi \quad (32)$$

where ρ_L is defined in Eq. (27). Again the integration may be carried out; however, computer results are best obtained by numerical integration of Eq. (32). Results of

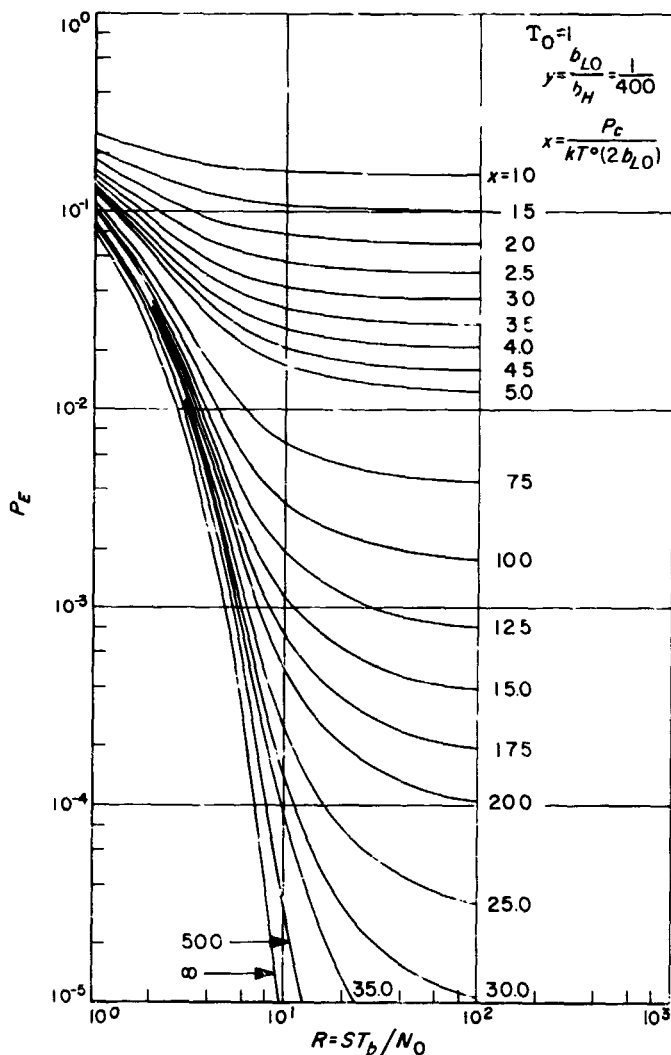


Fig. 10. Error probability P_E vs signal-to-noise ratio R in the data ST_b/N_0 ($r_0 = 2$; $Y_0 = 1$; PSK signaling assumed)

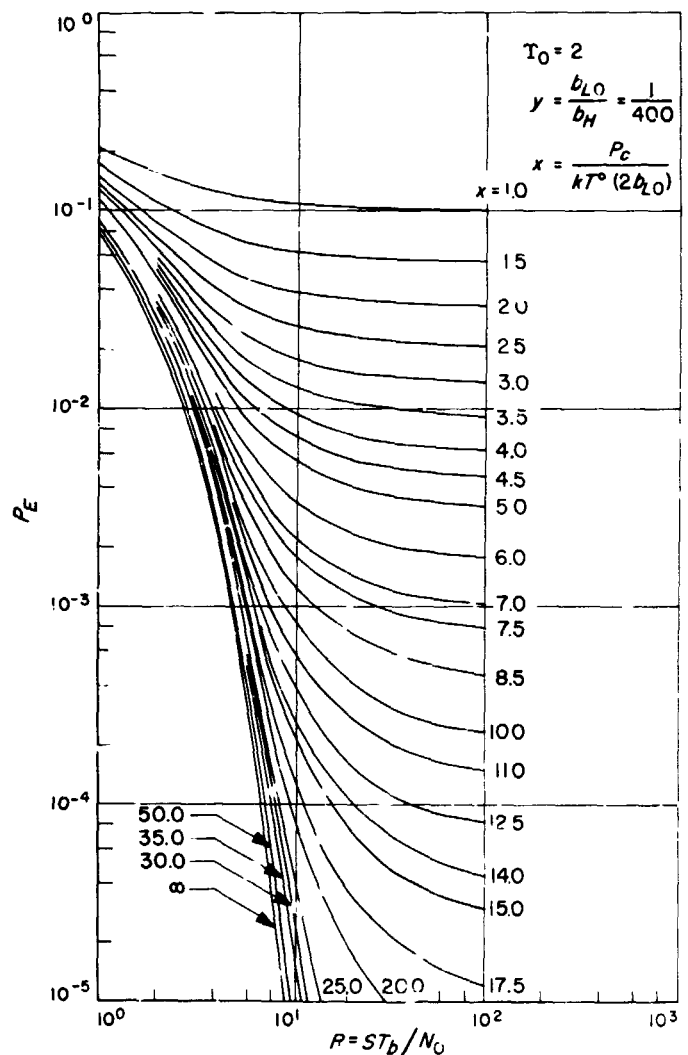


Fig. 11. Error probability P_E vs signal-to-noise ratio R in the data ST_b/N_0 ($r_0 = 2$; $Y_0 = 2$; PSK signaling assumed)

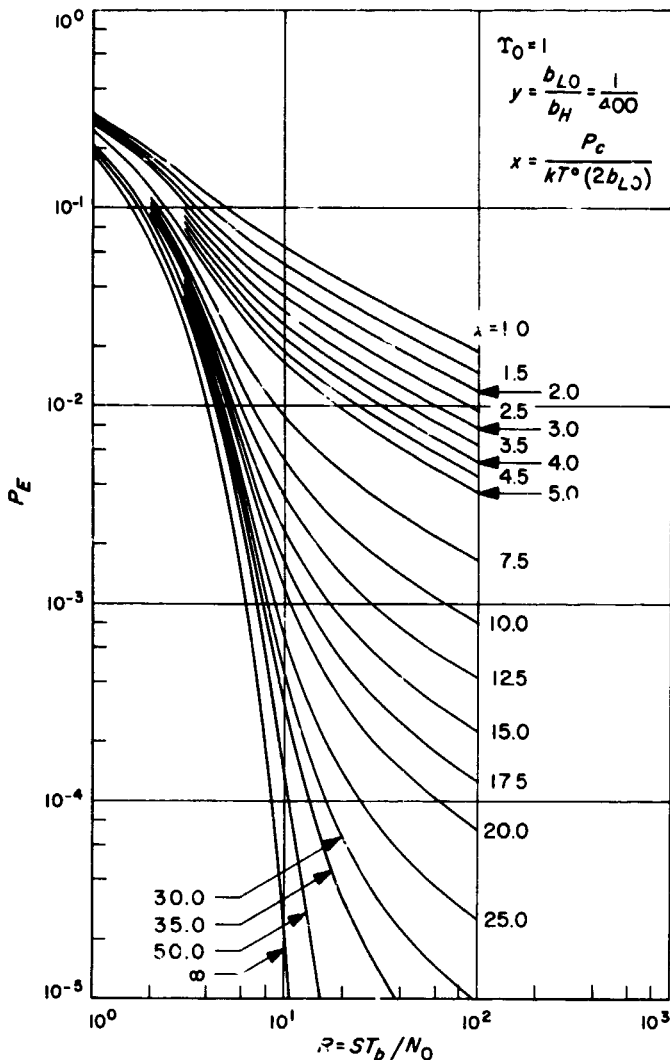


Fig. 12. Error probability P_E vs signal-to-noise ratio R in the data ST_b/N_0 ($r_0 = 2$; $\Upsilon_0 = 1$; DPSK signaling assumed)

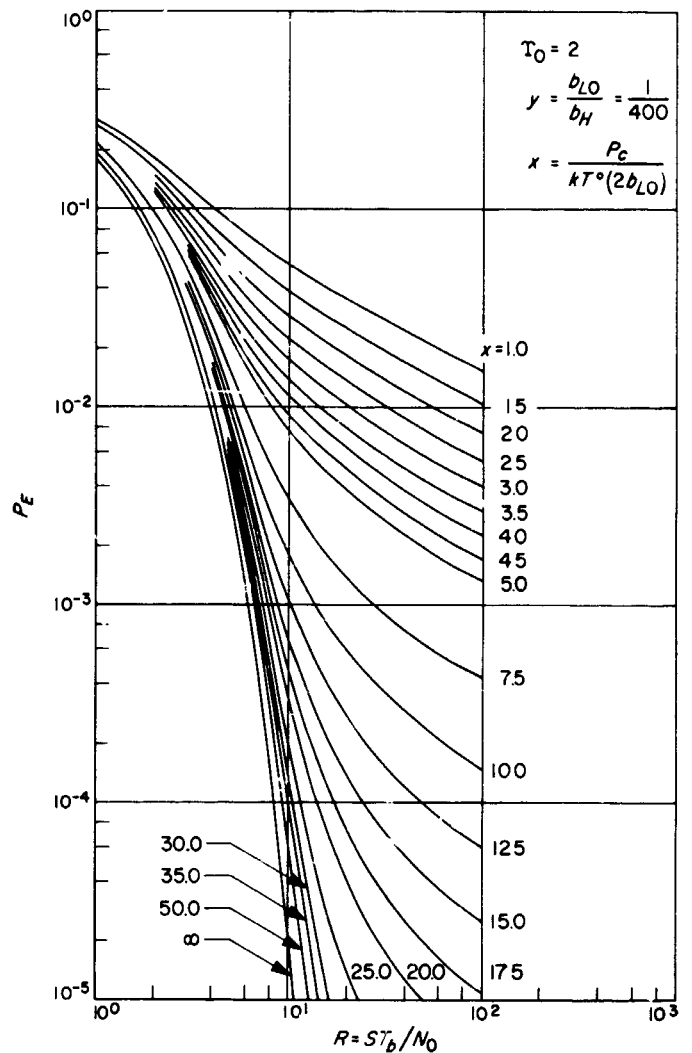


Fig. 13. Error probability P_E vs signal-to-noise ratio R in the data ST_b/N_0 ($r_0 = 2$; $\Upsilon_0 = 2$; DPSK signaling assumed)

these computations are illustrated in Figs. 12 and 13 with $\Upsilon_0 = 1$, $\Upsilon_0 = 2$, $r_0 = 2$, $y = 1/400$ for various values of $R = ST_b/N_0$ and $x = P_c/(kT^0)(2b_{LO})$.

e. Error rates in Pioneer-type data detectors. The conditional error probability in the *Pioneer* system mechanization is such that² the total error probability is given by

$$P_{E_t} = 2 \int_{-\pi}^{\pi} p(\phi) P_E(\phi) [1 - P_L(\phi)] d\phi \quad (33)$$

where $P_E(\phi)$ is given by Eq. (2). Performing the integration numerically on the IBM 7094 computer yields the results shown in Fig. 14 for $\Upsilon_0 = 2$, $y = 1/400$, and vari-

ous values of x and $R = ST_b/N_0$. The results in Fig. 14 are easily compared with those given in Fig. 10 for a *Mariner*-type system. From Figs. 10 and 14 it is clear that the performance of a DPSK system, illustrated in Fig. 12, is superior to either the *Mariner*- or *Pioneer*-type system. This is due to the fact that a DPSK system makes correct decisions if the frequency of the voltage-controlled oscillator remains at the frequency of the incoming RF carrier, i.e., phase lock is not as significant in a system which employs differentially coherent detection.

f. System performance when the phase error is not constant over the duration of the signal. In previous sections we have been concerned with the performance of various communications systems where the phase error

²J. Layland, private communication

is constant over the duration of the modulation, i.e., T_b sec. In certain situations, e.g., command systems and low-rate telemetry systems, the assumption that the phase error of the system remains constant for T_b sec becomes suspect, and it is therefore of interest to understand how system performance changes. The basic system parameter, which is a measure of how stable the phase error is over the signal duration, is the ratio of the data rate to the bandwidth of the carrier tracking loop (Ref. 13). In Ref. 13 it is shown that the decision variables which a correlation receiver has to work with are given by

$$q_k = \int_0^T \cos \phi(t) x_k(t) [x_2(t) - x_1(t)] dt + \int_0^{T_b} n'(t) dt; \quad k = 1, 2 \quad (34)$$

where $x_1(t)$ and $x_2(t)$ are the transmitted signals, and $n'(t)$ is additive white Gaussian noise with a single-sided spectral density of N_0 watts/cycle. To determine the error probability, one must determine the probability density of $p(q_k)$ and from this compute the probability that q_k is less than zero, given that $x_2(t)$ was transmitted and vice versa. In general, this is a very difficult, if not formidable, problem; however, an upper bound on the best that one can expect to do is to compute the mean and variance of q_k on the basis that q_k is Gaussian. Such a procedure has been used by this author in determining the performance of linear analog demodulators (Ref. 20). Using the same procedure as outlined in Ref. 20, it is easy to show that the mean of q is given by

$$\bar{q}_2 = 2ST_b(\overline{\cos \phi}) \quad (35)$$

and from Eq. (6) we find that

$$\overline{\cos \phi} = \frac{I_1(\rho_L)}{I_0(\rho_L)} = \mu \quad (36)$$

This function has been studied in detail in Ref. 21. The variance of q_2 is easily shown to be given by

$$\sigma_{q_2}^2 = 2ST_b N_0 \quad (37)$$

Similarly, the mean of q_1 becomes

$$q_1 = -2ST_b(\overline{\cos \phi})$$

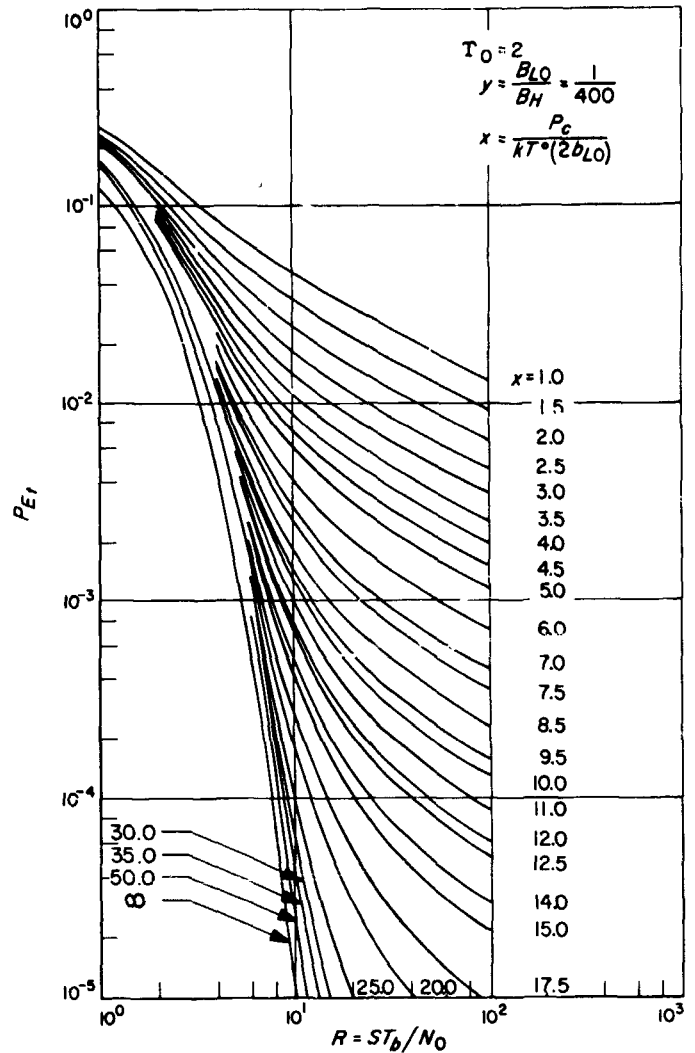


Fig. 14. Error probability P_E vs signal-to-noise ratio R in the data ST_b/N_0 ($r_0 = 2$; $\gamma_0 = 2$; Pioneer system; phase error assumed constant over duration of 1 bit)

and the variance of q_1 is

$$\sigma_{q_1}^2 = 2ST_b N_0 = \sigma_{q_2}^2 \quad (38)$$

If one characterizes the statistics of $p(q_k)$ as Gaussian and assumes equal probable signals, then the error probability for PSK systems is given by

$$P_E = \frac{1}{(2\pi)^{1/2}} \int_{(2\mu^2 R)^{1/2}}^{\infty} \exp\left(-\frac{y^2}{2}\right) dy; \quad (\text{PSK}) \quad (39)$$

This result agrees with one due to F. Reed in unpublished work³. For differentially coherent detection we have

$$P_E = \frac{1}{2} \exp[-\mu^2 R]; \quad (\text{DPSK}) \quad (40)$$

and the error rate for a *Pioneer*-type system becomes

$$P_{E_t} = 2P_E(1 - P_E) \quad (41)$$

³F. Reed, private communication of information developed for Motorola on contract 951700.

Equation (39) is plotted in Fig. 15 for various values of x , R with $y = 1/400$ and $\gamma_0 = 2$. Figure 16 illustrates a similar plot for DPSK systems, while Fig. 17 is a plot of Eq. (41). Thus, in any practical system we have upper and lower bounds on the error probability. The upper bound is for use in systems where the ratio of the data rate to the carrier-tracking loop bandwidth is large, i.e., the phase error is essentially constant over the duration of the signal. The lower bound is to be used in predicting the performance of systems where the ratio of the data rate to the carrier-tracking loop bandwidth is small, i.e., the phase error varies over the duration of the signal. For intermediate values of this ratio system performance lies between these two curves.

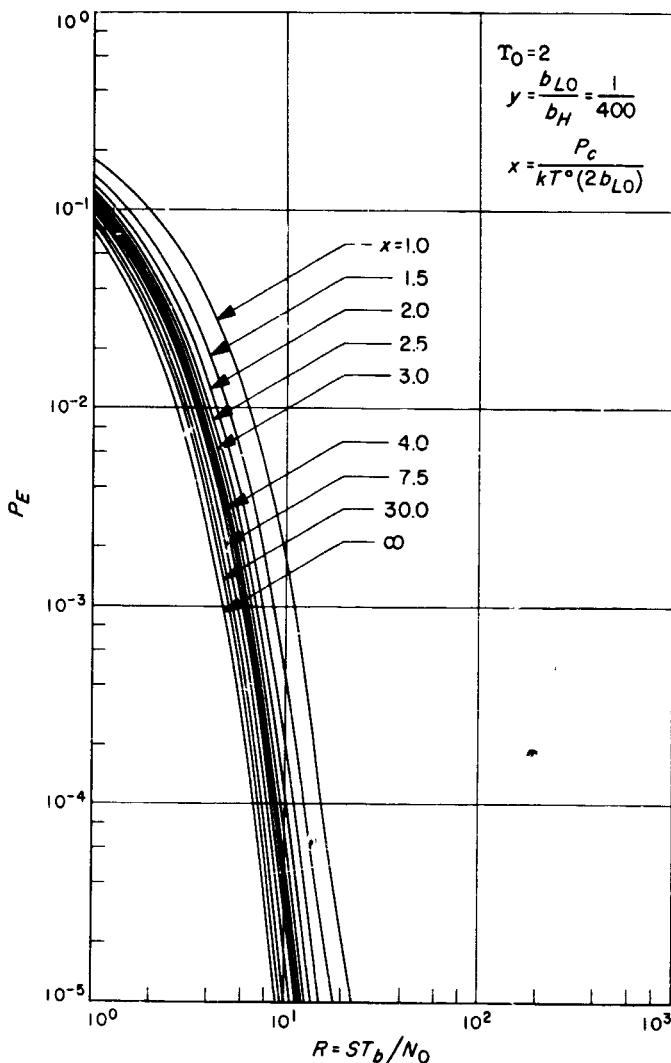


Fig. 15. Error probability P_E vs signal-to-noise ratio R in the data ST_b/N_0 ($r_0 = 2$; $\gamma_0 = 2$; phase error assumed to vary during transmission of 1 bit; PSK signaling assumed)

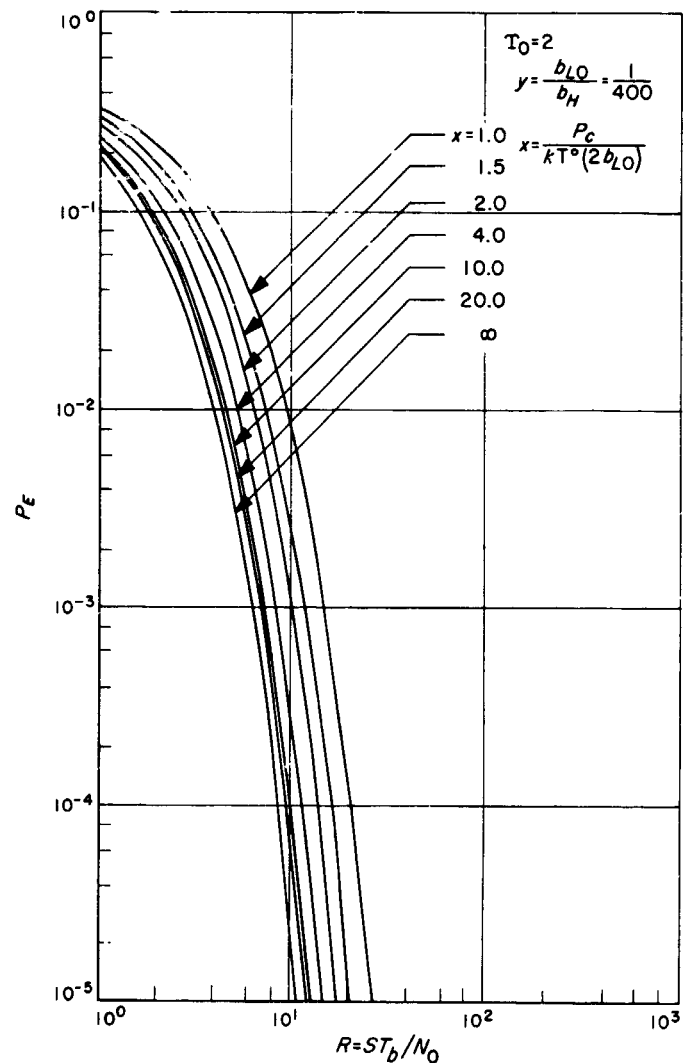


Fig. 16. Error probability P_E vs signal-to-noise ratio R in the data ST_b/N_0 ($r_0 = 2$; $\gamma_0 = 2$; phase error assumed to vary during transmission of 1 bit; DPSK signaling assumed)

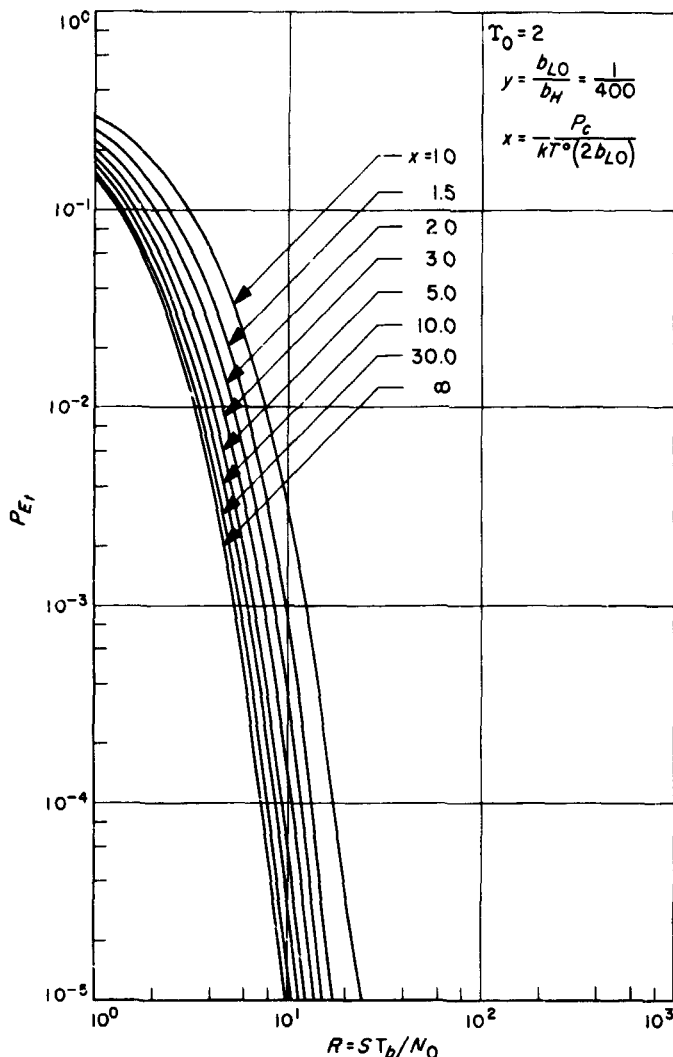


Fig. 17. Error probability P_E vs signal-to-noise ratio R in the data ST_b/N_0 ($r_0 = 2$; $\gamma_0 = 2$; Pioneer system; phase error assumed to vary during transmission of 1 bit)

2. Radio Losses in Block-Coded Communication Systems,

W. C. Lindsey

a. Introduction. In SPS 37-34, Vol. IV, pp. 242-247, SPS 37-36, Vol. IV, pp. 298-306, and Refs. 22 and 23, results were presented which allow one to optimally allocate the total transmitter power between the carrier and sidebands of a block-coded communication system. The purpose of this article is to evaluate the "radio losses" that are experienced in high-rate block-coded systems. The term "radio losses" needs defining. Here the term is taken to mean the degradation in system performance due to the fact that the modulation and demodulation processes are not perfect. The major contribution to this loss is due to the noisy reference derived by the carrier tracking loop in

the Deep Space Network and the phase modulation existing on the spacecraft's transmitted carrier that is due to the noise in the spacecraft's transponder receiver.

Two cases of the phenomenon are considered: (1) one-way reception where the spacecraft is operating with an auxiliary oscillator as a frequency reference, and (2) two-way reception. This situation corresponds to the case where the additive noise on the up-link affects the performance of the earth-based telemetry demodulator. We point out that the losses in one-way telemetry are the limiting cases for two-way reception (Ref. 23).

b. System performance. The conditional (conditioned on ϕ) word error probability for a block-coded system employing $(2^n, n)$ orthogonal codes has been shown (SPS 37-34, Vol. IV, pp. 242-247) to be given by

$$P_E(\phi) = 1 - \int_{-\infty}^{\infty} \frac{\exp\left(\frac{-y^2}{2}\right)}{(2\pi)^{1/2}} \{\text{erf}[y + (R)^{1/2} \cos \phi]\}^{2^{n-1}} dy \quad (1)$$

where $R = ST_b/N_0$ and

$$\text{erf}(x) = \frac{1}{(2\pi)^{1/2}} \int_{-\infty}^x \exp\left(\frac{-z^2}{2}\right) dz \quad (2)$$

For $(2^{n-1}, n)$ bi-orthogonal codes, the conditional (conditioned on ϕ) word error probability is given by

$$P_E(\phi) = 1 - \int_{-(2R)^{1/2} \cos \phi}^{\infty} \frac{\exp\left(\frac{-y^2}{2}\right)}{(2\pi)^{1/2}} \times \left[\int_{-y+(2R)^{1/2} \cos \phi}^{y+(2R)^{1/2} \cos \phi} \frac{\exp\left(\frac{-z^2}{2}\right)}{(2\pi)^{1/2}} dz \right]^{2^{n-1}-1} dy \quad (3)$$

where ϕ is the phase error due to the fact that the carrier tracking loop cannot track the phase of the observed carrier component with zero error. By averaging Eq. (1) over the probability distribution of ϕ , we obtain the average word error probability for either orthogonal or bi-orthogonal codes, i.e.,

$$P_{E_k}(n) = \int_{-\pi}^{\pi} p_k(\phi) P_E(\phi, n) d\phi, \quad k = 1, 2 \quad (4)$$

where $p_1(\phi)$ is the probability distribution of the phase error where the system is operating in a one-way mode, and $p_2(\phi)$ is the probability distribution of the phase error when the system is in two-way lock. In Ref. 13, it has been shown that

$$p_2(\phi) = \frac{I_0(\alpha_1^2 + \alpha_2^2 + 2\alpha_1\alpha_2 \cos \phi)^{1/2}}{2\pi I_0(\alpha_1) I_0(\alpha_2)}, \quad |\phi| \leq \pi \quad (5)$$

where

$$\begin{aligned} \alpha_1 &= \left(\frac{2P_{c1}}{N_{01}\omega_{L1}} \right) G^2 K(r_1, r_2, \beta) \\ \alpha_2 &= \frac{2P_{c2}}{N_{02}\omega_{L2}} = \frac{P_{c2}}{N_{02}b_{L2}} \\ K_R(r_1, r_2, \beta) &= \frac{r_1\beta}{r_2(r_1+1)} \left[\frac{r_2 + r_1r_2(\beta)(1+\beta) + \beta^2(1+\beta) + r_1\beta^3}{r_2(r_1+r_2)\beta + (r_2+r_1-2)\beta^2 + r_1\beta^3 + \frac{r_1\beta^4}{r^2}} \right] \\ \beta &= \frac{\omega_{L1}(r_1+1)}{\omega_{L2}(r_2+1)} \\ r_n &= \frac{(P_{cn})^{1/2} K_n \tau_{2n}^2}{\tau_{1n}}, \quad n = 1, 2 \\ \omega_{Ln} &= 2b_{Ln} = \frac{1}{2\pi j} \int_{-j\infty}^{j\infty} |H_n(s)|^2 dz \end{aligned} \quad (6)$$

and $H_n(s)$ is the closed-loop transfer function (in linear form) of the carrier tracking loops. On the other hand, $p_1(\phi)$ is obtained from $p_2(\phi)$ by allowing α_1 to approach infinity, i.e.,

$$\begin{aligned} p_1(\phi) &= \lim_{\alpha_1 \rightarrow \infty} p_2(\phi) \\ &= \frac{\exp[\alpha_2 \cos \phi]}{2\pi I_0(\alpha_2)}, \quad |\phi| < \pi \end{aligned} \quad (7)$$

where $\alpha_2 = \alpha = 2P_c/N_0\omega_L = P_c/N_0b_L$, i.e., one-way reception. Considerable experimental justification for the use of Eqs. (6) and (7) in characterizing the RF phase error is given in Refs. 18 and 19.

Equation (4) has been programmed, using Eqs. (1) and (7), on the IBM 7094 computer and evaluated numerically

for various values of the parameters R and α . The results of these computations are given in Fig. 18 for orthogonal codes with $n = 5, 6, 7$ and 8 . Similar results for two-way reception are shown in Figs. 19, 20, 21 and 22 for $n = 5, 6, 7$ and 8 . These results are obtained by substituting Eqs. (1) and (5) into Eq. (4) and performing the integration numerically on the IBM 7094 computer. Since the performance (Ref. 5) of block-coded systems which use orthogonal codes is, for all practical purposes, equivalent to the performance of a system which uses bi-orthogonal codes, the results in Figs. 18 through 22 may be used in the design of systems which use $(2^{n-1}, n)$ bi-orthogonal codes. The results are useful in evaluating the radio losses and designing high-rate block-coded systems.⁴ Similar results for uncoded systems are given in SPS 37-44, Vol. IV, pp. 282-290.

⁴Private communication, J. Knudsen and F. Reed.

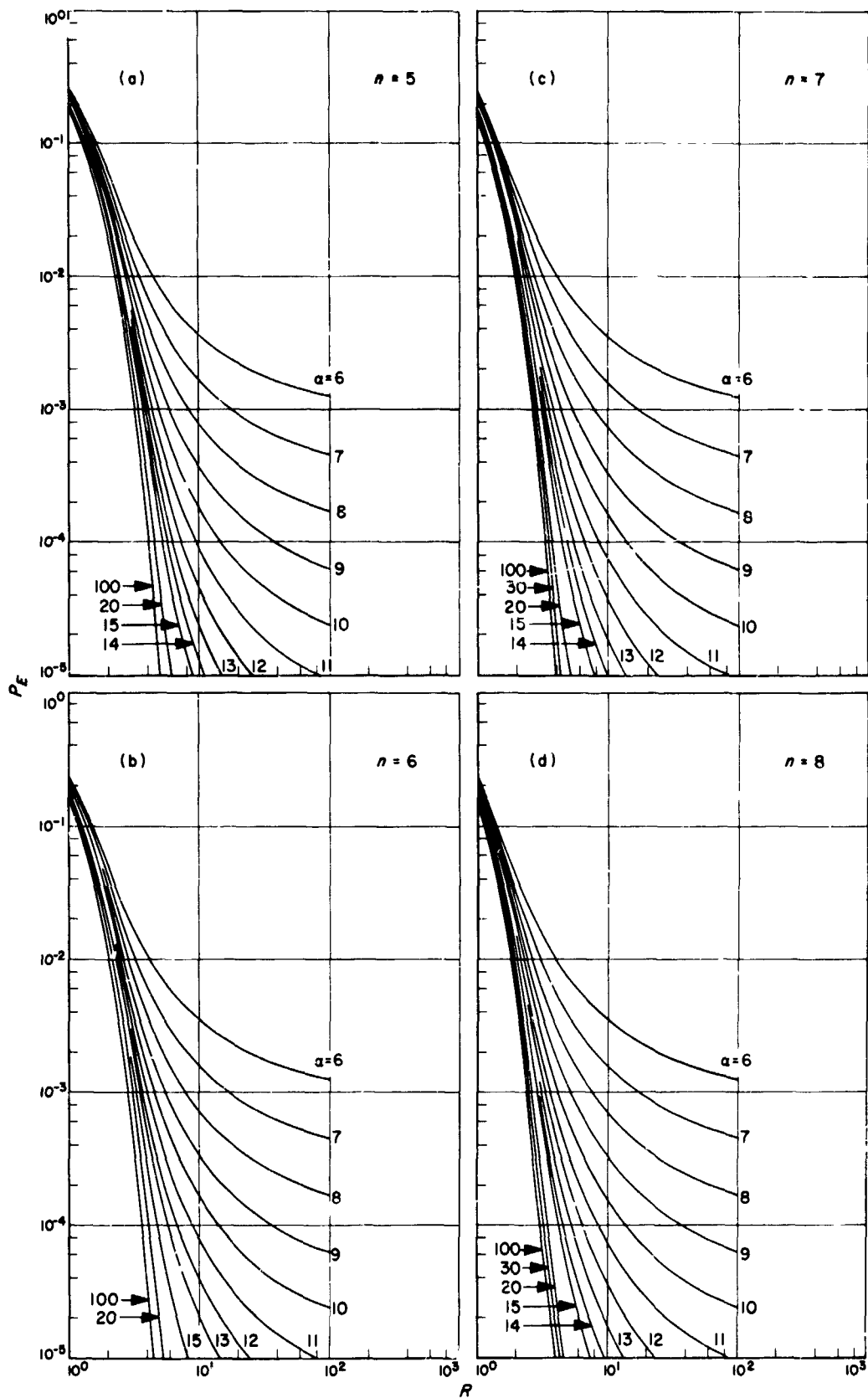


Fig. 18. Word error probability vs $R = ST_b/N_0$ for various values of $\alpha = P_c/N_0 b_L$: (a) $n = 5$, (b) $n = 6$, (c) $n = 7$, (d) $n = 8$

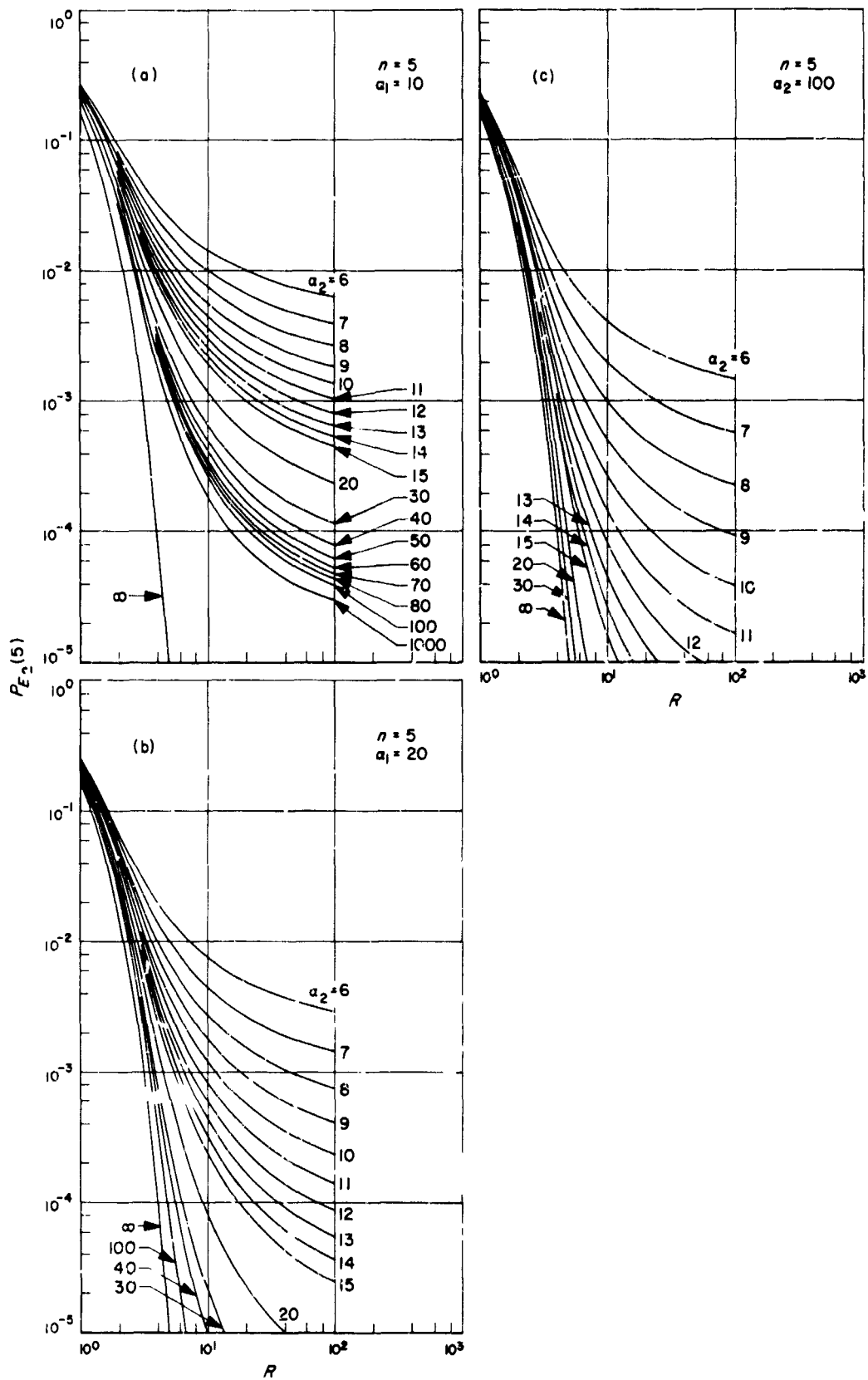


Fig. 19. Word error probability vs $R = ST_0/N_0$ for various values of α_2 with $n = 5$: (a) $\alpha_1 = 10$, (b) $\alpha_1 = 20$, (c) $\alpha_1 = 100$

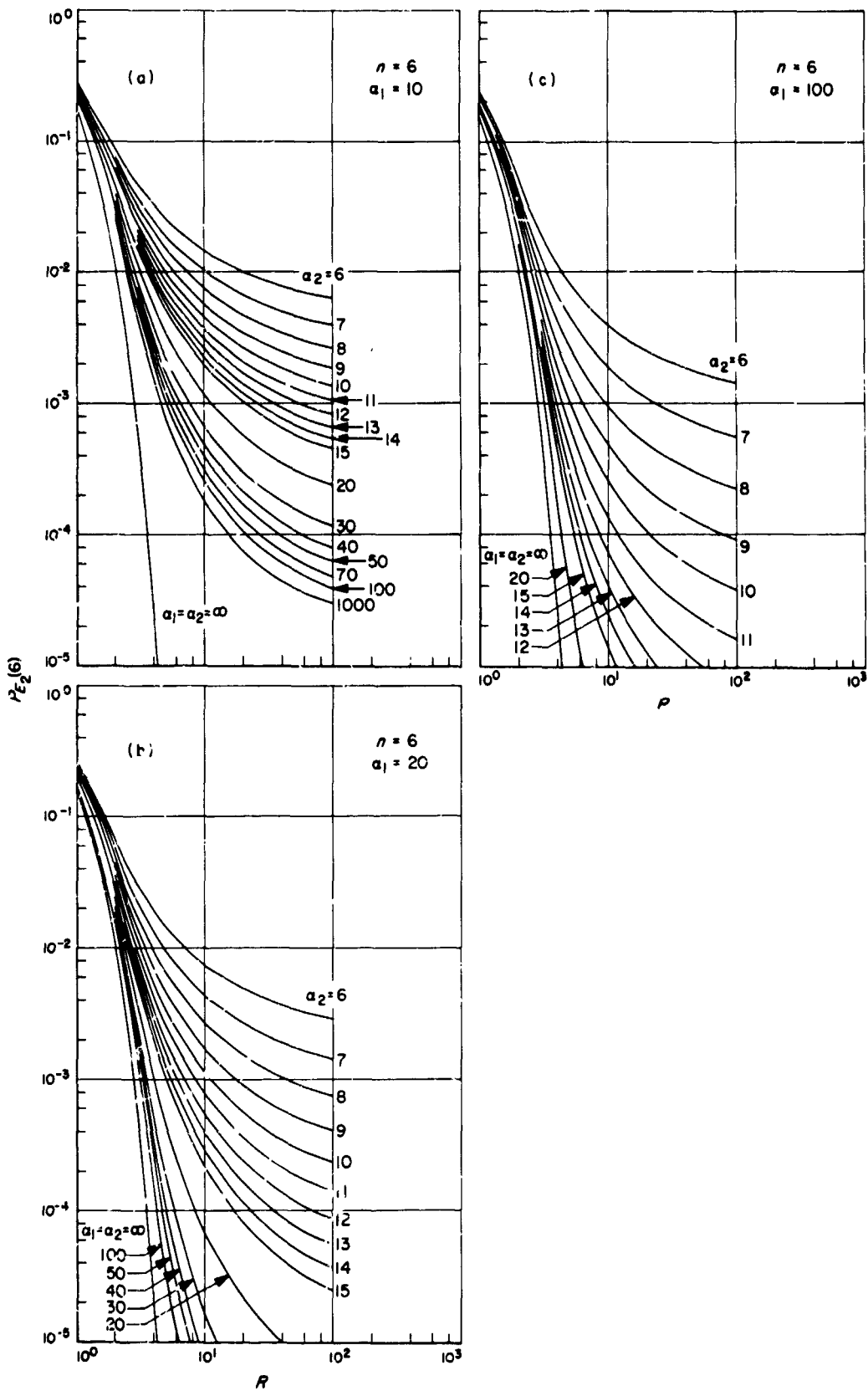


Fig. 20. Word error probability vs $R = ST_b/N_0$ for various values of α_2 with $n = 6$: (a) $\alpha_1 = 10$, (b) $\alpha_1 = 20$, (c) $\alpha_1 = 100$

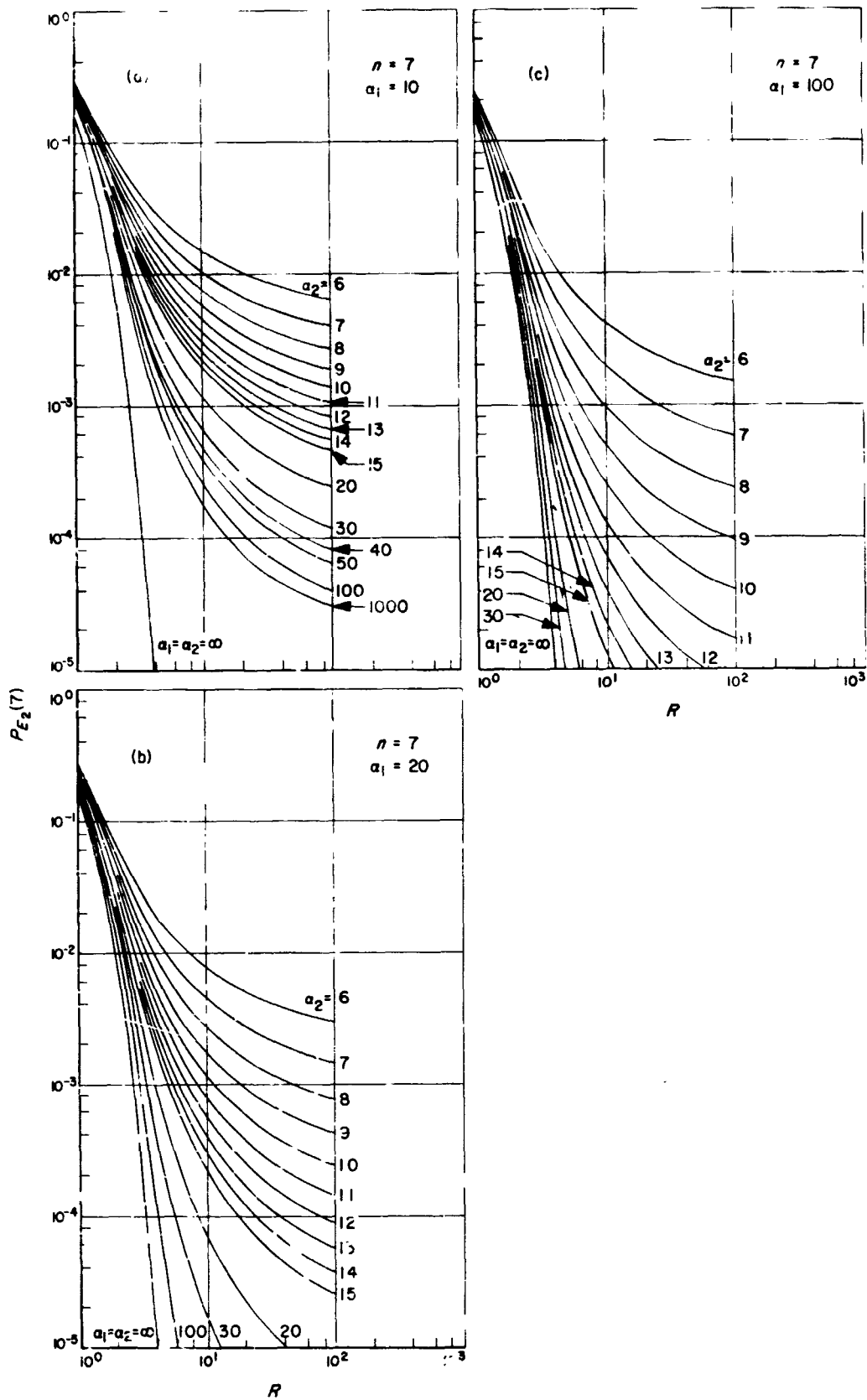


Fig. 21. Word error probability vs $R = ST_b/N_0$ for various values of α_2 with $n = 7$: (a) $\alpha_1 = 10$, (b) $\alpha_1 = 20$, (c) $\alpha_1 = 100$

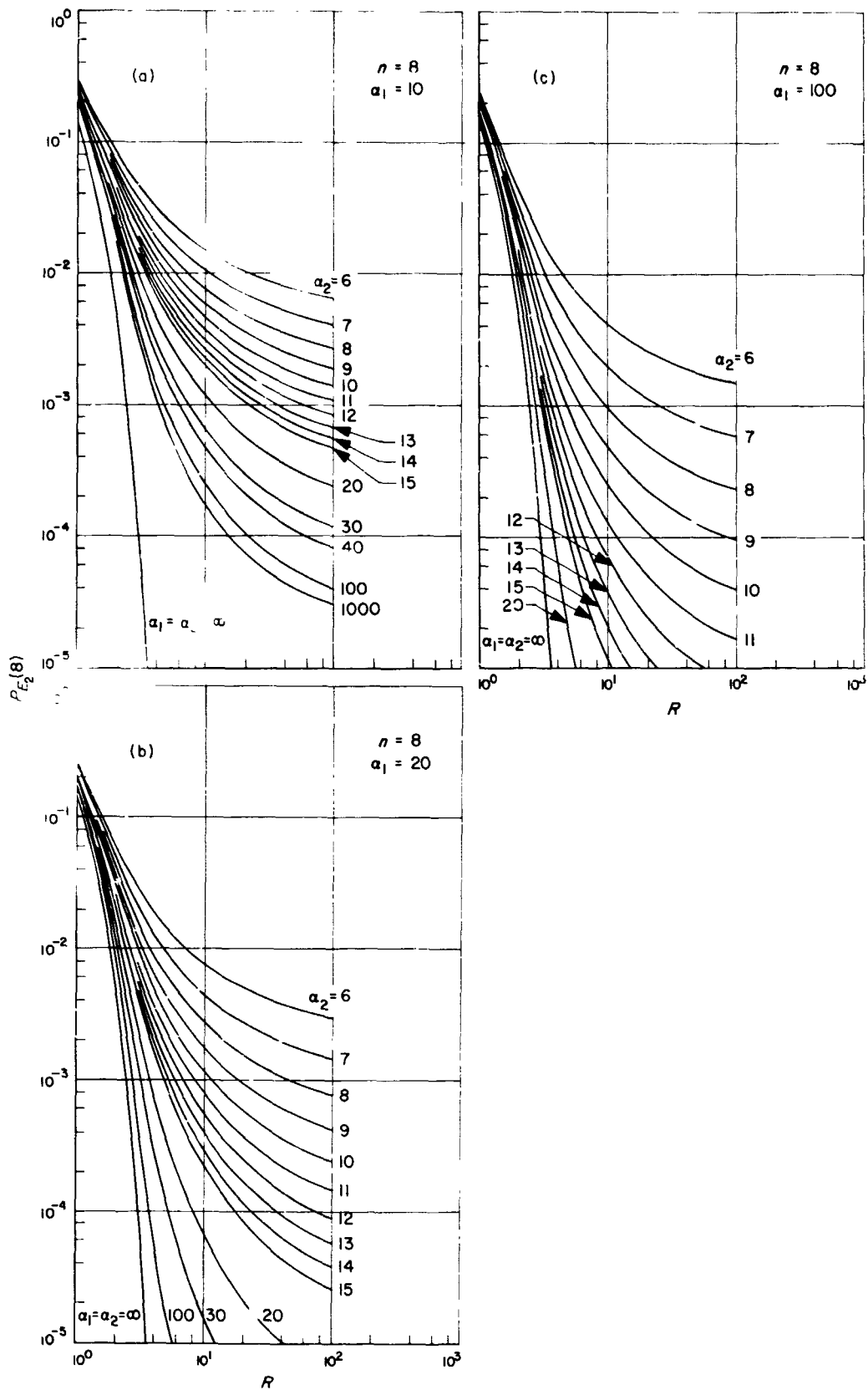


Fig. 22. Word error probability vs $R = ST_b/N_0$ for various values of α_2 with $n = 8$: (a) $\alpha_1 = 10$, (b) $\alpha_1 = 20$, (c) $\alpha_1 = 100$

3. The Effect of Filtering and Quantization on a Coded PSK Communication System, A. J. Viterbi²

Figure 23 illustrates a mechanization of the symbol detector for a coded binary phase-shift-keyed (PSK) communication system which avoids the integrate-and-dump circuit, since the latter may be quite difficult to mechanize at high data rates. This technique has been proposed for the *Mariner Mars 1969* telemetry system.⁶

The received signal heterodyned to baseband, $y(t)$, is normally operated on during the symbol period $kT_s \leq t < (k+1)T_s$ by an integrate-and-dump circuit which generates

$$\Delta y_k = \int_{kT_s}^{(k+1)T_s} y(t) dt \quad (1)$$

These samples are then fed to the digital decoder after very fine quantization (Ref. 5).

In the alternate mechanization shown in Fig. 23, the integrate-and-dump circuit is replaced by a low-pass filter. To obtain specific results we shall assume a one-stage resistance-capacitance filter whose impulse response is

$$h(\sigma) = e^{-\sigma/\tau} u(\sigma) \quad (2)$$

which is the simplest possible system to mechanize and in this sense represents a lower bound on performance. Note, however, that as the time constant $\tau \rightarrow \infty$, $h(\sigma)$ approaches the impulse response of an ideal integrator. Assuming a filter output $y(kT_s)$ at time kT_s , the output at time $(k+1)T_s$ due to a positive symbol of amplitude

²Consultant from Department of Engineering, University of California, Los Angeles.

⁶Easterling, M. F., private communication.

$(S)^{1/2}$ and white Gaussian noise of one-sided density N_0 will be

$$y[(k+1)T_s] = \int_0^{T_s} (S)^{1/2} u(T_s - \sigma) e^{-\sigma/\tau} d\sigma + \int_0^{T_s} n(T_s - \sigma) e^{-\sigma/\tau} d\sigma + y(kT_s) e^{-T_s/\tau} \quad (3)$$

Since the initial output for the k th symbol, $y(kT_s)$, is known exactly (within a quantization error), the computer can first calculate the quantity

$$\Delta y_k \triangleq y[(k+1)T_s] - y(kT_s) e^{-T_s/\tau} \quad (4)$$

From Eq. (3) it follows that

$$\Delta y_k = (S)^{1/2} \tau (1 - e^{-T_s/\tau}) + n_k \quad (5)$$

where n_k is a zero mean Gaussian random variable. Thus

$$E(\Delta y_k) = (S)^{1/2} \tau (1 - e^{-T_s/\tau}) \quad (6)$$

$$\text{var}(\Delta y_k) = \text{var}(n_k)$$

$$= \int_0^{T_s} \int_0^{T_s} \frac{N_0}{2} \delta(\gamma - \sigma) e^{-(\sigma+\gamma)/\tau} d\sigma d\gamma = \frac{N_0}{4} \tau (1 - e^{-2T_s/\tau}) \quad (7)$$

We now determine the degradation due to the filter alone without quantization. It is well known (Ref. 24) that the performance of the overall communication system depends only on the energy-to-noise ratio (bit or symbol) and the relative normalized inner products or distances between signals. Since each symbol of each signal has only been attenuated as shown in Eq. (5), the relative inner products are unchanged. The entire effect

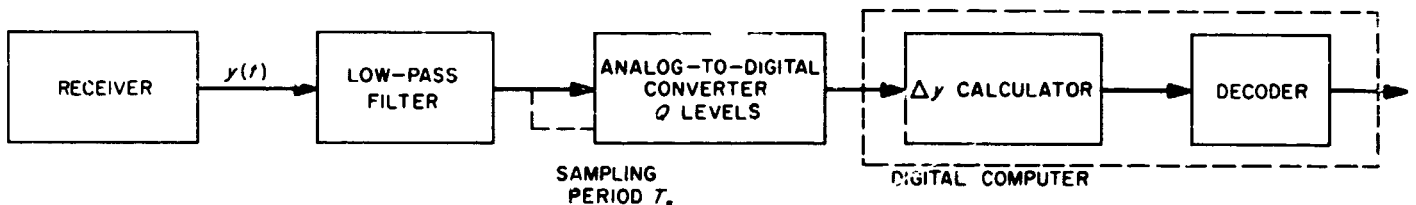


Fig. 23. Digital telemetry demodulator utilizing filtering and quantization

is then measured by the degradation of energy-to-noise ratio. This is obtained directly from Eqs. (6) and (7)

$$\frac{[E(\Delta y_k)]^2}{\text{var}(\Delta y_k)} = \frac{4S\tau(1 - e^{-T_s/\tau})^2}{N_0(1 - e^{-2T_s/\tau})} \triangleq \frac{2SI_s}{N_0} \left[\frac{2(1 - e^{-x})^2}{x(1 - e^{-2x})} \right] \quad (8)$$

where $x \triangleq T_s/\tau$. It is well known, and can be readily shown by using Eq. (1), that for an integrate-and-dump circuit the corresponding quantity is

$$\frac{[E(\Delta y)]^2}{\text{var}(\Delta y_k)} = \frac{2ST_s}{N_0}$$

Thus we conclude that the degradation factor due to the filter only, which we shall denote D_F , is

$$D_F(x) = \frac{2(1 - e^{-x})^2}{x(1 - e^{-2x})} \leq 1 \quad (9)$$

It follows readily from Eq. (9) that

$$\lim_{x \rightarrow 0} D_F(x) = 1$$

which is as expected since $x \rightarrow 0$ corresponds to $\tau \rightarrow \infty$, which corresponds to a perfect integrator as shown by Eq. (2). (Note that the differencing operation of Eq. (4) effectively converts a perfect integrator into an integrate-and-dump circuit.)

Thus, if quantization were not required, we should make the filter time constant as long as possible. On the other hand, with quantization a perfect integrator cannot be tolerated because this would convert white noise into a Wiener process, whose variance increases linearly with time. (Of course, this could be avoided by a series-blocking capacitor; but, as we shall see, it will not be required.) It is clear from Fig. 23 that the total dynamic range of the quantizer must be large enough to treat the entire range of signals plus all but the additional variation due to noise. Assuming that the truncation of noise values beyond $\pm 3\sigma$ will have little effect, we thus set the total dynamic range of the quantizer at

$$2A = 2(K + 3\sigma) \quad (10)$$

where A is total one-sided deviation of the quantizer about zero, and K is the magnitude of the maximum deviation from zero of $y(kT_s)$ due to signal only. Note that here σ^2 is the variance of $n(kT_s)$ or $y(kT_s)$ and not Δy_k , which is much less and is given by Eq. (7). The maximum deviation of $y(kT_s)$ due to signal only (i.e., of $E[y(kT_s)]$) depends on the code. If we assume that each code word has an equal number of zeros and ones and, furthermore, that the difference between the number of zeros and ones that can occur between the beginning of a word and any given symbol is never greater than k_M , (note that k_M cannot be greater than half the length of each word) then it readily follows from Eq. (6) that

$$K = E[y(k_M T_s)] = (S)^{1/2} \tau (1 - e^{-k_M T_s/\tau}) \quad (11)$$

On the other hand, if the code words do not have equal numbers of zeros and ones, the worst case becomes Eq. (11) with $k_M = \infty$. The variance σ^2 of $y(kT_s)$ or $n(kT_s)$ must be taken as the steady-state variance as $k \rightarrow \infty$, since we cannot set any limit to the duration of transmission and, in any case, the steady-state variance is closely approached after one or two word-times. It follows from Eq. (7), letting $T_s \rightarrow \infty$, that

$$\sigma^2 = \frac{N_0 \tau}{4} \quad (12)$$

Thus we have from Eq. (10) that the total dynamic range of the quantizer must be

$$2A = 2(S)^{1/2} \tau \left[1 - e^{-k_M T_s/\tau} + \frac{3}{2} \left(\frac{N_0}{S\tau} \right)^{1/2} \right] \quad (13)$$

Now we can assess the degrading effect of quantization. We assume Q levels and a uniform quantization scheme as shown in Fig. 24. It is also reasonable to assume that the quantization error in each level is uniformly distributed. (This may be somewhat inaccurate in the outermost levels which are affected only by noise, but since the probability that $y(t)$ will be at these high noise

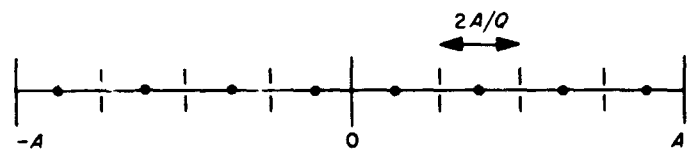


Fig. 24. Quantization scheme for 8 levels

levels is very small, it is felt that the effect will be negligible.) Then the probability density function of the quantization error or noise is

$$p_q(n_q) = \begin{cases} Q/2A, & \text{for } -A/Q \leq n_q \leq A/Q \\ 0, & \text{otherwise} \end{cases}$$

its mean is zero, and its variance is

$$\text{var}(n_q) = \frac{A^2}{3Q^2} = \frac{S\tau^2}{3Q^2} \left[1 - e^{-k_M x} + \frac{3}{2} \left(\frac{x}{R} \right)^{1/2} \right]^2 \quad (14)$$

where $x = T_s/\tau$ and $R = ST_s/N_c$. Since the quantization noise is essentially independent of the channel noise (except for the edge effect noted above), we may add the variance of the quantization noise of Eq. (14) to the variance due to channel noise of Eq. (7) to obtain the total variance

$\text{var}(\Delta y_k)_t =$

$$\frac{N_0\tau}{4} \left[(1 - e^{-2x}) + \frac{4R}{3x} \left(\frac{1 - e^{-k_M x} + \frac{3}{2} \left(\frac{x}{R} \right)^{1/2}}{Q} \right) \right] \quad (15)$$

where $R = ST_s/N_0$, $x = T_s/\tau$. Finally, from Eqs. (6) and (15) we obtain the effective degradation factor with quantization and filtering

$$D_{FQ}(x, R, k_M, Q) = \frac{[E(\Delta y_k)]^2}{\text{var}(\Delta y_k)_t} \left(\frac{2ST_s}{N_0} \right)^{-1} \\ = \frac{2(1 - e^{-x})^2}{x \left[1 - e^{-2x} + \frac{4R}{3x} \left(\frac{1 - e^{-k_M x} + \frac{3}{2} \left(\frac{x}{R} \right)^{1/2}}{Q} \right)^2 \right]} \quad (16)$$

where $R = ST_s/N_0$, $x = T_s/\tau$. Note that as $Q \rightarrow \infty$, this approaches the result without quantization of Eq. (9). Note also that for finite Q

$$\lim_{x \rightarrow \infty} D_{FQ}(x, R, k_M, Q) = 0$$

for now an infinite time constant (perfect integrator) would result in an infinite required dynamic range $2A$, which in turn would produce infinite quantization error for finite Q .

It should be emphasized that the result of Eq. (16) is essentially exact (except for the quantization edge effect mentioned above). However, this is merely a degradation in the effective energy-to-noise ratio. This is also the degradation in system performance if the noise affecting each word decision is Gaussian. Of course, the symbol quantization noise is uniform. On the other hand, the noise affecting a word decision is the result of adding all the symbol noises for the word. If the number of symbols per word is large (32 for the *Mariner* Mars 1969 biorthogonal system), we may reasonably invoke the central limit theorem for the sum of these independent equidistributed random variables with finite moments of all orders, and it is anticipated that the result of Eq. (16) will be a very good approximation to the actual system degradation.

Figures 25 to 28 show the degradation factor of Eq. (16) in dB on two different scales for $Q = 2^q$ ($q = 2, 3, \dots, 12$), for the (32, 6) biorthogonal code with $R = ST_s/N_0 = 0.45$ (which corresponds to $ST_B/N_0 = 2.4$ and bit error probability $P_B \approx 10^{-3}$). Figures 25 and 26 show on two different scales the degradation factor for the worst case ($k_M = 16$) if each code word had an equal number of zeros and ones. Figures 27 and 28 show on the same scales the degradation factors for the worst case (equivalent to $k_M = \infty$) when the code words are unbalanced. It appears that for $Q = 2^6$ the degradation can be kept to less than 0.1 dB over a wide range of $x = T_s/\tau$. The uppermost curve in each case is that of Eq. (9) without quantization.

We note finally that although quantization will also affect the integrate-and-dump circuit of Eq. (1), the effect will be much smaller since both the signal peak and noise variance will depend only on one symbol, thereby allowing a much narrower quantizer dynamic range and consequently a smaller quantization noise variance for the same number of levels.

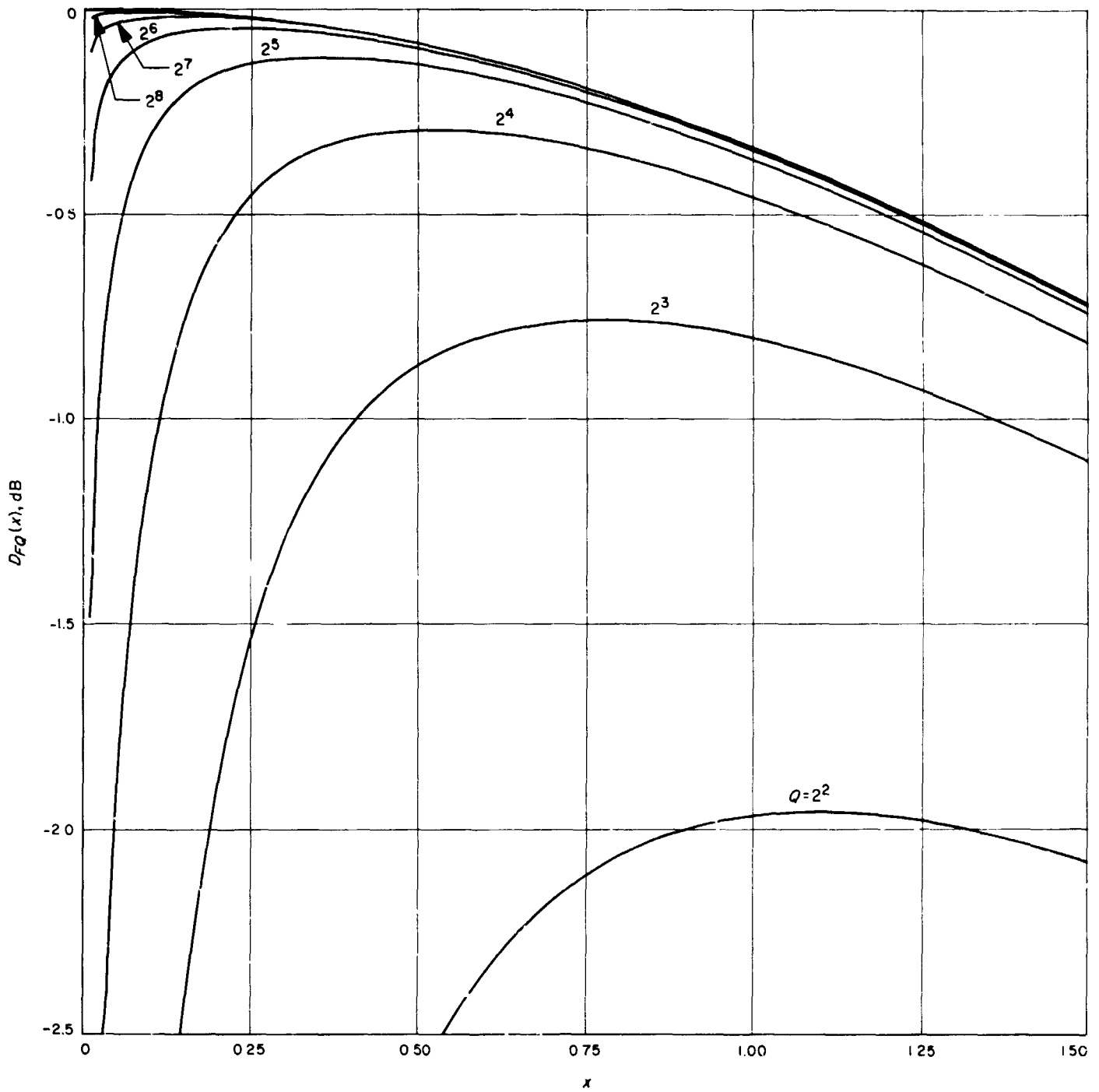


Fig. 25. Degradation factor for $k_M = 16$, $ST_s/N_0 = R = 0.45$, $ST_B/N_0 = 2.4$, $x = T_s/\tau$

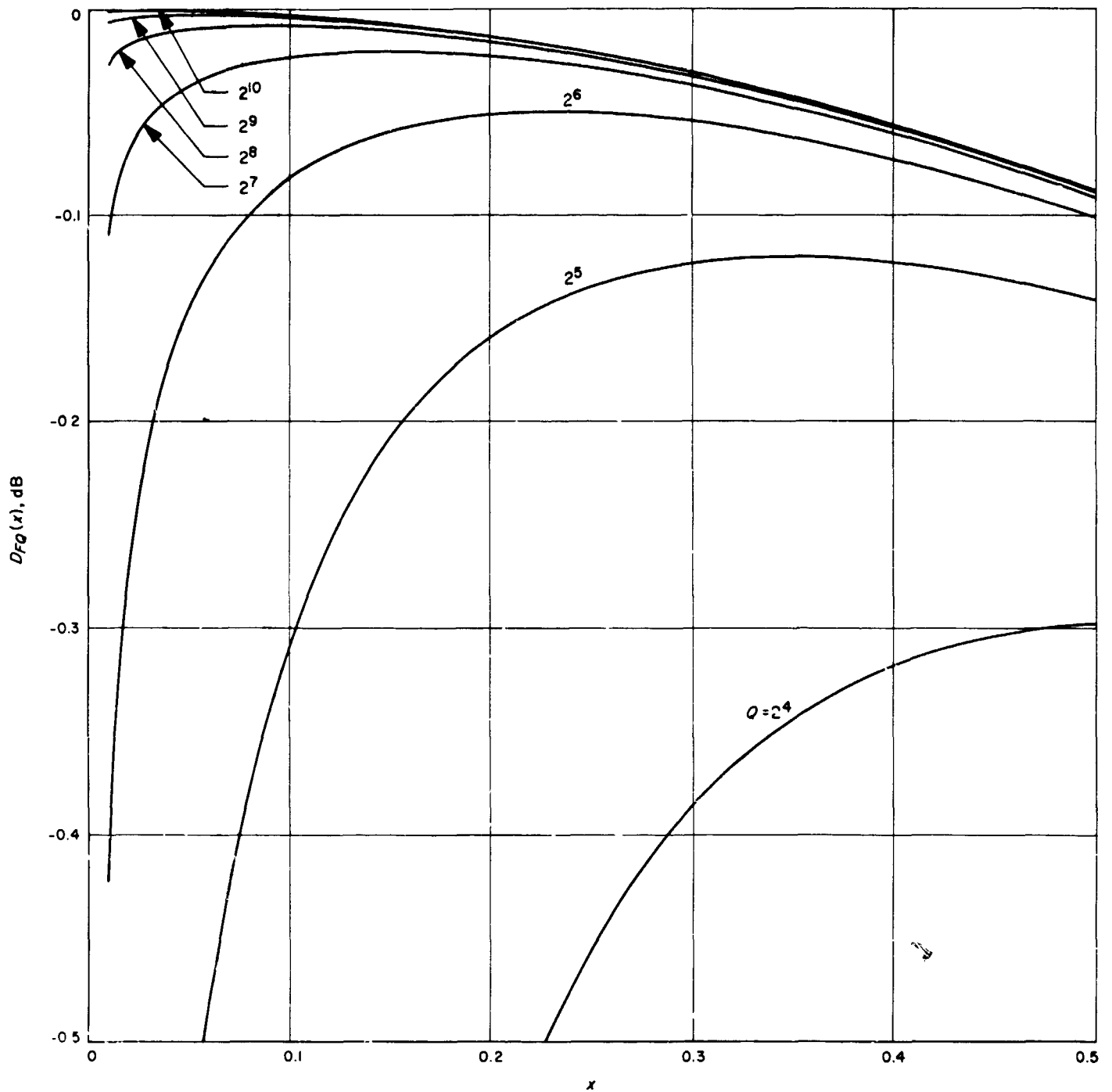


Fig. 26. Degradation factor of Fig. 25 on expanded scale

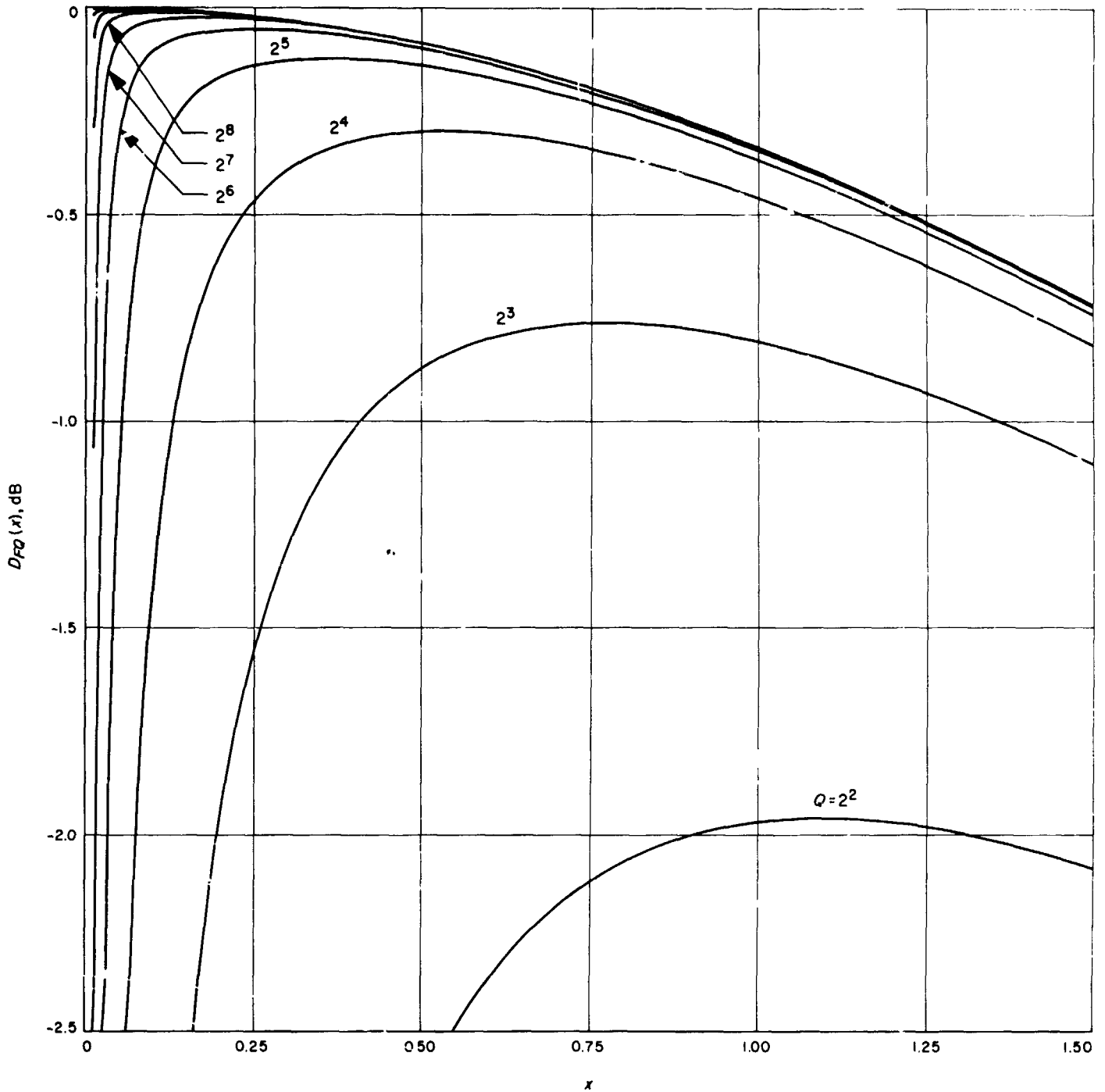


Fig. 27. Degradation factor for unbalanced code words ($k_M = \infty$), $ST_s/N_0 = R = 0.45$, $ST_B/N_0 = 2.4$, $x = T_s/\tau$

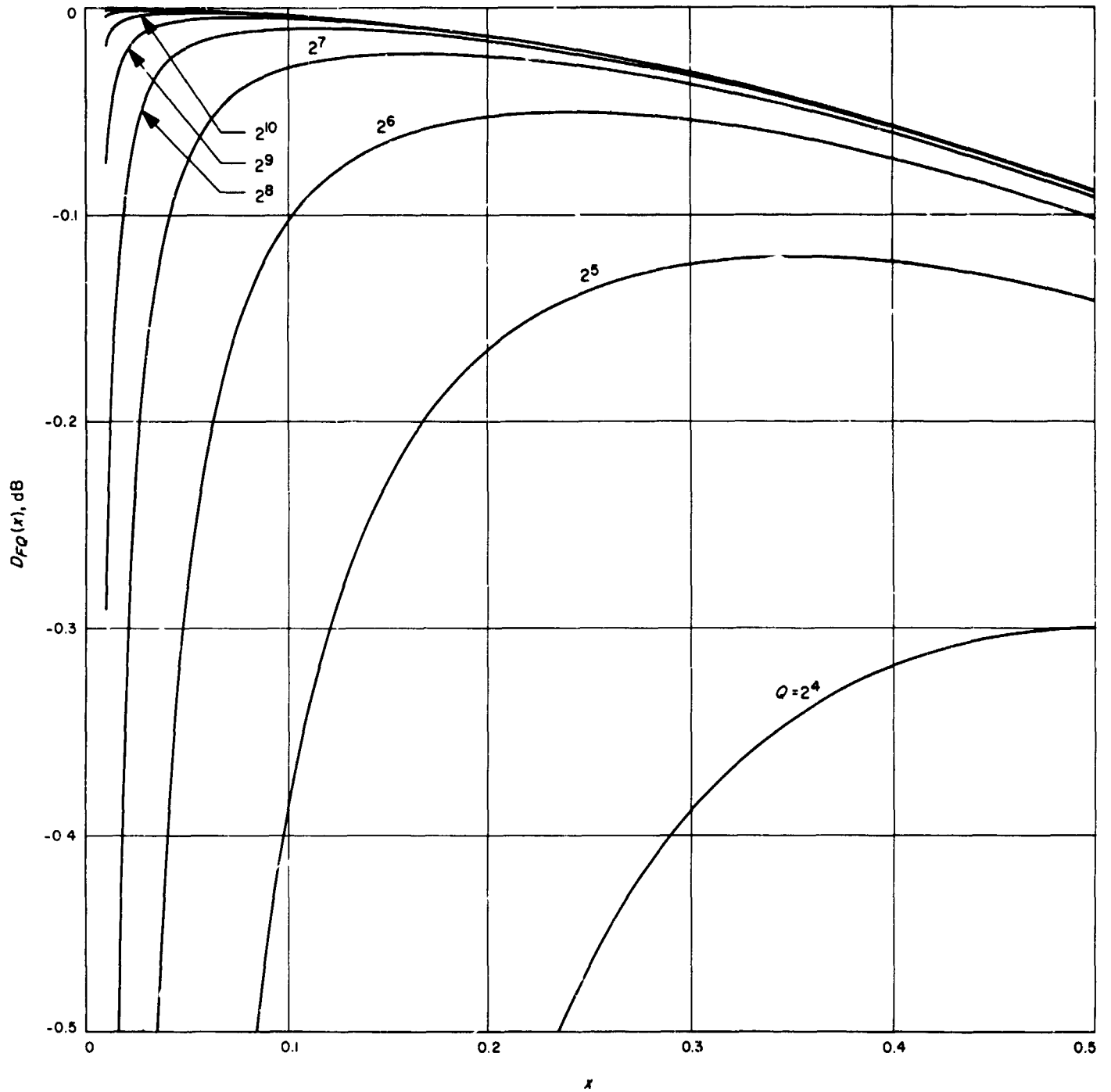


Fig. 28. Degradation factor of Fig. 27 on expanded scale

E. Information Processing, S. Zohar

1. Computation of the Derivatives of a Band-Limited Function

a. Introduction. In the processing of sampled data, the need sometimes arises to compute a high-order derivative of a band-limited function given by its (adequately spaced) samples.

Since the original continuous function is completely reconstructible from its samples, the determination of any derivative is a straightforward procedure. However, the expressions obtained are sometimes so ill-behaved numerically as to render the results absolutely meaningless. In the following discussion, we examine the cause of this behavior and devise a computational scheme that overcomes the difficulty.

The problem originally arose in the processing of planetary radar data. The algorithm described here has been successfully applied to the extraction of the planetary backscatter function from the return signal.

b. Basic formulation. Let $\rho(\cdot)$ be a band-limited function such that its Fourier transform $p(\nu)$ vanishes for $|\nu| > \frac{1}{2}$. We use indices to denote the samples. Thus,

$$\rho_k = \rho(k), \quad k \text{ integer} \quad (1)$$

Applying the sampling theorem, we can reconstruct $\rho(\tau)$ from its samples as follows:

$$\rho(\tau) = \sum_{k=-\infty}^{\infty} \rho_k f[\pi(k - \tau)] \quad (2)$$

where

$$f(x) = \frac{\sin x}{x} \quad (3)$$

Hence,

$$\rho^{(n)}(\tau) = \frac{d^n \rho(\tau)}{d\tau^n} = (-\pi)^n \sum_{k=-\infty}^{\infty} \rho_k [f^{(n)}(x)]_{x=\pi(k-\tau)} \quad (4)$$

We see that our problem is essentially the evaluation of the n th derivative of $\sin x/x$, which we proceed to do

now. Using the derivative operator D , we note that for real x

$$f^{(n)}(x) = \text{Im} \{ D^n (x^{-1} e^{ix}) \} \quad (5)$$

Applying Leibnitz's rule, we find that $f^{(n)}(x)$ is expressible in terms of partial sums of the sine and cosine series. In view of this, we introduce the following notation:

$$S_n(x) = \sum_{k=0}^{n-1} s_k(x); \quad C_n(x) = \sum_{k=0}^{n-1} c_k(x) \quad (6)$$

where

$$s_k(x) = (-1)^k \frac{x^{2k+1}}{(2k+1)!}; \quad c_k(x) = (-1)^k \frac{x^{2k}}{(2k)!} \quad (7)$$

and

$$S_\infty(x) = \sin x; \quad C_\infty(x) = \cos x \quad (8)$$

With this terminology, we get the following expressions for the derivatives of $f(x)$:

$$\left. \begin{aligned} f^{(2m)}(x) &= (-1)^{m+1} \frac{\cos x}{2m+1} \cdot \frac{S_m(x)}{s_m(x)} \\ &\quad + (-1)^m \frac{\sin x}{x} \cdot \frac{C_{m+1}(x)}{c_m(x)} \\ f^{(2m-1)}(x) &= (-1)^m \frac{\cos x}{2m} \cdot \frac{S_m(x)}{c_m(x)} \\ &\quad + (-1)^m \frac{\sin x}{x} \cdot \frac{C_m(x)}{s_{m-1}(x)} \\ &= (-1)^m \frac{x \cos x}{2m(2m+1)} \cdot \frac{S_m(x)}{s_m(x)} \\ &\quad + (-1)^m \frac{(2m-1) \sin x}{x^2} \cdot \frac{C_m(x)}{c_{m-1}(x)} \end{aligned} \right\} \quad (9)$$

While the above formulae are certainly correct as mathematical statements, they are almost useless when actual

numerical evaluation is considered. The reason lies in the behavior of the function

$$\gamma_n(z) = \frac{z^n}{n!} \quad (10)$$

for increasing n [$c_k(x), s_k(x)$ are essentially such functions]. While it is true that

$$\lim_{n \rightarrow \infty} \gamma_n(z) = 0$$

application of Stirling's approximation to $n!$ shows that, for a finite z , $\gamma_n(z)$ becomes a monotonically decreasing function of n only for (approximately)

$$n > ez \quad (11)$$

Before this n value is reached, however, $\gamma_n(z)$ may assume extremely large values. Since $S_n(x), C_n(x)$ are just sums of such terms with an alternating sign, it is obvious that cases may arise in which a reasonable relative error in a single term of the sum (say, 10^{-8}) could lead to computed $|S_n(x)|, |C_n(x)|$, which are orders of magnitude greater than the true values.

The resolution of this difficulty is taken up in the next section. Before we do that, however, we find it somewhat more convenient to reformulate our problem in terms of the functions

$$E_n(x) = \frac{S_n(x)}{s_n(x)}, \quad H_n(x) = \frac{C_{n+1}(x)}{c_n(x)} \quad (12)$$

These are polynomials of degree n in the variable $1/x^2$. [See definitions in Eqs. (6) and (7).] Expressing the derivatives in terms of these functions, we get

$$\left. \begin{aligned} f^{(2m)}(x) &= (-1)^{m+1} \frac{\cos x}{2m+1} E_m(x) \\ &\quad + (-1)^m \frac{\sin x}{x} H_m(x) \\ f^{(2m-1)}(x) &= (-1)^m \frac{x \cos x}{2m(2m+1)} E_m(x) \\ &\quad + (-1)^m (2m-1) \frac{\sin x}{x^2} H_{m-1}(x) \end{aligned} \right\} \quad (13)$$

We note that for $x=0$, the functions $E_n(x), H_n(x)$ become infinite, making Eq. (13) indeterminate and requiring the application of l'Hospital's rule. However, with $x=0$, the derivative can be obtained directly from the Taylor expansion of $\sin x/x$, yielding the result

$$\left. \begin{aligned} [f^{(2m)}(x)]_{x=0} &= \frac{(-1)^m}{2m+1} \\ [f^{(2m-1)}(x)]_{x=0} &= 0 \end{aligned} \right\} \quad (14)$$

Eqs. (13) and (14) are the final forms adopted here. Substitution of these in Eq. (4) will yield the desired derivative formula. We turn now to the resolution of our main difficulty, the computation of the functions $E_n(x), H_n(x)$.

c. The functions $E_n(x), H_n(x)$. We discuss here, in detail, only the computation of $E_n(x)$. Since the derivations for $H_n(x)$ are very similar, the corresponding results will be stated without proof later on. Our first step is to establish a recursion relationship. Starting with the definition, we have

$$E_n(x) = \frac{S_n(x)}{s_n(x)} = \frac{S_{n-1}(x) + s_{n-1}(x)}{\left[-\frac{x^2}{2n(2n+1)} \right] s_{n-1}(x)}$$

Denoting

$$e_n(x) = \frac{2n(2n+1)}{x^2} \quad (15)$$

we get the recursion

$$E_n(x) = [1 + E_{n-1}(x)] e_n(x) \quad (16)$$

We examine now the feasibility of using Eq. (16) to compute a sequence of $E_n(x)$. Suppose the error in $E_{n-1}(x)$ is $\Delta E_{n-1}(x)$, then we see that $\Delta E_n(x)$, the error in $E_n(x)$, is given by

$$\Delta E_n(x) = e_n(x) \Delta E_{n-1}(x) \quad (17)$$

The error in $e_n(x)$ itself can be neglected. It is the accumulation of errors which we should worry about. The

*Corresponding equations in the two cases are assigned the same number, except that a prime is added to the number for the $H_n(x)$ case.

stability of the recursion process obviously depends on the magnitude of $e_n(x)$. Thus, as long as

$$|e_n(x)| < 1$$

for all n in the sequence generated, an error injected in, say, $E_m(x)$ will be progressively attenuated in $E_{m+1}(x)$, $E_{m+2}(x)$, etc. Under these conditions, the desired sequence will be generated by a simple stable process starting with

$$E_0(x) = 0 \quad (18)$$

We observe, however, that $|e_n(x)|$ is a monotonically increasing function of n and as we proceed with the recursion we will eventually reach a point beyond which all

$$|e_n(x)| > 1$$

Any error introduced at this point and beyond it will be progressively magnified in subsequent terms, rendering the results completely meaningless.

The solution to this problem is quite simple. Rewriting Eq. (17) to obtain

$$\Delta E_{n-1}(x) = \frac{1}{e_n(x)} \Delta E_n(x) \quad (19)$$

we observe that for

$$|e_n(x)| > 1$$

we have here a stable process in the backward direction; that is, we can safely generate $E_{n-1}(x)$ from $E_n(x)$, etc.

This points to the following computational procedure: Our first step would be to determine α where

$$|e_\alpha(x)| = 1 \quad (20)$$

Applying Eq. (15), we get

$$\alpha(x) = \frac{1}{4} [(1 + 4\tau^2)^{1/2} - 1] \quad (21)$$

Now let

$$n_1(x) = [\alpha] \quad (22)$$

$$n_2(x) = n_1(x) + 1 \quad (23)$$

Obviously,

$$n_1 \leq \alpha < n_2 \quad (24)$$

Hence, $E_{n_1}(x)$ can safely be used to generate all $E_n(x)$ for $n \leq n_1(x)$. The remaining values (if any) will all have to be generated by a backward recursion from $E_{n_2}(x)$ where n_2 is the highest required n value.

How does one compute this $E_{n_2}(x)$? The answer is provided by a simple argument originally applied by J. C. P. Miller (Ref. 25) to the computation of Bessel functions. The reasoning is as follows: If the generated function is known to be bounded, it does not really matter what value we use for the initial value starting the recursion, provided we start with an index n sufficiently removed from the first index of interest. Since the initial error is finite, it will take only a finite number of recursions to reduce it below any permissible error.

Applying this idea to our case, we consider first the possible error in the initial value of the backward recursion. This is most easily obtained by requiring that $e_n(x)$ is actually a ratio of two adjacent s_k values. Specifically,

$$e_n(x) = \frac{s_{n-1}(x)}{s_n(x)} < 1$$

This means that for $n \geq n_2(x)$

$$|s_n(x)| < |s_{n-1}(x)|$$

Hence, we can apply to $S_n(x)$ the well-known theorem pertaining to alternating series and obtain

$$|S_n(x) - S_\infty(x)| \leq |s_n(x)|, \quad n \geq n_2(x) \quad (25)$$

Dividing by $|s_n(x)|$ we get

$$\left| \frac{E_n(x) - S_\infty(x)}{s_n(x)} \right| \leq 1, \quad n \geq n_2(x) \quad (26)$$

A reasonable choice for the initial value of the backward recursion is therefore the estimate

$$\hat{E}_n(x) = \frac{\sin x}{s_n(x)} \quad (27)$$

From Eq. (26), the absolute error in this term is bounded by 1. Let m be the highest n value for which $E_n(x)$ is required. To guarantee a negligible error in $E_m(x)$ we have to start the recursion with a higher n value. Let the initial estimate then be

$$\hat{E}_{m+k}(x) = \frac{\sin x}{s_{m+k}(x)} \quad (28)$$

where $k > 0$.

We consider now the determination of k for a specified error bound in $E_m(x)$. We have already seen that the absolute error bound on $E_{m+k}(x)$ is 1. Successively applying Eq. (19), we get

$$|\Delta E_m(x)| \leq \prod_{i=1}^k \frac{1}{|e_{m+i}(x)|} = \frac{x^{2k}}{(2m+2)_{2k}} \quad (29)$$

This inequality leads to the determination of a sufficiently large k . Let the error requirement be

$$|\Delta E_m(x)| \leq \epsilon \quad (30)$$

Then we set

$$|\Delta E_m(x)| \leq \frac{x^{2k}}{(2m+2)_{2k}} \leq \epsilon \quad (31)$$

Naturally, we are interested in the smallest k satisfying this inequality. Rewriting Eq. (31) explicitly

$$\epsilon \geq \frac{x}{2m+2} \cdot \frac{x}{2m+3} \cdots \frac{x}{2m+2k+1} \quad (32)$$

shows a simple way of determining this k on a computer. The relevant program would multiply factors as indicated on the right and test after each multiplication whether the bound ϵ has been reached.

A simpler, though somewhat wasteful, solution is based on the inequality

$$\frac{x^{2k}}{(2m+2)_{2k}} \leq \left(\frac{x}{2m+2} \right)^{2k} \quad (33)$$

Here we would set

$$\epsilon = \left(\frac{x}{2m+2} \right)^{2k} \quad (34)$$

getting

$$k = \frac{1}{2} \frac{\log \left(\frac{x}{2m+2} \right)}{\log \epsilon} \quad (35)$$

We have described here a method which will yield any desired $E_n(x)$ without error accumulation. Obviously, the method is most economical when $E_n(x)$ is required for a sequence of indices starting with $n = 1$. This method has been tested on the IBM 1620 computer with most encouraging results. The testing consisted of comparing results obtained with a different number of digits (from 8 to 28). Also, both the backward and forward recursions were extended (for test purposes only) one term beyond their proper range and the results compared; that is, $E_{n_1}(x)$ and $E_{n_2}(x)$ were computed by both recursions. In both tests, the slight discrepancies observed were consistent with the number of digits used.

It will be seen in the next section that the values of $E_n(z)$ for

$$x = \pi, 2\pi, \dots$$

play a major role in an important special case. We pause here briefly to establish the range of these parameters. Denoting

$$E_{nk} = E_n(k\pi), \quad k \text{ integer}, k \neq 0 \quad (36)$$

we observe that the Inequality (26) implies

$$|E_{nk}| \leq 1, \quad n \geq n_2 \quad (37)$$

This range can be further narrowed by applying the basic recursion Eq. (16):

$$E_{nk} = [1 - E_{n-1,k}] e_n(k\pi)$$

The square bracket term is non-negative because of Eq. (37), while $e_n(\tau)$ is negative for all non-negative integers n . Consequently,

$$E_{nk} \leq 0, \quad n \geq n_2$$

and combining with Eq. (37) the range is

$$-1 \leq E_{nk} \leq 0, \quad n \geq n_2 \quad (38)$$

We proceed now to remove the constraint on n in Eq. (38). We note that for $n < n_2$ (that is, $n \leq n_1$)

$$e_n(k\pi) \geq -1$$

Therefore, it for any $n < n_2$,

$$-1 \leq E_{n-1,k} \leq 0 \quad (39)$$

then

$$-1 \leq [1 + E_{n-1,k}] e_n(k\pi) \leq 0$$

that is,

$$-1 \leq E_{nk} \leq 0 \quad (40)$$

But

$$E_{0k} = 0$$

and certainly satisfies Eq. (39). Hence, we conclude that Eq. (40) holds for all $n < n_2$, and combining with Eq. (38) we establish

$$-1 \leq E_{nk} \leq 0$$

for all n . These bounds are the tightest that can be established. Thus, the upper bound is a member of the set, as we have already seen. The lower bound is a direct result of Eq. (25); but there, equality holds in the limit as $n \rightarrow \infty$. Hence, this is the case here too and we have

$$\lim_{n \rightarrow \infty} E_{nk} = -1$$

We turn now briefly to the second function appearing in Eq. (12), namely, $H_n(x)$. The recursion formula is

$$H_n(x) = 1 + H_{n-1}(x) h_n(x) \quad (16')$$

where

$$h_n(x) = -\frac{2n(2n-1)}{x^2} = \frac{c_{n-1}(x)}{c_n(x)} \quad (15')$$

The error propagation is governed by

$$\Delta H_n(x) = h_n(x) \Delta H_{n-1}(x) \quad (17')$$

Forward recursion can be used up to $n_1(x)$ where

$$n_1(x) = [\alpha] \quad (22')$$

$$\alpha = \frac{1}{4} [(1 + 4x^2)^{1/2} + 1] \quad (21')$$

The initial value for the forward recursion is

$$H_0(x) = 1 \quad (18')$$

Backward recursion is to be used down to

$$n_2(x) = n_1(x) + 1 \quad (23')$$

If $H_n(x)$ is required up to $n = m$ and the permissible absolute error in $H_m(x)$ is ϵ , the backward recursion should start with

$$H_{m+k}(x) = \frac{\cos x}{c_{m+k}(x)} \quad (28')$$

where k is determined by

$$\epsilon \geq \frac{x}{2m+1} \cdot \frac{x}{2m+2} \cdots \frac{x}{2m+2k+2} \quad (32')$$

Alternatively, an explicit though somewhat wasteful formula for k is

$$k = \frac{1}{2} \frac{\log \frac{x}{2m+1}}{\log \epsilon} - 1 \quad (35')$$

d. *The derivative formula.* Having resolved the difficulties associated with the functions $E_n(x), H_n(x)$, all that remains to be done is to substitute Eq. (13) [or Eq. (14)] in Eq. (4). The resulting expressions are:

$$\left. \begin{aligned} \frac{d^{2m} \rho(\tau)}{d\tau^{2m}} &= (-1)^{m+1} \pi^{2m} \sum_{k=-\infty}^{\infty} \left\{ \frac{\cos \pi(k-\tau)}{2m+1} E_m[(k-\tau)\pi] - \frac{\sin \pi(k-\tau)}{\pi(k-\tau)} H_m[(k-\tau)\pi] \right\} \rho_k \\ \frac{d^{2m-1} \rho(\tau)}{d\tau^{2m-1}} &= (-1)^{m+1} \pi^{2m} \sum_{k=-\infty}^{\infty} \left\{ \frac{(k-\tau) \cos \pi(k-\tau)}{2m(2m+1)} E_m[(k-\tau)\pi] + (2m-1) \frac{\sin \pi(k-\tau)}{\pi^2(k-\tau)^2} H_{m-1}[(k-\tau)\pi] \right\} \rho_k \end{aligned} \right\} (41)$$

Recalling the special treatment required in handling $E_n(0), H_n(0)$, we restrict the application of Eq. (41) to non-integral τ . When τ is an integer (n), one term in the infinite sum in Eq. (4) will require use of Eq. (14) rather than Eq. (13). In addition to that, however, all the remaining terms involving Eq. (13) are simplified since the associated trigonometric functions have integral multiples of π for their arguments. Taking advantage of the fact that $E_n(x)$ is an even function of x , substituting $k-n = r$, and using the terminology of Eq. (36), we get

$$\left. \begin{aligned} \left[\frac{d^{2m} \rho(\tau)}{d\tau^{2m}} \right]_{\tau=n} &= \frac{(-1)^{m+1} \pi^{2m}}{2m+1} \left\{ -\rho_n + \sum_{r=1}^{\infty} (-1)^r E_{mr} (\rho_{n+r} + \rho_{n-r}) \right\} \\ \left[\frac{d^{2m-1} \rho(\tau)}{d\tau^{2m-1}} \right]_{\tau=n} &= \frac{(-1)^{m+1} \pi^{2m}}{2m(2m+1)} \sum_{r=1}^{\infty} (-1)^r r E_{mr} (\rho_{n+r} - \rho_{n-r}) \end{aligned} \right\} (42)$$

We note the simplicity of Eq. (42) compared to Eq. (41). Of particular interest to us is the disappearance of the function $H_n(x)$ as well as the replacement of the continuous function $E_n(x)$ by the parameters E_{nr} . In view of the fact that the derivative of a band-limited function is likewise band-limited to the same frequency band, it is obvious that the m th derivative of $\rho(\tau)$ at any τ whatever can be obtained from its samples given by Eq. (42). Thus,

$$\frac{d^m \rho(\tau)}{d\tau^m} = \sum_{n=-\infty}^{\infty} f[\pi(n-\tau)] \left\{ \left[\frac{d^m \rho(\tau)}{d\tau^m} \right]_{\tau=n} \right\} \quad (43)$$

Consequently, we see that the derivative at any point could, in principle, be obtained without recourse to the continuous functions $E_n(x), H_n(x)$, using only the E_{nr} parameters. The advantage of the approach adopted here is that, while the simplicity of the formula for the sam-

ples of the derivative is maintained, we get a much more convenient formulation for points in between. Thus, Eq. (43) used with Eq. (42) involves a double summation as compared to the single summation in Eq. (41). Under usual circumstances, this point far outweighs the extra computations involved in evaluating $H_n(x)$.

In special cases, however, the combination of Eqs. (42), (43) might still prove to be faster than Eq. (41). This could be the case, for example, when a large number of derivatives is required and a large memory storage is available. In this case, one would initially compute and store all the required parameters. This would avoid a large amount of repetition and would appreciably speed-up the implementation of Eqs. (42), (43). Depending on the specific problem, the resulting computing time might be much shorter than that involved in Eq. (41).

We conclude with the application of Eq. (42) to determine derivatives at the origin of the autocorrelation $\rho(\tau)$

of a band-limited process. Using the fact that the autocorrelation is an even function, we get

$$\left. \begin{aligned} \left[\frac{d^{2m} \rho(\tau)}{d\tau^{2m}} \right]_{\tau=0} &= \frac{(-1)^{m+1} \pi^{2m}}{2m+1} \\ &\times \left\{ -\rho_0 + 2 \sum_{k=1}^{\infty} E_{mk} (-1)^k \rho_k \right\} \\ \left[\frac{d^{2m-1} \rho(\tau)}{d\tau^{2m-1}} \right]_{\tau=0} &= 0 \end{aligned} \right\} \quad (44)$$

This formula plays a key role in the solution of the planetary backscatter problem and provided the initial motivation for this investigation.

F. Data Compression Techniques, I. Eisenberger

1. A Goodness-of-Fit Test Using Six and Eight Quantiles

a. Introduction. The desire to achieve data compression of space telemetry arises from the fact that there is a limit to the total number of experimental observations that can be transmitted in a given time, thus limiting the number of experiments that can be performed simultaneously for given sample sizes. The aim of a data compression system is to transmit only "useful" information, discarding the remainder of the data. If the data compression ratio, the ratio of the number of observations taken to the number transmitted, is high enough, it will then be possible to perform additional experiments with a relatively small increase in cost. Or, data compression may be necessary on the ground communication links between an overseas Deep Space Station site and JPL, due to a limitation in the number of circuits available between JPL and overseas sites.

There are cases where the data is to be used to draw statistical conclusions from a histogram, such as in pulse height analyzers of the kind used in the "Chicago cosmic ray" experiment on board the *Pioneer* spacecraft. In such instances, it may be possible to achieve significant amounts of data compression with only a small loss of useful information by transmitting a small number of sample *quantiles* instead of all the sample values. The sample quantiles can then be used to perform the identical statistical analyses for which the histogram was originally intended. When data compression is done on the ground to make the best utilization of existing ground links, using quantiles may allow the experimenter to have usable data in real time

instead of having to wait several weeks or more for the complete received telemetry to arrive at the experimenter's laboratory.

A distribution-free goodness-of-fit test for large sample sizes, using sample quantiles, was given in Ref. 26, pp. 9-12. In addition, the special case where the null hypothesis assumes that the parent population is normally distributed with unknown parameters was also considered and a procedure was given which uses four quantiles. The object of this article is primarily to extend this procedure to six and eight quantiles.

b. Review of quantiles. To define a quantile, consider a sample of n independent values x_1, x_2, \dots, x_n taken from a distribution of a continuous type with distribution function $G(x)$ and density function $g(x)$. The p th quantile, or the quantile of order p of the distribution or population, denoted by ζ_p , is defined as the root of the equation $G(\zeta) = p$; that is,

$$p = \int_{-\infty}^{\zeta_p} dG(x) = \int_{-\infty}^{\zeta_p} g(x) dx$$

The corresponding sample quantile, Z_p , is defined as follows: If the sample values are arranged in non-decreasing order of magnitude,

$$x_{(1)} \leq x_{(2)} \leq \dots \leq x_{(n)}$$

then $x_{(i)}$ is called the i th order statistic and

$$Z_p = x_{([np]+1)}$$

where $[np]$ is the greatest integer $\leq np$.

If $g(x)$ is differentiable in some neighborhood of each quantile value considered, it has been shown (Ref. 27) that the joint distribution of any number of quantiles is, asymptotically,

$$E(Z_p) = \zeta_p$$

$$\text{var}(Z_p) = \frac{p(1-p)}{ng^2(\zeta_p)}$$

$$\rho_{12} = \left[\frac{p_1(1-p_2)}{p_2(1-p_1)} \right]^{1/2}$$

where ρ_{12} is the correlation between Z_{p_1} and Z_{p_2} , $p_1 < p_2$. The analyses will be based on the limiting distribution and moments of the sample quantiles.

c. *Testing a distribution using M quantiles.* Let H_0 denote the null hypothesis that the parent population has a probability distribution with density function $g(x)$ (which meets the above conditions on its derivative), and let K_1 denote the (composite) alternative hypothesis that the density function is not $g(x)$. Let $Z'_i, i = 1, 2, \dots, m$, be m sample quantiles of orders p_i and let ζ'_i denote the corresponding population quantiles. Assuming that $g(x)$ is completely specified under H_0 , the ζ'_i and $g(\zeta'_i)$ can be calculated and one has

$$E(Z'_i) = \zeta'_i \text{ and } \sigma_i^2 = \frac{p_i(1-p_i)}{ng^2(\zeta'_i)}$$

Since the (asymptotically) normally distributed random variables Z'_1, Z'_2, \dots, Z'_m are not independent, it is convenient to transform them into m new *independent* random variables x_1, x_2, \dots, x_m such that under H_0 , each x_i is distributed $N(0,1)$. In order to accomplish this, the following procedure is adopted. First, let

$$Z_i = \frac{Z'_i - \zeta'_i}{\sigma_i}, \quad i = 1, 2, \dots, m$$

then set

$$x_k = a_{kk}Z_k + \sum_{i=1}^{k-1} a_{ki}x_i, \quad k = 1, 2, \dots, m$$

and determine the a_i , recursively so as to satisfy the following conditions:

$$E(x_i) = 0 \quad (1)$$

$$E(x_i^2) = 1 \quad (2)$$

$$E(x_i x_j) = 0, i \neq j \quad (3)$$

It is immediately seen that by normalizing the Z'_i and putting $a_{11} = 1$, the first condition, $E(x_i) = 0$, is satisfied. Applying Conditions (2) and (3) results in the following general expressions for the k th set of coefficients:

$$a_{kk} = [1 - \rho_{ik}^2 - (a_{21}\rho_{1k} + a_{22}\rho_{2k})^2 - (a_{31}\rho_{1k} + a_{32}\rho_{2k} + a_{33}\rho_{3k})^2 - \dots - (a_{k-1,1}\rho_{1k} + a_{k-1,2}\rho_{2k} + \dots + a_{k-1,k-1}\rho_{k-1,k})^2]^{-1/2}$$

$$a_{k1} = -\rho_{1k}a_{kk}$$

$$a_{k2} = -(a_{21}\rho_{1k} + a_{22}\rho_{2k})a_{kk}$$

$$a_{k3} = -(a_{31}\rho_{1k} + a_{32}\rho_{2k} + a_{33}\rho_{3k})a_{kk}$$

$$a_{k,k-1} = -(a_{k-1,1}\rho_{1k} + a_{k-1,2}\rho_{2k} + \dots + a_{k-1,k-1}\rho_{k-1,k})a_{kk}$$

where ρ_{ij} is the correlation between Z'_i and Z'_j . The above transformations are derived in Ref. 26, where it is shown that the x_i are indeed independent normally distributed random variables, each with zero mean and unit variance. Thus, the likelihood function is the density function of the joint distribution of the x_i , given by

$$L(x_1, \dots, x_m) = \frac{1}{(2\pi)^{m/2}} \exp\left(-\frac{1}{2} \sum_{i=1}^m x_i^2\right)$$

$$y = \sum_{i=1}^m x_i^2$$

which has a maximum value of $(2\pi)^{-m/2}$. A *critical* (or *rejection*) region can now be designated as the interval $0 < L < A, A < (2\pi)^{-m/2}$, where A is determined such that, given H_0 , the probability of $L(x_1, \dots, x_m)$ lying in this interval is equal to ϵ , the significance level of the test. However, since $L(x_1, \dots, x_m)$ is a monotone function of

and $y = 0$ when $L = (2\pi)^{-m/2}$ and $y \rightarrow \infty$ when $L \rightarrow 0$, a critical region of the form $0 < L < A$ is equivalent to a critical region $y > B$, where B is determined so that the probability of $y > B$ equals ϵ .

Now, y has the chi-square distribution with m degrees of freedom, so that for a given value of ϵ , a value of B can easily be found in a table of percentage points of the chi-square distribution, such as that given in Ref. 28, pp. 130-131.

d. Testing a normal distribution with unknown parameters using six and eight quantiles. In practical situations, the null hypothesis is often made on the form of the density functions which may be a function of several unknown parameters. For example, one may wish to test the hypothesis that the parent population is normally distributed with unknown mean and variance. It is this case that will be considered and tests will be given using six and eight quantiles. The four-quantile case is given in Ref. 26.

In order to carry out this test when μ and σ are unknown, estimates of μ and σ are required and the same sample quantiles used for the test can also be used in the estimators. Optimum unbiased quantile estimators of μ and σ have been derived using up to twenty quantiles and are given in Ref. 26. However, since the orders of the quantiles which are optimum with respect to estimating μ are not, in general, those which are optimum with respect to estimating σ , suboptimum estimators of μ and σ were constructed using the same quantiles. The criterion used was minimization of the linear sum $\text{var}(\hat{\mu}) + c \text{var}(\hat{\sigma})$ for $c = 1, 2, 3$. The estimators that will be used here are those obtained for $c = 1$. Using six quantiles, these estimators are

$$\hat{\mu} = 0.0497(Z_1 + Z_6) + 0.1550(Z_2 + Z_5) + 0.2953(Z_3 + Z_4)$$

$$\hat{\sigma} = 0.1088(Z_6 - Z_1) + 0.1951(Z_5 - Z_2) + 0.1228(Z_4 - Z_3)$$

where

$$p_1 = 0.0237 \quad p_6 = 0.9769$$

$$p_2 = 0.1180 \quad p_5 = 0.8820$$

$$p_3 = 0.3369 \quad p_4 = 0.6631$$

Now, let Z be a sample quantile from a set of sample values taken from a normal population with density function $g(x)$. Let ζ^* denote the corresponding population quantile and ζ denote the corresponding population quantile of the standard normal distribution with density function $f(x)$. Then one has

$$p = \int_{-\infty}^{\zeta^*} g(x) dx = \int_{-\infty}^{(\zeta^* - \mu)/\sigma} f(x) dx = \int_{-\infty}^{\zeta} f(x) dx$$

Hence, one sees that, asymptotically,

$$E(Z) = \zeta^* = \mu + \zeta\sigma$$

and, since $g(\zeta^*) = 1/\sigma f(\zeta)$,

$$\text{var}(Z) = \frac{\sigma^2 p(1-p)}{nf^2(\zeta)}$$

so that the moments of the sample quantiles of normal distributions are expressible in terms of the standard normal. Thus, for the quantiles used above for estimating μ and σ , one has, replacing μ and σ by $\hat{\mu}$ and $\hat{\sigma}$,

$$E(Z_1) \cong \mu_1 = \hat{\mu} - 1.9936 \hat{\sigma} \quad E(Z_6) \cong \mu_6 = \hat{\mu} + 1.9936 \hat{\sigma} \quad \text{var}(Z_1) = \text{var}(Z_6) \cong \frac{7.5473 \hat{\sigma}^2}{n}$$

$$E(Z_2) \cong \mu_2 = \hat{\mu} - 1.1850 \hat{\sigma} \quad E(Z_5) \cong \mu_5 = \hat{\mu} + 1.1850 \hat{\sigma} \quad \text{var}(Z_2) = \text{var}(Z_5) \cong \frac{2.6633 \hat{\sigma}^2}{n}$$

$$E(Z_3) \cong \mu_3 = \hat{\mu} - 0.4209 \hat{\sigma} \quad E(Z_4) \cong \mu_4 = \hat{\mu} + 0.4209 \hat{\sigma} \quad \text{var}(Z_3) = \text{var}(Z_4) \cong \frac{1.6758 \hat{\sigma}^2}{n}$$

Recursive evaluation of the coefficients a_{ij} now provides the following transformation to independent variables for the six-quantile case, using the same quantiles for the test as were used to estimate μ and σ :

$$x_1 = \frac{0.3640 (n)^{1/2}}{\hat{\sigma}} (Z_1 - \mu_1)$$

$$x_2 = -0.4504x_1 + \frac{0.6721 (n)^{1/2}}{\hat{\sigma}} (Z_2 - \mu_2)$$

$$x_3 = -0.2455x_1 - 0.5451x_2 + \frac{0.9000 (n)^{1/2}}{\hat{\sigma}} (Z_3 - \mu_3)$$

$$x_4 = -0.1234x_1 - 0.2740x_2 - 0.4882x_3 + \frac{0.8904 (n)^{1/2}}{\hat{\sigma}} (Z_4 - \mu_4)$$

$$x_5 = -0.06312x_1 - 0.1401x_2 - 0.2497x_3 - 0.4834x_4 - \frac{0.7039 (n)^{1/2}}{\hat{\sigma}} (Z_5 - \mu_5)$$

$$x_6 = -0.02451x_1 - 0.05442x_2 - 0.09695x_3 - 0.1877x_4 - 0.3629x_5 + \frac{0.3954 (n)^{1/2}}{\hat{\sigma}} (Z_6 - \mu_6)$$

Although the above transformation is also used when μ and σ are known, it is important to note that the statistic

$$y = \sum_{i=1}^6 x_i^2$$

has only *four* degrees of freedom when μ and σ are unknown, since two degrees of freedom are lost in estimating μ and σ . Thus, to test H_0 using six quantiles, transform the observed values of Z_i (of order p_i) to the x_i by means of the above transformation; if

$$\sum_{i=1}^6 x_i^2 < B$$

accept H_0 . If

$$\sum_{i=1}^6 x_i^2 > B$$

reject H_0 . B is determined for six degrees of freedom when μ and σ are known, and for four degrees of freedom when they are estimated.

When eight quantiles are used, the suboptimum estimators are given by

$$\hat{\mu} = 0.0249 (Z_1 + Z_8) + 0.0764 (Z_2 + Z_7) + 0.1568 (Z_3 + Z_6) + 0.2419 (Z_4 + Z_5)$$

$$\hat{\sigma} = 0.0600 (Z_8 - Z_1) + 0.1249 (Z_7 - Z_2) + 0.1528 (Z_6 - Z_3) + 0.0789 (Z_5 - Z_4)$$

where

$$\begin{aligned}
 P_1 &= 0.0119 & P_8 &= 0.9881 \\
 P_2 &= 0.0604 & P_7 &= 0.9396 \\
 P_3 &= 0.1721 & P_6 &= 0.8279 \\
 P_4 &= 0.3711 & P_5 &= 0.6289
 \end{aligned}$$

and one also has

$$\begin{aligned}
 E(Z_1) &\cong \mu_1 = \hat{\mu} - 2.2603\hat{\sigma} & E(Z_8) &\cong \mu_8 = \hat{\mu} + 2.2603\hat{\sigma} & \text{var}(Z_1) = \text{var}(Z_8) &\cong \frac{12.2349\hat{\sigma}^2}{n} \\
 E(Z_2) &\cong \mu_2 = \hat{\mu} - 1.5515\hat{\sigma} & E(Z_7) &\cong \mu_7 = \hat{\mu} + 1.5515\hat{\sigma} & \text{var}(Z_2) = \text{var}(Z_7) &\cong \frac{3.9584\hat{\sigma}^2}{n} \\
 E(Z_3) &\cong \mu_3 = \hat{\mu} - 0.9459\hat{\sigma} & E(Z_6) &\cong \mu_6 = \hat{\mu} + 0.9459\hat{\sigma} & \text{var}(Z_3) = \text{var}(Z_6) &\cong \frac{2.1904\hat{\sigma}^2}{n} \\
 E(Z_4) &\cong \mu_4 = \hat{\mu} - 0.3290\hat{\sigma} & E(Z_5) &\cong \mu_5 = \hat{\mu} + 0.3290\hat{\sigma} & \text{var}(Z_4) = \text{var}(Z_5) &\cong \frac{1.6340\hat{\sigma}^2}{n}
 \end{aligned}$$

The transformation to the x_i is as follows:

$$x_1 = \frac{0.2859(n)^{1/2}}{\hat{\sigma}}(Z_1 - \mu_1)$$

$$x_2 = -0.4801x_1 + \frac{0.5576(n)^{1/2}}{\hat{\sigma}}(Z_2 - \mu_2)$$

$$x_3 = -0.2896x_1 - 0.6032x_2 - \frac{0.8130(n)^{1/2}}{\hat{\sigma}}(Z_3 - \mu_3)$$

$$x_4 = -0.1751x_1 - 0.3644x_2 - 0.5800x_3 + \frac{0.9581(n)^{1/2}}{\hat{\sigma}}(Z_4 - \mu_4)$$

$$x_5 = -0.1011x_1 - 0.2105x_2 - 0.3350x_3 - 0.5201x_4 + \frac{0.9311(n)^{1/2}}{\hat{\sigma}}(Z_5 - \mu_5)$$

$$x_6 = -0.05944x_1 - 0.1239x_2 - 0.1973x_3 - 0.3066x_4 - 0.5116x_5 + \frac{0.8033(n)^{1/2}}{\hat{\sigma}}(Z_6 - \mu_6)$$

$$x_7 = -0.03211x_1 - 0.06698x_2 - 0.1066x_3 - 0.1654x_4 - 0.2765x_5 - 0.4623x_6 + \frac{0.5806(n)^{1/2}}{\hat{\sigma}}(Z_7 - \mu_7)$$

$$x_8 = -0.01305x_1 - 0.02727x_2 - 0.04341x_3 - 0.06743x_4 - 0.1127x_5 - 0.1884x_6 - 0.3563x_7 - \frac{0.3109(n)^{1/2}}{\hat{\sigma}}(Z_8 - \mu_8)$$

The statistic

$$y = \sum_{i=1}^8 x_i^2$$

has eight degrees of freedom when μ and σ are known, but only six degrees of freedom when μ and σ are unknown.

e. Applying the test. The above tests were applied to two sets of sample values, each taken from non-normally distributed populations in order to test for normality. In Case A, the parent population was bimodal with a density function given by

$$g_A(x) = \frac{0.3}{(2\pi)^{1/2}} e^{-1/2 x^2} + \frac{0.7}{3(2\pi)^{1/2}} e^{-1/2 [(x-4)/3]^2}$$

200 sample values were generated from entries taken from a table of random numbers. The required sample quantiles to perform both the six- and eight-quantile tests were determined. The set of six quantiles gave the results, $\hat{\mu} = 2.813$, $\hat{\sigma} = 3.248$, as compared to $\mu = 2.8$, $\sigma = 3.156$. After transformation to independent variables under the null hypothesis that the population was normally distributed, the result

$$\sum_{i=1}^6 x_i^2 = 24.83 > 13.28$$

was obtained. Hence, H_0 is rejected at both the 0.01 and 0.05 levels. The set of eight quantiles gave the results,

$$\hat{\mu} = 2.805, \quad \hat{\sigma} = 3.250, \quad \sum_{i=1}^8 x_i^2 = 18.40 > 16.81$$

For this test, H_0 is again rejected at the 0.01 and 0.05 levels.

With respect to Case B, the parent population was also bimodal with a density function given by

$$g_B(x) = \frac{0.8}{(2\pi)^{1/2}} e^{-1/2 x^2} + \frac{0.2}{0.5(2\pi)^{1/2}} e^{-1/2 [(x-2)/0.5]^2}$$

The six-quantile test gave the results, $\hat{\mu} = 0.345$, $\hat{\sigma} = 1.208$ as compared to $\mu = 0.40$, $\sigma = 1.221$, and

$$\sum_{i=1}^6 x_i^2 = 16.99 > 13.28$$

The eight-quantile test gave the results

$$\hat{\mu} = 0.386, \quad \hat{\sigma} = 1.105, \quad \sum_{i=1}^8 x_i^2 = 30.15 > 16.81$$

Thus, both tests reject H_0 at both the 0.01 and 0.05 levels.

The same tests were then performed on two sets of sample values, each taken from a standard normal distribution. With $n = 200$ in both cases, the following results were obtained. From the first set, the six-quantile test gave

$$\hat{\mu} = 0.031, \quad \hat{\sigma} = 0.980, \quad \sum_{i=1}^6 x_i^2 = 3.38 < 9.49$$

The eight-quantile test gave

$$\hat{\mu} = 0.047, \quad \hat{\sigma} = 0.929, \quad \sum_{i=1}^8 x_i^2 = 5.69 < 12.59$$

From the second set, the six-quantile test gave

$$\hat{\mu} = -0.038, \quad \hat{\sigma} = 0.980, \quad \sum_{i=1}^6 x_i^2 = 5.93 < 9.49$$

The eight-quantile test gave

$$\hat{\mu} = -0.062, \quad \hat{\sigma} = 1.010, \quad \sum_{i=1}^8 x_i^2 = 9.37 < 12.59$$

Thus, in all cases, H_0 is accepted for $\epsilon = 0.05$ as well as for $\epsilon = 0.01$.

The power of the test, that is, the probability of rejecting H_0 when it is false, obviously depends upon the nature

of the true distribution (as well as on ϵ). In order to determine the power of the test relative to a specific alternate density function, one must find the probability that

$$\sum_{i=1}^m x_i^2 > B$$

under the simple alternative hypothesis H_1 , when the x_i are random variables resulting from transforming the Z_i under H_0 . Consequently, although the x_i are still normally distributed under H_1 , they are in general correlated and have means and variances other than 0 and 1, respectively. Under these conditions, the problem of determining the distribution of

$$y = \sum_{i=1}^m x_i^2$$

under H_1 is quite difficult. Accordingly, in order to estimate the power of the tests by "Monte Carlo" methods when H_0 is the hypothesis that the population in Case A is normally distributed with $\mu = 2.8$, $\sigma = 3.156$ and H_1 is the hypothesis that the population has a distribution with the true density function $g_A(x)$ given above, the Z_i were transformed to the x_i under H_0 , and then the first two moments and correlations of the x_i were computed under

H_1 . For the six-quantile case, 350 sets of the six x_i were generated from a table of random numbers, and for each set,

$$y = \sum_{i=1}^6 x_i^2$$

was computed. In 97.1% of the cases $y > 12.59$, and in 84.3% of the cases $y > 16.81$. For the eight-quantile case, 250 sets of the eight x_i were generated and for each set

$$y = \sum_{i=1}^8 x_i^2$$

was computed. For this case, in 93.0% of the cases $y > 15.51$, and in 83.6% of the cases $y > 20.09$.

Although the quantile estimators of μ and σ were derived on the basis of a normally distributed parent population, they are relatively insensitive to deviations from normality, as can be seen by comparing $\hat{\mu}$ and $\hat{\sigma}$ with the true means and standard deviations in Cases A and B where the parent populations were both bimodal. Thus, these estimators can be used effectively when the goodness-of-fit tests given here are applied to other types of density functions where the parameters are unknown but can be determined from knowledge of the mean or variance, or both.

References

1. Cranér, H., *Mathematical Methods of Statistics*. Princeton University Press, Princeton, New Jersey, 1946.
2. Balakrishnan, A. V., "Signal Selection Theory for Space Communication Channels," *Advances in Communication Systems: Vol. 1*. Academic Press, New York, N. Y., 1964.
3. Weber, C. L., "New Solutions to the Signal Design Problem for Coherent Channels," *IEEE Transactions on Information Theory*, April 1966.
4. Scholtz, R. A., and Weber, C. L., "Signal Design for Phase-Incoherent Communications," *Transactions IT*, October 1966.
5. Golomb, S. W., et al., *Digital Communications With Space Applications*. Prentice-Hall, New York, 1964.
6. Hall, M., Jr., "A Survey of Difference Sets," *Proc. Am. Math. Soc.*, Vol. 7, pp. 975-986, 1956.

References (contd):

7. Mann, H. B., *Introduction to Algebraic Number Theory*. The Ohio State University Press, Columbus, Ohio, 1955.
8. v.d. Waerden, B. L., *Modern Algebra*, Vol. 1, pp. 83-88. Frederick Ungar Publishing Co., Inc., New York, 1949.
9. Yamamoto, K., "Decomposition Fields of Difference Sets," *Pacific Journal of Mathematics*, Vol. 15, pp. 337-352, 1963.
10. du Castel, F., *Tropospheric Radiowave Propagation Beyond the Horizon*, pp. 56-57. Pergamon Press, New York, 1966.
11. *Meteorological and Astronomical Influences on Radio Wave Propagation*, p. 24. Edited by B. Landmark. Pergamon Press, New York, 1963.
12. *Advances in Radio Research*, pp. 53-120. Edited by J. A. Saxton. Academic Press, New York, 1964.
13. Lindsey, W. C., "Optimal Design of One-Way and Two-Way Coherent Communication Links," *IEEE Trans. Commun. Technol.*, Vol. Com-14, No. 4, pp. 418-431, August 1966.
14. Lindsey, W. C., *The Theory of Phase Coherent Communication Systems For Deep Space Applications*, Technical Report 32-986. Jet Propulsion Laboratory, Pasadena, Calif. (in press).
15. Lindsey, W. C., *A Wideband Adaptive Communication System*, Ph.D. thesis, Purdue University, Lafayette, Indiana, June 1962.
16. Lawton, J. G., "Theoretical Error Rates of Differentially Coherent Binary 'Kineplex' Data Transmission Systems," *Proc. IRE*, February 1959.
17. Tausworthe, R. C., *Theory and Practical Design of Phase-Locked Receivers*, Technical Report 32-819. Jet Propulsion Laboratory, Pasadena, Calif., February 15, 1966.
18. Lindsey, W. C., and Charles, F. J., *A Model Distribution For The Phase Error in Second-Order Phase-Locked Loops*, Technical Report 32-1017. Jet Propulsion Laboratory, Pasadena, Calif., October 1966.
19. Charles, F. J. and Lindsey, W. C., "Some Analytical and Experimental Phase-Locked Loop Results For Low Signal-to-Noise Ratios," *Proc. IEEE*, Vol. 54, pp. 1152-1166, September 1966.
20. Lindsey, W. C., *Optimum Coherent Linear Demodulation*, Technical Report 32-787. Jet Propulsion Laboratory, Pasadena, Calif., October 1, 1965. (Also appears in *IEEE Trans. Commun. Technol.*, Vol. Com-13, No. 2, June 1965.)
21. Lindsey, W. C., "Determination of Modulation Indices and Designing to Channel Coherent Communication Systems," *IEEE Trans. Commun. Technol.*, April 1966.
22. Lindsey, W. C., "Design of Block-Coded Communication Systems," *IEEE Trans. Commun. Technol.*, August 1967.

References (contd)

23. Lindsey, W. C., "On The Design Performance of Frequency Multiplexed, Phase-Modulated, Block Coded Communication Systems," presented at the National Telemetry Conference, San Francisco, Calif., May 16-18, 1967.
24. Viterbi, A. J., *Principles of Coherent Communication*, Chapter 8. McGraw-Hill Book Co., Inc., New York, 1966.
25. "Bessel Functions. Pt. II. Functions of Positive Integer Order," Vol. X of series "Mathematical Tables," *British Association for the Advancement of Science*, The University Press, Cambridge, England, 1931-46.
26. Eisenberger, I., and Posner, F. C., *Systematic Statistics Used for Data Compression in Space Telemetry*. Technical Report 32-510, Jet Propulsion Laboratory, Pasadena, Calif., October 1, 1963. (Also appears in *Journal of the American Statistical Association*, Vol. 60, pp. 97-133, Mar. 1965.)
27. Cramer, H., *Mathematical Methods of Statistics*. Princeton University Press, Princeton, N. J., 1946.
28. Pearson, E. S., and Hartley, H. O., *Biometrika Tables for Statisticians, Vol. 1*. Cambridge University Press, Cambridge, England, 1962.

N67-34779

XVIII. Communications Elements Research

TELECOMMUNICATIONS DIVISION

A. RF Techniques: 90-GHz mm Wave Work,

W. V. T. Rusch¹, S. D. Slobin¹, and C. T. Stelzried

During the period of April 4 through July 10, 1966, a series of lunation observations were carried out using the USC-JPL millimeter wavelength radio astronomy facility located on the JPL Mesa Antenna Range. Useful data were obtained on only 23 dates in this period, primarily because of bad weather. However, better measurement resolution was obtained during this experiment than during a similar lunation experiment in 1965, due to improved instrumentation and data reduction techniques.

1. Observations

The observational technique has been refined to yield a maximum amount of data for a given night's effort, while still maintaining accurate calibration standards. One drift curve sequence consists of the following operations: The center of the moon is tracked for 2 min and then the antenna tracking drive is turned off, allowing the moon to drift out of the antenna beam. After 2 min have passed, a gas tube noise output is recorded for 1 min. The antenna is then repositioned on the center of the moon for the following drift curve. All data taken are recorded by both

¹Consultant from the Electrical Engineering Department, University of Southern California.

a chart recorder and by a digital voltmeter. The output of the digital voltmeter is used to give quantitative data, while the chart recorder is used primarily to monitor the system performance. Before and after each night's runs, the gas tube noise output is calibrated by comparing it with the outputs of matched waveguide terminations heated to known temperatures. The analog and digital output of a typical drift curve may be seen in Fig. 1.

The output of each night's runs [which included the ratio moon output (digital)/gas tube output (digital), zenith angle for each drift curve, and complete gas tube calibration measurements] was recorded on IBM cards and submitted for computer evaluation.

2 Data Reduction

Figure 2 shows a typical computer data reduction print-out (program designated CTS 10). This program gives a least squares solution to the equation

$$\frac{T_{ant}}{T_{gt}} = \frac{T_{ant,cor}}{T_{gt}} (LO)^{-sec z} \quad (1)$$

or

$$TA = TAC (L_0)^{-sec z} \quad (2)$$

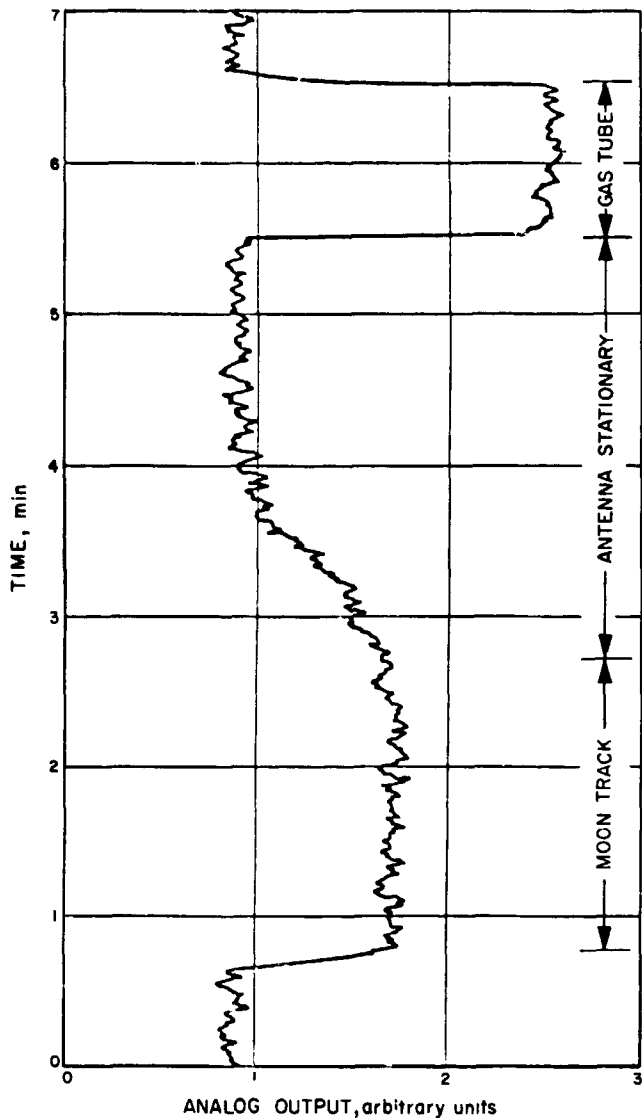


Fig. 1. Luration drift curve, showing analog and digital output

TIME			OUTPUT								
h	min	s	1	2	3	4	5	6	7	8	9
2	2	1	1	5	8	4	1	8	7	1	1
2	2	1	1	4	5	4	2	4	1	4	1
2	2	1	1	3	3	4	2	7	0	2	1
2	2	1	1	2	1	6	8	5	9	7	1
2	2	1	1	0	8	6	8	5	7	0	1
2	2	1	0	5	6	6	9	2	4	6	1
2	2	1	0	4	3	6	8	1	1	2	1
2	2	1	0	3	1	6	8	1	2	2	1
2	2	1	0	1	9	4	2	8	3	1	1
2	2	1	0	0	0	4	2	4	9	1	1
2	2	0	9	5	4	4	2	6	1	6	1
2	2	0	9	4	9	4	2	8	2	6	1
2	2	0	9	2	9	4	2	3	8	0	1
2	2	0	9	1	4	4	2	6	0	5	1
2	2	0	9	0	4	4	2	6	9	8	1
2	2	0	8	5	2	4	3	3	6	8	1
2	2	0	8	7	6	4	4	2	6	8	1
2	2	0	8	2	7	4	6	5	1	9	1
2	2	0	8	1	4	4	9	1	5	0	1
2	2	0	8	0	2	5	1	9	9	0	1
2	2	0	7	5	0	5	2	8	4	8	1
2	2	0	7	3	7	5	5	1	1	5	1
2	2	0	7	2	5	5	4	8	5	3	1
2	2	0	7	1	2	5	6	2	9	2	1
2	2	0	7	0	0	5	6	1	6	3	1
2	2	0	6	4	8	5	6	3	2	2	1
2	2	0	6	3	5	5	5	9	6	9	1
2	2	0	6	2	3	5	5	5	2	1	1
2	2	0	6	1	7	5	5	7	3	7	1
2	2	0	5	5	8	5	6	3	7	1	1
2	2	0	5	4	5	5	6	1	6	3	1
2	2	0	5	3	3	4	5	3	9	3	1
2	2	0	5	2	1	4	3	1	4	5	1
2	2	0	5	0	8	4	2	2	8	5	1
2	2	0	4	5	6	4	2	8	6	8	1

where

$$TA = \frac{T_{ant}}{T_{gt}} = \text{measured ratio of radio source antenna temperature divided by gas tube noise temperature contribution}$$

$$TAC = \frac{T_{ant, cor}}{T_{gt}} = \text{ratio of antenna temperature corrected for atmospheric loss, divided by gas tube noise temperature contribution}$$

$LO = L_0 = \text{zenith atmospheric loss } (LO > 1)$

$\sec z = \text{secant of the zenith angle } (z = 0 \text{ is overhead})$

The actual radio source disc temperature is given by

$$T_{disc} = \frac{T_{ant, cor}}{BCF} = \frac{TAC \times T_{gt}}{BCF} \quad (3)$$

where BCF is the beam correction factor defined by

$$BCF = \frac{G_0}{4\pi} \int_{source} f(\Omega) d\Omega \quad (4)$$

and

$G_0 = \text{net gain of the antenna}$

$f(\Omega) = \text{normalized antenna pattern}$

RADIO SOURCE MEASUREMENTS..... LUNAR DATA APRIL 30, 1966 (UP)					
TA	Z	TA(LN)	TA-TA(LN)	TA(TAY)	TA-TA(TAY)
0.86850	67.450	0.88031E 00	-0.11812E-01	0.87985E 00	-0.11345E-01
0.94350	65.130	0.90823E 00	0.35267E-01	0.90806E 00	0.35441E-01
0.98020	62.200	0.93752E 00	0.42679E-01	0.93766E 00	0.42536E-01
0.91990	59.800	0.95762E 00	-0.37720E-01	0.95799E 00	-0.38087E-01
0.89400	57.280	0.97574E 00	-0.81737E-01	0.97631E 00	-0.82310E-01
1.00750	54.620	0.99216E 00	0.15337E-01	0.99293E 00	0.14574E-01
1.04630	51.530	0.10084E 01	0.37874E-01	0.10094E 01	0.36921E-01
1.01180	48.970	0.10200E 01	-0.82138E-02	0.10211E 01	-0.93048E-02
0.99150	46.780	0.10288E 01	-0.37289E-01	0.10300E 01	-0.38485E-01
1.06390	44.730	0.10362E 01	0.27722E-01	0.10375E 01	0.26437E-01
1.07750	42.550	0.10433E 01	0.34237E-01	0.10446E 01	0.32865E-01
1.04250	40.180	0.10502E 01	-0.76686E-02	0.10516E 01	-0.91246E-02
TAC(LN)= 0.12545E 01		PETAC(LN)= 0.46382E-01		PETA(LN)= 0.27345E-01	
LO(LN)= 0.11455E 01		PELO(LN)= 0.23202E-01			
LO(LN)DB= 0.58996E 00		PELO(LN)DB= 0.87965E-01			
TAC(TAY)= 0.12587E 01		PETAC(TAY)= 0.46103E-01		PETA(TAY)= 0.27336E-01	
LO(TAY)= 0.11472E 01		PELO(TAY)= 0.23612E-01			
LO(TAY)DB= 0.59637E 00		PELO(TAY)DB= 0.89388E-01			
NO. ITERATIONS FOR EACH COMPLETE CYCLE= 2					

Fig. 2. Computer printout for lunation data reduction (April 30, 1966)

The beam correction factor is obtained from antenna gain and pattern calibrations. The USC 60-in. millimeter antenna has a higher gain and somewhat narrower beamwidth than when measured previously (1965).

A complete description of the solutions of Eq. (1) is given in SPS 37-36, Vol. IV, pp. 255-258. Referring to Fig. 2, TA represents the measured ratio of radio source antenna temperature divided by the gas tube noise temperature contribution. TAC represents the same quantity after correction for atmospheric attenuation. Quantities involving the notation (LN) represent solutions to Eq. (2) by linearizing the data with respect to the logarithmic equation

$$\ln(TA) = \ln(TAC) - \sec(z) \ln(LO) \quad (5)$$

Quantities involving the notation (TAY) represent solutions to Eq. (2) by linearizing the data using a Taylor series expansion of Eq. (2).

The logarithm linearization method introduces an unknown weighting factor that does not occur in the Taylor series method (Ref. 1). Therefore, the latter method was used to determine final values for lunar temperature during the lunation, utilizing Eqs. (3) and (4). The columns

$TA - TA(LN)$ and $TA - TA(TAY)$ indicate the error between the actual measured value of TA at a particular zenith angle and the calculated value $TAC(LO)^{-\sec z}$, by both methods. Quantities involving PE indicate the probable error of the associated quantities.

Accurate calibrations of the gas tube noise contribution were made throughout the lunation. A straight line is fitted to the values obtained for each day, and this new value is used as the average gas tube contribution for that day. This method smooths out the daily measurement errors for the gas tube contribution and accounts for long-term drifts in the gas tube.

3. Results

The resulting lunation curve for the period April 4 through July 10, 1966 is shown in Fig. 3. Comparison of this curve with the 1965 lunation curve indicates a reduced scatter of data points as well as a reduced uncertainty for each data point. The data from phase 180 to 270 deg are repeated for the sake of clarity. The increased accuracy was obtained by improving the instrumentation, increasing the period of the on-off cycle, and taking more data points. In addition, every data point in Fig. 2 is the result of averaging both pre- and posttransit data.

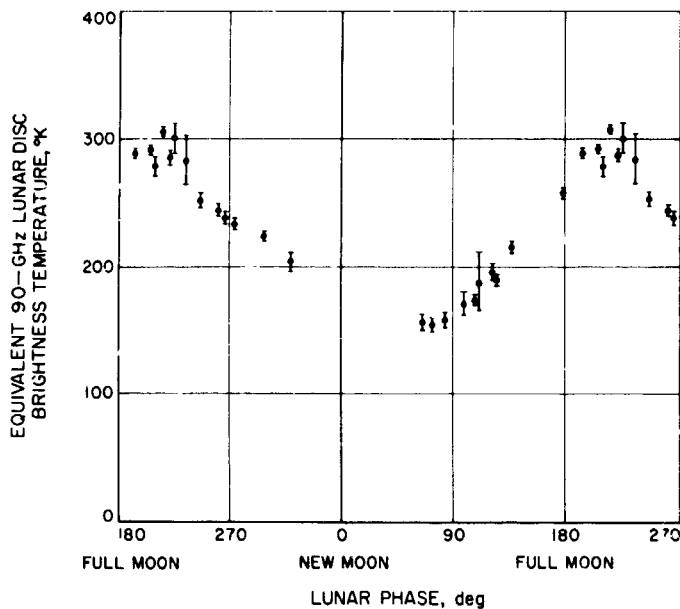


Fig. 3. Lunation curve (April 4 through July 10, 1966)

The error flags represent the probable error due to measurement dispersion only. The resulting scatter of the data points is attributed primarily to changing atmospheric loss rather than to experimental uncertainty, as the resolution of the radiometer is much higher than the spread of data would indicate. Changes in atmospheric loss during the course of a series of observations can frequently produce misleading data; and the process of averaging pre- and posttransit data usually results in smoothing the scatter but not eliminating it.

B. Quantum Electronics: Optical Communications Components, M. S. Shumate and J. C. Siddoway

1. Carbon Dioxide Laser Heterodyne Receiver, M. S. Shumate

The use of the nitrogen-carbon dioxide laser wavelengths ($\sim 10.6 \mu\text{m}$) for deep space communication has been discussed recently (Refs. 2 and 3), and although the desirability of such a communications system is subject to discussion, its feasibility has been adequately established (Ref. 2). This article describes an experiment leading toward a laboratory demonstration of a $10.6\text{-}\mu\text{m}$ laser heterodyne receiver.

Of the several pieces of equipment necessary for a $10.6\text{-}\mu\text{m}$ laser communications system, the receiver portion of the system is one of the least developed. The state of the art for efficient ($\sim 17\%$) (Ref. 4), high-power transmitters is adequate, although no space qualified laser transmitter has yet been constructed. Appropriate modu-

lators exist, and present day telescope technology is sufficient for both the transmitting and receiving antennas. A sketch of an optical heterodyne receiver is presented in Fig. 4.

A laboratory demonstration of a laser heterodyne receiver suitable for deep space communication is now being prepared. Previous heterodyne experiments with $10.6\text{-}\mu\text{m}$ carbon dioxide lasers have been reported (Ref. 5-7²).

However, most of the emphasis in these experiments has been on the narrow band detector performance; these experiments have not adequately simulated an optical receiver. The present experiment will use two separate lasers, one serving as a transmitter and the other as a local oscillator. The transmitter beam can be suitably attenuated and modulated in order to simulate a weak, broad band signal.

Construction of the various pieces of apparatus has begun. The laboratory facilities have been suitably modified to eliminate air conditioning noise and vibration from the table used for the experiment. A gas handling system for controlling and metering the gases used by the laser has been constructed, as well as two complete lasers. Peripheral monitoring apparatus has been purchased or fabricated.

"Heterodyne Operation of 10M Photoconductive Detectors" by C. J. Buczek, G. S. Picus, and D. E. Bode, to be published.

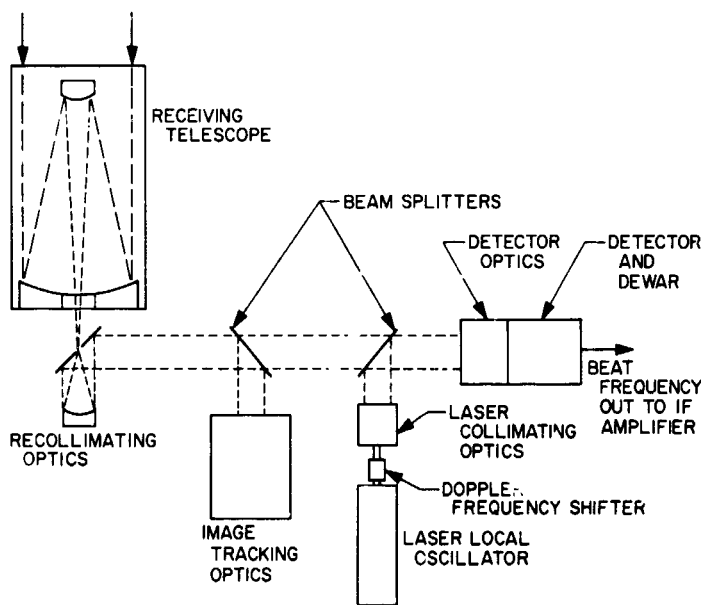


Fig. 4. Sketch of an optical heterodyne receiver

Prior to actual heterodyne experiments, it has been necessary to perform an accurate wavelength determination of the carbon dioxide laser lines, in order to calculate the optimum laser cavity length (SPS 37-39, Vol. IV, pp. 196-198). Experiments are also in progress to determine the discharge tube configuration. Problems involving frequency stability of the laser have occurred, the effect being due to thermal drifts and mechanical vibration of the laser cavity mirrors. Although present experiments indicate reasonable stability, it may be necessary to devise a frequency stabilizing technique in order to obtain the required laser frequency stability.

2. Isotopic CO₂ Laser Studies, J. C. Siddoway

The development of an efficient laser whose output is in a favorable atmospheric window has made the carbon dioxide laser a potential candidate for a future high data rate transmission link from deep space. However, there are many problems to be studied before the full potential

of such a system can be demonstrated. This summary describes a program to study:

- (1) Impurity and/or "gettering" effects which limit the lifetime of sealed-off CO₂ lasers.
- (2) The use of various isotopes to prevent radiation absorption by thermally excited CO₂ molecules in the atmosphere.
- (3) Isotopic lasers as possible local oscillators to account for Doppler shifts.

Three isotopes of carbon dioxide ($C^{12}O_2^{16}$, $C^{13}O_2^{16}$, $C^{14}O_2^{16}$) have been obtained for study. Since some of the reaction products formed in the discharge fall on the same mass number of parent molecules present in the laser, definite results concerning possible contaminants are difficult to obtain. (Two examples are: mass 28; N₂, CO and mass 44; CO₂, N₂O.) The use of isotopes to shift these lines on the

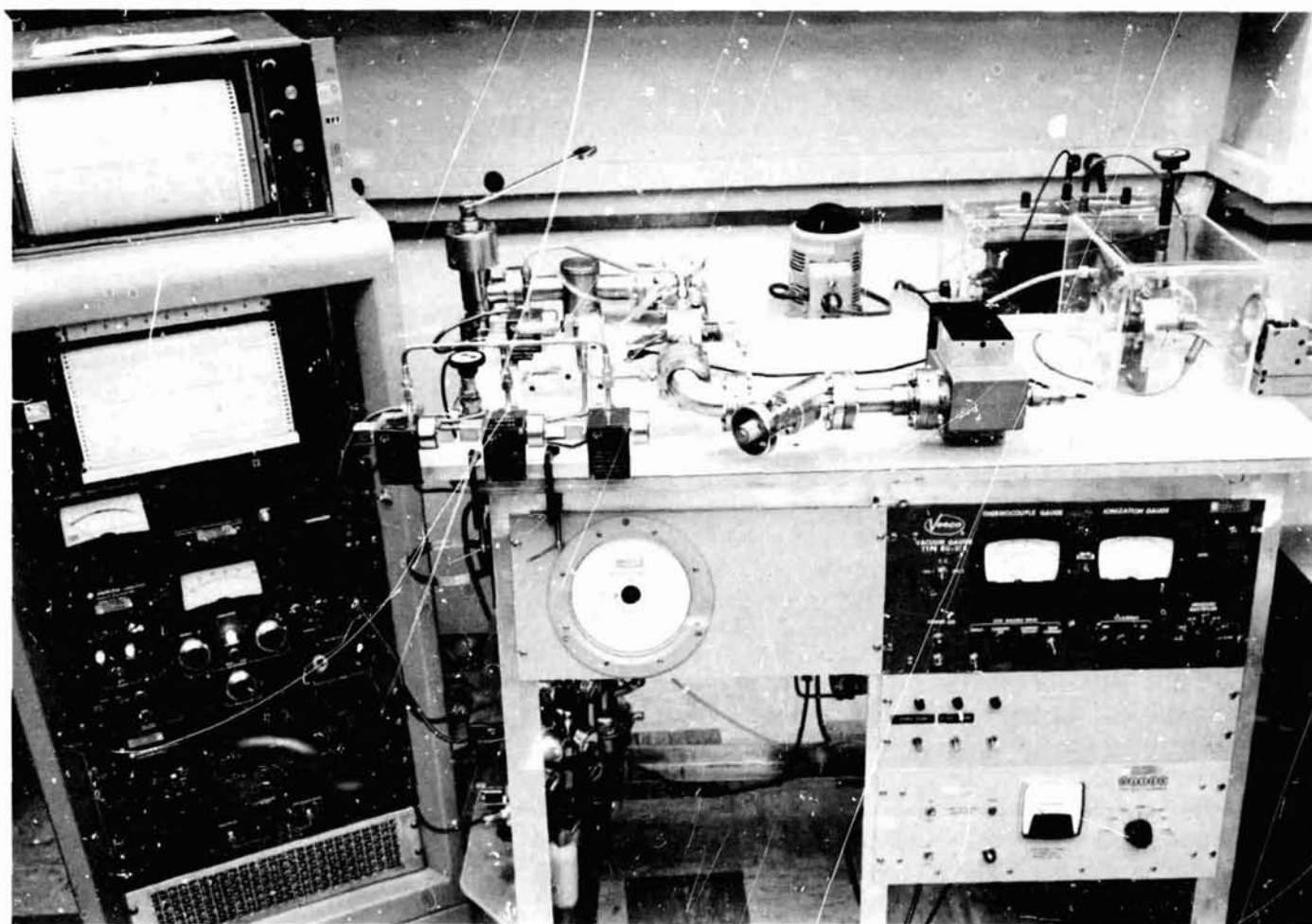


Fig. 5. Isotopic CO₂ laser

mass scale will make analysis much easier and more quantitative.

The isotopic wavelengths will be measured using a 0.75-m Spex grating monochrometer. Comparisons can then be made with the absorption spectra of the atmosphere to determine suitable operational wavelengths. Isotopic CO_2 may also be desirable for use in a receiver in a local oscillator since the calculated Doppler shift (~ 500 MHz) from a typical spacecraft operation is approximately an order of magnitude greater than the tuning capability allowed by the Doppler broadened linewidth.

a. Apparatus. The laser which has been constructed for the isotopic CO_2 studies is shown in Fig. 5. The water cooled discharge tube is 24 in. long with a $\frac{1}{2}$ -in. ID. Each end of the tube is equipped with bakeable high-vacuum (Conflat) flanges using copper gaskets for seals. The brewster window mounts and aluminum electrodes are attached to a mating flange through which $\frac{1}{8}$ -in. copper tubing has been run to provide cooling for the electrodes. The windows, polished flats of potassium chloride, are sealed with a low vapor pressure epoxy (Varian Torr Seal). Double sided Conflat inserts are used between the flanges to provide gas inlet and vacuum exhaust ports. The optical reflectors are gold coated, nearly opaque mirrors; one of 2-m radius of curvature and a flat through which a 3-mm diam hole provides output coupling.

Three Granville-Phillips variable leak valves control gases admitted into the discharge tube, and the pressure is monitored with a Wallace & Tiernan gauge. A fourth variable leak valve allows small samples of gas to flow from the discharge tube to the analysis chamber of a Varian quadrupole mass spectrometer and then to the vacuum system. Used in this fashion the instrument permits comparisons of background, impurities, relative amounts of the original gases before and after the discharge has been run, and new molecular species formed in the discharge.

The main vacuum system is a 2-in. mercury diffusion pump with two Granville-Phillips liquid nitrogen cold traps. (Mercury is used to prevent hydrocarbon contamination of the mass spectrometer.) Also, a Vac-Ion pump allows continuous pumping of the discharge without full time operation of the Hg pump and cold traps. High-vacuum fittings have been used throughout the apparatus so that pressures at least of the order of 10^{-6} mm Hg are attainable.

Construction of the apparatus is now complete, and initial operations have been concerned with leak checking and calibration. Lifetime studies have recently been started, but no definitive results have yet been obtained.

C. Propagation Studies: Planetary Entry Blackout, G. S. Levy

A study³ was conducted under a JPL contract to determine the effect of entry plasma on the telemetry link of a Mars lander. The effects of both frequency shift and attenuation were studied, and a report has been issued (Ref. 8). The plasma environment model used in this study was adopted from D. Spencer (Ref. 9). It was found that for the model used both attenuation and frequency shift can be significant effects.

As a spacecraft enters the atmosphere of Mars, a plasma column trailing the spacecraft is generated. The strength and the frequency of the signal originating from the spacecraft are greatly affected by the presence of this plasma column. The objective of this investigation was to obtain an estimation of the frequency shift as well as the attenuation of the signal passing through the plasma column based on an idealized model (Ref. 8, Fig. 6).

It is assumed for this model that: (a) the plasma is confined in a cylindrical column swept out by the spacecraft;

³Conducted by Dr. G. Cohn of Quantum Engineering, Pasadena, California.

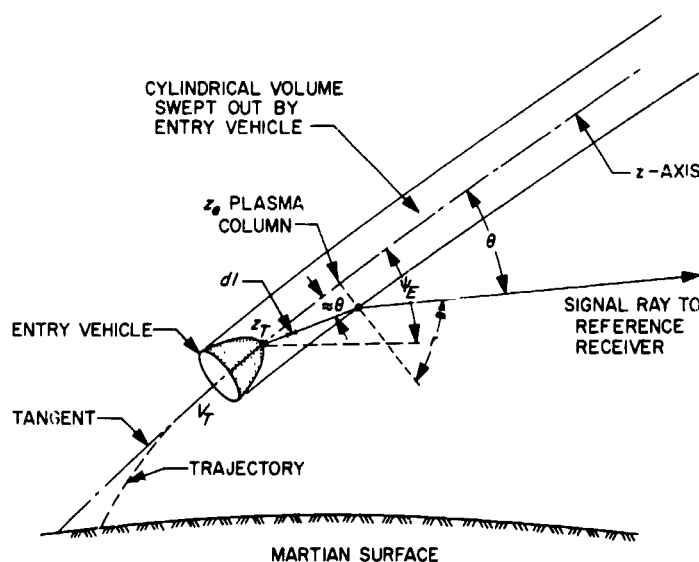


Fig. 6. Entry vehicle, trajectory and plasma column configuration

(b) the plasma is uniformly distributed over each circular cross section of the column; and (c) the density of the plasma varies along the column in accordance with the generation rate and the decay rate of the plasma for the nonfrozen flow model. Furthermore, it is assumed that the plasma medium may be adequately described by a cold plasma permittivity constant with loss (Ref. 9). The velocity, electron collision frequency and plasma frequency, as functions of altitude, are shown in Figs. 7-9.

1. Signal Attenuation

Under the W.K.B. approximations, the total signal attenuation A between the transmitter and the point where the signal emerges from the plasma column can be obtained from the following expression

$$A = \int_{l_T}^{l_e} \alpha dl \quad (1)$$

where α is the attenuation per unit length along the ray path; l_T is the location of the transmitter; and l_e is the location where the ray emerges from the plasma column. Expressing Eq. (1) in cylindrical coordinates with the

z -coordinate along the plasma cylinder axis and making use of the assumed plasma model, one has (Ref. 10)

$$A = \int_{z_T}^{z_e} \frac{\alpha(z)}{c \cos \theta} dz \quad (2)$$

where z_e , z_T and θ are shown in Fig. 6. $\alpha(z)$ is obtained using the cold plasma model with collision, (Refs. 3 and 9) or,

$$\alpha(z) = \frac{\omega}{c(2)^{1/2}} \left\{ \frac{\omega_p^2}{\omega^2 + \nu^2} - 1 + \left[\left(1 - \frac{\omega_p^2}{\omega^2 + \nu^2} \right)^2 + \left(\frac{\omega_p^2}{\omega^2 + \nu^2} \right)^2 \right]^{1/2} \right\} \quad (3)$$

where c is the velocity of light in vacuum; and the plasma frequency ω_p and the collision frequency ν are functions

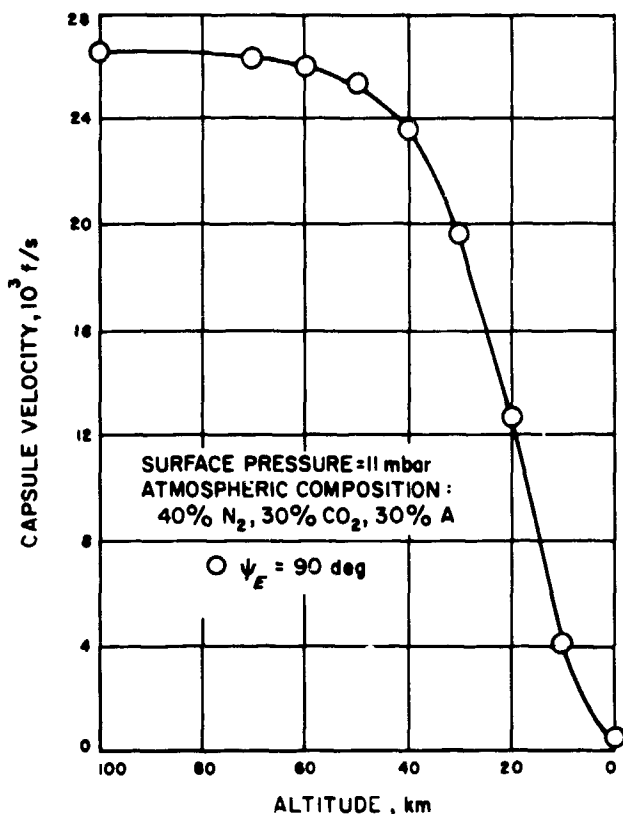


Fig. 7. Velocity versus altitude

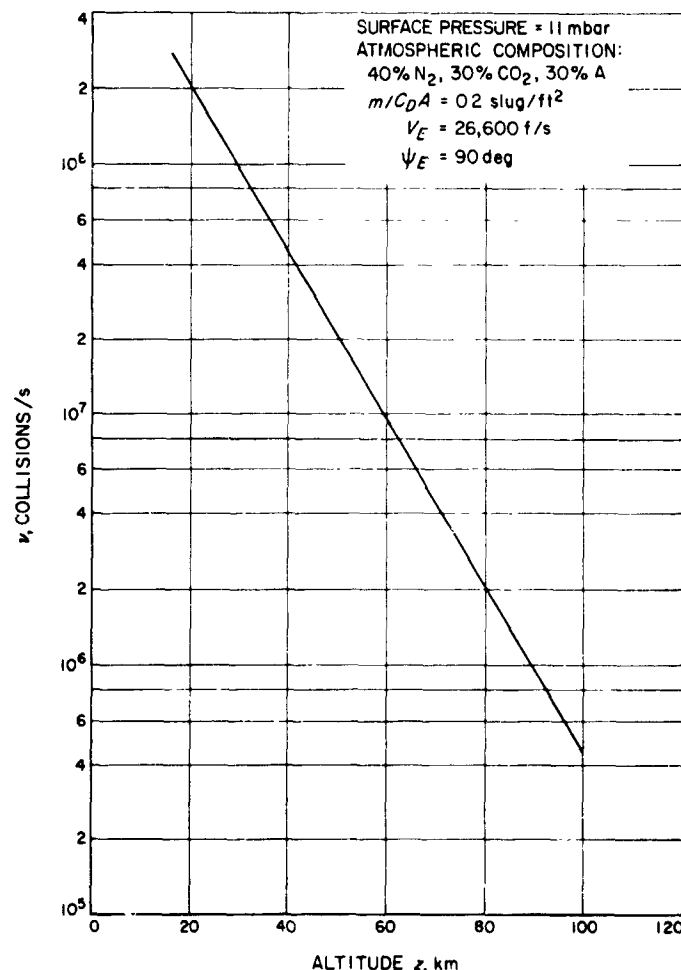


Fig. 8. Electron collision frequency versus altitude

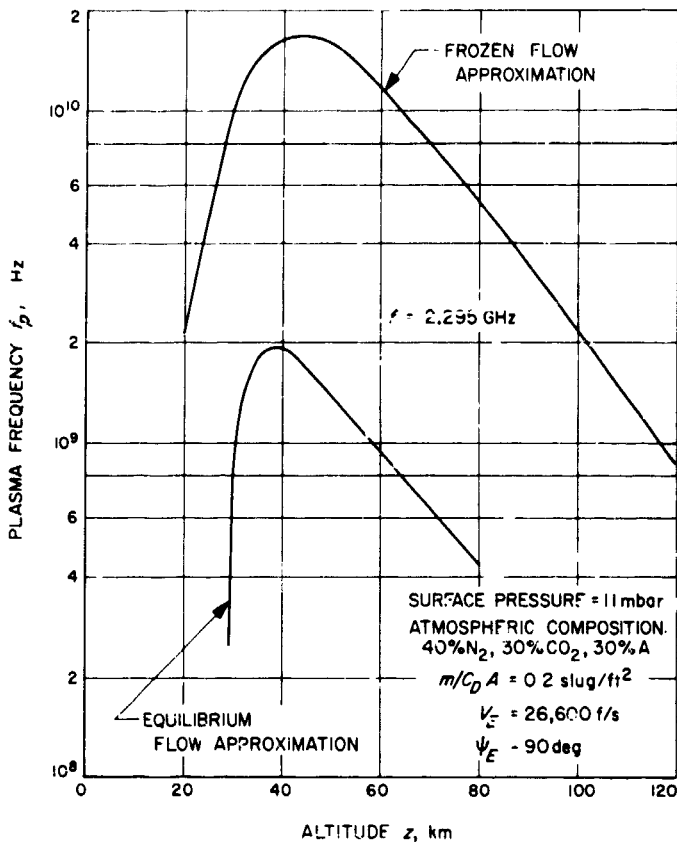


Fig. 9. Plasma frequency versus altitude

of z in accordance with the plasma density variation described in Ref. 10. The attenuation in dB/m within the plasma column is presented as a function of altitude for both frozen and equilibrium flow in Fig. 10.

2. Signal Frequency Shift

With the assumption that the velocity of the space vehicle is much less than the phase velocity of a plane wave in the plasma medium, the frequency of the received signal may be given as follows (Ref. 10):

$$f_R = f_T \left[1 + \frac{v_{Tl} - v_{Rl}}{v_p} - \int_{l_T}^{l_R} \frac{d}{dt} \left(\frac{1}{v_p} \right) dl \right] \quad (4)$$

where f_R and f_T are, respectively, the frequency of the received signal and the transmittal signal. $(v_{Tl} - v_{Rl})$ is the relative velocity between the transmitter and the receiver. v_p is the phase velocity of a plane wave in the plasma medium. l_R and l_T represent, respectively, the receiver location and the transmitter location. The second term in Eq. (4) represents the classical doppler frequency shift while the third term in Eq. (4) represents the frequency shift due to the changes in the internal properties

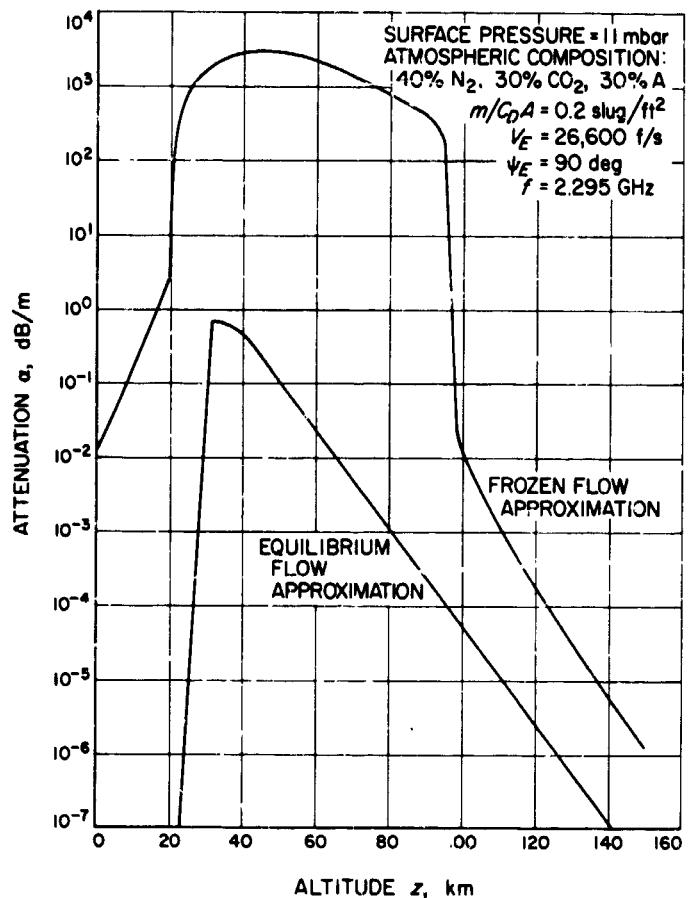


Fig. 10. The attenuation per unit length versus altitude

of the propagation path. Eq. (4) is derived from the phase kinematic considerations (Ref. 10)

Assuming that the phase velocity does not vary significantly within the signal ray path under consideration, one may make the following approximation for the last term in Eq. (4)

$$- \int_{l_T}^{l_R} \frac{d}{dt} \left(\frac{1}{v_p} \right) dl \approx - \frac{a}{\sin \theta} \frac{d}{dt} \left(\frac{1}{v_p} \right) \quad (5)$$

where a is the radius of the plasma column and θ is shown in Fig. 6. With the further assumption that the dependence on time is only due to the change in the spacecraft position for the frozen flow model, we have

$$\begin{aligned} - \int_{l_T}^{l_R} \frac{d}{dt} \left(\frac{1}{v_p} \right) dl &\approx - \frac{a}{\sin \theta} v_T \frac{d}{dl_T} \left(\frac{1}{v_p} \right) \\ &= - \frac{a v_T \sin \psi_E}{\sin \theta} \frac{d}{dz} \left(\frac{1}{v_p} \right) \end{aligned} \quad (6)$$

where ψ_E is defined in Fig. 6,

$$v_T = -\frac{v_{T1}}{\cos \theta}$$

and

$$\frac{1}{v_p} = \frac{1}{(2)^{1/2} C} \left\{ 1 - R + \left[(1 - R)^2 + \left(\frac{v}{\omega} R \right)^2 \right]^{1/2} \right\} \quad (7)$$

with

$$R = \frac{\omega_p^2}{\omega^2 + \nu^2}$$

3. Numerical Examples

Numerical computations were carried out for specific models representing the Martian atmosphere in accordance with Ref. 8. Results are shown in Figs. 11 and 12. In Fig. 11, the component frequency shift is plotted against the altitude of the Martian atmosphere. The symbols used in Fig. 11 are defined as follows (Ref. 10):

$$f_{STP} = \left(\frac{v_{T1}}{c} \right) f_T$$

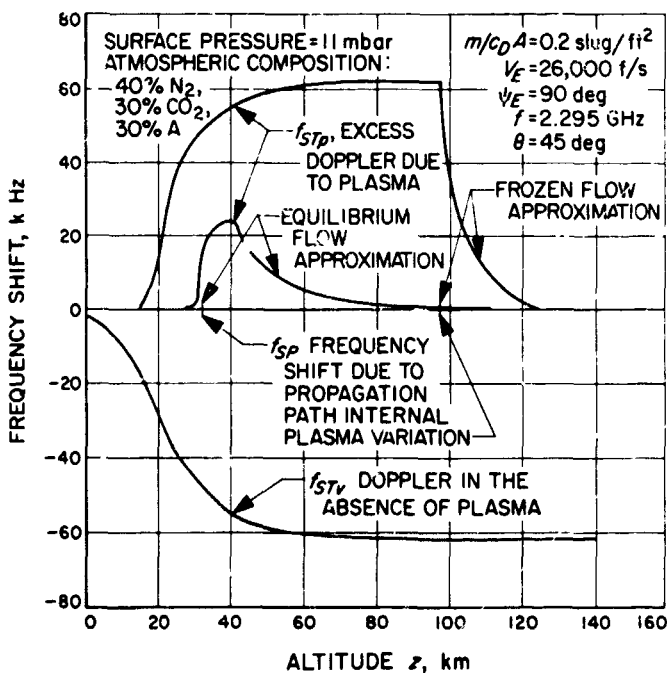


Fig. 11. Component frequency shift versus altitude

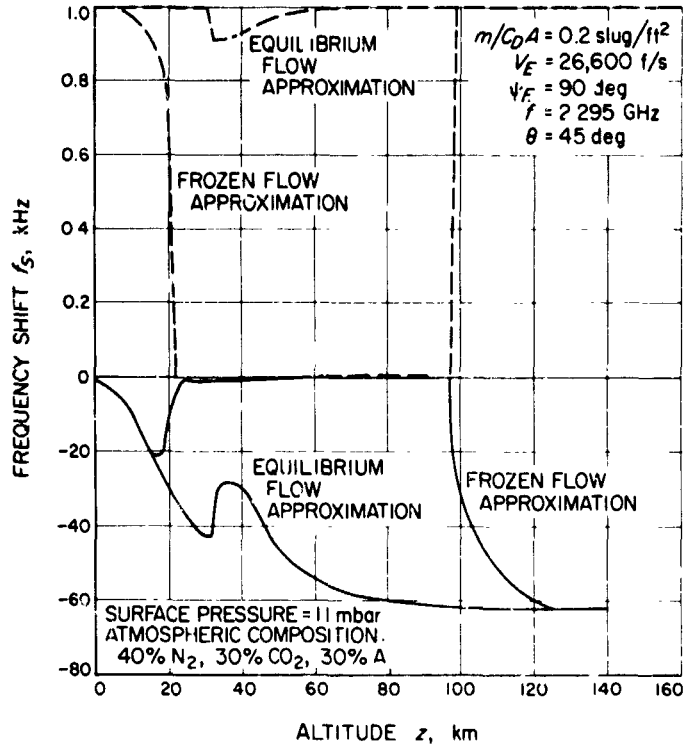


Fig. 12. Frequency shift and signal relative amplitude versus altitude

$$f_{STP} = \left(\frac{v_{T1}}{v_p} - \frac{v_{T1}}{c} \right) f_T$$

$$f_s = \left(\frac{v_{T1} - v_{R1}}{v_p} - \int_{l_1}^{l_2} \frac{d}{dt} \frac{1}{v_p} dl \right) f_T$$

$$f_{SP} = \left(- \int_{l_1}^{l_2} \frac{d}{dt} \frac{1}{v_p} dl \right) f_T$$

In Fig. 12, the total frequency shift f_s and the relative signal amplitude are both plotted against the altitude of the Martian atmosphere.

D. Low Noise Transponder Preamplifier Research, W. H. Higa

Spacecraft transponders currently use a mixer with a noise figure of ~ 8 dB as the input stage. A preamplifier could be used to improve the receiver sensitivity by at least 3 dB without too much difficulty. However, to realize the improvement with a minimum of additional dc power drain is of great importance for deep space probes. A figure of merit is defined as a starting point for solving this problem. Various possibilities are being compared.

The effective input noise temperature T_e of a preamplifier followed by a mixer is given by

$$T_e = T_1 + \frac{T_2}{G_1}$$

where

T_1 = noise temperature of preamplifier

G_1 = power gain of preamplifier

T_2 = noise temperature of mixer

Figure 13 shows a graph of T_e as a function of T_1 for different gains G_1 . Two horizontal reference lines for an 8-dB mixer and a 5-dB mixer are shown also.

An arbitrary figure of merit for a spacecraft preamplifier can be expressed as

$$M = \frac{T_e \times P_{dc} \times S}{R}$$

where

M = figure of merit

P_{dc} = dc power input

S = stability factor

R = reliability (e.g., mean time before failure)

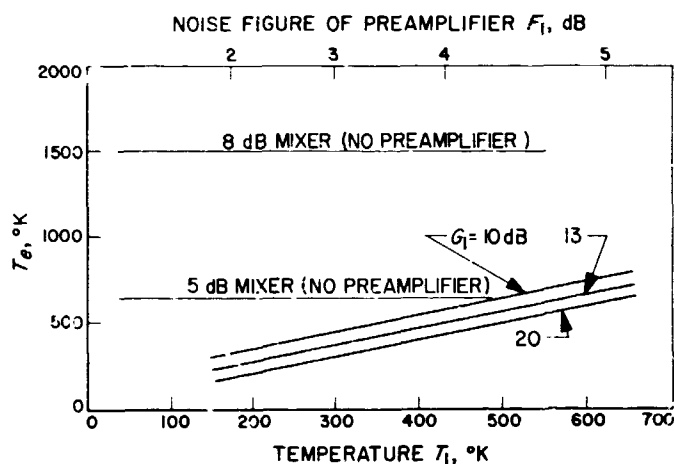


Fig. 13. Effective input noise temperature for different preamplifier noise temperatures (followed by 8-dB mixer) and different gains G_1 .

Clearly a low value of M is desirable. The stability factor S is a product of gain variation coefficients, such as $\Delta G_1/\Delta T$, $\Delta G_1/\Delta V_{dc}$ where

ΔT = change in ambient temperature

ΔV_{dc} = change in power supply voltage

Current developments in semiconductor devices make the following devices attractive competitors at 2115 MHz

- (1) Transistor amplifiers.
- (2) Tunnel diode amplifiers.
- (3) Parametric amplifiers with solid state pump.

In Table 1 typical values are compared for various parameters. The dc power requirements shown include losses in the regulating circuits employed. Potentially, the tunnel diode amplifier is most attractive in this respect.

The paramp is good from the point of view of noise temperature, while the transistor amplifier is good with respect to stability and reliability.

One each of the devices has been ordered, and an evaluation program will commence soon.

Table 1. A comparison of various parameters for three different solid state preamplifiers

Device	Noise figure typical, dB	Typical P_{dc} , W	Stability	Reliability	Typical gain, dB
Transistor	4-6	0.5	Good	Excellent	15
Tunnel diode	3-5	0.4	Fair	Good	15
Paramplifier	2-4	1.0	Poor	Fair	15

E. Thermally Isolated Transmission Lines,

C. T. Stelzried, T. Y. Otschi, and D. L. Mullen

Spacecraft onboard communication systems require microwave transmission lines with high reliability, low loss and light weight. Microwave transmission lines which provide thermal isolation are used in the construction of thermal calibration terminations (cold loads). These thermal terminations provide noise temperature calibration instrumentation for low noise receiving systems. The thermally isolated transmission lines are usually fabricated from thin-wall stainless steel. Copper plating is used to reduce the microwave insertion loss.

1. Description

A lightweight thermally isolated low-loss waveguide section has been fabricated with plastic. Fig. 14 shows a photograph of an H-band plastic waveguide test section (RFT 265) obtained from Maury Microwave Corporation, Montclair, California. This unit is 6.0 in. in length with $\frac{1}{16}$ -in. wall thickness. The section was fabricated by hand wrapping fiberglass tape to the desired thickness on a steel mandrel and impregnating with liquid plastic. The plastic flanges are an integral part of the section. The necessary conductive film on the interior and flange faces is provided by first spraying approximately 0.005-in. thick aluminum on the mandrel. The waveguide interior is given a thin gold flash for protection after fabrication.

2. Experimental Evaluation

Table 2 summarizes the measured interior dimensions for this particular test section at ambient and liquid nitrogen temperatures. Since plastic has a higher coefficient of expansion than metal, these dimensional changes are greater than would be obtained with stainless steel. The measured dissipative loss of this particular section at 8448 MHz was 0.0196 dB. This is in good agreement with a loss of 0.0258 dB measured for solid aluminum wave-length of the same length, fabricated by the electric discharge method, if account is taken for surface roughness. The dissipative loss is obtained by subtracting the reflected loss from the overall measured insertion loss.

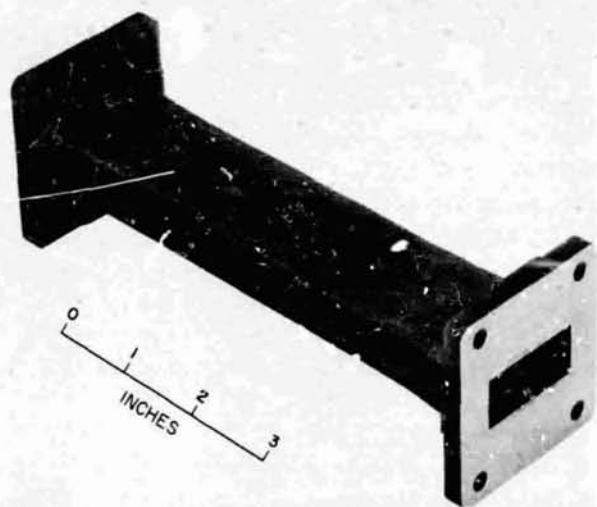


Fig. 14. WR 112 plastic waveguide

Table 2. Plastic H-band waveguide interior dimensions at ambient and liquid nitrogen temperatures

Waveguide opening dimensions, in.		
Standard opening	Actual opening	
	Ambient temperature	Liquid nitrogen temperature
1.122×0.497	1.124×0.503	1.120×0.500

The plastic and solid aluminum waveguides have a measured surface roughness of approximately 40 and 70 μ in. rms, respectively.⁴ The accuracy of the dissipative loss measurements accounting for instrumentation, mismatch errors, and measurement dispersion was approximately 0.0006 dB (probable error) and 0.0004 dB (probable error) for the plastic and aluminum waveguide sections, respectively.

3. Conclusion

The primary advantages of the plastic waveguide fabrication technique over conventional stainless steel sections are reduced cost and fabrication time. Special thin-wall stainless steel waveguide requires a factory mill run, which entails long lead time and user storage problems. The plastic section also has higher rigidity and less total weight than conventional stainless steel sections.

The primary disadvantages are the dimensional instability caused by the higher coefficient of expansion of the material and the thin conductive coating on the flanges. The flanges cannot be lapped due to the thin metal covering.

The close agreement in insertion loss between the solid aluminum and plastic waveguide sections indicates that the sprayed aluminum interior of the plastic waveguide provides a suitable microwave conductor.

F. RF Breakdown Studies, R. Woo, and H. Erpenbach

1. High Pressure RF Breakdown in Coaxial Transmission Lines at S-Band Frequencies, R. Woo

a. Introduction. The results of our investigations of multipacting breakdown have been reported in previous issues of SPS, Vol. IV. Multipacting breakdown occurs when the electron mean free path, the average distance traveled by the electrons between collisions, is greater

⁴Refer to JPL Inspection Report 56401, Account No. 421-00103-3330, sketch for part number.

than the electrode separation distance. If pressure is increased, the mean free path is shortened, and the principal electron production mechanism is no longer secondary electron emission but ionization by electron collision. If both the electron mean free path and the amplitude of oscillation of the electrons are appreciably less than the electrode separation distance, the main electron loss mechanism is diffusion to the electrodes. Under these conditions, RF breakdown is governed by the diffusion theory (Ref. 11).

It is within the limits of the diffusion theory that many microwave components fail. In certain gases, electrons are effectively removed by attachment to gas molecules; loss by recombination is generally negligible, since the charge concentrations are usually low. The subject of high pressure RF breakdown has been ably summarized by Brown, Francis, and MacDonald, Refs. 11-13, respectively.

The availability of engineering data for high pressure RF breakdown is essential for the successful design of high power RF components for future space missions. High pressure RF breakdown would be encountered in two main situations: (1) when there is a requirement to turn on the high power RF prior to launch and to leave it on during ascent through the earth's atmosphere, and (2) when high power RF components must operate in the vicinity, or on the surface of, a planet where pressure levels are a few torr, such as on Mars.

In this article we will present breakdown data in air for 1/8-in. rigid coaxial transmission line obtained at S-band frequencies, using the basic experimental setup described in SPS 37-44, Vol. IV, pp. 334-336. A three-dimensional surface representing both multipacting and higher pressure RF breakdown data will also be discussed. The simplicity and practical usefulness of such a plot is shown to be attractive to the design engineer.

b. Experimental setup and procedure. The schematic of the vacuum system used in the experiments is shown in Fig. 15. Air is admitted through the dessicant tube, which removes the moisture and carbon dioxide from the air. The swivel-type Stoke's-McLeod gauge used for measurement of pressure, has a 0-5000 μm scale. The dry-ice-acetone cold trap serves to prevent the diffusion of mercury vapor from the McLeod gauge to the remainder of the vacuum system.

Rose and Brown (Ref. 14) showed that the products of ionization from one breakdown measurement can reduce subsequent breakdown voltages by as much as 10%, if the

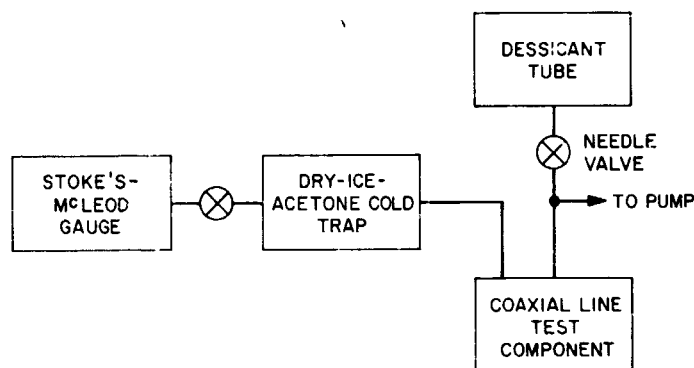


Fig. 15. Schematic of vacuum system

air is not changed. The system was, therefore, pumped down to 40 μm , and new air introduced before each breakdown measurement. Reproducibility of the power breakdown readings was within $\pm 2\%$ (equivalent to breakdown voltage reproducibility within $\pm 1\%$), while the accuracy of the readings was within $\pm 3\%$ (equivalent to breakdown voltage reproducibility within $\pm 1.5\%$).

c. Experimental results and discussion. Figure 16 shows the manner in which breakdown power varies with pressure for 1/8-in. coaxial transmission line at 1700 and 2400 MHz. An RF breakdown is determined by the electric field, but we have chosen to plot power, since this is the parameter of direct interest to the design engineer. It should be cautioned that these power readings correspond to a matched 50- Ω transmission line. Under mismatched conditions, the electric fields may be higher so that breakdown could occur at lower power levels.

The "parabolic" shape of the breakdown plots in Fig. 16 is typical of diffusion-controlled RF breakdown. The minimum of each breakdown plot occurs at the pressure p_{min} , where the electron-molecule collision frequency ν_c is approximately equal to the radian frequency ω ($\omega = 2\pi f$, where f is the frequency of the RF field), since the energy transfer to the electrons from the field is at a maximum. If the pressure is increased, the electron-molecule collision frequency increases, the energy gained by the electrons from the field per mean free path decreases, and the breakdown electric field (or power) must correspondingly increase.

In a perfect vacuum, the electrons oscillate with their velocity 90 deg out of phase with the RF field, and no energy is gained by the electrons from the field. The electrons gain energy from the field only by undergoing collisions with the gas molecules. A decrease in pressure for pressures lower than p_{min} , therefore, corresponds to an

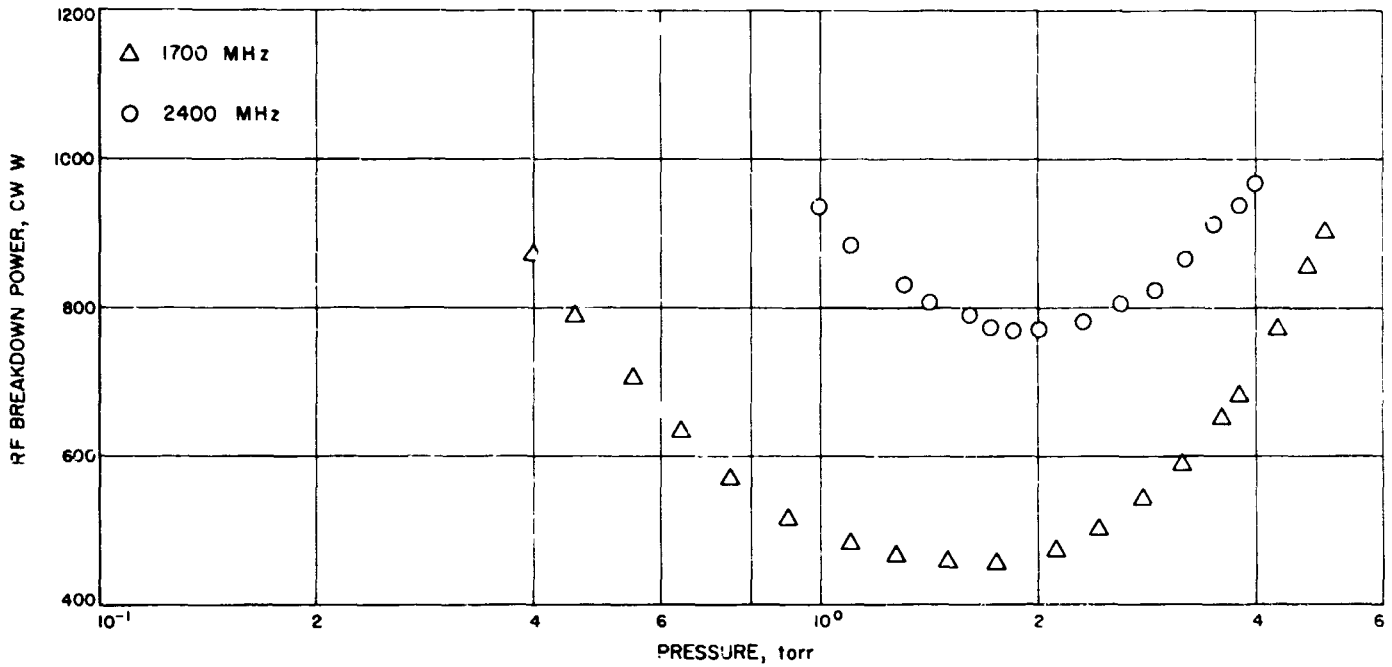


Fig. 16. RF breakdown power for 1 1/8-in. coaxial line at 1700 and 2400 MHz as a function of pressure

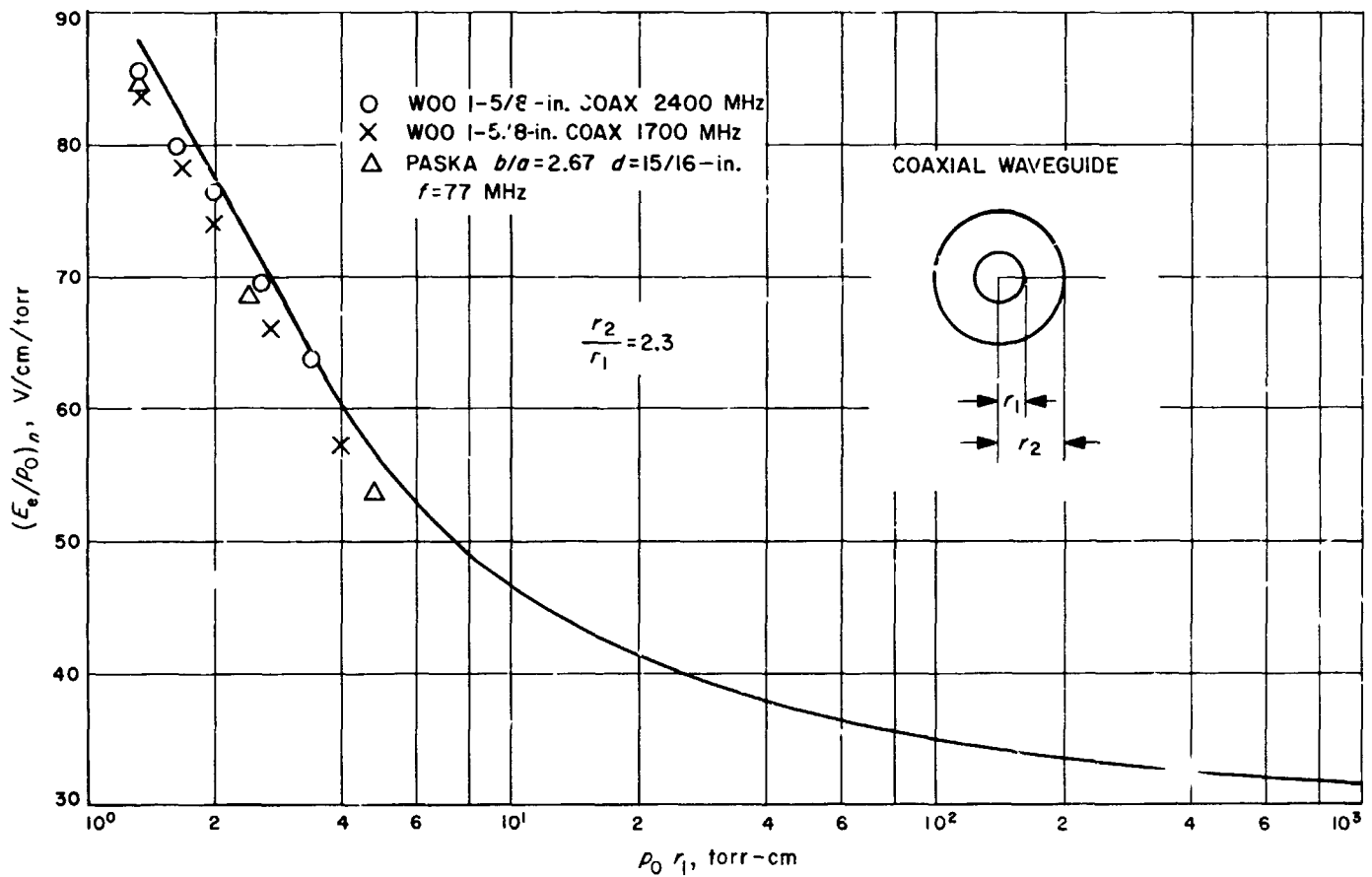


Fig. 17. Ratio of normalized CW breakdown field to pressure as a function of pressure times inner conductor radius

increase in loss of energy transfer from the field to the electrons. As a result, the breakdown field rises with decreasing pressure.

High pressure RF breakdown between coaxial electrodes has been investigated by Herlin and Brown (Ref. 15), and Gould (Ref. 16). Paska (Ref. 17) obtained some experimental data at 77 MHz. Unfortunately, the theoretical results of Herlin and Brown, and Gould, suffer from limitations. Shown in Fig. 17 is the theoretical curve of Gould, together with the experimental data of Fig. 16 and that of Paska using Gould's notation. As can be

seen, Gould's curve is limited to pr values greater than 1.4 torr-cm. In the case of the 1/8-in. coaxial line, data exist only for pressures greater than 1600 μm . One reason for this limitation is the concept of effective electric field, which is only satisfactory for higher values of pr .

Comparison of Herlin and Brown's data with our data indicated their breakdown power levels were approximately 10% lower. The reason is that they did not use fresh air for each breakdown measurement when determining the high frequency ionization coefficient ξ (Ref. 18). The main objection to either Gould's or Herlin and

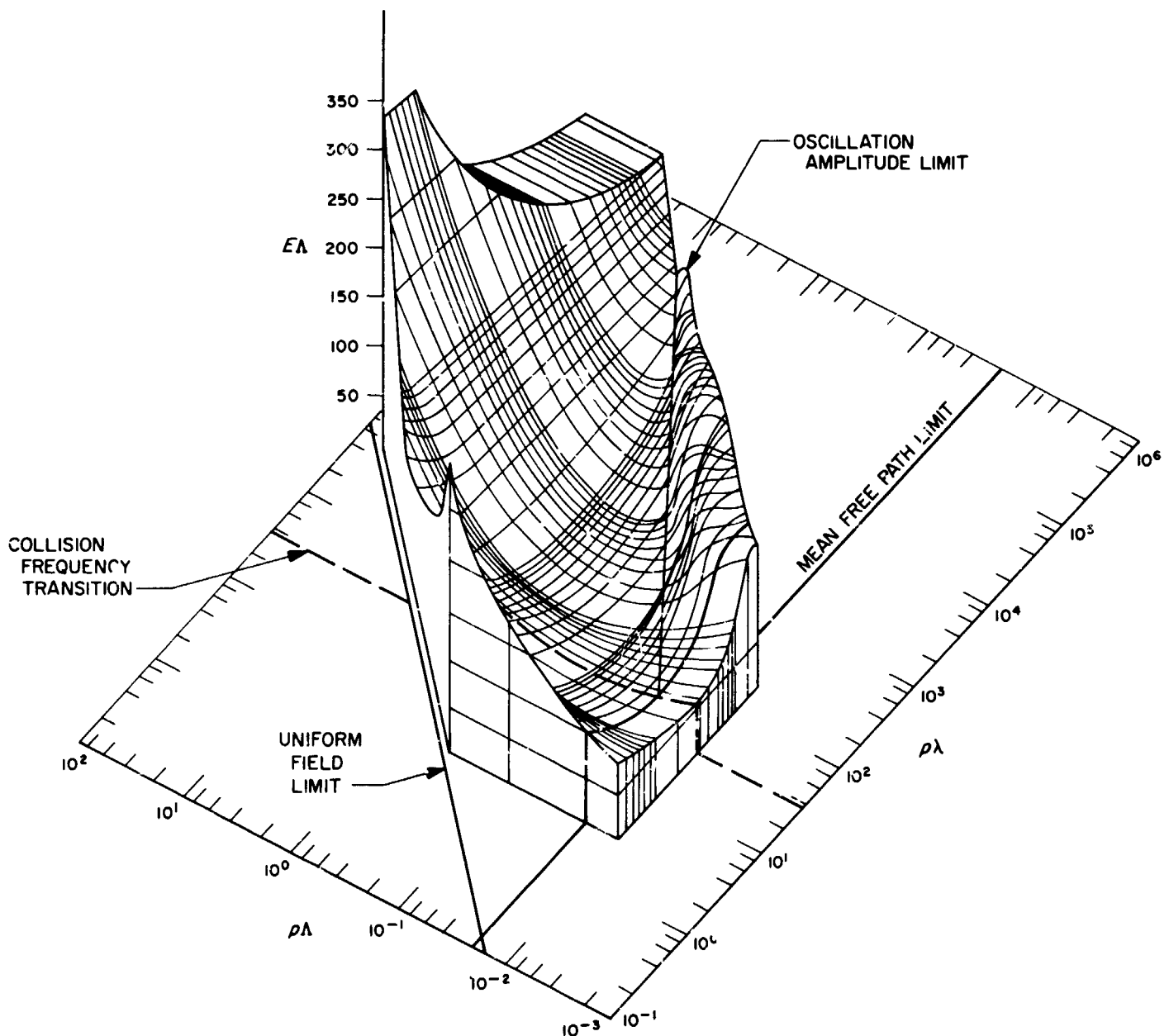


Fig. 18. Surface constructed from high pressure RF breakdown in hydrogen between parallel plates

Brown's theoretical curves, however, is their complexity. A design engineer is usually interested in the breakdown power level as a function of pressure for a fixed frequency and a given coaxial line. He is also interested in the effects of changing frequency or the line size. Such data are not conveniently or explicitly available in the theoretical curves.

A more meaningful and practical scheme of presenting the breakdown data is to use a three-dimensional plot, such as that described by MacDonald and Brown for parallel plates (Ref. 19) and shown in Fig. 18. They showed through dimensional analysis that the breakdown data for geometrically-similar configurations in a given gas can be represented by a single $p\Lambda$ - $p\lambda$ - $E\Delta$ surface. Λ is the characteristic diffusion length and, in the case of

parallel electrodes, is equal to d/π , where d is the electrode separation distance. It should be noted that the vertical axis could have been breakdown power rather than $E\Delta$.

Reproduced in Fig. 19 is the $p\Lambda$ - $p\lambda$ plane with the limits of the diffusion theory for hydrogen. In the case of air, these limits are approximately the same. A discussion of these limits is given in Ref. 19. The collision frequency transition represents the condition $\nu_c \sim \omega$. The limits for the data of Herlin, Brown, and Gould are also indicated.

The usefulness of Fig. 18 is realized when we examine a single 45-deg line on the $p\Lambda$ - $p\lambda$ plane. A single 45-deg line corresponds to a given electrode separation distance with frequency fixed and pressure varied. At this point we

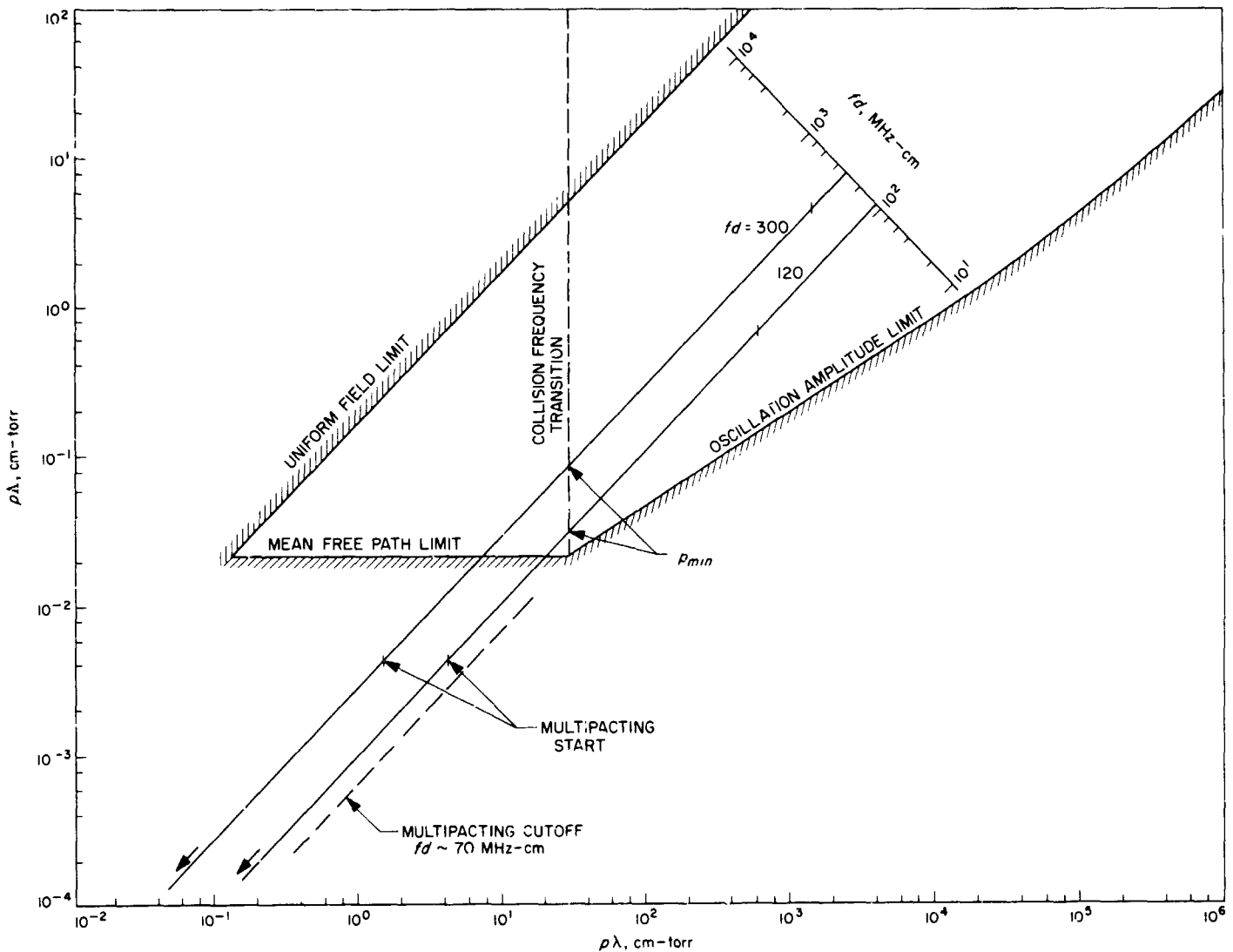


Fig. 19. Limits of applicability of diffusion theory of breakdown in hydrogen between parallel electrodes

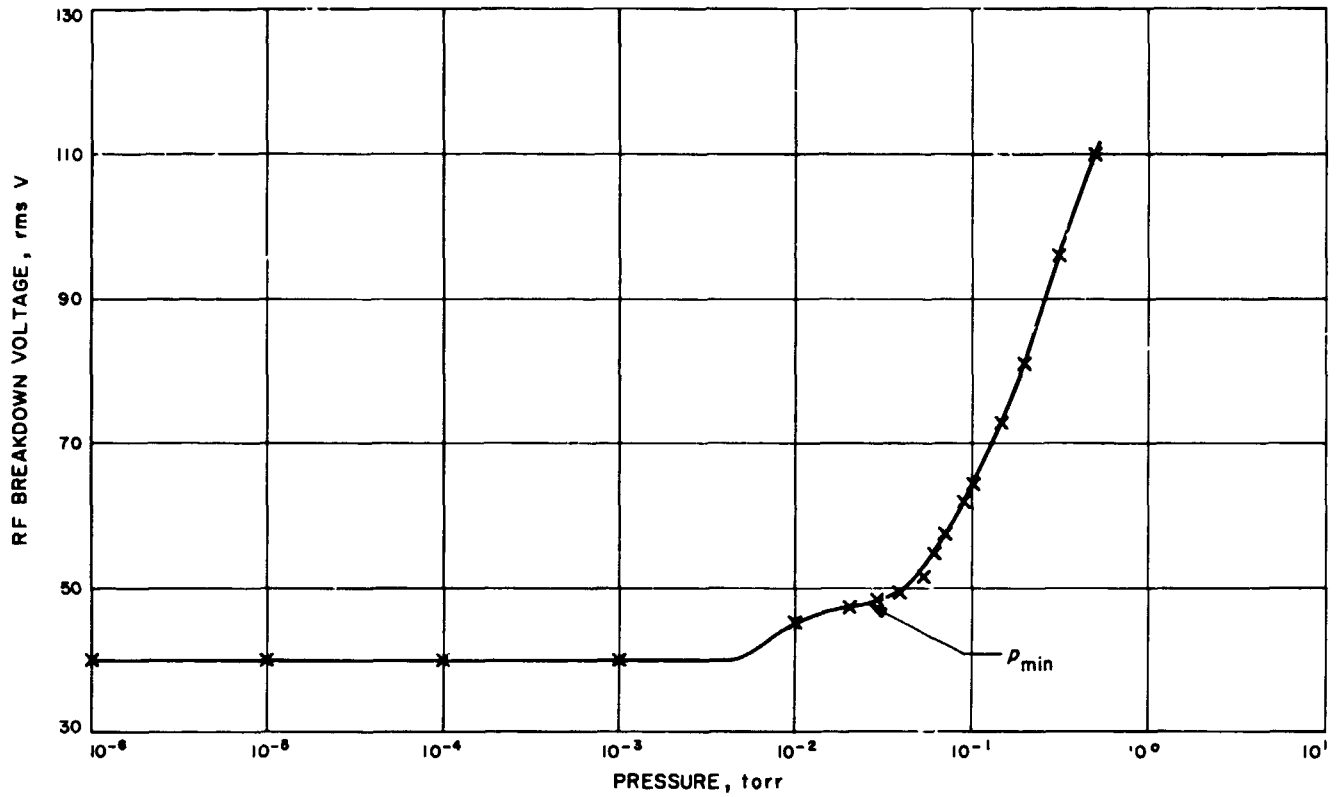


Fig. 20. RF breakdown voltage vs pressure for parallel plates; $f = 30$ MHz and $d = 4$ cm; $fd = 120$ MHz-cm

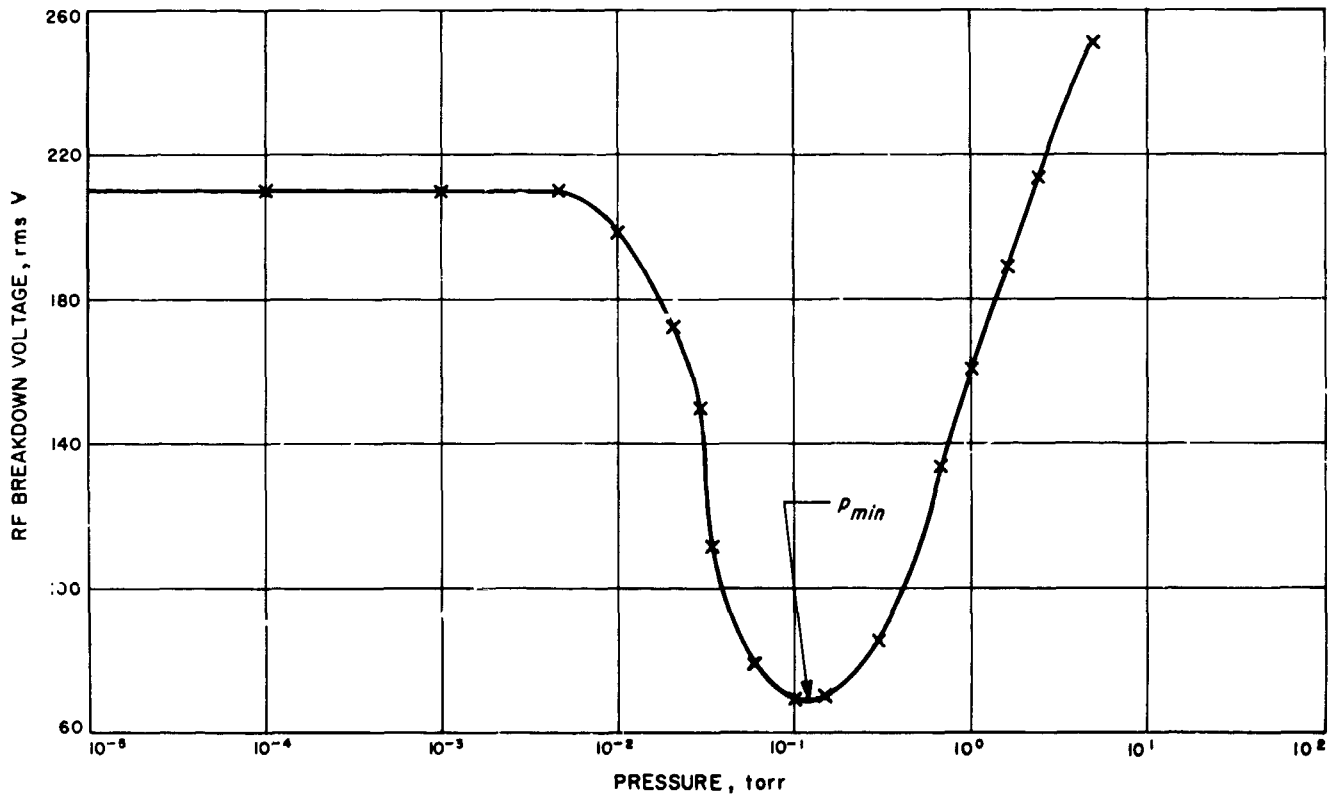


Fig. 21. RF breakdown voltage vs pressure for parallel plates; $f = 100$ MHz and $d = 3$ cm; $fd = 300$ MHz-cm

wish to add an important observation. Each 45-deg line corresponds to a fixed fd product, and this allows the inclusion of multipacting data in Fig. 18. To illustrate, we show in Figs. 20 and 21, breakdown data obtained for two parallel plates situations ($fd = 120$ MHz-cm and $fd = 300$ MHz-cm) with the experimental apparatus described in SPS 37-41, Vol. IV, p. 242. The 45-deg lines corresponding to these two situations, as well as to the multipacting cut-off fd value of 70 MHz-cm, (SPS 37-41, Vol. IV, p. 246) are drawn in Fig. 19. The vertical ticks on each line indicate the limits of the data.

The data in Figs. 20 and 21 represent two interesting situations. In Fig. 20 the multipacting breakdown voltage is less than that corresponding to p_{min} , while in Fig. 21 it is greater than that corresponding to p_{min} . On the three-dimensional plot of Fig. 18, the multipacting region is

represented by a surface composed of horizontal lines, which are at a 45-deg slope on the $p\lambda$ - $p\lambda$ plane. The cross-section of this surface is similar to Fig. 26 in SPS 37-41, Vol. IV, p. 246. If the vertical axis is power instead of voltage, the slopes of the phase-determined boundaries would be doubled. It should be noted that the $\frac{3}{2}$ -cycle multipacting mode occurs approximately 310 MHz-cm. For RF voltages lower than 200 V, the fd range for multipacting is significantly smaller than that for higher pressure RF breakdown.

In the case of breakdown in air between similar coaxial electrodes a surface can also be constructed. For convenience, the $E\lambda$ axis can be replaced by power. Presently the $b/a = 2.3$ (b and a are the radii of outer and inner electrodes) case is of interest. Shown in Fig. 22 is the

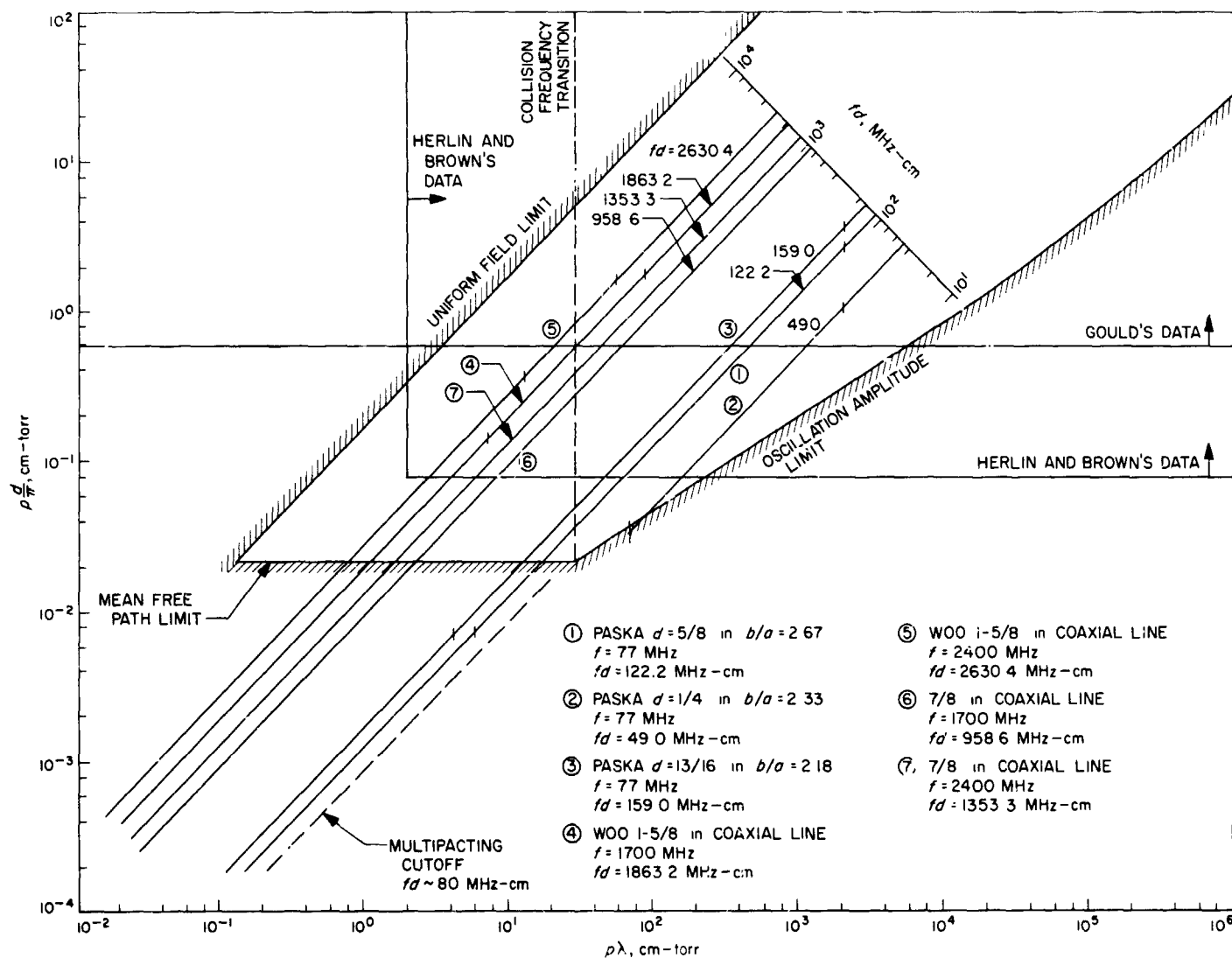


Fig. 22. Limits of applicability of diffusion theory of breakdown in air between coaxial electrodes; $b/a = 2.3$

$p\Delta$ - $p\lambda$ plane for $b/a = 2.3$ with the diffusion limits of Fig. 19. These represent a good approximation since the limits should not deviate significantly from that of parallel electrodes here the electrode separation distance is identical. The fd lines corresponding to our data, as well as to Paska's data are drawn. Breakdown data for $\frac{3}{8}$ -in. coaxial line at 1700 and 2400 MHz are currently being obtained and will be reported in SPS 37-46, Vol. IV.

It is clear from Fig. 22 that data are needed in the 200-1000 MHz cm fd range. This can be obtained either with the setup described in SPS 37-41, Vol. IV, p. 241, or with the current setup when a 1-kW 150-1000 MHz RF source, now on order, is delivered. Note that the former setup is advantageous in two respects: (1) large RF voltage can be achieved with the use of a lower power amplifier, and (2) voltages can be measured more conveniently and more accurately by using a vacuum tube voltmeter.

When these data are obtained they will be combined with the multipacting data, and the three-dimensional breakdown surface will be constructed. From the standpoint of the design engineer, the results will prove invaluable. By selecting the fd line corresponding to the coaxial line in question, the design engineer has available to him breakdown data for both the multipacting and higher pressure RF breakdown regions. In addition, he has information on the breakdown processes and the effects of changing either frequency or line size.

d. Conclusions. It has been shown that multipacting data can be included in the breakdown plots introduced by MacDonald and Brown for higher pressure RF breakdown. The 45-deg lines on the $p\Delta$ - $p\lambda$ plane correspond to constant fd situations and, when identified, can be very useful to the design engineer. By using this scheme for plotting the data, he can cover a wide range of breakdown parameters with a minimum number of experiments. Similar plots can be constructed for those gas media which correspond to extraterrestrial atmospheres.

2. Multipactor Research: Surface Preparation Studies — Secondary Electron Emission, H. Erpenbach

Investigation of reduced secondary electron emission from copper surfaces is continuing. In SPS 37-41, Vol. IV, pp. 207-209 we reported that the purity of hydrocarbon gases used for the deposition of thin carbon films on copper surfaces has a direct effect on the yield of secondary electrons. An attempt was made to obtain a research grade of gases for our work; however, these gases were not obtainable from our source in the quantities that we require

for our process. We obtained chemically pure ethane from another source with fewer impurities. Mass-spectrometer analysis of the above gas showed it to be 99.9% pure. The impurities were methane and ethylene.

Table 3 is a list of 10 copper targets that have been bombarded with ethane ions to form a thin carbon film over one surface. The current discharge density, time, and gas pressure were the same for each sample shown in the table. The tests were made after each target had been exposed to the atmosphere for a minimum of 24 h.

The δ maximum ratio of incident primary electrons to secondary electrons of the 10 targets in Table 3 average 0.98, compared to the 1.07 figure previously obtained with ethane gas of lower purity.

X-ray diffraction patterns made from two of the copper targets with carbon film deposits, show the films to be of a polycrystalline type; however, since the results are preliminary, further investigation will be made.

Application of the cleaning and carbon coating technique to waveguides for prevention of oxidation, thereby reducing the surface resistivity, is now being studied. Two waveguides are being evaluated for the cleaning process only, and later a carbon deposit will be applied.

To bombard an internal surface of a waveguide with ions, a gas pressure-voltage relationship is followed if the operation is performed in a conventional vacuum bell jar system that encloses the open ended waveguide.

Table 3. Compiled data

Gas	Sample No.	δ max
Ethane ↓	1	1.05
	2	0.98
	3	0.95
	4	1.01
	5	1.01
	6	0.98
	7	0.96
	8	0.95
	9	0.98
	10	0.97
	Δ	0.984

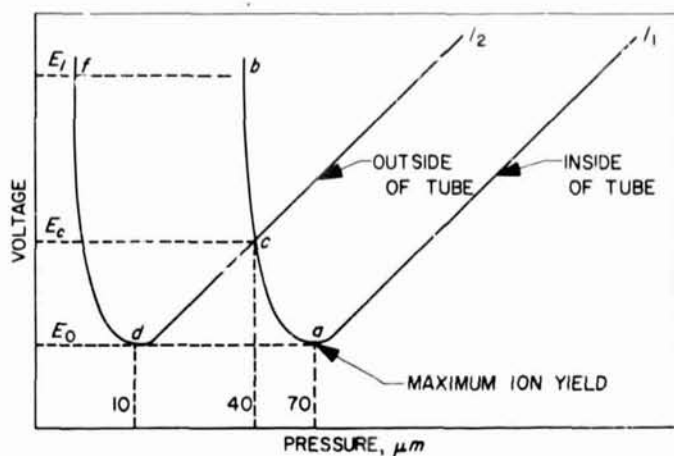


Fig. 23. Pressure-voltage curve

Fig. 23 illustrates the pressure-voltage required of any form of tube waveguide or cavity in which an ion discharge takes place while enclosed in a chamber. Since the l_1 and l_2 (ID and OD of tube or waveguide) are constant, we may plot the voltage against pressure instead of P_l and obtain the two curves for the two paths shown to Fig. 23. If the pressure in the chamber is progressively reduced from high values, the discharge, as shown by the ID curve passes more easily until at P_a the curve reaches the minimum a with the voltage E_0 . A further reduction of pressure demands a relatively large increase in potential, shown by the steeper slope between a and b . If the source of potential were limited to a maximum value E_1 , the discharge would cease at b . But at c the longer path becomes available, and the discharge passes the route via the outside of the tube, with a new minimum at d . At lower pressures the discharge passes with increasing difficulty and stops at l , when the limit of potential E_1 is reached.

The pressure P_c determines an unstable condition, where the discharge may pass on either the inside or outside of the tube; however, for our work the pressure is adjusted to the a portion of the curve or about $70 \mu m$ during the ion bombardment of the internal surface.

A hydrogen ion discharge is preferred to argon for the cleaning of the waveguides, as it seems to be more effective in reaching the internal corners of a rectangle. The reason is not known at this time, but possibly the increased gas pressure necessary for internal ion discharge work may be the cause, as the impurity content of the hydrogen is less than the argon.

Our next work will be the bombardment of copper surfaces with a newly designed 10-kV ion gun, which will allow us to work at lower pressures.

G. Spacecraft Antenna Studies, K. Woo and R. M. Dickinson

1. High Impact Cavity-Backed Spiral Antenna, K. Woo

a. Introduction. A high impact cavity-backed spiral antenna (SPS 37-41, Vol. IV, pp. 239-241) has been developed. It is capable of surviving an indirect impact of 10,000 g and is relatively compact and lightweight. (Refer to SPS 37-40, -42, -43, -44, Vol. IV, pp. 201-206, 180-181, 386-389, 336-338, respectively, for other high impact antennas.)

b. Antenna design. The antenna (Fig. 24) consists of a pair of copper planar Archimedean spirals printed on a

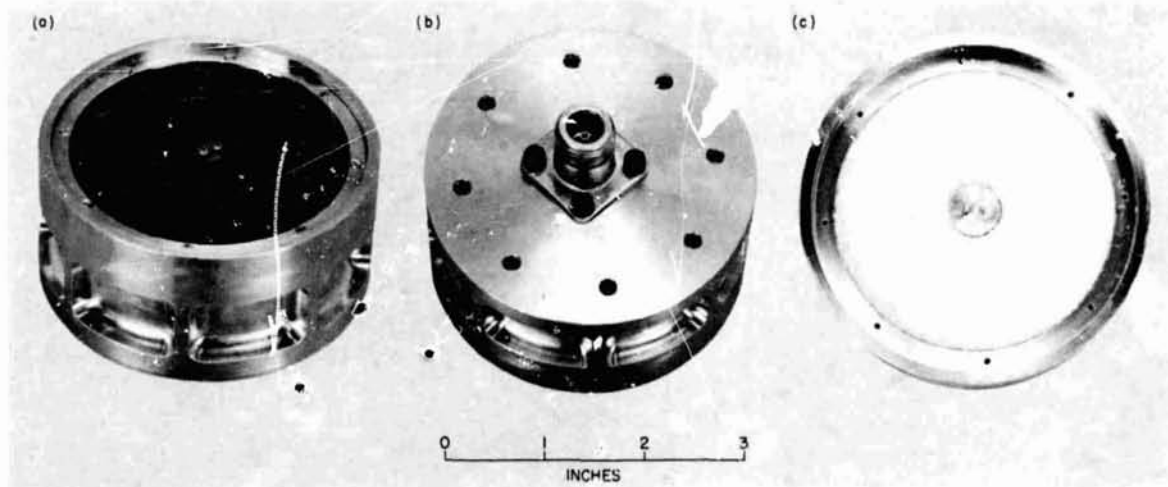


Fig. 24. High impact cavity-backed spiral antenna: (a) front; (b) rear; (c) interior

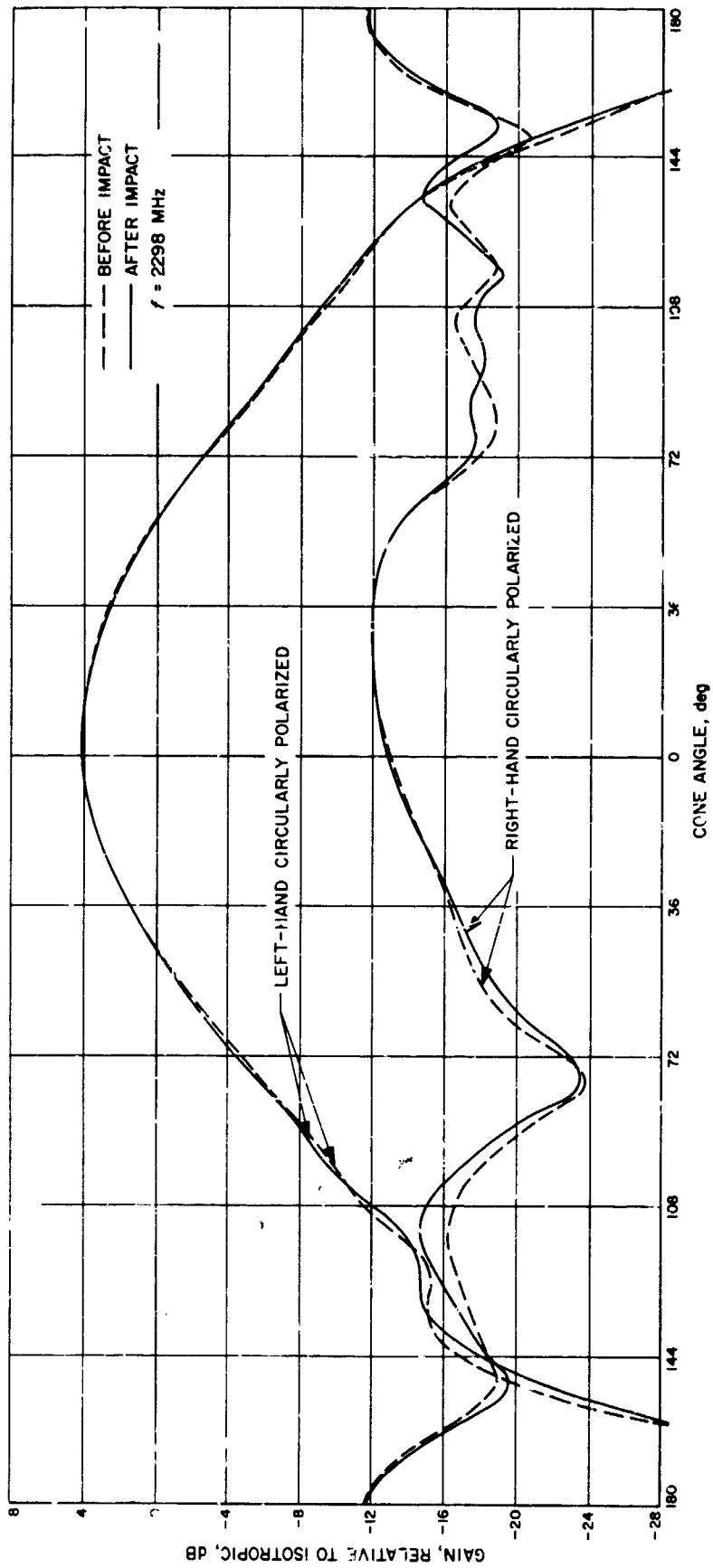


Fig. 25. Radiation patterns before and after impact

fiberglass board (0.135-in. thick) and backed by an aluminum cylindrical cavity (2.750-in. ID, 0.803-in. deep). For the purpose of preventing the board from flexing during high impact, the cavity is filled with low-loss foam, and the board is bonded to the foam. The foam is formed by mixing Eccofoam FPH³ (high temperature foam-in-place liquid resin) and catalyst 12-10H. Upon curing, the foam becomes rigid and adheres firmly to the cavity walls.

The input arms of the spirals are fed by a coaxial transmission line protruding into the cavity from the input connector at the rear. The arms, respectively, make contact with the center conductor (1/16-in. diam) and the ground stud (1/16-in. diam) of the feed line by means of a self-locking nut (0-80 thread). As the result of bonding the board, the feed contacts are capable of withstanding high impact and remain secure. When the spirals are energized, circularly polarized radiations are obtained in the forward direction.

c. Test results. An indirect impact test of the antenna at 10,000 g (0.6 ms duration) was performed. The antenna was attached in a test fixture, and then the fixture was impacted against a target. There was no visible damage to the antenna. The electrical performance of the antenna remained about the same. Figure 25 shows the radiation patterns at 2298 MHz of the left-hand circularly polarized and right-hand circularly polarized components taken before and after the impact. The input voltage standing wave ratio measured the same before and after the impact, 1.32.

Future work on the antenna will include

- (1) Improving the gain and axial ratio by reducing losses, wherever possible, and modifying the feed-line configuration.
- (2) Reducing antenna weight (present weight 0.71 lb) by further trimming the cavity walls.
- (3) Adapting the antenna to right-hand circular polarization by redesigning the spiral configuration.

2. Large Aperture Antenna Study, R. M. Dickinson

a. Introduction. This study is directed toward developing an analytical technique for evaluating the performance of large aperture spacecraft erectable antennas wherein the reflector is not a simple surface of revolution.

In order that an antenna be erectable (i.e., capable of being packaged into a small volume for launch and then

unfurled in space), the mechanical design sometimes compromises the reflector or mirror such that the erected surface deviates from the ideal parabola of revolution.

The surface deviations generally result in a loss of peak gain and increased wide angle or scattered radiation when compared to the normal paraboloidal antenna. This portion of the present study will be limited to investigating the effect on peak gain of "umbrella" reflector surface deviations.

Theoretical umbrella surfaces consist of a flexible reflecting material pulled uniformly between radial ribs. The particular example investigated used ribs that are parabolic in section. Surface equations for this type antenna reflector were derived in SPS 37-35, Vol. IV, pp. 273-278.

b. Peak gain calculation. Peak gain calculations were made by using the surface current integration technique, as outlined in Ref. 20. An attempt was made to formulate the calculations in a manner paralleling existing measurements. That is, to use the unit circularly polarized vectors of Ref. 21 in a spherical polar coordinate system in order to describe the currents and fields. However, this particular mathematical system runs afoul of the essential ambiguity at the poles where $\theta = 0$ or π . Therefore, a uniform in azimuth, linearly polarized feed system was used in the calculations, which is satisfactory for the peak or on-axis gain calculations, whereas the spherical circularly polarized wave representation is ambiguous on axis.

A computer program was written in Fortran II for the IBM 1620 using double, Simpson's 1/3 rule, numerical integration (Ref. 22). The program was checked by increasing the number of ribs to a very large quantity and comparing the calculated gain to the gain of a perfect paraboloid.

Calculations were made for reflector diameters from 4 to 75 wavelengths and for the cases of 8 to 20 ribs. All reflectors were of 0.35 focal length to diameter ratio, and a cosine-squared-feed power pattern was assumed.

The numerical integration increments were varied from 6 increments in θ by 6 increments in ϕ to 20×20 over a "gore" half. (The portion of the reflecting surface material between a pair of ribs is termed a gore. For peak gain calculations the two regions on either side of the gore radial center line are symmetrical with respect to the feed; and thus, only half a gore need be considered.)

³Distributed by Emerson and Cuming, Inc.

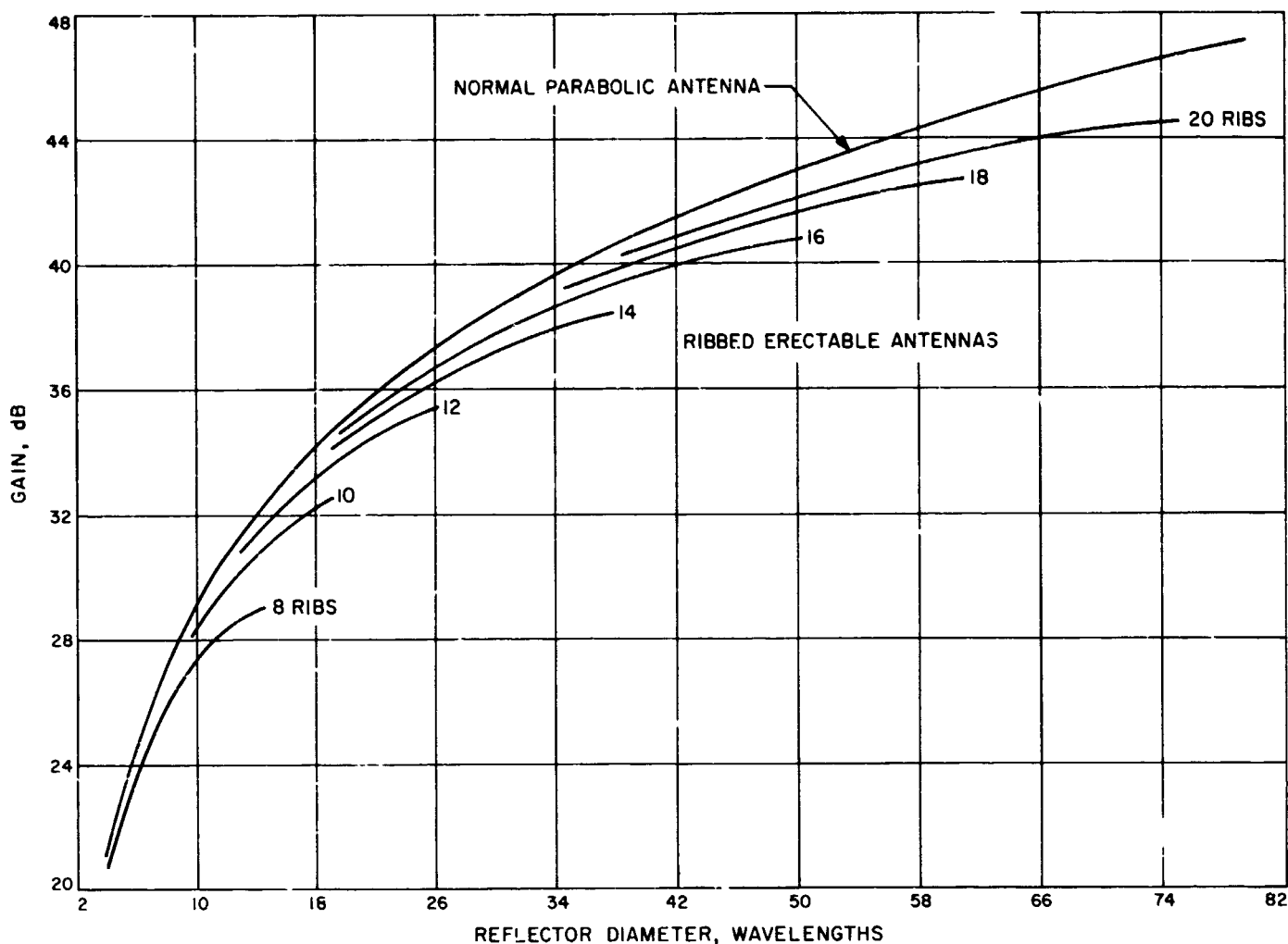


Fig. 26. Calculated peak gain of erectable and parabolic antennas with \cos^2 feed

The machine execution time varied from <2 to >10 min with a difference in the calculated gain of only several hundredths of a dB. Thus, most calculations were made using 6 increments in θ and ϕ .

Figure 26 shows the calculated gains as a function of reflector diameter in wavelengths for various numbers of radial parabolic ribs. The gain of a perfect paraboloid using the same feed is also shown for comparison.

The program effectively integrates the surface currents over an area with a circular boundary whose perimeter is the same as an equal diameter circular paraboloid. In actual construction, the radial ribbed erectable reflector would have scalloped edges. Thus, the projected aperture area of an erectable umbrella antenna would be less than the aperture area of an equal diameter circular paraboloid. Figure 27 shows the approximate gain reduction based upon the area loss with respect to a full paraboloid.

(Both curves of Figs. 26 and 27 are actually stepped functions but are drawn continuously for ease of graphing.)

c. Surface efficiency factor. The surface efficiency factor η_s is defined as the ratio of the peak gain of an equal aperture area ribbed reflector to a perfect paraboloid when both are excited by the same feed.

On the basis that the peak gain loss is proportional to the reflector surface deviation from parabolic, η_s was plotted as a function of the erectable peak surface deviation δ_{ms} , as shown in Fig. 28. The deviation is measured parallel to the focal axis.

The solid curve drawn through the calculated points of Fig. 28 is given by

$$\eta_s = \frac{G}{G_0} = \exp - (2.11\delta_{ms})^2 \quad (1)$$

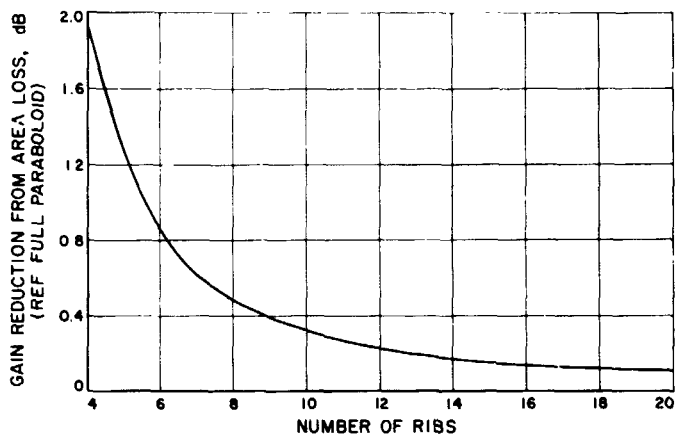


Fig. 27. Gain loss due to scalloped edges for radial ribbed reflectors

The greatest surface deviation occurs along the gore center line and has its maximum deviation from the true parabolic surface at the reflector edge.

$$\delta_{mx} = 1.794 D_\lambda / n^2 \quad (2)$$

where

D_λ = Reflector rib diameter in wavelengths

n = Number of ribs or gores

δ_{mx} = Maximum surface deviation in wavelengths measured parallel to the focal axis

Except at the ribs, where the surface deviation is assumed zero, points on this particular erectable reflector surface are always closer to the focus than the same points on a true paraboloid. Thus, all the surface deviations have the same sign. It may be possible to reduce the gain loss by defocussing the feed, such that the aperture has zero mean phase error. Gain calculations for this case will be made in the future.

d. Comparison with Ruze's tolerance theory. The form of Eq. (1) is similar to Eq. (11) in Ref. 23, wherein Ruze

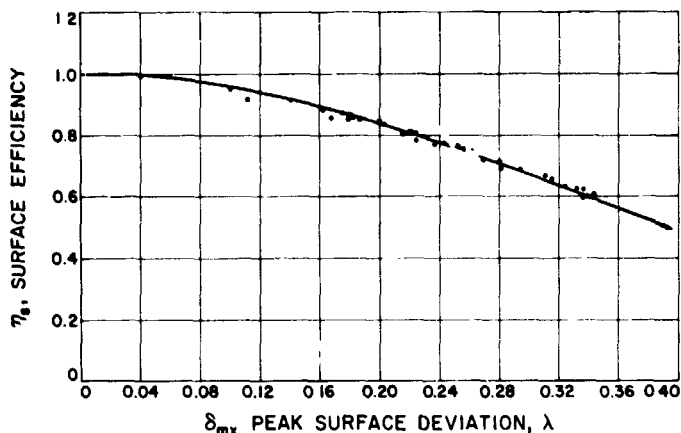


Fig. 28. Erectable "umbrella" antenna surface efficiency

relates gain reduction to the reflector rms surface deviation. However, Ruze's statistical tolerance theory for reflectors is based upon a uniform distribution of errors with zero mean phase error and is not applicable to the reflectors considered herein.

e. Design considerations. From the foregoing analysis, with reference to Fig. 26, it can be seen that a given value of required peak gain can be achieved by various combinations of diameter sizes and number of ribs. Possibly, the optimum design would produce the required gain with the least weight for spacecraft applications.

Since the weight of the reflecting screen is small in comparison to the rib weight, the optimum design in terms of dB per lb would possibly be the larger required diameter with the least number of ribs.

The absolute gain values in Fig. 26 are optimistic in that a cosine squared feed with no radiation beyond 90 deg was assumed for calculation simplicity. Nevertheless, the surface efficiency factor of Fig. 28 should be only secondarily influenced by the type of feed. In actual practice, the umbrella surfaces will likely be additionally degraded by construction tolerances and thermal distortions.

References

1. Stelzried, C. T., and Rusch, W. V. T., "Improved Determination of Atmospheric Opacity," *J. Geophys. Res.*, Vol. 72, p. 2445.
2. *Reference Data for Advanced Space Communication and Tracking Systems*, Report P67-09, Hughes Aircraft Company, Culver City, Calif., 1966 (Contract No. NAS 5-9637).
3. Wells, W. H., "Feasibility Studies of Optical Space Communications and Tracking," Space Optical Technology Conference, Huntsville, Ala., Nov. 2, 1965.
4. Whitehouse, D. R., "High Power CO₂ Laser," *NEREM Record*, p. 190, 1966.
5. Soref, R. A., *Electronics Letters*, Vol. 2, p. 410, Nov. 1966.
6. Teich, M. C., Keyes, R. J., and Kingston, R. H., *Appl. Phys. Lett.*, Vol. 9, p. 357, Nov. 15, 1966.
7. Brandewie, R. A., Haswell, W. T., III, Harada, R. H., *IEEE J. Quantum Elec.*, Vol. QE-2, p. 756, Nov. 1966.
8. Cohn, George I., *Preliminary Estimate of Perturbation in the Mars-Voyager-Mission Entry-Vehicle Telecommunications Link Caused by Ionization in the Martian Atmosphere*, Quantum Electronics, Pasadena, Mar. 1967. Jet Propulsion Laboratory Reorder 67-228, Pasadena, Calif.
9. Spencer, D. F., *An Evaluation of the Communication Blackout Problem for a Blunt-Mars-Entry Capsule and a Potential Method for the Elimination of Blackout*, Technical Report 32-594. Jet Propulsion Laboratory, Pasadena, Calif., Apr. 15, 1964.
10. Allis, W. P., Buchsbaum, S. J., and Bers, A., MIT Press, Cambridge, Mass., 1963.
11. Brown, S. C., *Handbuch der Physik*, Vol. 22, pp. 531-575. Edited by S. Flugge, Springer-Verlag, Berlin, 1956.
12. Francis, G., *Ionization Phenomena in Gases*, pp. 81-172. Butterworth's Scientific Publications, London, 1960.
13. MacDonald, A. D., *Microwave Breakdown in Gases*, John Wiley & Sons, Inc., New York, 1966.
14. Rose, D. J., and Brown, S. C., "Microwave Gas Discharge Breakdown in Air, Nitrogen, and Oxygen," *J. Appl. Phys.*, Vol. 28, pp. 561-563, 1957.
15. Herlin, M. A., and Brown, S. C., "Electrical Breakdown of a Gas Between Coaxial Cylinders at Microwave Frequencies," *Phys. Rev.*, Vol. 74, pp. 910-913, 1948.
16. Gould, L., *Handbook on Breakdown of Air in Waveguide Systems*, Microwave Associates Inc., Burlington, Mass., Apr. 1956.
17. Paska, R. P., *VHF Breakdown of Air at Low Pressures*, Report 944. Ballistic Research Laboratories, Aberdeen Proving Ground, Md., Aug. 1955.

References (contd)

18. Herlin, M. A., and Brown, S. C., "Breakdown of a Gas at Microwave Frequencies," *Phys. Rev.*, Vol. 74, pp. 291-296, 1948.
19. MacDonald, A. D., and Brown, S. C., "Limits for the Diffusion Theory of High Frequency Gas Discharge Breakdown," *Phys. Rev.*, Vol. 76, pp. 1629-1633, 1949.
20. Silver, S., *Microwave Antenna Theory and Design*, pp. 149-151, McGraw-Hill Book Co., Inc., New York, 1949.
21. Kales, M. L., "Part III—Elliptically Polarized Waves and Antennas—Complex Vector Representations of Elliptically Polarized Fields," *Proc. IRE*, pp. 544-549, May 1951.
22. Salvadori, M., and Baron, M., *Numerical Methods in Engineering*, pp. 176-178, Prentice-Hall, Inc., New York, 1952.
23. Ruze, J., "Antenna Tolerance Theory — A Review," *Proc. IEEE*, Vol. 54, No. 4, pp. 633-640, April 1966.

N67-34780

XIX. Spacecraft Radio

TELECOMMUNICATIONS DIVISION

A. Spacecraft Guidance Radar Beam Configuration Performance II, R. L. Horitor

1. Introduction

This report is the last part of an effort to analyze the beam configuration performance of spacecraft guidance radars. Such radars are used in closed loop guidance systems for lunar and planetary soft landing vehicles. Several factors influence the choice of a beam geometry for a particular guidance radar application. In the context of a Mars lander, the dominant ones are capsule trajectory angles, surface scattering variation, and the need to perform an altitude marking function. As the work in this article shows, the quality of the radar output data is affected by the geometry of the radar beam configuration. Hence, the performance of the beam configuration may be assessed by the quality of the radar output.

Previous work concerning the radar beam-to-surface incidence angles was reported in SPS 37-43, Vol. IV, pp. 376-380. Analyses of the altitude marking accuracy and slant range bias error of the beam geometry were presented in SPS 37-44, Vol. IV, pp. 328-334. This article analyzes the variances of the range and velocity estimates.

For all of these criteria, beam geometry performance varies with changes in the beam look angle. The results

of these reports can be used in picking a beam geometry suitable for a given set of spacecraft trajectory and attitude conditions.

The beam geometry chosen for this work is particularly applicable to a Mars retrorlander. Figure 1 illustrates a simple five-beam configuration with four beams pointed symmetrically at an angle from the fifth. There are several ways of combining the information from each of the five beams in order to generate the required output information. At various times in this summary, certain techniques use three, four or five beams to perform the required function.

2. Variances of Range and Velocity Estimates

In the Mars lander context, the velocity information may be used to follow a gravity turn. Components v_x and v_y are then used as null signals, while v_z is used to calculate the thrust command. Different weighting may, therefore, be given to component variances when judging performance. One criterion is the following:

$$FM(\theta; \alpha) = \alpha [\text{Var}(v_x) + \text{Var}(v_y)] + (1 - \alpha) \text{Var}(v_z), \quad 0 < \alpha < 1 \quad (1)$$

where α assigns relative importance to transverse and axial components according to an external value criterion. The

BLANK PAGE

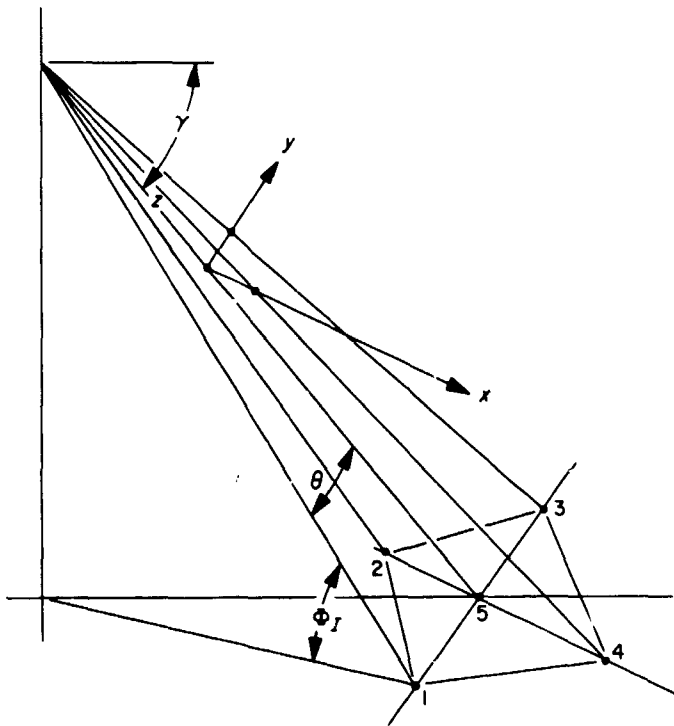


Fig. 1. Beam geometry

dependence on angle θ results from expressing velocity components (v_x, v_y, v_z) in terms of beam components (v_1, v_2, v_3, v_4, v_5). An important special case occurs when α is one half. Then $FM(\theta, 1/2)$ is one half the variance of the estimate of the total velocity vector.

$$\text{Var}[\mathbf{v}] = \text{Var}(v_x) + \text{Var}(v_y) + \text{Var}(v_z) = 2FM(\theta; 1/2) \quad (2)$$

Both of these criteria find some use in this work.

a. Three-beam system. A three-beam system may be chosen from the total system in Fig. 1 by choosing Beam 5 and the two other beams closest to the ground. This technique is useful for combating low trajectory angles, when two opposite beams may not intersect the surface.

With the geometry drawn as shown, the (v_x, v_y, v_z) components are expressed as follows:

$$\begin{aligned} v_x &= \frac{v_5}{\tan \theta} - \frac{v_2}{\sin \theta} \\ v_y &= \frac{v_5}{\tan \theta} - \frac{v_1}{\sin \theta} \\ v_z &= v_5 \end{aligned} \quad (3)$$

The following conditions apply to the v_i ,

$$E\{v_i v_j\} = E\{v_i\} \cdot E\{v_j\}, \quad i \neq j$$

$$E\{v_i\} = 0$$

$$\text{Var}\{v_i\} = \sigma_i^2 = \beta_i^2 \cdot \sigma_1^2, \quad \beta_1 = 1$$

The β_i depend on the antenna patterns, the surface reflectivity, the orientation of the beam system to the surface, and the velocity vector. They serve only as normalization factors whose derivation is extraneous to this discussion.

Substituting Eqs. (3) into the criterion for data quality, Eq. (1) gives

$$FM_3(\theta; \alpha) = \sigma_1^2 \left[\alpha(\beta_1^2 + \beta_2^2) \frac{1}{\sin^2 \theta} + \frac{2\alpha\beta_3^2}{\tan^2 \theta} + (1 - \alpha)\beta_5^2 \right] \quad (4)$$

Figure 2 shows that the minimum occurs at $\theta = \pi/2$. At that point

$$FM_3(\pi/2; \alpha) = \sigma_1^2 [\alpha(\beta_1^2 + \beta_2^2) + (1 - \alpha)\beta_5^2] \quad (5)$$

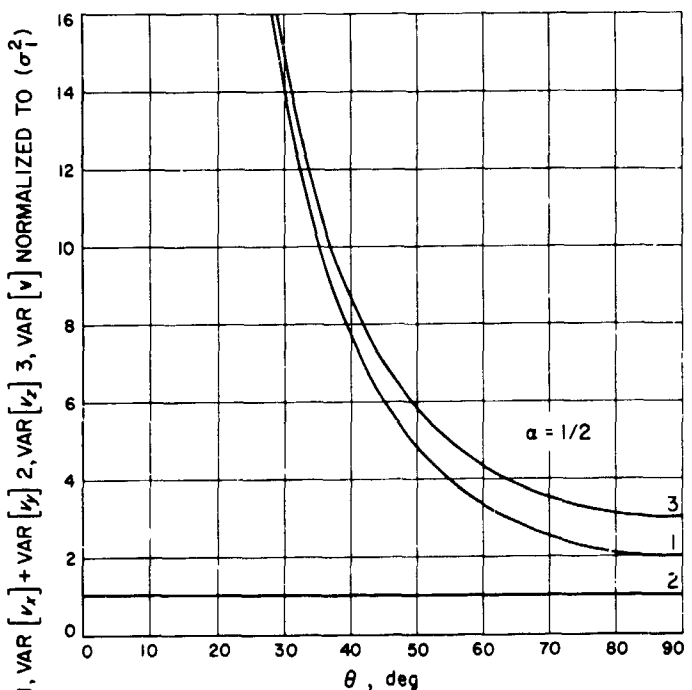


Figure 2. Velocity variances for three-beam system versus beam look-angle theta

The variance of the velocity vector when θ is $\pi/2$ is

$$\text{Var}(\mathbf{v}) = \sigma^2 (\beta_1^2 + \beta_2^2 + \beta_3^2) \quad (6)$$

If all the beam variances are equal

$$\text{Var}(\mathbf{v}) = 3\sigma_1^2 \quad (7)$$

The point is academic, since not all the beams can intersect the surface when θ is $\pi/2$. For example, at a 30-deg beam look angle,

$$\text{Var}(\mathbf{v}) = 15\sigma_1^2 \quad (8)$$

b. Four-beam system. This configuration uses only the outer four beams. It is useful primarily during the final descent portion of the trajectory when the system approaches vertical flight.

The velocity components (v_x, v_y, v_z) are expressed as follows:

$$\begin{aligned} v_x &= \frac{1}{2 \sin \theta} (v_4 - v_2) \\ v_y &= \frac{1}{2 \sin \theta} (v_3 - v_1) \\ v_z &= \frac{1}{4 \cos \theta} (v_1 + v_2 + v_3 + v_4) \end{aligned} \quad (9)$$

The variances of components are

$$\begin{aligned} \text{Var}(v_x) &= \frac{1}{4 \sin^2 \theta} \sigma_1^2 (\beta_2^2 + \beta_4^2) \\ \text{Var}(v_y) &= \frac{1}{4 \sin^2 \theta} \sigma_1^2 (\beta_1^2 + \beta_3^2) \\ \text{Var}(v_z) &= \frac{1}{16 \cos^2 \theta} \sigma_1^2 (\beta_1^2 + \beta_2^2 + \beta_3^2 + \beta_4^2) \end{aligned} \quad (10)$$

Substituting into the quality criterion, Eq. (1) yields

$$\text{FM}_4(\theta; \alpha) = \frac{\sigma_1^2}{4} (\beta_1^2 + \beta_2^2 + \beta_3^2 + \beta_4^2) \left[\frac{\alpha}{\sin^2 \theta} + \frac{(1-\alpha)}{4 \cos^2 \theta} \right] \quad (11)$$

Only one term in Eq. (11) depends on θ (Fig. 3). Minimizing $\text{FM}_4(\theta; \alpha)$ is not difficult. Letting $G(\theta)$ be the last term

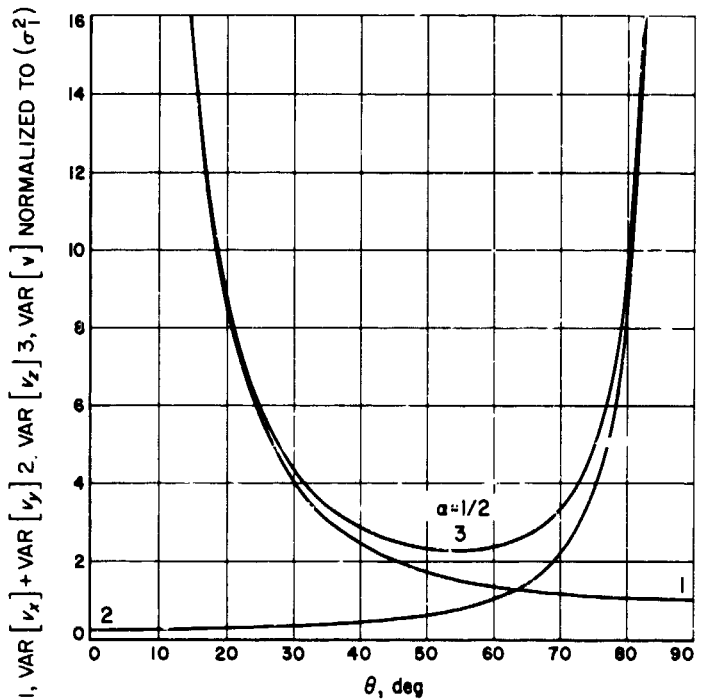


Fig. 3. Velocity variances for four-beam system versus beam look-angle theta

in Eq. (11) gives

$$\begin{aligned} G(\theta) &= \alpha \csc^2 \theta + (1-\alpha) \sec^2 \theta \cdot \frac{1}{4}, \quad 0 < \theta < \pi/2 \\ G'(\theta) = 0 &= -2\alpha \cot \theta \csc^2 \theta + \frac{1}{2} (1-\alpha) \tan \theta \sec^2 \theta \end{aligned} \quad (12)$$

Solving for θ begins with

$$(1-\alpha) \tan \theta \sec^2 \theta = 4\alpha \cot \theta \csc^2 \theta$$

or

$$(1-\alpha) \frac{\sin \theta}{\cos^3 \theta} = 4\alpha \frac{\cos \theta}{\sin^3 \theta}$$

which becomes

$$\tan^4 \theta = \frac{4\alpha}{1-\alpha}$$

$$\theta = \tan^{-1} \left[(2)^{1/2} \left(\frac{\alpha}{1-\alpha} \right)^{1/4} \right] \quad (13)$$

When α is $\frac{1}{2}$, the minimum variance is also achieved.

$$\begin{aligned}\theta &= \tan^{-1}(2)^{1/2} \\ \theta &= 54^\circ 44'\end{aligned}\quad (14)$$

This angle is the tetrahedron angle. For the presently accepted angle of 30 deg, the variance is $4\frac{1}{2}\sigma_i^2$, with equal beam variances. For the same conditions, the minimum variance is $2\frac{1}{4}\sigma_i^2$.

c. Five-beam system. When all five beams are used, two measurement techniques are possible. One system uses Beam 5 to measure v_z directly. The components (v_x, v_y) are derived from the other four beams. The relations are

$$\begin{aligned}v_x &= \frac{1}{2\sin\theta}(v_4 - v_2) \\ v_y &= \frac{1}{2\sin\theta}(v_3 - v_1) \\ v_z &= v_5\end{aligned}\quad (15)$$

Substituting into the figure of merit definition gives

$$FM_{51}(\theta; \alpha) = \frac{\sigma_i^2 \alpha}{4 \sin^2 \theta} (\beta_1^2 + \beta_2^2 + \beta_3^2 + \beta_4^2) + (1 - \alpha) \sigma_i^2 \beta_5^2 \quad (16)$$

Clearly, the minimum occurs at $\theta = \pi/2$. Assuming equal β_i , the v variance is minimum also.

$$\text{Var}(\mathbf{v}) = 2\sigma_i^2$$

Again, the point is academic, since not all the beams intersect the surface when θ is a right angle.

An interesting question is what region of θ allows $FM_5(\theta; \alpha)$ to be $< FM_4(\theta; \alpha)$. The terms with $\sin^2 \theta$ are equal, hence

$$\begin{aligned}(1 - \alpha) \sigma_i^2 \beta_5^2 &\leq \frac{(1 - \alpha) \sigma_i^2 (\beta_1^2 + \beta_2^2 + \beta_3^2 + \beta_4^2)}{16 \cos^2 \theta} \\ \cos^2 \theta &\leq \left[\frac{\beta_1^2 + \beta_2^2 + \beta_3^2 + \beta_4^2}{16 \beta_5^2} \right]\end{aligned}\quad (17)$$

Thus, when

$$\theta \geq \cos^{-1} \left[\frac{(\beta_1^2 + \beta_2^2 + \beta_3^2 + \beta_4^2)^{1/2}}{4\beta_5} \right] \quad (18)$$

$FM_5(\theta; \alpha)$ For equal weighting factors and equal variances,

$$\theta \geq \cos^{-1} \left(\frac{1}{2} \right)$$

or

$$\theta \geq 60 \text{ deg} \quad (19)$$

Whenever $\theta < 60$ deg, the four-beam variance is less than the five-beam variance. This result is surprising. The reason is that the noise averaging in the v_z component greatly offsets the $\sec^2 \theta$ multiplication effect.

Alternate five-beam system. Another estimate of v_z combines data from all five beams according to Eq. (20)

$$v_z = \frac{1}{3} \left[\frac{v_3 + v_1}{2 \cos \theta} + \frac{v_4 + v_2}{2 \cos \theta} + v_5 \right] \quad (20)$$

The estimates of the transverse components (v_x, v_y) remain unchanged from the previous examples.

$$v_x = \frac{v_4 - v_2}{2 \sin \theta}$$

$$v_y = \frac{v_3 - v_1}{2 \sin \theta} \quad (21)$$

Substituting these expressions into the figure of merit $FM_{52}(\theta; \alpha)$ yields

$$\begin{aligned}FM_{52}(\theta; \alpha) &= \frac{\sigma_i^2}{4} (\beta_1^2 + \beta_2^2 + \beta_3^2 + \beta_4^2) \\ &\times \left[\frac{\alpha}{\sin^2 \theta} + \frac{1 - \alpha}{9 \cos^2 \theta} \right] + \frac{\beta_5^2 \sigma_i^2}{9} (1 - \alpha)\end{aligned}\quad (22)$$

The variance of the total velocity is given by

$$2FM_{52}(\theta; 1/2)$$

$$\text{Var}(\mathbf{v}) = \frac{\sigma_i^2}{4} (\beta_1^2 + \beta_2^2 + \beta_3^2 + \beta_4^2)$$

$$\times \left[\frac{\alpha}{\sin^2 \theta} + \frac{1 - \alpha}{9 \cos^2 \theta} \right] + \frac{\sigma_i^2}{9} \beta_5^2 \quad (23)$$

This equation is nearly identical to the one minimized in subsection *b*. The minimum occurs at

$$\theta_M = \tan^{-1} \left[(3)^{1/2} \left(\frac{\alpha}{1-\alpha} \right)^{1/4} \right] \quad (24)$$

The velocity variance for equal variance beams and $\alpha = 1/2$ is

$$\text{Var}_M(\mathbf{v}) = 1\% \sigma_1^2 \quad (25)$$

with

$$\theta_M = 60 \text{ deg}$$

Plots of Eq. (23) appear in Fig. 4. At $\theta = 30$ deg by comparison, the variance is

$$\text{Var}(\mathbf{v}) = 4\% \sigma_1^2 \quad (26)$$

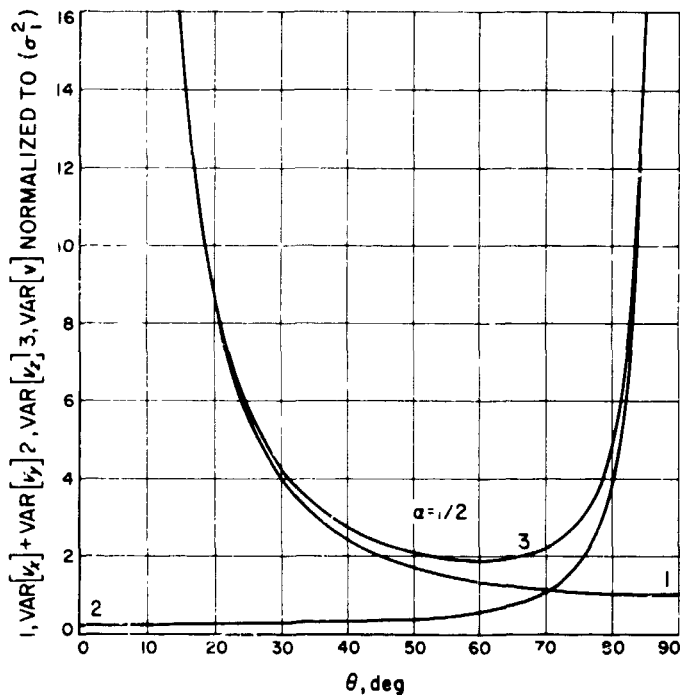


Fig. 4. Velocity variances for five-beam system versus beam look-angle theta

3. Range Estimation Variance

When only three of the five radar beams are used in a given estimation technique, range is measured directly along the roll axis, or Beam 5. Consequently, the variance of the estimate is just the variance of Beam 5. For the four-beam estimation technique, the estimation variance is reduced greatly by the averaging of four components.

The expression in Eq. (27) indicates that slant range is merely a sum

$$R_{s_4} = \frac{1}{4} (R_1 + R_2 + R_3 + R_4) \cos \theta \quad (27)$$

of the four range measurements along each of the outside beams. Since each measurement is independent of the others, the variance of the overall estimate is merely the sum of the variances of each beam weighted by the proper coefficients. This relation is expressed by Eq. (28).

$$\text{Var}(R_{s_4}) = \frac{\sigma_k^2}{16} [\epsilon_1^2 + \epsilon_2^2 + \epsilon_3^2 + \epsilon_4^2] \cos^2 \theta$$

$$\text{Var}(R_i) = \epsilon_i^2 \sigma_k^2 \quad (28)$$

Slant range may also be estimated by using the information gained from all five beams. This estimate is indicated in Eq. (29).

$$R_{s_5} = \frac{1}{5} [(R_1 + R_2 + R_3 + R_4) \cos \theta + R_5] \quad (29)$$

Again, all measurements are independent, and the variance can be written down in Eq. (30).

$$\text{Var}(R_{s_5}) = \frac{\sigma_k^2}{25} [(\epsilon_1^2 + \epsilon_2^2 + \epsilon_3^2 + \epsilon_4^2) \cos^2 \theta + \epsilon_5^2] \quad (30)$$

The variance expressions for the three-, four-, and five-beam estimates are plotted in Fig. 5. The relative variances are plainly indicated.

4. Conclusions

This series of articles has dealt with a very specialized guidance radar beam configuration. No attempt was made at generality, except for varying the beam look angles. The reason for choosing this configuration was the current interest in Mars lander type capsules and their requirements for radar. Clearly the same performance criteria will apply to any other class of beam configurations. The principal result contained in this summary is that the radar beam look angle chosen for the Mars capsule concept is much smaller than it should be. Greater marking accuracy as well as far less velocity estimate variance could be achieved by spreading the angles from 30 deg to something more like 50 deg. The best angle for marking accuracy is of course dependent upon what the trajectory angle will be at the time when the mark is

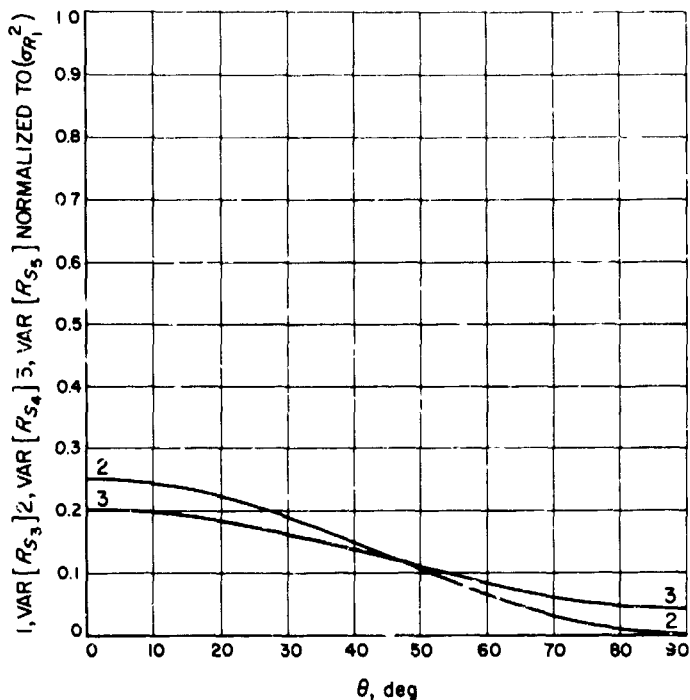


Fig. 5. Slant range variances for three-, four-, and five-beam systems versus beam look-angle theta

desired. This information could be used only if the Martian atmosphere were better known. Until such time, the beam configuration must be chosen on the basis of worst case. Range and velocity estimation variances could be greatly improved by increasing the beam look angles. Both of these considerations must be balanced against the slant range bias error, which gets worse with increased look angles.

The results of the articles referenced in SPS 37-33, -44, Vol. IV, should be helpful in designing radar systems for future missions.

B. Performance Margin and Cost Trade-off for Spacecraft Telecommunication System Design, M. K. Tam¹

1. Introduction

In the design of interplanetary spacecraft telecommunication systems, the "sum of the negative tolerances" philosophy has been used as a system management tool in controlling the telecommunication system parameters. In this design concept, the performance margin (expressed in dB) of a communication link is defined as the ratio of

¹Contract associate.

the nominal received signal level to the nominal threshold signal level; and the acceptance level of the system is chosen such that the magnitude of the performance margin is equal to or greater than the linear sum of the adverse tolerances for the various system parameters. This approach establishes a minimum level for the communication system performance with a high degree of confidence, provided the specified system tolerances are accurate.

The sum of the negative tolerances concept is a worst-case design technique for system design. While it is seemingly possible for any one of the system parameters to operate anywhere within its permissible range, the probability of all the parameters encountering their adverse tolerance limit simultaneously is extremely unlikely. This is because the tolerance of individual system parameters is usually randomly distributed in some continuous fashion, and the overall system tolerance, which is made up of the tolerance of all the individual parameters, tends to be normally distributed. However, for first generation systems or pioneering missions, the extra margin of safety achieved by this technique is highly desirable.

It is recognized that this technique does not permit controlled variation of design risk, nor does it specify the relationship between the tolerance and the variance of system parameters and express the meaning of the assigned tolerance statistically. Another possible and often suggested approach that serves the same purpose is by realistic handling of the system tolerances such as the rms method supplemented with a safety factor. These two approaches appear to be comparable, if the selected safety factor for the latter approach is adequate.

The same technique is not automatically applicable to follow-on missions, as the characteristics of the system become better understood. In this case, the design constraint on system tolerances may be relaxed to an extent that will optimize the trade-off between mission cost and design performance margin.

From the stand-point of communication performance margin, two methods can be adopted for cost reduction purposes. The first method is to narrow the tolerance limits of individual system parameters based on the experience of the past missions. The second method is to employ a probability design principle in relation to cost. Both methods can be employed concurrently. However, since the latter method offers a reasonable estimate of risk associated with the reduction in system performance

margin requirement, it is discussed and considered exclusively in this article.

The question of how much the performance margin of a communication link should be reduced under the influence of the cost-design margin trade-off is an operations research problem. In general, a problem of this nature involves a multitude of factors which may be of varying degrees of significance, depending upon the attitude and position of the individuals concerned. The parameters of interest may also be varied, depending upon the level of organization at which the operations research is taking place. Therefore, prior to the undertaking of an optimization problem, certain ground rules defining the preference, motivation, and emphasis of the individual should be established.

In the current study, the total cost of the mission rather than the cost of the communication system alone is optimized. The average mission cost, as a function of power-gain product, is obtained, and the point of diminishing returns is determined graphically. This relationship is demonstrated first by a Mars-distance mission and second by a long-distance mission, with a nominal power-gain product of 20 dBm over that of the former. Finally, a similar analysis reflecting the loss of scientific measurement capacity, as a result of the payload weight increase for a higher margin of performance, is also given. The latter analysis ignores the possibility that some scientific measurement capability can be accommodated by sacrificing operation time and bit error rate.

2. Average Cost of Mission Based on System Performance Margin

This subsection shows the development of an analytical model relating the average cost of a planetary mission and the margin of communication system performance. Here we make the hard assumption that the mission must be repeated unless all the objectives are satisfactorily met. The important elements to be considered are the tolerance distribution of the overall communication link and the average cost involved for lowering the design constraint in performance margin.

a. Distribution of overall system tolerance. The tolerance distribution of the overall communication link establishes the probability of the communication system to meet a given margin of performance. The overall system tolerance is the aggregate sum of the tolerances for individual system parameters, which are random variables of specific distributions. Since the exact nature of these distributions is not yet available, the over-all system dis-

tribution used in the current study is based on the following assumptions.

- (1) The communication link consists of 10 parameters. The distribution of the variation of these parameters is identical but independent.
- (2) The deviation from the design point of these parameters is rectangularly distributed (± 1 dB). Its standard deviation σ is 0.578 dB.
- (3) The over-all system tolerance is approximately normally distributed, based on the central limit theorem with a mean of 0 and a standard deviation σ_t equal to 1.83 dB.
- (4) System performance is considered unsuccessful if it does not meet all specifications, including bit error rate at encounter.

Based on the above assumptions, the distributions for the individual parameters and for the over-all system are shown in Fig. 6. The actual behavior of propagation of tolerances and the distribution of various system parameters will be investigated in a later study.

In Fig. 6(b), the probability of success for a given design margin of performance p is represented by the area under the normal curve up to the performance margin that is selected.

b. Expected number of flights to meet hardened objectives. Suppose that an infinite amount of money is available to accomplish a given mission and that successive attempts can be made until a successful flight is achieved

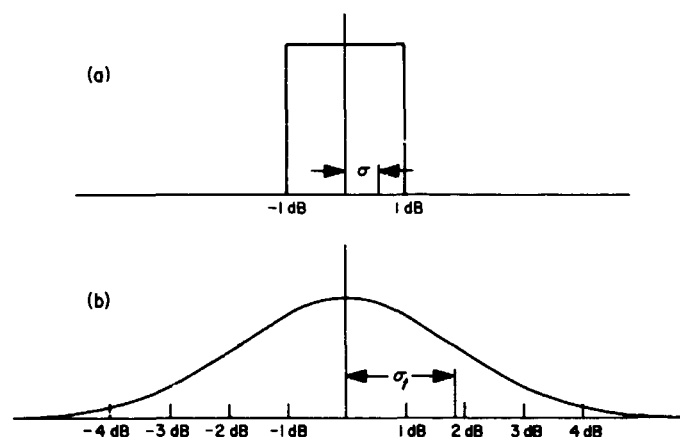


Fig. 6. Assumed distribution for deviation from design point: (a) individual parameters; (b) over-all system

for the first time. The sample space describing the success flights of this mission is as follows:

First flight	p
Second flight	qp
Third flight	q^2p
n th flight	$q^{(n-1)}p$

This is an infinite sample space in which p is the probability of success for each flight and p and q are related by

$$p + q = 1 \quad (1)$$

It is implied in this sample space that the i th flight is undertaken only when all the preceding flights have failed. In the present level of analysis, the probability of success of each flight reflects only the performance required of the communication system.

If x denotes the number of flights needed to achieve the first success, then

$$f(x) = q^{(x-1)} p, \quad x = 1, 2, 3, \dots, n \quad (2)$$

and the average value of x is found to be

$$\bar{x} = \sum_{x=1}^n xf(x) = p(1 + 2q + 3q^2 + 4q^3 + \dots) \quad (3)$$

It is known that

$$\frac{1}{(1-q)^2} = 1 + 2q + 3q^2 + 4q^3 + \dots \quad (4)$$

Therefore,

$$\bar{x} = \frac{p}{(1-q)^2} = \frac{1}{p} \quad (5)$$

Equation (5) shows that the average number of flights is inversely proportional to the probability of success of each flight.

c. Average cost. The average cost of the mission is the product of the cost for each flight and the average number of flights required to accomplish the mission. Therefore,

$$\bar{c} = u\bar{x} = \frac{u}{p} \quad (6)$$

where u is the total cost per flight.

The general relationship between the average cost of the mission (exclusive of the communication system and power required for the communication system) and the performance margin is shown in Fig. 7.

It can be visualized from Fig. 7 that if the design point with respect to the over-all system tolerance is used, the probability for the system to meet the required performance level is only 50%. Consequently, two flights are required on the average to achieve success of the mission. Conversely, if the sum of the negative tolerances procedure is followed, only one flight is required, as p for this case is essentially unity. It is interesting to note that the average number of flights is only slightly greater than unity when $3\sigma_t$ is chosen as the design constraint.

Figure 7 points out two characteristics that are significant.

- (1) The difference in cost between two performance levels near the upper tail of the cost-design level curve appears to be small.

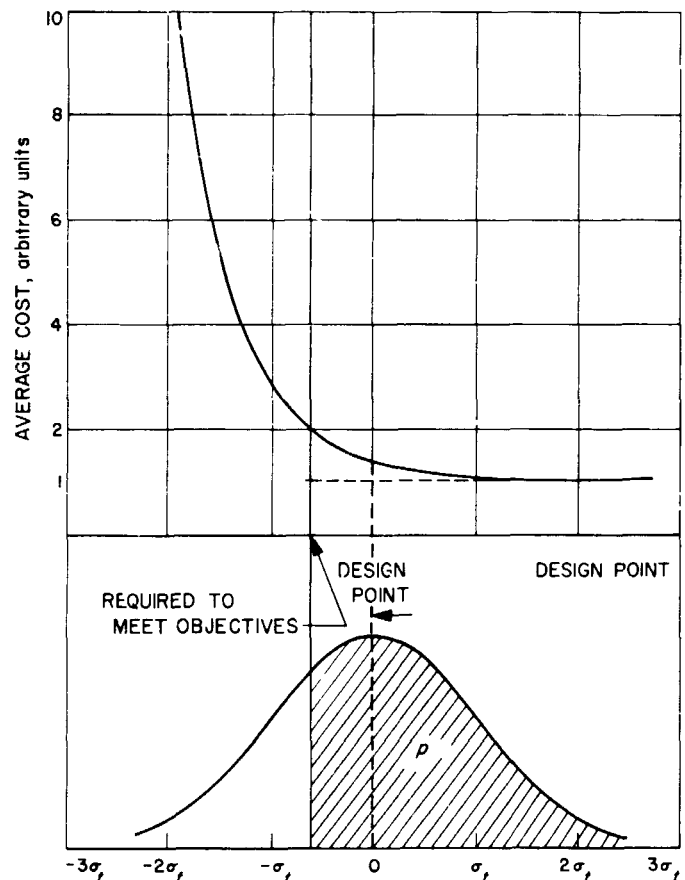


Fig. 7. General characteristics — average mission cost vs performance margin

- (2) The average mission cost rises rapidly as p decreases below 50%. This leads to the conclusion that design in this region is not desirable.

3. Average Cost of Transmitter Power

The average mission cost, as described in the preceding subsection, is valid for those outlays which are independent of the performance margin. To increase the performance margin of a communication system, additional costs and other economic factors will be incurred on certain portions of the spacecraft, depending upon the methods by which the additional performance is achieved. At present, one of the more feasible methods is to increase power and antenna gain of the spacecraft telecommunication system if operation time and bit-error rate are to be maintained. A shortcoming of this method is that, in addition to the cost required, it takes up already limited payload weight availability; and, as a consequence, design and utility restrictions imposed upon other subsystems may be created. This subsection outlines the relationship between cost and design constraints in terms of the product of transmitter power and antenna gain.

a. Relationship between weight and transmitter power and antenna gain. The relation defining the optimum weight as a function of power and antenna gain of the spacecraft transmitter has been investigated. For a symmetrical paraboloidal antenna, the relative weight in relation to power and antenna gain is expressed by

$$W = \frac{P}{k_1} + k_2 A = \frac{P_t}{k_1 \eta_r \eta_t} + \frac{k_2 \lambda^2}{4\pi \eta_a} G \quad (7)$$

where

P = raw power

A = antenna area

k_1 = raw power per unit weight

k_2 = antenna weight per unit area

P_t = available power at antenna

G = antenna gain

η_r = power regulator efficiency

η_t = transmitter efficiency

η_a = percent effective area of antenna ($A_{eff} = \eta_a A$)

λ = wavelength of transmitted signal

b. Cost of power-gain product. The term power-gain product here refers to the power-gain product $P_t G$ required to satisfy a given performance margin when all other parameters of the communication link are assumed constant. Although there are unlimited combinations of P_t and G that yield a given power-gain product, the combination which is optimum with respect to cost is used for this study. This optimum power-gain product denoted by M_0 is determined as follows:

Assuming the cost of power-gain product C_p is obtained by

$$C_p = q_1 W + q_2 P + q_3 A \quad (8)$$

in which q_1 , q_2 , and q_3 are cost per unit payload weight for launching, cost per unit raw power, and cost per unit antenna area, respectively. Then, combining Eqs. (7) and (8) yields

$$C_p = \alpha_1 P_t + \alpha_2 G \quad (9)$$

where

$$\alpha_1 = \frac{1}{\eta_r \eta_t} \left(\frac{q_1}{k_1} + q_2 \right) \quad (10)$$

and

$$\alpha_2 = \frac{(q_1 k_2 + q_3) \lambda^2}{4\pi \eta_a} \quad (11)$$

The optimum condition is obtained by taking

$$\frac{dC_p}{dG} = \frac{d}{dG} \left[\alpha_1 \frac{M_0}{G} + \alpha_2 G \right] = 0 \quad (12)$$

and the minimum cost is found to be

$$C_{p \min} = 2 (\alpha_1 \alpha_2)^{1/2} (M_0)^{1/2} \quad (13)$$

As a preliminary estimate, the various constants used in the above equations are listed in Table 1. It should be emphasized that the listed values are derived from limited data and are subject to further verification. In the meantime, they serve to provide a numerical estimate for demonstration purposes only.

With these constants,

$$C_{p \min} = 7400 (M_0)^{1/2} \quad (14)$$

Table 1. Various constants used for evaluating C_{pmin}

Constant	Value used	Remarks
k_1	5 W/lb	Solar panel at Mars distance
k_2	0.25 lb/ft	
η_r	0.8	
η_1	0.3	} Not constant for all power levels
η_2	0.5	
λ	0.1 m	
q_1	\$1000/lb	Not a linear function
q_2	\$20,000/W	
q_3	\$100,000/m	

Equation (14) is plotted in Fig. 8 with the power-gain product coordinate expressed in dBm

c. Cost of power-gain product reflecting weight reduction of science package. There is a considerable hidden cost due to the loss of payload weight resulting from over-design. For example, the over-design may result in the reduction of weight available for the scientific instrument package to such an extent that additional flights are required to complete all the planned measurements. This, in effect, increases the cost of the over-all mission. It is assumed that, on the average, the cost of the over-all mission is increased in proportion to the decrease in weight of the science package. If a weight ceiling for the combination of science and power packages is assumed to exist, a curve of the form shown in Fig. 9 can be constructed to show the weight capacity available for the science package in relation to the power-gain product.

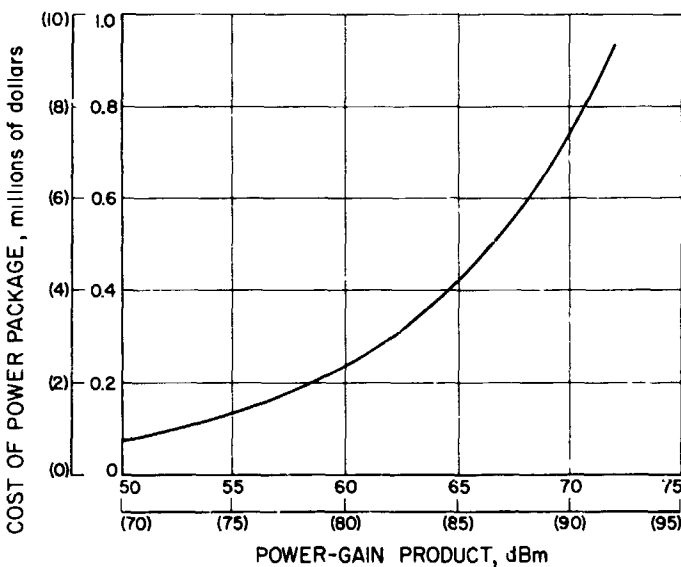


Fig. 8. Cost vs power-gain product

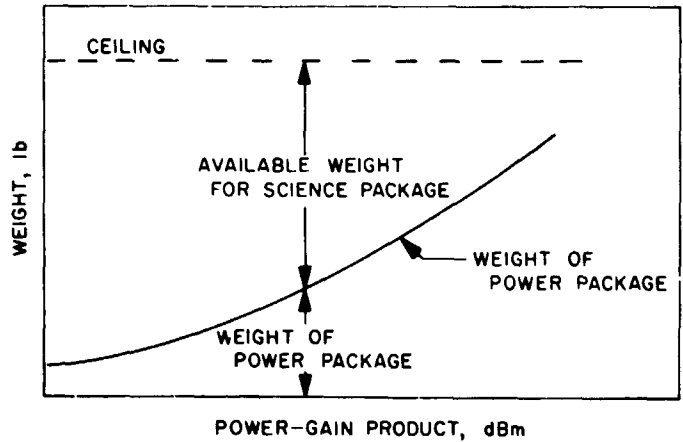


Fig. 9. Load limit for science package in relation to power-gain product

On this basis, it is possible to establish a price for each unit weight by taking the quotient of the cost of a spacecraft and the typical weight of the science package it carries. The cost for the excessive weight, due to a higher power-gain product requirement, is then determined by

$$C_w = q_s (W - W_0) \quad (15)$$

where

C_w = cost of excessive weight of power package

q_s = cost per unit weight due to loss of science measurement

W = actual weight of power package

W_0 = weight of power package with no safety margin for tolerance

With the information concerning the weight of the power package given in subsections 3a and 3b, and with the variable portion of the spacecraft cost assumed to be \$27,000,000, and with the weight of the science package to be 60 lb, the relationship between C_w and the power-gain product in terms of M_0 in dBm can be computed and plotted (Fig. 10). In optimization problems of this type, the optimum point is independent of the fixed cost and, therefore, can be ignored in the computation.

4. Total Average Cost of Mission

The total average cost of the mission is obtained by combining the average mission cost of the spacecraft (not including power package) and the average cost of the power package. The latter, derived in subsection 3, is modified by the factor \bar{x} to reflect the fact that the power

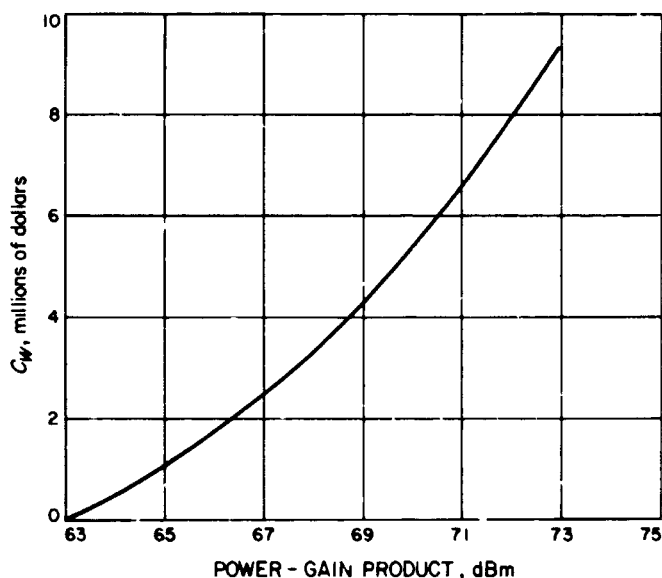


Fig. 10. C_w vs power-gain product

package is also subject to the same risk as the balance of the spacecraft.

Three composite performance-cost curves are presented. Figures 11 and 12 are based on direct cost of the power package only. While Fig. 11 represents the cost characteristics for a Mars mission with a nominal M_0 of 63 dBm, Fig. 12 is for a long-distance mission whose nominal M_0 is assumed to be 83 dBm. Figure 13 depicts the case which reflects the trade-off between scientific measurement capacity and communication system performance.

5. Weighting Function for Subjective Adjustment

The general characteristics of the total average cost of the mission, as illustrated in the preceding subsection, indicate that there exists an optimum power-gain product at which the mission cost is at the minimum. Theoretically, the power-gain product of the spacecraft telecommunication system should be designed around this optimum point, if the minimum average mission cost is the sole consideration for system design objective. Unfortunately, such an assumption oversimplifies the situation which the management team of a space exploration project must confront. At present, planetary explorations still attract world-wide attention, and design decision is heavily influenced by political pressure, as national prestige and institutional reputation are at stake. Therefore, the optimum power-gain product thus obtained can be used only as a guide toward the final design decision.

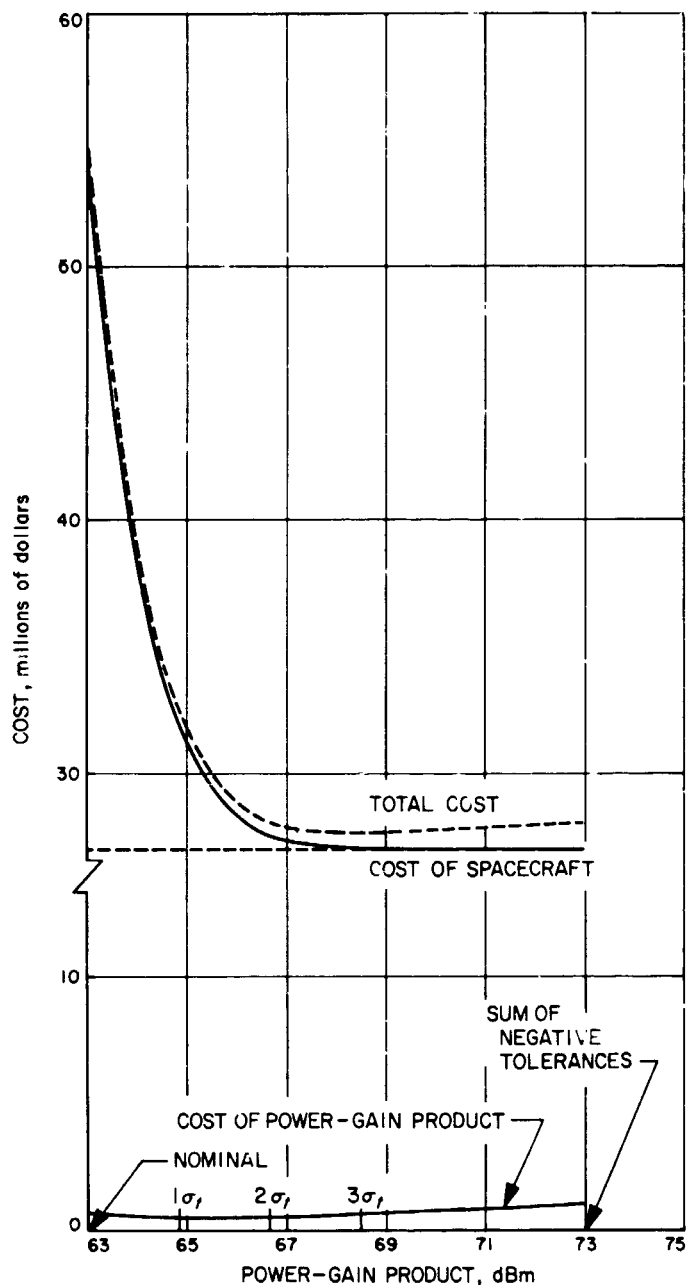


Fig. 11. Mars-distance mission performance-cost characteristics (10 component blocks each with ± 1.0 -dB tolerance rectangularly distributed)

The effectiveness of the average cost and performance analysis technique can be improved if a flexible, subjective weighting function, which reflects the degree of the current political pressure and the confidence of the management team in the design of the telecommunication system, is incorporated into the analysis. This weighting function should be monotonically decreasing with increasing power-gain product and asymptotically approaching

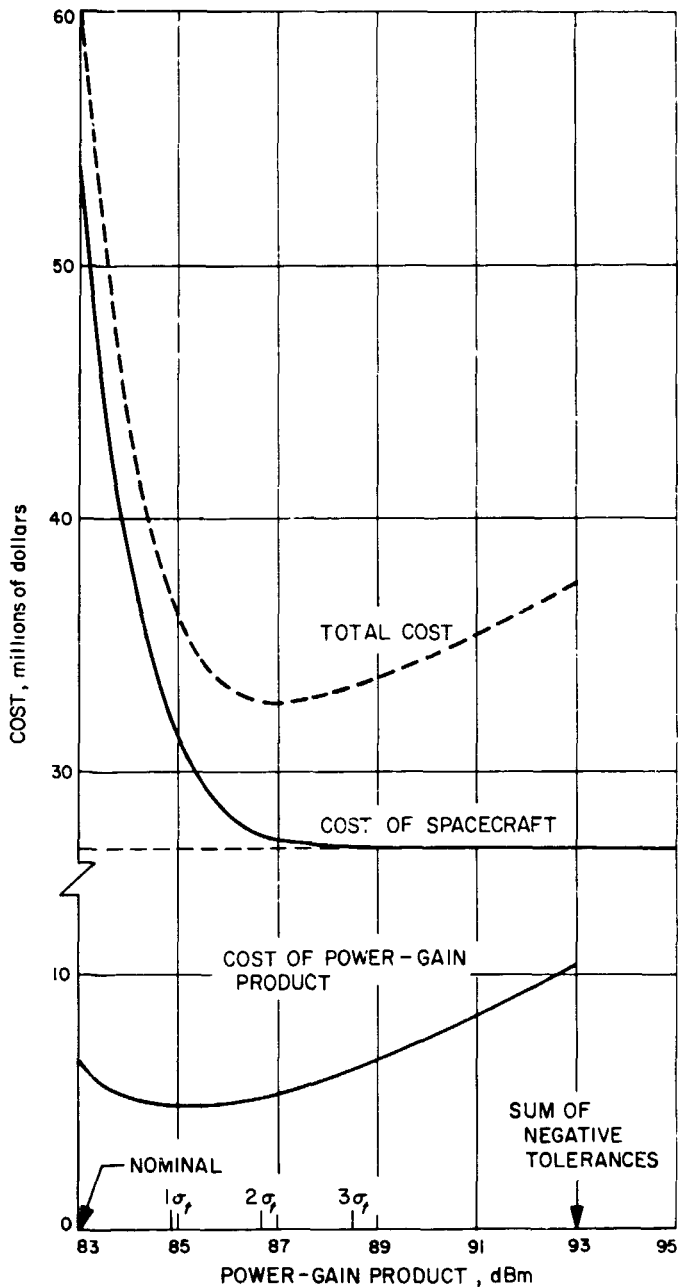


Fig. 12. Long-distance mission performance-cost characteristics (10 component blocks each with ± 1.0 -dB tolerance rectangularly distributed)

unity as the power-gain product increases without limit. In addition, the function can be modified by varying a single weighting factor. Among the many mathematical expressions that satisfy these requirements, Eq. (16) is regarded as most suitable. Hence,

$$W(z) = 1 + v \exp - \frac{z}{\sigma_0} \quad (16)$$

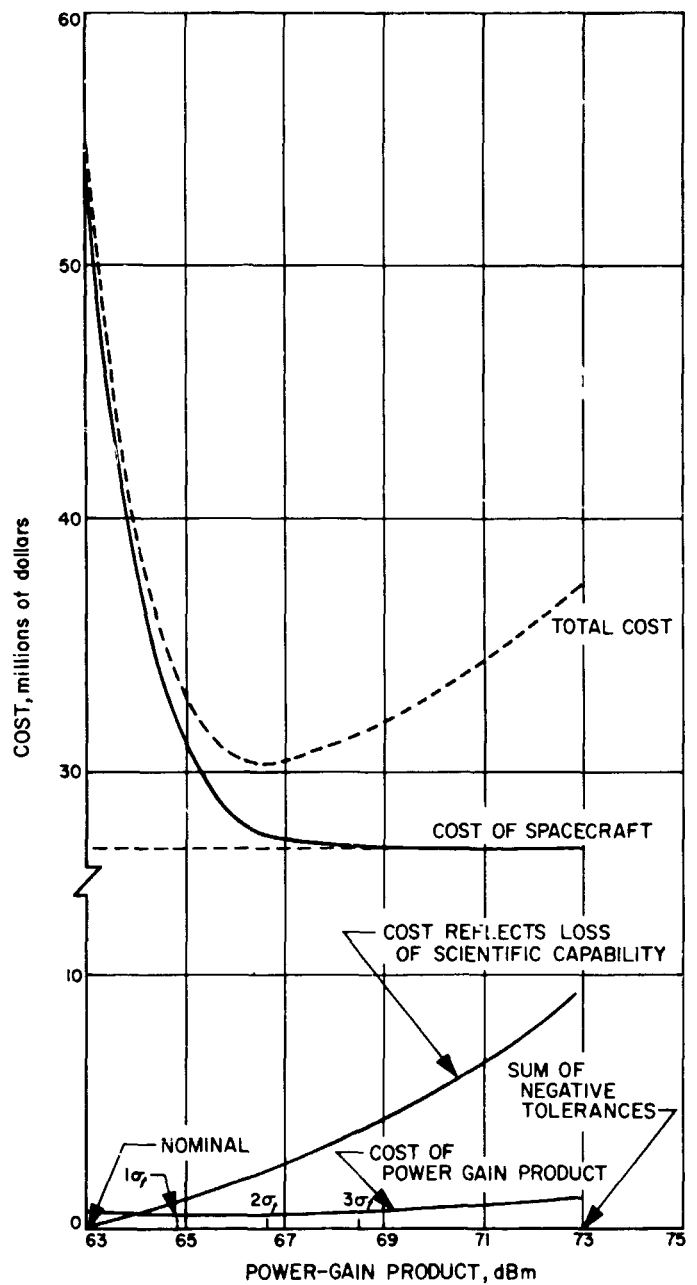


Fig. 13. Performance-cost characteristics (10 component blocks each with ± 1.0 -dB tolerance rectangularly distributed)

in which z is the power-gain product in terms of the standard deviation σ_0 , and v is the adjustable weighting factor of the function.

A revised cost function $C'(z)$ can be constructed according to Eq. (17)

$$C'(z) = W(z) C(z) \quad (17)$$

where $C(z)$ is the cost function of the mission. It can be shown that an optimum point in power-gain product at which $C'(z)$ is minimum exists. In relation to the optimum power-gain product for $C(z)$, this point is shifted toward the right side, with a displacement depending upon v . If v is determined, the optimum power-gain product for $C'(z)$ will be the desired margin for the telecommunication system.

The remaining problem is how to assign the weighting factor v . It can only be selected intuitively based on cumulative knowledge from past experience. To get some understanding for handling this factor, it is possible to obtain values for v so that the revised optimum power-gain product coincides with the margin of the sum of the negative tolerances approach and with any other arbitrary margin, such as the $3\text{-}\sigma$ point. With this information

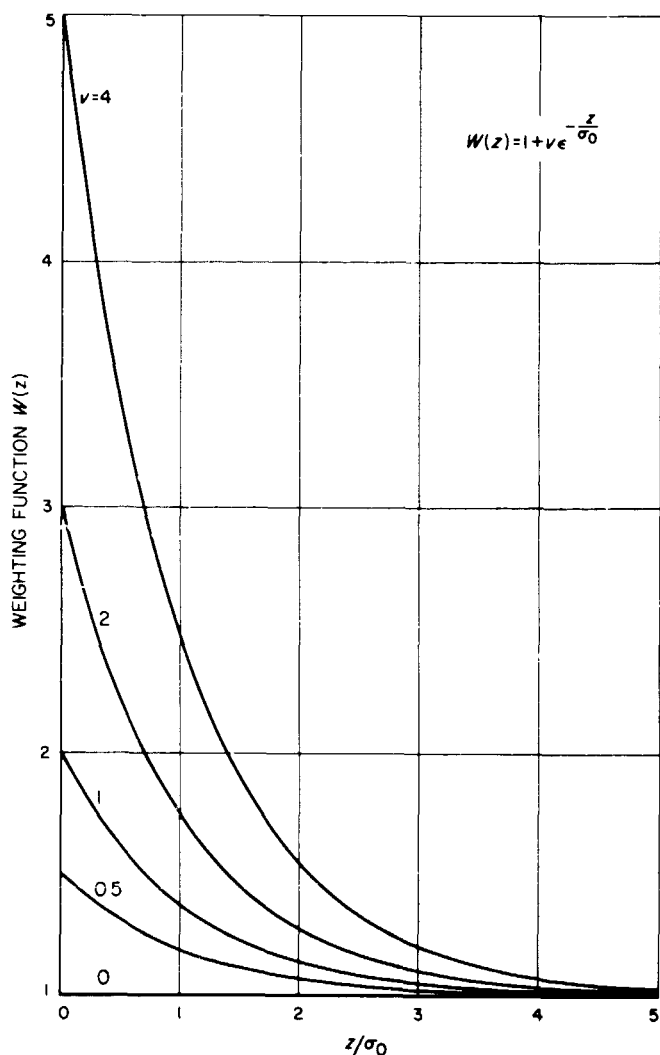


Fig. 14. Weighting function curves

as a guide, a reasonable value of v can be established according to circumstances at hand.

For demonstration purposes, a family of curves for the weighting function and for the corresponding $C'(z)$ are shown in Figs. 14 and 15, respectively. The cost function $C(z)$ used to construct Fig. 15 is the one for the long-distance mission, as shown in Fig. 12.

The unit used in the ordinate of the diagram shown in Fig. 15 may be misleading, as the $C'(z)$ curves for various v do not in fact represent the true cost. To avoid any misinterpretation, these curves are normalized with respect to their optimum point and are plotted in Fig. 16.

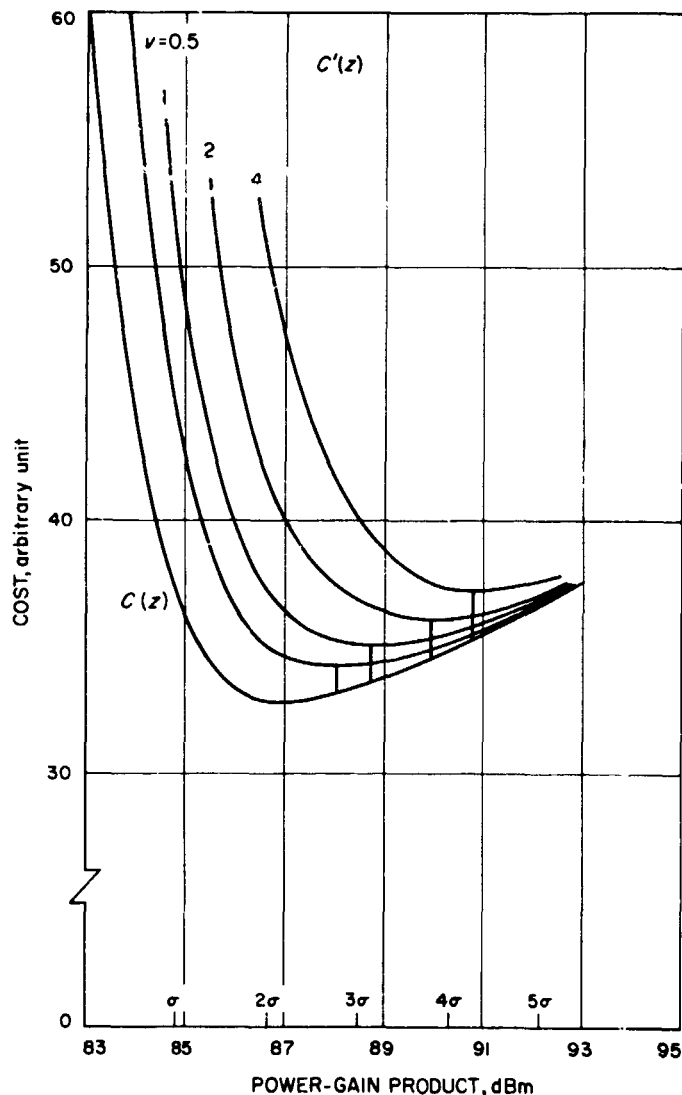


Fig. 15. Modified long-distance mission performance-cost characteristics (10 component blocks each with $\pm 1.0\text{-dB}$ tolerance rectangularly distributed)

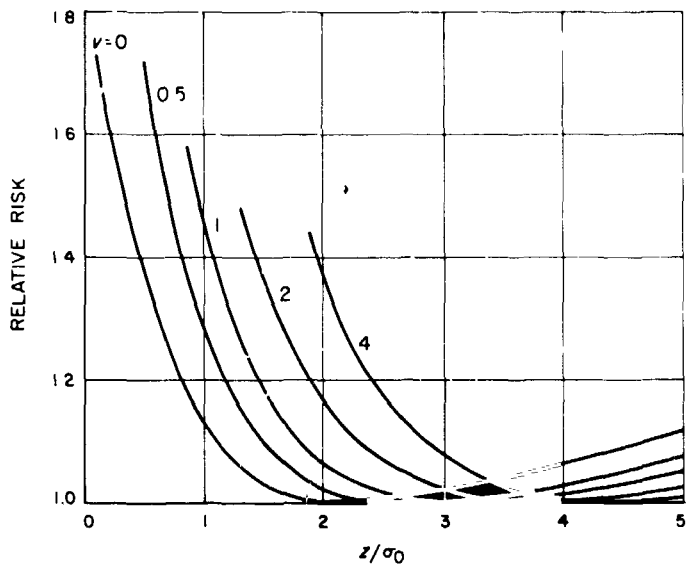


Fig. 16. Relative risk function corresponding to Fig. 15

The ratio of $C'(z)$ to its corresponding $C'(z_0)$, where z_0 is the optimum level, is defined as the relative risk function.

6. Conclusions

In each of the three cases considered in subsection 4, there exists an optimum power-gain product at which the total average mission cost is at the minimum. The optimum power-gain product occurs between the 2- σ and 3- σ points, depending upon the specific cases.

From the direct cost standpoint, and if the mission is confined within the Mars distance, it appears that the design constraint on performance margin is not critical beyond the 2- σ point, so far as the total mission cost is concerned. On the other hand, the optimum condition becomes more keenly defined for missions with longer distance, or when system capacity (such as scientific measurement capacity), is considered. Under these circumstances, it is beneficial to investigate the point of diminishing returns for each mission and to establish the design constraint accordingly, instead of employing the more arbitrary procedure of sum of the negative tolerances.

It has also been shown that if certain subjective measures are included in the analysis, the optimum strategy would be shifted toward the conservative side.

XX. Future Projects

ADVANCED STUDIES

A. Mission to a Comet: Constraints and Background Information, *R. G. Brereton and R. L. Newburn*

1. Introduction

When first observed far from the sun, a comet appears as a hazy area of light. Plunging into the inner parts of the solar system, it may appear to change in size, and it usually develops one or more extensive tails which may trail out to a length of more than 10^8 km. The most spectacular comets are possibly new comets, or those from far out in the solar system, which have not been subjected to repeated solar passages. It is obvious that material is used up, or "boiled off," in each passage near the sun.

Observations tell us that comets are very different from the earth and may be among the most interesting scientific bodies in our solar system. The nature of the observational information has led to many theories and a great deal of speculation. Perhaps comets are formed from interstellar dust, thus providing an accessible sample of

interstellar material, or perhaps they represent a sample of the original solar-system condensate. Knowledge of the chemical composition of the material in a comet could yield the best possible estimate of the composition of primordial matter and lead to important conclusions about the origin of the elements. The mechanics of a comet's formation and the effect of a cometary impact on a planetary atmosphere or surface are also of interest. Some have even speculated as to whether large lunar craters and other lunar surface features could be the scars of a cometary impact.

Because comets are so little understood, and because of the diversity of speculations about them, the selection of suitable and acceptable scientific objectives and experiments for a comet-intercept mission is not an easy task; further, it is one that must be subjected to review by a large segment, comprising many disciplines, of the scientific community. However, it is felt that such a mission may be the most important mission for purposes of cosmogonical research that will be within the capabilities of the early 1970s.

2. Mission Constraints

To derive the maximum scientific value from a comet-intercept mission, it is necessary to define several mission constraints that affect not only the choice of experiments and their unique requirements and techniques for implementation, but also the feasibility of the mission itself. These comet-mission constraints, as presently conceived, are discussed below.

The selection of a specific comet for an intercept mission will not be attempted here. This can be accomplished only after a detailed analysis has traded off the constraints listed below, as applied to particular comets, with technical data involving constraints on the launch vehicle, launch window, flight time, approach velocity, communication distance, guidance and control, and, finally, the mission's scientific objectives and the resulting scientific instruments.

a. Launch vehicle capability. The launch vehicle assumed here has at least the capabilities of an *Atlas/Centaur*. Because of the high injection-energy requirements for most comet missions and the relatively modest capability of the *Atlas/Centaur* launch vehicle, target selection is limited, as are spacecraft weight and the resulting scientific payload. Even so, preliminary trajectory analyses indicate that there will be several favorable comet apparitions from 1970 through 1976 that are amenable to study with a lightweight *Mariner*-type spacecraft. These opportunities are expected to allow the consideration of 110 to 150 lb of scientific payload for a particular mission. This is certainly adequate, and a select group of scientific experiments on an intercept probe of this type can be expected to contribute data toward a major advance in our understanding of comets.

b. Intercept miss distance. A spacecraft-comet encounter miss distance of less than 2500 km from some preselected part of the comet is desirable. Through Deep Space Instrumentation Facility tracking and programmed trajectory corrections, the spacecraft's location in space will be known, and, within limits, some adjustment will be possible. However, the comet's trajectory will be less well-known, and so the precise point and time of spacecraft-comet encounter will be largely dependent upon knowledge of the cometary orbital elements. This suggests that an extensive accompanying optical observation program of the comet will be necessary throughout the apparition, i.e., possibly for several weeks prior to spacecraft launch and also during the flight portion of the mission. This further suggests that the choices of

particular comets considered for the mission should be limited to those short-period comets whose orbital elements are already reasonably well-known and whose apparitions can be predicted to be bright enough to permit early recovery.

Previous studies (Ref. 1) of the trajectories, orbital determination techniques, and spacecraft guidance problems for a number of selected comet missions have indicated that the requisite 2500-km spacecraft-comet encounter miss distance is feasible. This would be without the complication of an on-board comet seeker for in-flight and terminal guidance. The general comet-selection and guidance procedure for achieving this accuracy in flyby distance is envisioned as follows:

- (1) Use data from earlier apparitions of selected short-period comets to determine their orbits (highly elongated), predict intercept points, etc., and then select the most suitable one as a likely target.
- (2) Begin optical tracking of the comet from several facilities at its first appearance to determine a more precise orbit and intercept point. It is possible that this phase could begin some months before launch.
- (3) Launch the spacecraft on the basis of item (2) above.
- (4) Track the spacecraft and the comet.
- (5) Use midcourse and terminal corrections to achieve final rendezvous.

c. Desirability of intercept close to perihelion. Except for the rare annual comets such as Schwassmann-Wachmann 1 and Oterma, comets usually become visible only as they approach the sun and become subject to increasing solar radiation. Their most active period is near perihelion; therefore, it is desirable to have the spacecraft-comet intercept occur at or near perihelion passage. This is also an important consideration for the following constraint.

d. Visibility from earth during intercept. This places a requirement on both the brightness and the trajectory of the comet. It is very desirable that the comet be visible from earth during the intercept phase to allow the correlation of data from the spacecraft's scientific instruments, earth observatories, and perhaps, by then, even orbiter observations. Thus, any comet chosen for this mission should be a visual comet or, at the least, one that is

capable of achieving a brightness of at least tenth magnitude during the intercept phase of the mission; this is especially desirable for carrying out any earth-based spectroscopic observations. This constraint is a difficult one, as few periodic comets have been observed to brighten to visual magnitudes as high as six.

e. Closing velocity. Closing velocities determine how long the spacecraft will be in a particular comet and also affect the design of the scientific instruments, their data rate, and the design of the scan platform. In most cases, the comet would overtake the spacecraft. A low closing velocity is desirable, with the comet flying slowly by the spacecraft; however, a differential velocity of up to 15 km/s would be acceptable.

f. Trajectory constraints for approach, fly-through, and recession from the comet. It is desirable to fly through the coma and as close to the nucleus as possible in order to observe the central core of the comet. The desired trajectory is expected to pass through the coma and, as discussed earlier, to within 2500 km of the nucleus. Further, the trajectory should offer an opportunity to perform scientific experiments on the comet's coma and tail during the approach and recession portion of the flight. It should be noted that, for most trajectories, the cometary tail cannot be intercepted on leaving the coma without a significant change in the course of the spacecraft.

g. Spacecraft hazard. The physical state and distribution of matter within a comet are largely unknown; thus, the actual coma penetration phase of this mission could involve a hazard to the spacecraft. For this reason, it may be desirable to include shielding for certain critical spacecraft components and also a real-time, or at least a high-data-rate, transmission capability for monitoring the spacecraft's engineering and scientific data. In this way, it may be possible to have information concerning a hazardous situation before loss of contact with the spacecraft. Fortunately, the intercept phases of most comet missions that are practicable seem to occur when the communication distance is very small, e.g., a few tenths of 1 AU. This could be an important advantage in sizing a communication link for high-data-rate transmission.

3. Comets: Observation and Theory

a. Orbital characteristics. The most precisely known characteristics of comets are their orbital elements, although even here the uncertainty is much larger than in the case of planetary orbits. Comets can be roughly divided into two classes: the "short-period" or just

"periodic" comets having periods up to 200 yr, with about 100 members currently known; and the "long-period" comets with periods averaging 50,000 yr or more and numbering possibly on the order of 10^6 to 10^{12} members.

A further distinction can perhaps be made among the "long-period" comets by distinguishing their orbits as hyperbolic or nonhyperbolic. It has been an important scientific question whether or not hyperbolic comets, entering from interstellar space, never before having been attached to the sun, do indeed exist. It is now universally recognized that many comets having hyperbolic orbits when moving near the sun were perturbed into those orbits from their former elliptical paths by the action of one or more of the planets, usually Jupiter. Such comets then are lost to the solar system for all future time.

Long-period comets are not completely randomly distributed. The number within a given inclination is roughly proportional to the sine of the inclination, with a deficiency from 100 to 120 deg and an excess from 120 to 150 deg. Their nodes are roughly uniform in distribution, but the distribution of aphelia, a measure of the direction from which comets have come, is nonuniform, there being numerous concentrations and several regions showing no comets (Ref. 2). There are definite groups of long-period comets having almost the same orbital elements, except for the time of perihelion passage. The famous sungrazers, of which Ikeya-Seki (1965f) is the most recent of seven known members, is such a group. These groups tend to cause a clustering in the distribution of aphelion points.

The periodic comets are definitely not randomly organized. More than two-thirds of the known examples have inclinations less than 20 deg. Only seven out of the total of 94 are in retrograde orbits, as opposed to about half of the long-period comets. The aphelia of 67 of the 94 periodic comets lie between 4 and 8 AU from the sun, with 52 of them between 4 and 6 AU. These 67 comets are usually referred to as Jupiter's comet family. Russell (Ref. 3) and Stromgren (Ref. 4) have shown conclusively that the action of Jupiter has indeed greatly changed their orbits, in effect capturing them from long-period orbits. In fact, Jupiter has played a major role in the determination of the orbits of most, if not all, the short-period comets. Even Halley's comet, with an aphelion distance of 35.3 AU, can at present come no nearer than 8 AU to the orbit of Neptune, but can come within 1 AU of that of Jupiter (Ref. 5). The other major planets have had measurable effects upon various comets, of course, but there is no good evidence that any of them have

comet families (Ref. 5). In fact, a study of cometary nodal distances (the distances from the sun at which a comet crosses the ecliptic plane) indicates that Jupiter and possibly the terrestrial planets Venus, earth, and Mars are the chief cometary perturbers.

The changes effected in the orbits of periodic comets by Jupiter are not small. For example, from 1858 to 1964, Jupiter's interaction with P/Pons-Winnecke changed the comet's period from 5.56 to 6.30 yr, its perihelion distance from 0.77 to 1.23 AU, its eccentricity from 0.755 to 0.639, and its inclination from 10.8 to 22.3 deg (Ref. 6). In 1886, P/Brooks 2 passed within two Jovian radii of Jupiter, and its period was changed from 31 to 7 yr in the one interaction (Ref. 6). P/Oterma had a period of 18.0 yr in 1934, 7.9 yr in 1950, and 19.2 yr in 1965.

Comets of the Jupiter family cannot be differentiated from minor planets (asteroids) on the basis of orbit alone. Roemer (Ref. 7) has remarked that "When I observed Comet Arend-Rigaux on its last apparition I found that it was completely stellar on all plates. The orbit is similar to that of a minor planet, but the object was designated as a comet because it on occasion showed some diffuseness. When Baade discovered Hidalgo he was undecided whether to call it a minor planet or a comet, but he decided on the former simply because more people were observing minor planets at the time and it would be better taken care of!"

b. Observed structure.

Nucleus. A comet consists of a nucleus, a coma, and usually one or more tails. The nucleus and coma together are called the head. The nucleus is the name given to the starlike point of light appearing at times within the coma. It requires a fairly large telescope and long focal length even to see the nucleus of most comets, and photography is also difficult due to the lack of contrast against the coma. Roemer has possibly had the most experience of any modern astronomer in this area, and she states (Ref. 8) "It is our experience that the overwhelming majority of comets have essentially starlike nuclei that can be observed photographically with the 40 inch, f/6.8 Ritchey-Chretien reflector, but that these nuclei almost invariably are fainter than magnitude 13 or 14 regardless of the total brightness of the comet." Roemer feels that it is likely the nucleus is a small solid body. Richter (Ref. 9) stated that "the term nucleus can be understood to refer to the optical center of the comet, and we can speak of the photometric nucleus." He notes that not all comets show anything that could be called a

nucleus, not even a central condensation, let alone a starlike nucleus, while some show a condensation resembling one or more planetary disks (Ref. 9). Most observational evidence seems to agree with Roemer's contention that such difficulties are due to inadequate apertures used by many observers.

In cases where a starlike cometary nucleus has existed of sufficient brightness to attempt slit spectroscopy, the result has been a Fraunhofer spectrum of reflected sunlight, with only a few weak gaseous emission lines superimposed (Ref. 9). These emission lines may well be from the surrounding coma. Photometrically, the nucleus seems to follow an inverse square law rather well, again what would be expected of a body shining by reflected radiation (Ref. 9). Assuming the nucleus is a compact body following Lambert's law of reflection, a radius may be calculated for any assumed albedo. Typical periodic comets show nuclear radii from 0.1 to 2 km, assuming an extremely high albedo of 0.70, and from 1 to 10 km, assuming an opposite extreme albedo of 0.02 (Ref. 10). If these values are typical of nuclear radii, it is obvious why small telescopes see so little and why even large ones still do not resolve a disk. For nearly parabolic comets, radii are typically twice as great, while exceptional objects in both categories may be 5 to 10 times larger (Ref. 10). Assuming a middle value for the albedo (0.25) and a mean density of 3 g/cm³, nuclear masses would typically lie in the range of 10¹⁷ to 10²⁰ g, with a few exceptional objects going as high as perhaps 3 × 10²² g. Whipple has reversed the problem and attempted to build a "new" Halley's comet from estimates of dust and gas loss by the comet at each perihelion passage. He finds a minimum total mass of 10¹⁷ to 10¹⁹ g (Ref. 11). No cometary mass has ever been measured gravitationally, and two comets have been observed to pass within the Jovian satellite system without causing a measurable effect upon the satellites. This is consistent with the masses discussed above.

If the comet is not a compact body, but rather a gravitationally associated cloud of dust, the masses are roughly the same while the dimensions are one to several orders-of-magnitude larger (Ref. 9). According to Lyttleton, the masses are again comparable to those discussed above, but there is no real nucleus (Ref. 12).

Coma. The head of a comet is quite large and very tenuous. Just how large is difficult to state, since the apparent size varies with the aperture, focal ratio, and detector used for the observation, as well as with the

distance of the comet from the sun. A typical diameter is 10^5 km although many cases of 10^6 km have been measured and 6×10^7 km is claimed for 1943 I (Ref. 13). Star trails can usually be photographed through at least the outer parts of the coma. In some cases, the coma appears to shrink in size as the comet approaches the sun, while in others it may grow (Ref. 9). The coma is roughly spherical in shape, and the nucleus is more or less at its center. This would seem to indicate an isotropic streaming of material from the nucleus (assuming the nucleus exists).

The spectrum of the head (coma) of a comet near perihelion consists most prominently of emission bands of CN and C_2 . Other neutral molecules that have been identified are C_3 , OH, NH_2 , and CH (Ref. 14). Forbidden lines of atomic oxygen were first identified by Swings and Greenstein in 1958. Atomic sodium is often identified in comets that closely approach the sun, i.e., nearer than 0.7 AU (Ref. 14). High-dispersion observations of the recent sun-grazer Ikeya-Seki (1965f) confirmed an earlier visual observation of atomic iron, and definitely added Ca I and Ca II while suggesting H, Sr II, Fe II, and Mg I in increasing order of doubt (Ref. 15). Several other workers obtained spectra of 1965f, and new information may soon be published. Ionized molecules are characteristic of the tail, but CO^+ , n_2^+ , CO_2^+ , CH^+ , and possibly OH^+ all may appear in the region of the head (Ref. 14). It is difficult to distinguish the head from the initial part of the tail where it leaves the comet. The head usually also exhibits a weak continuum of reflected sunlight, indicating the existence of scattering or reflecting particles (Ref. 13). The continuum seems in some cases to be slightly reddened (Ref. 14).

It is difficult to obtain any estimate of dust-particle mass or density in the coma. Some comet heads contain a great deal of dust, as shown by rather strong spectral continua; others contain virtually no dust. There is not even a direct correlation between dust in the coma and so-called dust tails, since the dust particles must be just the right size for light-pressure acceleration to form a proper dust tail (Ref. 13). Vanysek has attempted an estimate of dust in the coma from the continuum strength, assuming properties for the dust grains, and finds the total mass varies from about 3×10^7 g for P/Encke to almost 10^{12} g for objects such as Arend-Roland (Ref. 16). The coma of Arend-Roland was some 3×10^5 km in radius (Ref. 17). This implies a mean density of 10^{-20} g/cm³. Assuming the particles to be 1 μ m in diameter (Ref. 18) with a density of 3 g/cm³, they would have

a mass of about 1.5×10^{-12} g/particle, and there would be about 7×10^{-3} particles/m³. Assuming an inverse-square-density increase toward the nucleus, this would imply 70 particles/m³ at a distance of 1500 km from the center of the nucleus. The particle density would be considerably lower in a comet such as P/Encke, which is nearly as large but has much less dust. It must be recognized that these figures depend strongly on assumptions and could easily be in error by orders of magnitude.

The photometric behavior of the coma differs greatly from that of the nucleus (which follows a routine inverse square brightness with distance from the sun). Values have been measured from inverse 11.4 power to direct 1.77 power, although comets with inverse values greater than 2 are in the great majority (Ref. 9). Most of the visible light from the coma is the result of fluorescence excitation of gases by the sun, and the brightness of a comet must be, among other things, a function of the number of molecules of gas available for excitation and the efficiency of the detailed mechanism. These processes are not well-understood. Some additional discussion is included elsewhere in this article.

Tail The most spectacular feature of a great comet is its huge tail. P/Halley showed a tail at least 3×10^7 km long in 1910; that of Arend-Roland was 5×10^7 km in length; and the great comet of 1843 showed a tail 32×10^7 km long (Ref. 9). These tails may be 10^6 km in width (Ref. 9). Yet some faint comets never develop an appreciable tail, simply appearing as a small diffuse cloud. Other comets may develop more than one tail, and tails of the same or different comets may differ greatly in appearance and behavior at different times.

In 1903, Bredikhin developed, in considerable detail, the complete mechanical theory of cometary tails previously begun by Bessel (Ref. 14). This theory assumed that, once particles received an initial velocity from the comet nucleus, they moved strictly in a field of attraction force due to the sun and repulsive force of solar radiation pressure. If the repulsive force was strongly dominant, they were rapidly accelerated back from the nucleus, virtually in a straight line away from the sun. Such straight narrow tails were called Type I. If the repulsive force was weak, the tails were strongly curved and called Type II. A related weak acceleration tail called Type III was due to an outburst of particles with a small range of weak acceleration (as opposed to the usual continuous emissions of particles) which resulted in a nearly straight tail (Ref. 19).

A comet's tail generally lies in the plane of its orbit. Unless the earth is reasonably far out of that plane, it may be difficult to observe just how the tail is behaving. Tail spectra characteristically show emission due to CO^+ , N_2^+ , CO_2^+ , CH^+ , and OH^+ , and may show a continuum (Ref. 14). It is usual to place CN in the tail also (Ref. 9), but Wurm would deny this (Ref. 20). When the earth is far enough out of the plane of a comet's orbit, it is seen that the comet may have a pure ion tail that appears to be Bredikhin's Type I, a pure dust tail of Type II (or III), or both (Ref. 14). In fact, it can appear to have several tails. Any tail appearing to contain both ions and dust more than a few million kilometers from the nucleus is just a projection effect of one tail on top of the other. The accelerations in the ion tails are far greater than those that can be given to dust particles, and the dust particles show no ability to generate gas (Ref. 13). Either they are completely degased before they leave the coma, or they never had any significant amount of gas in them (Ref. 13).

Until recently, it was generally felt that the classical theory of Bredikhin was adequate for the dust tails (Ref. 21); however, Belton has suggested that some features of dust tails are unexplained by this theory and that the dust particles are probably charged and, with accompanying electrons, form a plasma (Ref. 22). This turns the nature of the dust-tail mechanism into a rather complex problem. Levin has even suggested that the evidence that Type II tails exhibit nothing but a continuum is not really valid, and that, in fact, the Type II tails are really primarily neutral gas tails plus some dust (Ref. 19). Levin still pictures the Type III tail as a pure dust structure, following Bredikhin's theory.

c. Theoretical structure (cometary models). Cometary models generally fall into two classes: the particulate or "sandbank" models; and the compact models, the most notable of which is Whipple's icy conglomerate model. None is completely satisfactory, but they offer insight into the problems of understanding comets and, above all, suggest what experiments may be crucial to ascertaining the true nature of comets.

For almost a century, the most prevalent view was that a comet consisted of a large number of solid particles of varying sizes, possessing some gravitational coherence and being in orbit about the sun—the sandbank model. In 1953, Lyttleton presented details of a cometary model in which gravitational coherence could operate only at a great distance from the sun, while at planetary distances each particle would be in its own independent Keplerian orbit about the sun (Ref. 12). On the basis of this model,

most periodic comets would have negligible self-attraction as compared to the solar action. Lyttleton suggests that collisions occur near perihelion between independent particles in the comet, due to the orbital crossings on the perihelion side of the latus rectum of the mean orbit. These collisions would shatter particles, offering fresh surfaces for desorption, and would perhaps effect direct gas production through intense local heating (Ref. 23). Even if this mechanism produces sufficient gas, which remains to be proved, the average comet begins to produce gas at a heliocentric distance of 2.5 to 3 AU, which in many cases is long before it crosses the latus rectum.

The theory that condensed gases might be present in comets was formulated in the nineteenth century. However, until some idea of the composition and quantity of gases and dust present in comets was obtained, and until certain other factors, such as the secular acceleration, appeared to be well-established, there was no reason to be overly suspicious of the sandbank theories. In 1950, Whipple (Ref. 24) proposed his icy conglomerate model, a model in which the nucleus was visualized "as a conglomerate of ices, such as H_2O , NH_3 , CH_4 , CO_2 or CO , (C_2N_2)², and other possible materials volatile at room temperature, combined in a conglomerate with meteoric material." The description was expanded in later papers (Refs. 25–28), and many other researchers have since made contributions.

It was soon pointed out by Delsemme and Swings (Ref. 29) that the sublimation rates in a vacuum were all wrong for such substances as CH_4 , NH_3 , and H_2O to be subliming simultaneously. Yet that had appeared to be required to obtain the spectroscopically observed daughter products. Delsemme and Swings suggested instead that the substances present were hydrates such as $\text{CH}_4 \cdot 6\text{H}_2\text{O}$. Various authors have since confirmed that, if there are CH_4 , NH_3 , CO_2 , etc., present in a comet, they must be present as such hydrates (in fact, probably as mixed hydrates) to satisfy thermodynamics (Ref. 30). (The vapor pressure of CH_4 in such a hydrate is decreased by 10^3 to 10^6 , for example.) There are now no conflicts with spectroscopic abundances of neutral molecules.

An interesting observation is that old comets (comets that have short periods and have been around the sun many times) show primarily gas spectra, whereas new comets show continua due to dust. This is just the opposite of what might be expected of a sandbank comet releasing absorbed gas. This adds structure to the icy conglomerate model, suggesting that meteoric material near the centers of old comets begins to adhere, making

available dust rare, while fine unconsolidated dust predominates near the surface of new comets or very small comets (Ref. 11). The possibility of cohering carbon dust at the center of comets also exists (Ref. 11). More elaborate models are now being built using Whipple's original concept.

A problem common to all theories is the source of the tremendous amounts of gas given off by a comet at each perihelion passage. It cannot be assumed that some of the particles are frozen gases, since they would be destroyed during the first perihelion passage. Levin's work on adsorbed gases seemed to offer possibilities (Ref. 9). The process was feasible, and the energetics were right. However, the mass of gas available comes nowhere near meeting that required for even one orbit, and it is impossible to replace it from the interplanetary medium for the next orbit, even if it were sufficient for the first (Ref. 11).

A somewhat related problem faced by any cometary model is survival from a close perihelion passage. The sun-grazing comets pass within about 1 solar radius of the solar surface at perihelion. Becklin and Westphal (Ref. 31), assuming the emissivities of iron, were able to fit observations of the head of Ikeya-Seki at 1.65, 2.2, 3.4, and 10 μm with a color temperature curve that reached 1000°K at 0.15 AU. At perihelion, the temperature must have been several times that value, far above the vaporization temperature of iron. Indeed, any particle of up to several-meters radius should certainly be vaporized during a passage within 4 radii of the sun (Ref. 12). Whipple has shown that only about 2% of the original comet would be available for recondensation, the remainder having been dissipated due to its gaseous random thermal velocities, together with light pressure effects as particles begin to recondense (Ref. 25). Yet Ikeya-Seki appeared virtually the same before and after perihelion passage.

d. Origin and evolution. The status of knowledge of the origin of comets is roughly the same as that of knowledge of the origin of the solar system: there are many ideas, none very acceptable, or at least none very well-developed. Knowledge of the evolution of comets is slightly better because they evolve very rapidly, and there is observational evidence of change.

Theories of cometary origin can be divided into two major classes: those based on interstellar origin, and those based on origin within the gravitational bounds of the solar system. The idea of interstellar origin dates back to Laplace. In the classic form of his theory, comets were

condensations in interstellar space. The original velocity distribution of the comets and the presence or lack of a resisting medium at the time of capture vary from theory to theory. There is no question that, under some of the conditions postulated, comets could be captured by the sun. The chief problem is accounting for the fact that strongly hyperbolic comets, which should be the rule of such an origin, do not appear to exist. Only special classes of distribution functions of cometary velocities result in an ellipse, rather than a hyperbola, as the preferred "capture" orbit.

Some theories regard the capture process as being over, a temporary event as the sun passed through an interstellar cloud. Others assume that comets are a natural part of interstellar space, filling the size spectrum between interstellar dust and small planets. A very recent theory of this type is that of Sekanina (Ref. 32).

Perhaps the most ingenious theory of interstellar origin is that of Lyttleton (Ref. 12). He observes that the sun travels through an interstellar dust cloud from time to time. The individual dust particles must then describe hyperbolic trajectories with respect to the sun that intersect along a line parallel to the relative velocity vector of the cloud and the sun. The particles are, in effect, gravitationally focused. Kinetic energy is lost through inelastic collisions, and material within about 100 to 1000 AU may be captured by the sun, depending upon the relative speed of the cloud.

Theories of origin within the solar system are also quite old, dating back to Lagrange. Most of the nineteenth century theories assumed comets were ejected by the major planets. The modern champion of the ejection hypothesis is Vsekhsviaty, who, in his more recent papers, has partially turned from the major planets to their satellites as sources (Ref. 33). The major objection to the ejection hypothesis has come in modern times with a better understanding of the conditions on the major planets and their satellites. Very few scientists are willing to accept the idea that a mass of 10^{19} g (a large comet) could be ejected volcanically from bodies such as we think the major planets and their satellites to be.

The most prominent current theory is that of Oort, based in part on the work of van Woerkom. It states that there is a great reservoir of comets, the total number being perhaps 10^{11} , at a mean distance from 30,000 to 100,000 AU (Ref. 34). These are said to be perturbed into the central part of the solar system by passing stars. As

evidence of this reservoir, a plot of the number of comets against the reciprocal semimajor axis shows a great preponderance at very large distances. Actually, the statistics are so poor, with most of the "reservoir" lying completely beyond the data points, that the "evidence" is very weak. The evidence in no way denies the existence of the reservoir, but neither does it confirm it. Oort's hypothesis in no way creates comets. It only moves the history one step further back.

4. Scientific Objectives and Experiments

The Space Science Board of the National Academy of Sciences (Ref. 35) has developed a rationale for exploration of the solar system. It stated that the exploration of the solar system is concerned with three central scientific problems of our time, defined as:

- (1) The origin and evolution of the earth, sun, and planets (moons, asteroids, and comets implied).
- (2) The origin and evolution of life.
- (3) The dynamic processes that shape man's terrestrial environment.

In terms of these major problems, the Board has further suggested a number of specific questions to guide cometary research. Some of these are shown in Table 1.

Obviously, the mission under consideration in this document cannot logically be addressed to the task of answering all questions specified by the Board, so some ordering is required. It would seem that the important questions can be divided into two groups. The first group is concerned with questions regarding the physical nature

Table 1. Scientific questions for guidance of cometary research

Question	Means for obtaining answer
(1) Are cometary nuclei single bodies of icy material?	A TV or bistatic radar experiment in a near-flyby probe seems best. (See photo-imaging and mass spectrometer experiments in Table 2.)
(2) If so, what compounds do the ices comprise?	An IR, UV, or microwave experiment could give direct evidence about the composition of the "snowball" itself. A mass spectrometer would recognize "boil off" products. (See dust detector experiment in Table 2.)
(3) What part do frozen free radicals play?	Item (2) above
(4) What is the structure of cometary dust?	A detailed answer would require a sophisticated approach involving sample return or complex on-board analysis of samples. Some information could be obtained by observing abrasion and penetration rates of spacecraft components during passage through the comet.
(5) Do stable isotope ratios in icy compounds or dust differ from the usual terrestrial and meteoritic values?	An answer would require a sophisticated approach involving sample return or complex on-board analysis of samples. Perhaps a good IR experiment could provide the answer.
(6) What is the age of the dust?	Item (5) above
(7) Can nuclear material be identified as primordial solar system condensates or as accumulated interstellar dust grains?	Unknown. The answer can only come from an evolution of knowledge about comets and the solar system.
(8) How long, on the average, have the present elliptical comets been in orbit?	Information about the boil-off rate, or the rate at which comets are affected and the mechanism of this, may suggest an answer. (See dust detector experiment in Table 2.)
(9) What is the composition and size distribution of cometary dust?	Information on the composition would probably require sample return or on-board analysis techniques. A penetration or Pegasus-type experiment would be useful for determining the size distribution. A simple dust detector [see item (4) above] would give much information on the mass velocity and energy distribution.
(10) How are tail gases ionized?	The search coil magnetometer, the vector magnetometer, energetic electron detectors in the range of a few to tens of kiloelectron-volts, the plasma detector, the mass spectrometer, the UV spectrometer, and perhaps TV experiments could each contribute to an understanding of this phenomenon.
(11) How are they accelerated away from the sun; if by the solar wind, what is the coupling mechanism?	Item (10) above
(12) What causes cometary bursts?	Item (10) above
(13) What are the compositions of the coma and tail gases?	Using both ground and spacecraft techniques, IR and UV spectroscopic studies would be useful. A mass spectrometer on a fly-through trajectory could provide some direct measurements. (See dust detector experiment in Table 2.)

and composition of the comet itself. For example, are cometary nuclei made up of single bodies of icy material, and, if so, what compounds do the ices comprise? What is the chemical nature of the material? Is the so-called sandbank model appropriate, and, if so, what are the nature and distribution of the particles? The second group is concerned with questions regarding the interaction of the cometary matter with solar corpuscular and electromagnetic radiation, and with interplanetary magnetic fields. For example, how are tail gases ionized? How are they accelerated away from the sun? If by the solar wind, what is the coupling mechanism? What is the effect of cosmic ray bombardment?

From the foregoing, it seems appropriate that the scientific objectives for an early comet mission should be to determine the comet's physical state, structure, composition, and the manner in which it reacts to its environ-

ment by investigating the comet at close proximity with the appropriate experiments. A select scientific payload to accomplish these broad objectives could include the following experiments: (1) photo-imaging, (2) mass spectrometer, (3) dust (solid particle) detector, (4) magnetic field detector, (5) plasma spectrometer, (6) Fourier spectrometer, and (7) cometary mass determination. These are described in Table 2.

5. Conclusion

Having considered the many questions about cometary phenomena that still remain unanswered and the possible importance of these questions in cosmogonical research, it is concluded that a comet-intercept space-probe mission is potentially the most important mission for the purposes of such research within the capabilities of the early 1970s.

Table 2. Scientific experiments for an early comet mission

Experiment	Weight, lb	Power, W	Objective
Photo-imaging	50	32 (max)	Examine the nucleus, if present, and determine its shape, size, albedo, and light-scattering properties; also, examine the over-all structure of the comet and observe any temporal and spatial changes
Mass spectrometer	12	15 (max)	Investigate the chemical nature of the gaseous material comprising the coma, and determine the distribution of such species and ionized constituents as can be identified
Dust (solid particles) detector	— ^a	2	Investigate the distribution, mass, and velocity of small solid particles throughout the coma and in space
Magnetic field detector (a 3-axis helium magnetometer plus a single-axis search coil magnetometer)	8	7	Examine magnetic fields in space and in the comet, and investigate the interaction between the comet and the ambient solar environment
Plasma spectrometer	20	10	Examine plasma streams in the comet and in space and obtain data on the interaction that must occur between the solar plasma and the cometary atmosphere
Fourier spectrometer	26	12	Examine, at close range, the gaseous envelope around the nucleus to decide on the origin of the radicals C ₂ , CN, etc.
Cometary mass determination	— ^a	— ^a	Determine the mass of the cometary nucleus as it may be indicated by tracking data

^a Not applicable.

References

1. Light, J. O., *Comet Mission Study*, Engineering Planning Document 376. Jet Propulsion Laboratory, Pasadena, Calif., 1966.
2. Tyror, J. G., "The Distribution of Perihelion Points of Long-Period Comets," *Mon. Not. Roy. Astron. Soc.*, Vol. 117, p. 370, 1957.

References (contd)

3. Russell, H. N., "On the Origin of Periodic Comets," *Astron. J.*, Vol. 33, p. 49, 1920.
4. Stromgren, E., "The Short-Period Comets and the Hypothesis of Their Capture by the Major Planets," *Pub. Obser., Copenhagen*, No. 144, 1947.
5. Porter, J. G., "The Statistics of Comet Orbits," Chap. 16, in *The Moon, Meteorites, and Comets*, Vol. IV, of *The Solar System*. Edited by G. P. Kuiper and B. M. Middlehurst. University of Chicago Press, Chicago, 1963.
6. Richter, N. B., *The Nature of Comets*, Chap. 2. Methuen and Company, Ltd., London, 1963.
7. Roemer, E., "Astrometric Observations and Orbits of Comets," *Astron. J.*, Vol. 66, p. 368, 1961.
8. Roemer, E., "Cometary Nuclei: Introductory Report," in *Memoires de la Société Royale des Sciences de Liège*. Series 5, Vol. XII, p. 15, 1966.
9. Richter, N. B., *The Nature of Comets*, Chap. 3. Methuen and Company, Ltd., London, 1963.
10. Roemer, E., "The Dimensions of Cometary Nuclei, in "Memoires de la Société Royale des Sciences de Liège, Series 5, Vol. XII, p. 23, 1966.
11. Whipple, F. L., "Problems of the Cometary Nucleus," *Astron. J.*, Vol. 66, p. 375, 1961.
12. Lyttleton, R. A., *The Comets and Their Origin*. Cambridge University Press, New York, 1953.
13. Wurm, K., "The Head (or Coma) of Comets: Introductory Report," in *Memoires de la Société Royale des Sciences de Liège*, Series 5, Vol. XII, p. 119, 1966.
14. Wurm, K., "The Physics of Comets," Chap. 17, in *The Moon, Meteorites, and Comets*, Vol. IV, of *The Solar System*, Edited by G. P. Kuiper and B. M. Middlehurst. University of Chicago Press, Chicago, 1963.
15. Thackeray, A. D., Feast, M. W., and Warner B., "Daytime Spectra of Comet Ikeya-Seki Near Perihelion," *Astrophys. J.*, Vol. 143, p. 276, 1966.
16. Vanysek, V., "Dust Grains in Cometary Atmospheres," in *Memoires de la Société Royale des Sciences de Liège*, Series 5, Vol. XII, p. 255, 1966.
17. Richter, N. B., *The Nature of Comets*, Chap. 4. Methuen and Company, Ltd., London, 1963.
18. Lilie, W., "The Nature of the Grains in the Tails of Comets 1956h and 1957d," *Astrophys. J.*, Vol. 132, p. 867, 1960.
19. Levin, B. J., "On the Bredikhin's Classification of Cometary Tails and the Nature of the Type II Tails," in *Memoires de la Société Royale des Sciences de Liège*, Series 5, Vol. XII, p. 323, 1966.
20. Wurm, K., "Structure and Development of the Gas Tails of Comets," *Astron. J.*, Vol. 66, p. 362, 1961.

References (contd)

21. Biermann, L., and Lust, R., "Comets: Structure and Dynamics of Tails," Chap. 18, in *The Moon, Meteorites, and Comets*, Vol. IV, of *The Solar System*, Edited by G. P. Kuiper and B. M. Middlehurst. University of Chicago Press, Chicago, 1963.
22. Belton, M. J. S., "The Dynamics of Type II Comet Tails," in *Memoires de la Société Royale des Sciences de Liège*, Series 5, Vol. XII, p. 317, 1966.
23. Lyttleton, R. A., "Introduction" to N. B. Richeson's *The Nature of Comets*. Methuen and Company, Ltd., London, 1963.
24. Whipple, F. L., "A Comet Model: I. The Acceleration of Comet Encke," *Astrophys. J.*, Vol. III, p. 375, 1950.
25. Whipple, F. L., "On the Structure of the Cometary Nucleus," Chap. 19, in *The Moon, Meteorites, and Comets*, Vol. IV, of *The Solar System*. Edited by G. P. Kuiper and B. M. Middlehurst. University of Chicago Press, Chicago, 1963.
26. Whipple, F. L., "A Comet Model: II. Physical Relations for Comets and Meteors," *Astrophys. J.*, Vol. 113, p. 464, 1951.
27. Whipple, F. L., "A Comet Model: III. The Zodiacal Light," *Astrophys. J.*, Vol. 121, p. 750, 1955.
28. Whipple, F. L., and Stefanik, R. P., "On the Physics and Splitting of Cometary Nuclei," in *Memoires de la Société Royale des Sciences de Liège*, Series 5, Vol. XII, p. 33, 1966.
29. Delsemme, A. H., and Swings, P., "Hydrates de Gaz Dans les Noyaux Cométaires et les Grains Interstellaires," *Ann. Astrophys.*, Vol. 15, p. 1, 1952.
30. Delsemme, A. H., "Occurrence des Hydrates de Gaz Dans les Noyaux Cométaires," in *Memoires de la Société Royale des Sciences de Liège*, Series 5, Vol. XII, p. 69, 1966.
31. Becklin, E. E., and Westphal, J. A., "Infrared Observations of Comet 1965f," *Astrophys. J.*, Vol. 145, p. 435, 1966.
32. Sekanina, Z., "Hyperbolic Comets and Oort's Hypothesis of Cometary Cloud," in *Memoires de la Société Royale des Sciences de Liège*, Series 5, Vol. XII, p. 443, 1966.
33. Vsekhsviatky, S. K., "Comet Cosmogony of Lagrange and the Problem of the Solar System," in *Memoires de la Société Royale des Sciences de Liège*, Series 5, Vol. XII, p. 495, 1966.
34. Oort, J. H., "Empirical Data on the Origin of Comets," Chap. 20, in *The Moon, Meteorites, and Comets*, Vol. IV, of *The Solar System*, Edited by G. P. Kuiper and B. M. Middlehurst. University of Chicago Press, Chicago, 1963.
35. *Space Research, Direction for the Future, Part I*, Space Science Board, National Academy of Sciences, National Research Council, Washington, D.C., 1965.